U.S. DEPARTMENT OF THE INTERIOR
U.S. GEOLOGICAL SURVEY

DATA AND RESULTS FROM R.V. ALEKSANDR VINOGRADOV CRUISES 91-AV-19/1, NORTH PACIFIC HYDROCHEMISTRY TRANSECT; 91-AV-19/2, NORTH EQUATORIAL PACIFIC KARIN RIDGE FE-MN CRUST STUDIES; AND 91-AV-19/4, NORTHWEST PACIFIC AND BERING SEA SEDIMENT GEOCHEMISTRY AND PALEOCEANOGRAPHIC STUDIES

Edited by

James R. Hein[1], Alexander S. Bychkov[2], and Ann E. Gibbs[1]

Open File Report 94-230

1994

[1]U.S. Geological Survey, 345 Middlefield Rd., ms 999, Menlo Park, CA 94025-3591
[2]Pacific Oceanological Institute, Far Eastern Branch Russian Academy of Sciences, 43 Baltiyskaya St., Vladivostok, 690041, Russia

IN MEMORIAM: DR. MIKHAIL F. STASHCHUK

We gratefully acknowledge the contributions of Dr. Mikhail F. Stashchuk, whose efforts made possible the Russian-U.S.A.-Canadian cooperative research program on which this report is based. Mikhail F. Stashchuk is a renowned Russian geologist and geochemist who passed away on March 5, 1991 at the age of 60. Mikhail headed the "Processes of Mineral Formation Laboratory" at the Pacific Oceanological Institute (POI), USSR Academy of Sciences, Vladivostok. This laboratory is involved in the study of ferromanganese crusts and nodules, phosphorites, the marine carbonate system, and other studies of marine geology and geochemistry. Mikhail is probably best known for his two books: "The Oxidation-Reduction Potential in Geology", which was first published in 1968 (Moscow, Nedra), but has been reprinted, translated, and published in the USA as well; and "Thermal Dynamics and its Application to Lithology", published in 1985, Moscow, Nauka. The former innovative book was one of the first to use thermodynamics to broadly describe the authigenic formation of iron and manganese minerals and the role of microorganisms in mineral formation. Among the many projects that Mikhail was working on at the time of his death, was putting the final touches on a major three and a half month expedition involving many Russian, U.S., and Canadian groups (see introductory chapter). Due to budgetary constraints, the cruise was cut from four to three legs, but the three legs were successfully completed between April and July 1991 aboard the Soviet ship R.V. Akademik Aleksandr Vinogradov.

The cooperative program was initiated in 1988 by Mikhail F. Stashchuk and James R. Hein, U.S. Geological Survey (USGS), through an MOU between the two groups. The program was named Geochemistry of Marine Sediments (GEMS), but involves most aspects of marine geochemistry. About 70 Soviet and 50 U.S. scientists were involved in the program before it ended in 1993. After nearly two years of development and planning by Stashchuk and Hein, two Canadian groups agreed to join in the first series of cruises: C.S. Wong of the Institute of Ocean Sciences (IOS), British Columbia representing JGOFS; and Kristin J. Orians of the University of British Columbia (UBC) who was part of GEMS. This was the first full-scale oceanographic expedition to be designed, developed, and carried out jointly.

Mikhail's persistence and commitment to the program to see that nothing jeopardized its success was comforting and commendable. He wanted to prove that the Soviets could deliver and that a successful scientific program would result. The success of the first series of cruises in our program is a tribute to Mikhail's vision and commitment. Personally, we will miss his diligence, good humor, diplomacy, kindness, and friendship and will remember our many visits to his laboratory with great fondness. The world scientific community has lost an enthusiastic and brilliant researcher.

CONTENTS

INTRODUCTORY REMARKS

James R. Hein, U.S. Geological Survey, 345 Middlefield Rd., ms 999, Menlo Park, CA, 94025-3591, USA and **Alexander S. Bychkov**, Pacific Oceanological Institute, Far Eastern Branch, Russian Academy of Sciences, 43 Baltiyskaja, Vladivostok 690041, Russia

This open file report provides shipboard and laboratory generated data, and discussions of those data, for three cruises undertaken by participants of a Russian, U.S., and Canadian cooperative program. The cruises were sponsored originally by a joint Russian Academy of Sciences-U.S. Geological Survey program on the Geochemistry of Marine Sediments (GEMS) under the leadership of Mikhail F. Stashchuk and James R. Hein. Upon the death of Dr. Stashchuk in March 1991, Alexander S. Bychkov took over as the Russian leader and JGOFS objectives were added to the planned cruises. At that time, C.S. Wong and colleagues of the Institute of Ocean Sciences, Canada joined the program to participate in the JGOFS objectives. In this introductory note, we provide a brief overview of the cruise objectives, all of which were accomplished for Legs, 1, 2, and 4 (Fig. 1; Table 1). Leg 3 had to be canceled because of budgetary constraints. This open file report is divided into separately authored chapters that deal with both general results from the three legs and studies directed to specific scientific problems.

The general objectives of the cruises were to study the physiochemical processes of mineral formation on the ocean floor; determine the geological and geophysical evolution of the North Pacific lithosphere; and determine the paleoceanographic evolution of the North Pacific. Specifically, studies were directed to the clarification of various aspects of Fe-Mn crust and nodule formation, including the distribution of trace elements in the deposits. Phosphorus distribution, migration, and concentration on seamounts was also a primary objective, as was the evolution of the seamounts. In abyssal areas, geochemical characteristics across redox boundaries were determined. Generally, investigations included sampling and analyses of seawater, bottom sediment, mineral deposits, and rock outcrop. All studies are included within the framework of the GEMS and JGOFS programs. All data have been distributed to the participants as specified by the World Ocean Agreement (WOA), which was signed by George Bush and Mikhail Gorbachev on 1 June 1990; the GEMS program was one of the three approved programs within the WOA.

Leg 1

Leg 1 (91-AV-19/1) occurred from 16 April to 6 May 1991 and consisted of a transect from Vladivostok, Russia to Hilo, Hawaii. The leg was designed by and headed by Alexander Bychkov (Pacific Oceanological Institute, POI, Russia), C.S. Wong (Institute of Ocean Sciences, IOS, Canada), and K.J. Orians (University of British Columbia, UBC, Canada) and many scientists from these institutes participated in the cruise (Table 2). Twenty-one hydrochemical and CTD stations were occupied including deep (to seafloor) and shallow (≤1200 m) water stations, which alternated every 2.5° of longitude (Table 1). The objectives were to study the geochemical characteristics of the water column, including the distribution of nutrients and the distribution of trace elements that predominantly reflect eolian processes.

Leg 2

Leg 2 (91-AV-19/2) occurred from 6-31 May 1991 from Hilo to Hilo and concentrated on the study of Karin Ridge in the U.S. Johnston Island Exclusive Economic Zone, centered at 168°W longitude and 17°N latitude in the North equatorial Pacific. The program for Leg two was established by Mikhail F. Stashchuk (POI) and James R. Hein (U.S. Geological Survey, USGS) and scientists from many Russian, U.S., and Canadian groups participated in the cruise (Table 3). Objectives included the characterization of ferromanganese oxyhydroxide crusts and the origin, distribution, and evolution of associated phosphorites, volcanic, and sedimentary rocks. The oxidation state of the manganese was determined by wet chemical techniques on surface scrapes of Fe-Mn crusts from different water depths immediately after their collection. This was done to understand the control of oxidation state on the incorporation of minor metals into the crusts. Two current meter moorings were installed on Karin Ridge five months prior to the cruise and were picked up during Leg 2. The moorings were deployed to determine the influence of water masses and currents on the formation and distribution of authigenic deposits. Operations included 12 dredges, 4 gravity cores, 2 box cores, 3 hydrochemistry stations, 14 CTD-oxygen stations, 4 bottom camera-video transects, and 2 free-floating sediment trap stations (Table 1).

Leg 4

Leg 4 (91-AV-19/4) occurred from 3 July to 2 August 1991 and began in Vladivostok and ended there after occupying 50 stations throughout the northwest Pacific and Bering Sea. Major accomplishments of this leg included deployment of four sediment traps, occupation of 16 hydrological stations, and recovery of 35 sediment cores. The hydrochemical part of the leg was designed by Alexander Bychkov (POI) and C.S. Wong (IOS), the sediment geochemistry by Lev Gramm-Osipov (POI) and Joris Gieskes (Scripps Institution of Oceanography, USA), and the paleoceanography by Sergey A. Gorbarenko (POI) and Lloyd Keigwin (Woods Hole Oceanographic Institute, USA). Many scientists from these and other institutions participated in Leg 4 (Table 4).

Work accomplished on these research cruises addresses significant scientific problems in geology, geochemistry, geophysics, and oceanography. The approach was interdisciplinary and multifaceted as is required to address such diverse but inter-related topics. Through this international cooperation, we used the best techniques and emphasized the strong points of each nation, which guaranteed great success and fulfillment of the objectives.

Many people and many hours of hard work were required to make this cooperative research successful. We would especially like to thank Captain Vladimir Karpov and the crew of the R.V. Vinogradov for excellent support in carrying out our mission. Many shipboard scientists and technicians (see Tables) and shore-based laboratory technicians deserve much credit. The operations personnel for POI, USGS, IOS, and UBC worked diligently to see that the cruises went smoothly. Inna Shapotina kindly translated several chapters from Russian to English. Much of the technical work for this report was completed by Ann E. Gibbs; without her untiring efforts, completion of this report would not have been possible. We sincerely thank all of these people and the many others that helped make this program a success.

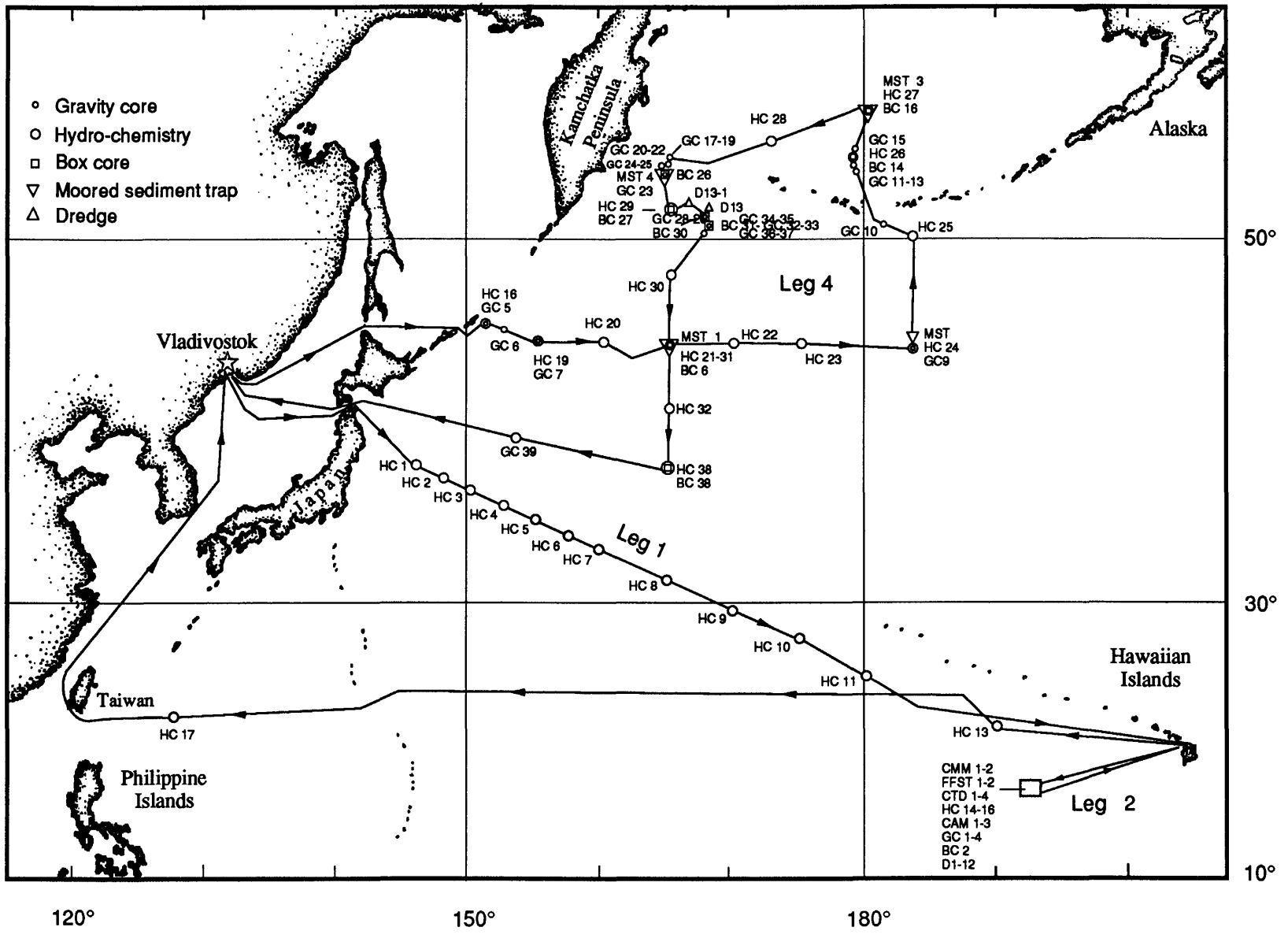

Figure 1. Trackline of R/V *Akademik Aleksandr Vinogradov* cruise 91-AV-19. Location of all operations undertaken during legs 1, 2, and 4 are shown.

Table 1. Compilation of operations completed during cruise 91-AV-19, Legs 1, 2, and 4

Operation	Date		Time		Location		Water Depth
	UTC	Ship	UTC	Ship	Latitude	Longitude	(m)
Dredge (D)							
D1	13 May	12 May	03:45	16:45	16°39.66' N	168°19.76' W	1900-1809
					16°40.23' N	168°16.96' W	
D2	14 May	13 May	05:44	19:44	16°34.06' N	168°25.66' W	No recovery
					16°36.21' N	168°19.76' W	(5100-4600)
D3	15 May	14 May	07:12	21:12	16°33.98' N	168°21.52' W	2600-2500
					16°35.54' N	168°18.75' W	
D4	17 May	16 May	00:16	14:16	16°34.03' N	168°28.71' W	3300-2900
					16°36.67' N	168°20.00' W	
D5	17 May	17 May	11:26	01:26	16°31.81' N	168°25.62' W	4300-3900
					16°34.50' N	168°20.90' W	
D6	19 May	18 May	00:30	14:30	17°05.4' N	168°26.5' W	No recovery
					17°06.6' N	168°29.0' W	(2100-1600)
D7	19 May	19 May	16:32	06:32	17°14.0' N	168°13.2' W	4850-4000
					17°14.5' N	168°16.7' W	
D8	20 May	20 May	14:20	04:20	17°14.2' N	168°13.3' W	4200-3700
					17°13.6' N	168°16.2' W	
D9	21 May	20 May	00:45	14:45	17°12.2' N	168°20.0' W	Lost bag
					17°11.6' N	168°21.1' W	(3200-2500)
D10	22 May	22 May	20:00	10:00	17°11.2' N	168°15.8' W	3400-2960
					17°10.7' N	168°18.6' W	
D11	23 May	22 May	02:30	16:30	17°12.5' N	168°18.6' W	3000-2450
					17°11.2' N	168°18.6' W	
D12	23 May	23 May	20:30	10:30	--	--	No recovery
					--	--	(2000-1600)
D13-1	--	22 July	--	17:03	51°41.9' N	166°30.0' E	No recovery
					51°41.8' N	166°31.9' E	
D13	--	24 July	--	06:15	51°31.0' N	167°37.0' E	1750-1590
					51°30.0' N	167°39.8' E	
Camera Survey (CAM)							
CAM 1	13 May	14 May	12:54	02:54	16°34.1' N	168°25.7' W	4200
			18:28	08:28	16°36.2' N	168°19.8' W	3600
CAM 2	15 May	16 May	12:34	02:34	16°41.1' N	168°19.0' W	1780
			18:36	08:36	16°40.2' N	168°12.7' W	2030
CAM 3	16 May	17 May	19:47	09:47	16°37.8' N	168°20.5' W	1800
			23:15	13:15	16°37.7' N	168°18.0' W	1750
CAM 4	21 May	21 May	06:15	20:15	17°09.6' N	168°22.0' W	1880
			10:50	00:50	17°09.7' N	168°27.2' W	1650
Box Cores (BC) and Gravity Cores (GC)							
GC 1	15 May	14 May	00:52	14:52	16°27.3' N	168°31.8' W	5130
GC 2	20 May	19 May	07:40	21:40	16°59.0' N	168°17.4' W	No recovery
GC 3	20 May	19 May	04:40	18:40	17°01.4' N	168°18.0' W	No recovery
GC 4	24 May	24 May	10:54	00:54	17°21.5' N	168°41.0' W	1670
GC 5	06 July	06 July	10:35	20:35	46°00.2' N	150°42.9' E	2110
GC 6	06 July	07 July	21:05	07:05	45°31.8' N	152°15.5' E	5510
GC 7	07 July	07 July	10:15	20:15	45°00.4' N	155°00.0' E	4930
BC 8	09 July	10 July	14:40	00:40	44°58.9' N	165°03.0' E	5860
GC 9	12 July	13 July	15:15	01:15	44°36.3' N	176°49.4' W	6110

Table 1 continued: Box Cores and Gravity Cores

Operation	------Date------		-----Time-----		----------Location----------		Water Depth
	UTC	Ship	UTC	Ship	Latitude	Longitude	(m)
GC 1	15 May	14 May	00:52	14:52	16°27.3' N	168°31.8' W	5130
BC 1	20 May	20 May	–	–	17°01.6' N	168°18.2' W	2170
GC 2	20 May	19 May	07:40	21:40	16°59.0' N	168°17.4' W	No recovery
GC 3	20 May	19 May	04:40	18:40	17°01.4' N	168°18.0' W	No recovery
GC 4	24 May	24 May	10:54	00:54	17°21.5' N	168°41.0' W	1670
BC 2	24 May	24 May	–	–	–	–	No recovery
GC 5	06 July	06 July	10:35	20:35	46°00.2' N	150°42.9' E	2110
GC 6	06 July	07 July	21:05	07:05	45°31.8' N	152°15.5' E	5510
GC 7	07 July	07 July	10:15	20:15	45°00.4' N	155°00.0' E	4930
BC 8	09 July	10 July	14:40	00:40	44°58.9' N	165°03.0' E	5860
GC 9	12 July	13 July	15:15	01:15	44°36.3' N	176°49.4' W	6110
GC 10	15 July	16 July	20:03	06:03	50°53.6' N	178°56.2' W	4000
GC 11	16 July	17 July	14:55	00:55	53°31.1' N	178°51.1' E	3060
GC 12	16 July	17 July	18:00	04:00	53°44.2' N	178°42.5' E	2600
GC 13	16 July	17 July	19:05	05:05	53°44.1' N	178°43.0' E	2630
BC 14	17 July	17 July	01:30	11:30	53°41.0' N	178°49.0' E	2920
GC 15	17 July	17 July	05:10	15:10	54°03.0' N	178°43.9' E	2330
BC 16	17 July	18 July	17:05	03:05	56°00.2' N	179°59.0' E	3815
GC 17	19 July	20 July	06:24	16:24	53°42.7' N	165°00.3' E	3970
GC 18	19 July	20 July	07:58	17:58	53°41.0' N	164°56.5' E	3820
GC 19	19 July	20 July	09:18	19:18	53°41.0' N	164°56.5' E	3800
GC 20	19 July	20 July	11:35	21:35	53°35.6' N	164°49.3' E	3430
GC 21	20 July	20 July	13:05	23:05	53°36.2' N	164°48.8' E	3500
GC 22	20 July	21 July	14:00	00:00	53°36.9' N	164°49.1' E	3550
GC 23	20 July	21 July	16:40	02:40	53°25.3' N	164°31.3' E	2860
GC 24	20 July	21 July	20:20	06:20	52°58.2' N	164°43.1' E	2970
GC 25	20 July	21 July	21:15	07:15	52°58.5' N	164°42.0' E	2970
BC 26	20 July	21 July	22:45	08:45	52°59.3' N	164°38.5' E	2970
BC 27	21 July	22 July	19:50	05:50	51°23.0' N	165°04.7' E	5120
GC 28	22 July	23 July	14:35	00:35	51°18.0' N	165°39.9' E	2340
GC 29	22 July	23 July	15:20	01:20	51°18.2' N	167°39.9' E	2340
BC 30	22 July	23 July	16:45	02:45	51°18.3' N	167°39.6' E	2340
BC 31	22 July	23 July	20:00	06:00	51°03.3' N	167°49.6' E	2700
GC 32	22 July	23 July	21:11	07:11	51°03.4' N	167°52.6' E	2860
GC 33	22 July	23 July	22:55	08:55	51°03.0' N	167°54.6' E	3000
GC 34	23 July	23 July	01:35	11:35	50°56.3' N	168°07.8' E	3750
GC 35	23 July	23 July	03:05	13:05	50°56.3' N	168°07.0' E	3670
GC 36	23 July	24 July	23:52	09:52	50°24.7' N	167°43.9' E	3300
GC 37	24 July	24 July	01:00	11:00	50°25.2' N	167°43.9' E	3300
BC 38	26 July	27 July	23:07	09:07	38°04.9' N	165°11.4' E	5370
GC 39	29 July	30 July	14:35	00:35	40°00.0' N	153°29.2' E	5620
			Temperature, Salinity, Oxygen Profiles (CTD)				
1/1	19 April	19 April	05:18	05:18	38°10.1' N	145°53.4' E	0-1000
1/2	2 April	20 April	00:13	10:13	38°10.3' N	145°50.3' E	0-1000
2	21 April	21 April	09:45	19:45	37°28.0' N	147°58.1' E	0-1000
3	22 April	22 April	03:45	14:54	36°50.9' N	149°59.3' E	0-1000
4	22 April	23 April	19:48	06:48	36°53.0' N	152°30.0' E	0-1000
5/1	23 April	23 April	08:48	19:48	35°00.5' N	155°00.1' E	0-1000
5/2	24 April	24 April	03:52	14:52	34°59.8' N	154°59.9' E	0-1000
6	24 April	25 April	15:54	02:54	24°05.1' N	157°29.5' E	0-1000
7	25 April	25 April	05:13	16:13	35°10.0' N	159°58.4' E	0-1000
8/1	26 April	26 April	10:52	21:52	31°21.4' N	164°59.9' E	0-1000

Table 1 continued: Temperature, Salinity, Oxygen Profiles

Operation	----Date----		----Time----		--------Location--------		Water Depth
	UTC	Ship	UTC	Ship	Latitude	Longitude	(m)
8/2	26 April	27 April	15:43	02:43	31°21.2' N	164°58.8' E	0-1000
9	27 April	28 April	18:02	06:02	29°30.9' N	170°01.0' E	0-1000
10	28 April	29 April	23:59	11:59	27°45.2' N	175°00.2' E	0-1000
11	30 April	01 May	20:53	08:53	25°18.6' N	179°59.3' W	0-1000
13	02 June	02 June	21:17	09:17	22°04.2' N	170°00.1' W	0-1000
14/1	13 May	13 May	15:45	05:45	16°27.3' N	168°30.6' W	0-1000
14/2	13 May	13 May	21:08	11:08	16°31.7' N	168°29.8' W	0-1000
14/3	16 May	15 May	01:57	15:57	16°31.8' N	168°29.7' W	0-1000
15/1	12 May	1 May	04:50	18:50	17°07.63' N	168°30.1' W	0-1000
15/2	18 May	17 May	07:06	21:06	17°04.88' N	168°28.3' W	0-1000
15/3	18 May	18 May	14:26	04:26	17°10.0' N	168°27.8' W	0-1000
16/1	21 May	21 May	16:17	06:17	17°14.0' N	168°07.0' W	0-1000
16/2	21 May	21 May	22:50	12:50	17°14.9' N	168°10.9' W	0-1000
16/3	2 May	21 May	05:13	19:13	17°17.6' N	168°12.1' W	0-1000
16/4	23 May	22 May	07:05	21:05	17°13.0' N	168°06.1' W	0-1000
17	14 June	14 June	10:17	19:17	22°00.0' N	127°35.0' E	0-1000
USGS							
CTDR 1	11 May	--	05:40	--	17°07.0' N	168°30.0' W	0-1888
CTDR 2	12 May	--	07:13	--	16°37.8' N	168°17.8' W	0-1615
CTDR 3	15 May	--	11:30	--	16°29.9' N	168°30.9' W	0-3507
CTDR 4	18 May	--	07:13	--	17°14.5' N	168°09.2' W	0-3514
			Hydrochemistry (HC)				
HC 1	21 April	21 April	00:30	10:30	38°14.3' N	145°50.9' E	5070
HC 3	22 April	23 April	21:45	08:45	36°50.9' N	149°59.4' E	5748
HC 5	24 April	24 April	08:00	19:00	34°57.8' N	155°02.3' E	4106
HC 7	26 April	26 April	01:40	12:40	34°10.4' N	159°59.2' E	4007
HC 8	27 April	27 April	07:20	18:20	31°21.4' N	164°59.9' E	5614
HC 9	28 April	28 April	16:25	04:25	29°30.7' N	170°00.8' E	5097
HC 10	30 April	30 April	01:05	13:05	27°46.5' N	174°59.4' E	4599
HC 11	01 May	02 May	19:15	07:15	25°18.1' N	179°59.8' E	5105
HC 13	02 June	02 June	21:17	10:17	22°04.2' N	170°00.1' W	4554
HC 14	14 May	13 May	01:05	15:05	16°33.0' N	168°27.4' W	4038
HC 15	18 May	18 May	13:20	03:20	17°09.8' N	168°27.8' W	1492
HC 16	21 May	21 May	02:05	16:05	17°14.9' N	168°11.1' W	4648
HC 17	14 June	14 June	11:25	19:25	21°59.7' N	127°36.0' E	4016
HC 18	06 July	06 July	09:30	19:30	45°00.0' N	150°44.0' W	1305
HC 19	07 July	07 July	11:30	21:30	45°00.8' N	155°00.6' W	3968
HC 20	08 July	09 July	17:15	03:15	44°59.5' N	160°00.6' E	1520
HC 21	10 July	10 July	07:45	17:45	44°55.8' N	165°04.5' E	5570
HC 22	11 July	11 July	03:35	13:35	44°58.9' N	170°02.3' E	1504
HC 23	12 July	12 July	03:32	13:32	45°01.6' N	175°04.1' E	1523
HC 24	13 July	13 July	11:17	21:17	44°35.8' N	176°49.7' W	5519
HC 25	15 July	15 July	04:10	14:10	50°26.2' N	176°34.9'	5692
HC 26	16 July	17 July	21:30	07:30	53°42.6' N	178°47.0' E	2533
HC 27	17 July	18 July	20:41	06:41	55°59.2' N	179°59.4' E	3011
HC 28	19 July	19 July	00:55	10:55	54°29.9' N	172°28.2'	3509
HC 29	21 July	21 July	13:30	23:30	51°22.7' N	165°05.0' E	4569
HC 30	24 July	25 July	15:57	01:57	48°28.6' N	165°01.0' E	1484
HC 31	25 July	25 July	11:15	21:15	45°00.6' N	164°59.7' E	1533
HC 32	26 July	26 July	07:00	17:00	41°30.6' N	165°00.1' E	1503
HC 33	27 July	27 July	04:35	14:35	38°02.7' N	165°07.3' E	4914

Free-Floating Sediment Trap (FFST)

Operation	Date		Time		Location		Water Depth
	UTC	Ship	UTC	Ship	Latitude	Longitude	
FFST 1	15 May	15 May	20:54	10:54	16°32.1' N	168°27.2' W	Deployed
	18 May	17 May	02:00	16:00	16°37.8' N	168°22.8' W	Retrieved
FFST 2	20 May	19 May	01:24	15:24	17°09.1' N	168°23.4' W	Deployed
	24 May	24 May	20:40	10:40	17°32.6' N	168°32.3' W	Retrieved

Moored Sediment Trap (MST)

MST 1	--	10 July	--	--	44°55.8' N	165°04.5' E	5330
MST 2	--	14 July	--	--	45°44.03' N	176°52.4' W	5800
MST 3	--	18 July	--	--	55°58.94' N	179°59.4' W	3820
MST 4	--	21 July	--	--	51°24.42' N	165°13.2' E	5000

Table 2. Scientific personnel of R.V. Akademik Aleksandr Vinogradov Cruise 91-AV-19/1, leg 1

Alexander S. Bychkov	Co-Chief Scientist	POI[1]
Lev M. Gramm-Osipov	Deputy Chief Scientist; leader geochemistry	POI
Anatoly N. Kalyagin	Deputy Chief Scientist; leader geology	POI
Viktor V. Abramov	Seawater sample collection	POI
Andrey G. Andreev	Total alkalinity determinations; loop-sample collection; Data processing	POI
Larisa A. Avdevnina	Determination of sulfur content in sediments	FEGI[2]
Ziniat Badredtinov	Rock collection and descriptions	FEGI
Ronald D. Bellegay	Sampling operations	IOS[3]
Alexander I. Beloglazov	X-ray observations	FEGI
Tatyana U. Butenko	Trace metals processing	IC[4]
Denis V. Chervonetsky	Manganese nodule adsorption properties	IC
Ruslan V. Chichkin	Mn oxidation state determinations	POI
Moisey F. Eyberman	X-ray observations	POI
Anna A. Gerasimova	Assisted geomorphology observations	POI
Viktoria A. Gladkaya	Total alkalinity determinations	POI
Vladimir V. Golozubov	Rock collection and descriptions	FEGI
Sergey A. Gorbarenko	Sediment collection and descriptions	POI
Vladimir V. Gusev	Phosphate mineralization studies	POI
Oleg S. Ibadullaev	Sediment trap deployment; GPS observations	POI
W. Keith Johnson	Total inorganic carbon determinations	IOS
Elena V. Kaplun	Manganese nodule adsorption properties	IC
Galina L. Kirillova	Geomorphology observations	ITG[5]
Valentina A. Kondratenko	Assisted geomorphology observations	POI
Gennady A. Krainikov	Chief of technical staff; support sampling ops.	POI
Nelly A. Krasnova	Report preparation	POI
Lyudmila N. Kurilenko	Trace metals processing	IC
Anatoly N. Levin	X-ray observations	IC
Yury A. Martynov	Rock collection and descriptions	FEGI
Hugh R.C. MacLean	Trace metals operations	UBC[6]
Brad A. McKelvey	Trace metals processing	UBC
Evgeny V. Mikhailik	Rock collection and descriptions	FEGI
Maya L. Mitnik	Meteorological observations	POI
Sergey B. Mokrov	Total calcium determinations	SPSU[7]
Anatoly V. Mozherovsky	X-ray observations	POI
Robert U. Mugo	Trace metals processing	UBC
Victor P. Nechaev	Sediment collection and descriptions	FEGI
Helen Nicolidakis	Seawater geochemistry	UBC
Rostislav A. Oktyabr'sky	Rock collection and descriptions	FEGI
Kristin J. Orians	Seawater geochemistry	UBC
Galina Yu. Pavlova	Total inorganic carbon determinations	POI
Nina N. Pankova	Interpreter	POI
Sergey P. Pletnev	Paleontological observations	POI
Wendy A. Richardson	Nutrients determinations	IOS
Irina G. Rodzik	Trace metals processing	IC
Anatoly N. Salyuk	Data and graphics processing	POI
Alexander F. Sergeev	Hydrological observations; collection of seawater	POI
Inna A. Shapotina	Interpreter	POI
Yury M. Shulga	Trace metals processing	POI
Glenn E. Smith	pCO_2 determination	IOS
Vladimir N. Soyfer	Collection and preparation for isotopic analysis	POI
Anna V. Sorochinskaya	Sediment collection and descriptions	POI
Nadezhda V. Sudakova	Dissolved oxygen determinations	POI
Alexander S. Svarichevsky	Geomorphology investigations	POI
Alexander I. Svininnikov	Rock collection and identifications	POI

Table 2 continued

Valery P. Tapinov	CTD measurements	POI
Pavel Ya. Tishchenko	pCO_2 and pH determinations; data processing	POI
Irina B. Tsoy	Paleontological observations	POI

[1]Pacific Oceanological Institute, Vladivostok, Russia
[2]Far East Geological Institute, Vladivostok, Russia
[3]Institute of Ocean Sciences, Sidney, Canada
[4]Institute of Chemistry, Vladivostok, Russia
[5]Institute of Tectonics and Geophysics, Khabarovsk, Russia
[6]University of British Columbia, Vancouver, Canada
[7]St. Petersburg State University, St. Petersburg, Russia

Table 3. Scientific personnel of R.V. Akademik Aleksandr Vinogradov Cruise 91-AV-19/2, leg 2

Alexander S. Bychkov	Co-Chief Scientist	POI[1]
James R. Hein	Co-Chief Scientist	USGS[2]
Lev M. Gramm-Osipov	Deputy Chief Scientist; leader geochemistry	POI
Anatoly N. Kalyagin	Deputy Chief Scientist; leader geology	POI
Viktor V. Abramov	Seawater sample collection	POI
Andrey G. Andreev	Total alkalinity determinations; Loop-sample collection; Data processing	POI
Larisa A. Avdevnina	Determination of sulfur content in sediments	FEGI[3]
Ziniat Badredtinov	Rock collection and descriptions	FEGI
Alexander I. Beloglazov	X-ray observations	FEGI
Tatyana U. Butenko	Trace metals processing	IC[4]
Denis V. Chervonetsky	Manganese nodule adsorption properties	IC
Hank Chezar	Photographer; camera sled operations	USGS
Ruslan V. Chichkin	Mn oxidation state determinations	POI
Moisey F. Eyberman	X-ray observations	POI
Anna A. Gerasimova	Assisted geomorphology observations	POI
Viktoria A. Gladkaya	Total alkalinity determinations	POI
Vladimir V. Golozubov	Rock collection and descriptions	FEGI
Sergey A. Gorbarenko	Sediment collection and descriptions	POI
Vladimir V. Gusev	Phosphate mineralization studies	POI
Oleg S. Ibadullaev	Sediment trap deployment; GPS observations	POI
Elena V. Kaplun	Manganese nodule adsorption properties	IC
Galina L. Kirillova	Geomorphology observations	ITG[5]
Valentina A. Kondratenko	Assisted geomorphology observations	POI
Gennady A. Krainikov	Chief of technical staff; support sampling ops.	POI
Nelly A. Krasnova	Report preparation	POI
Lyudmila N. Kurilenko	Trace metals processing	IC
Anatoly N. Levin	X-ray observations	IC
Yury A. Martynov	Rock collection and descriptions	FEGI
Hugh R.C. MacLean	Trace metals operations	UBC[6]
Evgeny V. Mikhailik	Rock collection and descriptions	FEGI
Maya L. Mitnik	Meteorological observations	POI
Sergey B. Mokrov	Total calcium determinations	SPSU[7]
Anatoly V. Mozherovsky	X-ray observations	POI
Victor P. Nechaev	Sediment collection and descriptions	FEGI
Helen Nicolidakis	Seawater geochemistry	UBC

Table 3 continued

Rostislav A. Oktyabr'sky	Rock collection and descriptions	FEGI
Kristin J. Orians	Seawater geochemistry	UBC
Galina Yu. Pavlova	Total inorganic carbon determinations	POI
Nina N. Pankova	Interpreter	POI
Sergey P. Pletnev	Paleontological observations	POI
Ransom W. Rideout	Marine Technician; sampling operations	USGS
Irina G. Rodzik	Trace metals processing	IC
Anatoly N. Salyuk	Data and graphics processing	POI
Majorie S. Schulz	CTD sampling and processing	USGS
Alexander F. Sergeev	Hydrological observations; Collection of seawater	POI
Inna A. Shapotina	Interpreter	POI
Yury M. Shulga	Trace metals processing	POI
Virginia K. Smith	Rock descriptions and processing	USGS
Vladimir N. Soyfer	Collection and preparation of samples for isotopes	POI
Anna V. Sorochinskaya	Sediment collection and descriptions	POI
Nadezhda V. Sudakova	Dissolved oxygen determinations	POI
Alexander S. Svarichevsky	Geomorphology investigations	POI
Alexander I. Svininnikov	Rock collection and identifications	POI
Valery P. Tapinov	CTD measurements	POI
Pavel Ya. Tishchenko	pCO_2 and pH determinations; Data processing	POI
Irina B. Tsoy	Paleontological observations	POI
Richard W. Viall	Electronics Technician; CTD and camera sled ops.	USGS
Juliet C. Wong	Rock descriptions and processing	USGS

[1]Pacific Oceanological Institute, Vladivostok, Russia
[2]United States Geological Survey, Menlo Park, USA
[3]Far East Geological Institute, Vladivostok, Russia
[4]Institute of Chemistry, Vladivostok, Russia
[5]Institute of Tectonics and Geophysics, Khabarovsk, Russia
[6]University of British Columbia, Vancouver, Canada
[7]St. Petersburg State University, St. Petersburg, Russia

Table 4. Scientific personnel of R.V. Akademik Aleksandr Vinogradov Cruise 91-AV-19/4, leg 4

Alexander S. Bychkov	Co-Chief Scientist	POI[1]
Lloyd D. Keigwin, Jr.	Co-Chief Scientist; paleoceanography	WHOI[2]
Lev M. Gramm-Osipov	Deputy Chief Scientist; leader geochemistry	POI
Anatoly N. Kalyagin	Deputy Chief Scientist; leader geology	POI
Viktor V. Abramov	Seawater sample collection	POI
Andrey G. Andreev	Total alkalinity determinations; loop-sample collection; data processing	POI
Larisa A. Avdevnina	Determination of sulfur content in sediments	FEGI[3]
Ziniat Badredtinov	Rock collection and descriptions	FEGI
Janet E. Barwell-Clarke	Nutrients determination	IOS[4]
Alexander I. Beloglazov	X-ray observations	FEGI
Ruslan V. Chichkin	Mn oxidation state determinations	POI
Moisey F. Eyberman	X-ray observations	POI
Valerie A. Forsland	Total inorganic carbon determination	IOS
Charles E. Franks	Coring operations	WHOI

Table 4 continued

Anna A. Gerasimova	Assisted geomorphology observations	POI
Viktoria A. Gladkaya	Total alkalinity determinations	POI
Vladimir V. Golozubov	Rock collection and descriptions	FEGI
Sergey A. Gorbarenko	Sediment collection and descriptions	POI
Oleg S. Ibadullaev	Sediment trap deployment; GPS observations	POI
Galina L. Kirillova	Geomorphology observations	ITG[5]
Valentina A. Kondratenko	Assisted geomorhphology observations	POI
Gennady A. Krainikov	Chief of technical staff; support sampling ops.	POI
Nelly A. Krasnova	Report preparation	POI
Yury A. Martynov	Hard rock collection and description	FEGI
Tatyana Matyunina	Rock collection and descriptions	POI
Hugh R.C. MacLean	Trace metals operations	UBC[6]
Evgeny V. Mikhailik	Rock collection and descriptions	FEGI
Anatoly V. Mozherovsky	X-ray observations	POI
Victor P. Nechaev	Sediment collection and descriptions	FEGI
Helen Nicolidakis	Geochemist	UBC
Rostislav A. Oktyabr'sky	Seawater geochemistry	FEGI
Kristin J. Orians	Seawater geochemistry	UBC
Galina Yu. Pavlova	Total inorganic carbon determinations	POI
Nina N. Pankova	Interpreter	POI
Alexander M. Pysarevsky	Eh measurements in bottom sediments	SPSU[7]
John B. Rapp	Gas and organic geochemistry sampling	USGS[8]
Irina A. Ryaben'kaya	Paleontological observations	POI
Anatoly N. Salyuk	Data and graphics processing	POI
Alexander F. Sergeev	Hydrological observations; collection of seawater	POI
Tatyana D. Shigaeva	Eh measurements in bottom sediments	SPSU
Yury M. Shulga	Trace metals processing	POI
Anna V. Sorochinskaya	Sediment collection and descriptions	POI
Timothy J. Soutar	Sediment trap deployment; assisted sampling ops.	IOS
Nadezhda V. Sudakova	Dissolved oxygen determinations	POI
Alexander S. Svarichevsky	Geomorphology investigations	POI
Alexander I. Svininnikov	Rock collection and identifications	POI
Pavel Ya. Tishchenko	pCO_2 and pH determinations; Data processing	POI
Frank A. Whitney	Hydrochemical analyses; chlorophyll analyses	IOS

[1]Pacific Oceanological Institute, Vladivostok, Russia
[2]Woods Hole Oceanographic Institute, Woods Hole, USA
[3]Far East Geological Institute, Vladivostok, Russia
[4]Institute of Ocean Sciences, Sidney, Canada
[5]Institute of Tectonics and Geophysics, Khabarovsk, Russia
[6]University of British Columbia, Vancouver, Canada
[7]St. Petersburg State University, St. Petersburg, Russia
[8]United States Geological Survey, Menlo Park, USA

— PAGE 17 FOLLOWS —

91-AV-19

LEG 1

Western North Pacific

— PAGE 19 FOLLOWS —

CADMIUM, ZINC, NICKEL, COPPER, LEAD, MANGANESE, AND COBALT IN THE WESTERN NORTH PACIFIC

Kristin J. Orians and Lu Yang, Departments of Oceanography and Chemistry, University of British Columbia, Vancouver, B.C., V6T 1Z4 CANADA

ABSTRACT

The distributions of dissolved cadmium, zinc, nickel, copper, lead, manganese and cobalt in the western North Pacific, along a transect from Japan to Hawaii, help to elucidate the biogeochemical processes that control those elements in the oceans and also demonstrate their use as physical tracers. Vertical profiles from the central gyre station (28°N, 175°E) agree well with previous results from nearby stations, confirming the reliability of sampling and analytical procedures used. The Kuroshio Current station (35°N, 155°E) has remarkably similar trace metal concentrations and vertical distributions to those observed in the central gyre. The station closest to Japan (38°N, 146°E) shows a surface enrichment (0 to 500 m) for all seven metals, and steeper concentration gradients in the upper waters, suggesting a coastal source for these elements and a shallowing of isopycnal surfaces in this region. A comparison of the surface concentrations in two stations west of the Kuroshio shows enhanced upwelling at the eastern station, furthest from the Japan coast. Elements that have a surface minimum (Cd, Zn, Cu, Ni), are elevated at this station, while elements that have a surface or near-surface maximum (Mn, Pb) are depleted. Just east of the Kuroshio there is evidence of a cold-core ring, bringing water from the coast out into the central gyre. This results in higher concentrations of all elements. These advective features are difficult to distinguish from salinity and temperature data alone.

The surface transect shows a higher degree of variability than found in vertical profiles. Advective processes, from both vertical upwelling and horizontal eddy transport, combined with local changes in the seasonal thermocline, the intensity of primary production and atmospheric input, all contribute to more variable surface water chemistry. One surprising aspect of the surface transect is the lack of a strong gradient from increased eolian inputs closer to the Asian dust and anthropogenic lead sources. Dust and lead fluxes are both thought to vary by nearly two orders of magnitude across this transect, yet the range observed for the trace elements is typically only a factor of three. Much of the expected input appears to be balanced by increased scavenging in the coastal region.

INTRODUCTION

The oceanic distributions of Cd, Zn, Ni, Cu, Pb, Mn, and Co have been investigated in a number of regions in the last decade since the development of sampling and analytical techniques that allow for contamination-free collection and analysis of low nanomolar levels of these elements (Bruland *et al.*, 1979; Bruland, 1983; Wong *et al.*, 1983). Cadmium, Zn, Ni, and Cu are nutrient-type elements (Boyle *et al.*, 1976, 1977; Bruland *et al.*, 1978; Bruland , 1980; Bruland and Franks, 1983; Yeats and Campbell, 1983; Danielsson *et al.*, 1985), having a surface depletion and deep water enrichment in the oceans. Cadmium distributions follow soft-tissue constituents, such as phosphate; Zn distributions follow the hard-part, silicate-type pattern; while Ni and Cu have more complex distributions, resulting from the combined effects of several processes. Nickel appears to be regenerated in both shallow and deep waters, following phosphate in the surface and silicate at depth. Copper has a nearly linear increase with depth. This has been interpreted as being the result of a combination of nutrient-type cycling, a pore water or sediment surface source and particle scavenging throughout the water column. Due to the general movement of deep waters from their formation in the North Atlantic and near Antarctica into the Indian and Pacific Oceans, all nutrient-type metals have a deep Pacific enrichment relative to the deep Atlantic.

Lead, Mn, and Co are scavenged-type elements, with short oceanic residence times and distributions that primarily reflect their external sources. Lead (Flegal and Patterson, 1983; Boyle *et al.*, 1986) has an eolian source, mainly from its use in leaded gasoline. With the decline in usage of leaded gasoline in the last decade, this flux has decreased. Combined with the rapid removal of Pb from surface waters via particle scavenging, Pb concentrations in surface waters have been steadily decreasing, resulting in a subsurface maximum in most regions. Particle scavenging also results in low concentrations in the deep waters, far from external sources. Manganese has multiple sources and a complex marine geochemistry (Bender *et al.*, 1977; Klinkhammer and

Bender, 1980; Martin and Knauer, 1980, 1984; Martin, *et al.*, 1985; Landing and Bruland, 1980, 1987; Yeats and Bewers, 1985; Sunda and Huntsman, 1988; Saager, *et al.*, 1989; Gordeyev and Atnashev, 1990). The available data give evidence of riverine sources dominating in coastal regions, small atmospheric sources observed in the central gyre surface waters, hydrothermal sources near mid ocean ridges, regeneration and transport in O_2 minimum zones and a photoreductive source in the surface waters. Manganese profiles thus typically show a surface maximum, a secondary maximum in the O_2 minimum zone, and low concentrations elsewhere. If in proximity to hydrothermal sources, another maximum may be observed at 2500 m depth. Less is known about Co. Cobalt is thought to be cycled with Mn in the O_2 minimum zone (Knauer, *et al.*, 1982; Sakamoto-Arnold and Johnson, 1987; Kremling and Hydes, 1988), though this covariation has recently been questioned (Coale *et al.*, 1990).

Few data on trace metal distributions are available from the western North Pacific, across the oligotrophic central North Pacific gyre, through the Kuroshio, and into the highly productive coastal region near Japan. Changing levels of primary production and the associated particle fluxes are expected to lead to changes in scavenging intensity (Coale and Bruland, 1985), drawing down the levels of some elements in highly productive regions. In addition, dust and lead sources are expected to increase by nearly two orders of magnitude (Duce *et al.*, 1991) from the central gyre towards the Asian coast. In the western North Pacific these two processes should have opposing effects on the distribution of trace elements that have significant eolian sources and short surface residence times. Surface levels of the nutrient-type elements are expected to vary with upwelling and other advective processes to a greater extent, as external inputs are not the dominant control on their distribution.

This paper presents data on the surface distribution of Cd, Zn, Ni, Cu, Pb, Mn, and Co across the western North Pacific, with three depth profiles at selected locations along the transect. These data help to elucidate the biogeochemical controls on the distribution of trace metals in the Pacific Ocean. In addition, the use of these trace metals as physical tracers of water mass movement in this area is demonstrated.

METHODS

Samples were collected with Go-flo® bottles suspended on Kevlar® line, filtered at sea through 0.45 μm polycarbonate membrane filters (Poretics) with N_2 over-pressure, then acidified in acid-cleaned polyethylene storage bottles with approximately 2 mL 6N HCl/liter (pH 2), following procedures similar to those developed by Bruland *et al.* (1979). Samples were then processed and analyzed in our shore-based clean laboratory via a multi-elemental technique using Chelex-100 resin with inductively coupled plasma mass spectrometry (ICP-MS) detection. Cobalt was analyzed by graphite furnace atomic absorption spectroscopy (GFAAS) instead of ICP-MS, due to problems with background interference from the seawater matrix at mass 59 on the ICP-MS at these low levels. Stored, acidified samples (1L) were spiked with ^{62}Ni, adjusted to pH 8.0 ± 0.1 with NH_4OH, then pumped at 0.6-0.8 mL/min. through 2 mL of Chelex-100 resin (in Na form – equivalent to ~1ml in acid form). Columns were rinsed with NH_4Ac and H_2O, then eluted with 8 mL 2.0N HNO_3. The isotopes used for mass spectral determination were: ^{55}Mn, ^{60}Ni, ^{65}Cu, ^{66}Zn, ^{111}Cd, and ^{208}Pb. Isotope dilution was used for Ni, using a ^{62}Ni spike, as both ^{60}Ni and ^{62}Ni are relatively free of interferences. Indium, added to the column eluent, was used as an internal standard for the ICP-MS analysis of other metals to correct for variable sensitivity and matrix effects; a standard calibration was used for Co on the GFAAS.

Metal recoveries from stored acidified seawater samples, using this Chelex-100 method, were estimated by stable spike addition. Quantitative recoveries ($100 \pm 5\%$) were found for all elements except Pb. Pb recoveries of 84±2% were consistent and easily corrected for. Seawater detection limits for 1 liter samples (after the 125-fold concentration factor) were in the range of 2-10 pmol/kg for all elements except Zn, which had a detection limit of 60 pmol/kg. Precision of triplicate analyses on samples subdivided after collection, was 3-7%. Analysis of standard reference seawater samples from the National Research Council of Canada (NRC), verified the accuracy of the method, within the 99% confidence limit. Details of the technique will be presented elsewhere.

RESULTS AND DISCUSSION

The Study Site

Seawater samples for this study were collected from the Russian research vessel *"Aleksandr Vinogradov"* in the spring of 1991. The sampling locations are shown in Fig. 1, referred to as AV-HS (Aleksandr Vinogradov Hydro Stations) 1 through 16. Samples from 25 m depth were collected at all stations for the surface transect, with depth profiles collected at AV-HS 1, 5 and 10. The coastal region (AV-HS 1 and 2) west of the Kuroshio is characterized by low temperature and low salinity waters, originating from a combination of the southward flowing Oyashio, entrained waters from the Sea of Japan and fluvial sources. The Kuroshio (AV-HS 3-5) is characterized by warmer, higher salinity surface waters, advected northwards from the equatorial region. The surface waters then continue getting warmer and saltier to the southeast, into the central gyre (AV-HS 6-16), with two exceptions. Station AV-HS 6 has colder, lower salinity surface waters compared to the two adjacent stations. As will be discussed in more detail later, we believe this to be a cold-core ring, bringing water from the coastal region across the Kuroshio and into the central gyre. At stations AV-HS 14-16, the surface waters are warmer yet lower in salinity. These stations are in the North Equatorial Current (NEC), which brings water from the coast of North America across the Pacific. In the vertical profiles, the North Pacific intermediate water (NPIW) can be seen as a salinity minimum at 250 m near the coast and at 700 m in the Kuroshio and central gyre stations. A seasonal thermocline and halocline between 25 and 50 m can be seen at AV-HS 10, leading to increased stratification of the surface layer at this station. The main thermocline is at approximately 500 m in the Kuroshio and central gyre and shallows to 250 m in the coastal station.

Trace Metal Distributions

Cadmium

Dissolved Cd vertical distributions are shown in Fig. 3a. The profile from the North Pacific central gyre, at AV-HS 10, shows the expected phosphate-type distribution, with concentrations of 0.01 nmol/kg in the surface waters, a broad maximum of 1.0 nmol/kg centered at 1500 m, and deep water concentrations of 0.80 nmol/kg. These data agree well with previous data from this region (Bruland, 1980; Bruland *et al.*, 1993). In the Kuroshio Current (AV-HS 5), ~4000 km to the northwest, both the distribution and concentrations of dissolved Cd are remarkably similar to the central gyre. In the coastal region west of the Kuroshio (AV-HS 1) the surface values increase to 0.2 nmol/kg and the mid-depth maximum is shallower, following the rising isopycnal surfaces in this region. The surface transect (Fig. 3b) shows that the surface values at stations 10 and 5 are low in comparison to nearby stations. This is difficult to interpret as vertical profiles were not sampled at most of the other stations, but could be due to increased stratification at this station within the seasonal thermocline or decreased eolian sources at this station. Dissolved Cd in the upper 25 m varies from 0.01 to 0.14 nmol/kg (average 0.08 nmol/kg) with no general trend across the central gyre (stations 6-14). Dissolved Cd surface concentrations are slightly depleted in the Kuroshio (stations 3-5) relative to the central gyre (average 0.05 nmol/kg), then increase significantly toward the coast to 0.19-0.33 nmol/kg (stations 1-2) with the outcropping of isopycnal surfaces and the potential presence of continental sources. A slight Cd enrichment is observed in the surface waters at AV-HS 14, 15, and 16, in the low salinity North Equatorial Current (NEC). The Cd enrichment observed in the NEC may be of coastal origin from North American sources, via the California Current, where somewhat elevated levels of Cd (0.04-0.25 nmol/kg) are found (Bruland, 1980; Knauer and Martin, 1980). The phosphate/cadmium relationship for all of these data shows a linear correlation that can be described by:

$$[Cd]\ (nmol/kg) = 0.322[PO_4]\ (\mu M) + 0.013 \quad (R^2 = 0.994). \qquad \text{Eq. 1}$$

Similar results were found in the central and eastern North Pacific by Bruland *et al.* (1978), Bruland (1980) and Knauer and Martin (1980), demonstrating that it is valid to use Cd as a paleotracer for nutrients throughout the Pacific Ocean.

Zinc

Dissolved Zn (Fig. 4a) has the expected silicate-type profile in the central North Pacific gyre (AV-HS 10). Low concentrations in the surface waters (0.5 nmol/kg), a deep maximum at 3000 m (9 nmol/kg), and slightly depleted levels in the deepest waters (8 nmol/kg), are all in agreement with previous results (Bruland, 1980; Bruland *et al.*, 1993). At the Kuroshio station (AV-HS 5) there is a small decrease in Zn levels in the mid-waters (500-3000 m) relative to the central gyre station, which may or may not be significant. Analysis of the AV-HS 10 samples was performed before Zn process blanks were well controlled, resulting in

less confidence in those values. There is a significant increase in the upper 2000 m at the coastal station (AV-HS 1), associated with the shallowing of isopycnal surfaces in this region and a potential coastal source for Zn. The surface transect (Fig. 4b) shows dissolved Zn concentrations at 25 m varying from 0.4 to 1.0 nmol/kg across the central gyre and Kuroshio (excluding station 6), then increasing to 1.8 nmol/kg in the coastal stations west of the Kuroshio. We believe that the anomalous value of 2.3 nmol/kg at AV-HS 6, just east of the Kuroshio, is from a cold core ring, advected into the central gyre from the coastal region. This station is anomalous for all elements analyzed. The Zn/Si relationship for all of these data shows a linear correlation, described by:

$$[Zn]\ (nmol/kg) = 0.0556\ [Si]\ (\mu M) + 0.5137\ \ (R^2 = 0.978). \qquad \text{Eq. 2}$$

Similar results were found by Bruland (1980), again showing that trace metal / nutrient correlations hold in this region of the oceans.

Nickel

Dissolved Ni concentrations (Fig. 5a) in the central gyre (AV-HS 10) show the expected nutrient-type profile (Bruland, 1980), with concentrations of 3.8 nmol/kg in the surface waters, increasing in the upper 1500 m to a broad maximum of 11.4 nmol/kg between 1500 and 3000 m. A slight decrease at the bottom may be seen by a single sample at 4600 m with a Ni concentration of 10 nmol/kg. Like Cd and Zn, there is little difference between the Kuroshio Current profile (AV-HS 5) and the central gyre, but the coastal station (AV-HS 1) does show higher surface values (6 nmol/kg) and a shallowing of the mid-depth maximum to 1000-1500 m. The surface transect (Fig. 5b) shows dissolved Ni concentrations in the upper 25 m varying from 3.3 to 7.3 nmol/kg with a general increase towards the west into the coastal region, reflecting continental sources for this element. A similar increase was observed to the east, towards the coast of North America (Bruland, 1980). Comparisons with PO_4 and Si show behavior intermediate between the shallow regeneration associated with soft-parts and the deeper regeneration associated with hard-parts – we do not, however, find better correlations with PO_4 in the upper 800 m and better correlations with silicon in the deep waters, as was observed by Bruland (1980). Plots of Ni *vs.* PO_4 and Ni *vs.* Si both show curvature throughout the water column.

Copper

Dissolved Cu concentrations (Fig. 6a) show a combination of a nutrient-type and a scavenged-type profile. In the central gyre (AV-HS 10), concentrations of 0.5 nmol/kg are found in the surface waters, steadily increasing into the deep ocean to concentrations of 3 nmol/kg, in agreement with previous data from this region (Bruland, 1980; Bruland *et al.*, 1993). Like the other nutrient-type metals there is little difference between the profiles in the Kuroshio (AV-HS 5) and the central gyre, though it is possible that the central gyre deep waters are slightly enriched in dissolved Cu. No obvious explanation for this enrichment is found - an analytical error cannot be ruled out. The coastal station (AV-HS 1) is significantly higher in dissolved Cu throughout the water column. The surface concentration in the westward station is 1 nmol/kg and deep water is almost 4 nmol/kg. The deep water residence time of dissolved Cu was previously estimated at roughly 1000 years, using a vertical advection-diffusion model (Craig, 1974; Boyle, 1977; Bruland, 1980; Bruland and Franks, 1983). Application of this model to the data from stations AV-HS 1 and 10 also gives a deep water residence time of approximately 1000 years (1030 and 1070 years, respectively). The surface transect (Fig. 6b) shows dissolved Cu concentrations in the upper 25 m varying from 0.4 to 1.0 nmol/kg with a small, possibly significant, increase towards the west across the central gyre and the Kuroshio, then increasing sharply in the coastal stations to 1.2 nmol/kg. This reflects the shallowing of isopycnal surfaces and a coastal source for dissolved Cu, as reported for the eastern boundary of the Pacific as well (Bruland, 1980). A higher dissolved Cu concentration is found in the surface at station AV-HS 6 (1.6 nmol/kg), again consistent with the eastward advection of coastal waters by a cold-core ring.

Lead

Dissolved Pb concentrations in the central gyre (AV-HS 10 - Fig. 7a and b), show the expected scavenged-type profile, with concentration of 60 pmol/kg in the surface waters, increasing to 70 pmol/kg at 250 m, then decreasing to 20 pmol/kg at depth. These data agree well with previous results from this region (Flegal and Patterson, 1983; Bruland *et al.*, 1993). The depleted values in the upper 200 m at this station show the decreased eolian source of Pb from declining use of leaded gasoline over the last couple decades. Dissolved Pb concentrations below 250 m at the Kuroshio Current station (AV-HS 5 - Fig. 7a and c) are essentially the same as at the central gyre station, but the surface depletion is not evident. This station is closer to Asian lead sources, which may account for the small increase in dissolved Pb in the near surface waters (80 pmol/kg), compared to the central gyre. In addition, these surface waters are of advective origin, from more southern

locations, which may have higher Pb concentrations. The coastal station (AV-HS 1 - Fig. 7a and d) again shows similar deep water values to those observed in the central gyre, somewhat lower concentrations in the mid-waters, from 700-100 m (40 pmol/kg *vs.* 60-80 pmol/kg), then a sharper increase to similar surface concentrations (80 pmol/kg). The surface transect (Fig. 7e) shows a general increase from the central gyre (30-40 pmol/kg) to the coast (80 pmol/kg). This doubling of the surface Pb concentration, towards the Asian continent, is less than might be expected from known source gradients (Duce *et al.*, 1991), suggesting that additional lead input may be scavenged from the surface waters in the coastal region. We suspect that higher values would be found closer to the Asian sources, but were unable to sample near Japan from the Russian research vessel. A high Pb concentration (115 pmol/kg) is found at the site of the proposed cold-core ring (AV-HS 6). The coastal source of this water could easily come from a region with higher lead concentrations than found at AV-HS 1.

Manganese

Dissolved Mn concentrations (Fig. 8a) in the central gyre (AV-HS 10) show the expected scavenged-type profile, with concentrations of 1 nmol/kg in the surface waters and lower values in the deep waters (0.2 nmol/kg). Regeneration and transport in the O2 minimum zone is also seen as a maximum at 1000 m, with a Mn concentration of 0.6 nmol/kg. These data agree well with previous data from this region (Landing and Bruland, 1980, 1987; Bruland *et al.*, 1993). In the Kuroshio Current station (AV-HS 5), similar values are found in the surface and deep waters, but the mid-depth maximum is strengthened (1.0 nmol/kg). The coastal station (AV-HS 1) has even higher Mn levels in the shallowing O_2 minimum, with a broader maximum of 1.3-1.6 nmol/kg at 250-800 m. The increase in dissolved Mn concentrations in the O_2 minimum zone closer to the continental slope support the contention that this maximum is primarily advective in origin, rather than from *in situ* reduction of particulate manganese oxides in the open ocean. The oxygen concentration at the minimum is actually higher in the coastal region than in the central gyre (50 µM at AV-HS 1 vs. 40 µM at AV-HS 10), and thus cannot explain the coastal Mn enrichment. Without data on the amount of particulate Mn, which is likely to be higher near the continent, we cannot make an accurate estimate the rate of *in situ* dissolved Mn production at the two locations. The most likely explanation for the coastal Mn enrichment, however, appears to be horizontal advection from the location of contact of the O_2 minimum with the continental slope. The surface values are also elevated in the coastal region, reaching nearly 2 nmol/kg. The surface transect (Fig. 8b) shows slightly increasing Mn values across the central gyre from east (0.9 nmol/kg) to west (1.4 nmol/kg), somewhat lower levels in the Kuroshio Current (~1 nmol/kg), and a significant increase in the coastal region (1.9 nmol/kg). This factor of two increase in Mn surface values from the central gyre to the coastal region is consistent with a fluvial source for Mn, as observed in other regions (Landing and Bruland, 1987; Saager *et al.*, 1989; Gordeyev and Atnashev, 1990).

Cobalt

Dissolved Co was not measured in the central gyre (AV-HS 10) since the column eluent was no longer available once it was determined that this element needed to be analyzed by GFAAS rather than ICP-MS. The Kuroshio (AV-HS 5) and coastal (AV-HS 1) stations however (Fig. 9a), do show a manganese-type profile, with concentration of 25-30 pmol/kg in the surface waters, a maximum of 40 pmol/kg between 500 and 1200 m, and deep water concentrations of 10-20 pmol/kg. These data agree reasonably well with previous data from the North Pacific (Knauer *et al.*, 1982), though there is significant scatter in our data. In addition to the similarities, there are some distinct differences between Co and Mn. In the Kuroshio, the Co mid-depth maximum is broader and shallower than that seen for Mn, whereas in the coastal station they are more tightly coupled. It is not clear why this is so, but the differing behavior of Co and Mn is in agreement with the results of Coale *et al.* (1990). The surface enrichment, relative to the upper thermocline, is smaller for Co at both locations. This may reflect a reduced reactivity of Co in photoredox cycles and/or a lower input of Co from eolian and fluvial sources. The surface transect (Fig. 9b) is missing several points, again due to analytical difficulties, but shows no apparent trend. The lack of a significant coastal enrichment supports the hypothesis that dissolved Co may have lower input of from eolian and/or fluvial sources than dissolved Mn.

The Central Gyre

The central North Pacific gyre is an oligotrophic region with low surface trace element concentrations, due to distance from continental sources and slow rates of vertical exchange. The vertical exchange can be further reduced in the upper water column by a seasonal thermocline formed in the summer-time. Evidence of a seasonal thermocline at the central gyre station (AV-HS 10) was found above 50 m in late April, 1991, with

elevated temperature and salinity (Fig. 2a, b). Increased stratification may explain the lower concentrations observed for Cd, Ni, and Cu at this station in comparison to nearby stations in the central gyre, since vertical exchange provides a significant source of nutrients and nutrient-type elements to the surface waters of the open ocean. It is also possible, however, that the seasonal thermocline is more widespread. Data are not available beneath 25 m from the other central gyre stations to verify this. Atmospheric sources are also significant for these elements in the open ocean (Duce *et al.*, 1991). Sporadic and patchy eolian deposition may be an important factor leading to the observed surface water variability. The lower concentration of dissolved Mn at this station is not easily explained by the presence of a seasonal thermocline, as the source of Mn to the surface is believed to be a combination of fluvial, eolian, and photoreductive origins, rather than vertical exchange. Variable eolian input is a more likely explanation for the Mn variations. The variations in surface water Pb levels do not follow the other elements, however, suggesting a more complex situation. Although ratios of Cd, Cu, and Ni to Pb in marine aerosols do vary somewhat, the range is not large (Duce *et al.*, 1991), and it is expected that Pb would also be effected by changes in eolian input. Enhanced effects of scavenging over time in the seasonally stratified surface layer may also contribute to the decreased trace metal levels observed.

The Coastal Region and Evidence of a Cold-Core Ring in the Central Gyre

In the coastal region, west of the Kuroshio Current, the surface waters are from a number of sources. Sub-Arctic waters are advected down with the Oyashio Current, some water is entrained from the Sea of Japan outflow, and fluvial sources are present. In addition, mixing along outcropping isopycnal surfaces leads to effects similar to upwelling. The station closest to Japan (38°N, 146°E) shows a surface enrichment (0 to 500 m) for all seven metals, suggesting a coastal source for these elements and a shallowing of isopycnal surfaces in this region. A comparison of the surface concentrations in the two stations west of the Kuroshio shows indications of upwelling at the eastern station (AV-HS 2), farthest from the Japan coast. Elements that have a surface minimum (Cd, Zn, Cu, Ni), are elevated at this station, while elements that have a surface or near-surface maximum (Mn, Pb) are depleted. Immediately to the east of the Kuroshio, at AV-HS 6 (34°N, 157°E), is an indication of a cold-core ring, bringing water from the coastal side of the Kuroshio Current into the central gyre. This results in higher concentrations of all elements. These advective features are both seen in a reduced salinity and temperature at stations AV-HS 2 and AV-HS 6, but the difference between upwelling and eddy transport is not obvious from temperature or salinity alone. The use of multiple trace metals, with different depth dependent distributions, helps to elucidate the origin of the low temperature and salinity waters at these two stations.

Effect of Atmospheric Source Gradient on Surface Ocean Metal Concentrations

The surface transect shows a higher degree of variability than observed in the vertical profiles. This reflects changes caused by advective transport, the presence and intensity of a seasonal thermocline, the amount of primary production and associated particle fluxes, and the rate of atmospheric input. Atmospheric fluxes vary with proximity to the continental and with local weather conditions. Wet deposition requires a rain event and dry deposition varies with wind strength and direction. Dust and Pb fluxes are both thought to vary by nearly two orders of magnitude across this transect, increasing with proximity to the Asian continent (Duce *et al.*, 1991). One of the most surprising features of the surface transect reported here is the lack of a strong gradient in surface water trace metal concentrations from this increased eolian input. The range observed for Pb, the element with the greatest expected eolian source, is only two-fold. Copper and Mn also only vary by a factor of 2-3. The largest gradient is seen for dissolved Cd, with a 4-30 fold enrichment in the coastal versus open ocean. This increase is attributed more to rising isopycnals and potential fluvial sources, rather than atmospheric source gradients. Much of the expected eolian input close to the Asian sources appears to be balanced by increased scavenging in the coastal region. It is also likely that sampling closer to the coast of Japan (not permitted from the Russian ship) would have shown the effects of these increased inputs to a greater extent.

CONCLUSIONS

Vertical profiles of Cd, Zn, Ni, Cu, Pb, Mn, and Co from the North Pacific central gyre (28°N, 175°E) agree well with previous results from nearby stations, demonstrating contamination-free sampling and reliable analytical procedures. Concentrations and distributions for these elements are remarkably similar in the Kuroshio and the central gyre. Cadmium, Zn, Ni, Cu, Pb, Mn, and Co all show an enrichment in the upper 500 m in the coastal region, west of the Kuroshio, from outcropping isopycnals and continental sources. The

nutrient-type trace elements, Cd, Zn, and Ni, all show similar relationships to Si and PO_4 throughout the western and eastern North Pacific, demonstrating the validity of using these elements as paleotracers for nutrients in the western regions of the Pacific Ocean as well. In addition to a surface depletion and deep water enrichment, dissolved Cu is scavenged from the deep waters of the western North Pacific with a residence time of approximately 1000 years, consistent with previous results from other regions. The dissolved Mn maximum in the O_2 minimum zone is intensified closer Asia, in agreement with an advective source from the location of contact of the O_2 minimum with the continental slope, rather than from *in situ* reduction of particulate manganese oxides in the open ocean.

Surface distributions across the western North Pacific show the utility of trace elements as physical tracers. Local upwelling can be seen by enrichments of elements with a surface minimum (Cd, Zn, Cu, Ni) and depletion of elements with a surface or near-surface maximum (Mn, Pb). Eddy transport, from the coastal region into the central gyre, on the other hand, results in higher concentrations of all elements. These advective features both lead to reduced salinity and temperature, and are difficult to distinguish on this basis. The use of multiple trace metals, with different depth dependent distributions, helps to elucidate the origin of the low temperature and salinity waters in these two instances. The high degree of surface variability reflects advective transport, as well as changes in the seasonal thermocline, the amount of primary production, and the magnitude of atmospheric input. The surface transect presented here shows a lack of a strong gradient in trace metal concentrations that might be expected from the increased eolian inputs closer to Asian sources. Much of the expected input appears to be balanced by increased scavenging in the coastal region.

ACKNOWLEDGMENTS

We thank the scientists from the Pacific Oceanological Institute in Vladivostok, Russia, for collaboration on this research expedition. Invaluable assistance with sample collection by the crew of the research vessel "*Aleksandr Vinogradov*" and from H. Maclean, B. McKelvey, and H. Nicolidakis are gratefully acknowledged. The temperature, salinity and nutrient data were provided by the Institute of Ocean Sciences, Sidney, B.C.. We also thank Mikhail Stashchuk, Alexander Bychkov, and James R. Hein for development of the Vinogradov cruises. This work was funded by the Natural Science and Engineering Research Council of Canada.

REFERENCES

Bender, M. L., Klinkhammer, G. P., and Spencer, D. W., 1977, Manganese in seawater and the marine manganese balance: Deep-Sea Research, v. 24, p. 799-812.

Boyle, E. A., Sclater, F. F., and Edmond, J. M., 1976, On the marine geochemistry of cadmium: Nature, v. 263, p. 42-44.

Boyle, E. A., Sclater, F. F., and Edmond, J. M., 1977, The distribution of dissolved copper in the Pacific: Earth and Planetary Science Letters, v. 37, p. 38-54.

Boyle, E. A., Chapnick, S. D., and Shen, G. T., 1986, Temporal variability of lead in the western North Atlantic: Journal of Geophysical Research, v. 91, p. 8573-8593.

Bruland, K. W., Knauer, G. A., and Martin, J. H., 1978, Cadmium in northeast Pacific waters: Limnology and Oceanography, v. 23, p. 618-625.

Bruland, K. W., Franks, R. P., Knauer, G. A., and Martin, J. H., 1979, Sampling and analytical methods for the determination of copper, cadmium, zinc, and nickel at the nanogram per liter level in seawater: Anal. Chim. Acta, v. 105, p. 233-245.

Bruland, K. W., 1980, Oceanographic distributions of cadmium, zinc, nickel, and copper in the North Pacific: Earth and Planetary Science Letters, v. 47, p. 176-198.

Bruland, K. W., 1983, Trace Elements in Seawater: *in* Riley, J. P. and Chester, R. (eds.) Chemical Oceanography. Academic Press, London, v. 8, p. 57-220.

Bruland, K. W., and Franks, R. P., 1983, Mn, Ni, Cu, Zn, and Cd in the western North Atlantic: *in* C.S. Wong, *et al.* (eds.), Trace Metals in Sea Water. Plenum Press, New York, p. 395-415.

Bruland, K. W., Orians, K. J., and Cowen, J. P., 1993, Reactive trace metals in the stratified central North Pacific: In preparation for Geochimica et Cosmochimica Acta.

Coale, K. H. and Bruland, K. W., 1985, ^{234}Th:^{238}U disequilibria within the California Current: Limnology and Oceanography v. 30, p. 22-33.

Coale, K. H., Johnson, K. S., Chapin, T., and Stout, P. M., 1990, The contrasting behaviour of manganese and cobalt in seawater from the southern California Borderlands and the Equatorial Pacific: EOS Abstracts, v. 71(43), p. 1413.

Craig, H., 1974, A scavenging model for trace elements in the deep sea: Earth and Planetary Science Letters, v. 23, p. 149-159.

Danielsson, L. G., Magnusson, B., and Westerlund, S., 1985, Cadmium, copper, iron, nickel, and zinc in the north east Atlantic Ocean: Marine Chemistry, v. 17, p. 23-41.

Duce, R. A. *et al.*, 1991, The atmospheric input of trace species to the world ocean: Global Biogeochemical Cycles, v. 5, p. 193-259.

Flegal, A. R. and Patterson, C. C., 1983, Vertical concentration profiles of lead in the central Pacific at 15°N and 20°S: Earth and Planetary Science Letters, v. 64, p. 19-32.

Gordeyev, V. V. and Atnashev, V. B., 1990, Dissolved manganese in the northeastern Atlantic Ocean: Oceanology, v. 30, p. 58-63.

Jickells, T. D. and Burton, J. D., 1988, Cobalt, copper, manganese, and nickel in the Sargasso Sea: Marine Chemistry, v. 23, p. 131-144.

Klinkhammer, G. P. and Bender, M. L., 1980, The distribution of manganese in the Pacific Ocean: Earth and Planetary Science Letters, v. 46, p. 361-384.

Knauer, G. A. and Martin, J. H., 1980, Phosphorus-cadmium cycling in northeast Pacific waters: Journal of Marine Research, v. 39, p. 65-76.

Knauer, G. A. and Martin, J. H., and Gordon, R. M., 1982, Cobalt in the north-east Pacific Ocean: Nature, v. 297, p. 49-51.

Kremling, K. and Hydes, D., 1988, Summer distribution of dissolved Al, Cd, Co, Cu, Mn, and Ni in surface waters around the British Isles: Continental Shelf Research, v. 8, p. 89-106.

Landing, W. M. and Bruland, K. W., 1980, Manganese in the North Pacific: Earth and Planetary Science Letters, v. 49, p. 45-56.

Landing, W. M. and Bruland, K. W., 1987, The contrasting biogeochemistry of iron and manganese in the Pacific Ocean: Geochimica et Cosmochimica Acta, v. 51, p. 29-43.

Martin, J. H. and Knauer, G. A., 1980, Manganese cycling in northeast Pacific waters: Earth and Planetary Science Letters, v. 51, p. 266-274.

Martin, J. H. and Knauer, G. A., 1984, Vertex: manganese transport through oxygen minima: Earth and Planetary Science Letters, v. 67, p. 35-47.

Martin, J. H., Knauer, G. A., and Broenkow, W. W., 1985, Vertex: the lateral transport of manganese in the northeast Pacific: Deep-Sea Research, v. 32, p. 1405-1427.

Saager, P. M., De Barr, H. J. W., and Burkill, P. H., 1989, Manganese and iron in Indian Ocean waters: Geochimica et Cosmochimica Acta, v. 53, p. 2259-2267.

Sakamoto-Arnold, C. M. and Johnson, K. S., 1987, Determination of picomolar levels of cobalt in seawater by flow injection analysis with chemiluminescence detection: Analalytical Chemistry, v. 59, p. 1789-1794.

Sunda, W. G. and Huntsman, S. A., 1988, Effect of sunlight on redox cycles of manganese in the southwestern Sargasso Sea: Deep-Sea Research, v. 35, p. 1297-1317.

Wong, C.S., Boyle, E.A., Bruland, K.W., Burton, J.D., and Goldberg, E.D., (eds.), 1983, Trace Metals in Sea Water. Plenum Press, New York.

Yeats, P. A. and Bewers, J. M., 1985, Manganese in the western north Atlantic Ocean: Marine Chemistry, v. 17, p. 255-263.

Yeats, P. A. and Campbell, J., 1983, Nickel, copper, cadmium, and zinc in the northwest Atlantic Ocean: Marine Chemistry, v. 12, p. 43-58.

Table 1. Total dissolved Cd, Zn, Ni, Cu, Pb, Mn, and Co in the Northwest Pacific

Station	Trace Metal Concentrations							
	Depth (m)	Cd (nmol/kg)	Zn (nmol/kg)	Ni (nmol/kg)	Cu (nmol/kg)	Pb (pmol/kg)	Mn (nmol/kg)	Co (pmol/kg)
AV-HS 1 (38°14' N, 145°51' E)	25	0.186	1.48	5.60	1.08	76	1.95	26
	50	0.219	1.97	5.12	1.17	95	1.93	29
	75	0.280	1.58	6.37	1.15	65	1.39	34
	100	0.299	1.52	6.13	1.25	66	1.10	27
	250	0.440	2.99	6.86	1.29	53	1.63	47
	499	0.844	7.02	9.35	1.48	40	1.32	30
	770	0.970	8.86	10.68	1.56	40	1.25	26
	1036	0.966	9.24	11.53	1.48	39	0.72	16
	1489	0.984	9.83	11.76	2.37	47	0.63	11
	2326	0.861	9.14	11.09	2.52	23	0.37	12
	2759	0.837	8.77	10.88	2.87	23	0.34	9
	4689	0.823	8.14	10.87	3.86	20	0.34	6
AV-HS 2 (37°28' N, 147°58' E)	25	0.333	1.84	7.07	1.20	72	1.55	N.A.
AV-HS 3 (36°51' N, 149°59' E)	25	0.058	0.56	5.36	0.77	79	1.17	N.A.
AV-HS 4 (35°53' N, 152°30' E)	25	0.063	1.06	5.18	0.84	87	1.27	N.A.
AV-HS 5 (34°58' N, 155°02' E)	25	0.024	0.37	4.53	0.56	78	0.96	22
	50	0.060	0.37	4.62	0.74	61	1.09	23
	75	0.027	0.45	4.40	0.53	83	0.97	16
	100	0.028	0.34	4.67	0.65	76	0.96	16
	262	0.047	0.66	4.71	0.59	77	0.87	19
	410	0.208	1.10	6.68	0.85	59	0.57	33
	692	0.637	3.91	8.28	1.08	47	0.55	38
	1013	0.865	6.44	11.02	1.48	39	1.01	40
	1502	0.960	7.80	11.62	1.43	39	0.60	24
	2526	0.896	8.08	11.94	1.67	28	0.35	24
	3051	0.918	8.36	11.78	2.09	20	0.33	18
AV-HS 6 (34°05' N, 157°30' E)	25	0.130	2.28	7.31	1.61	115	1.95	N.A.
AV-HS 7 (33°10' N, 159°58' E)	25	0.094	0.70	5.43	0.87	77	1.37	N.A.
AV-HS 8 (31°21' N, 165°00' E)	25	0.064	0.89	5.07	0.84	68	1.35	N.A.
AV-HS 9 (29°31' N, 170°01' E)	25	0.072	0.74	5.23	0.92	62	1.38	N.A.
AV-HS 10 (27°47' N, 174°59' E)	25	0.010	0.48	3.73	0.55	62	1.03	N.A.
	50	0.018	0.44	3.80	0.55	63	0.97	N.A.
	75	0.014	0.50	3.61	0.52	63	0.96	N.A.
	100	0.021	0.56	3.68	0.57	67	0.95	N.A.
	238	0.076	0.82	3.97	0.59	71	0.38	N.A.
	388	0.216	1.16	4.78	0.75	59	0.25	N.A.
	511	0.397	5.43	5.91	1.01	59	0.27	N.A.
	1009	0.969	7.99	10.30	1.60	43	0.60	N.A.
	1492	1.002	8.13	11.28	1.72	24	0.35	N.A.
	2615	0.928	9.15	11.28	2.55	31	0.24	N.A.
	3116	0.879	8.64	11.51	2.53	12	0.32	N.A.
	4599	0.788	8.12	10.31	3.12	20	0.19	N.A.
AV-HS 11 (25°18' N, 178°00' E)	25	0.065	0.56	4.81	0.89	42	1.41	N.A.
AV-HS 14 (16°28' N, 168°30' W)	25	0.086	0.38	3.30	0.42	31	0.97	25
AV-HS 15 (17°04' N, 168°28' W)	25	0.139	0.56	3.82	0.52	48	0.84	39
AV-HS 16 (17°14' N, 168°07' W)	25	0.102	0.58	3.29	0.52	46	1.04	26

N.A. = Not Analyzed

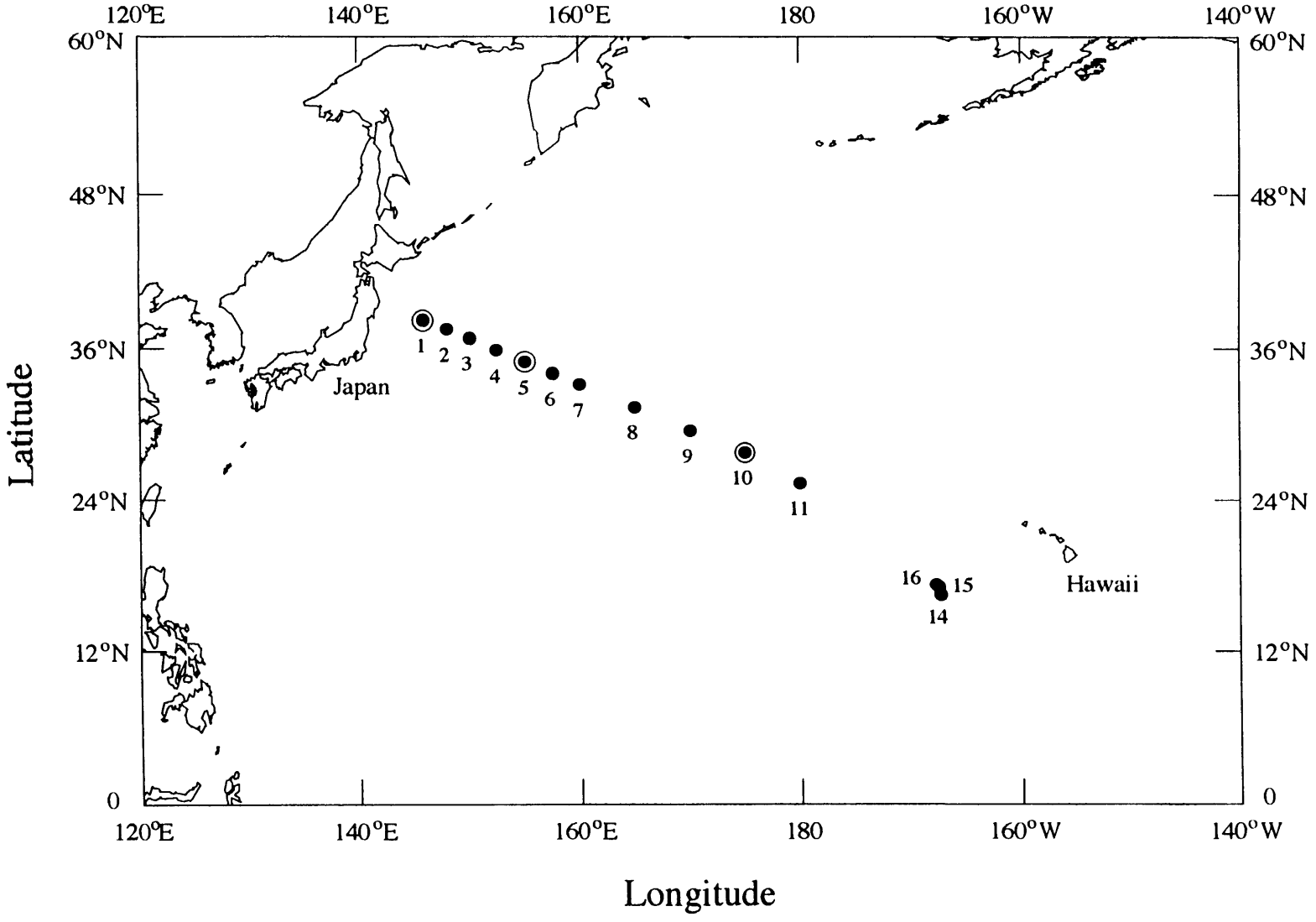

Figure 1. Map of the study area, sampled from the Russian research vessel *Aleksandr Vinogradov* in the spring of 1991. Filled circles show station locations, referred to as AV-HS (Aleksandr Vinogradov Hydro Stations) 1 through 16. Samples from 25 m depth were collected at all stations for the surface transect, with depth profiles collected at AV-HS 1, 5, and 10 (shown as double circles). See Table 1 for coordinates of stations.

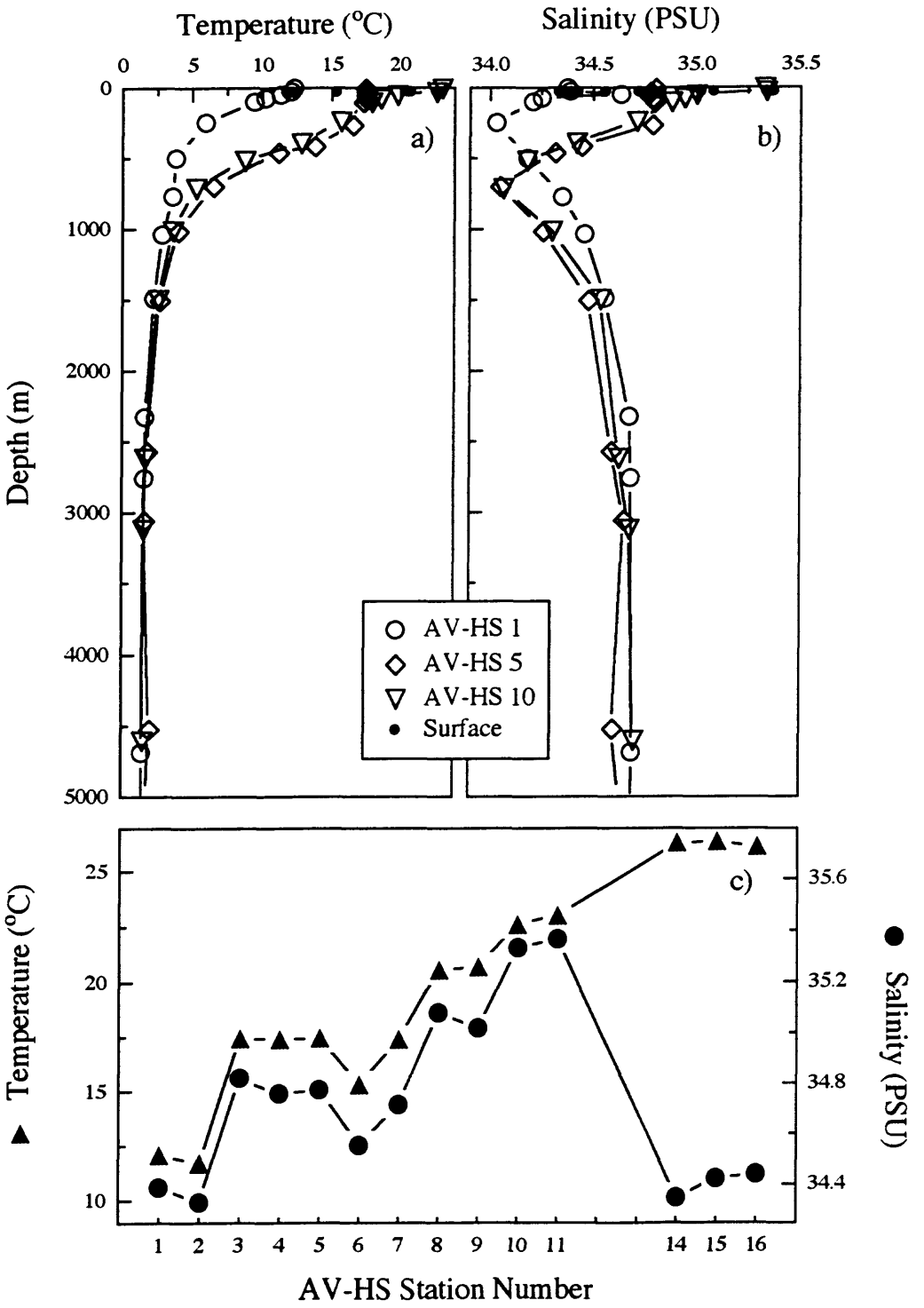

Figure 2. Distribution of a) Salinity (in psu, practical salinity units) and b) Temperature *versus* depth at stations AV-HS 1 (open circles), AV-HS 5 (open diamonds), and AV-HS 10 (open triangles). Surface (25 m) values at stations AV-HS 1 through 16 are also shown (small filled circles). c) Surface (25 m) salinity (filled circles) and temperature (filled triangles) plotted *versus* station number. See Fig. 1 and Table 1 for station locations.

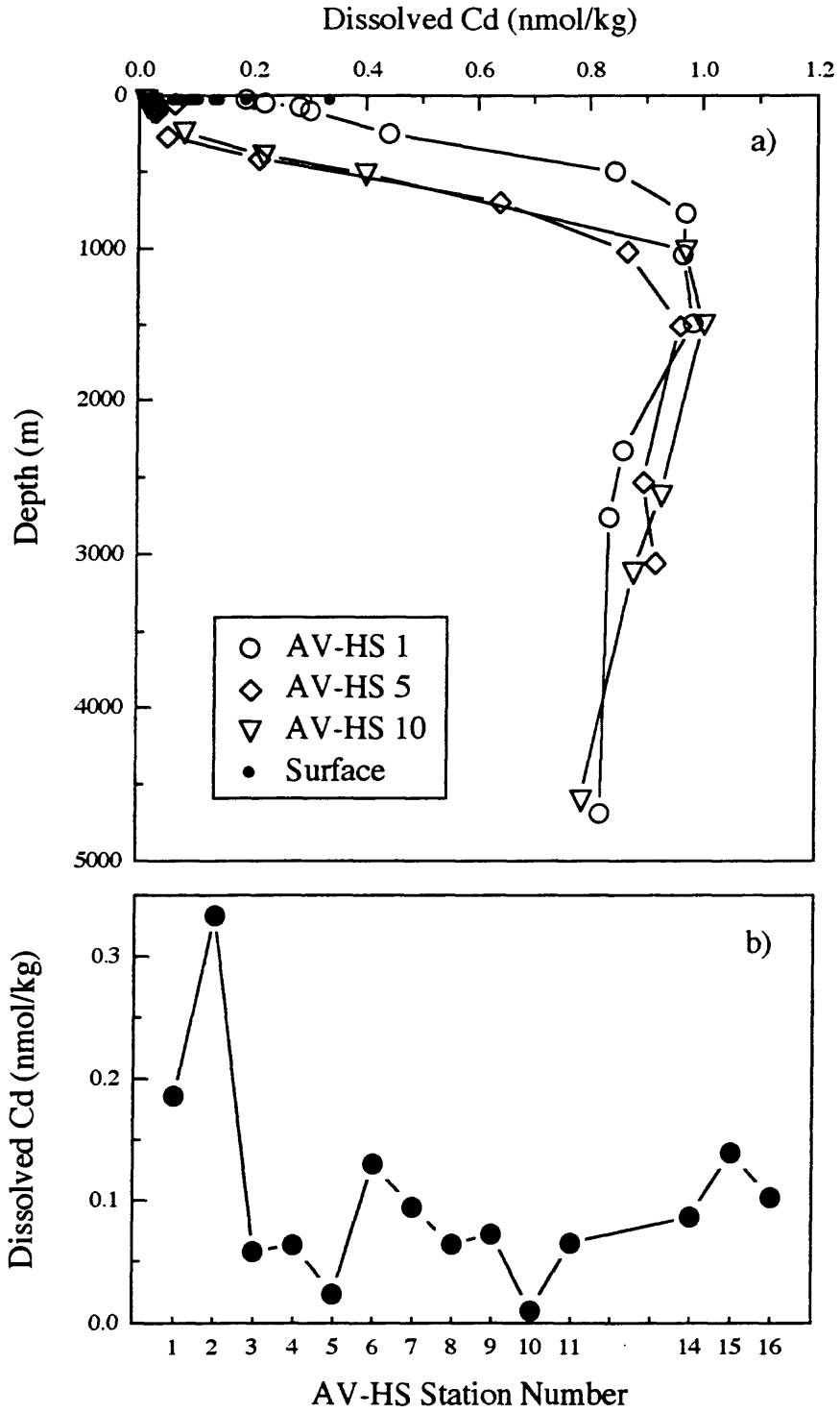

Figure 3. a) Distribution of dissolved cadmium *versus* depth at stations AV-HS 1 (open circles), AV-HS 5 (open diamonds), and AV-HS 10 (open triangles). The surface (25 m) values at stations AV-HS 1 through 16 are also shown (small filled circles). b) Dissolved cadmium at 25 m plotted *versus* station number. See Fig. 1 and Table 1 for station locations.

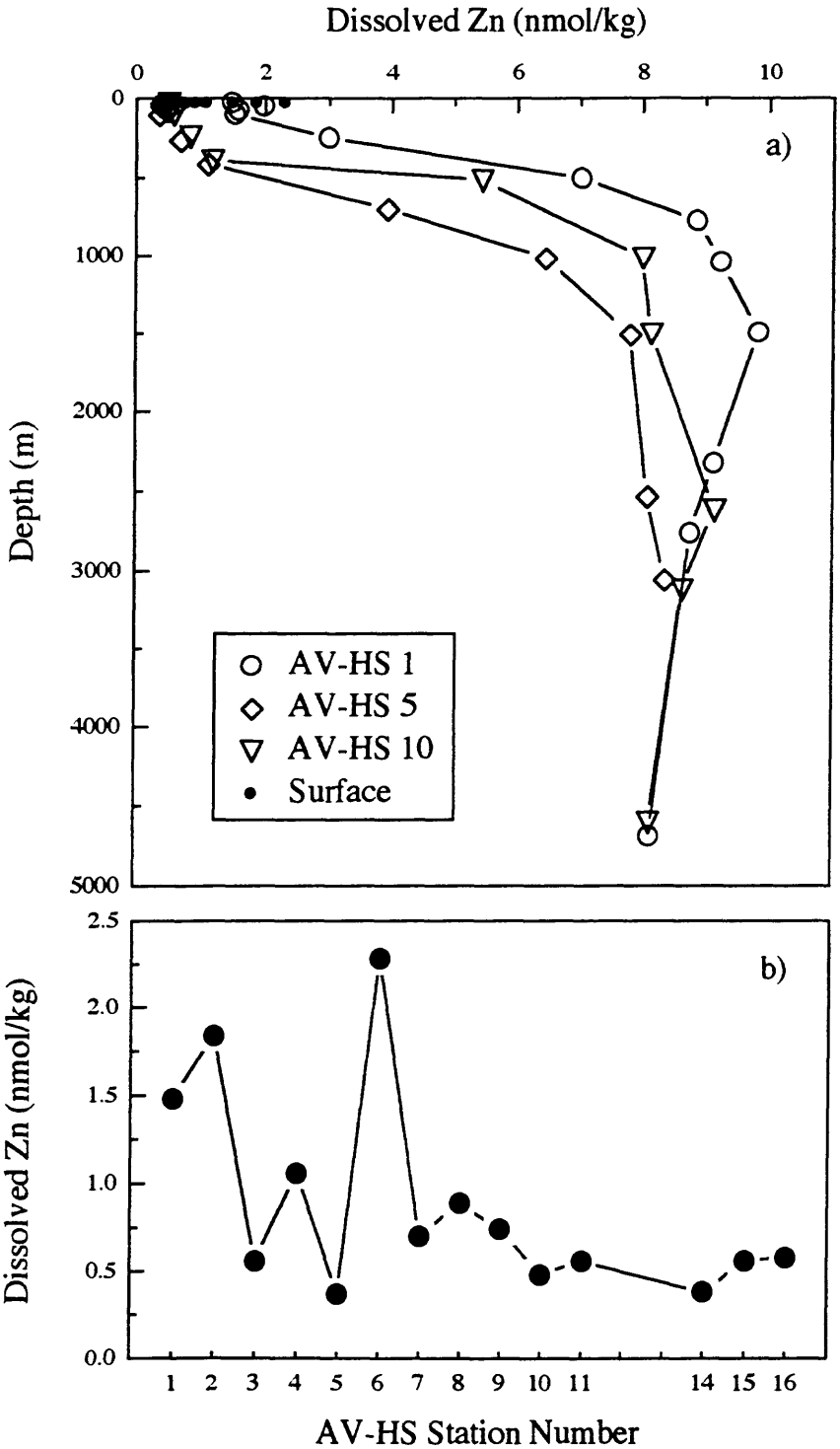

Figure 4. a) Distribution of dissolved zinc *versus* depth at stations AV-HS 1 (open circles), AV-HS 5 (open diamonds), and AV-HS 10 (open triangles). Surface (25 m) values at stations AV-HS 1 through 16 are also shown (small filled circles). b) Dissolved zinc at 25 m plotted *versus* station number. See Fig. 1 and Table 1 for station locations.

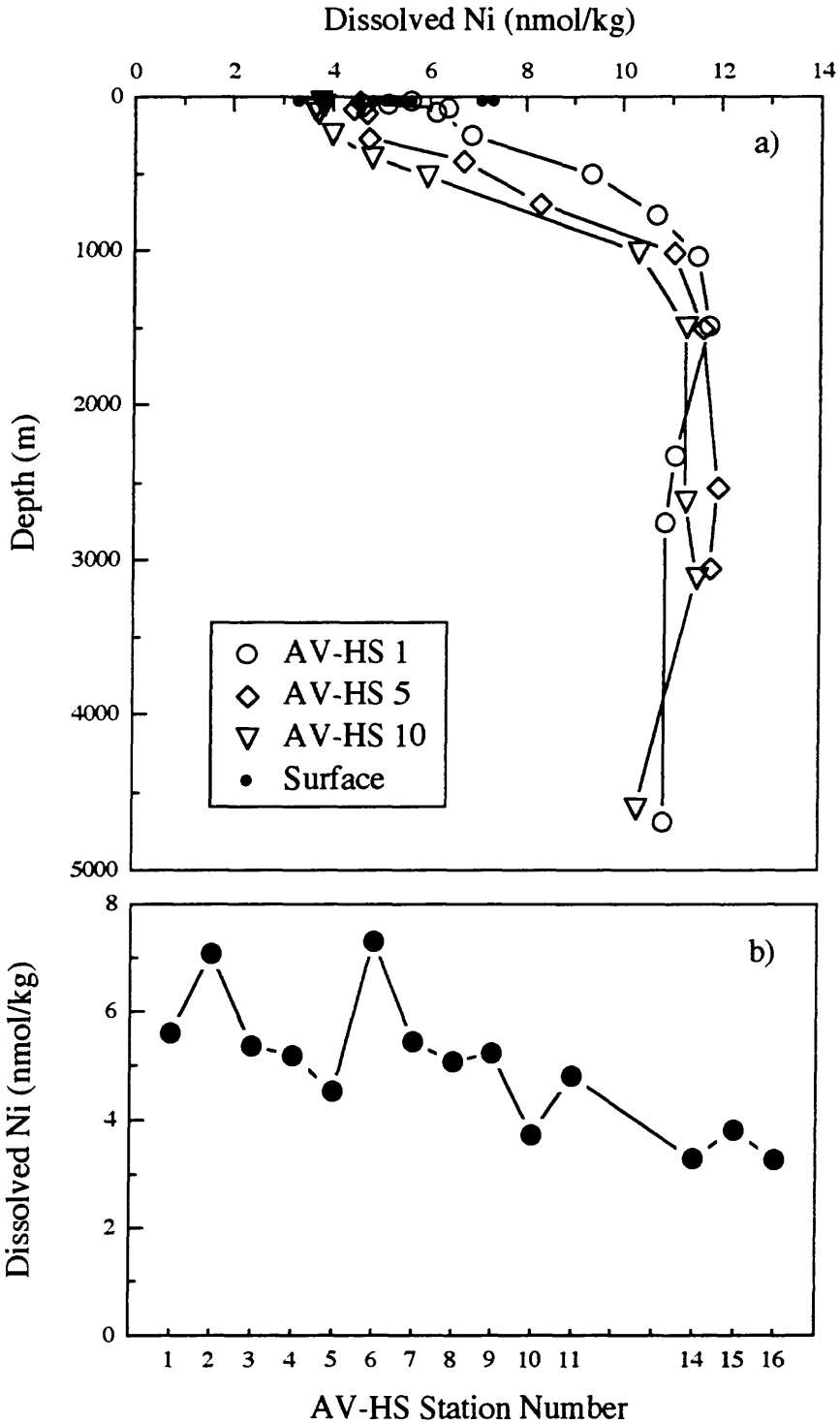

Figure 5. a) Distribution of dissolved nickel *versus* depth at stations AV-HS 1 (open circles), AV-HS 5 (open diamonds), and AV-HS 10 (open triangles). Surface (25 m) values at stations AV-HS 1 through 16 are also shown (small filled circles). b) Dissolved nickel at 25 m plotted *versus* station number. See Fig. 1 and Table 1 for station locations.

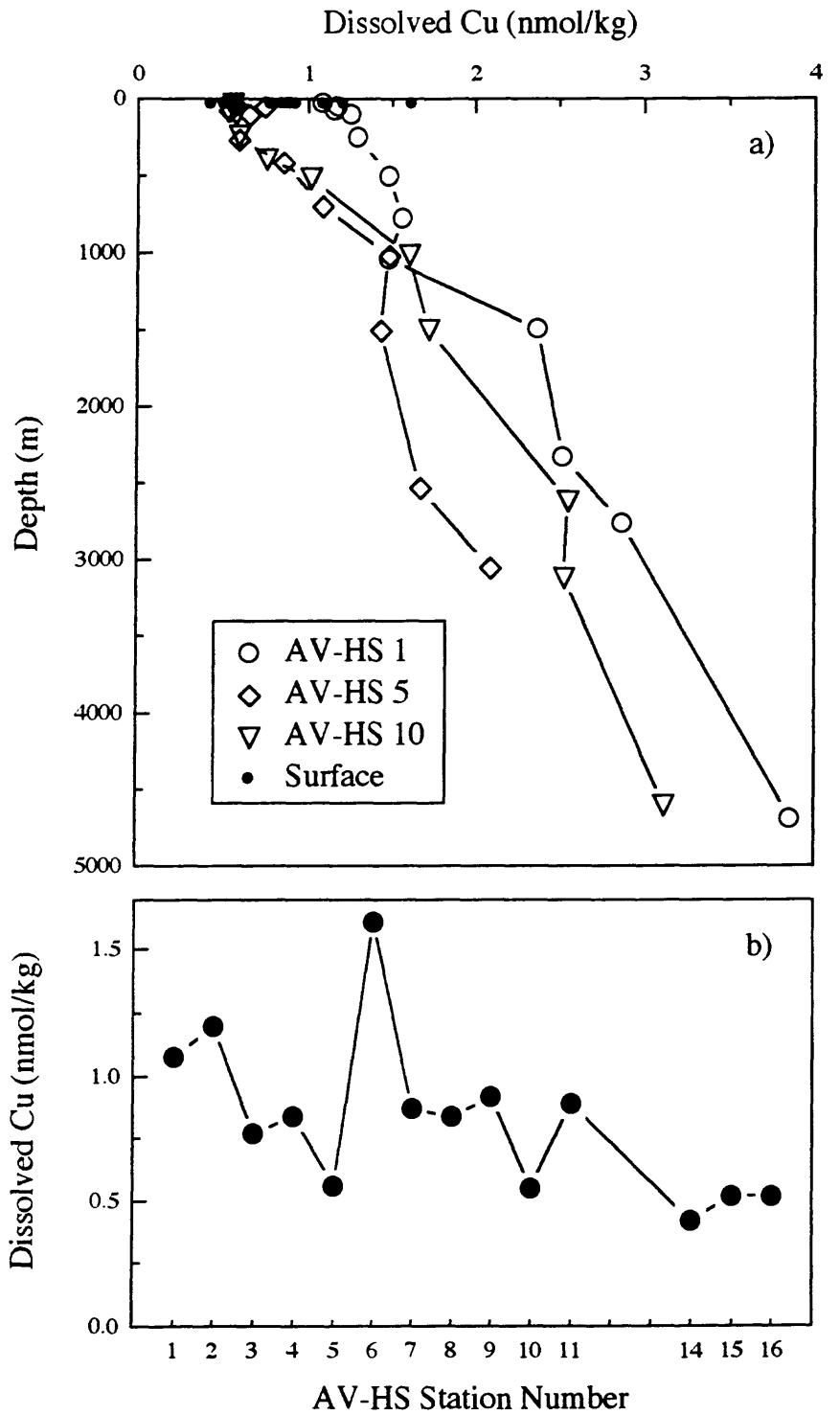

Figure 6. a) Distribution of dissolved copper *versus* depth at stations AV-HS 1 (open circles), AV-HS 5 (open diamonds), and AV-HS 10 (open triangles). Surface (25 m) values at stations AV-HS 1 through 16 are also shown (small filled circles). b) Dissolved copper at 25 m plotted *versus* station number. See Fig. 1 and Table 1 for station locations.

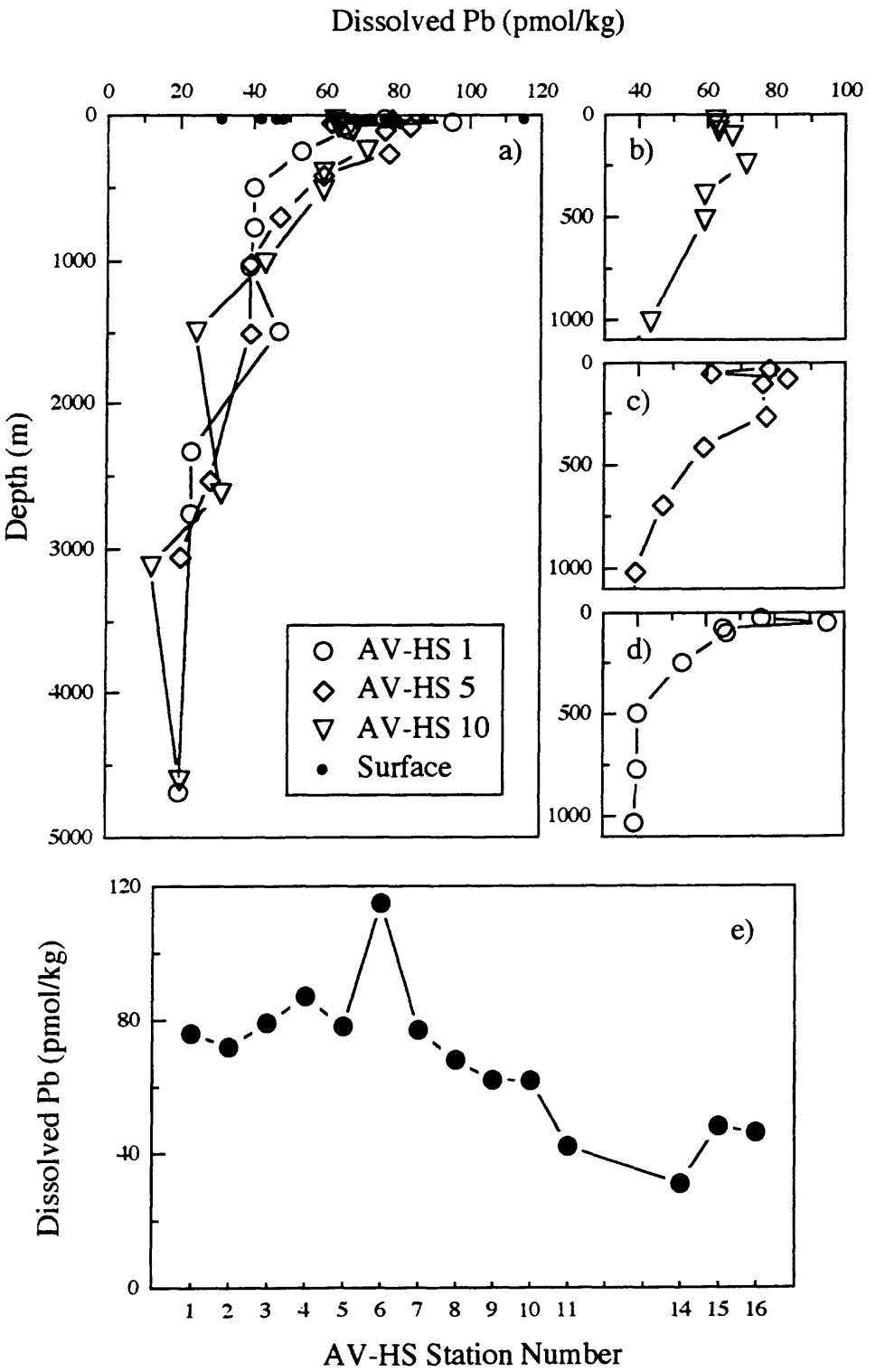

Figure 7 a) Distribution of dissolved lead *versus* depth at stations AV-HS 1 (open circles), AV-HS 5 (open diamonds), and AV-HS 10 (open triangles). Surface (25 m) values at stations AV-HS 1 through 16 are also shown (small filled circles). Also shown in b), c), and d) are expanded views of the upper 1000 m at AV-HS 10, AV-HS 5, and AV-HS 1, respectively. e) Dissolved lead at 25 m plotted *versus* station number. See Fig. 1 and Table 1 for station locations.

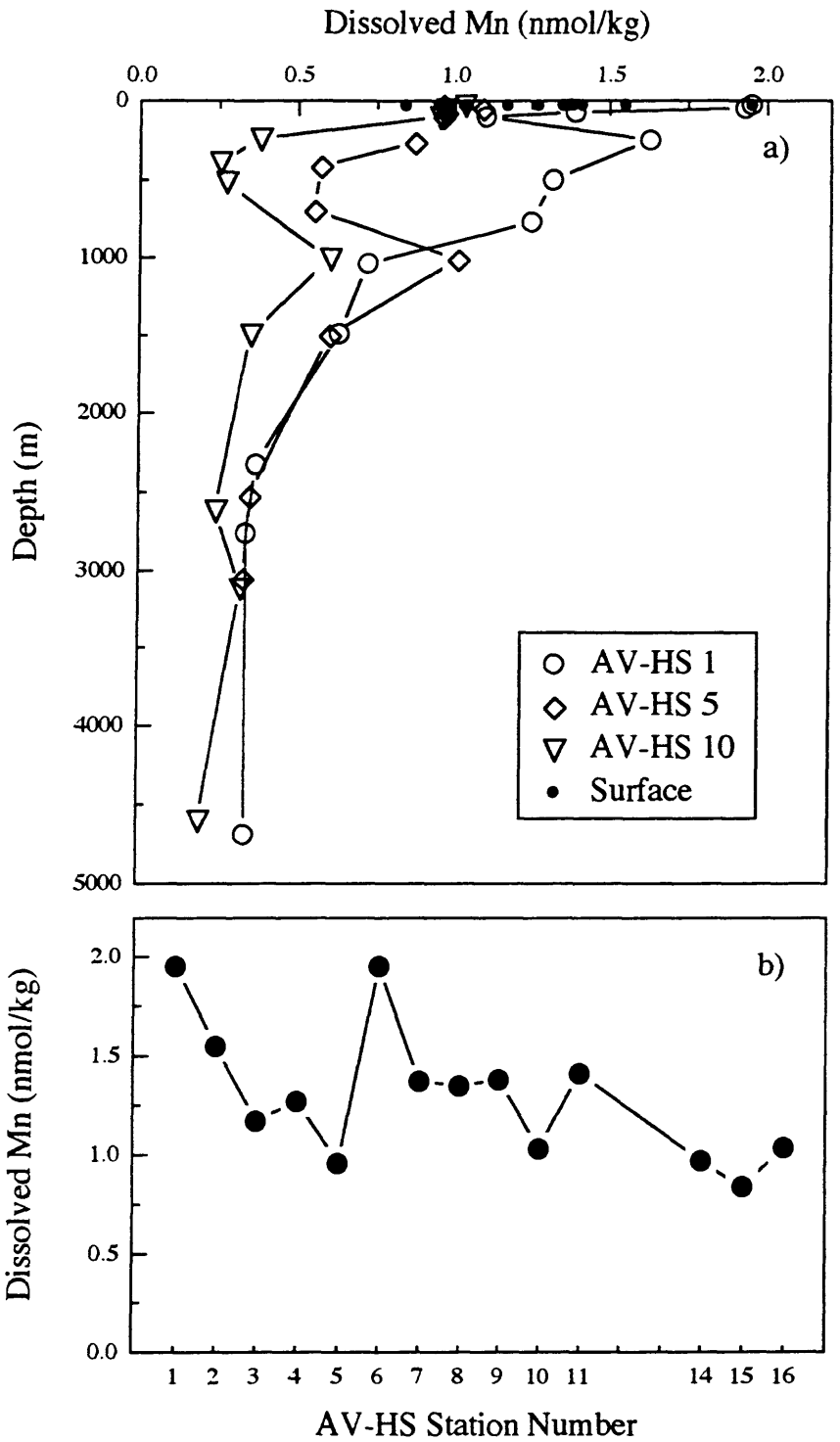

Figure 8. a) Distribution of dissolved manganese *versus* depth at stations AV-HS 1 (open circles), AV-HS 5 (open diamonds), and AV-HS 10 (open triangles). Surface (25 m) values at stations AV-HS 1 through 16 are also shown (small filled circles). b) Dissolved manganese at 25 m plotted *versus* station number. See Fig. 1 and Table 1 for station locations.

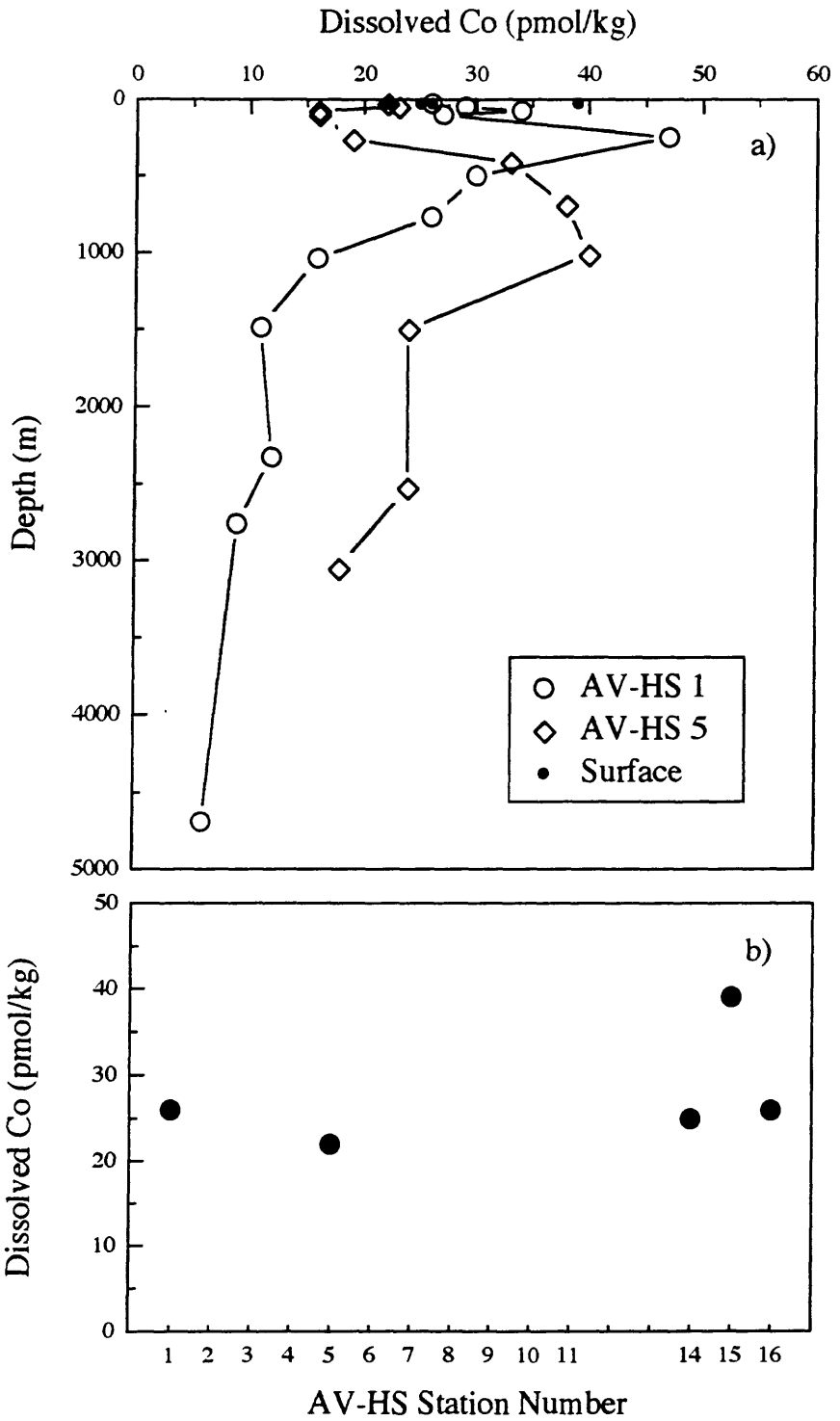

Figure 9. a) Distribution of dissolved cobalt *versus* depth at stations AV-HS 1 (open circles) and AV-HS 5 (open diamonds). Surface (25 m) values at stations AV-HS 1 through 16 are also shown (small filled circles). b) Dissolved cobalt at 25 m plotted *versus* station number. See Fig. 1 and Table 1 for station locations.

91-AV-19

LEG 2

Karin Ridge

— PAGE 39 FOLLOWS —

DESCRIPTION AND COMPOSITION OF FE-MN CRUSTS, ROCKS, AND SEDIMENTS COLLECTED ON KARIN RIDGE, R.V. ALEKSANDR VINOGRADOV CRUISE 91-AV-19/2

James R. Hein[1], Lev M. Gramm-Osipov[2], Ann E. Gibbs[1], Anatoly N. Kalyagin[2], William M. d'Angelo[3], Victor P. Nachaev[4], Paul H. Briggs[5], Alexander S. Bychkov[2], Alicé S. Davis[1], Vladimir V. Gusev[2], Hank Chezar[1], Sergey A. Gorbarenko[2], John H. Bullock[5], Gennady A. Kraynikov[2], David F. Siems[5], Evgeny V. Mikhailik[4], Hezekiah Smith[3], Moisey F. Eyberman[2], Marjorie J. Schutt[1], Alexander I. Beloglazov[4], Anatoly V. Mozherovsky[2], and Ruslan V. Chichkin[2]

[1]U.S. Geological Survey, Menlo Park, CA; [2]Pacific Oceanological Institute, Vladivostok; [3]U.S. Geological Survey, Reston, VA; [4]Far East Geological Institute, Vladivostok; [5]U.S. Geological Survey, Denver, CO

INTRODUCTION

From 9-31 May 1991, scientists from the Russian Academy of Sciences, U.S. Geological Survey, and University of British Columbia, Canada, participated in a cooperative cruise (91-AV-19/2) to Karin Ridge in the Johnston Island Exclusive Economic Zone (EEZ; Figs. 1-6) of the United States. The main objective of the cruise was to understand what geological, geochemical, and oceanographic parameters control the origin and evolution of ferromanganese oxyhydroxide crusts (hereafter called Fe-Mn crusts). The strategy was to study the water column, Fe-Mn crusts, and associated substrate rocks and sediments. Here, we present detailed descriptions of dredged and cored samples, chemical and mineralogical compositions, statistical analyses of the chemical data, bathymetric maps, and bottom camera photographs and descriptions. Chemical analyses of Fe-Mn crusts include major and minor elements, platinum group elements (PGEs), and rare earth elements (REEs). Brief petrographic descriptions of the volcanic and sedimentary rocks and paleontology of the sedimentary rocks are also presented. Comparisons are made with other central Pacific Fe-Mn deposits and the origin of the Karin Ridge deposits is discussed.

METHODS

Bottom sampling of Karin Ridge was completed using a 1-m circular chain bag dredge, large-diameter gravity corer, and box corer (Table 1). Because sediment cover is thin on the ridge, the three gravity core and two box core attempts on the ridge flanks recovered little sediment; however, one box core recovered about 2 kg of crust. A gravity core taken in abyssal deposits adjacent to the southwest base of the ridge recovered 3.4 m of sediment. Twelve dredges were attempted, with eight recoveries. Dredging was designed to sample along two transects, one on the south and the other on the north flank of Karin Ridge, in intervals spanning 500 m water depth each from the ridge base to the summit of. In addition, 2 kg of rocks were recovered in a box core taken on the summit of the north study area and 10 kg of rocks were caught by the camera sled when it collided with a rock outcrop during a transect on the summit in the north study area.

Satellite navigation was used, as Global Positioning System navigation was not available. Satellite fixes were available for about six hours each day, consequently, exact locations of some operations were not always possible and locations were adjusted according to bathymetry where appropriate. The three camera tows were all completed during times when satellites were available.

X-ray diffraction analyses were conducted on a Phillips diffractometer, with Cu-kα radiation and a curved-crystal carbon monochromator. Abundances of major oxides in substrate rocks were determined by X-ray fluorescence spectroscopy (Taggart et al., 1987), Fe(II) by colorimetric titration (Peck, 1964), CO_2 by coulometric titration (Engleman et al., 1985), H_2O^+ by water evolved at 950°C as determined coulometrically by Karl-Fischer titration (Jackson et al., 1987), and H_2O^- by sample weight difference at 110°C for greater than 1 hour (Shapiro, 1975). The low totals for the phosphorite samples occur because fluorine and sulfur were not determined and therefore are not included in the totals. High fluorine (to 4.4%) and sulfur (to 2.1% SO_3) contents are typical of marine carbonate fluorapatite (Cullen and Burnett, 1986; Burnett et al., 1987; Hein et al., 1993). The compositions of two glass samples from a hyaloclastite were determined by electron microprobe. For Fe-Mn crusts, the concentrations of most major and minor

elements were determined by inductively coupled plasma-atomic emission spectrometry, except those of K, Zn, and Pb, which were determined by flame atomic-absorption spectroscopy, and those of As, Cr, and Cd, determined by graphite-furnace atomic absorption spectroscopy on air-dried samples (Aruscavage et al., 1989). Concentrations of platinum-group elements for Fe-Mn crusts and substrate rocks, and rare earth elements for Fe-Mn crusts, were determined by inductively coupled plasma-mass spectrometry (Lichte et al., 1987a,b).

For Q-mode factor analysis, each variable percentage was scaled to the percent of the maximum value before the values were row-normalized and cosine theta coefficients calculated. Factors were derived from orthogonal rotations of principal component eigenvectors using the Varimax method (Klovan and Imbrie, 1971). All communalities are ≥0.99. The usnal Pearson product moment correlation coefficient was used to calculate the correlation coefficient matrices.

BATHYMETRY AND BOTTOM PHOTOGRAPHY

Karin Ridge is the northwest terminus of the Line Islands Ridge. The sinuous crest of Karin Ridge varies in morphology from rounded to razor-back (Figs. 1-4). The central part of the ridge, where this study took place, forms a wide flat summit with steep flanks (Figs. 5, 6). Sediment cover on the ridge is thin as indicated by GLORIA side-scan sonar images (Frontispiece), single-channel seismic reflection profiles (Hein et al., 1987a), and bottom photography (Figs. 7, 8). The large notch in the central south flank of the ridge probably represents a huge landslide scar (Figs. 2, 7).

Four bottom camera stations were occupied, three in the southern study area and one in the northern area (Figs. 5-8). Camera station 1 (CAM 1) crossed seafloor characterized by rock outcrops that are partly to completely covered with a thin layer of carbonate sediment. Pebble- to cobble-sized talus rests on the sediment surface in places. Generally, rock outcrops alternate with sediment-covered sections. Feeding tracks and trails are noted on the sediment surface, but current ripples are rare. In places, the rock outcrops are bedded and are probably composed of volcaniclastic breccia and sandstone deposits, especially in the shallower part of the camera transect. Camera station 2 (CAM 2) begins with a seafloor characterized by rock outcrops partly covered by a thin layer of sediment. The outcrops are generally bedded and may be reworked hyaloclastite deposits like those recovered in dredge D1. Nodule fields occur in places on the sediment surface. The nodules are probably talus, thinly coated by Fe-Mn oxyhydroxides, unlike typical abyssal plain Fe-Mn nodules. The sediment generally shows current ripples in a wide variety of forms: scalloped, long-crested, symmetric, asymmetric, interference ripples, and others. Again, moving upslope, rock outcrops alternate with sediment-covered sections. The seafloor is predominantly rock outcrops for the final quarter of the transect. Camera station 3 (CAM 3) begins with rock outcrops partly to completely covered by a thin layer of current-rippled carbonate sediment. The middle third of the transect is predominantly rock outcrops that vary from bedded volcaniclastic rocks to pillow basalt. The rock surface has a botryoidal texture typical of Fe-Mn crust growth. The final third of the transect is alternating outcrops of rock and sediment. Degraded current ripples characterize the sediment surface. Pebbles line the current-ripple troughs in places. Camera station 4 (CAM 4) begins with rock outcrops and adjacent expanses of sediment densely populated with nodules. Feeding tracks and trails are common on the sediment surface, as is talus debris. Sediment is current rippled with rock fragments lining the troughs. The nature of the seafloor over the central third of the transect is unknown because the camera sled was too far above the seafloor to record bottom images. The final third of the transect is rock outcrops alternating with sections of sediment cover. All rock outcrops in all four transects are coated with Fe-Mn crusts.

PETROLOGY, MINERALOGY, AND GEOCHEMISTRY

Rock Types and Ages

Various dredge attempts recovered 15 to 350 kg of Fe-Mn crusts and associated substrate rocks (Tables 2, 3). Breccia was the dominate substrate rock type recovered, followed by basalt, mudstone, and hyaloclastite. The breccia is composed of basalt clasts in: 1) a hyaloclastite matrix; 2) sandy volcaniclastic matrix; 3) phosphorite cement; or 4) mixtures of 1 through 3. Minor rock types include phosphorite, limestone, and volcaniclastic sandstone. Hyaloclastite, whether matrix for breccia or as a rock type, is always nearly completely altered to smectite and zeolites. Hyaloclastite and breccia are most

common on the upper ridge flanks, mudstone on mid-flank areas, and basalt on the middle and lower flanks.

Several volcanic rock samples are being processed for radiometric dating; the results will be presented elsewhere. However, rocks collected during other cruises to Karin Ridge yield radiometric ages of about 84 m.y., Late Cretaceous (Schlanger et al., 1984; Hein et al., 1990). The oldest fossil age that has been reported previously is Eocene (Hein et al., 1990). A brown mudstone from dredge D10 (Table 3), as well as samples from a number of other dredges contain foraminifera that indicate a Cretaceous age (see Pletnev et al., this volume). Fossil and radiometric age dating indicate that Karin Ridge formed in the Late Cretaceous and that sedimentation began soon after. Eocene volcanism, found in other parts of the Line Islands ridge, has not been found to have occurred on Karin Ridge, although many sedimentary rocks of Eocene age were recovered.

Phosphorites from dredge D4 are various shades of brown and contain much admixed opaque debris including Fe-Mn oxyhydroxides (probably todorokite), hematite, and magnetite. Relict volcanic glass fragments occur and the phosphorites are probably carbonate fluorapatite (CFA)-replaced hyaloclastite. Phosphorite in dredge D5 shows relict textures of zeolite crystals, smectite, and volcanic glass and again probably represent CFA-replaced altered hyaloclastite. Basalts from dredge D7 vary from highly plagioclase-phyric, with tachylitic to cryptocrystalline groundmass and large (centimeter size) phenocrysts that are anhedral to subhedral, to rocks with less abundant plagioclase phenocrysts, with rare rounded clinopyroxene phenocrysts; rare iron-oxide pseudomorphs after olivine also occur in some rocks. Most of the basalts are highly altered to smectite, hematite, and zeolites. Vesicles are partly to completely filled with bladed, prismatic, and blocky zeolites and reddish-brown to greenish smectite. Palagonite rims are common on many rock samples. Basalts from dredge D8 include: 1) Highly vesicular, tachylitic to microcrystalline basalt with sparse plagioclase phenocrysts and iron-oxide pseudomorphs after olivine; 2) highly plagioclase-phyric, pilotaxitic basalt with large, anhedral to subhedral plagioclase phenocrysts that have many devitrified glass inclusions; 3) moderately vesicular, fine grained, plagioclase-rich basalt with seriate texture. These basalts are also highly altered, with similar vesicle fills as described for dredge D7 basalts. Basalt collected by CAM-1 is vesicular, intersertal to intergranular with sparse plagioclase and clinopyroxene microphenocrysts. Vugs and vesicles are irregular in shape, lined by smectite, and contain euhedral crystals of zeolite. Basalts from dredge D11 include: 1) Highly plagioclase-phyric, hyalopilitic to intersertal basalt; rare, rounded clinopyroxene phenocrysts occur; plagioclase phenocrysts are large (centimeter size) and contain devitrified glass inclusions; a thin glass rind contains some sideromelane that is too full of microlites for good glass analyses; 2) highly vesicular, sparsely plagioclase-phyric basalt. Centimeter-size, anhedral to subhedral plagioclase phenocrysts are very altered; vesicles are small and round, and the groundmass has a pilotaxitic to intersertal texture. Hyaloclastite from dredge D11 contains large pieces of highly vesicular palagonite, with small areas containing fresh sideromelane; plagioclase phenocrysts are large and fresh.

A gravity core (GC1) taken at the base of south flank in abyssal deposits (water depth 5130 m; Fig. 6)), recovered a 3.4 m core consisting of beds containing various amounts of mixed pelagic and volcaniclastic debris (Table 4). Some beds are extensively bioturbated. The volcaniclastic beds were probably transported from the adjacent Karin Ridge by turbidity currents. Pelagic beds consist of foraminifera and nannofossils. A small amount of sediment collected in box core BC-1 (Table 4) also consists of foraminifera and nannofossils and is age dated as Pleistocene or Holocene (see Pletnev et al., this volume).

X-Ray Mineralogy

Breccias are composed of plagioclase, pyroxene, and alteration products of these minerals and volcanic glass, including smectite, phillipsite, and clinoptilolite (Table 5). Some breccias had a carbonate matrix that subsequently was replaced by carbonate fluorapatite (CFA), other breccias have a matrix of fine-grained volcanogenic minerals. Hyaloclastites are composed of the same minerals as breccia. Fresh basalt contains plagioclase and pyroxene, but is commonly altered to various extents to smectite and probably X-ray amorphous iron hydroxides. In some basalt samples, vesicles are filled with calcite and in others, with phillipsite. Mudstones are composed of volcanogenic minerals and their alteration products, much like breccias. However, mudstones also contain nodules of clinoptilolite, smectite, and phillipsite that were probably originally volcanic ash layers, redistributed by bioturbation and later altered to clay minerals and zeolites. Phosphorites are replaced carbonates and hyaloclastites and are composed of CFA and various admixtures of volcanogenic minerals and their alteration products. In general, the replacement

minerals CFA, phillipsite, and smectite are very common components of the rocks on Karin Ridge. Eolian quartz occurs in trace amounts in some samples (Table 5).

Geochemistry

The most phosphorus-rich rocks (D1-10, D4-12-1B) analyzed have CaO/P_2O_5 ratios of 1.59 and 1.60 (Table 6). These ratios fall near the high end of the range for the theoretical chemical compositions of carbonate fluorapatites, 1.50-1.60 (Manheim and Gulbrandsen, 1979). Minor excess Ca over P may be the result of the presence of Ca associated with plagioclase, phillipsite, or relict calcite in the replaced rocks. Some of the phosphorites are very pure, consisting of over 80% CFA. Several other elements characteristic of phosphorites were not analyzed for here, but have been determined recently for other phosphorites collected from equatorial Pacific seamounts: mean F, Cl, SO_3, and Sr contents are 3.44%, 0.011%, 1.52%, and 0.12%, respectively (Hein et al., 1993).

The composition of a breccia altered to nearly pure smectite shows a very high MgO content (12.9%; Table 6; CAM 1-1C). High MgO, coupled with high Al_2O_3 and Fe_2O_3 contents (9.55 and 11.2%, respectively), indicate that the smectite is probably saponite.

The composition of a vesicular basalt and two basaltic glass samples show similar SiO_2, Al_2O_3, and other oxide contents, except K_2O and MgO contents, which are much different (Table 6). The glass has higher MgO and lower K_2O relative to the vesicular basalt.

The rock types, mineralogy, and chemistry of samples studied here are consistent with those collected and analyzed in previous studies (e.g., Hein et al., 1990).

FERROMANGANESE CRUSTS

Fe-Mn crusts are virtually always current smoothed and polished, whether recovered from the north or south flank of Karin Ridge and apparently independent of water depth. Other surface textural types include botryoidal, subdued botryoidal, lizard-skin (very fine-scale botryoids), and granular (very porous). Currents caused mechanical erosion of the crusts, reducing their thicknesses and smoothing primary botryoidal surfaces, which produced a complete range of textures from botryoidal to smooth-polished. We speculate that lizard-skin texture is produced by renewed growth on an originally current-smoothed surface. Granular textures form in areas removed from direct exposure to currents and are common on the sides or undersides of substrate rocks. Most crusts collected during cruise 91/AV-19/2 are composed of one dense massive black layer, however, some of the thicker crusts have up to three distinct layers. The inner parts of some crusts contain CFA veins and paper-thin laminae, similar to what are found for crusts from other areas (Halbach et al., 1982). CFA varies from dark to pale brown and massive to porous.

Maximum crust thicknesses for different dredges vary from 2-80 mm, with mean values ranging from <1-35 mm. Such thicknesses are typical of Fe-Mn crusts recovered from central Pacific seamounts (Hein et al., 1985; 1987b; 1988; 1990). These results show that thickness distributions are highly variable, as 160 mm-thick crusts were recovered in 1986 within kilometers of the south flank transect described here (Hein et al., 1990). Crust thicknesses are greater from the southern ridge flank transect than along the northern transect (Table 2). Also, crusts are apparently thicker from the shallower-water dredges along both transects, and become only patinas on rocks from the base of the ridge on the northern flank transect.

Fe-Mn nodules compose 80% of dredge D5, 20% of dredge D4, and minor amounts of other dredges. Nodules are generally small, less than 30 mm in diameter and most have a relatively large nucleus compared with abyssal plain nodules. About 70% of the nodules are typical seamount-type nodules, that is, they have a large nucleus, which is essentially completely encrusted talus debris. Nuclei of abyssal nodules and 30% of those from Karin Ridge have a very small nucleus relative to the thickness of Fe-Mn layers. Nuclei of nodules from Karin ridge include older nodule and crusts fragments and all rock types mentioned above. Nodules apparently become more abundant with water depth along the sampling profile on the south flank of the ridge. The dredge from about 3000 m contains 20% nodules, whereas that from about 4000 m contains 80% nodules. Shallower-water dredges contain only a few percent of nodules. Along the sampling profile on the north flank of the ridge, nodules were recovered only from the deepest dredge (D7), where they compose about 2% of the dredge haul.

Growth rates of the crusts were determined using the empirical equation of Puteanus and Halbach (1988), which depends on Co and P contents. Mean growth rates for bulk crusts range from 3 to 32 mm/m.y., with a mean of 12 mm/m.y. Crust surfaces accreted at rates ranging from 3 to 13 mm/m.y., with

a mean of 8 mm/m.y. These growth rates indicate that on the average growth of the outermost layer was slower than the mean growth rates of the crusts as a whole. This is also demonstrated by growth of the three layers analyzed for crust D1-2, which show a progressively slower growth rate, from 12 to 7 to 3 mm/m.y. over the history of crust formation. Finer-scale sampling would no doubt define greater variability in crust growth rates than indicated here. In general, growth rates determined here are faster than those found for crusts from other studies, which are mostly less than 8 mm/m.y., but range up to 15 mm/m.y. (Hein et al., 1992b). This difference is probably due to the deeper sampling sites here than in many other studies. Higher oxygen contents in waters below the oxygen minimum zone would promote oxidation and accretion of the oxyhydroxides. The Fe-Mn nodule (D4-6-1) with a very high Cu content may have formed diagenetically (see below), which is supported by its apparently very fast rate of growth, 128 mm/m.y.

Minimum ages for crusts can be determined from the growth rates and crust thicknesses. Hiatuses, or periods of non-growth are relatively common in crusts and are not measurable by chemical age-dating methods. Minimum ages for bulk crusts range from 14 to 0.5 m.y., that is middle Miocene to late Pleistocene. The surface layer (0.5 mm) of crusts range in age from 40-170 k.y, with a mean age of 70 k.y. These ages are probably close to the true ages of the surface layer for each crust.

X-Ray Diffraction Mineralogy

Great care was taken in sampling crusts for chemical and mineralogical analyses. All contamination from recent sediment was removed, which was especially critical in the porous crust layers. Also, special attention was paid to obtaining a clean separation of the lower crust layers from the substrate. Any minerals or elements determined to exist in the various deposits were incorporated into those layers during deposition or diagenesis and are not due to sampling procedures or post-depositional infiltration of sediment. Finally, all encrusting organisms and other debris were cleaned from the crust surfaces before sampling. Bulk always refers to the entire crust thickness whether composed of layers or not.

Bulk crusts and nodules and layers of crusts are composed of 92-100% δ-MnO_2 (vernadite), which has only two X-ray reflections at about 2.42Å and 1.41Å (Table 7). The δ-MnO_2 varies from moderately well crystalline to the more common very poorly crystalline. X-ray amorphous Fe oxyhydroxide epitaxially intergrown with δ-MnO_2 is also a dominant phase. The Fe phase is not crystallized to goethite in any of the crusts as has been found in a small percentage of crusts from equatorial Pacific seamounts (Hein et al., 1990; Hein, Kang et al., 1990). CFA composes 9% of the inner half of Fe-Mn crust D1-2C and 3% of the outer surface of Fe-Mn crusts D4-8, -12 (Table 7). Phosphatization of the outer layers of Fe-Mn crusts has not been described before and it has always been the inner layers that are phosphatized. We do not think that samples D4-8, 12 is an exception and suggest that the CFA was incorporated into the crusts as a detrital mineral along with plagioclase and quartz. The substrate rock from dredge D4 is phosphorite-rich and phosphorite particles were probably eroded from nearby outcrops and transported by bottom currents (Tables 2, 3). Typical detrital and eolian minerals make up the remainder of the crusts, including quartz (to 8%), plagioclase (to 4%), and K-feldspar (to 3%). It is rare to find quartz in abundances as great as 8% in crusts and we speculate that its high content in the surface scrape CAM 1-1B is the result of contamination during sample preparation; bulk crust CAM 1-1A and surface scrape CAM 1-1D, 1-5 from the same dredge do not contain quartz. Most of the quartz and part of the plagioclase are eolian and the remainder of the plagioclase and K-feldspar are reworked from local outcrops and incorporated into the crusts during precipitation of the Fe-Mn oxyhydroxides. Calcite is rare in crusts and most commonly dissolves before accretion of more than a millimeter of crust (Hein, Kang, et al., 1990) and was detected in only one surface scrape of crusts from Karin Ridge.

Geochemistry

Chemical compositions were determined for 31 samples from Karin Ridge, including 12 bulk crusts, 14 surface scrapes of crusts, 3 layers from one crust, and 2 nodule samples, one being a composite composition of four bulk nodules (Tables 8-12). The mean Fe and Mn contents of the 12 bulk crusts are 15.1% and 15.7%, respectively, yielding a Mn/Fe ratio of 1.1 (Table 11). Iron content is about the same, but Mn content is much lower than it is for the average central Pacific crust (Table 13). On a hygroscopic water-free basis, the Fe and Mn contents are 21.6% and 22.6%, respectively. The mean composition of crust surface samples is about the same as the mean composition of bulk crusts (Tables 11-13). This is

uncommon and surface layers in previous studies generally have much greater Co contents, higher Ni and Pb contents, but somewhat lower Cu contents (Hein, Kang, et al., 1990). This is probably the result of a greater mean water depth for dredge hauls in this study. Most of the metals in crust surface samples decrease with increasing water depth, with the exception of Cu, which increases with depth (Table 12). Most of the metals and the Mn/Fe ratios are lower in crusts from this study as compared to their values for crusts from other central Pacific studies (Table 13). Again, this is the result of different water depths among the various studies. The higher Fe relative to Mn is due to increasing Fe content with water depth. The thickest crusts analyzed generally have more Mn, P, Ni, and Mo and less Fe, Al, and Cr than thinner crusts (Table 13).

Three layers of a thick crust (D1-2) were analyzed (Tables 8-10). On a hygroscopic water-free basis, the following elements decrease regularly through all three layers with depth in the crust from the surface: Fe, Na, Mg, P, Co, and As; whereas Ca, Ni, Zn, Ba, Sr, and Ce increase with depth in the crust. This is the opposite trend normally found for P, which is commonly most abundant in the lower crust layers. Cobalt is more than double and Ce is less than half their respective contents from the base to surface of the crust (4829 to 10020 ppm and 2759 to 1214 ppm, respectively; Table 9). In addition, Si, Al, Ti, and Cr (aluminosilicate-associated elements) have their lowest contents in the lowermost layer, whereas CO_2, Mo, V, and Pb have their highest concentrations in the lowermost layer. In a general way, these trends may indicate that the CCD rose and then deepened, the oxygen minimum zone became better developed, and surface-water productivity increased as the crust grew. In addition, the ridge may have subsided during crust growth. As the crust grew, it received increased clastic input.

There are notable differences in the composition of nodules and crusts from this study (Table 13). Copper is significantly enriched in the nodules (mean 1800 ppm) compared to crusts (780 ppm). Mean Al and P contents are higher in the nodules, whereas mean Fe, Mn, Co, and Mo contents are lower in the nodules. These compositional differences between seamount crusts and nodules also contrast with results from other studies, where the two types of deposits generally have similar compositions. The differences in samples studied here maybe the result of diagenetic enrichment of Cu in the nodules, either from reactions in the soft sediment, or more likely from diagenetic reactions in the underlying sedimentary rocks.

Regardless of the compositional differences described in the preceding paragraphs, all the samples studied here fall within the central Pacific hydrogenetic crust field on the Bonatti et al. (1972) Fe-Mn-(Cu+Ni+Co)x10 ternary diagram (Fig. 9). The crust field is defined by 308 bulk crust analyses for samples collected from the central Pacific region (Hein et al., 1992a). The mean Co+Ni+Cu content for bulk crusts is 0.72%, very low in regards to economic considerations. On a hygroscopic water-free basis, this trace metal sum is 1.03%.

Platinum Group Elements (PGEs)

We report the concentrations of Pt, Pd, Rh, Ru, and Ir for six bulk crusts (Tables 8-11, 13). Platinum varies from 88-150 ppb (131-223 ppb on hygroscopic water-free basis), with a mean content of 113 ppb (165 ppb). This mean content is much lower than the mean for central Pacific crusts, especially those from the Marshall Islands (489 ppb; Table 13). The PGEs show significant enrichments over lithospheric (except Pd; Parthé and Crocket, 1978) and seawater abundances (Hodge et al., 1986; Goldberg, 1987; Colodner, 1991), but show depletions over solar system abundances (mean composition of C1 chondrites; Fig. 10; Anders and Ebihara, 1982). Ruthenium and Pt show a positive anomaly on a seawater normalized plot, which is comparable to trends that occur for Fe-Mn crust compositions in other parts of the central Pacific (Hein, Kang, et al., 1990; Hein, Ahn, et al., 1992). Comparisons of the ratios of each PGE to Ir and Pt for crusts, seawater, the lithosphere, and the solar system indicate that Pt, Ir, Ru, and most of the Rh are derived predominantly from seawater, whereas the Pd and to a lesser extent Ru and Rh are derived from both clastic debris and seawater. The extraterrestrial component (meteorite debris) in the bulk crusts must be small, certainly no more than 10-15% of the PGEs could have been derived from such a source. In general, the PGEs reflect the hydrogenetic input to the crusts.

Rare Earth Elements

Six bulk crusts were analyzed for REEs. Total REE concentrations range from 0.22% to 0.31% (Table 14). These contents are much higher than mean contents for other parts of the equatorial Pacific (Hein et al., 1987a, Hein, Kang, et al., 1990; Hein, Ahn, et al., 1992). These relatively higher contents are

due to the samples being recovered from deep-water sites. Generally, REE abundances increase in crusts with increasing water depth (Aplin, 1984; De Carlo and McMurtry, 1992). In our samples, this increase in abundance with water depth is due to increases in the light REEs (LREEs). The heavy REEs (HREEs) either do not change with water depth, or may decrease slightly with increasing water depth. Also, there is a significant and consistent increase in fractionation of Ce from the other REEs with water depth (Table 14; Figs. 11, 12), which was also noted to occur to a lesser extent in samples described by De Carlo and McMurtry (1992). Unlike the results from De Carlo and McMurtry (1992), Ce concentrations increase with increasing water depth.

Chondrite-normalized REE patterns (Haskin et al., 1968) show LREE enrichment, a positive Ce anomaly, small negative Eu anomaly, and possibly a small positive Gd anomaly. These characteristics are typical of hydrogenetic crusts (Hein et al., 1988). Unlike the other REEs, soluble Ce^{+3} is oxidized to insoluble Ce^{+4} at the Fe-Mn surface and fixed in predominantly Fe and Mn phases, thus creating a large positive Ce anomaly on both shale- and chondrite-normalized plots (Goldberg et al., 1963; Piper, 1974). The Ce anomaly, Ce* (normalized 2Ce/La+Pr), ranges from 1.29 to 1.65 and increases with increasing water depth.

All the crusts have a small positive Gd anomaly. The Gd anomaly was first discovered to occur in seawater by De Baar et al. (1985) and in Fe-Mn crusts by Hein et al. (1988). The Gd anomaly occurs in patterns for crusts from the Marshall Islands (Hein et al., 1988) and Micronesia (Hein, Ahn, et al., 1992), but is rarely present in other crusts analyzed from the Johnston Island EEZ (Hein et al., 1987a). De Baar et al. (1985) attributed the Gd/Tb fractionation in seawater to anomalous properties associated with the shift from an exactly half-filled 4f electron shell.

The HREE depletion results from their formation of more stable carbonate complexes in seawater compared to the LREEs, and consequently the HREEs are more difficult to fix in the crusts than are the LREEs (Cantrell and Byrne, 1987). This may also explain why the HREEs do not increase in crusts with increasing water depth as do the LREEs.

Interelement Relationships: Correlation Coefficient Matrices

Correlation coefficient matrices were calculated from the compositions of 12 bulk crusts (Table 15) and from data for 14 crust surface samples (Table 16). Matrices also include water depth, latitude, longitude, and crust thickness.

For bulk crusts, strong positive correlations are found among the following selected elements: **Mn**: Ni, Co, Mo, Ir; **Si**: Al, K, Fe, Ti; **Ca**: P, CO_2, Sr, Mo; **Ti**: Fe; Cu: Ba; **Pt**: Ru, Ir, Co, Ni. Many more statistically significant moderately strong to weak correlations occur (Table 15). All elements are associated with one or more mineral phases(s) in the crusts. We interpret the correlations in Table 15 to indicate the following phases and their associated elements: **δ-MnO_2**: Mn, Mo, Co, Na, Ca, Sr, V, Pb, Cd, Mg, Ir, Ru, Pt, Rh; **aluminosilicate**: Si, Al, Cr, K, Fe, Ti, Pd, Ce, Y; **titanomagnetite**: Ti, Fe; **CFA**: Ca, P, CO_2, Sr, V, Pb, Mo; **residual biogenic** phase: Ba, Cu, Zn, Ca, Sr, Mg, Mo, V, Ce, Y, P, Pd. Both the CFA and residual biogenic phases increase with increasing crust thickness. It is common for the CFA phase to increase with crust thickness for samples collected throughout the central Pacific. Generally, elements of the δ-MnO_2 and CFA phases are negatively correlated with those of the aluminosilicate phase.

The PGEs are apparently distributed among several different crust phases. A strong association exists among Pt, Ir, Ru, and Rh. This group shows a preference to the manganese phase and to a lesser extent to the CFA phase. Palladium is closely associated with the aluminosilicate phase, but also is associated with the residual biogenic phase.

For crust surface samples, strong positive correlations are found among the following selected elements: **Mn**: Mo, Ni, Cd, Co, As, Ca; **Si**: Al, Ba, Ti, Fe; **Ca**: Sr, Mo, Ni, Mn, Y, Cd, Co; **water depth**: Ce, Ti, Cu, Al (negative correlations: P, CO_2, Sr, Y, V, Mn, Ni, Zn, Mo, Pb, Cd); **latitude**: Si, Fe (negative correlations: As, Mn, Ni, Co, Mo). Many more statistically significant moderately strong to weak correlations occur (Table 16). We interpret the correlations in Table 16 to indicate the following phases and their associated elements: **δ-MnO_2**: Mn, Mo, Ni, Co, Cd, As, Ca, Sr, Pb, V, Y; **aluminosilicate**: Si, Al, Ba, Ti, Fe, Ce, K, Cu; **chrome spinel**: Cr; **CFA**: Ca, CO_2, Y, Sr, V; **calcite**: Ca, CO_2, Sr; **residual biogenic**: Ba, Ce, Cu, Fe, Ca, Na, AS, Mg. Some notable differences occur between the bulk crusts and crust surface samples. For example, in the crust surface data, As is strongly associated with the δ-MnO_2 and Ba, Ce, and Cu are associated with the aluminosilicate phase. In addition, the CFA and residual biogenic phases are only weakly developed.

Several elements have correlations with latitude and water depth. Correlations with latitude are not an artifact of changing water depths with latitude as there is no correlation between latitude and water depth; also, the mean water depths of dredges from the northern and southern study areas are about the same. In general, elements associated with the aluminosilicate phase increase with increasing water depth and those associated with the manganese and biogenic phases decrease with increasing water depth. In addition, the aluminosilicate phase increases with latitude (that is, in crusts in the northern area), whereas the manganese phase decreases with latitude--that is, it increases with proximity to the equator.

Grouping of Elements: Q-Mode Factor Analysis

Q-mode factor analysis was completed for the 12 bulk crusts and 14 crust layer samples (Figs. 13, 14). The elements grouped by Q-mode factor analysis for bulk crusts can be assigned to four factors, three of which are essentially the same as those interpreted from the correlation coefficient data. Q-mode factors did not include what we would interpret as CFA or titanomagnetite phases, but did define what we call a Cr spinel phase. Q-mode factor analysis places P, Zn, and As in the manganese phase, which indicates that the elements that compose CFA are associated with the manganese phase. This type of relationship is commonly noted for thin crusts that have not been phosphatized (Hein, Kang, et al., 1990). This relationship indicates that there are at least two mechanisms that incorporate phosphorus into crusts: syndepositional adsorption and later-stage diagenesis. Factor analysis puts Ba and Cu into the aluminosilicate phase for both bulk and surface crust groups, and adds Na as well in the former group.

For crust surface data, Q-mode factor analysis defined the same four factors as for bulk crust data and in addition defined a fifth phase that we interpret to be either a Fe oxyhydroxide or Fe phosphate phase (Fig. 14). Factor analysis adds P and Zn to the δ-MnO_2 phase and Mg to the aluminosilicate phase, compared to groupings interpreted from correlation coefficients. The chief differences between the main phases as defined by factor analysis in bulk crusts and crust surfaces include: Manganese phase, no Na and Mg and added Y to crust surface data; no Cr, Y, Na and added Ce and Mg to crust surface aluminosilicate phase.

The statistical data show that the partitioning of elements in crusts is complex and that many elements occur in several crust phases. Element distributions may depend on location of formation--that is both geographic and water depth locations. Distributions may also depend on crust thickness, which reflects growth rates and probably diagenesis within the crusts.

SUMMARY AND CONCLUSIONS

Rocks and Fe-Mn crusts were collected from 10 locations on the central part of the Cretaceous-age Karin Ridge, U.S. Johnston Island EEZ. In addition, a 3.4 m gravity core was collected from near the base of the ridge. Karin Ridge has a sharp to rounded crest that supports only thin sediment cover. Dredged rocks include predominantly breccia composed of basalt clasts and basalt, with smaller amounts of mudstone, hyaloclastite, sandstone, limestone, and phosphorite. The breccia has a hyaloclastite, sandy volcaniclastic, and/or phosphorite matrix-cement. Phosphorites are predominantly CFA-replaced hyaloclastites and carbonates. Basalts are generally highly altered, sparsely to highly vesicular, and contain various amounts of plagioclase and pyroxene phenocrysts. The gravity core from near the base of the ridge consists of alternating pelagic carbonate deposits and volcaniclastic turbidites that originated from the ridge.

Fe-Mn crusts are predominantly current smoothed and polished. Most crusts are composed of one dense massive black layer, however, some thicker crusts have up to three distinct layers. The inner part of some crusts contain CFA veins and paper-thin laminae. Maximum crust thicknesses for different dredges vary from 2-80 mm, with mean values ranging from <1-35 mm. Crust thicknesses are greater from the southern ridge-flank transect then they are along the northern flank transect. Crusts are also thicker in the shallower-water dredges from both transects and are only patinas on rocks from the base of the ridge along the northern transect. Fe-Mn nodules are abundant in some dredges and apparently are more abundant with increasing water depth. Growth rates of crusts vary from 3-32 mm/m.y., with a mean of 12 mm/m.y. The outermost 0.5 mm of the crusts accreted at a slower mean rate of 8 mm/m.y. Minimum ages for crusts vary from 0.5-14 m.y., and for the outermost 0.5 mm, from 40-170 ka.

Bulk Fe-Mn crusts are composed of 92-100% δ-MnO_2 (vernadite), with small amounts of quartz, plagioclase, K-feldspar, and CFA. On a hygroscopic water-free basis, bulk crusts have mean Fe and Mn

contents of 21.6% and 22.6 %, respectively, with a mean Mn/Fe ratio of 1.1. The mean Co content is 0.59% and the mean Co+Ni+Cu content is 1.03%. Copper is relatively high (mean 0.22%) in seamount nodules compared to crusts (mean 0.11%), and indicates that nodules may have grown by both diagenetic and hydrogenetic processes. The metal contents of the crusts, including the PGEs, are lower than they are for central Pacific crusts from other studies; this reflects the greater water depths for most of the dredges studied here (mean water depth 3170 m) compared to those from other studies. Many of the metals are known to decrease in crusts from increasing water depth. In contrast, total REEs are higher in crusts from this study than they are in crusts from other studies; this is also due to water depth, where REEs (especially the LREEs) generally increase in crusts with increasing water depth. The REEs and most of the PGEs (Ir, Pt, Ru, Rh) are derived from seawater, whereas Pd is derived from clastic debris as well as seawater.

Q-mode factor analysis and correlation coefficient matrices can be interpreted to define the following crust phases and their associated elements: δ-MnO_2 (Mn, Co, Ni, Mo, Na, Ca, Sr, V, Pb, Cd, Mg, P, Zn, As, Ir, Ru, Pt); aluminosilicate (Si, K, Fe, Ti, Mg, Ba, Cu, Na); CFA (P, CO_2, Sr, Mo); and residual biogenic (Ba, Cu, Zn, Ce, Ca, Sr, Mg, V); minor titanomagnetite, Cr spinel, and Fe phosphate phases may also occur. In general, elements associated with the aluminosilicate phase increase with increasing water depth and increasing latitude. In contrast, many elements associated with the manganese phase decrease with increasing latitude--that is, the manganese phase increases with proximity to the equator.

ACKNOWLEDGMENTS

We thank the captain and crew of the RV Aleksandr Vinogradov for their help and cooperation in making this a successful program. We thank Ransom Rideout and Richard Viall for technical help and Marjorie Schulz, Virginia Smith, and Juliet Wong for help with collection, description, and sampling of rocks and sediments.

REFERENCES CITED

Anders, E. and Ebihara, M., 1982, Solar-system abundances of the elements. Geochimica et Cosmochimica Acta, v. 46, p. 2363-2380.

Aplin, A.C., 1984, Rare earth element geochemistry of central Pacific ferromanganese encrustations. Earth and Planetary Science Letters, v. 71, p. 13-22.

Aruscavage, P.J., Kirschenbaum, H., and Brown, F., 1989, Analytical methods: The determination of 27 elements in ferromanganese materials: in Manheim, F.T. and Lane-Bostwick, C.M. (eds.), Chemical Composition of Ferromanganese Crusts in the World Ocean: A Review and Comprehensive Database. U.S. Geological Survey Open File Report 89-020, 200 p. plus 3 appendices.

Bonatti, E., Kraemer, T., and Rydell, H., 1972, Classification and genesis of submarine iron-manganese deposits. in Horn, D.R. (ed.), Ferromanganese Deposits On the Ocean Floor. Washington, D.C., National Science Foundation, p. 149-166.

Burnett, W.C., Cullen, D.J., and McMurtry, G.M., 1987, Open-ocean phosphorites--in a class by themselves? in Teleki, P.G., Dobson, M.R., Moore, J.R., and von Stackelberg, U. (eds.), Marine Minerals, D. Reidel, Dordrecht, p. 119-134.

Cantrell, K.J. and Byrne, R.H., 1987, Rare earth element complexation by carbonate and oxalate ions. Geochimica et Cosmochimica Acta, v. 51, p. 597-605.

Colodner, D.C., Boyle, E.A., and Edmond, J.M., 1991, Platinum in seawater. Abstracts and Program, 1992 Ocean Sciences Meeting, EOS, Transactions of the American Geophysical Union, v. 72, no. 51, p. 44.

Cook, H.E., Johnson, P.D., Matti, J.C., and Zemmels, I., 1975, Methods of sample preparation and X-ray diffraction data analysis (X-ray mineralogy laboratory, Deep Sea Drilling Project, University of California Riverside). in Hays, D.E., Frakes. L.A., et al., Initial Reports of the Deep Sea Drilling Project, U.S. Government Printing Office, Washington, D.C., v. 28, p. 999-1007.

Cullen, D.J. and Burnett, W.C., 1986, Phosphorite associations on seamounts in the tropical southwest Pacific Ocean. Marine Geology, v. 71, p. 215-236.

De Baar, H.J.W., Brewer, P.G., and Bacon, M.P., 1985, Anomalies in rare earth distributions in seawater: Gd and Tb. Geochimica et Cosmochimica Acta, v. 49, p. 1961-1969.

De Carlo, E.H. and McMurtry, G.M., 1992, Rare earth element geochemistry of ferromanganese crusts from the Hawaiian Archipelago. Chemical Geology. v. 95, p. 235-250.

Engleman, E.E., Jackson, L.L., and Norton, D.R., 1985, Determination of carbonate carbon in geological materials by coulometric titration. Chemical Geology, v. 53, p. 125-128.
Goldberg, E.D., Koide, M., Schmitt, R.A., and Smith R.H., 1963, Rare earth distribution in the marine environment. Journal of Geophysical Research, v. 68, p. 4209-4217.
Goldberg, E.D., 1987, Heavy metal analyses in the marine environment--approaches to quality control. Marine Chemistry, v. 22, p. 117-124.
Halbach, P., Manheim, F.T., and Otten, P., 1982, Co-rich ferromanganese deposits in the marginal seamount regions of the central Pacific basin--results of the Midpac '81. Erzmetall, v. 35, p. 447-453.
Haskin, L.A., Haskin, M.A., Frey, F.A., and Wildeman, T.R., 1968, Relative and absolute terrestrial abundances of the rare earths. in Ahrens, L.H. (ed.), Origin and Distribution of the Elements, 1, Pergamon, Oxford, p. 889-911.
Hein, J.R., Ahn, J.-H., et al., 1992, Geology, geophysics, geochemistry, and deep-sea mineral deposits, Federated States of Micronesia: KORDI-USGS R.V. *Farnella* cruise F11-90-CP. U.S. Geological Survey Open File Report 92-218, 191 pp.
Hein, J.R., Bohrson, W.A., Schulz, M.S., Noble, M., and Clague, D.A., 1992b, Variations in the fine-scale composition of a central Pacific ferromanganese crust: Paleoceanographic implications. Paleoceanography, v. 7, p. 63-77.
Hein, J.R., Fleishman, C.L., Morgenson, L.A., Bloomer, S.H., and Stern, R.J., 1987b, Submarine ferromanganese deposits from the Mariana and Volcano volcanic arcs, west Pacific. U.S. Geological Survey Open File Report 87-281, 67 p.
Hein, J.R., Kang, J-K., et al., 1990, Geological, geochemical, geophysical, and oceanographic data and interpretations of seamounts and Co-rich ferromanganese crusts from the Marshall Islands, KORDI-USGS R.V. *Farnella* cruise F10-89-CP. U.S. Geological Survey Open File Report 90-407, 246 p.
Hein, J.R., Kirschenbaum, H., Schwab, W.C., Usui, A., Taggart, J.E., Stewart, K.C., Davis, A.S., Terashima, S., Quinterno, P.J., Olson, R.L., Pickthorn, L.G., Schulz, M.S., Morgan, C.L., 1990, Mineralogy and geochemistry of Co-rich ferroman-ganese crusts and substrate rocks from Karin Ridge and Johnston Island, *Farnella* Cruise F7-86-HW. U.S. Geological Survey Open File Report 90-298, 80 pp.
Hein, J.R., Schulz, M.S., and Gein, L.M., 1992a, Central Pacific cobalt-rich ferromanganese crusts: Historical perspective and regional variability. in Keating, B. H. and Bolton, B. R. (eds.), Geology and Offshore Mineral Resources of the Central Pacific Basin, Springer-Verlag, New York, p. 261-283.
Hein, J.R., Schwab, W.C., Foot, D.G., Masuda, Y., Usui, A., Davis, A.S., Fleishman, C.L., Barna, D.L., Pickthorn, L.-B., Larson, D.A., Ruzzi, P., Benninger, L.M., and Gein, L.M., 1987a, *Farnella* cruise F7-86-HW, cobalt-rich ferromanganese crust data report for Karin Ridge and Johnston Island, central Pacific. U.S. Geological Survey Open File Report 87-663, 34 p.
Hein, J.R., Schwab, W.C. and Davis, A.S., 1988, Cobalt and platinum-rich ferromanganese crusts and associated substrate rocks from the Marshall Islands. Marine Geology, v. 78, p. 255-283.
Hein, J.R., Yeh, H.-W., Gunn, S.H., Sliter, W.V., Benninger, L.M., and Wang, C.-H., 1993, Two major Cenozoic episodes of phosphogenesis recorded in equatorial Pacific seamount deposits. Paleoceanography, v. 8, p. 293-311.
Hodge, V., Stallar, M., Koide, M., and Goldberg, E.D., 1986, Determination of platinum and iridium in marine waters, sediments, and organisms. Analytical Chemistry, v. 58, p. 616-620.
Jackson, L.L., Brown, F.W., and Neil, S.T., 1987, Major and minor elements requiring individual determination, classical whole rock analysis, and rapid rock analysis: in, Baedecker, P.A. (ed) Methods for Geochemical Analysis. U.S. Geological Survey Bulletin 1770, p. G1-G23.
Klovan, J.E. and Imbrie, J., 1971, An algorithm and FORTRAN-IV program for large-scale Q-mode factor analysis and calculation of factor scores. Mathematical Geology, v. 3, p. 61-77.
Lichte, F.E., Golightly, D.W., and Lamothe, P.J., 1987a, Inductively coupled plasma-atomic emission spectrometry. in Baedecker, P.A. (ed.), Methods for Geochemical Analysis. U.S. Geological Survey Bulletin 1770, p. B1-B10.
Lichte, F.E., Meier, A.L., and Crock, J.G., 1987b, Determination of the rare earth elements in geological materials by inductively coupled plasma-mass spectrometry. Analytical Chemistry, v. 59, p. 1150-1157.
Manheim, F.T. and Gulbrandsen, R.A., 1979, Marine Phosphorites. in Burns, R.G. (ed.), Marine Minerals, Mineralogical Society of America Short Course Notes, v. 6, p. 151-173.
Parthé, E. and Crocket, J.H., 1978, Platinum group: in Wedepohl, K.H. (ed.) Handbook of Geochemistry, v. II/5, Springer-Verlag, Berlin, p. 78-A1-78-O7.
Peck, L.C., 1964, Systematic analysis of silicates. U.S. Geological Survey Bulletin 1170, 89 p.

Piper, D.Z., 1974, Rare earth elements in ferromanganese nodules and other marine phases. Geochimica et Cosmochimica Acta, v. 38, p. 1007-1022.

Pletnev, S.P., Ryaben'kaya, I., and Quinterno, P.J., 1994, Biostratigraphic results of cruise 91-AV-19/2, Karin Ridge, central Pacific Ocean. In Hein, J.R., and Bychkov, A.S., Data and Results From R.V. Aleksandr Vinogradov Cruises 91-AV-19/1, North Pacific Hydrochemistry Transect; 91-AV-19/2, North Equatorial Pacific Karin Ridge Fe-Mn Crust Studies; and 91-AV-19/4, Northwest Pacific and Bering Sea Sediment Geochemistry and Paleoceanographic Studies. U.S. Geological Survey Open File Report (In press, this volume).

Puteanus, D. and Halbach, P., 1988, Correlation of Co concentration and growth rate: a method for age determination of ferromanganese crusts. Chemical Geology, v. 69, p. 73-85.

Schlanger, S.O., Garcia, M.O., Keating, B.H., Naughton, J.J., Sager, W.W., Haggerty, J.A., and Philpotts, J.A., 1984, Geology and geochronology of the Line Islands. Journal of Geophysical Research, v. 89, p. 11,261-11,272.

Schulz, M.S. and Hein, J.R., 1991, Petrography and chemistry of hydrothermal manganese oxyhydroxides from the Mariana and Izu-Bonin volcanic arcs, West Pacific. U.S. Geological Survey Open File Report 91-557, 80 p.

Shapiro, L., 1975, Rapid analysis of silicate, carbonate, and phosphate rocks--revised edition. U.S. Geological Survey Bulletin 1401, 76 p.

Taggart, J.E., Lindsay, J.R., Scott, B.A., Vivit, D.V., Bartel, A.J., and Stewart, K.C., 1987, Analysis of geologic materials by wavelength-dispersive X-ray fluorescence spectrometry. in Baedecker, P.A. (ed.), Methods for Geochemical Analysis. U.S. Geological Survey Bulletin 1770, p. E1-E19.

Table 1. Station locations and operations on Karin Ridge for cruise 91-AV-19/2; see Figs. 1, 5, and 6 for locations

Station	Operation	Location
1	CM 1	Summit, northern area
1	CTDR 1	Summit, northern area
2	CM 2	Summit, southern area
3	D1	Northeast flank below summit
2	CTDR 2	Summit, southern area
4	HC 1	Southern area
5	D2	No recovery
6	CAM 1	Southwest flank
4	GC 1	Abyssal apron off southwest flank
7	D3	Southwest flank below summit
4	CTDR 3	Lower southwest flank
4	HC 2	Southern area
8	CAM 2	Summit, southern area
9	FFST 1	--
10	D4	Southwest flank
11	D5	Southwest flank
12	HC 3	Southern area
13	D6	No recovery
14	CTDR 4	Northeast flank
15	D7	Northeast flank
16	FFST 2	--
17	BC 1	Summit, northern area
18	GC 2	No recovery
19	D8	Northeast flank
20	D9	No recovery
21	CAM 3	Upper southwest flank and summit margin
14	HC 4	Northern area
14	GC 3	No recovery
22	D10	Northeast flank below summit
23	D11	Northeast flank below summit
14	HC5	Northern area
24	D12	No recovery
25	GC 4	Summit, northern area
26	BC 2	No recovery
27	CAM 4	Summit, northern area

CM = current meter mooring; CTDR = temperature, salinity, oxygen profiles; D = dredge; HC = hydrochemistry; CAM = camera survey; GC = gravity core; BC = box core; FFST = free-floating sediment trap

Table 2. Dredge summary for cruise 91-AV-19/2, Karin Ridge

Dredge Number	Location	Water Depth Corrected (m)	Recovery (Kg)	Crust Thickness (Max. mm)	Crust Thickness (Av. mm)	Dominant Substrate	Comments
D1	South ridge top	1900-1809	60	80	35	Hyaloclastite	--
D2	Base south flank	5100-4600	0	--	--	--	No recovery
CAM-1	South flank	4200-3600	10	8	5	Breccia	Collected on camera sled
D3	South flank	2600-2500	15	63[1]	30[1]	Breccia	Reworked crusts
D4	South flank	3300-2900	200	35	10	Basalt	Much phosphorite
D5	South flank	4300-3900	120	35	25	Basalt	80% nodules
D6	North ridge top	2100-1600	0	--	--	--	No recovery
D7	North flank	4850-4000	20	2	<1	Basalt	Talus
BC-1	North ridge top	2170	2	10	8	Breccia	Collected in box core
D8	North flank	4200-3700	70	22	10	Mudstone, basalt, breccia	Crusts on mudstone
D9	North flank	3200-2500	0	--	--	--	Lost dredge bag
D10	North flank	3400-2960	300	30	18	Mudstone	Monolithic
D11	North flank	3000-2450	350	25	10	Breccia	Cobbly breccia
D12	North ridge top	2000-1600	0	--	--	--	No recovery

[1]Recent growth layers have maximum thickness of 15 mm, which occur on old crust fragments up to 50 mm thick; average thickness of recent growth layers is 10 mm

Table 3. Location and description of dredge hauls, cruise 91-AV-19/2, Karin Ridge

Dredge No.	Latitude (°N)	Longitude (°E)	Total Recovery (Kg)	% Broken From Outcrop	% Talus	% of Rocks in Dredge Encrusted	Description of Ferromanganese Oxyhyroxides	Substrate Description
D1	16°39.66' 16°40.23'	168°19.76' 168°16.96'	60	20	80	99	Large to small botryoids on surface, current smoothed in places, granular on bottoms & sides; 1 to 3 layers: 1. outer, massive, mod-erately porous, 2. middle, porous to vuggy, 3. inner, dense, massive, with CFA veins & laminae; fragments of only inner & side layers; dendrites & disseminated in substrate in places; thickness: max.=80mm, av.=35mm	100% yellow-green altered hyaloclastite with CFA veins, laminae, and cement in places; 1 sample of bedded hyaloclastite; in places a CFA lamina separates crust from substrate; CFA pale to dark brown, very dense
D2	—	—	0	—	—	—	No Recovery	-
CAM-1	16°34.06'16° 36.21'	168°25.66' 168°19.76'	10	70	30	100	Thin crusts with current-smoothed botryoidal surface, polished, also lizard skin; 1 layer, massive, porous in places; thickness: max.=8mm, av.=5mm	75% breccia composed of brown, red-brown, & yellow-red-brown altered massive to vesicular basalt clasts & hornblende crystals in fine-grained matrix of same material; 25% two basalt talus cobbles, one gray, vesicular aphanitic, the other reddish-gray, plagioclase phyric
D3	16°33.98' 16°35.54'	168°21.52' 168°18.75'	15	100	0	100	Pronounced to subdued botryoids, current polished in places, lizard skin; young crust growth to 15 mm thick, resting on fragments of older, reworked, dense, massive, CFA-rich crusts (to 50 mm thick), which are probably the inner layers of once thick crusts; crust & Fe-Mn nodule fragments as clasts in breccia; Fe-Mn oxide cement in breccia	100% breccia composed of clasts of gray, red-brown, & brown basalt & fragments of Fe-Mn oxide crusts & nodules with dense, massive cement of Fe-Mn oxides and CFA; CFA veins
D4	16°34.03' 16°36.67'	168°28.71' 168°20.00'	200	10	90	100	Current smoothed & polished surfaces on crusts & nodules; nodules compose 20% of dredge haul, 70% have a large nucleus, 30% small nucleus; nuclei include nodule fragments (20%), hyaloclastite (30%), mudstone (20%), basalt (10%), CFA (10%), limestone (10%); most nodules are several coalesced nodules; crusts have 1 layer that is black, dense, & massive; vuggy in places with CFA infilling vugs; some crusts grew on fragments of older crusts; several rocks of intimately intermixed Fe-Mn oxides & CFA; thickness: max.=35mm, av.=10mm	90% pillow basalt fragments including a 80 kg complete pillow boulder; aphanitic to highly vesicular, some plagioclase phyric; altered outer cooling rind; some vesicles infilled with CFA or calcite; 5% breccia composed of highly altered vesicular red-brown basalt clasts in CFA cement or yellow-green altered hyaloclastite matrix; rare clasts of sandstone & CFA; 5% phosphorite, hard, dense gray-brown; gray, borings, & inpregnated with Fe-Mn oxides; pale brown softer, massive, burrowed
D5	16°31.81' 16°34.50'	168°25.62' 168°20.90'	120	99 10[1]	1 90[1]	100	80% small (to 60mm, av. 25mm diameter) nodules with smooth, granular, & lizard-skin surfaces; nuclei of Fe-Mn nodule fragments (60%), phosphorite (30%), basalt & hyalo-clastite (10%); 30% with small & 70% with large nucleus; crust with current-smoothed surface with up to 4 massive layers; thickness: max.=35mm, av.=25mm; several rocks of intimately intermixed Fe-Mn oxides and CFA	80% nodules; 18% pillow basalt fragment, vesicular, plagioclase phyric; 2% pale brown to cream-colored phosphorite, some intimately intermixed with Fe-Mn oxides

Table 3 Continued

D6	–	–	0	–	–	–	No recovery	–
D7	17°14.0' 17°14.5'	168°13.2' 168°16.7'	20	0	100	100 patina	Smooth to granular patchy patina on most rocks; 2% small nodules to 20mm (av. 6mm) diameter, dense & black, mostly pancake type	99% basalt: gray, aphanitic to plagio-clase phyric; as above but vesicular; some with alteration rinds; gray & brown aphanitic, sparsely vesicular & plagioclase phyric; 1% brown mud; cream-colored phosphorite pebble
BC-1	17°01.6'	168°18.2'	2	100	0	100	Botryoidal, smoothed, & lizard skin surface; 1 massive layer; thickness: max.=10mm, av.=8mm	Breccia composed of basalt clasts in CFA cement & altered hyaloclastite matrix; 1 siliceous sponge fragment; foraminiferal sand
D8	17°14.2' 17°13.6'	168°13.3' 168°16.2'	75	100	0	100	Current-smoothed, polished, subdued botryoidal, lizard-skin, & granular surfaces; 1 massive black layer, except 2 crusts on breccia have 2 massive layers separated by 1-mm thick porous zone; lines & infills borings in mudstone; thickness: max.=22mm, av.= 10mm	34% brown mudstone, borings, burrows; 33% basalt: a) vesicular mugearite, b) vesicular pillow fragments, c) gray plagioclase phyric; 33% breccia: a) red-brown, brown, & gray basalt clasts in altered hyaloclastite matrix, b) pillow breccia with CFA layers & vesicle fill, CFA cement & altered hyaloclastite matrix, highly vesicular basalt clasts
D9	–	–	0	–	–	–	Lost dredge bag	–
D10	17°11.2' 17°10.7'	168°15.8' 168°18.6'	300	100	0	100	Current-smoothed, lizard-skin, subdued botryoidal, granular, & current-polished surfaces; 1 black, dense, massive layer in sharp contact with substrate; lines borings; thickness: max.=30mm, av.=18mm	>99% mudstone: brown, poorly consolidated, burrows in places, yellowish to pale brown burrow fill, rarely bored; <1% phosphorite
D11	17°12.5' 17°11.2'	168°18.6' 168°18.6'	350	100	0	100	Current-smoothed, subdued botryoidal, polished, lizard-skin, & granular surfaces; 1 black dense to porous layer; thickness: max.=25mm, av.=10mm	100% breccia: a) brown basalt clasts (granule to cobble size) in yellow-green hyaloclastite matrix, poorly consoli-dated; b) brown, poorly consolidated, composed of brown to gray basalt (granule to cobble size) clasts in sandy volcaniclastic matrix; CFA lenses
D12	–	–	0	–	–	–	No recovery	–

[1]If nodules are considered talus; CFA = carbonate fluorapatite

Table 4. Location and description of box cores (BC) and gravity cores (GC), cruise 91-AV-19/2; GC-1 is from abyssal apron off southwest flank of Karin Ridge

Core No.	Water Depth (m)	Latitude (°N)	Longitude (°E)	Interval (cm)	Description
GC-1[1]	5130	16°27.3'	168°31.8'	0-52	5YR5/2, brown sandy mud, burrows increase down-section, gradational contact
				52-56	10YR4/2, dark yellowish-brown silty sand, calcareous, fissile, horizontal bedding, sharp planar contact
				56-76	5YR3/2 transition to 10YR/82 from 65-69 cm due to burrowing of mud; more calcareous with depth; contact sharp & irregular
				76-79	10YR8/2, pale orange, foraminiferal sand with lens of pale brown mud 10YR5/4 yellowish brown calcareous sandy mud with 5YR5/2 brown mud burrows; sharp planar contact
				79-92	10YR7/4, laminae & lenses (to 4 mm thick) of clean & muddy foraminiferal sand; sharp planar contact
				92-98	10YR8/2 to 5YR2/2, calcareous sandy mud; sharp irregular contact
				98-109	10YR8/2, foraminiferal sand; sharp irregular contact 5YR2/2 dark brown mud to 128 cm, then 10YR6/2 yellowish brown mud with dark
				109-111	brown burrows; sharp irregular contact
				111-138	Foraminiferal sand with dark sand-sized grains of volcanic glass, Fe-Mn crust fragments, & others; sharp irregular contact
				138-141	5YR2/2, brown grades into 10YR6/2, pale brown with brown burrows; calcareous sandy mud; contact gradational
				141-168	10YR8/2 to 5Y8/1, foraminiferal sand with dark sand-sized grains (10-50%); fissile horizontal bedding; sharp irregular contact
				168-202	10YR5/4, yellowish-brown calcareous sandy mud with dark brown burrows; sharp irregular contact
				202-218	5YR2/2, foraminiferal sand; fissile horizontal bedding, sharp planar contact Dark brown mud with burrows; sharp irregular contact
				218-220	10YR7/4, foraminifera-rich sandy silt with mud clasts to 2-3 cm; sharp planar contact
				220-240	Dark brown calcareous mud with foraminifera-rich lenses that increase in
				240-247	abundance down-section; gradational contact
				247-261	

Table 4 continued

Core No.	Water Depth (m)	Latitude (°N)	Longitude (°E)	Interval (cm)	Description
GC-1[1] cont.	--	--	--	261-280	10YR6/2, yellowish-brown foraminiferal sand with dark sand-sized grains (30-50%); sharp irregular contact
				280-307	5YR3/2, 10YR6/2, 5YR5/2, pale brown calcareous sandy mud with dark brown burrows decreasing down-section; upper 5 cm more pale & fissile; sharp irregular contact at base
				[285-320]	Section cut by coarse-grained, well sorted, pale yellowish-brown foraminiferal sand dike, 1-5 mm thick
				307-325	Dark brown mud with burrows; upper contact cut by dike
				325-345	10YR6/2, pale yellowish-brown calcareous sandy mud, homogeneous, rare burrows
BC-1	2170	17°01.6'	168°18.2'	--	Only rocks & Fe-Mn crusts; bottom plate did not seal & sediment was lost; traces of carbonate ooze
GC-2	--	--	--	--	No recovery
GC-3	--	--	--	--	No recovery
GC-4	1670	17°21.5'	168°41.0'	--	Core catcher only, pale brown foraminiferal sand with fragments of Fe-Mn crust
BC-2	--	--	--	--	No Recovery

[1]Description by V. Nechaev

Table 5. X-ray diffraction mineralogy of substrate rocks from cruise 91-AV-19/2, Karin Ridge

Sample Number	Major (>25%)	Moderate (5-25%)	Minor/Trace (<5%)	Rock/Sediment
D1-1	CFA[1]	Smectite	--	Phosphatized hyaloclastite
D1-10	CFA	--	Smectite, plagioclase	Phosphatized hyaloclastite
CAM 1-1C	Smectite	--	Plagioclase	Volcaniclastic breccia[2]
CAM 1-3	Plagioclase, pyroxene	--	Smectite	Vesicular basalt
D3-2	Plagioclase	CFA	Smectite, clinoptilolite	Basalt clast from breccia
D4-12-1B	CFA	Phillipsite	Plagioclase?, smectite?, quartz?	Phosphorite, poorly consolidated
D5-6	Phillipsite	--	--	Zeolite nodule
D8-6-2B	Plagioclase, smectite	Phillipsite	Clinoptilolite, pyroxene	Brown mudstone
D10-1-1	Plagioclase	Clinoptilolite, CFA, smectite	Pyroxene?, quartz?	Brown partly phosphatized mudstone
D10-1-2	Plagioclase, smectite	--	Clinoptilolite	Yellow waxy burrow fill in sample D10-1-1
D10-2-1	Clinoptilolite	--	Quartz?	Pale yellow burrow fill in brown mudstone
D10-4	Smectite	--	--	Greyish-yellow mudstone
D11-1-1A	Plagioclase	Smectite	--	Altered breccia
D11-1-1B	Plagioclase	--	--	Grey-brown crystals in breccia
D11-2-2	Plagioclase, pyroxene	Smectite	--	Yellowish-green breccia
D11-3-4	Calcite	--	--	Vesicle fill in basalt

[1]CFA is carbonate fluorapatite
[2]All breccias are sedimentary, and most are volcaniclastic

Table 6. Chemical composition of selected substrate rocks from cruise 91-AV-19/2, Karin Ridge

	D1-10	CAM 1-1C	CAM 1-3	D4-12-1B	D8-6-2B	D10-1-1	D11-3-3a	D11-3-3b
SiO_2 wt. %	21.6	38.5	47.5	15.6	41.1	44.1	49.5	50.6
Al_2O_3	7.12	9.55	16.7	4.00	14.1	10.9	14.5	14.8
FeO	<0.01	0.69	1.79	--	0.46	0.42	12.7	11.2
Fe_2O_3	8.20	11.2	10.2	2.61	13.4	10.0	-	-
MgO	1.85	12.9	2.89	1.39	2.63	2.51	5.26	5.66
CaO	25.0	2.81	8.33	36.8	1.14	4.63	9.14	8.41
Na_2O	1.54	1.76	3.25	1.05	2.57	3.27	2.36	2.43
K_2O	1.63	1.00	2.44	1.47	2.04	2.40	1.21	1.38
TiO_2	1.71	2.15	3.93	0.24	3.19	2.12	4.21	3.48
P_2O_5	15.6	0.25	0.94	23.2	0.40	2.42	0.42	0.31
MnO	0.32	0.18	0.10	0.66	0.22	0.05	Cl = 0.04	Cl = 0.04
LOI	13.9	19.5	3.72	9.54	19.1	16.7	SO_3 = 0.18	SO_3 = 0.38
Total	98.47	100.49	101.79	96.56	100.35	99.52	99.53	98.69
H_2O^+	2.33	3.72	0.54	1.25	0.84	1.23	-	-
H_2O^-	7.30	12.54	2.75	3.60	14.01	11.00	-	-
CO_2	2.26	0.21	0.02	3.40	0.07	0.35	-	-
Rock Type	Phosphatized hyaloclastite	Altered breccia	Vesicular basalt	Phosphorite	Mudstone	Partly phosphatized mudstone	Glass from hyaloclastite	Glass in plagioclase, hyaloclastite

Analysis by X-ray fluorescence, except D11 by microprobe; LOI is loss on ignition at 925°C; double dash means could not be determined due to interference, single dash means not determined; all iron calculated as FeO for glass samples; MnO and LOI not determined for D11; low totals for phosphorite are due to high F and S contents; X-ray fluorescence analysts: M.J. Schutt and D.F. Siems; microprobe, A. Davis

Table 7. X-ray diffraction mineralogy of Fe-Mn crusts and nodules from cruise 91-AV-19/2, Karin Ridge

Sample Number	Type & Interval (mm)[1]	δ-MnO_2 (%)[2]	Others (%)
D1-2A	Crust layer (0-10)	99	1-quartz
D1-2B	Crust layer (10-30)	99	1-quartz
D1-2C	Crust layer (30-72)	91	9-CFA
D1-2D	Bulk crust (0-72)	96	4-CFA
D1-2E	Surface scrape (0-0.5)	99	1-quartz
D1-3	Surface scrape (0-0.5)	>99	<1-quartz?
D1-5	Surface scrape (0-0.5)	>99	<1-quartz; halite
D1-2, -3, -5	Composite surface scrape (0-0.5)	99	1-quartz
CAM 1-1A	Bulk crust (0-6)	100	–
CAM 1-1B	Surface scrape (0-0.5)	92	8-quartz
CAM 1-1D & CAM 1-5	Composite surface scrape (0-0.5)	99	1-halite
D3-1A	Surface scrape (0-0.5)	98	2-quartz+plagioclase+calcite
D3-1B	Bulk crust (0-13)	98	1-quartz; 1-plagioclase
D4-6-1	Nodule (0-45) + nucleus	96	2-plagioclase; 2-quartz
D4-8, -12	Composite surface scrape (0-0.5)	96	3-CFA; 1-plagioclase+quartz
D4-12-1A	Bulk crust (0-16)	97	2-plagioclase; 1-quartz
D5-1-1	Composite of 4 nodules + nuclei (0-25)	96	3-plagioclase; 1-quartz
D5-2	Surface scrape (0-0.5)	99	1-quartz
D5-3-1	Bulk crust (0-30)	99	1-quartz
BC-1-2	Surface scrape (0-0.5)	99	1-quartz
D8-3-1	Bulk crust (0-7)	99	1-quartz
D8-3-2	Surface scrape (0-0.5)	>99	<1-quartz
D8-4-1	Bulk crust (0-16)	94	3-K-feldspar; 2-plagioclase; 1-quartz
D8-4-2	Surface scrape (0-0.5)	99	1-quartz
D8-1, -3, -4, -5, -6	Composite surface scrape (0-0.5)	99	1-quartz
D8-6-2A	Bulk crust (0-18)	99	1-quartz
D10-1-3	Surface scrape, granular crust (0-0.5)	99	1-quartz
D10-1-4	Bulk granular crust (0-15)	95	4-plagioclase; 1-quartz
D10-1-5	Bulk lizard-skin crust (0-15)	97	2-plagioclase; 1-quartz
D10-1-6	Surface scrape, lizard skin type (0-0.5)	>99	<1-quartz
D11-1-2	Bulk crust (0-10)	97	2-plagioclase; 1-quartz
D11-1-3	Surface scrape (0-0.5)	100	–
D11-2-1	Bulk crust (0-11)	99	1-quartz
D11-2-3	Surface scrape (0-0.5)	99	1-plagioclase

[1]Intervals measured from outer surface of crusts and nodules

[2]Percentages were determined by using the following weighting factors relative to quartz set at 1: δ-MnO_2 70 (Hein et al., 1988); carbonate fluorapatite (CFA) 3.1; plagioclase 2.8; calcite 1.65; smectite 3.0; phillipsite 17.0; pyroxene 5.0; (from Cook et al., 1975); the limit of detection for each mineral falls between 0.2 and 1.0%, except the manganese minerals which are greater, perhaps as much as 5-10% for δ-MnO_2

Table 8. Chemical composition of ferromanganese oxyhydroxide crusts and nodules

	D1-2A[1]	D1-2B	D1-2C	D1-2D	D1-2,3,5	CAM1-1A	CAM1-1B	CAM1-1D	D3-1A	D3-1B	D4-6-1	D4-12-1A
Fe wt. %	14.0	13.0	9.1	12.0	13.0	13.0	13.0	14.0	13.0	13.0	12.0	16.0
Mn	19.0	18.0	20.0	19.0	18.0	18.0	16.0	17.0	17.0	18.0	13.0	15.0
Mn/Fe	1.4	1.4	2.2	1.6	1.4	1.4	1.2	1.2	1.3	1.4	1.1	0.9
Si	2.9	3.0	1.0	2.0	2.9	3.2	3.0	2.9	3.2	3.8	7.5	5.1
Na	1.4	1.3	1.2	1.3	1.5	1.4	1.9	2.2	1.5	1.4	1.3	1.3
Al	0.37	0.57	0.17	0.33	0.37	0.36	0.41	0.41	0.54	0.68	2.0	0.97
K	0.43	0.52	0.44	0.43	0.39	0.34	0.37	0.39	0.35	0.45	1.00	0.48
Mg	0.89	0.82	0.75	0.8	0.96	0.96	1.00	1.00	0.99	0.86	0.86	0.78
Ca	1.9	2.1	7.6	3.2	2.1	2.1	1.9	1.8	1.9	1.8	3.0	1.8
Ti	0.88	0.94	0.47	0.78	0.72	0.72	0.85	0.85	0.78	0.93	0.94	1.2
P	0.39	0.33	0.24	0.75	0.43	0.41	0.32	0.31	0.36	0.28	0.81	0.29
H_2O^+	9.7	8.9	7.9	7.2	8.1	9.8	8.0	8.5	8.5	10.8	9.6	11.1
H_2O^-	22.2	23.4	19.7	24.3	27.2	21.6	27	26.9	25.2	20.3	19.8	19.7
CO_2	0.41	0.35	1.20	0.53	0.69	0.42	0.52	0.38	0.61	0.38	0.44	0.37
LOI	35.9	37.2	32.8	38.0	40.7	35.7	40.7	41.4	38.9	34.2	31.6	32.6
Ni ppm	3000	3300	3600	3400	2900	2900	2400	2400	3200	3800	2600	2100
Cu	230	770	750	670	120	120	350	350	410	980	2300	1800
Zn	490	610	710	590	500	470	420	410	560	580	540	550
Co	7100	4200	3500	4900	6600	6400	5200	5000	4400	4900	2500	3100
Ba	1100	1800	2200	1700	750	730	740	760	840	1300	1500	1600
Mo	440	380	710	510	300	290	200	240	230	350	170	250
Sr	1400	1400	1600	1400	1200	1200	1100	1100	1100	1200	1000	1200
Ce	860	1300	2000	1300	820	780	1100	1100	670	770	930	1100
Y	170	140	160	150	150	150	140	140	140	130	190	140
V	580	540	620	560	560	540	460	450	540	500	350	480
Pb	1500	1200	2100	1500	1300	1300	1100	1300	1300	1300	840	950
Cr	6.1	3.8	4.0	2.3	5.1	5.5	30.0	3.4	3.5	4.1	7.7	5.9
Cd	2.5	2.2	2.7	2.5	3.0	3.1	2.5	2.3	2.9	2.7	1.9	1.8
As	260	200	160	190	250	210	220	230	230	210	110	190
Interval[2]	L 0-10	L 10-30	L 30-72	B 0-72	S 0-0.5	B 0-6	S 0-0.5	S 0-0.5	S 0-0.5	B 0-13	B 0-45	B 0-16
Type	Crust	Crust	Crust	Crust	Crust	Crust	Crust	Crust	Crust	Crust	Nodule	Crust

Table 8 Continued

	D4-8,12	D5-1-1	D5-2	D5-3-1	BC 1-2	D8-3-1	D8-3-2	D8-4-1	D8-4-2	D8-6-2A	D8-1, 3-6	D10-1-3
Fe wt. %	15.0	14.0	15.0	15.0	13.0	17.0	14.0	16.0	16.0	17.0	15.0	17.0
Mn	16.0	14.0	14.0	17.0	17.0	15.0	15.0	13.0	14.0	14.0	14.0	13.0
Mn/Fe	1.1	1.0	0.9	1.1	1.3	0.9	1.1	0.8	0.9	0.8	0.9	0.8
Si	3.3	5.1	3.9	3.1	3.4	4.0	3.6	5.6	4.4	4.0	4.5	4.7
Na	1.5	1.3	1.6	1.3	1.5	1.2	1.5	1.3	1.4	1.2	1.5	1.5
Al	0.43	1.50	0.62	0.54	0.43	0.66	0.60	1.30	0.84	0.74	0.85	0.77
K	0.34	0.55	0.38	0.37	0.36	0.36	0.39	0.50	0.42	0.34	0.45	0.42
Mg	0.99	0.92	0.96	0.80	0.94	0.81	0.95	0.83	0.96	0.77	0.92	0.95
Ca	1.9	2.0	1.7	1.7	2.2	1.6	1.7	1.6	1.6	1.6	1.7	1.7
Ti	0.80	1.30	0.93	1.20	0.72	1.20	0.94	1.30	1.00	1.30	0.98	0.99
P	0.39	0.42	0.32	0.28	0.40	0.31	0.33	0.29	0.32	0.29	0.33	0.35
H_2O^+	11.7	9.1	9.6	6.8	6.7	9.4	7.1	8.7	7.6	7.4	8.2	6.6
H_2O^-	26.3	23.5	26.8	24.1	27.0	21.8	27.7	21.4	25.8	24.8	25.2	25.4
CO_2	0.48	0.35	0.47	0.32	0.70	0.39	0.42	0.33	0.42	0.38	0.46	0.43
LOI	39.4	35.7	40.0	37.2	40.2	35.0	40.7	33.9	39.1	37.4	38.3	38.0
Ni ppm	2100	2600	1600	2300	2800	1600	1900	1500	1400	1400	1600	1300
Cu	470	1300	480	770	200	630	460	610	500	790	530	380
Zn	450	480	460	470	490	460	430	460	430	460	430	470
Co	4000	3400	3800	4200	5400	3600	4000	2800	3400	3000	3400	3400
Ba	800	1200	820	1400	810	1200	760	1300	850	1400	870	930
Mo	190	170	130	320	240	250	150	210	110	250	130	96
Sr	1100	940	1000	1200	1200	1200	1000	1100	1000	1100	1000	1100
Ce	1100	1200	1400	1300	750	1400	1400	1300	1600	1300	1400	1300
Y	140	150	130	170	150	170	130	170	130	170	130	140
V	500	400	460	490	520	470	450	460	460	480	470	450
Pb	1100	930	1000	1000	1200	1300	990	930	1000	1000	1100	1200
Cr	2.9	12.0	5.7	2.0	5.1	4.2	6.4	11.0	7.3	3.8	9.8	6.7
Cd	2.4	4.7	2.2	1.8	2.8	2.3	2.3	1.7	2.3	1.6	2.4	1.9
As	230	150	200	210	220	190	170	190	150	210	150	190
Pt ppb	-	-	-	130	-	-	-	-	-	88	-	-
Pd	-	-	-	0.5	-	-	-	-	-	0.5	-	-
Rh	-	-	-	9.5	-	-	-	-	-	7.5	-	-
Ru	-	-	-	14	-	-	-	-	-	11	-	-
Ir	-	-	-	3.9	-	-	-	-	-	3.0	-	-
Interval[2]	S 0-0.5	B 0-25	S 0-0.5	B 0-30	S 0-0.5	B 0-7	S 0-0.5	B 0-16	S 0-0.5	B 0-18	S 0-0.5	S 0-0.5
Type	Crust	Nodules	Crust	Crust	Crust	Crust	Crust	Crust	Crust	Crust	Crust	Crust

Table 8 Continued

	D10-1-4	D10-1-5	D10-1-6	D11-1-2	D11-1-3	D11-2-1	D11-2-3
Fe wt. %	16.0	17.0	16.0	15.0	15.0	14.0	15.0
Mn	13.0	14.0	14.0	16.0	15.0	17.0	15.0
Mn/Fe	0.8	0.8	0.9	1.1	1.0	1.2	1.0
Si	6.1	4.3	4.0	3.7	3.3	3.3	3.4
Na	1.3	1.2	1.3	1.3	1.5	1.3	1.6
Al	1.30	0.62	0.51	0.58	0.30	0.50	0.41
K	0.52	0.35	0.37	0.39	0.32	0.39	0.35
Mg	0.79	0.76	0.86	0.80	0.97	0.82	1.00
Ca	1.7	1.6	1.7	1.7	1.9	1.7	1.9
Ti	1.20	1.00	0.89	0.97	0.72	1.00	0.78
P	0.30	0.30	0.37	0.29	0.41	0.29	0.38
H_2O^+	12.7	8.1	7.8	7.4	6.2	7.8	6.6
H_2O^-	21.0	22.5	27.6	24.4	27.0	24.1	26.6
CO_2	0.34	0.38	0.54	0.41	0.61	0.41	0.52
LOI	33.4	35.4	40.0	37.5	40.4	37.5	38.6
Ni ppm	1600	1600	1600	2400	2000	2700	2100
Cu	790	710	350	740	260	750	230
Zn	510	510	470	440	460	460	440
Co	3100	3200	3600	4900	3700	5400	4200
Ba	1500	1300	830	1100	740	1100	740
Mo	220	280	120	300	170	320	170
Sr	1100	1200	1100	1100	1100	1200	1100
Ce	960	1000	1200	870	930	940	990
Y	170	150	140	170	150	170	150
V	460	510	470	450	520	450	450
Pb	990	1200	1100	1000	1100	1200	1100
Cr	19.0	3.5	3.4	5.9	5.2	5.6	2.5
Cd	1.7	1.7	2.1	1.9	2.4	2.2	2.4
As	130	180	170	160	170	150	160
Pt ppb	100	89	-	150	-	120	-
Pd	1.2	1.3	-	0.6	-	0.8	-
Rh	7.6	6.1	-	8.0	-	8.0	-
Ru	13	11	-	14	-	14	-
Ir	3.1	2.8	-	3.6	-	3.7	-
Interval[2]	B 0-15	B 0-15	S 0-0.5	B 0-10	S 0-0.5	B 0-11	S 0-0.5
Type	Crust	Crust	Crust	Crust	Crust	Crust	Crust

- Major and minor elements determined by Inductively Coupled Plasma-Atomic Emission Spectrometry (ICP-AES): except K, Zn, Pb by Flame Atomic Absorption Spectroscopy, and As, Cr, Cd by Graphite-Furnace Atomic Absorption Spectroscopy; Pt group elements determined by ICP-Mass Spectroscopy
- Analysts: W.M. d'Angelo, J.H. Bullock, H. Smith

[1]Sample numbers that are identical except for suffixes -A, -B, -C, and -D represent different sample intervals from the same crust

[2]Intervals are measured from the outer surface of the crust; B = bulk, the entire crust thickness was sampled and analyzed; L = layer; N = nodule; S = scraped surface: 0-0.5 mm; Dash (-) means not analyzed

Table 9. Hygroscopic water-free (0% H_2O^-) composition of ferromanganese oxyhydroxide crusts from Table 8

	D1-2A	D1-2B	D1-2C	D1-2D	D1-2,3,5	CAM1-1A	CAM1-1B	CAM1-1D	D3-1A	D3-1B	D4-6-1	D4-12-1A
Fe wt. %	19.8	18.9	12.6	17.8	20.0	18.4	20.2	21.4	19.5	17.9	16.4	21.7
Mn	26.8	26.2	27.6	28.2	27.7	25.4	24.9	26.0	25.6	24.8	17.8	20.3
Si	4.1	4.4	1.4	3.0	4.5	4.5	4.7	4.4	4.8	5.2	10.3	6.9
Na	2.0	1.9	1.7	1.9	2.3	2.0	3.0	3.4	2.3	1.9	1.8	1.8
Al	0.52	0.83	0.23	0.49	0.57	0.51	0.64	0.63	0.81	0.94	2.74	1.31
K	0.61	0.76	0.61	0.64	0.60	0.48	0.58	0.60	0.53	0.62	1.37	0.65
Mg	1.26	1.19	1.03	1.19	1.47	1.36	1.56	1.53	1.49	1.18	1.18	1.06
Ca	2.7	3.1	10.5	4.8	3.2	3.0	3.0	2.7	2.9	2.5	4.1	2.4
Ti	1.24	1.37	0.65	1.16	1.11	1.02	1.32	1.30	1.17	1.28	1.29	1.62
P	0.55	0.48	0.33	1.11	0.66	0.58	0.50	0.47	0.54	0.39	1.11	0.39
H_2O^+	13.7	13.0	10.9	10.7	12.4	13.9	12.4	13.0	12.8	14.9	13.1	15.0
CO_2	0.58	0.51	1.66	0.79	1.06	0.59	0.81	0.58	0.92	0.52	0.60	0.50
Ni ppm	4234	4802	4967	5052	4456	4100	3733	3664	4810	5229	3558	2842
Cu	325	1120	1035	996	184	170	544	534	616	1349	3147	2436
Zn	692	888	980	877	768	664	653	626	842	798	739	744
Co	10020	6112	4829	7281	10140	9047	8088	7633	6613	6743	3421	4196
Ba	1552	2619	3035	2526	1152	1032	1151	1160	1263	1789	2053	2166
Mo	621	553	980	758	461	410	311	366	346	482	233	338
Sr	1976	2037	2208	2080	1844	1696	1711	1679	1653	1651	1368	1624
Ce	1214	1892	2759	1932	1260	1103	1711	1679	1007	1060	1273	1489
Y	240	204	221	223	230	212	218	214	210	179	260	189
V	819	786	855	832	860	763	715	687	812	688	479	650
Pb	2117	1746	2897	2229	1997	1838	1711	1984	1954	1789	1149	1286
Cr	8.6	5.5	5.5	3.4	7.8	7.8	46.7	5.2	5.3	5.6	10.5	8.0
Cd	3.5	3.2	3.7	3.7	4.6	4.4	3.9	3.5	4.4	3.7	2.6	2.4
As	367	291	221	282	384	297	342	351	346	289	151	257

Table 9 Continued

	D4-8,12	D5-1-1	D5-2	D5-3-1	BC 1-2	D8-3-1	D8-3-2	D8-4-1	D8-4-2	D8-6-2A	D8-1, 3-6	D10-1-3
Fe wt. %	22.3	20.3	22.9	22.3	20.2	24.0	22.1	22.6	24.2	25.4	22.6	25.7
Mn	23.8	20.3	21.4	25.2	26.4	21.2	23.7	18.4	21.2	20.9	21.1	19.7
Si	4.9	7.5	5.9	4.6	5.3	5.6	5.7	7.9	6.7	6.0	6.8	7.1
Na	2.2	1.8	2.4	1.9	2.3	1.7	2.3	1.8	2.1	1.8	2.2	2.2
Al	0.64	2.18	0.95	0.80	0.67	0.93	0.95	1.84	1.27	1.11	1.28	1.17
K	0.51	0.80	0.58	0.55	0.56	0.51	0.62	0.71	0.64	0.51	0.68	0.64
Mg	1.47	1.34	1.47	1.19	1.46	1.14	1.50	1.17	1.45	1.15	1.38	1.44
Ca	2.8	2.9	2.6	2.5	3.4	2.3	2.7	2.3	2.4	2.4	2.6	2.6
Ti	1.19	1.89	1.42	1.78	1.12	1.69	1.49	1.84	1.51	1.94	1.47	1.50
P	0.58	0.61	0.49	0.42	0.62	0.44	0.52	0.41	0.48	0.43	0.50	0.53
H_2O^+	17.4	13.2	14.7	10.1	10.4	13.3	11.2	12.3	11.5	11.1	12.3	10.0
CO_2	0.71	0.51	0.72	0.47	1.09	0.55	0.66	0.47	0.64	0.57	0.69	0.65
Ni ppm	3122	3779	2448	3413	4351	2256	3003	2119	2121	2092	2406	1968
Cu	699	1889	734	1143	311	888	727	862	757	1180	797	575
Zn	669	698	704	698	761	649	680	650	651	687	647	711
Co	5946	4941	5814	6233	8391	5077	6323	3956	5150	4483	5113	5146
Ba	1189	1744	1255	2078	1259	1692	1201	1837	1288	2092	1308	1408
Mo	282	247	199	475	373	353	237	297	167	374	195	145
Sr	1635	1366	1530	1781	1865	1692	1581	1554	1515	1644	1504	1665
Ce	1635	1744	2142	1929	1165	1974	2213	1837	2424	1942	2105	1968
Y	208	218	199	252	233	240	205	240	197	254	195	212
V	743	581	704	727	808	663	711	650	697	717	707	681
Pb	1635	1352	1530	1484	1865	1833	1565	1314	1515	1494	1654	1816
Cr	4.3	17.4	8.7	3.0	7.9	5.9	10.1	15.5	11.1	5.7	14.7	10.1
Cd	3.6	6.8	3.4	2.7	4.4	3.2	3.6	2.4	3.5	2.4	3.6	2.9
As	342	218	306	312	342	268	269	268	227	314	226	288
Pt ppb	-	-	-	193	-	-	-	-	-	131	-	-
Pd	-	-	-	0.7	-	-	-	-	-	0.7	-	-
Rh	-	-	-	14.1	-	-	-	-	-	11.2	-	-
Ru	-	-	-	21	-	-	-	-	-	16	-	-
Ir	-	-	-	5.8	-	-	-	-	-	4.5	-	-

Table 9 Continued

	D10-1-4	D10-1-5	D10-1-6	D11-1-2	D11-1-3	D11-2-1	D11-2-3
Fe wt. %	22.0	24.5	24.9	22.3	23.6	20.7	23.3
Mn	17.8	20.2	21.8	23.8	23.6	25.2	23.3
Si	8.3	6.2	6.3	5.5	5.1	4.9	5.2
Na	1.7	1.7	2.0	1.9	2.3	2.0	2.5
Al	1.78	0.89	0.79	0.86	0.47	0.74	0.64
K	0.71	0.51	0.58	0.58	0.50	0.58	0.54
Mg	1.08	1.10	1.34	1.19	1.52	1.21	1.55
Ca	2.3	2.3	2.6	2.5	3.0	2.5	3.0
Ti	1.65	1.44	1.39	1.44	1.13	1.48	1.21
P	0.41	0.43	0.58	0.43	0.64	0.43	0.59
H_2O^+	17.4	11.7	12.2	11.0	9.7	11.6	10.2
CO_2	0.47	0.55	0.84	0.61	0.96	0.61	0.81
Ni ppm	2196	2309	2493	3575	3141	4000	3261
Cu	1084	1025	545	1102	408	1111	357
Zn	700	736	732	655	722	682	683
Co	4255	4618	5610	7298	5811	8000	6522
Ba	2059	1876	1293	1638	1162	1630	1149
Mo	302	404	187	447	267	474	264
Sr	1510	1732	1714	1638	1728	1778	1708
Ce	1318	1443	1870	1296	1461	1393	1537
Y	233	216	218	253	236	252	233
V	631	736	732	670	817	667	699
Pb	1359	1732	1714	1489	1728	1778	1708
Cr	26.1	5.1	5.3	8.8	8.2	8.3	3.9
Cd	2.3	2.5	3.3	2.8	3.8	3.3	3.7
As	178	260	265	238	267	222	248
Pt ppb	137	128	-	223	-	178	-
Pd	1.6	1.9	-	0.9	-	1.2	-
Rh	10.4	8.8	-	11.9	-	11.9	-
Ru	18	16	-	21	-	21	-
Ir	4.3	4.0	-	5.4	-	5.5	-

Table 10. Statistics for 31 Fe-Mn bulk crusts, crust layers, and nodules from Karin Ridge, data from Table 8

		N	MEAN	MEDIAN	SD[1]	MIN[2]	MAX[3]	NM[4]
Fe	wt. %	31	14.4	15.0	1.8	9.1	17.0	21.3
Mn		31	15.7	15.0	2.0	13.0	20.0	23.2
Mn/Fe		31	1.1[5]	1.1	0.3	0.8	2.2	1.1
Si		31	3.8	3.8	1.2	1.0	7.5	5.6
Na		31	1.4	1.4	0.2	1.2	2.2	2.1
Al		31	0.67	0.57	0.39	0.17	2.00	0.97
K		31	0.42	0.39	0.12	0.32	1.00	0.62
Mg		31	0.89	0.89	0.08	0.75	1.00	1.30
Ca		31	2.1	1.8	1.1	1.6	7.6	3.0
Ti		31	0.94	0.94	0.20	0.47	1.30	1.38
P		31	0.36	0.33	0.12	0.24	0.81	0.53
H_2O^+		31	8.5	8.1	1.6	6.2	12.7	12.5
H_2O^-		31	24.2	24.4	2.6	19.7	27.7	0
CO_2		31	0.47	0.42	0.17	0.32	1.20	0.70
LOI		31	37.3	37.5	2.7	31.6	41.4	-
Ni	ppm	31	2313	2300	715	1300	3800	3403
Cu		31	639	530	465	120	2300	924
Zn		31	491	470	66	410	710	722
Co		31	4203	4000	1140	2500	7100	6220
Ba		31	1118	1100	381	730	2200	1634
Mo		31	255	240	128	96	710	372
Sr		31	1153	1100	141	940	1600	1699
Ce		31	1131	1100	288	670	2000	1670
Y		31	151	150	16	130	190	222
V		31	487	470	54	350	620	719
Pb		31	1166	1100	238	840	2100	1718
Cr		31	6.6	5.2	5.5	2.0	30.0	9.7
Cd		31	2.3	2.3	0.6	1.6	4.7	3.5
As		31	188	190	35	110	260	279
Pt	ppb	6	113	110	25	88	150	165
Pd		6	0.8	0.7	0.3	0.5	1.3	1.2
Rh		6	8	8	1	6	9	11
Ru		6	13	13	1	11	14	19
Ir		6	3.35	3.35	0.44	2.80	3.90	4.92
Depth[6]		9	3059	3100	807	1855	4100	-

[1]Standard deviation
[2]Minimum
[3]Maximum
[4]Mean of hygroscopic water free data (0% H_2O^-) for bulk crusts from Table 9; less-than values were normalized from the values of one half their respective limits of detection
[5]Ratio of the Fe and Mn means, not a mean of the summation of ratios
[6]Water depth in meters

Table 11. Statistics for 12 bulk Fe-Mn crusts from Karin Ridge, data from Table 8

	N	MEAN	MEDIAN	SD[1]	MIN[2]	MAX[3]	NM[4]
Fe wt. %	12	15.1	15.5	1.7	12.0	17.0	21.6
Mn	12	15.7	15.5	2.0	13.0	19.0	22.6
Mn/Fe	12	1.1[5]	1.0	0.3	0.8	1.6	-
Si	12	4.0	3.9	1.1	2.0	6.1	5.7
Na	12	1.3	1.3	0.1	1.2	1.4	1.8
Al	12	0.71	0.64	0.32	0.33	1.30	1.00
K	12	0.41	0.39	0.06	0.34	0.52	0.59
Mg	12	0.81	0.80	0.05	0.76	0.96	1.17
Ca	12	1.8	1.7	0.4	1.6	3.2	2.6
Ti	12	1.07	1.10	0.19	0.72	1.30	1.53
P	12	0.34	0.29	0.13	0.28	0.75	0.49
H_2O^+	12	8.9	8.4	1.8	6.8	12.7	12.7
H_2O^-	12	22.5	22.1	1.8	19.7	24.8	0
CO_2	12	0.39	0.38	0.05	0.32	0.53	0.56
LOI	12	35.6	35.5	1.8	32.6	38.0	-
Ni ppm	12	2275	2200	794	1400	3800	3265
Cu	12	780	745	380	120	1800	1112
Zn	12	497	470	51	440	590	712
Co	12	4125	3900	1162	2800	6400	5932
Ba	12	1302	1300	257	730	1700	1868
Mo	12	296	285	80	210	510	426
Sr	12	1183	1200	83	1100	1400	1698
Ce	12	1085	1050	227	770	1400	1560
Y	12	159	170	14	130	170	229
V	12	487	480	35	450	560	699
Pb	12	1139	1100	185	930	1500	1635
Cr	12	6.1	4.8	4.7	2.0	19.0	8.6
Cd	12	2.1	1.8	0.5	1.6	3.1	3.0
As	12	185	190	26	130	210	265
Pt ppb	6	113	110	25	88	150	165
Pd	6	0.8	0.7	0.3	0.5	1.3	1.2
Rh	6	8	8	1	6	9	11
Ru	6	13	13	1	11	14	19
Ir	6	3.3	3.3	0.4	2.8	3.9	4.9
Depth[6]	8	3170	3140	786	1855	4100	-
Thickness[7]	12	19	15	18	6	72	-

[1]Standard deviation
[2]Minimum
[3]Maximum
[4]Mean of hygroscopic water free data (0% H_2O^-) for bulk crusts from Table 9; less-than values were normalized from the values of one half their respective limits of detection
[5]Ratio of the Fe and Mn means, not a mean of the summation of ratios
[6]Water depth in meters
[7]Crust thickness in millimeters

Table 12. Statistics for 14 crust surfaces from Karin Ridge, data from Table 8

	N	MEAN	MEDIAN	SD[1]	MIN[2]	MAX[3]	NM[4]
Fe Wt %	14	14.6	15.0	1.3	13.0	17.0	22.3
Mn	14	15.4	15.0	1.5	13.0	18.0	23.6
Mn/Fe	14	1.1[5]	1.0	0.2	0.8	1.4	1.1
Si	14	3.6	3.4	0.6	2.9	4.7	5.5
Na	14	1.6	1.5	0.2	1.3	2.2	2.4
Al	14	0.53	0.47	0.18	0.3	0.85	0.82
K	14	0.38	0.37	0.03	0.32	0.45	0.58
Mg	14	0.96	0.96	0.04	0.86	1.00	1.47
Ca	14	1.8	1.8	0.2	1.6	2.2	2.8
Ti	14	0.85	0.85	0.10	0.72	1.00	1.30
P	14	0.36	0.35	0.04	0.31	0.43	0.55
H_2O^+	14	7.9	7.9	1.4	6.2	11.7	12.2
H_2O^-	14	26.5	26.8	0.8	25.2	27.7	0
CO_2	14	0.52	0.50	0.10	0.38	0.70	0.80
LOI	14	39.7	40.0	1.0	38	41.4	-
Ni ppm	14	2093	2050	585	1300	3200	3213
Cu	14	364	365	123	120	530	556
Zn	14	459	455	39	410	560	703
Co	14	4293	4000	942	3400	6600	6593
Ba	14	803	805	58	740	930	1231
Mo	14	177	170	60	96	300	271
Sr	14	1086	1100	66	1000	1200	1667
Ce	14	1126	1100	276	670	1600	1727
Y	14	140	140	8	130	150	215
V	14	483	465	38	450	560	741
Pb	14	1135	1100	109	990	1300	1741
Cr	14	6.9	5.1	6.9	2.5	30.0	10.7
Cd	14	2.4	2.4	0.3	1.9	3.0	3.7
As	14	196	195	34	150	250	300
Depth[6]	9	3059	3100	807	1855	4100	-

[1]Standard deviation
[2]Minimum
[3]Maximum
[4]Mean of hygroscopic water free data (0% H_2O^-) for bulk crusts from Table 9; less-than values were normalized from the values of one half their respective limits of detection
[5]Ratio of the Fe and Mn means, not a mean of the summation of ratios
[6]Water depth in meters

Table 13. Mean concentrations of selected elements in various groups of Fe-Mn crusts from Karin Ridge compared with deposits from other areas

	Fe %	Mn %	Mn/Fe[6]	Al %	P %	Co ppm	Cu ppm	Ni ppm	Mo ppm	Cr ppm	Pt ppb
All bulk crusts, n = 12 (Pt = 6)	15.1	15.7	1.1	0.71	0.34	4125	780	2275	296	6.1	113
Crust surface, ≤ 0.5 mm, n = 14	14.6	15.4	1.1	0.53	0.36	4293	364	2093	177	6.9	--
Bulk crusts ≤ 10 mm thick, n = 3	15.0	16.3	1.1	0.53	0.34	4967	497	2300	280	5.2	--
Bulk crusts 10-20 mm thick, n =7 (Pt = 4)	15.6	14.9	1.0	0.87	0.29	3643	919	2100	269	7.6	99
Bulk crusts ≥ 20 mm, n = 2	13.5	18.0	1.3	0.43	0.51	4550	720	2850	415	2.1	--
Bulk nodules, n = 2	13.0	13.5	1.0	1.75	0.62	2950	1800	2600	170	9.9	--
Johnston Island EEZ bulk crusts mean[1], n = 97 (Pt = 25)	13.7	19.2	1.4	0.63	0.47	5792	848	3518	380	6.4	174
Marshall Islands EEZ bulk crusts mean[2], n = 61 (Pt = 20)	12.2	18.8	1.5	0.53	1.51	5136	841	4166	410	11.1	489
Central Pacific bulk crusts mean[3], n = 311 (Al, Mo, Cr=170; Pt=29)	15.7	23.0	1.46	0.58	0.91	7900	1200	4700	390	8.3	240
Stratabound Mn mean, active Mariana arc[4], n = 26 (Pt = 8)	1.5	42.3	28.2	0.65	0.09	100	235	296	594	3.1	13
Manganiferous sandstone mean, active Mariana arc[5], n = 18 (Pt=9)	6.8	17.3	2.5	4.6	0.09	157	393	314	184	24.5	18

[1]Hein et al. (1990); [2]Hein, Kang et al. (1990); [3]Hein et al. (1992a); [4]Schulz and Hein (1991); [5]Hein et al. (1987b);
[6]Ratio of means, not mean of the summation of ratios

Table 14. Concentrations of rare earth elements (ppm) in Fe-Mn crusts, Karin Ridge

	D5-3-1	D8-6-2A	D10-1-4	D10-1-5	D11-1-2	D11-2-1
La[1]	410	450	400	420	400	430
Ce	1500	1700	1200	1300	1100	1200
Pr	95	110	87	93	81	89
Nd	380	430	350	370	330	360
Sm	83	95	76	81	70	76
Eu	19	22	18	19	17	17
Gd	78	89	74	81	74	78
Tb	13	14	12	13	12	13
Dy	70	79	70	72	70	72
Ho	13	14	13	13	14	14
Er	34	37	35	35	37	37
Tm	4.9	5.4	5.0	5.0	5.4	5.4
Yb	32	34	34	33	35	36
Σ REE	2732	3079	2374	2535	2245	2427
Ce*[2]	1.63	1.65	1.37	1.40	1.29	1.30
Interval	B 0-30[3]	B 0-18	B 0-15	B 0-15	B 0-10	B 0-11
Water Depth	4300-3900	4200-3700	3400-2960	3400-2960	3000-2450	3000-2450

[1]Analyses by Inductively Coupled Plasma - Mass Spectrometry (ICP-MS); analyst: P.H. Briggs
[2]Ce* = 2Ce/La+Pr, cerium anomaly from chondrite-normalized data
[3]Intervals are measured from the outer surface of the crust; B = bulk, the entire crust thickness was sampled and analyzed

Table 15. Correlation coefficient matrix for 12 bulk Fe-Mn oxyhydroxide crusts listed in Table 8; n = 12, except for Pt, Pd, Rh, Ru, and Ir = 6; zero point of correlation for 12 and 6 points at the 95% confidence level is |0.575| and |0.813|, respectively

	Depth	Lat.	Long.	Fe	Mn	Fe/Mn	Si	Na	Al	K	Mg	Ca	Ti	P	H_2O^+	H_2O^-	CO_2	LOI	Ni
Lat.	0.175																		
Long.	-0.018	0.180																	
Fe	0.583	0.631	0.493																
Mn	-0.472	-0.691	-0.499	-0.891															
Fe/Mn	-0.565	-0.642	-0.502	-0.967	0.963														
Si	0.329	0.416	0.528	0.648	-0.868	-0.790													
Na	-0.260	-0.651	-0.357	-0.780	0.580	0.662	-0.153												
Al	0.270	0.367	0.505	0.545	-0.814	-0.708	0.949	-0.112											
K	-0.295	-0.051	0.393	-0.057	-0.290	-0.131	0.617	0.317	0.755										
Mg	0.150	-0.414	-0.440	-0.590	0.498	0.556	-0.246	0.757	-0.289	-0.133									
Ca	-0.605	-0.485	-0.168	-0.729	0.652	0.753	-0.610	0.284	-0.468	0.069	0.173								
Ti	0.563	0.440	0.483	0.806	-0.786	-0.843	0.658	-0.546	0.719	0.268	-0.571	-0.644							
P	-0.533	-0.342	-0.162	-0.621	0.554	0.661	-0.590	0.132	-0.453	0.003	0.119	0.980	-0.592						
H_2O^+	-0.012	-0.121	0.346	0.079	-0.276	-0.182	0.656	0.341	0.575	0.610	0.208	-0.179	0.095	-0.240					
H_2O^-	-0.083	0.267	-0.430	-0.089	0.227	0.168	-0.608	-0.360	-0.529	-0.565	-0.272	0.204	-0.096	0.267	-0.871				
CO_2	-0.675	-0.188	-0.103	-0.622	0.644	0.712	-0.705	0.095	-0.661	-0.225	0.147	0.848	-0.738	0.859	-0.299	0.354			
LOI	-0.183	0.075	-0.547	-0.324	0.486	0.424	-0.801	-0.165	-0.734	-0.644	-0.055	0.347	-0.343	0.384	-0.859	0.956	0.514		
Ni	-0.640	-0.681	-0.412	-0.938	0.917	0.946	-0.648	0.749	-0.583	0.012	0.504	0.603	-0.778	0.471	-0.027	-0.008	0.563	0.247	
Cu	-0.252	-0.216	0.740	0.238	-0.182	-0.259	0.335	-0.089	0.347	0.454	-0.536	-0.143	0.395	-0.242	0.307	-0.369	-0.210	-0.443	-0.049
Zn	-0.661	-0.587	0.176	-0.458	0.372	0.447	-0.130	0.310	-0.052	0.428	-0.070	0.602	-0.350	0.513	0.344	-0.388	0.393	-0.276	0.558
Co	-0.322	-0.434	-0.616	-0.824	0.857	0.853	-0.712	0.658	-0.749	-0.365	0.727	0.423	-0.849	0.346	-0.179	0.217	0.538	0.467	0.785
Ba	-0.343	-0.126	0.434	0.131	-0.178	-0.151	0.160	-0.301	0.334	0.512	-0.719	0.313	0.373	0.299	0.064	-0.029	0.045	-0.152	-0.099
Mo	-0.711	-0.493	-0.378	-0.783	0.829	0.852	-0.827	0.266	-0.696	-0.133	0.074	0.860	-0.688	0.813	-0.410	0.399	0.806	0.572	0.775
Sr	-0.543	-0.555	-0.140	-0.619	0.717	0.711	-0.703	0.136	-0.621	-0.119	0.082	0.843	-0.601	0.822	-0.232	0.123	0.749	0.299	0.610
Ce	0.352	0.180	0.269	0.402	-0.271	-0.321	-0.027	-0.638	0.139	-0.046	-0.477	0.093	0.574	0.202	-0.388	0.280	-0.047	0.144	-0.474
Y	0.445	0.680	-0.158	0.440	-0.438	-0.456	0.150	-0.479	0.205	-0.147	-0.267	-0.344	0.499	-0.231	-0.360	0.546	-0.278	0.362	-0.612
V	-0.253	-0.636	-0.296	-0.568	0.600	0.640	-0.587	0.263	-0.566	-0.255	0.351	0.770	-0.678	0.761	-0.128	0.023	0.616	0.204	0.515
Pb	-0.471	-0.296	-0.349	-0.617	0.698	0.736	-0.688	0.176	-0.687	-0.313	0.362	0.673	-0.755	0.690	-0.114	0.086	0.778	0.313	0.635
Cr	0.081	0.377	0.160	0.237	-0.594	-0.428	0.790	0.121	0.801	0.701	-0.016	-0.255	0.327	-0.243	0.668	-0.412	-0.405	-0.552	-0.377
Cd	-0.243	-0.524	-0.408	-0.767	0.783	0.822	-0.564	0.649	-0.593	-0.225	0.832	0.493	-0.799	0.436	0.129	-0.172	0.547	0.111	0.767
As	0.353	-0.554	-0.093	-0.151	0.348	0.260	-0.393	0.130	-0.350	-0.401	0.322	0.135	-0.073	0.112	-0.273	-0.029	0.025	0.086	0.230
Pt	-0.320	-0.340	-0.603	-0.781	0.750	0.830	-0.490	0.760	-0.416	0.023	0.725	0.760	-0.448	-0.577	-0.343	0.399	0.179	0.481	0.826
Pd	-0.409	0.381	0.270	0.342	-0.595	-0.505	0.684	-0.182	0.488	0.455	-0.361	-0.182	-0.306	0.887	0.665	-0.877	-0.051	-0.828	-0.371
Rh	0.359	-0.749	-0.747	-0.654	0.681	0.654	-0.448	0.696	-0.202	0.065	0.684	0.696	0.284	-0.870	-0.261	0.395	-0.412	0.414	0.573
Ru	-0.321	-0.400	-0.675	-0.935	0.723	0.851	-0.304	0.965	-0.176	0.340	0.930	0.965	-0.312	-0.511	-0.040	0.139	-0.025	0.243	0.867
Ir	-0.028	-0.601	-0.772	-0.898	0.907	0.924	-0.630	0.789	-0.467	-0.028	0.868	0.789	-0.172	-0.812	-0.397	0.465	-0.062	0.554	0.884
Thick	-0.501	-0.361	-0.125	-0.464	0.425	0.485	-0.509	-0.015	-0.294	0.129	-0.245	0.855	-0.267	0.857	-0.378	0.380	0.605	0.410	0.356

	Cu	Zn	Co	Ba	Mo	Sr	Ce	Y	V	Pb	Cr	Cd	As	Pt	Pd	Rh	Ru	Ir
Zn	0.433																	
Co	-0.453	0.018																
Ba	0.624	0.603	-0.598															
Mo	-0.106	0.574	0.550	0.253														
Sr	-0.009	0.645	0.398	0.299	0.864													
Ce	0.067	-0.122	-0.554	0.504	-0.005	0.163												
Y	-0.361	-0.803	-0.232	-0.129	-0.367	-0.465	0.434											
V	-0.273	0.574	0.398	0.077	0.669	0.764	-0.022	-0.581										
Pb	-0.385	0.459	0.580	-0.119	0.733	0.801	-0.097	-0.423	0.706									
Cr	0.001	-0.100	-0.341	0.078	-0.532	-0.533	-0.188	0.298	-0.450	-0.449								
Cd	-0.413	0.279	0.830	-0.488	0.490	0.516	-0.414	-0.489	0.585	0.777	-0.298							
As	-0.061	0.143	0.109	-0.071	0.182	0.250	0.258	-0.398	0.523	0.206	-0.671	0.328						
Pt	-0.150	-0.673	0.805	-0.588	0.648	0.007	-0.300	0.471	-0.538	-0.247	-0.166	0.574	-0.135					
Pd	-0.376	0.871	-0.383	0.202	-0.437	0.155	-0.525	-0.668	0.248	0.483	0.523	-0.136	-0.576	-0.505				
Rh	0.473	-0.511	0.470	0.022	0.460	0.083	0.382	0.754	-0.322	-0.509	-0.133	0.301	0.231	0.653	-0.716			
Ru	0.080	-0.448	0.804	-0.406	0.546	0.124	-0.307	0.610	-0.654	-0.175	0.121	0.710	-0.361	0.870	-0.339	0.755		
Ir	0.094	-0.621	0.813	-0.406	0.749	0.289	0.039	0.610	-0.449	-0.162	-0.252	0.668	0.042	0.844	-0.620	0.888	0.908	
Thick	0.020	0.561	0.056	0.648	0.803	0.755	0.425	-0.134	0.599	0.417	-0.274	0.061	0.136	-0.035	-0.355	0.580	0.028	0.285

Table 16. Correlation coefficient matrix for 14 Fe-Mn crust surfaces listed in Table 8; n = 14; the zero point correlation for 14 points at the 95% confidence level is |0.531|

	Depth	Lat.	Long.	Fe	Mn	Fe/Mn	Si	Na	Al	K	Mg	Ca	Ti	P	H_2O^+	H_2O^-	CO_2	LOI	Ni
Lat.	0.037																		
Long.	-0.075	0.255																	
Fe	0.328	0.547	0.284																
Mn	-0.543	-0.607	-0.109	-0.874															
Fe/Mn	-0.535	-0.566	-0.136	-0.926	0.979														
Si	0.392	0.619	0.220	0.794	-0.876	-0.841													
Na	0.328	-0.521	-0.479	-0.368	0.377	0.313	-0.510												
Al	0.534	0.395	0.182	0.536	-0.671	-0.617	0.885	-0.323											
K	0.481	0.275	0.004	0.310	-0.399	-0.361	0.656	-0.006	0.826										
Mg	-0.014	-0.516	-0.124	-0.386	0.439	0.394	-0.563	0.608	-0.356	-0.333									
Ca	-0.804	-0.328	-0.063	-0.703	0.795	0.794	-0.685	0.090	-0.712	-0.523	0.270								
Ti	0.800	0.327	0.079	0.617	-0.766	-0.722	0.802	-0.085	0.884	0.779	-0.326	-0.895							
P	-0.918	0.062	0.269	-0.183	0.406	0.378	-0.344	-0.440	-0.574	-0.539	-0.082	0.723	-0.778						
H_2O^+	0.220	-0.690	0.373	-0.081	0.190	0.115	-0.173	0.122	-0.011	-0.072	0.188	-0.067	0.042	-0.129					
H_2O^-	-0.073	-0.034	-0.196	-0.277	0.253	0.270	-0.484	0.131	-0.617	-0.393	-0.166	0.251	-0.338	0.216	-0.129				
CO_2	-0.864	-0.124	-0.127	-0.540	0.563	0.598	-0.441	-0.323	-0.546	-0.235	-0.293	0.405	-0.467	0.709	-0.133	-0.005			
LOI	0.030	-0.392	-0.339	-0.552	0.549	0.543	-0.691	0.488	-0.625	-0.314	0.118	0.307	-0.378	0.027	0.050	0.808	0.157		
Ni	-0.620	-0.561	-0.205	-0.895	0.942	0.954	-0.820	0.269	-0.631	-0.469	0.421	0.811	-0.790	0.420	0.076	0.122	0.671	0.380	
Cu	0.797	0.037	0.310	0.399	-0.556	-0.542	0.556	-0.077	0.719	0.431	-0.099	-0.787	0.781	-0.728	0.448	-0.448	-0.734	-0.344	-0.552
Zn	-0.710	-0.230	-0.079	-0.288	0.350	0.395	-0.144	-0.444	-0.142	-0.315	-0.097	0.437	-0.446	0.525	-0.004	-0.238	0.691	-0.205	0.553
Co	-0.526	-0.534	-0.298	-0.804	0.879	0.891	-0.758	0.376	-0.608	-0.196	0.309	0.793	-0.652	0.393	0.020	0.390	0.584	0.577	0.799
Ba	0.163	0.251	0.199	0.576	-0.561	-0.535	0.830	-0.415	0.804	0.574	-0.443	-0.450	0.622	-0.258	0.047	-0.699	-0.264	-0.714	-0.462
Mo	-0.597	-0.594	-0.175	-0.852	0.985	0.959	-0.862	0.382	-0.689	-0.369	0.423	0.832	-0.791	0.465	0.135	0.255	0.609	0.532	0.927
Sr	-0.851	-0.258	-0.092	-0.439	0.674	0.651	-0.559	0.074	-0.679	-0.440	0.096	0.872	-0.792	0.739	-0.147	0.248	0.751	0.256	0.671
Ce	0.834	0.367	0.175	0.647	-0.769	-0.754	0.712	-0.096	0.739	0.654	-0.287	-0.871	0.915	-0.682	0.090	-0.108	-0.807	-0.206	-0.879
Y	-0.852	-0.048	-0.118	-0.306	0.523	0.475	-0.556	0.044	-0.772	-0.615	0.206	0.811	-0.866	0.809	-0.336	0.268	0.726	0.170	0.553
V	-0.802	-0.305	0.094	-0.529	0.661	0.660	-0.460	-0.300	-0.439	-0.410	0.041	0.718	-0.738	0.765	0.089	-0.015	0.854	0.142	0.709
Pb	-0.593	-0.417	-0.239	-0.428	0.670	0.622	-0.451	0.331	-0.357	-0.088	0.217	0.556	-0.504	0.345	-0.021	-0.181	0.418	0.108	0.693
Cr	0.366	-0.183	-0.274	-0.273	-0.015	0.080	-0.091	0.341	0.021	0.155	0.188	-0.009	0.168	-0.375	-0.054	0.043	-0.065	0.173	0.009
Cd	-0.639	-0.398	-0.065	-0.848	0.849	0.876	-0.639	-0.002	-0.434	-0.295	0.286	0.782	-0.713	0.502	0.058	0.023	0.762	0.241	0.894
As	-0.414	-0.855	-0.152	-0.642	0.799	0.780	-0.690	0.407	-0.534	-0.314	0.410	0.641	-0.549	0.274	0.447	0.128	0.398	0.439	0.746

	Cu	Zn	Co	Ba	Mo	Sr	Ce	Y	V	Pb	Cr	Cd
Zn	-0.304											
Co	-0.714	0.241										
Ba	0.502	0.242	-0.541									
Mo	-0.644	0.359	0.919	-0.561								
Sr	-0.867	0.465	0.737	-0.269	0.728							
Ce	0.727	-0.655	-0.642	0.376	-0.792	-0.833						
Y	-0.921	0.350	0.552	-0.440	0.593	0.887	-0.822					
V	-0.505	0.758	0.538	-0.162	0.683	0.633	-0.753	0.546				
Pb	-0.529	0.521	0.611	0.000	0.715	0.723	-0.722	0.548	0.540			
Cr	0.094	-0.342	0.176	-0.164	-0.017	-0.086	0.142	-0.160	-0.221	-0.185		
Cd	-0.494	0.556	0.750	-0.386	0.847	0.555	-0.741	0.455	0.819	0.515	0.020	
As	-0.381	0.415	0.767	-0.238	0.804	0.651	-0.628	0.374	0.542	0.690	0.063	0.562

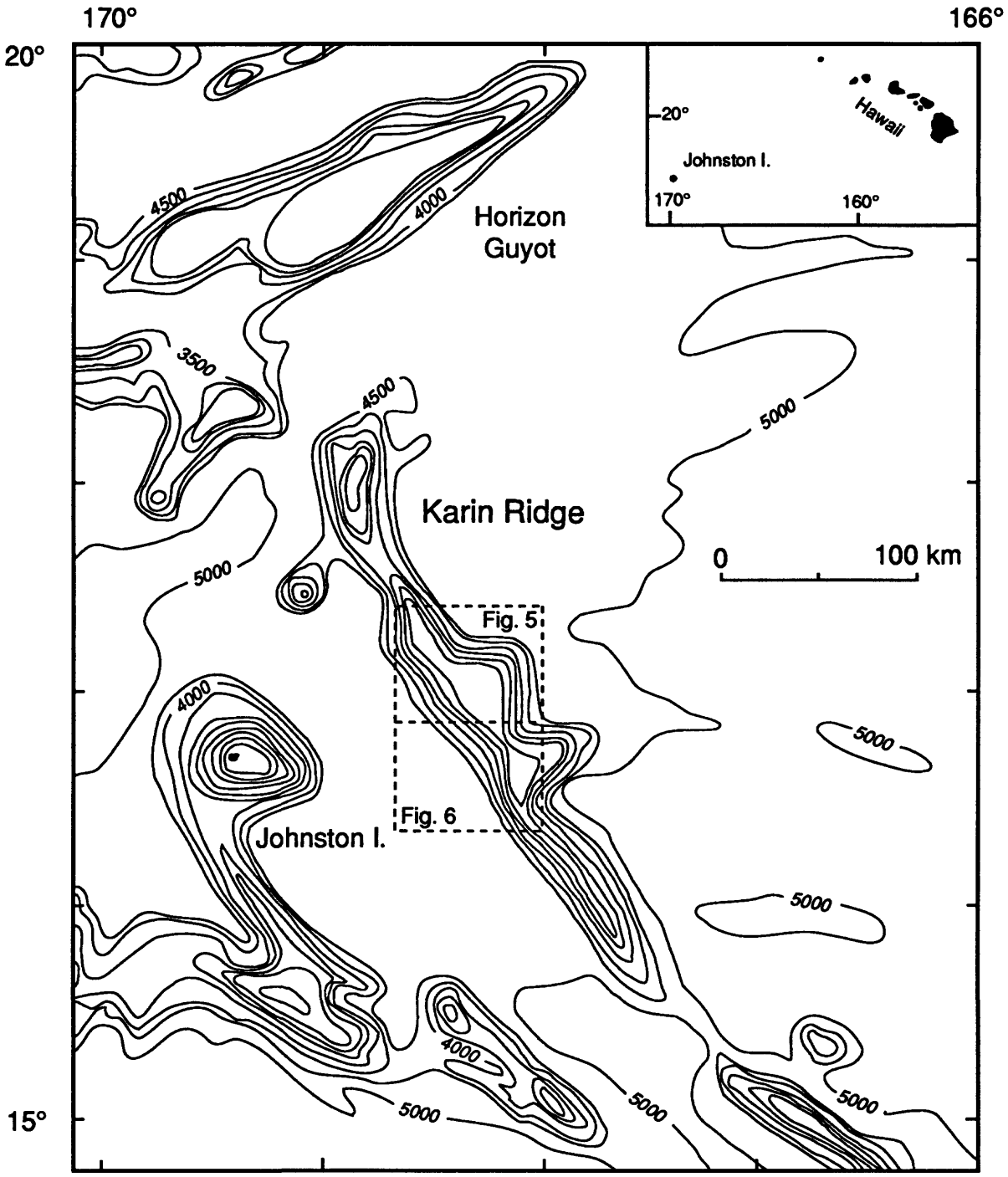

Figure 1. Regional map of Karin Ridge and adjacent areas, central Pacific. Contour interval is 500 m. Dashed boxes show locations of Figures 5 and 6.

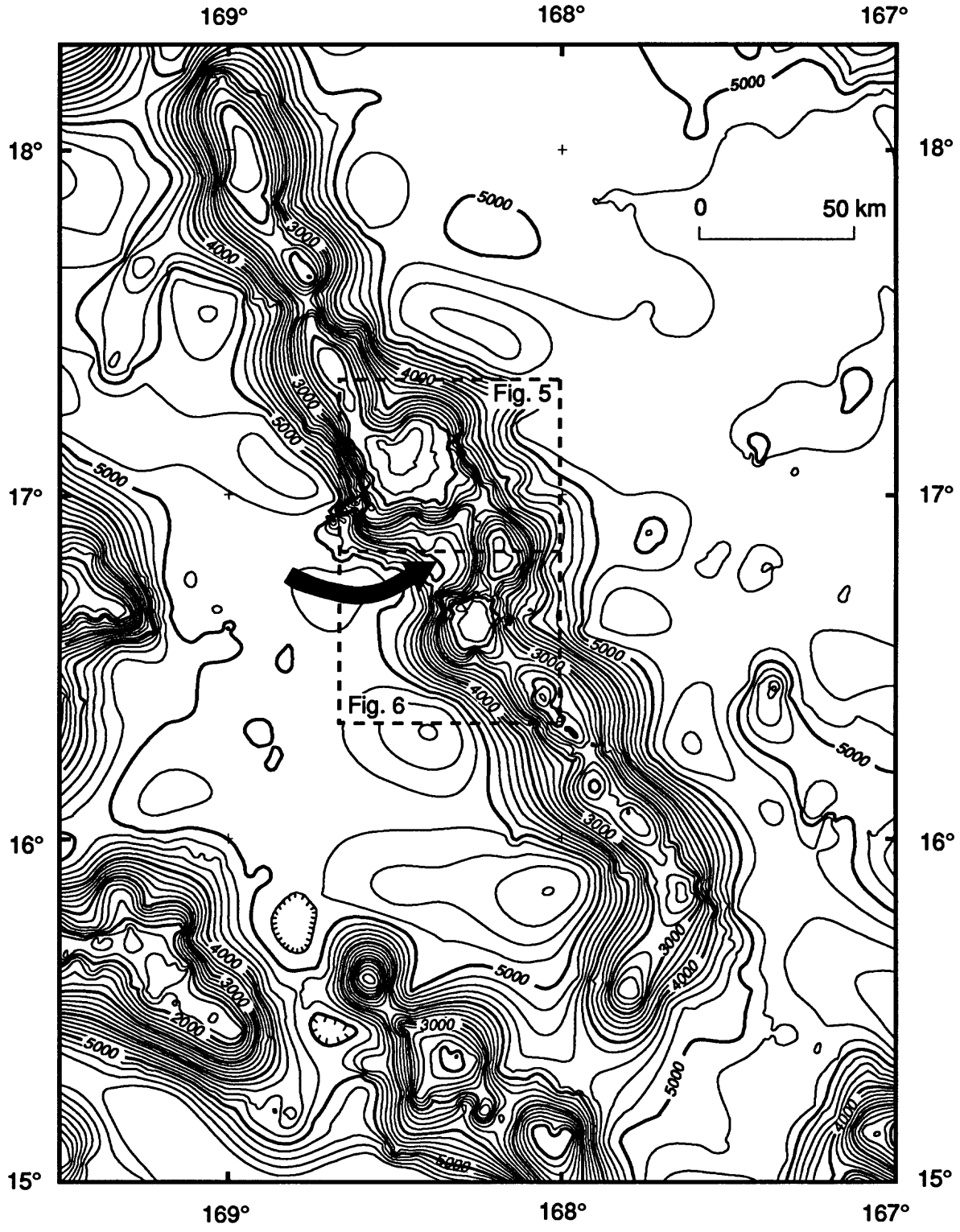

Figure 2. Bathymetric map of Karin Ridge. Bathymetry was generated at the U.S. Geological Survey using data from five U.S.G.S. cruises. Arrow identifies possible landslide scar. Dashed boxes show locations of Figures 5 and 6. Contour interval is 200 m.

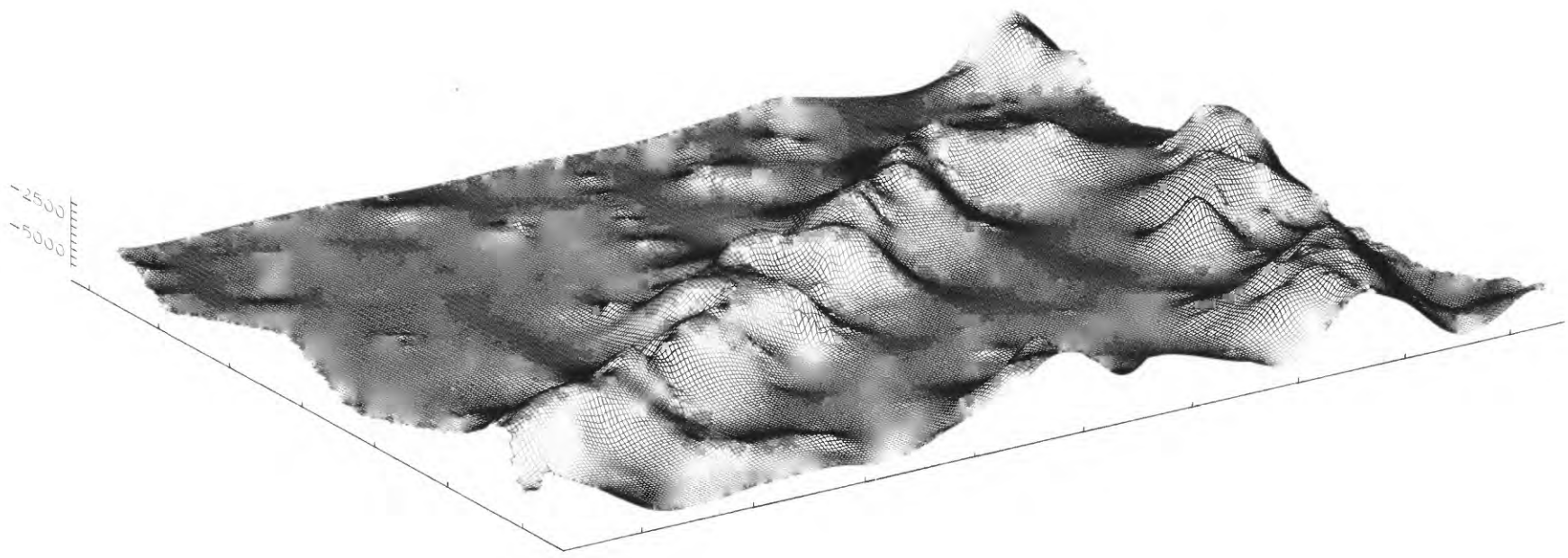

Figure 3. Computer generated physiographic map of Karin Ridge derived from bathymetry in Figure 2. View is looking to the southeast from 305° azimuth at 20° elevation; vertical exaggeration is 5 times; ridge is centered on 168° W longitude and 17° N latitude.

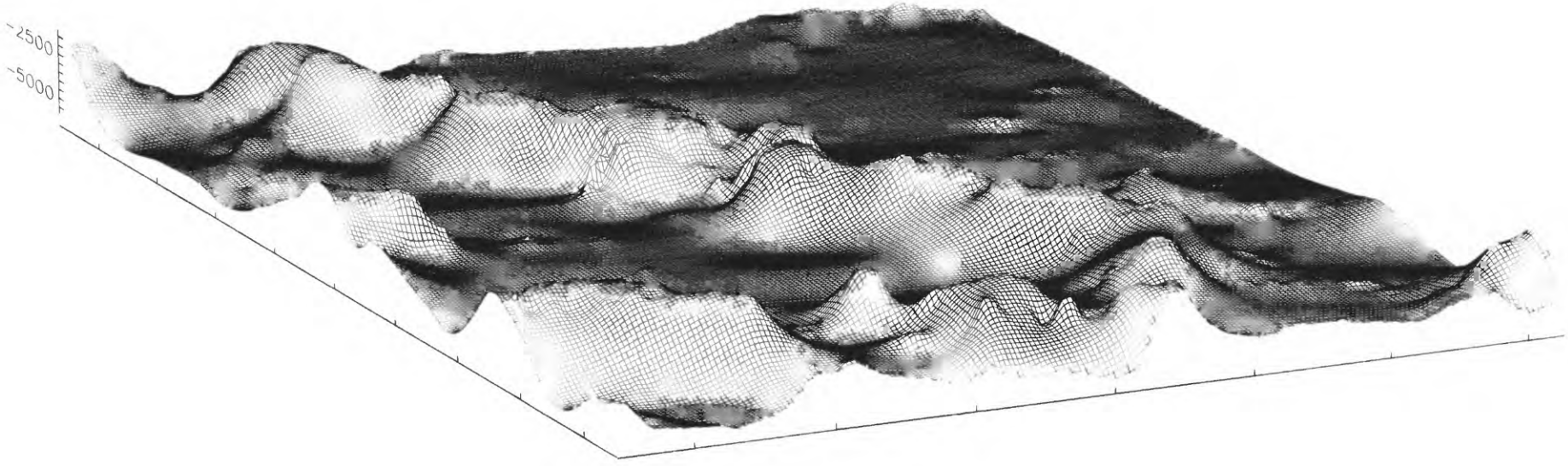

Figure 4. Same as Figure 3 except view is looking to the northeast from 205° azimuth at 15° elevation.

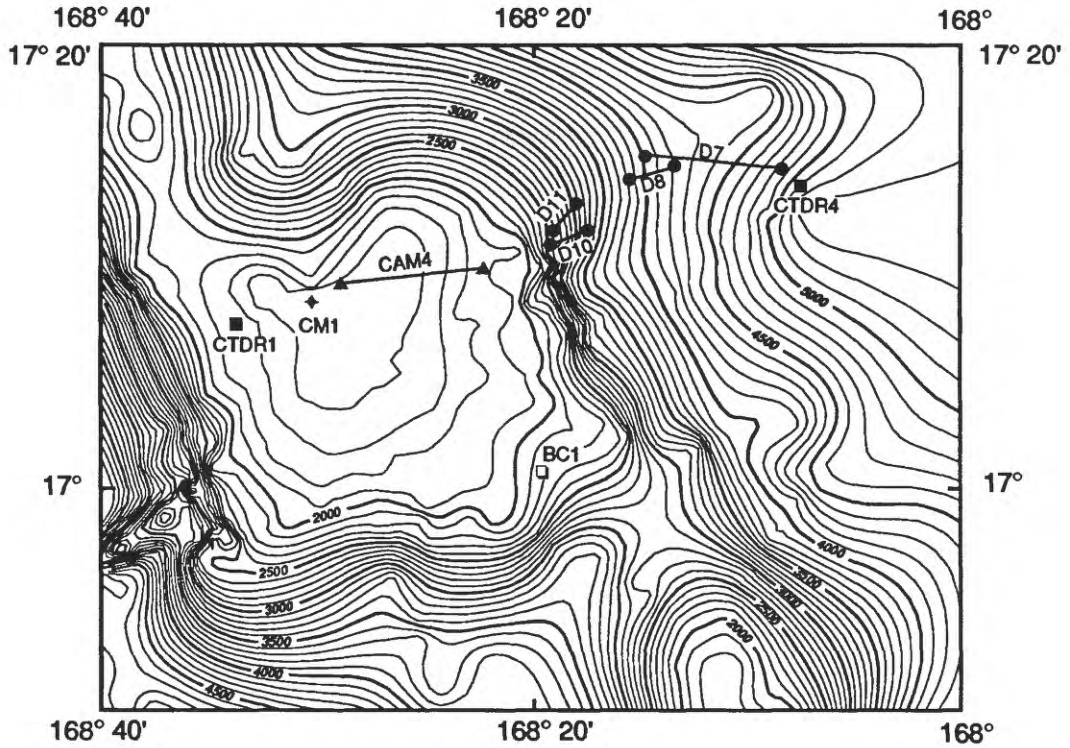

Figure 5. Study area 1 for cruise 91-AV-19/2 over Karin Ridge. Bathymetry for Figs. 5 and 6 was generated from five U.S. Geological Survey cruises. Contour interval is 100 m. D=dredge, CTDR=temperature-salinity-oxygen profile, CAM=camera-video survey, CM=current meter station, BC=box core, GC=gravity core.

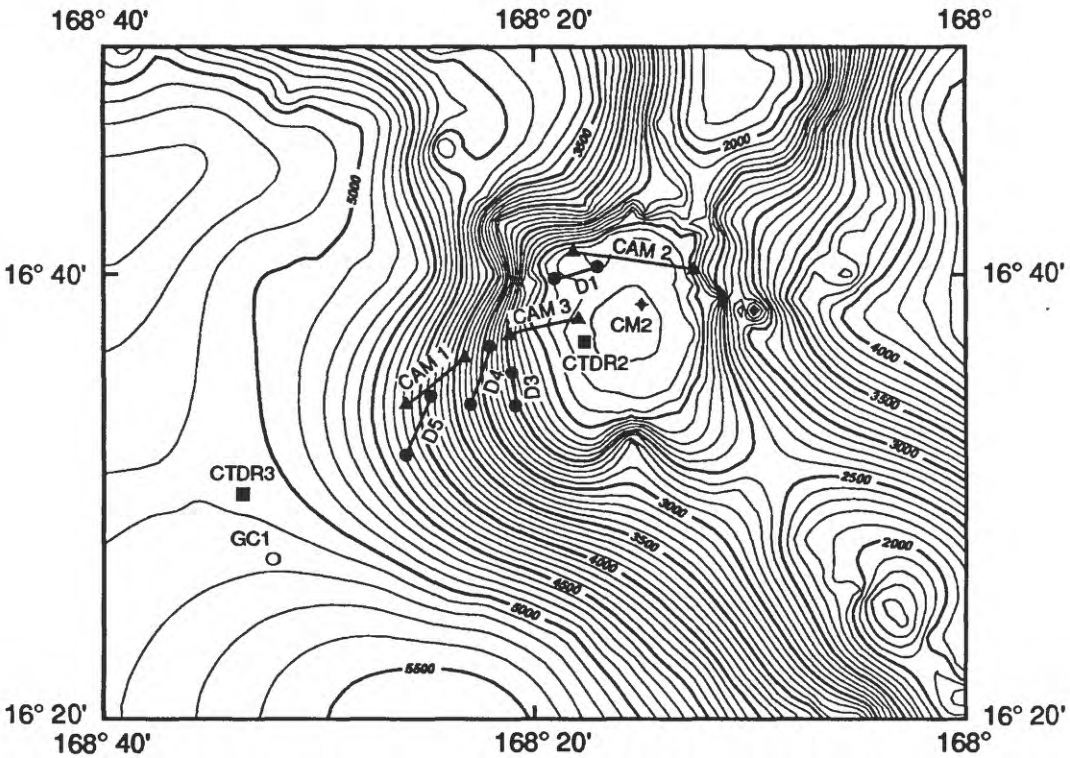

Figure 6. Study area 2 for cruise 91-AV-19/2 over Karin Ridge. See Fig. 5 for abbreviations.

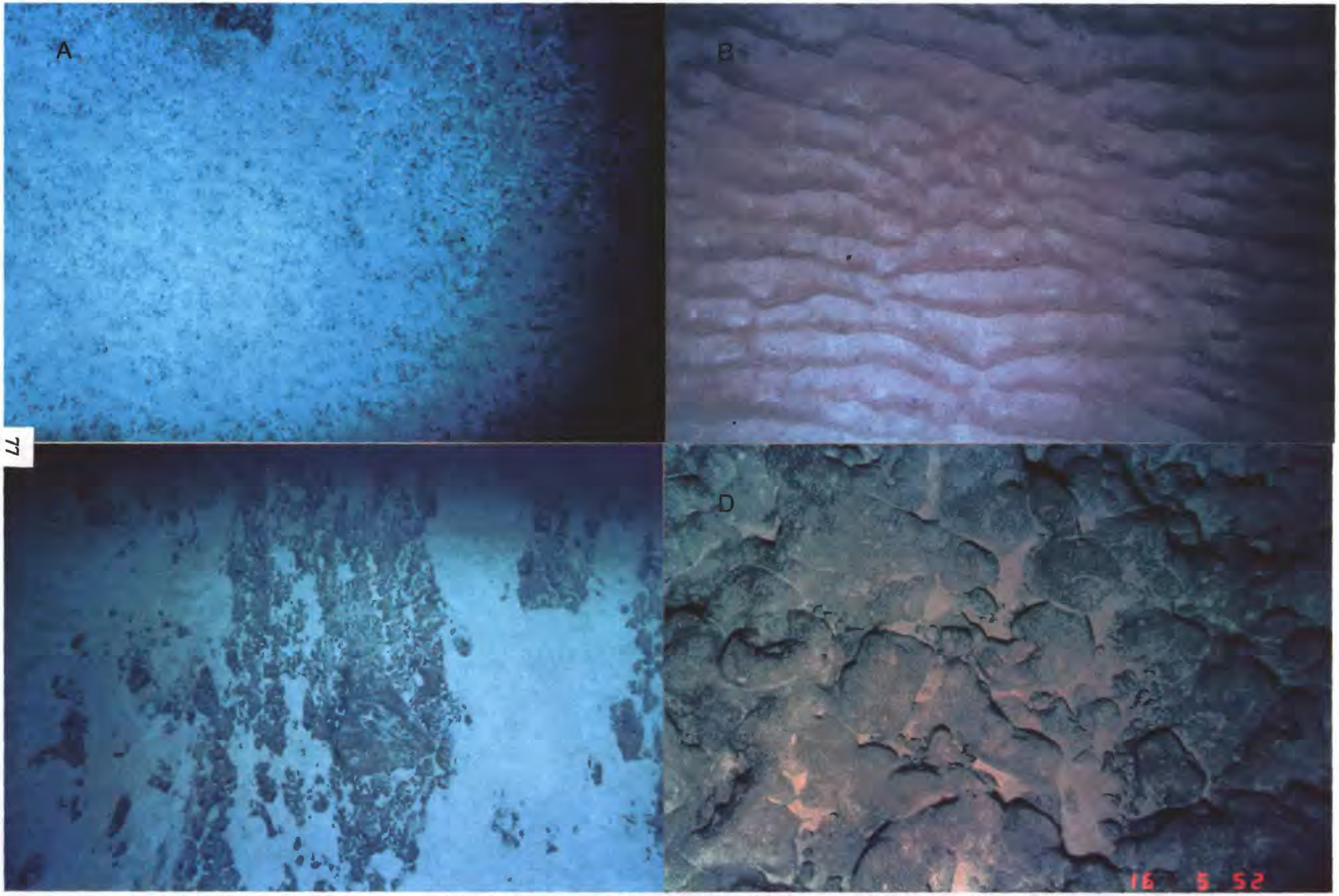

Figure 7. Bottom photographs of northern summit (A, B; CAM 4; water depth about 1800 m) and southern summit (C, D; CAM 2; water depth about 2000 m) areas; about 6 m^2 area of seafloor shown in each photo. **A.** Degraded ripple marks in carbonate ooze; troughs filled with Fe-Mn crust-coated pebbles; note feeding track in upper right quadrant. **B.** Degraded asymmetric ripple marks in carbonate ooze. **C.** Partly buried linear outcrop coated with Fe-Mn crusts displaying a smooth surface texture. **D.** Volcaniclastic breccia (?) outcrop coated with Fe-Mn crusts displaying a botryoidal surface texture; carbonate ooze infills lows.

BLANK

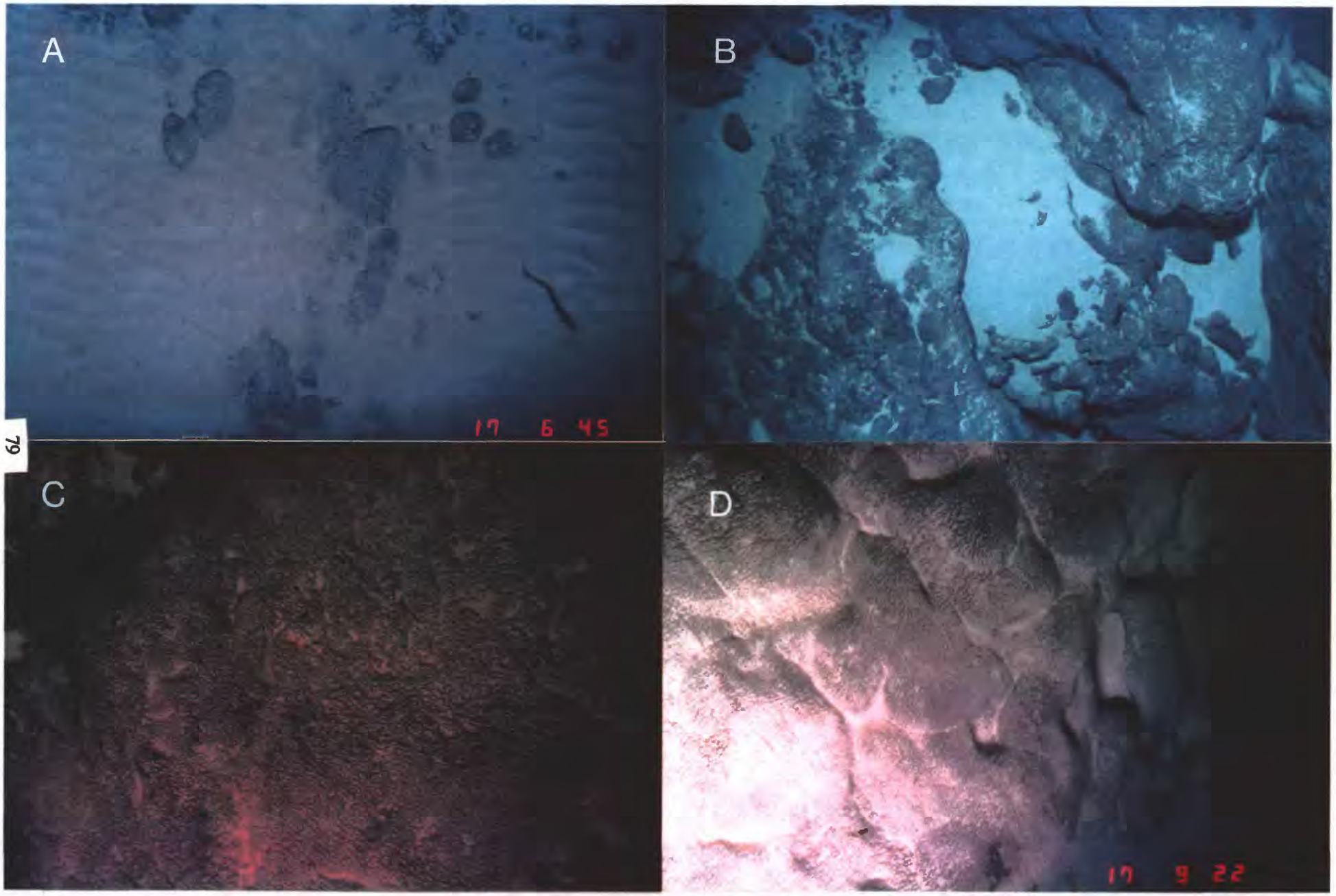

Figure 8. Bottom photographs of southern summit area, CAM 3, from about 1800 m (A) to about 1750 m (D) water depths; about 6 m^2 area of seafloor shown in each photo. **A.** Asymmetric ripple marks in carbonate ooze are degraded near rocks where preferential erosion occurs; note rat-tail fish in lower right quadrant. **B.** Outcrop forming a steep cliff with small shelves that support carbonate ooze; Fe-Mn crust with smooth surface coats the outcrop. **C.** Flat-horizontal outcrop coated with well-developed botryoidal Fe-Mn crust; light dusting of carbonate ooze. **D.** Pillow basalt forming steep cliff and coated with well-developed botryoidal Fe-Mn crust; light dusting of carbonate ooze on cliff face, being thicker at the base.

BLANK

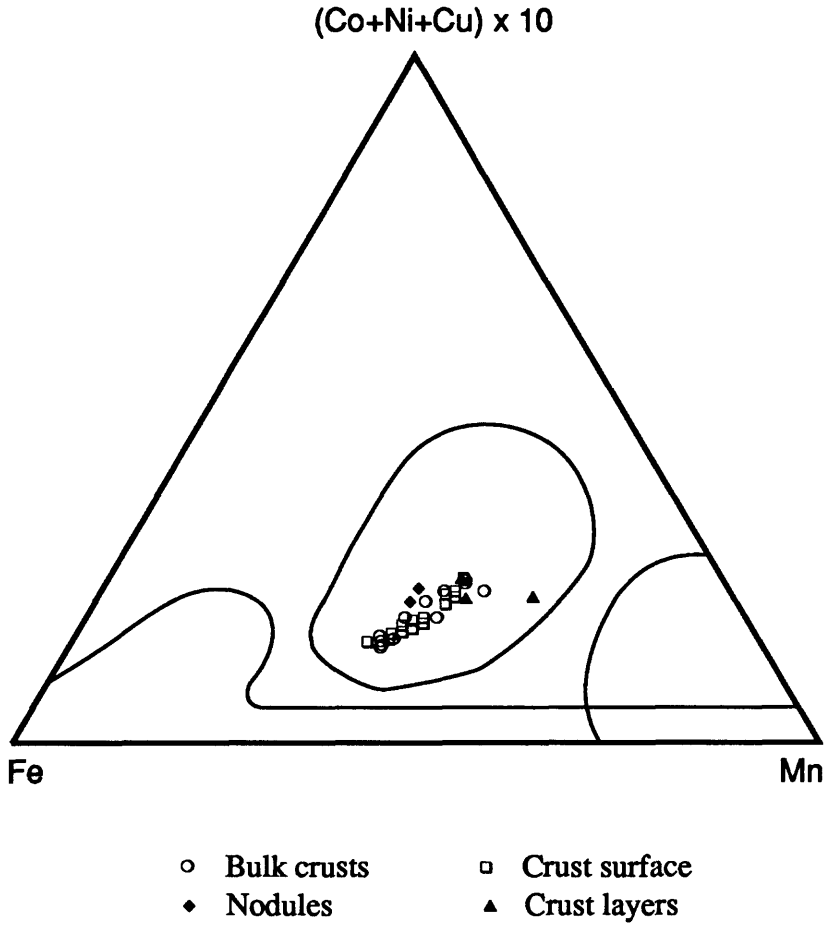

Figure 9. Ternary diagram after Bonatti et al. (1972) for 12 bulk Fe-Mn crusts, 14 crust surfaces, 3 crust layers, and 2 Fe-Mn nodules. The central field is for 308 bulk hydrogenetic crusts from the central Pacific (Hein et al., 1992a), the field along the base is for hydrothermal deposits, and the field around the Mn apex is a hydrothermal and diagenetic field (after Bonatti et al., 1972).

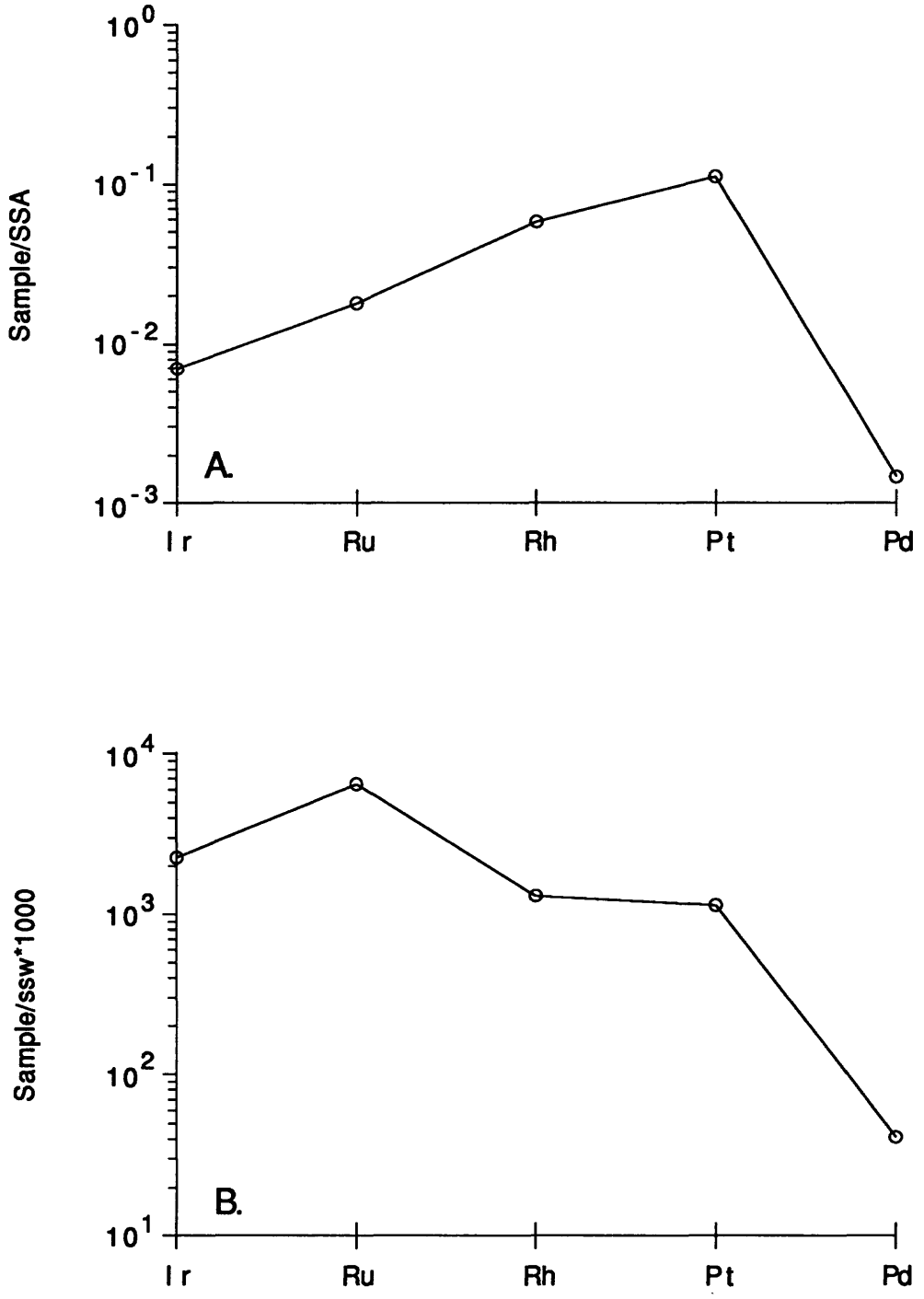

Figure 10. **A.** Mean PGE concentrations in 6 bulk crusts normalized to solar system abundances (same as C1 chondrite concentrations) taken from Anders and Ebihara (1982). **B.** Mean PGE concentrations in 6 bulk crusts normalized to surface seawater abundances taken from Goldberg (1987), except Rh which is set to 6 pg/l (see Hein, Kang, et al., 1990).

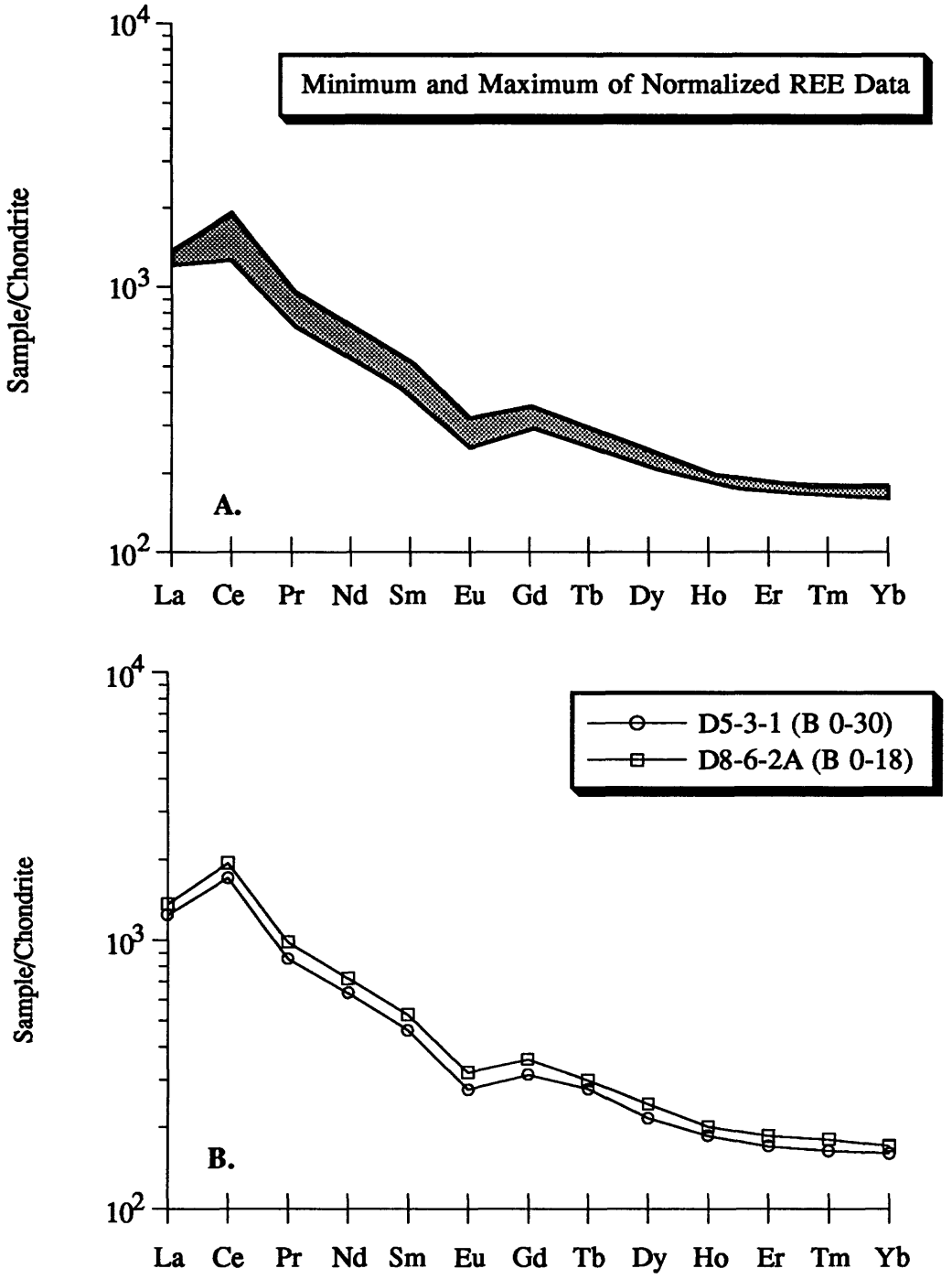

Figure 11. **A.** Chondrite-normalized REE plot. Shaded field represents complete data set of 6 bulk crust samples (see Table 14). Chondrite composition for Figs. 11 and 12 from Haskin et al. (1968). **B.** Chondrite-normalized REE plot of crusts from dredges D5 and D8. B = bulk, followed by sample interval in millimeters.

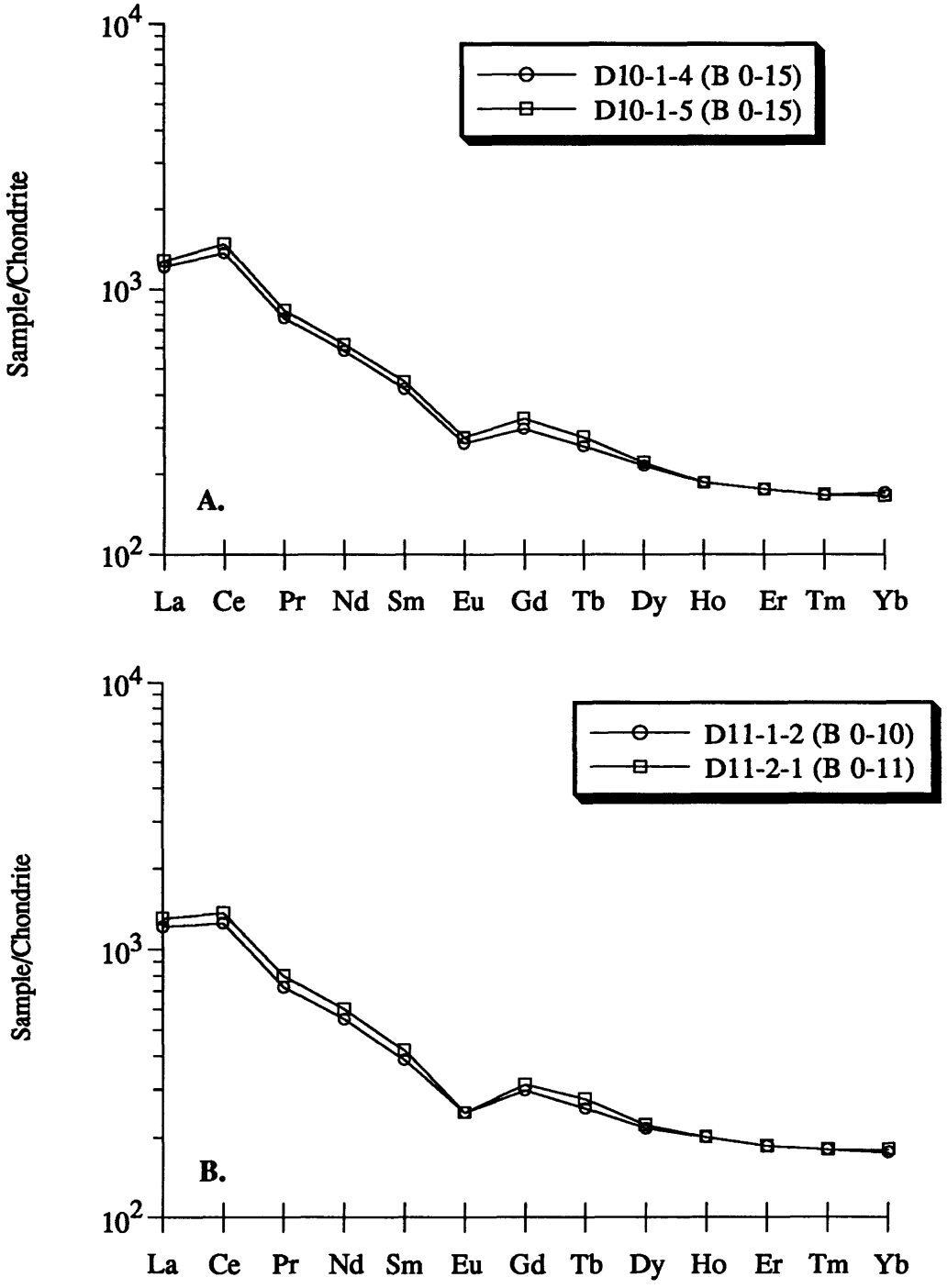

Figure 12. **A.** Chondrite-normalized REE plot of crusts from dredge D10. **B.** Chondrite-normalized REE plot of crusts from dredge D11. B = bulk, followed by sample interval in millimeters.

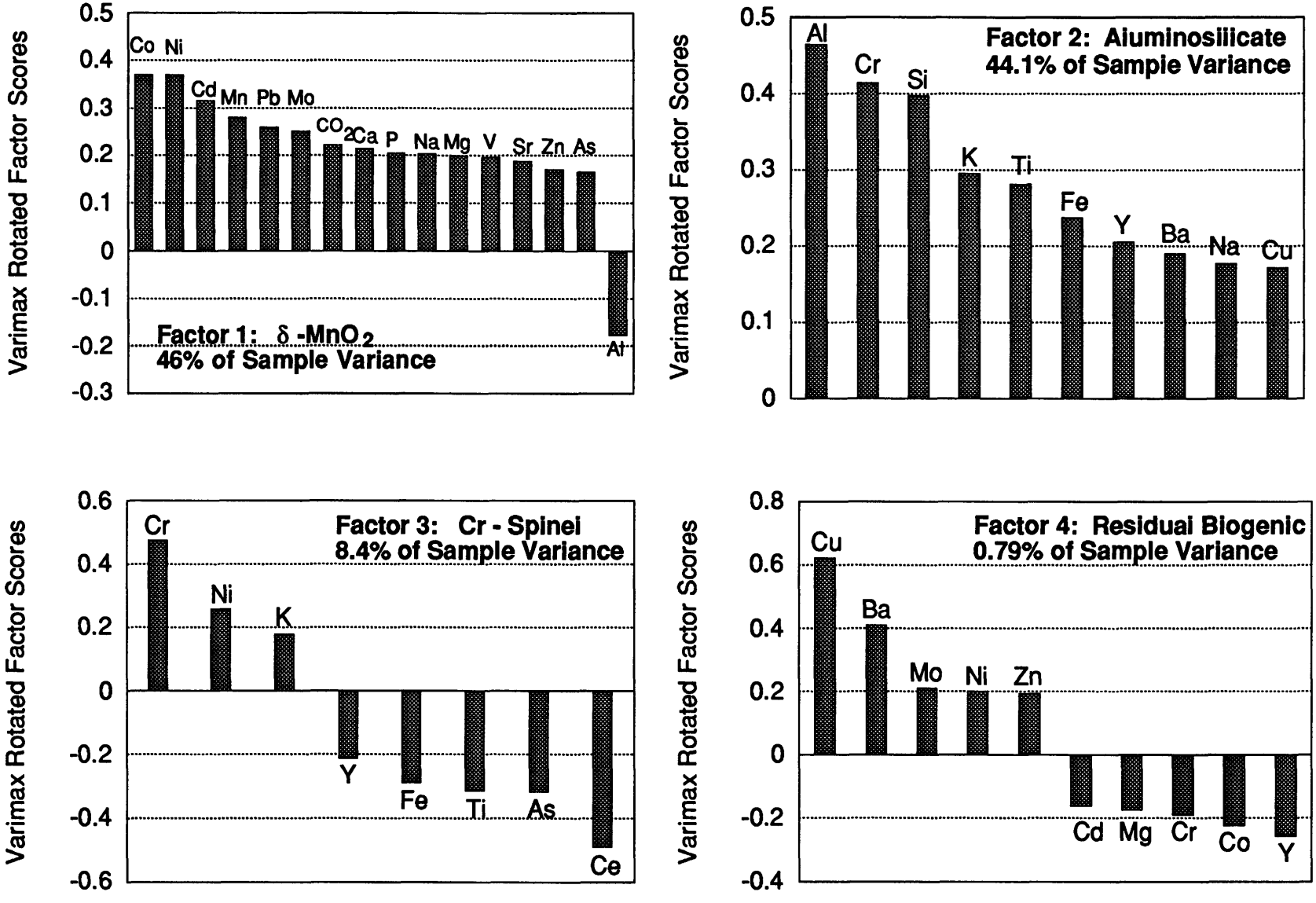

Figure 13. Four Q-mode factors for chemical data from 12 bulk crusts (Table 8). Factor scores between 0 and |0.160| are not included because random noise makes it difficult to resolve the orientation of the factor to within 10° of an absolute direction in variable space.

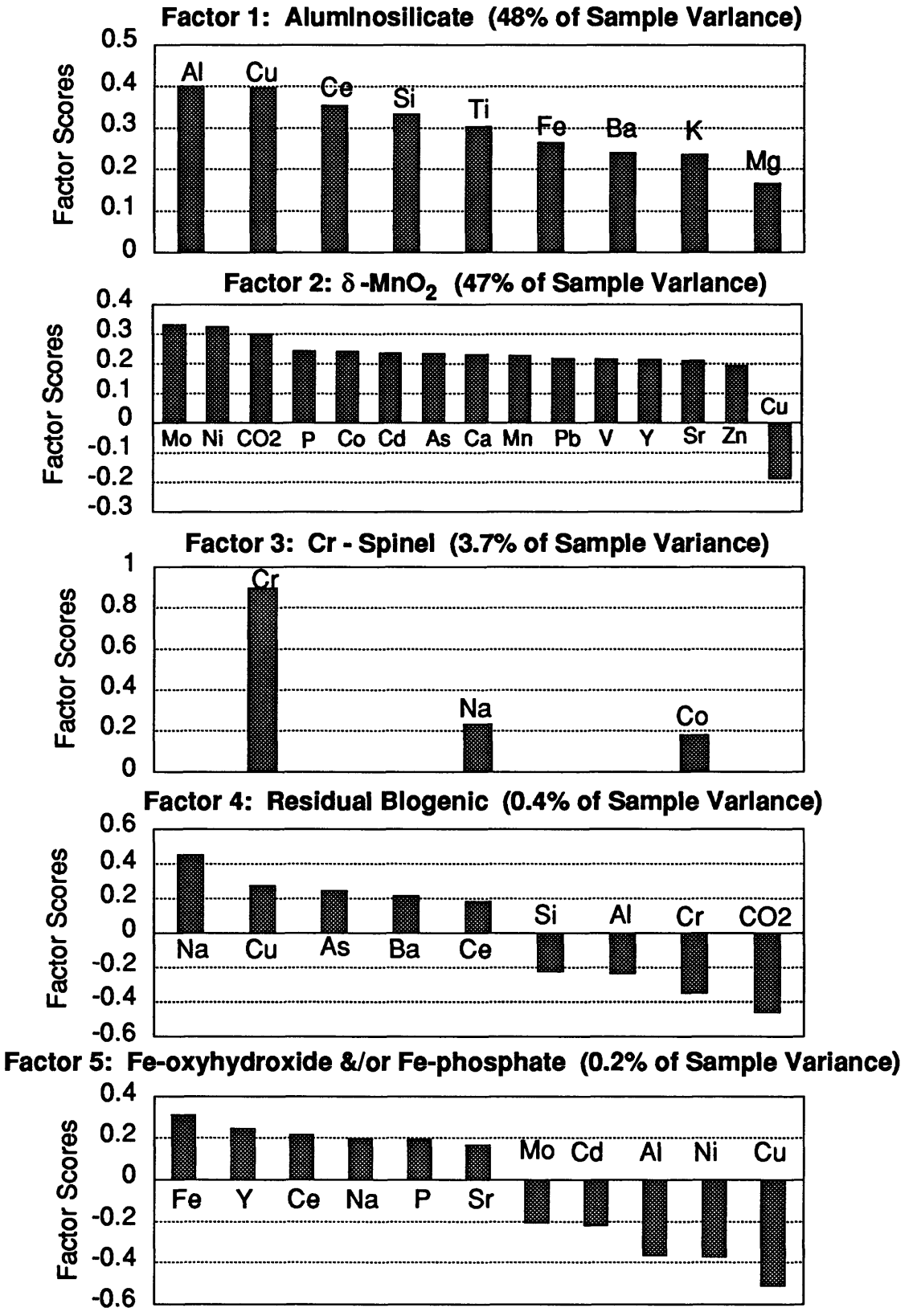

Figure 14. Five Q-mode factors for data from 14 crust surfaces. Factor scores between 0 and |0.160| are not included because random noise makes it difficult to resolve the orientation of the factor to within 10° of an absolute direction in variable space.

BIOSTRATIGRAPHIC RESULTS OF CRUISE 91-AV-19/2, KARIN RIDGE, CENTRAL PACIFIC OCEAN

Sergey P. Pletnev[1], Irina Ryaben'kaya[1], and Paula J. Quinterno[2]

[1]Pacific Oceanological Institute, Far Eastern Branch, Russian Academy of Sciences, 43 Baltiyskaja, Vladivostok 690041, Russia; [2]U.S. Geological Survey, 345 Middlefield Road MS 999, Menlo Park, CA 94025, USA

Sedimentary rocks collected during Leg 2 of the R/V *Akademik Vinogradov* Cruise 91-AV-19 to Karin Ridge yielded foraminifers, radiolarians, and calcareous nannofossils of Early Cretaceous through Quaternary age (Tables 1 and 2).

Upper Cretaceous

A siltstone from dredge sample D4-12 contains poorly preserved specimens of the planktonic foraminifer *Dicarinella* sp. and the benthic foraminifers *Gavelinella* sp. cf. *G . nacatochensis* and *Tritaxia* sp. cf. *T. tricarinata* (Reuss). The presence of these foraminifers indicates a Late Cretaceous age. The presence of *Rotalipora* in GC-1 indicates reworking of late Albian or Cenomanian foraminifers. The Maastrichtian planktonic foraminifer species, *Abathomphalus mayaroensis* (Bolli), occurs in siltstone sample D10-1 and is accompanied by *G. arca* (Cushman) and benthic species *Serovaina orbicella* (Bandy) and *Quinqueloculina* sp. Tests are secondarily mineralized with calcite, which makes identifications difficult.

Radiolarians in the Late Cretaceous siltstone sample D10-1 include the following species in varied states of preservation: *Stichocapsa rotunda* (Hinde), *Holocryptocanium barbui* (Dumitrica), *Pseudodictyomitra carpatica* (Dumitrica), *Crucella theokaftensis* (Baumgartner), *Archeodictyomitra brouweri* (Tan Sin Hok), *Thanarla pulchra* (Squinabol), *Alievium antiguum* (Pessagno), *Pseudodictyomitra lodogaensis* (Pessagno), *Artostrobium urna* (Foreman), and *Amphipyndax pluosis* (Foreman). Table 2 lists ranges for these species.

Stichocapsa rotunda (Hinde) is known to occur in Late Jurassic through the Vallanginian or Hauterivian deposits in the North Pacific (Foreman, 1975); Baumgartner (1984) defined the range as Upper Tithonian through Hauterivian for Mediterranean rock sequences.

Holocryptocanium barbui (Dumitrica) was originally described from Cenomanian strata in the Romanian Carpathians (Dumitrica, 1970). In Tethys deposits it is known to range from the Upper Berriasian to the Hauterivian or later (zones D, E1, and E2 on the basis of the Unitary Associations of Baumgartner, 1984). In Japan, this species occurs in rocks as old as Callovian (Matsuoka, 1989). A late Albian and Cenomanian range is reported for *H. barbui* from Sakhalin, Kamchatka, Cuba, the North Pacific, and California (Vishnevskaya, 1990). Teraoka and Kurimoto (1986) reported that this species occurs in rocks of Barremian through Cenomanian ages in southwest Japan.

Pseudodictyomitra carpatica (Dumitrica) occurs in rocks of latest Jurassic (Tithonian) through Cenomanian ages in the Tethys area (Baumgartner, 1984). According to data presented by Teraoka and Kurimoto (1986), it is present in Albian and Cenomanian strata in southwest Japan. Schaaf (1984) reported that this species occurs in rocks in the Mediterranean area, with questionable first and last occurrences in the lower Valanginian and the Turonian, respectively.

Crucella theokaftensis (Baumgartner) is known from Callovian through Tithonian strata and may extend into the Berriasian and Valanginian (Baumgartner, 1980).

Archeodictyomitra brouweri (Tan Sin Hok) is known to range from the Berriasian or Valanginian through the Barremian (Teraoka and Kurimoto, 1986).

Alievium antiguum (Pessango) is reported by Pessagno (1972) to occur in late Aptian strata of the Blake-Bahama Basin and in early Cenomanian strata in California (Pessango, 1976). The occurrence of *A. antiguum* in Mediterranean and Koryak highland Hauterivian deposits is discussed by Schaaf (1984) and Vishnevskaya (1988), respectively. The species is noted to occur in late Albian and Cenomanian deposits on Kamchatka and in Cuba by Vishnevskaya (1990).

Thanarla pulchra (Squinabol) is known to range from the from Late Jurassic (Tithonian) through Barremian in the Mediterranean area (Schaaf, 1984). It also occurs in California in lower Cenomanian strata (Dumitrica, 1975), and Pessagno (1977) stated that this species may range into the upper Cenomanian or lower Turonian.

Table 1. Age of sedimentary rocks from Karin Ridge based on foraminifers.

Sample	Rock Type	Foraminifers	Age	Comments
BC1-1		*Candeina nitida, Globigerinoides conglobatus, G. ruber, G. triloba, Globorotalia menardii, G. truncatulinoides, G. tumida, Orbulina universa, Sphaeroidinella dehiscens.*	Quaternary	Nannofossils present include: *Ceratolithus cristatus, C. telesmus, Gephyrocapsa caribbeanica, G. oceanica, Helicosphaera sellii?, Rhabdosphaera claviger, Scapholithus fossilis.*
D1-10	Phosphatized hyaloclastite	*Globigerina triloculinoides, Planorotalites pseudomenardii, Morozovella acuta, M. aequa, Acarinina pentacamerata*	late Paleocene, early Eocene	
D1-1-1	Foraminiferal sand (filling void in crust)	*Sphaeroidinellopsis disjuncta, Globigerina nepenthes*	late Miocene	Reworked Paleogene forms.
D4-8	Breccia	*Acarinina pentacamerata, Globigerina pseudoeocaena, Globigerina triloculinoides, Morozovella velascoensis, Globotruncana* sp.	Late Cretaceous, Paleocene	Mixed ages.
D4-4/2	Sandstone	*Gaudryina pyramidalis*	Late Cretaceous	Foraminifers very rare.
D4-12	Calcareous siltstone	*Dicarinella* sp. *Globotruncana* sp, *Gavelinella* cf. *nacatochensis, Tritaxia* cf. *tricarinata*	Late Cretaceous	Foraminifers rare.
D8-6-1	Siltstone	*Morozovella velascoensis*	late Paleocene	Foraminifers very rare.
D8-6	Argillite	*Trochammina* sp., *Haplophragmoides* sp.		Benthic deep water forms.
D10-1	Siltstone	*Globotruncana arca, Globotruncana mayaroensis, Seroviana orbicella, Quinqueloculina* sp.	Late Cretaceous	Poor preservation; secondary mineralization.
D10-F	Fe-Mn nodule	*Globorotalia truncatulinoides*	early or middle Pleistocene	The assemblage was washed into the void in the nodule.
D-11-1	Poorly cemented breccia	*Globorotalia menardii, G. truncatulinoides, G. tumida, Globigerinoides conglobatus*	Pleistocene	The assemblage reflects the last stage of sedimentation.
Cam 1-1		*Acarinina pseudotopilensis*		
Cam 1-6	Foraminiferal sand	*Globigerinoides obliquus*	End of late Miocene or early Pliocene	
GC-1, core catcher	Foraminiferal sand	*Globorotalia truncatulinoides, Sphaeroidinella excavata*	Pleistocene	Redeposited upper Cretaceous *Rotalipora.*
GC-2, core catcher	Foraminiferal sand	*Globorotalia truncatulinoides, Sphaeroidinella excavata, Pulleniatina finalis*	late Pleistocene	Rare reworked Oligocene foraminifers.

Note: Foraminifers sparse and too poorly-preserved to identify; calcareous nannofossils absent in D7-1 and D8-6-2B.

Artostrobium urna (Foreman) is present in Japan in the Kitanada and Iwamatsu formations in strata of Coniacian and Santonian ages (Nakaseko *et al.*, 1979; Yao, 1984; Kumon *et al.*, 1986; Teraoka and Kurimoto, 1986). Schaaf (1985) discussed the use of *A. urna* as a zonal marker in deep sea drilling cores and coastal sections on Majorca where radiolarian data are correlated with the paleomagnetic scale and nannoplankton. The *A. urna* Zone was defined by Riedel and Sanfilippo (1974) and is based on the earliest morphotypic appearance of *A. urna* (probably in the Coniacian). However, according to Foreman (1975), the first occurrence of *A. urna* may extend down into the mid-Turonian or earlier.

Amphipyndax plousis (Foreman) occurs in upper Campanian strata of the Onari Formation of Japan (Iwata and Tajika, 1986) in an interval that is probably correlative with the *Phaseliforma carinata* Subzone of Pessagno (1976).

In addition to the species discussed above, several species with longer stratigraphic ranges are also present. They are *Novixitus* sp., *Archeodictyomitra* sp., *Archeospongoprunum* sp., *Spongurus* sp., *Paronaella* sp., *Hagumastra* sp., *and Praenocaryomma* sp.

The siltstone sample from D10-1 contains two distinct radiolarian assemblages: lower Cretaceous species such as *S. rotunda, H. barbui,* and others (Table 2), and the upper Cretaceous species *Artostrobium urna* and *A. plousis.* The occurrence together of these two groups suggests reworking of Lower Cretaceous radiolarians into Upper Cretaceous strata.

Table 2. Ranges of radiolarian species in sample D10-1 (Karin Ridge). Ranges are as reported in the literature; those in question are noted by a dashed line.

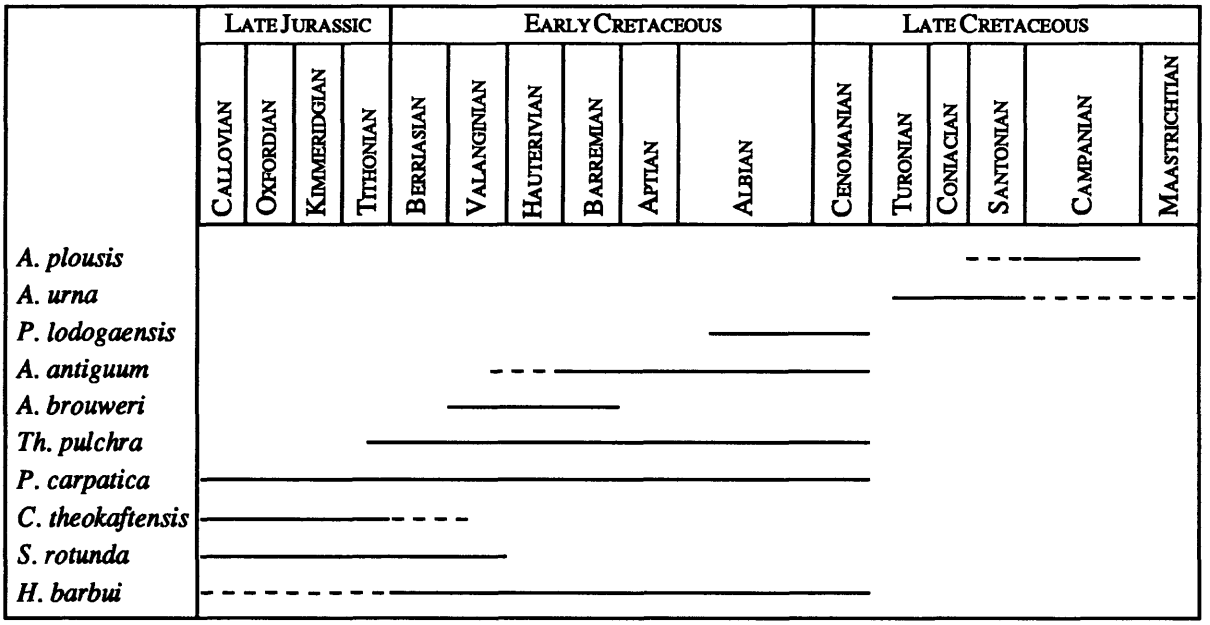

Upper Paleocene or Lower Eocene

Well-preserved specimens of the planktonic foraminifers *Globigerina triloculinoides* (Plummer), *Planorotalites pseudomenardii* (Bolli), *Morozovella acuta* (Toulmin), *M. aequa* (Cushman and Renz), *M. aragonensis* (Nuttall), *M. velascoensis* (Cushman), *and Acarinina pentacamerata* (Subbotina) were found in phosphatized breccias (samples D1-10, D4-8) and a siltstone (sample D8-6/1). The samples are, therefore, assigned a late Paleocene or early Eocene age.

Miocene and Pliocene

A foraminiferal sand (D-1-1-1) filling a cavity in an iron-manganese crust (sample D-1-1), contains the planktonic foraminifers *Sphaeroidinellopsis disjuncta* (Fmlay) and *Globigerina nepenthes* (Todd). The overlapping ranges of these two species allow assignment to Neogene planktonic foraminiferal Zones N14-

N17 (Bolli and Saunders, 1985), which corresponds to an age range of approximately 11.5-5.5 Ma on the Cenozoic time scale of Harland *et al.* (1990). The cavity containing the foraminifers is 18 mm from the outer edge of the crust; therefore, the maximum rate of growth is calculated to be 1.5-3.3 mm/m.y., assuming the sand did not filter into the cavity significantly after the crust accreted.

The only specimens of *Globigerinoides obliquus* (Bolli) obtained from Karin Ridge were recovered from a foraminiferal ooze that adhered to the underwater camera when it came in contact with the seafloor (Cam 1-6). This species is known to occur in the Miocene and Pliocene.

Quaternary

A layer of foraminiferal sand within an iron-manganese nodule (sample D10-F) includes the planktonic foraminifers *Globorotalia truncatulinoides* (d'Orbigny), *Gl. tosaensis* (Takayanagi & Saito), *Gl. tumida* (Brady), *Gl. inflata* (d'Orbigny), *Globigerinoides ruber* (d'Orbigny), and *Gs. conglobatus* (Brady). The presence of *Gl tosaensis* (Takayanagi & Saito) indicates that the nodule was formed prior to the pre-Brunhes paleomagnetic epoch (approximately 0.7 Ma). Apparently, these foraminifers filtered into the cavity after formation of the crust.

A Pleistocene fauna characterized by common *Globorotalia menardii* (d'Orbigny) and *Globigerinoides conglobatus* (Brady) is observed in a poorly cemented breccia (sample D11-1).

The late Pleistocene and Holocene planktonic foraminifers *Globorotalia truncatulinoides* (d'Orbigny), *Sphaeroidinella excavata* (Banner & Blow), and *Pulleniatina finalis* (Banner & Blow) are present in the foraminiferal sand of GC-2. Fragments of the large diatom, *Ethmodiscus rex* (Rattray), were found in the upper part of the core; this species is common in Pliocene and Pleistocene deposits.

Foraminifers in GC-2, recovered from a water depth of 5100 m, provide information on the sedimentary history of the Karin Ridge area. The core is characterized by several alternating layers of silt and sand which we interpret to be turbidites. The number of foraminiferal tests in the different sediment layers varies greatly; foraminifers are sparse in the following intervals: (325-345, 261-280, 218-220, 168-202, 109-111, 76-79 cm). Oligocene species correspond to the following Paleogene zones (from oldest to youngest) of Hardenbol and Berggren (1978): *Pseudohastigerina micra* (Cole), *Globorotalia opima* (Bolli), and *Globigerina ciperoensis* (Bolli). Smaller tests, including *P. micra* (Cole) and *Chiloguembelina cubensis* (Palmer), dominate the 335-345 cm interval, suggesting that this layer is part of a graded turbidite deposit. Cretaceous species are also found in some intervals (*Rotalipora* sp., *Abathomphalus mayaroensis* (Bolli)), as well as species of late Paleocene age (*Planorotalites pseudomenardii* (Bolli), *Morosovella velascoenis* (Cushman)), and the lower Eocene (*Morozovella subbotinae* (Morozova), *M. aragonensis* (Nuttall)). Foraminiferal tests are sparse in the argillaceous layers, which suggests deposition close to the calcite compensation depth. In the upper 2 cm of the core, the Pleistocene index species *Globorotalia truncatulinoides* (d'Orbigny) is present with poorly preserved lower Eocene planktonic foraminifers. Sharks teeth and relatively deep-water benthic foraminifers (*Hoeglundina elegans* (d'Orbigny), *Oridorsalis umbonatus* (Reuss), *Gyroidina* sp.) are also present in the sediments. The presence of older, reworked tests in the sediment may be explained by their greater resistance to dissolution during diagenesis compared to the younger forms.

Present-day sediments in the Karin Ridge area consist mostly of muds that are being deposited under conditions similar to muds of Pleistocene age. As in the Pleistocene sediments, pelagic sedimentation is periodically interrupted by turbidite deposition resulting in interbeds of silt and sand containing foraminifers that have been displaced from shallower-water deposits. Dissolution of the transported calcareous material is slight as a result of the high rates of turbidite sedimentation.

REFERENCES

Baumgartner, P.O., 1980, Late Jurassic Hagiastridae and Patulibracchiidae (Radiolaria) from the Argolis Peninsula (Peloponnesus, Greece): Micropaleontology, v. 26, no. 3, p. 274-322.

Baumgartner, P.O., 1984, A Middle Jurassic-Early Cretaceous low-latitude radiolarian zonation based on Unitary Associations and age of Tethyan radiolarites: Eclogae Geologicae Helvetiae, v. 77, no. 3, p. 729-837.

Bolli, H.M. and Saunders, J.B., 1985, Oligocene to Holocene low latitude planktonic foraminifera, *in* Bolli, H.M , Saunders, J.B., and Perch-Nielsen, K. (eds.), Plankton Stratigraphy: Cambridge, Cambridge University Press, p. 155-262.

Dumitrica, P., 1970, Cryptocephalic and cryptothoracic Nassellaria in some Mesozoic deposits of Romania: Revue Roumaine de Geologie, Geophysique et Geographie, Serie de Geologie, v. 14, no. 1, p. 45-124.

Dumitrica, P., 1975, Cenomanian Radiolaria at Podul Dimbovitei: Micropaleontological guide to the Mesozoic and Tertiary of the Romanian Carpathians, *in* 14th European Micropaleontological Colloquium, Romania. Institute of Geology and Geophysics, Bucharest, p. 87-89p.

Foreman, H., 1973, Radiolaria of Leg 10 with systematics and ranges for the families Amphipyndacidae, Artostrobiidae, and Theoperidae, *in* Worzel, J. L., Bryant, W., *et al.*, Initial Reports of the Deep Sea Drilling Project, v. 10, Washington, D.C. (U.S. Government Printing Office), p. 407-474.

Foreman, H., 1975, Radiolaria from the North Pacific, Deep Sea Drilling Project, Leg 32, *in* Larson, R. L., Moberly, R., *et al.*, Initial Reports of the Deep Sea Drilling Project, Washington, D.C. (U.S. Government Printing Office), v. 32, p. 579-676.

Hardenbol, J. and Berggren, W.A., 1978, A new Paleogene numerical time scale, *in* Cohee, G.V., Glaessner, M.F., and Hedberg, H.D. (eds.), Contributions to the Geologic Time Scale, papers given at the Geological Time Scale Symposium 106.6, 25th IGC Sydney, Australia, August, 1976, Tulsa: American Association of Petroleum Geologists, Studies in Geology 6, p. 213-234.

Harland, W.B., Armstrong, R.L., Cox, A.V., Craig, L.E., Smith, A.G., and Smith, D.G., 1990, A geologic time scale, 1989: Cambridge University Press, 263p.

Iwata, K. and Tajika, J., 1986, Late Cretaceous Radiolarians of the Yubetsu Group, Tokoro Belt, Northeast Hokkaido: Journal of the Faculty of Science, Hokkaido University, Series IV, v. XXI, no. 4, p. 619-644.

Kumon, F., Matsuyama, H., Nakajo, K., 1986, Revised latest Jurassic to Cretaceous radiolarian assemblages from the Hidakagawa Group in the Shimanto Belt, Kii Peninsula: Kaseki (Fossils), no. 41, p. 17-27.

Matsuoka, A., 1989, Radiolarian fossils from the Koyamada formation (lowest Cretaceous) of the Somanakamure Group, northeast Japan: Kaseki (Fossils), no. 46, p. 11-16.

Nakaseko, K., Nishimura, A., Sugano, K., 1979, Cretaceous Radiolaria in the Shimanto belt, Japan: News of Osaka Micropaleontologist Special Volume, no. 2, p. 1-49.

Pessagno, E., 1972, Cretaceous Radiolaria: Bulletins of American Paleontology, v. 61, no. 270, p. 267-325.

Pessagno, E., 1976, Radiolarian zonation and stratigraphy of the Upper Cretaceous portion of the Great Valley Sequence, California Coast Ranges: Micropaleontology, Special Publication, no. 2, 95 p.

Pessagno, E., 1977, Lower Cretaceous Radiolarian Biostratigraphy of the Great Valley Sequence and Franciscan Complex, California Coast Ranges: Cushman Foundation for Foraminiferal Research, Spec. Publ. no. 15, 87p.

Riedel, W., Sanfilippo, A., 1974, Radiolaria from the Southern Indian Ocean, *in* Davies, T.A., Luyendyk, B.P., *et al.*, Initial Reports of the Deep Sea Drilling Project, Washington, D.C., (U.S. Government Printing Office), v. 26, p. 771-813.

Schaaf, A., 1984, Radiolarians of the Lower and Middle Cretaceous; biology and classification (Les radiolaires du Cretace inferieur et moyen: Biologie et Systematique), Sciences Geologiques, no. 75, 189 p. (In French)

Schaaf, A., 1985, A new biochronological outline of the Lower and Middle Cretaceous; radiolarian biozones (Un Nouveau canevas biochronologique du cretace inferieur et moyen: Les Siozones a radiolaries), Sciences Geologiques, no. 38, p. 227-269. (In French)

Teraoka, Y., Kurimoto, C., 1986, Cretaceous stratigraphy of the Shimanto Terrane in the Uwajima area, west Shikoku, Southwest Japan, with reference to the stratigraphic distribution of mega- and radiolarian fossils: Bulletin of the Geological Survey of Japan, v. 37, no. 8, p. 417-453.

Vishnevskaya, V.S., 1988, O vozmozhnostyakh raschleneniya yursko-paleotsenovykh vylkanogenno-kremnistykh formatsii severo-zapadnogo obramleniya Patsifiki (v predelakh SSSR)/Possibilities of separation of the Jurassic-Paleocene volcano-siliceous formations of the northeastern Pacific rim (within the USSR)/Essays on Geology of Kamchatka and the Koryak Highlands. M.: Nauka, p. 8-17.

Vishnevskaya V.S., 1990, Alb-senomanskie radiolyarii severo-zapadnoy Patsifiki kak kluch k paleotektonicheskim rekonstruktsiyam v regione/ Albian-Cenomanian radiolarian of the Northwest Pacific as a key to paleotectonic reconstructions in the region (in Russian): Pacific Geology, no. 2, p. 3-15.

Yao, A., 1984, Subdivision of the Mesozoic complex in Kii-Yura Area, southwest Japan and its bearing on the Mesozoic basin development in the Southern Chichibu Terrane: Journal of Geosciences Osaka City University, v. 27, art. 2, p. 41-103.

—PAGE 93 FOLLOWS—

ADSORPTION PROPERTIES OF FERROMANGANESE CRUSTS AND NODULES

Stashchuk, M.F.[1], Chervonetsky, D.V.[2], Kaplun, E.V.[2], Chichkin, R.V.[3], Avramenko, V.A.[2], Tishchenko, P.Ya.[3], Gramm-Osipov, L.M.[3]

[1]Deceased; [2]Institute of Chemistry, Far Eastern Branch Russian Academy of Sciences, 159 Stoletia Vladivostku Ave., Vladivostok, 690022, Russia;[3] Pacific Oceanological Institute, Far Eastern Branch, Russian Academy of Sciences, 43 Baltiyskaja, Vladivostok 690041, Russia

INTRODUCTION

It is generally known that ferromanganese crusts and nodules (FCN) are natural collectors for a number of elements, such as Ni and Co and so emerges an interest in their sorption from saline solutions like seawater. This study addresses the sorption properties of FCN recovered from Karin Ridge (Pacific Ocean, 16° 40' N, 168° 20' W) during Leg 2 of the R/V "*Akademik Aleksandr Vinogradov*" cruise 91-AV-19. We present data on the degree of oxidation (method of reversal potentiometric titration), specific surface area (method of low temperature nitrogen adsorption), and ion-exchange sorption of transition metals (sorption of Co and Ni by static method).

METHODS

Measurement of FCN specific surface area by nitrogen adsorption method was conducted using a system similar to the one described in Kiselev and Dreving (1973). The system contains 1) a service unit for the vacuuming system, gas inlet, and manometer, and 2) a measuring unit consisting of calibrated vessels, manometer, and picnometer for samples. The sorption values were calculated from the equilibrium nitrogen pressure change onto the adsorbent at 77° K at known volume. The "consecutive" adsorption isotherm was obtained when the next equilibrium in turn had been stated after the gas portion inlet. Then the isotherm was treated according to the BET method, and the sample specific surface area value was obtained taking the area occupied by a nitrogen molecule to be equal to 16.8 $Å^2$ (Young and Crowell, 1962).

Sample Preparation

For analysis, FCN were divided into a surface sample "S" ($\leq$ 1 mm sampling depth) and a volume sample "V" ($\geq$ 5-6 mm sampling depth). Each sample was granulated (the main fraction 1-2 mm), weighed, and placed into a picnometer. Drying was conducted under vacuum at 130-140° C down to a residual pressure of 0.5×10^{-3} torr for 2-2.5 hours, and then treated under the same conditions for an additional hour. These treatment conditions were considered acceptable since no structural transformation of the primary Fe-Mn mineral (vernadite) was observed. Specific surface area measurements completed on one sample that was treated repeatedly did not exceed the error of measurement. The correct sample weigh was made ashore, back in the laboratory.

Co^{+2} and Ni^{+2} adsorption was determined on the basis of experiments on sorption from a constant volume (static method). Seawater passed through a nucleapor filter (0.4 5 μm) was taken as the background solution. Amounts of Co and Ni adsorbed were calculated as a ratio of initial and equilibrium concentration differences in a known volume to the FCN sample mass. Measurements were carried out at standard conditions:

initial concentrations	12, 24, 36, 48 μg/ml
solution volume 50 ml	
FCN sample mass	100 mg

Samples in solution were shaken for 48 hours. A previous, preliminary investigation on ion-exchange sorption kinetics in the same system has shown that this time period is adequate to establish equilibrium (Kaplun *et al.*, 1990).

Determination of oxidation number was made as described in Gramm-Osipov *et al.* (1987).

RESULTS AND DISCUSSION

Specific surface area values are presented in Table 1. Samples are identified by dredge number (D) and sample type (S or V). CAM1 represents FCN recovered in the frame of a deep-water camera sled.

The significant value of the specific surface area that is not a characteristic of natural minerals and does not result from the grain size of the sample is of significant interest. The range of the specific surface areas (200-400 m^2/g) is similar to that of silica gel, and, therefore, may be due to a silica gel-type structure.

Variations in water depth during dredging (up to 500 m) and the inability to know the specific water depth of individual samples makes it difficult to determine the dependence between water depth and specific surface area of a sample. However, specific surface area tends to increase with water depth.

As a rule (5 of 7 samples), "S" samples have a greater surface area than "V" samples. The differences vary from 1 to 20 %. The fact that precipitation of "S" and "V" intervals occurred during different time periods may be the reason for the variation in FCN properties through the layers. However, it is possible that since FCN have a porous structure, they are in equilibrium with seawater both at the FCN surface as well as the underlying layers due to diffusion processes. In other words, physical and chemical formation of FCN inner layers may not end as new layers are added.

Results of measuring the specific surface area of the same sample over time are interesting. The specific surface area of FCN decreased up to 20% during the first four weeks and up to 40% during eight weeks. Obviously, when a sample is brought to the surface, its *in situ* conditions (temperature, hydrostatic pressure, humidity) change. So the FCN structure maintained under hydrostatic pressure, which established the formation and development of its structure, also changes. It should be mentioned that since there is no unambiguous relation between the results of experiments onboard ship and in the laboratory, the "aging" should be considered when collecting samples. Otherwise, FCN should be transported in a preserved state, for example in a thermostatic autoclave.

Results of measuring the degree of oxidation (n) have shown that n varies over time for all FCN samples (Table 2), but the necessity of making the measurements on FCN properties, including the sorption equilibria, appears to be of great importance; the time between the sample recovery and analysis should be as small as possible.

Values of Co^{+2} and Ni^{+2} sorption on samples analyzed soon after recovery are given in Table 3. The cation sorption on a given sample is characterized by the Henry constant (Hc = ratio of sorption to concentration, when concentration tends to zero). Figures 1-2 show the dependence of Hc on the degree of oxidation for Co^{+2} and Ni^{+2}. The sorption value decreases with increasing n at adsorption on "V" samples; the relationship is unclear for "S" samples due to significant data scatter. The ion-exchange sorption process on non-stoichiometric manganese oxide results in an increase of adsorbent degree of oxidation (Table 2), in agreement with results presented by Kaplun *et al.* (1990). Figure 3 shows the dependence of Henry constants ratio (Co^{+2}/Ni^{+2}) on n. Cobalt is adsorbed more selectively than Ni, and the selectivity coefficient decreases with increasing the degree of oxidation. This observation may be useful in considering the problem of transition metal distributions in FCN. Selective sorption of Co compared with that of Ni on FCN (todorokite) was found by van der Weijden (1976).

Since a relation between n and FCN specific surface area was not found, the dependence between the Henry constants, divided by the specific surface area, and n is presented in Figs. 4-5 to confirm the connection between n and the ability of a given sample to adsorb cations. One can see that the dependence type has not changed. In other words, the specific surface area influences the sorption to a lesser extent than does n.

One should mention that some of our results differ with conclusions made by Kaplun *et al.* (1990), especially with regard to FCN extraction ability of metal cations with the degree of oxidation. But, it should be taken into account that manganese oxides with artificially stated n and FCN samples that had aged for a long time, were used by Kaplun *et al.* (1990).

Table 1. Specific surface area of FCN (Ssp)

Sample	Collection Date	Water Depth Beg - End (m)	Ssp: after 1 day (m^2/g)	Ssp: after 4 weeks (m^2/g)	Ssp: after 8 weeks (m^2/g)
D1S	13-May-91	1810-1840	281	195	160
D1V			277	230	221
D3S	15-May-91	2520-1965	318	252	190
D3V			250	189	157
D4S	17-May-91	3150-2850	381	336	325
D4V			355	316	313
D5S	18-May-91	4300-3900	321	298	278
D5V			318	-	-
D8S	21-May-91	3700-4200	320	-	-
D8V			365	326	-
D10S	22-May-91	2960-3400	367	-	-
D10V			342	-	-
D11S	23-May-91	2500-3000	292	-	-
D11V			335	-	-
CAM1S	15-May-91	3600-4200	328	-	-

S = surface sample; ≤ 1 mm sampling depth; V = volume sample; ≤ 5-6 mm sampling depth

Table 2. Oxidation numbers of FCN samples

Sample	Before Sorption May	After Sorption Co^{+2}	Ni^{+2}	10 Weeks Later (Without Sorption) July
D1S	1.8701	1.9270	-	-
D1V	1.9571	1.9590	-	-
D3S	1.8560	1.9650	1.9720	-
D3V	1.9091	1.9290	1.9650	-
D4S	1.9008	1.9170	1.9310	1.9560
D4V	1.9114	1.9680	1.9698	1.9490
D5S	1.8580	1.9699	1.9530	1.9440
D5V	1.8990	-	-	-
D8S	1.8810	1.9210	1.9220	1.9640
D8V	1.9261	1.9640	1.9300	1.9460
D10S	1.8340	1.9310	1.9220	1.9400
D10V	1.9037	1.9430	1.9460	1.9550
D11S	1.8690	1.9670	1.9690	1.9220
D11V	1.8920	1.9790	1.9560	1.9340

Table 3. Henry constants for Co and Ni sorption on FCN

Sample	Co^{+2} κ_H	Ni^{+2} κ_H	$Co^{+2}\kappa_H / Ni^{+2}\kappa_H$	$Co^{+2}\kappa_H / S_{sp} * 10^2$	$Ni^{+2}\kappa_H / S_{sp} * 10^2$
D1S	-	2.23	-	-	0.79
D1V	-	0.75	-	-	0.27
D3S	1.81	2.60	0.696	0.56	0.82
D3V	8.59	2.26	3.800	3.44	0.90
D4S	3.30	5.37	0.621	0.86	1.41
D4V	7.27	3.55	2.050	2.04	1.00
D5S	3.83	-	-	1.19	-
D5V	4.25	-	-	1.34	-
D8S	4.69	1.89	2.480	1.47	0.59
D8V	5.20	1.67	3.110	1.42	0.46
D10S	5.03	9.17	0.550	1.37	2.50
D10V	11.0	3.26	3.370	3.22	0.95
D11S	4.33	7.16	0.605	1.48	2.45
D11V	25.8	5.97	4.310	7.70	1.78

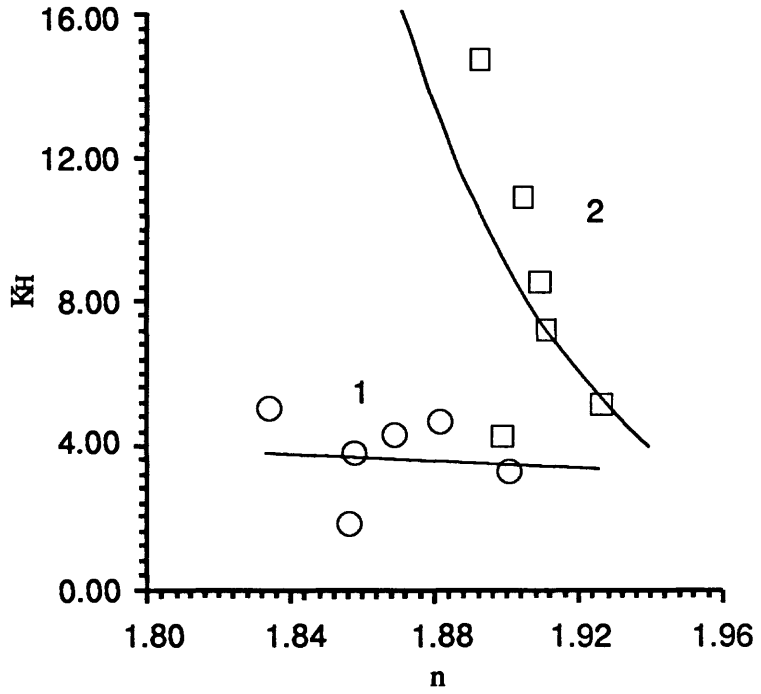

Figure 1. KH ratio dependence on the sample oxidation number. 1 = surface, 2 = volume samples.

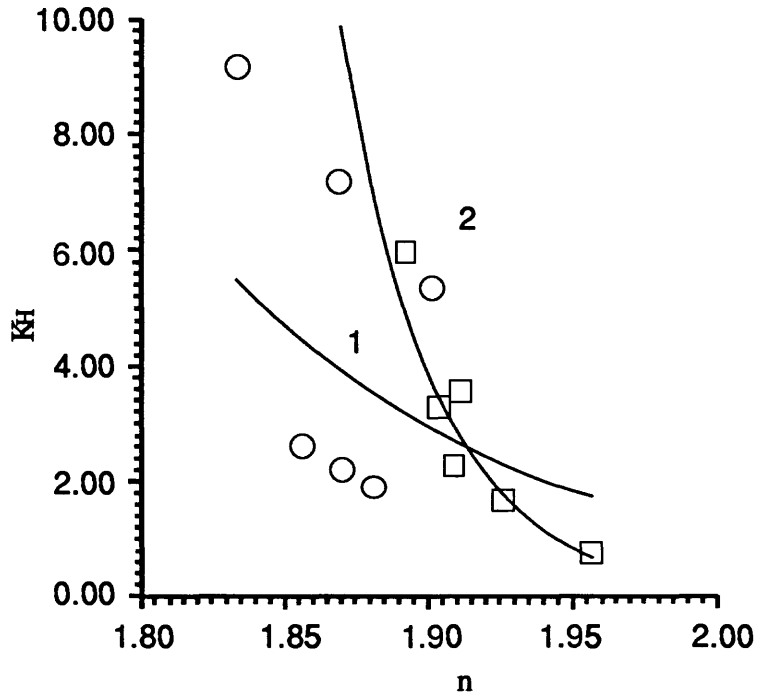

Figure 2. KH ratio dependence on the sample oxidation number. 1 = surface, 2 = volume samples.

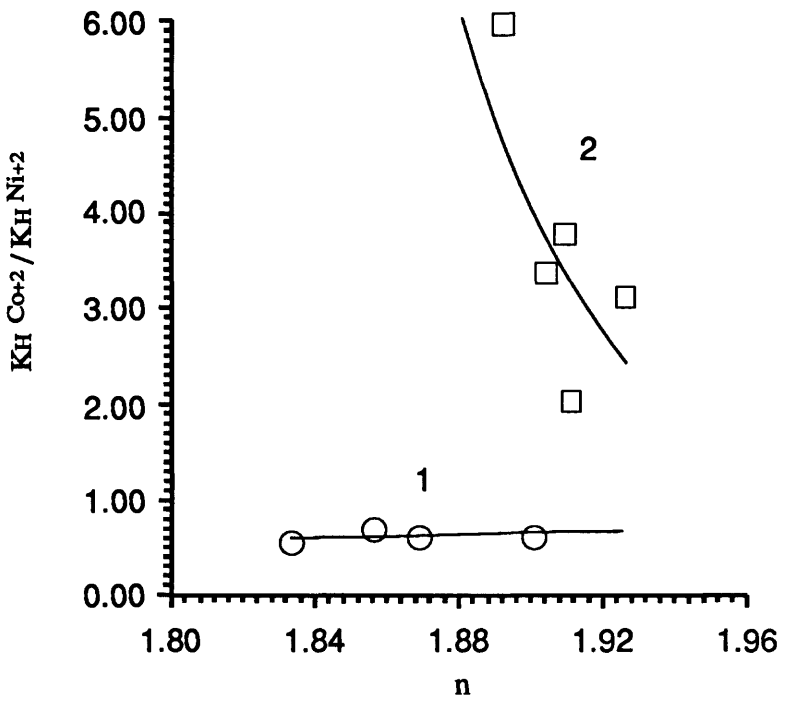

Figure 3. KH ratio dependence on the sample oxidation number. 1 = surface, 2 = volume samples.

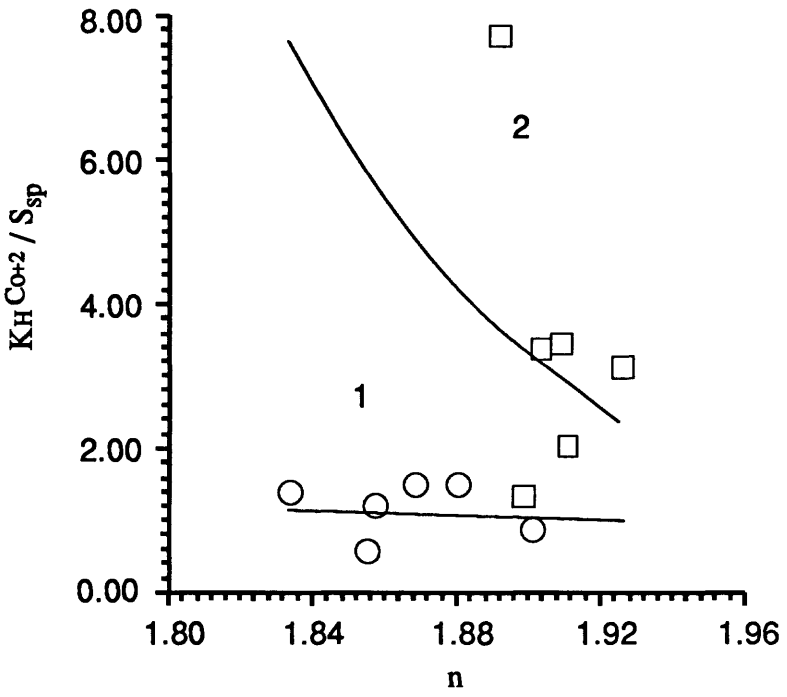

Figure 4. The dependence of KH related to specific surface area on oxidation number. 1 = surface, 2 = volume samples.

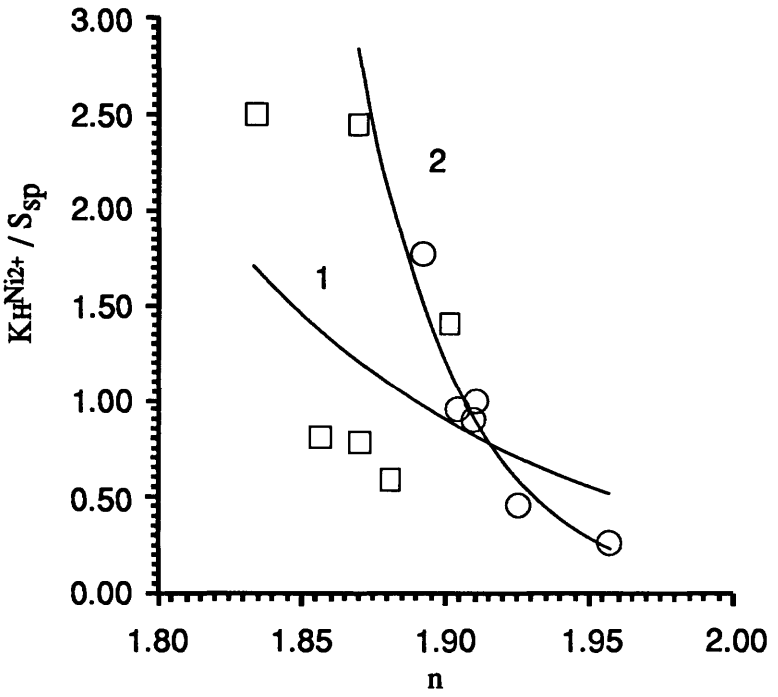

Figure 5. The dependence of KH related to specific surface area on oxidation number. 1 = surface, 2 = volume samples.

REFERENCES

Gramm-Osipov, L.M., Petrova, V.V., Volkova, T.I., and Tishchenko, P.Ya., 1987. Changing of oxidation degree of manganese micronodules in sediments of the Central Pacific : Geokhimiya, v. 6, p. 862-867. (In Russian)

Kaplun, E.V., Butenko, T.U., Avramenko, V.A., and Stashchuk, M.F., 1990. Co, Ni adsorption by vernadites with different oxidation numbers: Doklady Nauk, Academy of Sciences, USSR, v. 4, p. 312-314.

Kiselev, A.V. and Dreving, V.P., 1973. Experimental methods in adsorption and molecular chromatography: Moscow State University Press, 447 p.

van der Weijden, C.H., 1976. Some geochemical controls on Ni and Co concentrations in marine ferromanganese deposits: Chemical Geology, v. 18, p. 65-80.

Young, D.V. and Crowell, A.D., 1962. Physical adsorption of gases: Butterworths, London.

MANGANESE GEOCHEMISTRY IN THE KARIN RIDGE REGION: PRELIMINARY PHYSIOCHEMICAL DESCRIPTION

Lev M. Gramm-Osipov[1], James R. Hein[2], and Ruslan V. Chichkin[1]

[1]Pacific Oceanological Institute, Far Eastern Branch, Russian Academy of Sciences, 43 Baltiyskaja, Vladivostok 690041, Russia; [2]U.S. Geological Survey, 345 Middlefield Road MS 999, Menlo Park, CA 94025, USA

To study the influence of physiochemical conditions on the composition and genesis of Fe-Mn deposits is thought to be most convenient in those sites of the seafloor where conditions change significantly, for example, around volcanic edifices. From the top to the bottom of large rises, pressure ranges within hundreds of atmospheres, temperature within several degrees, pH within tenths, oxygen concentrations within tenths of mmol, and salinity by about 0.1‰. However, interactions between the present physiochemical conditions (determined and measured) and the composition of Fe-Mn deposits is valid only with respect to the surfaces of the deposits exposed to seawater. Hence, the best results will be obtained with analyses of the thinnest uppermost Fe-Mn crust layers that it is possible to sample, which represents the youngest age.

Fe-Mn crust characteristics must be chosen to correlate with physiochemical conditions and to describe the processes of formation of the solid phase. Physical chemistry can provide the needed information, whereas the chemical composition of the crusts fail to serve as an important comparative characteristic because it is associated with kinetic factors that cannot presently be estimated. Also chemical composition is of limited value because manganese minerals within Karin Ridge deposits are composed mostly of vernadite (δ–MnO_2) and little evidence exists as to how it varies in crystallinity and lattice structure with water depth. The same is also true of Fe minerals, represented by X-ray amorphous compounds ($FeOOH \cdot x\ H_2O$) and goethite. The one characteristic that may be meaningful for understanding interactions between physiochemical conditions and the compositions of Fe-Mn deposits is thought to be oxidation number "n" of the manganese oxide. Oxidation degree "n" is the ratio O/Mn. The oxidation number of manganese oxide changes as a result of the reaction of disproportionation with concentrations of Mn^{2+} and H^+ (Tye, 1976) in a solution:

$$MnO_2 + Mn^{2+} + 2H_2O = 2MnOOH + 2H^+ \qquad (1)$$

The correlation between concentrations of Mn^{2+} and H^+ in a solution and an oxidation number as determined experimentally is described by the equation:

$$\ln aMn^{2+} = 25.056 - 4.605\ pH + \ln [(2-n)^4/(2n-3)] \qquad (2)$$

($T = 25°$ C, $P = 1$ atm) (Tishchenko and Gramm-Osipov, 1985)

Manganese oxide (including manganese minerals) is a composite solid solution of oxyhydroxide δ–Mn(IV) and Mn(III):$[(MnO_2)_{2n-3}\ (MnOOH)_{4-2n}]$ (Gramm-Osipov *et al.*, 1991). By using this equation we determined the reasons for the variability of the oxidation number of manganese micronodules in red clays in the central Pacific (Gramm-Osipov *et al.*, 1987) and for the elevated Mn concentrations in pore water of these sediments (Pysarevsky *et al.*, 1989).

Thus knowing the *in situ* pH in seawater, the dissolved Mn concentrations, and "n" for Fe-Mn crusts, we can determine the correlation between "n" and concentration of Mn and pH by equation (2). For example, with pH and Mn concentrations being known, "n" of the solid phase can be calculated. However, it should be taken into account that no absolute agreement can be achieved between the values, because equation (2) is valid only for standard conditions ($T=25°$ C, $P=1$ atm) and for δ–MnO_2. However, the direction of changes can be determined. In addition, the correlation between physiochemical conditions in the mineral-forming environment and the processes of Fe-Mn crust formation can be determined alternatively by agreement between the concentrations of calculated Mn in seawater and Mn determined chemically in the same seawater.

More recently, we showed (Gramm-Osipov *et al.*, 1989) that the Mn concentration in seawater 150-600 m below the sea surface is governed by the reaction of hausmanite formation:

$$3Mn^{2+} + 0.5O_2 + 3H_2O = Mn_3O_4 + 6H^+ \quad (3)$$

below 150-600 m level - by the reaction:

$$Mn^{2+} + 0.25O_2 + 1.5H_2O = MnOOH + 2H^+ \quad (4)$$

Freshly precipitated MnOOH as a result of a disproportionation reaction (1) is transformed into oxyhydroxide with an oxidation number of 1.800-1.999. Manganese concentrations calculated in seawater by reactions (3) and (4) can vary by two to four times from measured concentrations, though the pattern of the profiles of concentrations do not differ (Klinkhammer and Bender, 1980; Bruland, 1983). Thus, we assume that reactions (3) and (4) are the reactions that describe the concentrations and distribution of Mn in the water column.

METHODS

A thin layer (about ≤0.5 mm) was removed from the surface of Fe-Mn crusts using a dental drill onboard ship immediately after recovery of the samples. The powders produced were subsequently analyzed onboard ship for mineral composition and oxidation number.

Oxidation number

About 2-4 mg of powdered sample was placed in a beaker (100 ml) and 10 ml of 0.01 $(NH_4)_2Fe(SO_4)_2$ was added and stirred with a magnetic stirrer until total dissolution of the oxide. Excess Fe^{2+} was determined by potentiometric inverse titration of 0.01 N $KMnO_4$ (V_1 (volume in ml), with pH=1.0-1.5. A platinum tabular electrode served as an indicator, the potential of which was measured on a "PH-121" pH-meter with respect to "EVL-1M3" reference electrode. A jump of the potential at the equivalence point was 300-400 mV.

Next, the same beaker was used to titrate Mn^{2+} with the same $KMnO_4$ solution (V_2, ml) to obtain Mn^{2+} ions, which formed a pyrophosphate complex by adding hot $Na_2H_2P_2O_7$ solution (5 g per 50 ml water). It was experimentally found that pH 6-7 is optimal for titration; this second jump of potential equaled 50-60 mV. It is not necessary to determine absolute concentrations of potassium permanganate and $(NH_4)_2Fe(SO_4)_2$ for calculating oxidation number, but rather it is enough to know the volume of $KMnO_4$ solution (V_0) going into titration of a 10 ml solution of $NH_4Fe(SO_4)_2$. Oxidation number is calculated from the formula:

$$n=1+5/2\ (V_0-V_1/4V_2-V_1) \quad (5)$$

The error of determination depends both on the precision of the burette used and on the magnitude of the jump of potential at the equivalence point. In our experiment using a burette graduated with a 0.01 ml scale, and taking into account onboard conditions, the measurement error for oxidation number is ±0.007 relative units.

X-ray diffraction analyses of mineral composition of samples was performed on a DRON-1 diffractometer (expedition version). CuKα radiation with a flat graphite monochromator was used: V = 34 KV, I = 30 mA. The monochromator allowed for the establishment of constant conditions of analysis for all samples.

RESULTS

Table 1 shows dissolved Mn concentrations in seawater in the area of Karin Ridge calculated from equation (4) (all necessary thermodynamic data and methods are from Gramm-Osipov *et al.*, 1989) and the oxidation number for Fe-Mn crusts from Karin Ridge. Mn concentrations in seawater were also calculated from equation (2) (Table 1).

Consistent with other studies, the major Mn mineral of Fe-Mn crusts on Karin Ridge is vernadite (δ–MnO_2) (See chapter by Hein *et al.*, this volume). This allows us to infer that oxidation number predominantly characterizes the mineral δ–MnO_2.

The data from Table 1 show that maximum values of oxidation number (though different in absolute values) both on the southwest and northeast flanks of Karin Ridge occur in Fe-Mn crusts sampled at the

shallowest water depths (about 2,000 m). The oxidation number for crusts collected in deep water down both flanks first drops and then tends to increase. However, the highest "n" values for crusts recovered from the lowermost dredging intervals (4200-3900 m), are not as large as those found for crusts from the ridge summit (1.978 - southwest summit, and 1.966 - southeast summit).

The calculations for Mn concentrations in the seawater column in the Karin Ridge area show (Table 1) that from the depth of about 300 m and deeper concentrations become rather close to those observed for open ocean water samples (Klinkhammer and Bender, 1980; Bruland, 1983). High Mn (II) concentrations are observed rather well in the oxygen-deficient layer and tend to decrease outside its confines. Thus, the theoretical distribution of dissolved Mn is well consistent with observed values.

These results are interesting because the degree of oxidation of Mn in the Fe-Mn crusts does not mirror the relative contents of oxygen as presently distributed in the seawater profile (see chapter by Gibbs *et al.*, this volume).

Table 1. Oceanographic conditions, dissolved Mn concentrations, and oxidation number of Fe-Mn crusts.

Sample number	Water depth (m)	pH	Temp °C	O_2 10^{-3} mol/kg	Measured Mn[1] nmol/kg	Calculated Mn (Eq. 4) nmol/kg	Calculated Mn (Eq. 2) nmol/kg	Oxidation number "n"
Station 14								
1	0	8.22	26.52	0.203	-	0.044	-	-
2	11	8.23	26.50	0.209	-	0.041	-	-
3	22	8.24	26.45	0.203	0.971	0.041	-	-
4	34	8.24	26.48	0.202	-	0.040	-	-
5	53	8.25	26.44	0.204	0.798	0.039	-	-
6	79	8.24	25.59	0.208	-	0.042	-	-
7	107	8.24	24.61	0.210	1.099	0.043	-	-
8	131	8.21	22.99	0.207	-	0.054	-	-
9	154	8.17	21.40	0.197	-	0.069	-	-
10	180	8.11	18.10	0.172	-	0.110	-	-
11	202	8.07	16.84	0.167	-	0.141	-	-
12	254	8.01	12.54	0.154	-	0.228	-	-
13	306	7.97	10.12	0.143	0.368	0.326	-	-
14	410	7.78	8.06	0.067	-	1.020	-	-
15	511	7.75	6.80	0.038	0.414	1.456	-	-
16	586	7.74	6.44	0.036	-	1.567	-	-
17	670	7.74	5.89	0.046	-	1.475	-	-
18	775	7.74	5.44	0.045	0.409	1.583	-	-
19	1032	7.78	4.32	0.054	0.297	1.292	-	-
20	1096	7.77	4.04	0.058	0.337	1.387	-	-
21	1413	7.81	3.06	0.077	0.308	1.118	-	-
22	1505	7.88	2.92	0.077	-	0.832	-	-
23	2002	7.84	2.22	0.113	0.370	0.948	0.02	1.978
24	2505	7.85	1.88	0.126	0.290	0.893	0.50	1.950
25	3002	7.88	1.62	0.129	0.097	0.784	0.37	1.952
26	3515	7.88	1.54	0.132	-	0.778	0.16	1.961
27	4038	7.88	1.48	0.154	0.146	0.771	0.09	1.966
Station 15								
1	0	8.21	26.41	0.203	0.843	0.048	-	-
2	52	8.22	26.43	0.206	1.009	0.044	-	-
3	102	8.23	25.02	0.209	0.412	0.046	-	-
4	127	8.21	23.37	0.208	-	0.052	-	-
5	152	8.16	20.86	0.194	-	0.076	-	-
6	178	8.14	19.02	0.188	-	0.092	-	-
7	204	8.03	15.23	0.155	-	0.183	-	-
8	252	7.97	11.78	0.141	0.189	0.301	-	-
9	304	7.94	10.07	0.139	-	0.376	-	-
10	396	7.82	7.92	0.081	0.455	0.822	-	-
11	506	7.74	6.88	0.098	-	1.188	-	-
12	604	7.73	5.98	0.045	0.532	1.552	-	-

Table 1. continued

Sample number	Water depth (m)	pH	Temp °C	O_2 10^{-3} mol/kg	Measured Mn[1] nmol/kg	Calculated Mn (Eq. 4) nmol/kg	Calculated Mn (Eq. 2) nmol/kg	Oxidation number "n"
Station 15 continued								
13	701	7.74	5.47	0.051	-	1.468	-	-
14	799	7.74	5.12	0.052	0.368	1.523	-	-
15	1005	7.76	4.28	0.057	0.418	1.439	-	-
16	1196	7.78	3.50	0.062	0.412	1.315	-	-
Station 16								
1	0	8.22	26.26	0.203	1.036	0.045	-	-
2	50	8.23	26.06	0.208	1.036	0.043	-	-
3	75	8.23	25.93	0.208	-	0.044	-	-
4	100	8.23	24.35	0.215	1.022	0.046	-	-
5	125	8.20	22.76	0.212	-	0.056	-	-
6	150	8.17	21.02	0.195	-	0.070	-	-
7	175	8.26	18.88	0.185	-	0.052	-	-
8	200	8.10	17.68	0.177	-	0.116	-	-
9	304	7.95	10.13	0.137	0.239	0.358	-	-
10	400	7.79	8.46	0.069	-	0.966	-	-
11	506	7.72	7.41	0.041	0.391	1.593	-	-
12	607	7.72	6.35	0.041	-	1.626	-	-
13	701	7.73	5.73	0.046	0.372	1.586	-	-
14	802	7.73	5.20	0.053	-	1.603	-	-
15	1001	7.75	4.30	0.055	0.313	1.477	-	-
16	1196	7.76	3.62	0.096	0.409	1.279	-	-
17	1494	7.79	2.73	0.083	0.260	1.197	-	-
18	2001	7.83	2.20	0.114	0.263	0.991	0.12	1.966
19	2506	7.85	1.80	0.123	0.213	0.898	0.16	1.962
20	3018	7.89	1.63	0.135	0.188	0.740	-	-
21	3510	7.85	1.52	0.133	0.199	0.893	0.60	1.948
22	4023	7.88	1.48	0.153	0.165	0.769	0.16	1.961
23	4521	7.89	1.37	0.167	-	0.721	-	-

[1] Data from K. Orians (written communication, 1993)

REFERENCES

Bruland, K.W., 1983, Trace elements in sea-water: *in* Riley, J.P. and Chester, R. (eds.), Chemical Oceanography. Academic Press, London, v. 8, p. 157-221.

Gibbs, A.E., Sergeev, A.F., Salyuk, A.N., Hein, J.R., Tapinov, V.P., and Bychkov, A.S., 1994, Hydrological parameters and water structure over Karin Ridge, Central Pacific: this volume, p. 169-186.

Gramm-Osipov, L.M., Petrova, V.V., Volkova, T.I., and Tishchenko, P.Ya, 1987, Changing of oxidation degree of manganese micronodules in sediments of the Central Pacific: Geokhimiya, v. 6, p. 862-867. (In Russian)

Gramm-Osipov, L.M., Tishchenko, P.Ya., Stashchuk, M.F., Volkova, T.I., Chichkin, R.V., and Shulga, Yu.M., 1989, Ferro-Manganese system: in Ilychev, V.I. (ed.), Chemistry of sea water and authigenic mineral formation. Nauka, p. 112-203, (In Russian).

Gramm-Osipov, L.M., Volkova, T.I., and Chichkin, R.V., 1991, Manganese dioxide behavior in water solutions (experimental data): Geokhimiya, v. 12, p 1692-1699, (In Russian).

Hein, J.R., Gramm-Osipov, L.M., *et al.*, 1994, Description and composition of Fe-Mn crusts, rocks, and sediments collected on karin ridge, R.V. *Aleksandr Vinogradov* cruise 91-AV-19/2: this volume, p. 39-86.

Klinkhammer, G.P. and Bender, M.L., 1980, The distribution of manganese in the Pacific Ocean: Earth and Planetary Sciences Letters, v. 46, p. 361-384. (In Russian)

Pysarevsky, A.M., Tishchenko, P.Ya., Gramm-Osipov, L.M., and Nikolayev, Yu.I., 1989, The MnO_2/Mn^{2+} system as the potential control of Eh in red clays: Doklady, Academy of Sciences of USSR, v. 306, p. 195-198, (In Russian).

Tishchenko, P.Ya. and Gramm-Osipov, L.M., 1985, Solid phase formation of manganese in the ocean: Doklady, Academy of Sciences of USSR, v. 280, p. 231-232 (In Russian).

Tye, F.L., 1976, Manganese dioxide electrode: relationship between activities and stoichiometry for compositions near to MnO_2: Electrochimica Acta, v. 21, p. 415-420.

PHYSICAL PROPERTIES OF ROCKS AND SEDIMENTS FROM KARIN RIDGE (CENTRAL EQUATORIAL PACIFIC) AND THE BERING SEA

Alexander I. Svininnikov

Pacific Oceanological Institute, Far Eastern Branch, Russian Academy of Sciences, 43 Baltiyskaja, Vladivostok 690041, Russia

ABSTRACT

Physical properties including compressional wave-velocity, bulk density, porosity, and natural radiation were measured on basalt, trachyte, hyaloclastite, mud, and Fe-Mn crust samples. Rocks were collected by dredging and sediments by gravity and box corers from Karin Ridge (central equatorial Pacific), the northwest Pacific, and the Bering Sea during Legs 2 and 4 of the *Aleksandr Vinogradov* cruise 91-AV-19.

Basalts from Karin Ridge have high vesicularity, variability in values of bulk properties, and low sonic velocity and bulk density. The properties reflect their subaerial origin and indicate they formed at far shallower paleodepths than their present locations. Fe-Mn crusts differ in acoustic properties from rocks and sediments associated with them. Radiation values of Fe-Mn crusts are larger than for the rocks and sediments. Thus, radiometric surveys can be used to search for crusts and in estimating their thickness.

INTRODUCTION

To use optical, acoustic, gravimetric, and radiometric methods in studying the sea floor, the physical properties of rocks, sediment, minerals, and water masses must be known. Shipboard measurements of compressional-wave velocity, sound velocity anisotropy, wet-bulk density, porosity, and natural radiation are directly related to the composition and texture of the rocks, sediments, and mineral deposits. New data included in this report supplement and support previously obtained results from the DSDP and facilitate geoacoustic and petrophysical modeling of the sea floor.

METHODS

Physical properties of collected rocks were measured on sample cubes measuring 40 to 100 mm on a side, under a natural seawater saturated state.

Wet-bulk density of rocks was determined by hydrostatic weighing using a DR-2 density meter (Kobranova *et al.*, 1977). The wet-bulk density of sediments was determined on undisturbed, 50 cm^3 seawater-saturated samples using the formula $\rho = Po/Vo$, where Po = weight of sea water-saturated sample and Vo = volume of undisturbed sediments; the volume of the inner cylinder of the core is 50 cm^3.

Water content, defined as wp/ws x 100, where wp = weight of pore fluid and ws = weight of wet sediment, was estimated by weighing a sample before and after air drying at 105°C. The formula M=(Po-Pc)/Po was used to calculate water content, where Pc = weight of sediment sample after drying at 105°C.

Porosity (Ratio of pore volume to sample volume) was calculated using the formula $n = (Po-Pc)/(Vo \times \rho sw(1-C))$, where ρsw = density of seawater in pores; C = % salinity / 100 (e.g. if salinity = 3.5% then C=0.035). Effective porosity was estimated by centrifuging, drying, and saturation using the free water saturation technique (Starostin, 1979).

Sound velocity was measured by the impulse transmission method, using a set of devices such as UK-10P, UDM-1, UD-11UA, UK-14P, UK-16P, frequency meter F3-54A, G5-54 generator, oscillographs, and lead-zirconate-titanate transducers with resonance frequencies of 60, 100, 600, 800, 1800, 2500, and 5000 kHz. Transducers were fixed on sliding calipers to facilitate measurements of distances between them with 0.05 mm accuracy. The error in reading the onset of signal arrival was -0.01 microseconds (mcs). Instruments were calibrated by velocity measurements in standards of KOU-2 set, quartz ultrasonic delay line, Plexiglas, and water samples of known temperature. Longitudinal wave velocity in such porous materials, as in most sediments and rocks, is greatly influenced by water saturation where velocity increases as pores are filled with water. To protect samples dredged or recovered with grabs from drying,

measurements were carried out immediately after recovery; samples remained in a seawater filled container until measurements could be made. Sediment samples were isolated from air with a waterproof cover. Once aboard ship, the temperature of samples changed from an initial 1.5°C to 20-35°C, causing a velocity increase of 5%. In the interest of corrections, temperature was controlled during the measurements. We used a mercury thermometer scaled at 0.02°C. Velocity dependence on temperature was estimated by heating samples that had been refrigerated.

Longitudinal wave velocity measurements in sediments were made through a polyethylene film (0.05 mm thick) enveloping the sample. The outer surface of the film was covered with a liquid lubricant or water at the contact with the transducers.

Velocity anisotropy was estimated by longitudinal wave velocity measurements in a minimum of three orthogonal directions: V1 = longitudinal wave velocity parallel to layering, schistosity, predominant orientation of minerals, and elongation of oriented structures; V2 = perpendicular to V1; V3 = velocity across layering, schistosity, etc., or transverse to bedding (Belikov *et al.*, 1970). The anisotropy coefficient was calculated using the formula: A = (V1-V3) x 100% / V4, where V4 = average velocity value (Table 1; Fig. 1). In order to measure the velocity anisotropy of longitudinal waves in sediments, it is commonly sufficient to make measurements in only two directions: along and across bedding (which is usually the same as across and along a sediment core). Initially, measurements were carried out across a sediment core (along bedding) every 2-10 cm depending on sediment homogeneity. The core was then cut into sections 10-15 cm long and velocity was measured along the core (across bedding).

Natural radiation was measured in seawater, sediment, and rock samples using techniques of gamma-ray determinations detailed in the manual on petrophysical property determinations in samples (Kobranova *et al.*, 1977). Gamma-ray activity in samples and specimens was measured using laboratory-ZM-701 radiometer consisting of ZWN-21M high-voltage source, A-22M analyzer with a regulated window, P-21 counter, SSU-70 scintillometer with a NaJ(Tl) detector (d=40mm, l=25mm), S2-56 oscillograph, and F3-54 frequency meter. Affective coefficient of measurements at 40K is 14%. Measurements were carried out on 50 cm^3 samples by exposure to the detector for the time necessary to count 100,000 impulses. The measurement was then computed by dividing 100,000 impulses by the count time (in minutes, min) and is given in Table 1 as Total count. Relative gamma-ray activity values in rocks and crusts, given in Table 1 as Net, is the difference between the total intensity of gamma quantum induced by major U, Th, and K radioactive elements distributed in the rocks, and a minimum value measured in tholeiitic basalts of the East Pacific Rise, the sample used for background value measurements (sample V13-2/15). During tests of sediments, ground rocks, and crusts, background radiation was measured on a control aluminum sample-box 50 cm^3 in volume, with walls 0.5 mm thick, filled with pure ground quartz. The difference between the number of counted impulses per minute in the sample and the control sample-box, is given as Net in Tables 2 and 4, and in Fig. 2, plotted against rock density.

Some samples of major rock and crust types dried at 105°C and ground to grain sizes of less than 0.25 mm were kept in the sample-box until equilibrium and then measured. The results are given in Table 2 as the ratio of natural radiation relative to the mass and volume of the samples.

RESULTS

Physical properties were measured in samples of mud, hyaloclastite, basalt, trachyte, phosphorite, and Fe-Mn crusts dredged from the slopes of Karin Ridge (Table 1). Physical properties of sea floor sediments from the northwest Pacific Ocean and the southern part of the Bering Sea, along track lines that crossed environments of pelagic and hemipelagic sedimentation were also measured. Sediments from the North Pacific and Bering Sea include red clay, poorly siliceous clays, and siliceous clays .

Wet-Bulk Density

Wet-bulk density ranges from 1.35 to 1.59 g/cm^3 in poorly-siliceous clay and up to 2.66-2.68 g/cm^3 in massive basalt and phosphorite. Density of sediments increase to maximum values in samples from the deepest stratigraphic intervals. Wet-bulk density of basalts, alkalic basalts, and trachytes (2.06-2.66 g/cm^3) depends greatly on vesicularity and to a lesser degree on the mineral composition of the rocks. Primary vesicularity of basalts, caused by the amount of volatiles in the magma and the water depth of eruption (hydrostatic pressure), records the paleoenvironmental conditions under which the volcanic rocks formed (Jones, 1969; Moore and Schilling, 1973; Svininnikov, 1989).

Highly vesicular basalts, with densities of 2.06-2.54 g/cm^3, compose the lower-middle section of the flanks of Karin Ridge (CAM1, D4, D5, D7, and D8), higher-density basalts (ranging from 2.35 to 2.66 g/cm^3) occur at dredge sites D3, D4, and D11. At water depths from 4.5 to 3 km, the density of the

volcanic rocks decreases gradually up slope from 2.52 to 2.22 g/cm^3.

Phosphatized limestone and phosphorite have densities of 2.09 g/cm^3 and 2.68 g/cm^3, respectively. The latter represents the maximum density for Karin Ridge rocks.

Density of Fe-Mn crusts (1.9-2.15g/cm^3) depends on the amount and composition of clayey, clastic, and fragmental carbonate particles in the crust, the type of included rock fragments, and the type of Fe-Mn minerals. Density is also dependent on crust texture. The outer crust layer A (samples D1-1/5; D11/3; D1-1/2; D1-1/1; D1-1/9; D1-1/6; D1-1/11) have densities of 1.95-2.14 g/cm^3, significantly lower than the inner crust layers (2.34 g/cm^3) as well as basalt.

Sonic Velocity

Compressional-wave velocity ranges from 1.52 to 5.14 km/sec. Sound velocities for weakly-lithified and unconsolidated sediments and for volcaniclastic rocks (mudstone, hyaloclastite) increase with grain-size and consolidation (Table 1). Claystones (Samples D10-1a, 1b, 1c) have velocities from 1.59 to 1.7 km/s. In consolidated claystones and hyaloclastites sound velocity reaches 1.8 km/s and 2.2 km/s, respectively. Phosphatized limestones have velocities averaging 2.26 km/s. Velocity varies from 2.24 to 3.53 km/s in Fe-Mn crusts. Low velocities were measured in porous layer A (Samples D1-1/5: Vp=2.78 km/s, D1-1/6: Vp=2.76 km/s), in crusts formed on poorly consolidated hyaloclastite substrate (Samples D11-2: Vp=2.46 km/s and D4-8: Vp=2.78 km/s), and in mudstone (Samples D10-2: Vp=2.8 km/s and D8-6/2: Vp=2.78 km/s). In the inner layer B of crusts, sound velocity reached 3.84 km/s in some samples (Sample D1-1), but more common values are about 3.35 km/s.

Velocity anisotropy in Fe-Mn crusts is not always distinctive, commonly not high, and is closely associated with heterogeneity, zonation, and layering of the samples. In nearly all varieties of crusts, sound velocities measured along layering (horizontal direction) is higher than velocity measured in the direction normal to the crust surface. Transverse anisotropy will no doubt be of intermediate values (more precisely, quasi-anisotropic with a vertical axis of the symmetry).

Elastic properties of basalts, trachytes, and sedimentary rocks are inversely proportional to porosity. Compressibility of seawater in pores is higher than that of mineral particles and the framework rock. Pore-space water content in highly vesicular basalt (Samples D4-13c/1; D4-18;D4-8a; D8-6/7) reaches 50% of rock volume, which lowers the sound velocity in them to 3.05-3.07 km/s. With decreasing porosity, velocity increases up to 4.72 km/s in massive aphyric basalts (Samples D4-13, D11-3) and 4.99 km/s in leucocratic plagioclase basalts (Sample D7-5; Fig. 1). Generally, measured velocities are consistent with values common for basalts and alkalic volcanic rocks of oceanic islands, ridges, and plateaus.

Sound Velocity - Density Relationships

The relationship between sound velocity and density is of interest for rock density estimations based on acoustic wave velocities and rock-type (Figs. 3, 4).

In sedimentary and volcaniclastic rocks with density of 1.35-1.90 g/cm^3, sound velocity gradually increases from 1.56 to 2.30 km/s. In basalt, velocity increases from 3.05 to 4.99 km/s as density increases from 2.06 to 2.54 g/cm^3. Data points on the plot satisfactorily define a straight line, but can be better defined by a second or third order polynomial regression (Fig. 3).

Data points associated with phosphorites and phosphatized limestones show a considerable deviation from the regression line. Limestones have longitudinal wave velocities values 2 km/s lower than basalts with the same density values. Sound velocity in Fe-Mn crusts is lower than it is in basalts with equivalent density. Deviation from the regression line is explained by differences in texture, i.e. framework structure in vesicular basalts, massive and granular in phosphorites, and fracture porosity in phosphatized limestones and crusts.

Natural Radiation

Gamma-ray activity of Karin Ridge rocks and sediments varies within 780 imp/min (Table 1). Radiation in volcanic rocks varies within 345 imp/min. Minimum values of 25-99 imp/min were determined for basalt samples (Samples D4-13-1/4, D4-13c/2, and D11-3). Alkaline basalts and trachytes emit radiation of 120-366 imp/min, proportionally increasing with increasing alkalinity.

Sediments and sedimentary rocks are characterized by relatively low radiation values of 22-85 imp/min in claystones, and 97-123 imp/min in hyaloclastites. A slight increase in gamma-ray activity in some hyaloclastite samples results from an increase in iron and manganese hydroxides contents (Sample D4-8/1).

Maximum values (271-800 imp/min) were measured in Fe-Mn crusts. Their radiation emissions change somewhat from the surface inward, reflecting changing ratios of Fe-Mn hydroxides and clastics plus carbonate particles. Qualitative ratios between crusts and substrate materials chiefly influence the radiation values of crusts. To estimate the radiation of major rock types, it is necessary to exclude the influence of density and heterogeneity of the samples. So carefully selected samples were dried and ground to the grain-size of 0.25 mm prior to being placed in hermetically sealed aluminum containers. After radiation equilibrium in the samples had been achieved, measurements were recorded (Table 2).

Physical Properties of Sediments

New data obtained on sound velocities, porosity, and water content of sediments of the Pacific Ocean and Bering Sea (Tables 3-8, Figs. 5 -10) are consistent with data obtained earlier for these areas (Svininnikov *et al.*, 1984). We confirm the increase in sound velocity, porosity, and water content, and the decrease in density as the biogenic silica content of muds increases (Figs. 6, 8). These changes result from the framework structure of the sediments. A slight radiation increase is accompanied by an increase of clay content and degree of oxidation of the sediment. Maximum radiation is characteristic of horizons rich in Fe-Mn micronodules (Table 4; Fig. 7).

CONCLUSIONS

Physical properties, including compressional-wave velocity, bulk density, porosity, and natural radiation, were measured on basalt, trachyte, hyaloclastite, claystone, Fe-Mn crusts, and sediments from Karin Ridge (central equatorial Pacific), the northwest Pacific, and the southern Bering Sea during Legs 2 and 4 of the *Aleksandr Vinogradov* Cruise 91-AV-19. Results show that: 1) High vesicularity of basalts from Karin Ridge, along with density and sound velocity, are probably explained by shallow water eruption of these rocks. Rocks with framework texture (vesicular basalts) have lower density than rocks that are massive, strongly fractured, and granular (phosphorites, phosphatized limestones, diabases), but all have similar velocities.

2) Natural radiation of Fe-Mn crusts is considerably higher than in substrate rocks, associated sediments, and seawater. This characteristic can possibly be used as a tool in the exploration for Fe-Mn crusts and estimation of their thickness.

3) Low contents of clay minerals and carbonate in siliceous sediments of the northwestern Pacific and Bering Sea are accompanied by a decrease in density and an increase in sound velocity relative to muds. Increased radiation reflects high clay mineral contents and sediment oxidation.

4) Deep-sea sediments with abundant Fe-Mn micronodules show high radiation values.

Table 1. Physical Properties of Rocks, *R.V. Vinogradov* cruise 91-AV-19

Sample #	Wet Bulk Density (g/cc)	Sound Velocity V1 (km/sec)	V2 (km/sec)	V3 (km/sec)	V4 (km/sec)	A	Natural Gamma Radiation Total Count	Net
D1-1/1: Fe-Mn crust	2.07	3.24	3.16	3.14	3.18	3.4	1980	582
D1-1/2: Fe-Mn crust	2.07	3.36	3.03	2.92	3.10	14.1	1802	407
D1-1/3: Fe-Mn crust	2.03	3.40	3.39	3.29	3.36	3.2	1744	351
D1-1/4: Fe-Mn crust	2.34	3.91	3.86	3.82	3.86	2.4	1686	302
D1-1/5: Fe-Mn crust	1.95	2.83	2.74	2.73	2.77	3.6	1720	351
D1-1/6: Fe-Mn crust	2.12	3.81	3.08	2.76	3.22	32.7	1781	407
D1-1/7: Fe-Mn crust	2.42	3.80	3.51	3.49	3.60	8.6	1645	271
D1-1/8: Fe-Mn crust	2.44	3.84	3.80	3.63	3.72	5.5	1690	361
D1-1/9: Fe-Mn crust	2.08	3.84	3.76	3.00	3.53	23.6	1664	299
D1-1/10: Fe-Mn crust	2.42	4.19	3.72	3.66	3.86	13.8	1731	366
D1-1/11: Fe-Mn crust	2.14	3.64	3.29	3.14	3.35	15.1	1788	423
D1-6: Fe-Mn crust	1.94	3.22	3.14	-	3.18	-	2133	702
D1-8: Fe-Mn crust	2.15	3.44	-	2.81	3.12	-	1938	487
D4-8: Fe-Mn crust	1.92	2.81	2.76	2.33	2.63	18.4	2119	747
D4-8/1: Hyaloclastite	1.85	2.23	2.19	2.18	2.20	2.2	1464	128
D4-12: Fe-Mn crust	1.99	2.91	2.89	2.80	2.87	4.0	1996	624
D4-12/2: Phosph. Limestone	2.09	2.52	-	2.01	2.26	-	1604	52
D7-8: Phosphorite	2.68	4.35	4.34	3.79	4.16	13.1	1614	137
D8-6/1: Claystone	1.59	1.80	1.78	1.76	1.78	2.4	1484	85
D8-6/2: Fe-Mn crust	1.96	2.85	2.74	2.53	2.71	11.9	2115	800
D10-1a: Mud	1.51	1.65	1.64	1.63	1.64	1.5	-	-
D10-1b: Mud	1.53	1.73	1.70	1.69	1.70	2.4	1548	63
D10-1c: Mud	1.35	1.64	1.58	1.56	1.59	4.8	1507	22
D10-2: Fe-Mn crust	1.99	2.89	2.82	2.69	2.81	7.0	2040	545
D11-2: Fe-Mn crust	1.90	2.46	2.07	2.01	2.03	-	2.34	531
D11-2a: Hyaloclastite	1.64	-	-	-	-	-	1539	97
D11-2a/1: Hyaloclastite	1.71	1.94	1.93	1.88	1.92	3.2	-	-
D11-2b: Hyaloclastite	1.77	-	-	-	-	-	1560	106
D3-2: Basalt	2.52	4.84	4.77	4.34	4.65	10.6	1570	176
D4-13: Basalt	2.63	4.88	4.79	4.47	4.71	8.7	1713	341
D4-13b/1: Basalt	2.17	3.64	3.61	3.52	3.59	3.3	1494	158
D4-13b/2: Basalt	2.23	3.83	3.60	3.46	3.63	10.0	1549	213
D4-13c/1: Basalt	2.21	3.86	3.76	3.68	3.77	4.8	1468	118
D4-13c/2: Basalt	2.21	3.56	3.54	3.52	3.54	1.2	1450	99
D4-13c/3: Basalt	2.22	3.76	3.54	3.50	3.60	7.4	1402	51
D4-13c/4: Basalt	2.06	3.14	3.02	3.01	3.05	4.1	1377	26
D4-1a: Basalt	2.30	4.30	4.06	4.05	4.14	6.2	1443	107
D4-1b: Basalt	2.10	3.71	3.69	3.52	3.64	5.1	1469	133
D4-8a: Basalt	2.11	3.29	3.03	2.88	3.07	13.4	1571	171
D5-2: Basalt	2.48	4.23	4.15	3.94	4.11	7.3	1463	77
D7-3: Basalt	2.44	4.37	4.25	4.23	4.28	3.4	1525	101
D7-3a: Basalt	2.48	4.99	4.61	4.33	4.65	14.2	1571	147
D7-3b: Basalt	2.39	4.44	4.38	4.20	4.34	5.6	1600	115
D7-5: Basalt	2.54	5.14	4.93	4.89	4.99	5.0	1596	172
D8-1: Basalt	2.33	4.43	4.10	3.96	4.16	11.1	1714	229
D8-4: Basalt	2.48	4.39	4.35	4.25	4.33	3.3	1551	103
D8-6/7: Basalt	2.17	3.28	3.04	3.04	3.12	7.8	1564	165
D11-3: Basalt	2.66	4.85	4.67	4.64	4.72	4.3	1411	21
D11-3/1: Basalt	2.35	3.87	3.80	3.73	3.70	3.7	1607	122
CAM-1-3: Basalt	2.41	4.28	4.24	3.95	4.16	7.9	1567	143
CAM-1-4: Trachyte	2.37	3.89	3.77	3.63	3.77	5.3	1796	366

Dash means not analysed; V1= longitudinal wave velocity along layering, schistocity, predominant orientation of minerals, and/or elongation of oriented structures; V2=velocity perpendicular to V1 orientation; V3= velocity transverse to layering, schistocity, etc.; V4= average velocity; A=anisotropy coefficient.

Table 2. Natural gamma radiation of Karin Ridge rocks, Fe-Mn crusts, and seawater.

Sample	Rock Type	Natural Gamma Radiation			
		Total Count	Net	Weight Radiation	Volume Radiation
D10-1	Mud	1494	62	1.19	1.74
D11-2b	Hyaloclastite	1489	55	0.83	1.47
D11-2a	Hyaloclastite	1477	51	0.79	1.30
D4-1	Basalt	1483	82	1.34	2.95
D10-2	Fe-Mn crust	1833	428	6.51	12.96
D11-2	Fe-Mn crust	1826	429	6.34	12.56
HS15	Seawater	1333	9	0.02	0.02

Table 3. Physical properties of sediments, *R.V. Vinogradov* cruise 91-AV-19/2; GC-1.

T ℃	H cm	L mm	t mcs	Vm m/s	Vw m/s	Vr	V20 m/s	VSIT m/s	DEN g/cm^3	Imp
17.00	3	136.8	69.23	1587	1514	1.049	1598	1565	-	-
17.10	5	140.5	69.41	1637	1514	1.081	1647	1613	1.46	2404
17.21	10	145.2	72.76	1626	1514	1.074	1636	1602	-	-
17.31	15	147.9	80.50	1503	1514	0.992	1512	1481	-	-
17.41	20	146.2	79.10	1508	1515	0.996	1517	1486	-	-
17.52	25	150.5	82.20	1504	1515	0.992	1512	1481	-	-
17.62	30	153.8	84.20	1507	1515	0.995	1515	1484	-	-
17.72	35	156.5	86.30	1502	1516	0.991	1509	1478	1.49	2249
17.83	40	159.4	88.40	1499	1516	0.989	1506	1475	-	-
17.93	45	160.5	88.80	1505	1516	0.992	1511	1481	-	-
18.03	50	158.2	84.50	1554	1517	1.025	1561	1529	-	-
18.14	55	159.3	89.20	1484	1517	0.979	1491	1460	-	-
18.24	60	160.2	89.40	1491	1517	0.983	1497	1466	1.25	1871
18.34	65	158.8	88.30	1494	1518	0.984	1500	1469	-	-
18.45	70	163.2	91.00	1498	1518	0.987	1503	1472	-	-
18.55	75	162.5	91.00	1490	1518	0.982	1495	1465	-	-
18.66	80	166.3	93.30	1494	1518	0.984	1499	1468	-	-
18.76	85	168.5	94.40	1501	1519	0.988	1505	1474	1.55	2333
18.86	90	168.0	94.50	1493	1519	0.983	1497	1467	-	-
18.97	95	164.9	93.00	1484	1519	0.977	1488	1457	-	-
19.07	110	163.8	90.60	1511	1520	0.994	1515	1484	-	-
19.17	115	163.3	90.00	1516	1520	0.997	1519	1488	-	-
19.28	120	163.4	90.00	1517	1520	0.998	1520	1489	1.45	2204
19.38	125	162.9	89.70	1516	1520	0.997	1519	1488	-	-
19.48	130	162.3	89.70	1509	1521	0.993	1512	1481	-	-
19.59	135	158.6	87.30	1509	1521	0.992	1511	1480	1.53	2312
19.69	140	163.2	91.20	1495	1521	0.982	1497	1466	-	-
19.79	145	161.9	90.10	1498	1522	0.985	1500	1469	1.42	2130
19.90	150	162.6	90.90	1493	1522	0.981	1494	1464	-	-
20.00	155	159.4	88.20	1502	1522	0.987	1503	1473	-	-

Dash means not analyzed; T= temperature of sediments; H = sampling horizon (sub-bottom depth); L= base of measuring (distance between transducers that sound waves travel - travel distance); t = travel time through sample; Vm = uncorrected (measured) velocity; Vw = sound velocity in the sea water at given temperature and pressure; Vr = relative velocity (Vr=Vm/Vw); V20 = sound velocity in sediments at 20°C; VSIT = sound velocity in the sediments at *in situ* conditions (with bottom pressure and temperature taken into account); DEN = wet-bulk density; Imp - impedance.

Table 4. Physical properties of sediments, *R.V. Vinogradov* cruise 91-AV-19/4

Site	H	P1	P2	P0	Wet Bulk Density	Porosity	WV	Sound Velocity Vr	Sound Velocity V20	Natural Gamma Radiation Total Count	Natural Gamma Radiation Net
	cm	g	g	g	g/cm3	%	%		m/sec		
GC-6	40	76.95	33.32	14.68	1.25	88.0	70.1	1.000	1524	1436	18
GC-7	2	79.87	37.00	14.87	1.30	86.5	66.0	1.006	1533	1512	94
"	20	79.87	36.32	14.73	1.30	87.9	66.9	0.999	1522	1488	59
"	30	78.75	36.25	14.28	1.29	85.8	65.9	0.997	1519	1438	12
"	45	79.95	38.48	14.63	1.31	83.7	63.5	0.982	1497	1437	7
"	65	81.85	42.70	15.08	1.34	79.0	58.6	0.985	1501	1484	54
GC-9	2	83.69	42.48	15.21	1.37	83.2	60.2	0.996	1518	1542	113
"	60	84.29	43.70	14.55	1.39	81.9	58.2	0.974	1484	1467	69
"	130	82.82	41.50	14.74	1.36	83.4	60.7	0.979	1492	1467	49
"	220	81.90	40.24	15.00	1.34	84.1	62.3	0.977	1489	1405	41
GC-13	10	74.83	33.56	15.14	1.19	83.3	69.1	1.002	1527	1408	22
"	30	74.20	32.10	14.96	1.18	85.0	71.1	0.999	1522	1497	11
"	50	78.74	36.50	15.34	1.27	85.2	66.6	0.987	1504	1407	21
"	70	75.83	34.87	14.73	1.22	82.7	67.0	0.988	1506	1411	25
"	90	78.35	37.77	14.84	1.27	81.9	63.9	0.989	1507	1401	6
"	110	81.75	41.20	15.27	1.33	81.8	61.0	0.979	1492	1427	32
"	130	76.40	34.27	14.89	1.23	85.0	68.5	0.997	1519	1422	27
"	160	79.34	39.10	14.90	1.29	81.2	62.4	0.981	1495	1477	49
"	170	79.62	39.82	14.78	1.30	80.3	61.4	0.981	1495	1405	10
"	190	82.14	41.50	15.30	1.34	82.0	60.8	0.982	1497	1440	20
"	210	81.34	41.45	14.81	1.33	80.5	60.0	0.984	1500	1415	10
"	230	80.84	41.13	14.99	1.32	80.1	60.3	0.981	1495	1424	14
"	250	80.34	40.33	14.75	1.31	80.7	61.0	0.980	1494	1440	35
"	265	82.14	42.27	14.80	1.35	80.5	59.2	0.986	1503	1424	24
"	285	81.55	41.77	14.77	1.34	80.3	59.6	0.984	1500	1422	42
"	305	85.07	46.34	14.82	1.41	78.2	55.1	0.989	1507	1461	61
"	320	83.13	43.26	14.93	1.36	80.5	58.5	0.985	1501	1442	42
"	350	79.97	39.02	14.71	1.31	82.6	62.7	0.986	1503	1428	28
"	370	80.42	38.65	14.62	1.32	84.3	63.5	0.990	1509	1446	19
"	395	80.22	39.30	14.69	1.31	82.6	62.4	0.983	1498	1436	16
"	410	81.30	40.32	15.09	1.32	82.7	61.9	0.987	1504	1415	15
"	432	83.42	43.83	14.38	1.38	79.9	57.3	0.985	1501	1423	27
"	450	81.94	42.62	14.82	1.34	79.3	58.6	0.990	1509	1394	11
"	470	82.33	42.12	14.82	1.35	81.1	59.6	0.987	1504	1392	28
"	490	80.12	39.10	14.84	1.31	82.8	62.8	0.985	1501	1407	17
"	510	79.65	38.82	14.85	1.30	82.4	63.0	0.989	1507	1380	6
"	530	77.52	34.85	14.72	1.26	86.1	67.9	0.992	1512	1419	17
"	550	80.70	39.44	14.95	1.32	83.3	62.8	0.992	1512	1427	29
"	570	80.25	39.57	15.01	1.30	82.1	62.4	0.990	1509	1420	22
"	590	79.52	37.80	14.78	1.29	84.2	64.4	0.989	1507	1432	34
"	605	80.84	39.92	14.74	1.32	82.6	61.9	0.993	1513	1418	20
BC-16	30	77.40	35.19	14.71	1.25	85.2	67.3	0.996	1518	1386	6
"	48	77.15	34.22	14.48	1.25	86.6	68.5	0.997	1520	1393	10
GC-20	15	86.95	51.32	14.56	1.45	71.9	49.2	0.987	1504	1470	62
"	30	88.40	54.20	14.75	1.47	69.0	46.4	0.988	1505	1492	91
"	40	87.32	53.50	14.70	1.45	68.3	46.6	0.993	1513	1486	66
"	58	87.22	52.61	14.70	1.45	69.8	47.7	0.985	1501	1490	98
GC-24	15	86.23	49.95	14.73	1.43	73.2	50.7	0.991	1510	1468	86
"	40	82.67	44.09	14.75	1.36	77.9	56.8	0.978	1490	1436	58
"	70	86.43	49.85	14.77	1.43	73.8	51.0	0.981	1495	1398	38
BC-26	10	81.82	47.77	14.71	1.34	68.7	50.7	0.991	1510	1461	69
"	38	84.37	49.20	14.76	1.39	71.0	50.5	0.993	1513	1447	58
BC-27	13	87.00	53.85	14.94	1.44	66.9	46.0	0.980	1494	1461	51
"	38	80.15	44.55	14.95	1.30	71.8	54.6	0.985	1501	1432	28
"	50	83.01	46.72	14.94	1.36	73.2	53.3	1.028	1567	1436	38

H= Sampling depth; P1= weight of seawater-saturated sediment sample and aluminum sample box; P2= weight of dry sediment sample and aluminum sample box; P0= weight of aluminum sample box; WV= humidity= (P1-P2)/(P1-P0)*100%; Vr= relative velocity (Vr=Vm/Vw); V20= sound velocity in sediments at 20°C. Bolded values indicates micronodule horizons

Table 5. Physical properties of sediments, *R.V. Vinogradov* cruise 91-AV-19/4; GC-6.

T °C	H cm	L mm	t mcs	Vm m/s	Vw m/s	Vr	V20 m/s	VSIT m/s	DEN g/cm^3	Imp
10.00	35	71.60	29.98	1491	1490	1.000	1524	1493	-	-
10.00	40	72.70	30.72	1491	1490	1.000	1524	1493	1.25	1905
10.00	45	71.40	29.77	1495	1490	1.003	1528	1497	-	-

Dash means not analyzed, headings as in Tables 3 and 4.

Table 6. Physical properties of sediments, *R.V. Vinogradov* cruise 91-AV-19/4; GC-7

T °C	H cm	L mm	t mcs	Vm m/s	Vw m/s	Vr	V20 m/s	VSIT m/s	DEN g/cm^3	Imp
6.00	2	114.75	59.22	1483	1475	1.006	1532	1501	1.30	1992
6.00	5	118.00	61.49	1482	1475	1.004	1530	1499	-	-
6.00	10	132.15	71.11	1480	1475	1.003	1529	1497	-	-
6.00	15	134.05	72.90	1470	1475	0.996	1518	1487	-	-
6.00	20	136.90	74.63	1474	1475	0.999	1522	1491	1.30	1973
6.00	25	129.55	69.96	1467	1475	0.995	1515	1484	-	-
6.00	30	136.20	74.33	1470	1475	0.997	1519	1487	1.29	1959
6.00	35	137.70	75.28	1472	1475	0.998	1520	1489	-	-
6.00	40	137.35	75.33	1466	1475	0.994	1514	1483	-	-
6.00	45	143.15	79.24	1467	1475	0.995	1515	1484	-	-
6.00	50	141.35	79.01	1449	1475	0.982	1496	1465	1.31	1960
6.00	55	137.95	76.34	1455	1475	0.986	1502	1472	-	-
6.00	60	135.70	74.55	1459	1475	0.989	1507	1476	-	-
6.00	65	133.90	73.65	1453	1475	0.985	1500	1470	1.34	2011

Dash means not analyzed, headings as in Tables 3 and 4.

Table 7. Physical properties of sediments, *R.V. Vinogradov* cruise 91-AV-19/4; GC-9.

T °C	H cm	L mm	t mcs	Vm m/s	Vw m/s	Vr	V20 m/s	VSIT m/s	DEN g/cm^3	Imp
7.00	2	130.20	70.09	1474	1479	0.996	1518	1487	1.37	2080
7.03	5	134.00	73.91	1449	1479	0.980	1492	1462	-	-
7.06	10	141.00	79.04	1444	1479	0.976	1487	1456	-	-
7.09	15	137.00	75.79	1453	1479	0.982	1496	1465	-	-
7.13	20	142.00	79.90	1441	1479	0.974	1483	1453	-	-
7.16	25	142.00	79.51	1448	1480	0.978	1490	1460	-	-
7.19	30	140.00	78.26	1445	1480	0.977	1488	1457	-	-
7.22	35	141.00	78.92	1446	1480	0.977	1488	1458	-	-
7.25	40	140.00	77.92	1451	1480	0.981	1494	1463	-	-
7.28	45	140.00	78.10	1448	1480	0.978	1490	1460	-	-
7.31	50	141.00	78.97	1445	1480	0.976	1487	1456	-	-
7.34	55	144.00	81.07	1444	1480	0.976	1486	1456	-	-
7.38	60	145.00	81.92	1442	1480	0.974	1483	1453	1.40	2077
7.41	65	149.00	84.60	1443	1481	0.975	1485	1455	-	-
7.44	70	148.00	83.83	1445	1481	0.976	1486	1456	-	-
7.47	75	145.00	81.77	1444	1481	0.975	1486	1455	-	-
7.50	80	147.00	83.02	1447	1481	0.977	1488	1458	-	-
7.53	85	147.00	83.10	1445	1481	0.976	1486	1456	-	-
7.56	90	147.00	83.09	1445	1481	0.976	1487	1456	-	-
7.59	95	144.00	81.00	1446	1481	0.976	1487	1456	-	-
7.63	100	144.00	80.78	1450	1481	0.979	1491	1460	-	-
7.66	105	139.00	77.55	1446	1482	0.976	1486	1456	-	-
7.69	110	135.00	74.74	1446	1482	0.976	1487	1457	-	-
7.72	115	133.00	73.43	1445	1482	0.975	1485	1455	-	-
7.75	120	141.00	78.21	1459	1482	0.984	1500	1469	-	-
7.78	125	144.00	80.68	1451	1482	0.979	1492	1461	-	-
7.81	130	148.00	83.47	1451	1482	0.979	1491	1461	1.36	2028
7.84	135	148.00	83.78	1445	1482	0.975	1485	1455	-	-
7.88	140	150.00	84.99	1448	1482	0.977	1488	1458	-	-
7.91	145	150.00	84.90	1450	1483	0.978	1490	1459	-	-
7.94	150	150.00	85.01	1448	1483	0.977	1488	1457	-	-
7.97	155	150.00	85.10	1447	1483	0.976	1486	1456	-	-
8.00	160	149.00	84.13	1451	1483	0.979	1491	1460	-	-
8.03	165	150.00	84.71	1453	1483	0.980	1493	1462	-	-
8.06	170	153.00	86.62	1456	1483	0.982	1495	1465	-	-
8.09	175	152.00	86.09	1453	1483	0.980	1492	1462	-	-
8.13	180	153.00	86.88	1451	1483	0.978	1491	1460	-	-
8.16	185	154.00	87.76	1448	1483	0.976	1487	1457	-	-
8.19	190	150.00	84.93	1449	1484	0.977	1488	1458	-	-
8.22	195	150.00	84.85	1451	1484	0.978	1490	1459	-	-
8.25	200	149.00	83.93	1455	1484	0.980	1494	1463	-	-
8.28	205	148.00	82.59	1466	1484	0.988	1505	1474	-	-
8.31	210	149.00	81.66	1495	1484	1.008	1535	1503	-	-
8.34	215	149.00	84.20	1450	1484	0.977	1488	1458	-	-
8.38	220	149.00	84.19	1450	1484	0.977	1488	1458	1.34	1995
8.41	225	148.00	83.48	1451	1484	0.977	1489	1458	-	-
8.44	230	148.00	83.26	1454	1485	0.980	1492	1462	-	-
8.47	235	148.00	83.26	1454	1485	0.980	1492	1462	-	-
8.50	240	147.00	82.81	1450	1485	0.977	1488	1457	-	-

Dash means not analyzed, headings as in Tables 3 and 4.

Table 8. Physical properties of sediments, *R.V. Vinogradov* cruise 91-AV-19/4; GC-13.

T °C	H cm	L mm	t mcs	Vm m/s	Vw m/s	Vr	V20 m/s	VSIT m/s	DEN g/cm^3	Imp
7.50	5	142.4	77.50	1490	1481	1.006	1533	1502	-	-
7.54	10	147.0	80.94	1484	1481	1.002	1526	1495	1.19	1816
7.59	15	145.2	78.12	1514	1481	1.022	1557	1525	-	-
7.63	20	148.0	81.64	1483	1481	1.001	1525	1494	-	-
7.68	25	148.7	82.32	1480	1482	0.999	1521	1490	-	-
7.72	30	148.3	82.00	1480	1482	0.999	1522	1491	1.19	1811
7.76	35	149.1	82.94	1473	1482	0.994	1514	1483	-	-
7.81	40	150.1	84.00	1467	1482	0.990	1507	1477	-	-
7.85	45	154.4	86.85	1468	1482	0.990	1509	1478	-	-
7.90	50	150.6	84.58	1463	1482	0.987	1503	1472	1.27	1909
7.94	55	149.4	83.66	1464	1483	0.988	1504	1474	-	-
7.99	60	151.6	85.22	1463	1483	0.987	1503	1472	-	-
8.03	65	153.4	86.36	1465	1483	0.988	1505	1474	-	-
8.07	70	152.2	85.50	1465	1483	0.988	1505	1474	1.22	1836
8.12	75	145.8	81.15	1465	1483	0.988	1505	1474	-	-
8.16	80	146.9	82.16	1461	1483	0.985	1500	1469	-	-
8.21	85	148.0	82.88	1461	1484	0.985	1500	1469	-	-
8.25	90	147.0	81.82	1468	1484	0.989	1507	1476	1.27	1914
8.29	95	152.0	83.79	1493	1484	1.006	1533	1501	-	-
8.34	100	156.0	88.40	1460	1484	0.984	1499	1468	-	-
8.38	105	156.7	89.86	1444	1484	0.973	1482	1452	-	-
8.43	110	156.0	88.87	1453	1484	0.979	1491	1460	1.33	1983
8.47	115	149.1	84.27	1450	1485	0.977	1488	1457	-	-
8.51	120	138.6	75.68	1476	1485	0.994	1514	1483	-	-
8.56	125	137.5	74.81	1478	1485	0.996	1517	1486	-	-
8.60	130	141.5	77.38	1481	1485	0.997	1519	1488	1.23	1868
8.65	135	143.0	78.93	1471	1485	0.990	1509	1478	-	-
8.69	140	139.0	76.80	1460	1485	0.983	1497	1466	-	-
8.74	145	142.0	79.10	1455	1486	0.979	1492	1461	-	-
8.78	150	145.0	80.60	1465	1486	0.986	1502	1471	-	-
8.82	155	154.0	87.20	1458	1486	0.981	1494	1464	-	-
8.87	160	158.0	89.90	1458	1486	0.981	1495	1464	1.29	1928
8.91	165	160.0	91.40	1456	1486	0.980	1493	1462	-	-
8.96	170	156.0	88.50	1459	1486	0.981	1495	1464	1.30	1943
9.00	175	155.0	87.90	1457	1487	0.980	1493	1463	-	-
9.04	180	155.0	87.70	1461	1487	0.982	1497	1466	-	-
9.09	185	153.0	86.40	1459	1487	0.982	1495	1465	-	-
9.13	190	148.0	82.90	1461	1487	0.982	1496	1466	1.34	2005
9.18	195	152.0	85.90	1456	1487	0.979	1492	1461	-	-
9.22	200	150.0	84.20	1462	1487	0.983	1497	1467	-	-
9.26	205	150.0	84.00	1465	1488	0.985	1501	1470	-	-
9.31	210	150.0	84.10	1464	1488	0.984	1499	1468	1.33	1993
9.35	215	150.0	84.40	1459	1488	0.980	1493	1463	-	-
9.40	220	152.0	85.60	1461	1488	0.982	1496	1465	-	-
9.44	225	153.0	86.30	1461	1488	0.982	1496	1465	-	-
9.49	230	150.0	84.30	1460	1488	0.981	1494	1464	1.32	1973
9.53	235	149.0	83.70	1459	1489	0.980	1493	1462	-	-
9.57	240	151.0	84.90	1462	1489	0.982	1496	1465	-	-
9.62	245	152.0	85.90	1456	1489	0.978	1490	1459	-	-
9.66	250	148.0	83.00	1459	1489	0.980	1493	1462	1.31	1955
9.71	255	146.0	81.40	1463	1489	0.982	1497	1466	-	-
9.75	260	150.0	83.80	1469	1489	0.986	1502	1472	-	-
9.79	265	147.0	81.80	1468	1490	0.986	1501	1471	1.35	2027
9.84	270	149.0	84.00	1454	1490	0.976	1486	1456	-	-
9.88	275	149.0	83.20	1468	1490	0.985	1500	1470	-	-
9.93	280	151.0	84.60	1467	1490	0.984	1500	1469	-	-
9.97	285	148.0	82.60	1466	1490	0.984	1499	1468	1.34	2008
10.01	290	150.0	83.60	1472	1490	0.988	1505	1474	-	-
10.06	295	152.0	85.00	1472	1491	0.987	1504	1473	-	-
10.10	300	151.0	84.30	1472	1491	0.988	1504	1474	-	-

Table 8. continued

T °C	H cm	L mm	t mcs	Vm m/s	Vw m/s	Vr	V20 m/s	VSIT m/s	DEN g/cm^3	Imp
10.15	305	153.0	85.50	1475	1491	0.989	1507	1476	1.41	2125
10.19	310	155.0	87.10	1471	1491	0.986	1503	1472	-	-
10.24	315	155.0	87.20	1469	1491	0.985	1501	1470	-	-
10.28	320	153.0	85.80	1470	1491	0.985	1501	1470	1.36	2042
10.33	325	150.0	83.70	1471	1492	0.986	1502	1471	-	-
10.37	335	146.0	81.30	1465	1492	0.982	1496	1465	-	-
10.41	342	146.0	81.20	1467	1492	0.983	1498	1467	-	-
10.46	345	147.0	81.60	1472	1492	0.986	1503	1472	-	-
10.50	350	148.0	82.30	1471	1492	0.986	1502	1471	1.31	1968
10.55	355	148.0	81.90	1479	1492	0.991	1509	1478	-	-
10.59	360	151.0	83.80	1481	1492	0.992	1512	1481	-	-
10.64	365	145.0	80.50	1467	1493	0.983	1497	1467	-	-
10.68	370	147.0	81.30	1477	1493	0.990	1507	1477	1.32	1990
10.72	375	148.0	82.30	1471	1493	0.986	1501	1471	-	-
10.77	380	150.0	83.30	1478	1493	0.990	1508	1477	-	-
10.81	385	153.0	86.60	1456	1493	0.975	1485	1455	-	-
10.86	390	153.0	85.60	1473	1493	0.986	1503	1472	-	-
10.90	395	151.0	84.50	1469	1494	0.983	1498	1467	1.31	1962
10.94	400	155.0	87.00	1472	1494	0.986	1502	1471	-	-
10.99	405	151.0	84.40	1470	1494	0.984	1499	1469	-	-
11.03	410	146.0	80.80	1474	1494	0.987	1503	1472	1.32	1984
11.08	415	153.0	85.00	1484	1494	0.993	1512	1481	-	-
11.12	420	149.0	82.70	1476	1494	0.988	1505	1474	-	-
11.16	425	148.0	81.10	1493	1495	0.999	1522	1491	-	-
11.21	432	149.0	82.90	1473	1495	0.985	1501	1470	1.38	2072
11.25	435	150.0	83.70	1471	1495	0.984	1499	1468	-	-
11.30	440	149.0	82.80	1475	1495	0.986	1503	1472	-	-
11.34	445	150.0	83.00	1483	1495	0.992	1511	1480	-	-
11.39	450	158.0	88.60	1480	1495	0.990	1507	1477	1.34	2020
11.43	455	157.0	86.40	1506	1495	1.007	1534	1502	-	-
11.47	460	154.0	86.10	1476	1496	0.987	1504	1473	-	-
11.52	465	162.0	91.50	1477	1496	0.987	1504	1473	-	-
11.56	470	163.0	92.20	1476	1496	0.987	1503	1472	1.35	2029
11.61	475	160.0	90.20	1476	1496	0.986	1503	1472	-	-
11.65	480	158.0	88.90	1475	1496	0.986	1501	1471	-	-
11.69	485	156.0	87.00	1484	1496	0.992	1511	1480	-	-
11.74	490	158.0	88.90	1475	1497	0.985	1501	1470	1.31	1966
11.78	495	160.0	90.10	1477	1497	0.987	1504	1473	-	-
11.83	500	158.0	88.90	1475	1497	0.985	1501	1470	-	-
11.87	505	157.0	88.00	1478	1497	0.988	1504	1474	-	-
11.91	510	158.0	88.50	1481	1497	0.989	1507	1476	1.30	1959
11.96	515	158.0	88.40	1483	1497	0.990	1509	1478	-	-
12.00	518	158.0	88.40	1483	1497	0.990	1509	1478	-	-
12.05	522	156.0	87.00	1484	1498	0.991	1509	1478	-	-
12.09	525	158.0	88.30	1485	1498	0.991	1510	1479	-	-
12.14	530	158.0	88.20	1486	1498	0.992	1512	1481	1.26	1905
12.18	535	157.0	87.70	1483	1498	0.990	1509	1478	-	-
12.22	540	155.0	86.70	1478	1498	0.986	1502	1472	-	-
12.27	545	154.0	85.70	1483	1498	0.990	1508	1477	-	-
12.31	550	155.0	86.20	1486	1499	0.992	1511	1480	1.32	1994
12.36	555	158.0	88.50	1481	1499	0.988	1506	1475	-	-
12.40	560	159.0	89.00	1484	1499	0.990	1509	1478	-	-
12.44	565	159.0	88.80	1488	1499	0.992	1512	1481	-	-
12.49	570	159.0	89.00	1484	1499	0.990	1508	1477	1.31	1976
12.53	575	158.0	88.20	1486	1499	0.991	1510	1479	-	-
12.58	580	159.0	88.60	1491	1499	0.994	1515	1484	-	-
12.62	585	157.0	87.30	1490	1500	0.994	1514	1483	-	-
12.66	590	156.0	87.00	1484	1500	0.989	1507	1476	1.30	1959
12.70	595	159.0	88.70	1489	1500	0.993	1513	1482	-	-
12.74	600	159.0	88.90	1486	1500	0.991	1509	1478	-	-
12.78	605	158.0	88.00	1490	1500	0.993	1513	1482	1.32	1997

Dash means not analyzed, headings as in Tables 3 and 4.

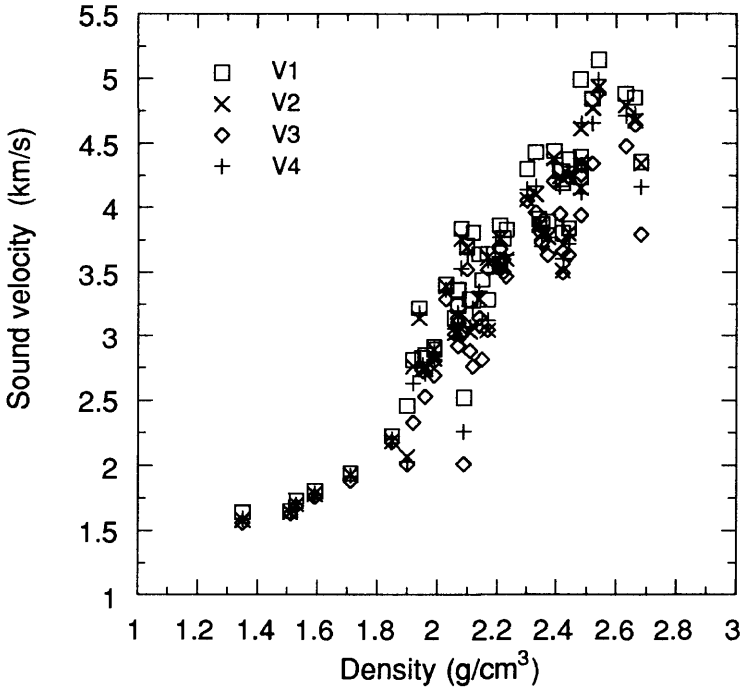

Figure 1. Sound velocity versus wet-bulk density of sediemntary and volcanic rocks from Karin Ridge.

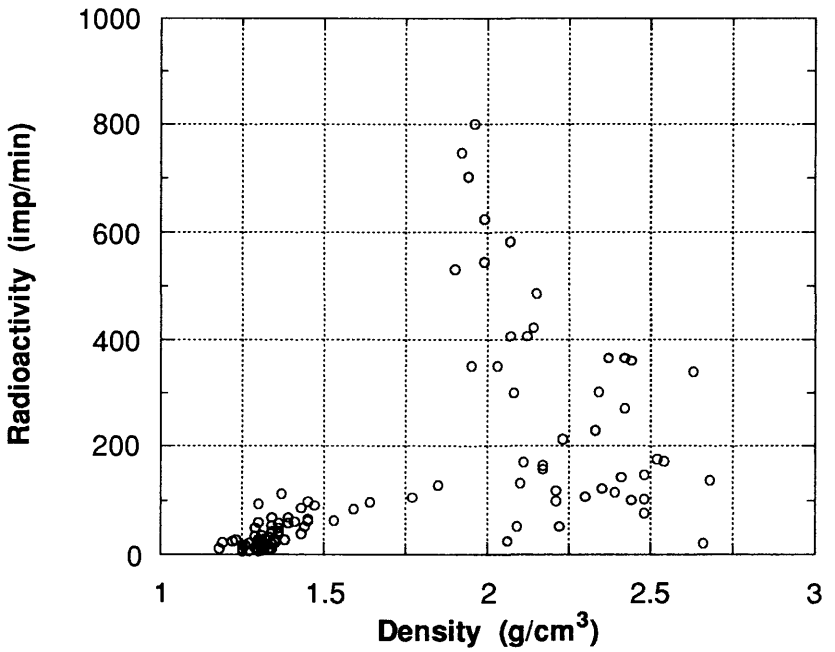

Figure 2. Natural radiation of sedimentary and volcanic rock samples from Karin Ridge.

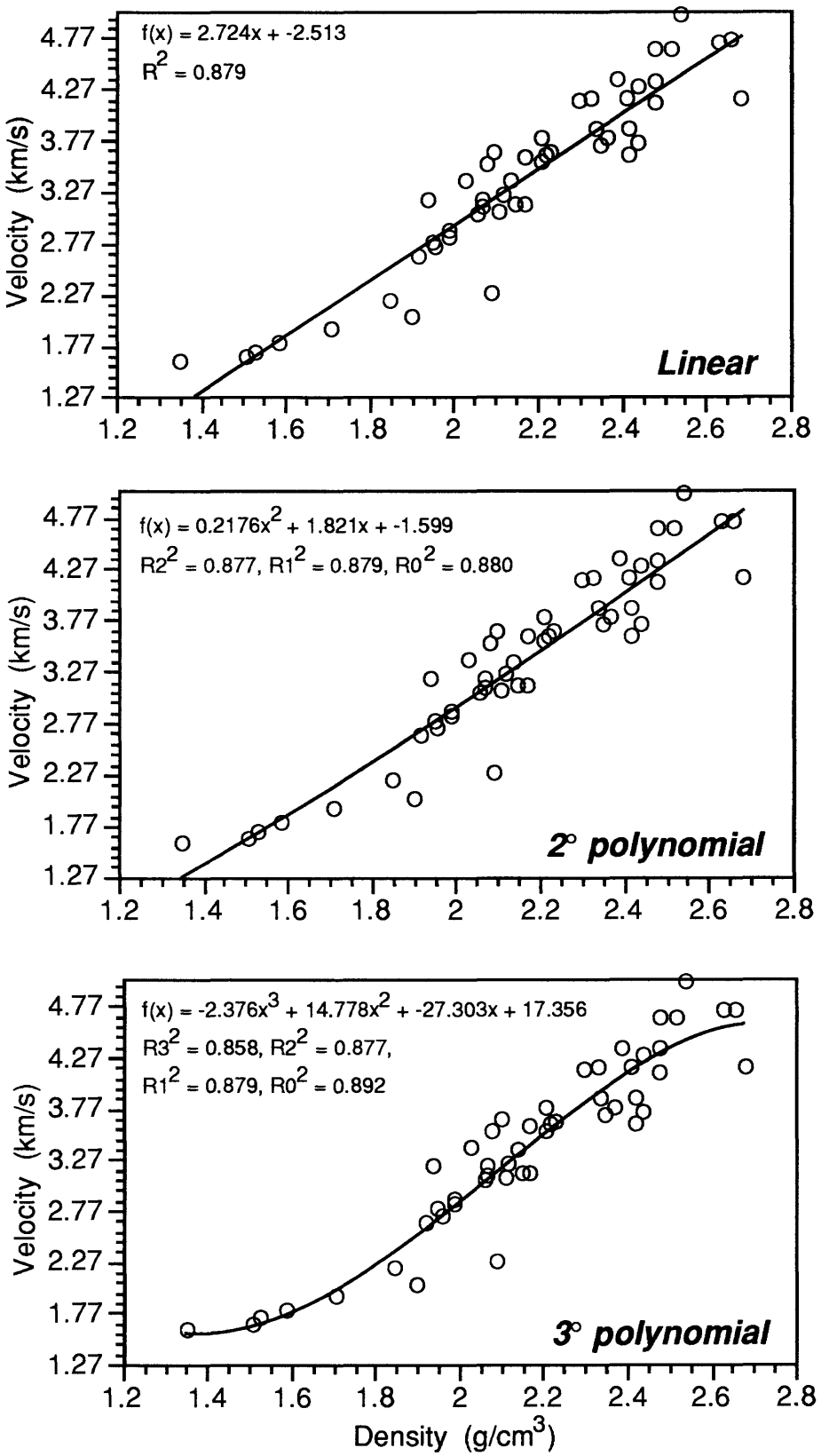

Figure 3. Relationship between compressional-wave velocity (average, V4) and wet bulk density; data from Table 1.

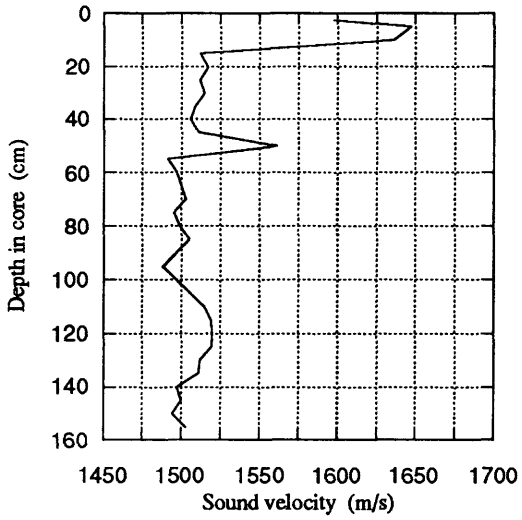

Figure 4. Velocity profile for sediments from gravity core GC-1.

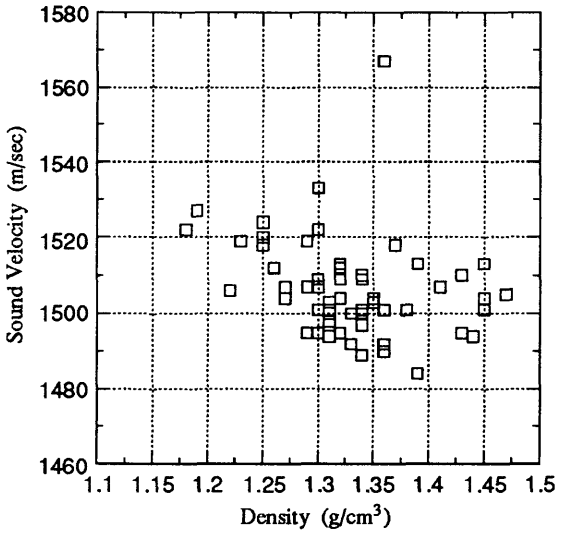

Figure 5. Sound velocity versus wet-bulk density for sediment samples from northwest Pacific and Bering Sea.

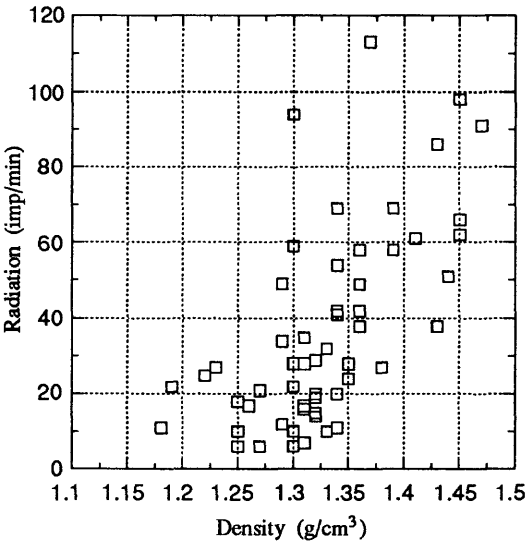

Figure 6. Natural radiation versus wet-bulk density for sediment samples from northwest Pacific and Bering Sea.

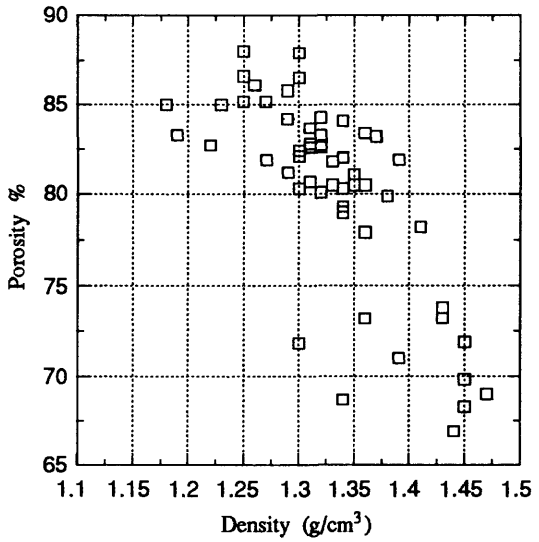

Figure 7. Porosity versus wet-bulk density for sediment samples from northwest Pacific and Bering Sea.

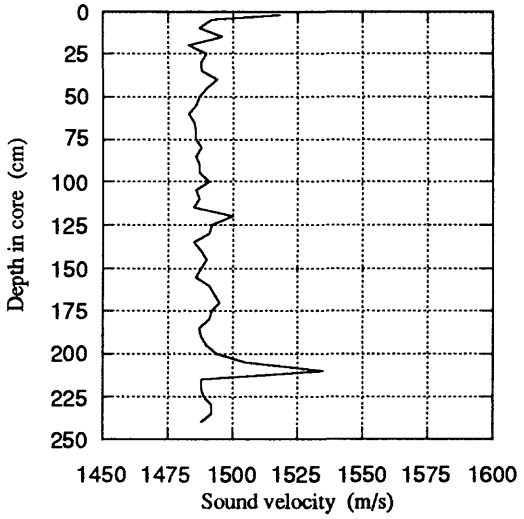

Figure 8. Sound velocity profile for sediments from gravity core GC-9, from the northwest Pacific

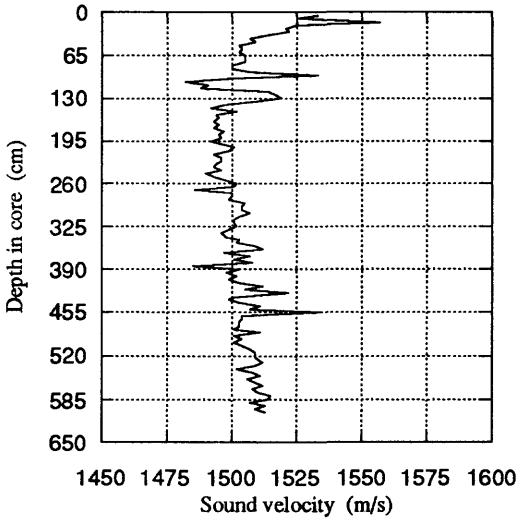

Figure 9. Sound velocity profile for sediments from gravity core GC-13, from the Bering Sea.

ACKNOWLEDGMENTS

Ann E. Gibbs and James R. Hein improved the English and reviewed this paper.

REFERENCES

Belikov, B.P., Alexandrov, K.S., and Ryjova, T.V., 1970. Elastic properties of minerals and rocks: Nauka. Moscow, 276 p. (In Russian)

Jones, J.G., 1969. Pillow lavas as depth indicators: American Journal of Science, v. 267, p. 181-195.

Kobranova, V.H., Izvekov, B.I., Patsevich, S.L., and Shvartsman, S.D., 1977. Determination of petrophysical characteristics from samples: Nedra, Moscow, 432 p. (In Russian)

Moore, J.G. and Schilling, J.G., 1973. Vesicles, water, and sulfur in Reykjanes Ridge basalts: Contributions to Mineralogy, Petrology, v. 41, p. 105-118.

Starostin, V.I., 1979. Structural-petrophysical analysis of endogene ores fields: Nedra, Moscow, 240 p. (In Russian)

Svininnikov, A.I., 1989. Sound velocity and density in volcanic rocks of the Japan Sea: *in* Konovalov Yu. (ed.), New data on the geology of the sea floor in Western Pacific. USSR Academy of Science Far Eastern Branch, Pacific Oceanological Institute, Vladivostok, p. 96-105 (In Russian)

Svininnikov, A.I., Markov, U.D., Lelikov, E.P., and Gramm-Osipov, L.M., 1984. Physical properties of sediments from northwestern Pacific: Pacific Ocean Geology, v. 1, p. 8-12 (In Russian)

CLASTIC COMPONENTS IN SEDIMENTS AND SEDIMENTARY ROCKS OF HAWAII AND KARIN RIDGE

Victor P. Nechaev[1], Sergei A. Gorbarenko[2], Anna V. Sorochinskaya[2], Eugene V. Mikhailik[1], Vladimir V. Golozubov[1], and Wayne C. Isphording[3]

[1]Far East Geological Institute, Far Eastern Branch, Russian Academy of Sciences, Vladivostok, 690022, Russia; [2]Pacific Oceanological Institute, Far Eastern Branch, Russian Academy of Sciences, 43 Baltiyskaja, Vladivostok 690041, Russia; [3]Department of Geology-Geography, University of South Alabama, Mobile, AL 36688, U.S.A.

INTRODUCTION

This work addresses the subject of clastic grains in modern sediments and their paleoceanic significance, which is part of the Russia-USA program "Geochemistry of Marine Sediments", coordinated by Mikhail F. Stashchuk and Alexander S. Bychkov (Pacific Oceanological Institute, Russian Academy of Sciences) and James R. Hein (U.S. Geological Survey). Research was conducted in two parts, the first consisted of the study of modern sediments deposited in various geological settings that are well studied. The second part is devoted to the geological evolution of less well known oceanic areas as recorded in sediments. Data on modern sediments that are indicative of their geological settings serve as a key to interpreting changes in sediments with time. All the investigations were carried out using heavy mineral assemblages in addition to mineralogy of the fine-sand (0.05-0.1 mm) fraction of sediments, X-ray diffractometry, biostratigraphy, and so on.

Deposits from Hawaii Island and Karin Ridge were collected prior to and during Cruise 91-AV-19/2 on the Russian R.V. *Akademik Aleksandr Vinogradov* (Table 1). Beach sands from Maui and Oahu Islands were sampled by W.C. Isphording in July 1990.

We studied modern sands from the Hawaiian Islands as examples of sediments derived from shield and post-shield hot-spot volcanoes. In addition, a large data set of heavy mineral analyses, representing Cenozoic (mainly Quaternary) sediments from various tectonic settings of the North Pacific, were included in the study. These data were obtained during previous studies (Markov *et al.*, 1989, 1992; Nechaev, 1991). Mineral compositions of these deposits serve as a key to deciphering the records contained in Cretaceous and Cenozoic sediments and sedimentary rocks of Karin Ridge. Because of the limitations of our data set, the main objective of this work is to show the utility of our methodology rather than to define the precise evolution of Karin Ridge.

METHODS

For mineral analysis, the 0.05-0.1 mm fraction was separated from sediments and sedimentary rocks by wet sieving; sedimentary rocks were disaggregated by crushing. Heavy minerals were then extracted using tribromomethane (2.9 g/cm^3) and identified using the petrographic microscope. When necessary, mineral identification was made with the help of X-ray diffraction, conducted by M.F. Eiberman (Pacific Oceanological Institute, Russian Academy of Sciences). All mineral analyses were carried out by V.P. Nechaev and A.V. Sorochinskaya (Tables 2-5).

Interpretation of data is based on comparison between the mineralogical composition of the sediments and various crystalline rocks, as described by Nechaev (1991 and references therein).

RESULTS

Hawaiian Sediments

Beach sands were collected at seven sites along the eastern coast of Hawaii (Fig. 1; Table 1). Most of the sands (H2-H6) lie on tholeiitic basalt of Mauna Loa and Kilauea shield volcanoes. Two samples

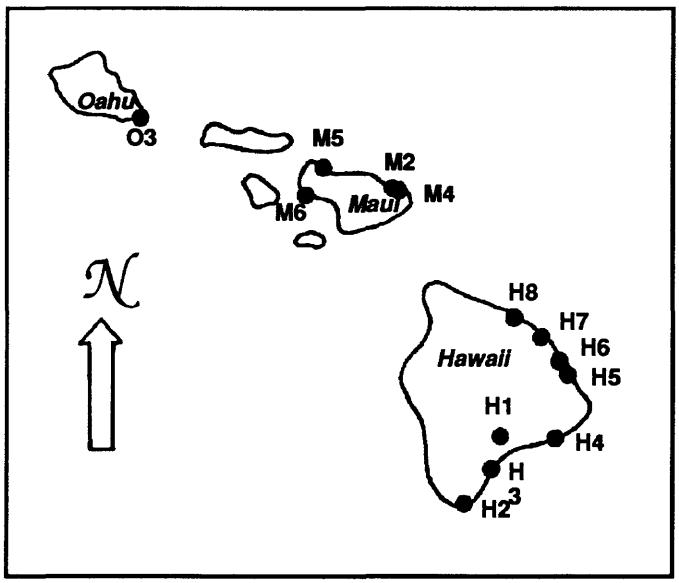

Figure 1. Sampling locations on the Hawaiian Islands.

(H7, H8) represent sediments deposited in the area of postshield volcanic rocks of Mauna Kea Volcano. Sand-size tephra (H1) was sampled on basalts near Kilauea crater; its source is unknown to the authors. Beach sands of Maui and Oahu Islands were deposited on volcanoes exposing both shield and postshield volcanic rocks as major units (Clague, 1987 and references therein).

According to mineral analyses, all the Hawaiian sediments consist of volcanic clasts: basaltic groundmass, volcanic glass, feldspar, olivine, clinopyroxene, magnetite, etc.; products of their alteration: smectite, Fe-Mn hydroxides, epidote, and others; and various bioclasts (Tables 2 and 3). Heavy mineral assemblages of these deposits may be distinguished from those of sediments belonging to other intraoceanic environments by their relatively high contents of olivine, iddingsite, brown (Ti-rich) clinopyroxene, and magnetite (Fig. 2). All these minerals were derived from Hawaiian Islands volcanic rocks, which contain them as dominant heavy mineral components (Clague, 1987).

Three volcaniclastic associations can be distinguished among the Hawaiian heavy minerals (Fig. 3). The first, in which olivine is dominant (samples H2-H6 and M2), was collected on tholeiitic shield lava of Kilauea, Mauna Loa, and East Maui volcanoes and may serve as an indicator of hot-spot shield volcanism. Postshield volcanism is indicated by a magnetite-olivine-clinopyroxene association (samples H7, H8, M4-M6, and O3, all collected from postshield or rejuvenated alkalic lava of Mauna Kea, East and West Maui, and Koolau volcanoes). The third association, in which brown Ti-rich augite is dominant, was defined in tephra collected from the Kilauea shield volcano and is attributed to the pyroclastic-type of hot-spot volcaniclastics. The same clinopyroxene-rich assemblage predominates in Quaternary mud collected from four cores obtained in the Pacific basin between 500 and 1000 km southeast of Hawaii (Markov *et al.*, 1992). The Ti-rich augite content in the heavy fraction of these sediments gradually increases from 75% in the core furthest from the island of Hawaii to 97% in the core closest to the island. Pelagic sediments further to the east contain only minor amounts of this mineral (see positions of the points "East Pacific Basin near Clarion Fracture Zone" on Fig. 2). Thus, the most powerful volcanic explosions on the Hawaiian hot spot may have distributed their fine-grained clastics far away from the volcanic centers. This suggestion is not surprising because hypersthene, green clinopyroxene, hornblende, and magnetite, undoubtedly derived from volcanic arcs, predominate in most pelagic deposits located in the central Pacific (Nechaev, 1991 and references therein). Nevertheless, we can not exclude the possibility that the clinopyroxene-rich assemblage found in the eastern Pacific mud may be derived from local hot-spot produced volcanoes. This problem requires additional study. On the basis of data obtained by Markov *et al.* (1992), we define one more heavy mineral association related to hot-spot edifices, based on Quaternary sediments from the area of the Hawaiian-Emperor bend (see Fig. 1). Magnetite associated with Ti-rich clinopyroxene and two pyroxenes-hornblende assemblage, characterizes this tectonic setting (see Figs. 2, 3). The enrichment in magnetite (the most stable volcaniclastic mineral) and paucity of olivine (the least

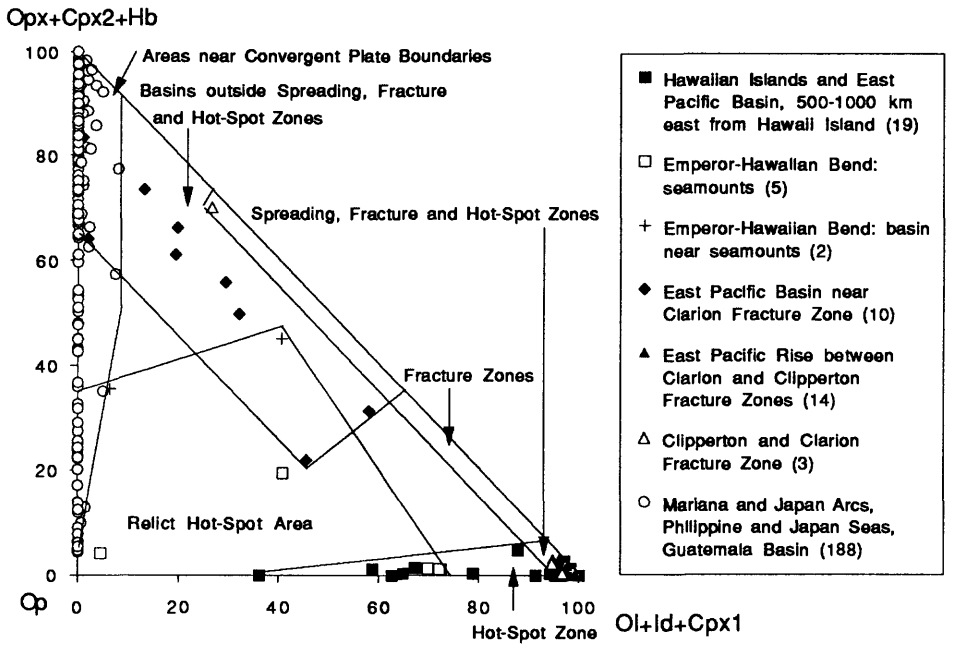

Figure 2. Heavy mineral compositions of sediments from different tectonic settings of the North Pacific; data from Table 3, Markov et al. (1989, 1992), and Nechaev (1991). Mineral abbreviations are the same as in Tables 3 and 5. Bracketed numbers in legend indicate the number of analyses used to define the fields.

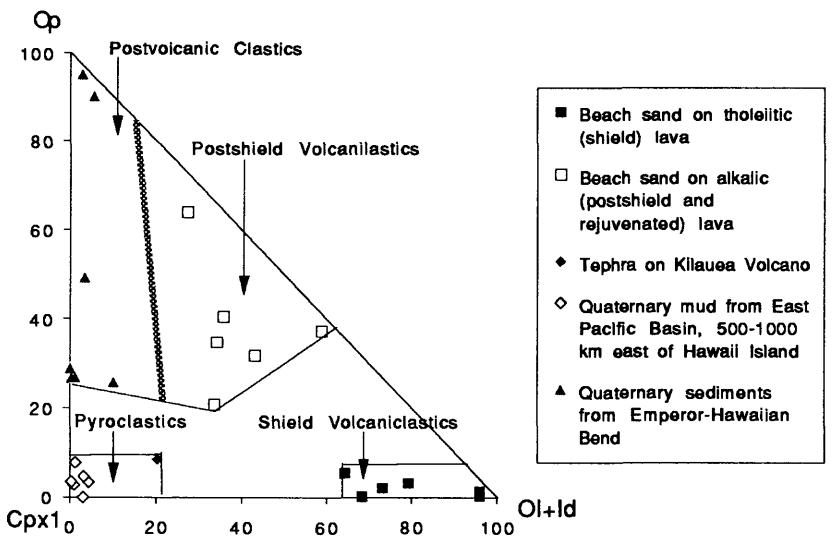

Figure 3. Major differences between heavy clastic mineral assemblages related to Hawaiian hot-spot evolution. Data from Table 3 and Markov et al. (1989, 1992). Mineral abbreviations are the same as in Tables 3 and 5.

stable mineral) in the relict hot-spot sediments are possibly due to weathering and reworking of first cycle hot-spot sediments. Both of these processes occur while hot-spot volcanic islands evolve into guyots. Clastic material derived from the erosion of magmatic rocks during weathering and reworking is much less abundant than that supplied during the volcanically active stage. As a result, sediments aquire relatively high amounts of clastic minerals derived from other sources, such as island arcs and active continental margins, where volcaniclastic grains are distributed far from their provenances through powerful volcanic explosions and pumice drift. This type of material may be characterized by the association of orthopyroxene, green clinopyroxene, green-brown hornblende, and magnetite (Nechaev, 1991). The abundance of these minerals in pelagic sediments from local basins in the relict hot-spot area is markedly higher than in deposits covering seamounts (compare positions of the points "Emperor-Hawaiian Bend: seamounts" and "Emperor-Hawaiian Bend: basin near seamounts" on Fig. 2).

Heavy Mineral Assemblages of Sediments and Sedimentary Rocks from Karin Ridge

Samples were collected by gravity core and dredge. Stations were located along two transects across the flanks of the central part of the ridge (Fig. 4). Seven lithologic units may be distinguished in this sequence.

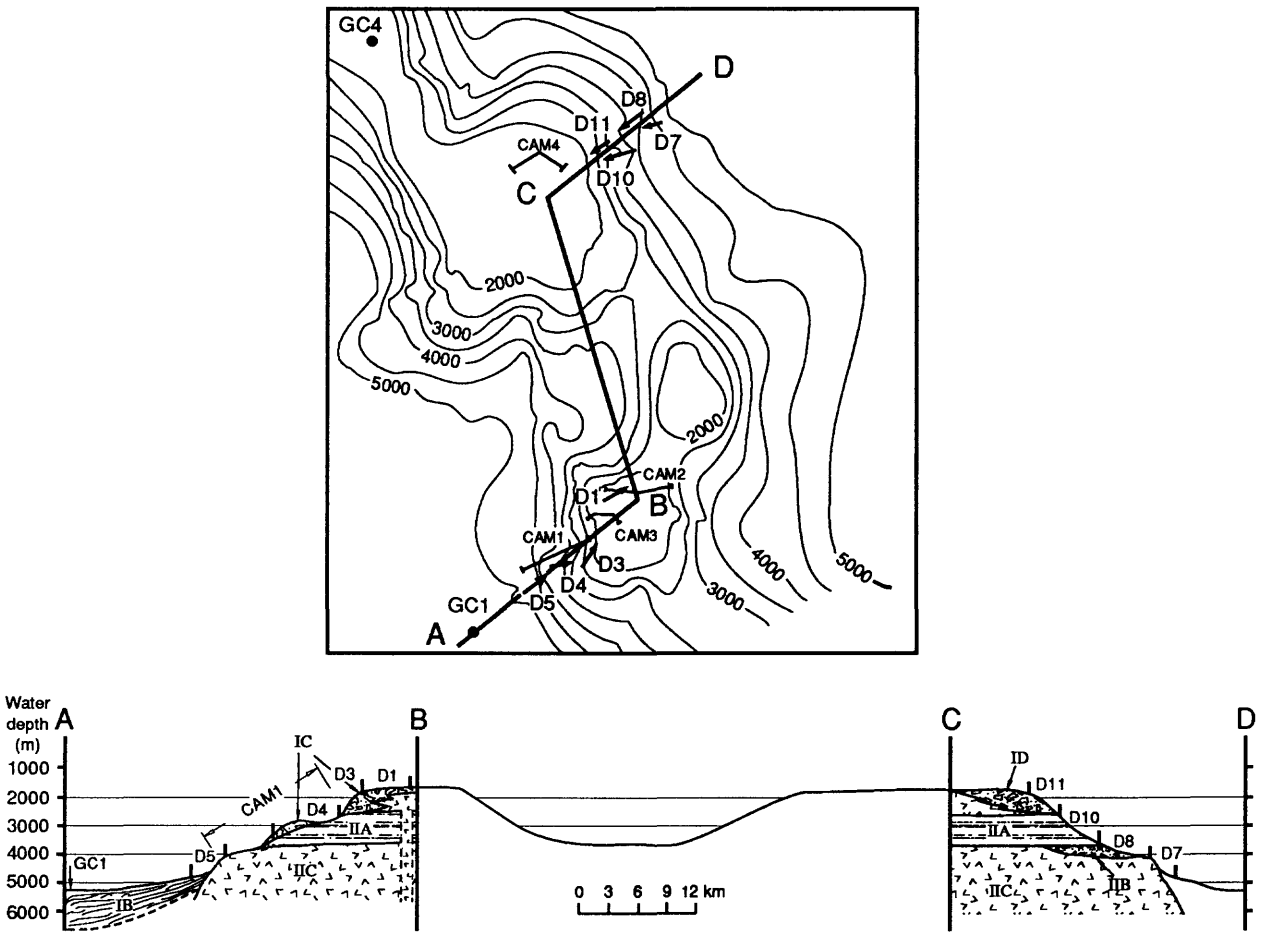

Figure 4. Schematic lithological cross-section of Karin Ridge. Arrows indicate dredge samples used in this study (see Figs. 2, 5, and 6 in Hein *et al.*, this volume, for bathymetric map and station locations.

Foraminiferal sand sampled by gravity core GC4 (summit of the northern area) is designated Unit IA. According to video-camera data, thin patches of foraminiferal sand occur on the summit of the ridge. Pletnev *et al.* (this volume) determined the age of this sediment to be late Pleistocene; some reworked Oligocene species also occur in the sediment. The mineral composition of this sand is close to that in sediments of the Hawaiian-Emperor bend and postshield volcaniclastic deposits of the Hawaiian Islands (Tables 4, 5; Figs. 5, 6).

Turbidite sands and pelagic clay, sampled by gravity core GC1 (abyssal apron; southwest flank of Karin Ridge), are designated Unit IB. The content of foraminifers in these sediments varies markedly from single tests in the muds to more than 1000 tests/g in the sands. Redeposited Oligocene species predominate in the sands. Rarely, the sands also contain Late Cretaceous, late Paleocene, and early Eocene species. The uppermost muds contain Pleistocene planktonic foraminifera, relatively deep-water benthic species of uncertain age, and the diatom *Ethmodiscus rex* (Pletnev *et al.*, this volume). Stratigraphically lower muds contain rare, poorly preserved, early Eocene foraminifers. Considering these data, and taking into account the poor lithification of the sediments, we questionably date the sediment as Oligocene(?). The uppermost mud may be Pleistocene, or younger. The occurrence of Paleogene deposits near the sediment surface is not unexpected, and the paucity of young sediments is well known in the abyssal region to the east of the study area (Creager and Scholl *et al.*, 1973). In particular, Paleogene sediments were recovered by gravity cores in the western part of the eastern Pacific basin between 15°N and 20°N during a R.V. *Akademik A. Vinogradov* cruise in 1989 (Markov *et al.*, 1992; see Fig. 1); in these cores fractures occur in Paleogene deposits, similar to those that occur in GC1, interval 280-325 cm. Perhaps, these fractures indicate tectonic activity in the region during some time in the late Oligocene or Neogene.

Sediments of Unit IB include a complex heavy mineral assemblage comparable with that of modern sediments on and near the relict hot-spot studied in the area of the Hawaiian-Emperor bend (Figs. 5, 6); however, significant differences exist in heavy mineral compositions of sediments from Karin Ridge area. All samples contain hot-spot volcaniclastic minerals in the dominant assemblage (brown clinopyroxene, olivine, iddingsite > orthopyroxene, green clinopyroxene, hornblende). In contrast, Quaternary pelagic clay, collected in local basins near seamounts of the Hawaiian-Emperor bend, contains island-arc volcaniclastic minerals in the dominant assemblage (orthopyroxene, green clinopyroxene, hornblende > brown clinopyroxene, olivine, iddingsite). They plot in the upper-left section of the field *Relict Hot-Spot Area* on Fig. 2 (its lower-right section is occupied by sediments from the seamounts). Mineral compositions of Unit IB sediments (especially sands) can be distinguished from other Karin Ridge deposits by their relatively high contents of epidote, pale-colored amphiboles, and garnet, which were probably derived from erosion of metamorphosed magmatic rocks (Fig. 7). Similar increases in metamorphic mineral contents have been found in late Oligocene and early Neogene sediments of the Philippine Sea, where they most likely reflect some tectonic events (Nechaev, 1991). Thus, we consider the mineralogical characteristics, fractures, and turbidite structures of Unit IB sediments as evidence of relatively high tectonic (without volcanic) activity in the region during the Oligocene and (or) early Neogene.

Other components of Unit IB sediments include heterogeneous volcanic clasts (groundmass of various volcanic rocks, colorless and brown volcanic glass, plagioclase, K-feldspar, quartz), barite, francolite, phillipsite, clinoptilolite, smectite, illite, chlorite, kaolinite, Fe-Mn hydroxides, and bioclasts (Foraminifera, Radiolaria, fish teeth).

Breccia located on the southwestern flank of Karin Ridge (CAM 1-1, D4-2, and D4-8) are designated Unit IC. Late Cretaceous-Eocene foraminifers were found in these deposits (Pletnev *et al.*, this volume) and, therefore, the breccias are Eocene or younger. Strongly altered breccia (samples D4-2 and D4-8) include the heavy mineral association (magnetite, brown clinopyroxene, olivine, iddingsite), the same assemblage as those from Hawaiian-Emperor bend, but with some additional characteristics (Figs. 5, 6). The altered breccias do not contain island-arc volcaniclastic minerals (Fig. 5). Relatively fresh breccia (CAM 1-1), contains predominantly brown clinopyroxene, indicating a hot-spot pyroclastic origin.

Breccia located on the upper part of the northeastern flank (D11-1/1, D11-2, D11-3) is designated Unit ID. No age-diagnostic fossils were found. Their age may be tentatively designated as Eocene, because of their location above Unit IIA mudstones containing Cretaceous through Paleocene foraminifers (see below). These breccias contain a heavy mineral association close to that of both shield and postshield hot-spot volcanoes (olivine together with iddingsite, which results from olivine alteration, and, in lesser amounts, magnetite are the dominant heavy clastic minerals, see Figs. 5, 6).

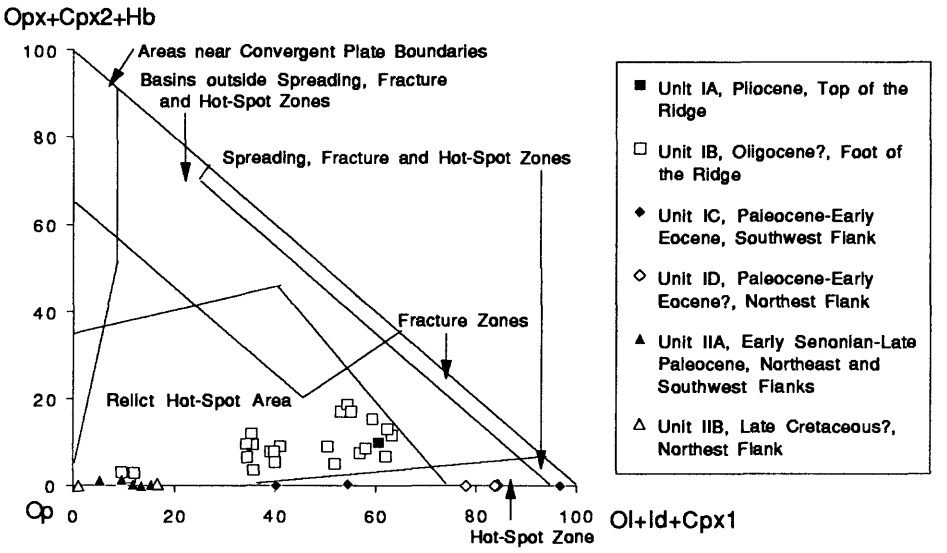

Figure 5. Heavy mineral assemblages in sediments and sedimentary rocks from Karin Ridge relative to various tectonic settings of the North Pacific (see Fig. 2). Mineral abbreviations are the same as in Tables 3 and 5.

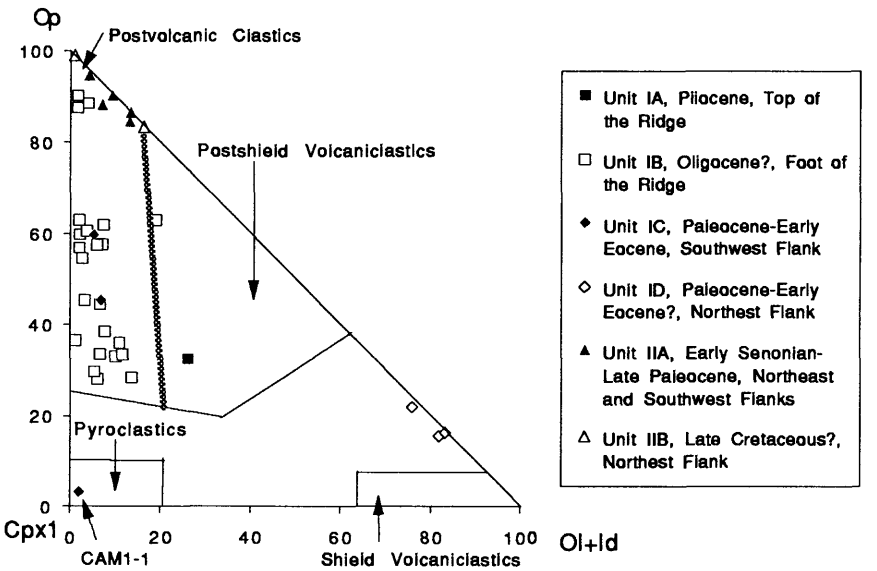

Figure 6. Heavy mineral assemblages in sediments and sedimentary rocks from Karin Ridge compared to rocks and sediments from the Hawaiian Ridge (see Fig. 3). Mineral abbreviations are the same as in Tables 3 and 5.

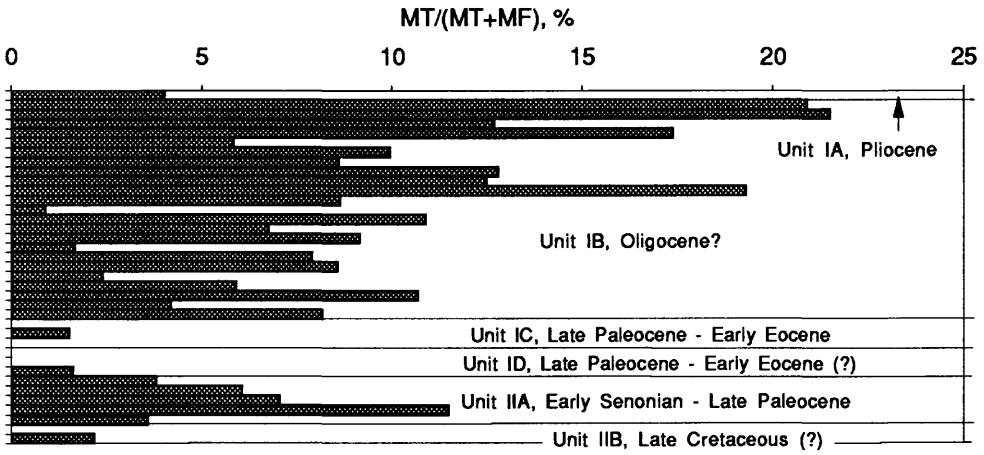

Figure 7. Temporal changes in relative contents of metamorphic (MT=AM+Ep+Grn) and mafic (MF=Ol+Id+Opx+Cpx+Cpx2+Hb) components in the heavy mineral fraction of Karin Ridge sediments. Mineral abbreviations are the same as in Tables 3 and 5.

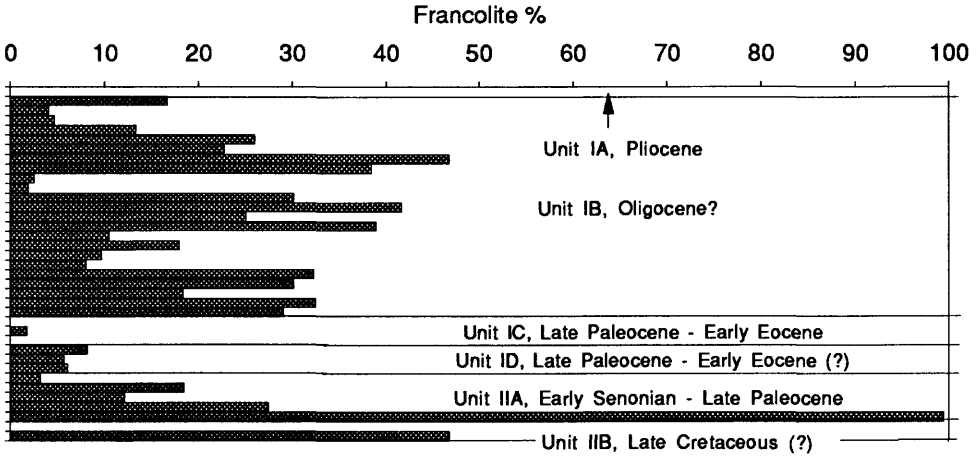

Figure 8. Temporal changes of francolite contents in the heavy mineral fraction of Karin Ridge sediments

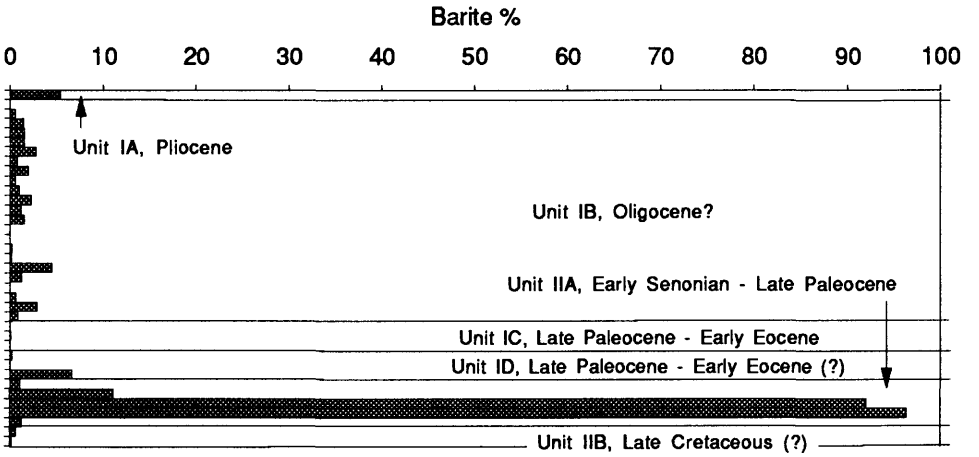

Figure 9. Temporal changes of barite contents in the heavy mineral fraction of Karin Ridge sediments.

The rock-forming components in Units IC and ID breccias are the same as those in Unit IB (see Table 4). According to petrologic study (Martynov *et al.*, this volume), coarse clasts are represented by volcanic rocks (hawaiites, alkaline basalts, plagioclase-phyric basalts) that are comparable in composition to those from Hawaiian postshield volcanoes.

Thus, the altered breccias of unit IC were, most likely, deposited at a hot-spot during volcanic activity or just after activity ceased, whereas fresh breccia resulted from related explosive volcanism. The breccias of Unit ID might have been deposited during the same volcanic episode, but at an adjacent volcanic center. The latter probably contained shield volcanic rocks (tholeiites?) supplying sediments with olivine and iddingsite. Subsequently, most breccias were deeply weathered, which resulted in significant reductions in amounts of olivine and pyroxene, and formation of smectite and zeolite. Most likely at the same time, barite, and francolite crystallization occurred. The probable Eocene age of the deposits is consistent with the ^{40}Ar-^{39}Ar ages of volcanic rocks (ranging from 59 to 36 Ma) as well as with the paleomagnetic and paleontological ages of Line Islands ridge rocks, although the Eocene ages were determined for rocks located to the south of Karin Ridge (Schlanger *et al.*, 1984).

Mudstones noted above (Samples D8-6, D10-1) associated with phosphorites (D4-12/2) were recovered from water depths of 2600-2500 and 3800-3500 m on both the northeast and southwest flanks of Karin Ridge, although they are more abundant in dredged material from the northeast flank. These rocks are designated Unit IIA (early Senonian through late Paleocene). The age range is determined from foraminiferal assemblages: late Paleocene, sample D8-6; Late Cretaceous, D10-1; and late Senonian, D4-12 (Pletnev *et al.*, this volume). Besides volcanic clasts (groundmass of volcanic rocks, feldspar, magnetite, olivine, Ti-rich clinopyroxene) and their alteration products (smectite, zeolite, iddingsite, Fe-Mn hydroxide), the sedimentary rocks of Unit IIA contain the following: (1) metamorphic minerals (epidote, amphibole, garnet; see Fig. 7); (2) rare island-arc type volcaniclastic grains, defined by the green clinopyroxene-orthopyroxene-hornblende association of heavy minerals, (3) common terrigenous minerals (illite, chlorite, kaolinite, quartz - all identified by X-ray diffraction), (4) bioclasts (fish teeth, Foraminifera, Radiolaria), and (5) authigenic barite and francolite. Note that Unit IIA deposits are the most enriched in barite and francolite compared to all the sedimentary rocks studied (Fig. 8, 9). Perhaps, local upwelling in the area during the Late Cretaceous or Paleogene resulted in high bioproductivity and, consequently, barite and francolite mineralization (see Hein *et al.*, 1993). The highest content of fish teeth (3.4% of the total 0.05-0.1 mm fraction) associated with the highest francolite content in sample D4-12/2, supports the late Senonian age for this upwelling-related mineralization (Table 4). A heavy mineral association (magnetite >> olivine > clinopyroxene) for all these deposits indicates the postvolcanic (relict) stage of the hot-spot with no input from volcanic arcs, or active continental margins (see Figs. 5, 6). Moreover, the relatively abundant metamorphic grains (Fig. 7) indicate that they were deposited after tectonic activity had taken place in the region.

The lower parts of the ridge between 3800-3500 and 5200-5100 m water depth consist of plagioclase-phyric basalts and hawaiites (Unit IIC), comparable in composition to postshield hot-spot volcanoes (Martynov *et al.*, this volume) and strongly altered breccias (IIB). The latter were found only on the northeastern slope of the ridge (samples D8-3 and D8-7a; Table 1). The heavy mineral assemblage in the breccias is close to that of Unit IIA mudstones, so the breccias may be one of the sources for the mudstones. No age-diagnostic fossils were found in Unit IIB breccias, but taking into account ages of the overlying mudstones, the breccia age is most likely Late Cretaceous. This suggestion is consistent with a K-Ar age (84-80 Ma) of Karin Ridge volcanic rock (Hein *et al.*, 1990), ^{40}Ar-^{39}Ar ages ranging from 93 to 70 Ma of volcanic rocks from other Line Islands ridge edifices, as well as the paleomagnetic and paleontological ages of Line Islands ridge rocks (Schlanger *et al.*, 1984).

CONCLUSIONS

All data presented support the hypothesis first proposed for the origin of the Line Islands chain by Crough and Jarrard (1981); the Karin Ridge area may have experienced hot-spot activity twice; sometime during the Cretaceous (before Maastrichtian, according to the oldest foraminifers in mudstones of Unit IIA overlying volcanic rocks cropping out in the lower part of the ridge), and again sometime during Paleogene (most probably Eocene) time.

The Cretaceous volcanic edifices were strongly eroded and in places buried under thick pelagic deposits during the Maastrichtian through Paleocene. During the Late Cretaceous, upwelling probably existed above the ridge, which resulted in phosphatic mineralization of the deposits, although most phosphatization in the region is of late Eocene and early Oligocene ages (Hein, *et al.*, 1993).

During Oligocene and Miocene time, when volcanism was over, the area was subjected to tectonism. Turbidites and landslides formed on the ridge flanks and spread debris onto the adjacent basins.

During the late Miocene trough Holocene, sedimentation on the ridge was relatively minor. Foraminiferal sands accumulated on the ridge above the CCD; below the CCD muds were deposited.

Finally, we would like to emphasize that our conclusions are preliminary. We have prepared this paper in order to interest other researchers in the central Pacific region and in our methodology.

Table 1. Description of samples, their location, and age

Sample	Location	Depth, m	Morphologic Setting	Lithology	Age
HAWAIIAN ISLANDS					
H1	2 km south of Volcano Observatory		Near Kilauea Crater	Sand-sized tephra, greenish gray	---
H2	Ka Lae (South Point)	0	Southern slope of Mauna Loa Volcano	Beach sand greenish gray	Holocene
H3	Punaluu Harbor	0	Southwestern slope of Kilauea Volcano	Beach sand black	Holocene
H4	Near Kamoamoa Camp	0	Southern slope of Kilauea Volcano	Beach sand black	Holocene
H5	Puhi Bay	0	Eastern slope of Mauna Loa Volcano	Beach sand calcareous, gray	Holocene
H6	Hilo Bay	0	Eastern slope of Mauna Loa Volcano	Beach sand dark gray	Holocene
H7	Near Lewuawehe Point	0	Eastern slope of Mauna Kea Volcano	Beach sand dark gray	Holocene
H8	Near Laupahoehoe Point	0	Eastern slope of Mauna Kea Volcano	Beach sand dark gray	Holocene
M2	Near Kalalu Point	0	Northeastern slope of Haleakala Volcano	Beach sand black	Holocene
M4	Near Hanualete Point	0	Northeastern slope of Haleakala Volcano	Beach sand black	Holocene
M5	1 km northwest of Wainee River mouth	0	Northeastern slope of Puu Kukui Volcano	Beach sand gray	Holocene
M6	Kalili Beach	0	Southern slope of Puu Kukui Volcano	Beach sand gray	Holocene
O3	Near easternmost tip of Oahu Island	0	Southeastern slope of Koolau Mountain Range	Beach sand gray	Holocene
KARIN RIDGE					
Unit IA					
GC4 0-5cm	17°21.5'N 168°11.0'W	1670	Top of ridge	White Foram sand, containing Mn crust clasts	Late Pleistocene
Unit IB					---
GC1 0-52cm	16°27.3'N 168°31.8'W	5130	Foot of ridge	Brown mud	Pleistocene?
52-56cm	16°27.3'N 168°31.8'W	5130	Foot of ridge	Sandy silt brown mud	---
56-76cm	16°27.3'N 168°31.8'W	5130	Foot of ridge	Dark brown mud on the top and pale brown mud below	---
76-79cm	16°27.3'N 168°31.8'W	5130	Foot of ridge	White Foram sand	Oligocene?
79-92cm	16°27.3'N 168°31.8'W	5130	Foot of ridge	Mud mottled (dark and pale brown)	---
92-98cm	16°27.3'N 168°31.8'W	5130	Foot of ridge	Foram sand layers, muddy to different degree	---

Table 1. continued

Sample	Location	Depth, m	Morphologic Setting	Lithology	Age
Unit IB continued					
98-109cm	16°27.3'N 168°31.8'W	5130	Foot of ridge	Mud dark brown	---
109-111cm	16°27.3'N 168°31.8'W	5130	Foot of ridge	White Foram sand	Oligocene?
111-138cm	16°27.3'N 168°31.8'W	5130	Foot of ridge	Mud dark brown on top and pale brown below	---
138-141cm	16°27.3'N 168°31.8'W	5130	Foot of ridge	White Foram sand	---
141-168cm	16°27.3'N 168°31.8'W	5130	Foot of ridge	Mud mottled (dark and pale brown)	---
168-202cm	16°27.3'N 168°31.8'W	5130	Foot of ridge	White Foram sand	Oligocene?
202-218cm	16°27.3'N 168°31.8'W	5130	Foot of ridge	Mud mottled (dark and pale brown)	---
218-220cm	16°27.3'N 168°31.8'W	5130	Foot of ridge	White Foram sand	Oligocene?
220-240cm	16°27.3'N 168°31.8'W	5130	Foot of ridge	Mud dark brown	---
240-247cm	16°27.3'N 168°31.8'W	5130	Foot of ridge	Foram sand muddy in upper part of layer	---
247-261cm	16°27.3'N 168°31.8'W	5130	Foot of ridge	Mud dark brown	---
261-280cm	16°27.3'N 168°31.8'W	5130	Foot of ridge	White Foram sand	Oligocene?
*280-307cm	16°27.3'N 168°31.8'W	5130	Foot of ridge	Mud mottled (dark and pale brown)	---
*307-325cm	16°27.3'N 168°31.8'W	5130	Foot of ridge	Mud dark brown	---
325-345cm	162°7.3'N 168°31.8'W	5130	Foot of ridge	Mud calcareous, pale brown	Oligocene?
* There are Foraminifer sand dikes and several fractures crossing muds over the interval 280-325 cm at the angle of 20-25° to the vertical core axis					
Unit IC, Southwest Flank					
CAM1-1	16°34.1'-16°36.2'N 168°25.7'-168°19.8'W	3000-3050	Southwestern slope	Breccia volcaniclastic, dark green	---
D4-2	16°34.0'-16°36.7'N 168°28.7'-168°20.0'W	3500-2900	Southwestern slope	Breccia volcaniclastic, deeply altered, greenish-yellow	---
D4-8	16°34.0'-16°36.7'N 168°28.7'-168°20.0'W	3500-2900	Southwestern slope	Breccia volcaniclastic, deeply altered, greenish-yellow	Late Paleocene-Early Eocene
Unit ID, Northest Flank					
D11-1/1	17°12.5'-17°11.2'N 168°18.6'-168°20.0'W	2700-2450	Northeastern slope	Breccia volcaniclastic brownish gray	---
D11-2	17°12.5'-17°11.2'N 168°18.6'-168°20.0'W	2700-2450	Northeastern slope	Breccia volcaniclastic, graded, deeply altered, greenish-yellow	---
D11-3	17°12.5'-17°11.2'N 168°18.6'-168°20.0'W	2700-2450	Northeastern slope	Breccia volcaniclastic, deeply altered, greenish-yellow	---

Table 1. continued

Sample	Location	Depth, m	Morphologic Setting	Lithology	Age
Unit IIA, Southwest Flank					
D4-12/2	--	--	Southwestern slope	Phosphorite pale gray	Early Senonian
Unit IIA, Northest Flank					
D10-1b	17°11.2'-17°10.7'N 168°15.8'-168°18.6'W	3600-3400	Northeastern slope	Mudstone pale brown	Maastrichtian
D10-1bw	17°11.2'-17°10.7'N 168°15.8'-168°18.6'W	3600-3400	Northeastern slope	Mudstone light brown	---
D10-1w	17°11.2'-17°10.7'N 168°15.8'-168°18.6'W	3600-3400	Northeastern slope	White mudstone	---
Unit IIB, Northest Flank					
D8-3	17°14.2'-17°13.6'N 168°13.3'-168°16.2'W	4200-3600	Northeastern slope	Breccia volcaniclastic, deeply altered, greenish-yellow	---
D8-6	17°14.2'-17°13.6'N 168°13.3'-168°16.2'W	4200-3600	Northeastern slope	Mudstone brown	Late Paleocene
D8-7a	17°14.2'-17°13.6'N 168°13.3'-168°16.2'W	4200-3600	Northeastern slope	Breccia volcaniclastic, deeply altered, greenish-yellow	---

Capital letters in the sample numbers indicate either the island where the sample was collected (H=Hawaii, M=Maui, O=Oahu) or the type of sampler (GC=gravity-corer, D=dredge, CAM=bottom camera).

Table 2. Mineral analyses (volume %) of Hawaii Island sands (0.05-0.1 mm fraction)

Sample	L	Gl	Fsp	HV	Sm	Hd	Cc	Si	Ft	No.
H1 (tephra)	-	12.5	23.9	33.5	2.7	25.4	-	-	-	335
H2 (beach sand)	20.8	0.8	6.5	11.8	45.7	4.1	10.2	-	0.2	245
H3 (beach sand)	6.7	47.3	6.7	12.0	17.3	4.3	5.7	-	-	300
H4 (beach sand)	-	73.5	16.7	4.5	1.0	2.2	1.8	-	0.2	490
H5 (beach sand)	-	0.3	3.2	1.3	-	7.3	88.0	-	-	317
H6 (beach sand)	77.5	4.0	2.0	8.0	-	8.5	-	-	-	500
H7 (beach sand)	21.7	0.3	4.1	9.2	50.0	6.1	8.4	0.3	-	392
H8 (beach sand)	80.2	0.3	1.8	11.1	2.3	1.5	2.8	-	-	389

L=groundmass of volcanic rocks, Gl=volcanic glass, Fsp=feldspar and, in minor amounts, undifferentiated quartz, HV=heavy minerals, Sm=smectite, Hd=Fe-Mn hydroxides, bioclasts: Cc=calcareous, Si=siliceous, Ft=fish teeth; No.=number of grains counted

Table 3. Heavy mineral analyses (volume %) of sediments from the Hawaiian Islands (0.05-0.1 mm fraction)

Sample	Ol	Id	Cpx1	Cpx2	Opx	Hb	Am	Ep	Op	Bi	Ap	Rt	Sph	No.
H1 (tephra)	16.8	2.9	69.0	-	-	-	-	1.7	8.3	-	-	-	1.4	351
H2 (beach sand)	95.0	0.3	2.9	-	-	0.6	-	-	1.2	-	-	-	-	341
H3 (beach sand)	62.4	1.3	29.8	-	-	0.2	0.2	-	5.4	-	0.7	-	-	463
H4 (beach sand)	74.9	0.7	16.8	-	-	-	0.3	2.1	3.1	-	0.3	-	1.7	291
H5 (beach sand)	69.3	0.8	23.9	-	-	-	0.4	-	2.0	-	2.8	0.4	0.4	251
H6 (beach sand)	66.6	-	30.6	2.4	0.1	0.1	-	-	0.1	-	-	-	-	700
H7 (beach sand)	58.2	-	3.8	-	-	-	-	0.4	36.8	0.8	-	-	-	239
H8 (beach sand)	23.6	1.5	8.0	-	-	-	-	-	58.3	7.0	1.0	-	0.5	199
M2 (beach sand)	94.4	0.3	3.8	-	1.27	-	-	-	0.3	-	-	-	-	395
M4 (beach sand)	33.3	0.3	45.3	0.3	-	-	-	-	20.8	-	-	-	-	318
M5 (beach sand)	33.2	1.1	30.7	0.4	-	-	-	-	34.6	-	-	-	-	280
M6 (beach sand)	34.1	1.4	23.4	1.1	-	-	-	-	40.1	-	-	-	-	646
O3 (beach sand)	41.6	0.8	24.9	1.4	-	-	-	-	31.2	-	-	-	-	365

Ol=olivine, Id=iddingsite, Cpx=clinopyroxene (1=brown, 2=green), Opx=orthopyroxene, Hb=green and brown hornblende, Am=pale colored amphibole, Ep=epidote, Bi=biotite, Ap=crystalline apatite, Rt=rutile, Sph=sphene, Op=opaque minerals (magnetite, ilmenite), No.=number of grains counted

Table 4. Mineral analyses (volume %) of sediments and sedimentary rocks from Karin Ridge (0.05-0.1 mm fraction)

Sample,-interval in cm	L	Fsp	Gl	HV	Ba	Fr	Zl	Sm	Hd	Cc	Si	Ft	No.
Unit IA, Top of the Ridge													
GC4 (foram sand)	-	-	-	0.7	-	-	-	-	5.1	94.2	-	-	277
Unit IB, Abyssal Apron adjacent to Ridge (Station GC1)													
0-52 (mud)	-	14.2	2.0	4.5	-	8.5	24.9	45.0	-	-	-	0.9	353
52-56 (sandy silt)	-	10.4	1.7	11.5	-	6.6	21.0	37.1	8.2	3.2	-	0.3	348
56-76 (mud)	-	7.7	-	9.0	-	1.9	25.4	39.4	-	16.6	-	-	359
76-79 (foram sand)	-	1.2	0.4	2.7	-	-	3.1	4.3	-	88.4	-	-	257
79-92 (mud)	-	3.9	2.5	5.7	-	3.9	6.8	16.4	3.2	57.6	-	-	280
92-98 (foram sand)	-	2.5	1.1	0.7	-	-	8.8	10.2	-	76.7	-	-	284
98-109 (mud)	-	9.1	2.6	9.5	-	12.6	29.2	28.6	4.3	3.8	-	0.3	349
109-111 (foram sand)	-	7.0	0.8	6.8	-	1.9	7.6	31.0	2.5	41.4	-	1.1	355
111-138 (mud)	-	17.8	0.9	8.8	-	3.3	27.8	34.4	6.0	0.9	-	-	331
138-141 (foram sand)	-	11.8	0.6	3.6	-	-	2.0	32.2	3.9	45.2	-	0.7	307
141-168 (mud)	-	7.1	0.2	4.7	-	3.9	22.8	18.0	7.7	35.5	-	-	338
168-202 (foram sand)	-	0.4	0.7	0.8	-	-	2.3	3.4	-	92.3	-	-	261
202-218 (mud)	-	0.8	1.1	1.1	-	1.1	4.5	9.5	1.5	80.5	-	-	262
218-220 (foram sand)	-	6.0	-	3.0	-	0.7	1.5	2.6	-	86.2	-	-	268
220-240 (mud)	-	9.0	3.0	5.9	-	2.6	29.4	40.7	5.0	4.5	-	-	422
240-247 (foram sand)	-	6.1	2.5	5.2	-	1.3	14.8	24.5	3.5	41.2	-	0.8	519
247-261 (mud)	-	12.5	5.3	5.0	-	6.1	28.9	31.3	8.5	1.2	-	1.2	342
261-280 (foram sand)	-	4.3	0.6	0.6	-	0.6	1.9	13.9	4.0	74.0	-	-	323
280-285 (mud)	-	5.6	3.2	2.6	-	3.2	38.5	42.6	2.0	1.8	-	0.6	340
285-307 (mud)	-	11.2	2.6	2.6	-	4.2	23.8	40.2	1.4	13.2	-	0.7	453
307-325 (mud)	-	7.3	3.6	3.2	-	2.8	16.1	38.5	4.8	22.9	-	0.4	248
325-335 (mud)	-	0.7	1.6	-	-	0.3	6.9	11.2	2.0	77.2	-	-	303
335-345 (mud)	-	1.1	1.9	1.5	-	2.6	4.2	4.9	0.4	83.3	-	-	264
Unit IC, Southwest Flank													
CAM1-1 (breccia)	5.1	-	-	4.8	-	0.3	0.3	88.0	1.4	-	-	-	351
D4-2 (breccia)	0.4	11.2	-	0.4	-	1.9	2.3	83.0	0.8	-	-	-	258
D4-8 (breccia)	0.3	9.6	-	1.7	-	-	-	86.4	1.3	-	0.3	0.3	301
UNIT ID, Northeast Flank													
D11-1/1 (breccia)	-	1.7	-	0.5	-	-	41.8	34.9	1.0	-	-	-	424
D11-2 (breccia)	-	-	-	0.7	-	-	6.3	92.6	0.4	-	-	-	270
D11-3 (breccia)	-	2.3	-	16.7	-	-	-	56.2	2.3	-	-	-	306
UNIT IIA, Southwest Flank													
D4-12/2 (phosphorite)	0.6	0.9	-	1.6	0.3	66.6	0.9	2.5	23.2	-	-	3.4	323
UNIT IIA, Northeast Flank													
D10-1b (mudstone)	13.5	6.7	-	0.7	-	-	-	79.1	-	-	-	-	297
D10-1bw (mudstone)	5.7	2.8	-	0.6	0.3	1.4	9.9	73.4	5.7	-	-	0.3	353
D10-1w (mudstone)	0.3	1.0	-	1.0	14.9	2.6	64.7	11.9	3.3	-	-	0.3	303
UNIT IIB, Northeast Flank													
D8-3 (breccia)	-	-	-	0.5	-	-	-	77.1	21.4	0.5	0.5	-	210
D8-6 (breccia)	-	-	-	5.1	-	-	39.7	55.2	-	-	-	-	315
D8-7a (breccia)	4.7	11.5	-	4.3	-	1.3	-	76.2	2.1	-	-	-	235

Ba=barite, Fr=francolite, the other symbols are the same as Table 2

Table 5. Heavy mineral analyses (volume %) of sediments and sedimentary rocks from Karin Ridge (0.05-0.1 mm fraction)

Sample,-interval in cm	Ol	Idd	Cpx1	Cpx2	Opx	Hb	Am	Ep	Grn	Zr	Op	Bi	Ap	Rt	Sph	Ba	Fr	No.
Unit IA, Top of the Ridge																		
GC4 (foram sand)	17.9	3.6	33.9	4.5	1.8	2.7	1.8	0.9	-	-	26.8	-	0.9	-	-	5.4	-	112
Unit IB, Abyssal Apron adjacent to Ridge (Station GC1)																		
0-52 (mud)	4.3	2.0	30.6	4.3	0.3	7.3	1.1	11.8	-	-	20.7	-	-	-	-	-	16.7	372
52-56 (sandy silt)	5.1	0.6	40.2	0.6	0.3	5.1	1.2	13.0	-	-	28.7	-	0.3	-	-	0.6	4.1	331
56-76 (mud)	2.0	0.7	42.2	0.2	0.2	4.0	1.0	6.2	-	-	37.2	-	-	-	-	1.5	4.7	403
76-79 (foram sand)	0.9	2.3	6.1	0.7	-	0.9	-	2.3	-	-	72.0	-	-	-	-	1.6	13.4	575
79-92 (mud)	3.2	5.1	35.4	3.2	-	4.8	0.6	2.6	-	-	17.4	-	-	-	-	1.6	26.0	311
92-98 (foram sand)	2.8	2.8	31.4	6.6	0.3	5.9	-	5.5	-	-	18.3	0.7	0.3	-	-	2.8	22.8	290
98-109 (mud)	1.5	1.8	16.4	0.8	-	1.8	0.3	1.8	-	-	26.9	0.3	0.5	-	-	0.8	46.8	391
109-111 (foram sand)	4.3	1.4	27.4	1.8	0.2	1.6	0.9	4.5	-	-	16.6	-	0.7	-	-	2.0	38.5	441
111-138 (mud)	3.2	1.6	30.2	2.5	-	4.4	0.6	5.4	-	-	47.6	0.6	0.6	-	-	0.6	2.5	315
138-141 (foram sand)	1.3	0.3	7.3	0.5	-	2.3	0.4	2.4	-	-	81.5	-	1.0	0.3	-	1.0	1.9	798
141-168 (mud)	2.3	1.0	35.2	2.3	-	5.7	0.7	3.7	-	0.3	15.1	0.7	0.3	-	-	2.3	30.2	298
168-202 (foram sand)	2.0	8.3	9.8	1.0	-	1.0	-	0.2	-	0.2	34.1	0.2	0.2	-	-	1.2	41.7	410
202-218 (mud)	2.3	1.8	29.8	1.3	-	4.7	1.0	3.9	-	-	27.2	-	1.3	-	-	1.6	25.1	386
218-220 (foram sand)	1.7	1.5	28.3	3.2	0.5	6.1	1.0	2.0	-	-	15.9	-	1.0	-	-	-	39.0	410
220-240 (mud)	0.9	0.6	27.7	1.7	0.3	3.5	0.3	3.2	-	-	49.6	1.5	0.3	-	-	-	10.5	343
240-247 (foram sand)	0.6	0.3	45.4	3.9	0.3	2.5	0.3	0.6	-	-	26.6	1.4	-	-	-	0.3	18.0	361
247-261 (mud)	1.4	0.2	28.9	2.8	0.5	7.0	0.5	2.8	0.2	-	45.4	0.2	0.3	-	-	0.2	9.7	575
261-280 (foram sand)	0.4	1.1	8.8	0.7	-	1.8	0.2	1.0	-	-	72.8	0.4	0.7	-	-	4.5	8.0	838
280-285 (mud)	0.9	0.6	25.2	1.9	-	3.9	-	0.8	-	-	32.3	0.4	0.4	-	-	1.3	32.3	532
285-307 (mud)	1.7	0.5	21.8	1.5	0.2	4.6	-	1.9	-	-	37.1	0.3	0.2	-	-	-	30.2	487
307-325 (mud)	1.1	2.1	39.2	5.6	-	5.3	1.4	4.6	0.4	-	18.0	2.8	0.4	-	-	0.7	18.4	283
325-335 (mud)	0.2	3.9	17.3	1.7	-	4.3	0.2	1.0	-	-	34.9	0.2	0.2	0.5	-	2.9	32.5	415
335-345 (mud)	0.5	0.7	25.2	0.5	0.2	4.4	-	2.8	-	0.2	34.7	0.2	0.2	0.2	-	0.9	29.1	429
Unit IC, Southwest Flank																		
CAM1-1 (breccia)	-	2.0	94.3	-	-	-	-	-	-	-	3.2	0.6	-	-	-	-	-	348
D4-2 (breccia)	0.3	4.8	33.9	-	-	-	-	0.6	-	0.1	58.1	0.1	-	-	0.1	0.1	1.8	685
D4-8 (breccia)	2.7	4.1	47.1	-	-	0.3	-	-	-	-	44.9	0.3	0.3	-	-	-	-	292
UNIT ID, Northeast Flank																		
D11-1/1 (breccia)	1.1	73.5	2.4	-	0.1	-	-	-	-	-	14.2	0.1	-	-	-	0.3	8.2	880
D11-2 (breccia)	0.6	77.6	0.6	-	-	-	-	-	-	-	15.2	0.1	0.1	-	-	-	5.7	696
D11-3 (breccia)	0.8	64.3	1.9	-	-	-	0.3	0.8	-	-	18.8	0.3	0.3	-	-	6.6	6.1	378
UNIT IIA, Southwest Flank																		
D4-12/2 (phosphorite)	0.4	8.6	0.4	0.4	-	0.9	-	0.4	-	-	87.1	0.4	-	-	-	1.3	99.5	233
UNIT IIA, Northeast Flank																		
D10-1b (mudstone)	1.3	8.0	-	-	-	-	0.2	0.4	-	-	59.9	0.2	0.2	-	-	11.1	18.5	449
D10-1bw (mudstone)	-	11.1	1.9	-	-	0.2	0.5	0.5	-	0.2	71.2	0.5	1.5	-	0.2	92.0*	12.1	413
D10-1w (mudstone)	0.3	2.7	0.8	0.3	-	0.5	0.3	0.3	-	-	67.5	-	-	-	-	96.4*	27.5	400
UNIT IIB, Northeast Flank																		
D8-3 (breccia)	-	1.0	-	-	-	-	-	-	-	-	98.0	0.3	-	-	-	0.7	-	292
D8-6 (breccia)	1.9	4.1	3.9	-	-	0.2	0.2	0.2	-	0.4	74.1	0.6	-	-	-	1.1	3.2	463
D8-7a (breccia)	0.2	8.4	0.2	-	-	0.2	-	0.2	-	-	43.9	-	-	-	-	0.2	46.8	592

Grn=garnet, Zr=zircon, Ba=barite, Fr=francolite, the other symbols are the same as Table 2.
*percentages of the other minerals in the analysis were determined separately from this dominant one; the marked mineral identifications were checked by X-ray diffraction.

ACKNOWLEDGMENTS

We are indebted to all the Leg members with whom we worked on board the Russian vessel *Akademik Aleksandr Vinogradov* especially to our American colleagues: James R. Hein, Henry Chezar, Ransom Rideout, Marjorie S. Schulz, Virginia K. Smith, Rick Vail, and Juliet C. Wong, because it was our first experience with joint USA-Russia study at sea.

We would also like to thank James R. Hein, US Geological Survey and Lloyd Kegwin, WHOI, for improving the English and for kindly reviewing this paper.

REFERENCES

Clague, D.A., 1987, Hawaiian alkaline volcanism: *in* Fitton, J.G. and Upton, B.G.J. (eds.) Alkaline igneous rocks. Geological Society Special Publication 30, p. 227-252.

Creager, J., Scholl, D. *et al.*, 1973, Initial Reports of the Deep Sea Drilling Project, Vol. 19. Washington (U.S. Government Printing Office), 913 p.

Crough, S.T. and Jarrard, R.D., 1981, The Marquesas-Line swell: Journal of Geophysical Research, v. 86, p. 11,763-11,771.

Hein, J.R., *et al.*, 1994, Description and composition of fe-Mn crusts, rocks, and sediments collected on Karin Ridge, R.V. *Aleksandr Vinogradov* Cruise 91-AV-19/2: this volume, p. 39-86.

Hein, J.R., Hsueh-Wen Yeh, Gunn, S.H., Sliter, W.V., Benninger, L.M., and Chung-Ho Wang, 1993, Two major Cenozoic episodes of phosphogenesis recorded in Equatorial Pacific seamount deposits: Paleoceanography, v.8, p. 293-311.

Hein, J.R., Kirschenbaum, H., Schwab, W.C., *et al.*, 1990, Mineralogy and geochemistry of Co-rich ferromanganese crust and substrate rocks from Karin Ridge and Johnston Island, *R.V. Farnella* cruise F7-86-HW: U.S. Geological Survey Open File Report 90-298, 80 p.

Markov, Yu.D., Vashenkova, N.G., Nechaev, V.P., and Ryapolova, N.V, 1989, Sedimentology in the eastern and central Pacific. Part 1: Sediment deposition on seamounts and East Pacific Rise: Preprint. Far Eastern Branch of Russian Academy of Sciences Report, Pacific Oceanological Institute, Vladivostok, 37 p. (In Russian)

Markov, Yu.D., Kulinich, R.G., Lin'kova, T.I., Nechaev, V.P., Biryulina, M.G., Vashenkova, N.G., Ivanov, Yu.Yu., and Pushkar, V.S., 1992, Sedimentology in the eastern and central Pacific. Part 2: Sediment deposition and stratigraphy of soft sediments in Clarion Fracture Zone and Guatemala Basin: Preprint. Far Eastern Branch of Russian Academy of Sciences Report, Pacific Oceanological Institute, Vadivostok, 47 p. (In Russian)

Martynov, Y.A., Oktyabr'sky, R.A., and Badredtinov, Z.G., 1994, Petrography, mineral composition, and major and trace element geochemistry of igneous rocks from Karin Ridge: this volume, p.

Nechaev, V.P., 1991, Evolution of the Philippine and Japan Seas from the clastic sediment record: Marine Geology, v. 97, p. 167-190.

Pletnev, S.P., Ryaben'kaya, I., and Quinterno, P.J., 1994, Biostratigraphic results of Cruise 91-AV-19/2, Karin Ridge, central Pacific Ocean: this volume, p. 87-92.

Schlanger, S.O., Garcia, M.O., Keating, B.H., Naughton, J.J., Sager, W.W., Haggerty, J.A., Philpotts, J.A., and Duncan, R.A., 1984, Geology and geochronology of the Line Islands: Journal of Geophysical Research, v. 89, p. 11,261-11,272.

PETROGRAPHY, MINERAL COMPOSITION, AND MAJOR AND TRACE ELEMENT GEOCHEMISTRY OF IGNEOUS ROCKS FROM KARIN RIDGE

Yury A. Martynov, Ziniat G. Badredtinov, and Rostislav A. Oktyabr'sky

Far East Geological Institute, Russian Academy of Sciences, Vladivostok 69022, Russia

INTRODUCTION

Karin Ridge, studied during Leg 2 of the R/V *Akademik A. Vinogradov* cruise 19, is located at the northern termination of the Line Islands. Information about the geology, petrology, and geophysics of the Line Islands chain is presented by Schlanger *et al.* (1976), Winterer (1973), Schlanger *et al.* (1984), Sager and Keating (1984), Epp (1984), Duncan and Clague (1985), and others.

The Line Islands compose one of the longest linear features of the Pacific plate, comparable in size to the Hawaiian-Emperor volcanic chain. Some geological and morphological features of the two chains differ. The morphology of the Line Islands is more complicated and changes at the intersection, or projected intersection, of the Clarion, Clipperton, and Galapagos fracture zones (Haggerty *et al.*, 1982). The volcanic history of the Line Islands is also temporally more complex than that of the Hawaiian-Emperor chain. DSDP drilling in the central Line Islands, the radiometric age dating of dredged rocks, and paleontological age dating define middle through Late Cretaceous and Eocene volcanic edifices or ridge-building volcanic events. Eocene volcanic events took place from 15°N to 9°S and Cretaceous events took place from 18°N to 9°S (Schlanger *et al.*, 1984). The wide geographic distribution of both volcanic events over a distance of several thousands of kilometers indicates that the Line Island chain was not formed by a single hot spot.

Predominant volcanic rock types of the Line Islands are alkalic basalts and hawaiites (Schlanger *et al.*, 1984). Tholeiitic basalts and phonolites were dredged only from the central part of the chain. Major, trace, and rare earth element analyses indicate that the rocks are typical oceanic island alkalic lavas, comparable with alkalic Hawaiian rocks.

Karin Ridge was studied chiefly during U.S. Geological Survey cruise F7-86-HW (Hein *et al.*, 1990). The predominant rock types recovered include sedimentary breccias and alkalic basalts. Breccia consists of basalt clasts in various kinds of cement and matrix. Relatively fresh volcanic rocks are alkalic basalts. Differentiated compositions include hawaiites and benmoreites. Two samples were defined as transitional basalt.

The aim of this report is to give brief petrological descriptions and evaluate the petrogenetic relationships among the various types of volcanic rocks recovered from two profiles along the flanks of Karin Ridge (See Fig. 1, Nechaev *et al.*, this volume).

METHODS

Thirteen samples from Karin Ridge were analyzed for major and trace element composition. Eleven samples from Kilauea and Mauna Loa volcanoes were also analyzed in order to estimate the accuracy of the analytical technique.

Major element abundances were determined using wet chemical techniques and trace element contents were determined with XRF, both at the Far East Geological Institute of the Academy of Sciences, Russia. The accuracy of the results were verified by replicate analyses of standard samples of andesite AGB-1, granodiorite GSP-1 (USA), gabbro SGD-1A, and andesite DVA and DVB (Russia). Analitical errors for trace elements are better than 10%. Analyses of minerals were performed using a Camebax-type microprobe at the Institute of Volcanology (Petropavlovsk - Kamchatka). Working conditions were 20 kV accelerating voltage and a sample current of 50 nA. Matrix corrections were applied according to Bence and Albee (1968). Natural silicates (sanidine for Si, K, Na, Al, diopside for Ca and Mg, olivine for Fe, ilmenite for Ti, rhodonite for Mn), carefully checked against other standards for composition, were used as standards. Relative errors due to counting statistics were 3 % 2Q. Raw data were corrected on-line for drift, dead-time, and background.

PETROGRAPHY AND MINERAL COMPOSITIONS

Alkalic basalts

Pillow-fragments of alkalic basalts broken from outcrops are relatively fresh and moderately vesicular (5-15%). Vesicles are commonly filled with phillipsite and smectite. Porphyritic alkalic basalts contain up to 20% phenocrysts of plagioclase, olivine, and rarely, subequal proportions of both olivine and clinopyroxene (D4-13B/1; D4-13B/2; Table 1). Groundmass is microlitic and aphanitic. Predominant minerals in the groundmass are plagioclase, olivine, and rarely clinopyroxene. Cores of plagioclase phenocrysts (0.1-2.0 mm) range in composition from An65 to An60 with normal zoning up to 5% An content (Fig. 1). Phenocryst cores are usually replaced by zeolite, especially in altered samples. Groundmass plagioclase (0.01-0.8 mm) compositions range from An60 to An50 and typically contain inclusions of brown volcanic glass. Cores of these crystals are rarely replaced by zeolite. Olivine phenocrysts vary in abundance and size (0.15-0.8 mm), and are typically replaced by iddingsite and iron oxides. Augitic clinopyroxene occurs in unaltered euhedral grains both as phenocrysts and as a groundmass mineral. Pyroxene phenocrysts display little compositional zoning, with increasing ferrosilite and wollastonite end members from core to rim. Aluminum oxide contents range from 2.54% in the core to 6.03% in the rim (Table 2, Fig. 2), which could indicate decreasing total P or rapid cooling during crystallization. Glass and associated opaque minerals are typically replaced by smectite.

Transitional basalts

Transitional basalts are massive, rarely vesicular pillow-fragments (up to 100x100x50 mm) coated with an Fe-Mn patina. Up to 5% of the vesicles are filled with smectite. Textures vary from porphyritic to glomerophyric, containing plagioclase phenocrysts (20%) and microlites. In samples D7-3 and D7-6, phenocryst and groundmass clinopyroxene is present. Fe-Ti oxides occur only in the groundmass. Abundances of plagioclase and opaque minerals increase from the quenched margin to the center of the pillow-fragments.

Plagioclase phenocrysts (0.3-0.6mm) most commonly occur in clots, typically including an opaque mineral and devitrified glass, and are locally replaced by zeolite. Phenocrysts display both normal and reverse zoning. The composition of phenocryst cores varies from An43 to An83, both in the group of samples and within a single sample, whereas phenocryst rim and groundmass plagioclase typically show little compositional variation (about 60-63% An) (Fig. 1).

Clinopyroxene phenocrysts commonly display well defined reverse zoning with increasing wollastonite and enstatite end members from core to rim (Table 2). Aluminum oxide contents increase rapidly from core (1.50) to rim (up to 4.45%). It is interesting to note the similarity between plagioclase and clinopyroxene phenocryst rim compositions in alkalic and transitional basalts, and the distinct differences in their cores (Fig. 2).

Glass in the transitional basalts is typically palagonite composed of smectite and palagonite.

Hawaiites

Hawaiites occur as pillow-fragments (D5-2) in breccia, which are commonly cemented by Fe-Mn oxyhydroxides. The rocks are predominantly massive or sparsley vesicular (up to 5%), but in some samples vesicles increase to 25-30%. About 10% of the vesicles are filled with smectite, carbonate, and rarely zeolite and Fe-Mn minerals. Hawaiites are generally porphyritic with glomerophyric areas, and rarely aphanitic. Phenocrysts (5-20%) of plagioclase, olivine, and magnetite are common. In samples CAM-1/3 and D3-1, sparse brown clinopyroxene is present. Groundmass textures vary from hyalopilitic to intersertal, and pilotaxitic, locally microlitic in aphanitic samples. The groundmass consists of plagioclase, olivine, magnetite, rarely clinopyroxene, and/or anorthoclase. In samples D3-1 and D3-3A, sparse apatite is present.

Plagioclase phenocrysts (0.15-1.5 mm) are commonly zoned, ranging in composition from An58 in the cores to An30 in the rims. Large phenocrysts may include altered glass, olivine, and magnetite. Some plagioclase cores are replaced by colorless zeolite (phillipsite) and/or smectite. Groundmass plagioclase (about 0.01-0.5 mm) ranges in composition from An50 to An30. Groundmass anorthoclase, containing up to 30% Or, was identified in Sample D3-2B (Table 2).

Euhedral olivine phenocrysts (0.1 to 0.6 mm) typically occur in clusters with rare titanomagnetite, and are completely altered to iddingsite and iron oxides. Groundmass olivine is commonly skeletal and is replaced by iddingsite. An important feature of hawaiites is the presence of Fe-Ti oxides (up to 15-20%) both in euhedral phenocrysts (0.1-0.6 mm) and as a groundmass mineral (0.01-0.03 mm). Titanomagnetite phenocrysts commonly occur in clusters with olivine (D5-2), occasionally with inclusions of olivine.

Clinopyroxene (0.01-0.02 mm) was identified only in the groundmass in samples CAM1-3, D5/2, D3-1, and D3-2B. In aphanitic hawaiites, clinopyroxene is typical only of the rocks with intersertal texture. Glass (up to 50-70%) is usually replaced by smectite, especially in the aphanitic hawaiites.

Trachyte

A fragment of vesicular (about 10%) trachyte (50x50x100 mm), coated with Fe-Mn crust (~50 mm thick), was recovered in CAM1-4. Vesicles are typically filled with smectite. The trachyte texture is porphyritic with sodic plagioclase phenocrysts (up to 10%) and variable amounts of Fe-Ti oxides.

Alkali feldspar laths (0.01-0.1mm), trace amounts of pyroxene, and magnetite dominate the groundmass. Plagioclase phenocrysts (0.5-0.1mm) range in composition from An_{45} to An_{40} and typically have included groundmass magnetite and apatite. Euhedral phenocrysts of magnetite are locally replaced by smectite, while pyroxene and magnetite are replaced by iron oxides. Alkali feldspar in the trachyte groundmass regularly varies in composition from 11 to 42% Or (Table 2).

ALTERATION OF VOLCANIC ROCKS

Volcanic rocks analyzed in this study are moderately to strongly altered at the initial stage of oceanic halmyrolysis including replacement of volcanic glass by smectite, filling of microfractures and vesicles with zeolite, and replacement of olivine and some magnetite by Fe oxides. Rare hematite, goethite, and secondary alkali feldspar were also detected by X-ray diffraction (shipboard analysis by M.F. Eiberman, A.P. Mazherovsky, and A.N. Levin). Carbonate occurs only in samples D4-13T/1 and D4-15/1. The assemblage of secondary minerals indicates formation under oxidizing conditions at low temperature and pressure.

Alteration intensity for the rocks depends greatly on their structural characteristics and vesicle content. For example, the pillow-fragments, which are divided into three parts based on their structure (marginal, transitional, and central). In the marginal zone (1-2 cm), sparse phenocrysts of rock-forming minerals, abundant clay minerals replacing volcanic glass, and typical dark-brown color were observed. In some samples (D3-2B), the Fe-Mn crust that coats the pillow-fragments penetrates into the marginal zone and fills some vesicles. The transitional zone is characterized by relatively numerous vesicles and phenocrysts; vesicles are commonly filled with smectite and/or zeolite (phillipsite). Olivine and magnetite phenocrysts are replaced by Fe oxides. Zeolite usually replaces plagioclase phenocryst cores and fills microfractures in groundmass. The central zone is similar to the transitional zone but shows less low-grade metasomatic alteration. Each zone of the pillow-fragments clearly shows the difference in major and trace element contents as a result of redistribution during submarine weathering. This is especially apparent for the highly altered marginal zones, which differ from the relatively fresh central zones by high contents of Rb, K_2O, and Fe_2O_3 and low concentrations of FeO, CaO, MgO, P_2O_5, and Y (Table 3), although the latter typically is considered as an alteration resistant element. A sharp decrease of Co in the marginal zone was observed in some samples (D4-13A/1 and D4-13B/1). Unusually high Co, Ni, and V contents in the marginal zone of sample D4-4 are most likely the result of contamination by Co- and Ni-enriched Fe-Mn crusts that are known to occur in the area (Hein *et al.*, 1990).

Concentrations of so-called alteration-resistant elements (except Y) in each zone are constant and vary only within the limits of analytical accuracy.

These data suggest that Ca, Mg, P, Y, and probably Co were removed, and Fe, K, and Rb added, during low-temperature alteration of the volcanic rocks. At least for two studied pillow-fragments (D4-13A and D4-13B/1) this element mobility is clearly shown (Table 3) and the data for Fe, K, Rb, Mg, and Ca are in good agreement with experimental results of the interactions between seawater and basalts (Seyfried and Bishoff, 1979; Rona, 1988). Cobalt removal from basalt is probably a result of replacement of magnetite and glass by Fe-oxides and smectite and is in good agreement with the inverse relationship between Fe and Co in studied samples.

MAJOR AND TRACE ELEMENTS GEOCHEMISTRY

Alteration of volcanic rocks severely limits the use of element abundances to determine original magma types. This is especially true for MgO which, due to replacement of olivine, shows unrealistically low contents in the basaltic rocks and has no significant correlation with Ni, Co, or incompatible trace element abundances (Table 4). Potassium and Rb are believed to be mobile in aqueous fluids due to their low ionic potentials (Pearce, 1983), so their high contents in the basalts may be the result of alteration.

The best method to estimate primary composition and magmatic type of altered samples is the use of empirically established so called alteration-resistant minor and trace elements (Sr, Ba, Zr, Nb, partially Ti and Y, REE) which preserve their primary concentrations even in fairly altered rocks (Bass *et al.*, 1973). Igneous rocks from both northern and southern Karin Ridge generally plot in the fields for alkalic rocks (Figs. 3a-c), and transitional basalts from the northern area display distinctly low P_2O_5, Sr, Zr, and Nb contents, thus may be classified as transitional basalt or ocean islands tholeiite. Major element compositions (Fig. 4) show other differences in basic rocks of Karin Ridge. K_2O and P_2O_5 contents are generally lower and Al_2O_3 higher in the transitional basalts relative to alkalic ones. On the other hand, the hawaiites from both northern and southern study areas on Karin Ridge show similar major and trace elements abundances (Fig. 4-5).

Elements with low distribution coefficients (K_D) between typical basalt rock-forming minerals (olivine, plagioclase, clinopyroxene, and spinel) and melt may be used to test if the collected magmatic rocks were cogenetic. Because Nb is an alteration-resistant element, abundances of incompatible (P_2O_5, K_2O, Rb) and moderately incompatible elements are shown as a function of Nb content (Fig. 5). All elements except for P_2O_5 and Y form positive coherent trends defined for all Karin Ridge lavas with the highest abundances in hawaiites and trachyte. Thus, all of studied rocks were presumably derived either from a similar mantle source or from sources with similar incompatible element ratios. In spite of their mobility in aqueous fluid, the highly regular evolution of K_2O and Rb concentrations in studied samples gives strong evidence for the preservation of their primary contents, even in relatively highly altered rocks. Alternatively, a very scattered trend of Y may be caused by alteration; as mentioned above, the element contents regularly change from core to margin of the pillow fragments (Table 3). Highly variable P_2O_5 abundances in alkalic basalts probably reflect contamination of samples with phosphate minerals.

Frey *et al.* (1990) used Sr/X ratios (where X is a highly incompatible element) in identifying a possible parent composition and the petrogenetic processes leading to the origin of volcanic rock sequences. The Sr/Nb ratio in volcanic rocks of Karin Ridge (Fig. 6) is markedly lower than it is in postshield alkalic lavas of Mauna Kea Volcano, Hawaii, but the relationships between basalts and hawaiites for each suite are very similar. Both magma groups define distinct but subparallel paths reflecting different parental magma compositions. A decrease in Sr/Nb ratio within basic and hawaiite lava suites indicates the important role of low-pressure feldspar dominating fractionation in creating both magma types. But the transition from basalt to hawaiite requires a segregation of a clinopyroxene +olivine, plagioclase-poor assemblage at moderate pressures (Frey *et al.*, 1990). In such a way, alkalic and transitional basalts of Karin Ridge showing distinct geochemical characteristics might have been produced by fractional crystallization of a common parental magma. This model is strongly supported by mineralogical data, because in transitional basalt with the highest Sr/Nb ratio, plagioclase and clinopyroxene phenocrysts display features that are typical of accumulative mineral phases, i.e., a wide range of core compositions and well-defined reverse zoning. Relatively low Ni, Sr, and P_2O_5 contents in trachyte (Fig. 5, Table 4) give evidence for plagioclase, apatite, and mafic mineral segregation in the genesis of this magma type.

An assemblage of Karin Ridge volcanic rocks and their geochemistry are similar to those of postshield alkalic lavas from Mauna Kea volcano, Hawaii (Frey *et al.*, 1990), although some differences were observed. Karin Ridge basalts have distinctly higher K_2O, Rb, and P_2O_5 contents and K_2O/Nb, Rb/Nb ratios (Fig. 5), that might reflect alkali element enrichment of their mantle source. Unlike many Hawaiian tholeiitic and alkalic basalts, volcanic rocks from Karin Ridge have a significantly higher Ti/V ratio (Fig. 7). According to Shervais (1982), this ratio is a sensitive indicator of oxygen fugacity conditions during both partial melting and fractional crystallization. However, the differences in Ti/V ratios of igneous rocks may also reflect different mineral assemblages in the melt. For example, the variation in garnet/olivine ratio must substantially change Ti/V ratios in produced melts, because garnet typically has a higher distribution coefficient for V (8) than olivine (0.09). Thus the difference between alkalic rocks of Karin Ridge and Hawaii might be the result of their differences in either oxygen fugacity or melted mineral assemblages.

CONCLUSIONS

1. Igneous rocks dredged from the Karin Ridge are alkalic and transitional basalts, hawaiites, and trachytes, partially altered by low temperature processes under oxidizing conditions.

2. Transitional and alkalic basalts from the northern and southern Karin Ridge study areas differ in major (K_2O, P_2O_5, and Al_2O_3) and trace element (Sr, Zr, and Nb) contents, but may have been produced

by low-pressure plagioclase dominating fractionation of a common parental magma. Hawaiites are the result of segregation of a plagioclase-poor assemblage at moderate pressures.

3. The assemblage of Karin Ridge volcanic rocks and their geochemistry are similar to those of postshield alkalic lavas (basaltic and hawaitic substage) from Mauna Kea Volcano, Hawaii. The difference between the compared rocks from the two areas might be the result of compositional differences of mantle sources and/or total P and oxygen fugacity conditions during magma evolution.

Table1. Petrographic summary of Karin Ridge volcanic rocks

Samples	Phenocrysts	Groundmass	Alteration
Alkalic basalts			
D4-13A/1	Ol+Pl(>50)	Ol+Pl(50)+Gls	Ol (Hd)
D4-13T/1	Ol+Cpx+Pl(58-50)	Ol+Cpx+Pl+Gls	Ol (Hd) Pl (Ze)
D4-13T/2	Ol+Cpx+Pl	Ol+Cpx+Pl(50)+TiMt+Gls	Ol (Hd) Gls (Sm)
D4-13B/2	Ol+Pl(65-58)	Pl+Gls+TiMt	Gls (Sm)
D4-13G/1	Ol+Pl(62-55)	Ol+Pl(55-45)+Gls+TiMt	Ol (Hd)
D4-1/4	Ol+Pl	Pl+Gls+TiMt	
Transitional basalts			
D7-3	Ol+Pl(55)	TiMt+Pl(50)+Gls	Gls (Sm)
D7-5C	Pl(55)	TiMt+Pl(45)+Gls	Gls (Sm)
D7-5T	Pl(50)	Pl+Gls	Gls (Pg,Hd)
D11-3/1	Pl(55-50)	Ol+Pl(45-40)+Gls	Pl(Ze) Ol(Id) Fs(Sm)
D11-3/2	Pl(65-50)	TiMt+Pl(50-40)+Gls	Gls (Sm)
D11-3A	Ol+Pl	TiMt+Ol+Pl+Gls	
Hawaiites			
D5-2	TiMt+Ol+Pl(55-45)	TiMt+Ol+Cpx+Pl(45-40)+Gls	Pl (Ze) Ol (Hd)
CAM 1/3	Cpx+Ol+Pl(60-40)	Ol+Cpx+Pl(45-35)+Gls+TiMt	Ol (Hd)
D3-1	TiMt+Cpx+Ol+Pl(68)	Ap+TiMt+Cpx+Pl(65-50)+Gls	Ol (Cc) Gls (Sm)
D3-2A	Ol+Pl(65-50)	Ap+TiMt+Ol+Pl+Gls	Pl (Ze) Ol (Hd)
D3-2T	Ol+TiMt+Pl(58-43)	Ol+TiMt+Cpx+Or+Pl+Gls	Ol(Hd) Fs(Sm) Gls(Sm)
D8-1	TiMt+Pl(62-50)+Ol	TiMt+Ol+Pl(50-45)+Gls	Pl(Ze) Ol(Id) Gls(Sm)
D8-2	TiMt+Ol+Pl(>50)	TiMt+Pl(50-45)+Gls	Ol(Id) Pl(Ze) Gls(Sm)
D8-4	Pl(68)	TiMt+Ol+Pl(50-45)+Gls	Ol(Id) Pl(Ze) Gls(Sm)
Trachyte			
CAM 1/4	TiMt+Pl(36-45)	Ap+TiMt+Pl+Or	

TiMt=opaque minerals; Ol=olivine; Cpx=clinopyroxene; Pl=plagioclase with An content in parentheses; Or=feldspar; Ap=apatite; Gls=glass; Ol(Hd) (Cc) (Id)=olivine replaced with Fe-Ti oxides, carbonate, and iddingsite respectively; Pl(Sm) (Ze)= plagioclase replaced by smectite and zeolite; Gls(Pg)=palagonite.

Table 2. Selected mineral analyses

	FELDSPAR								
	Alkalic basalt		Hawaiite				Transitional basalt		
	D4-13T/1		D3-2B				D7-3		
	mph	grm	ph(c)	ph(r)	grm	grm	ph(r)	ph(c)	ph(r)
SiO_2	52.38	53.84	52.95	57.29	60.54	65.80	52.81	46.95	54.97
Al_2O_3	30.05	29.73	29.13	26.33	24.06	21.28	29.05	32.28	29.68
CaO	13.14	12.48	11.60	8.43	5.87	2.19	11.91	16.19	12.49
Na_2O	3.54	3.98	4.28	5.66	6.73	6.73	3.89	1.82	3.72
K_2O	0.27	0.34	0.34	0.70	1.41	5.00	0.35	0.08	0.27
Total	101.20	101.80	98.88	99.05	99.64	101.79	98.91	98.38	99.10
An(%)	65.51	62.11	58.75	43.21	29.76	10.76	61.51	82.72	63.89
Ab(%)	32.87	35.85	39.21	52.51	61.72	59.92	36.34	16.81	34.46
Or(%)	1.63	2.04	2.05	4.28	8.53	29.32	2.16	0.47	1.66

Table 2. continued

CLINOPYROXENE

	Alkalic basalt D4-13T/1		Transitional basalt D7-3			
	mph	mph	ph(c)	ph(r)	ph(c)	grm
SiO_2	51.68	48.41	51.23	51.36	49.16	48.92
TiO_2	1.03	2.73	0.46	0.59	1.42	1.47
Al_2O_3	2.54	2.73	1.50	1.71	4.25	4.45
Cr_2O_3	0.03	0.00	0.00	0.00	0.10	0.13
FeO	8.75	9.25	16.25	12.78	9.58	9.24
MnO	0.23	0.18	0.69	0.44	0.23	0.17
MgO	16.39	12.58	10.95	13.29	13.99	13.62
CaO	18.17	21.59	18.07	18.96	19.74	20.03
Na_2O	0.05	0.11	0.24	0.24	0.28	0.31
Total	98.89	100.88	99.39	99.48	98.75	98.38
Woll	38.01	46.62	39.30	39.98	42.30	43.37
En	47.70	37.78	33.13	38.98	41.69	41.02
Fs	14.29	15.53	27.57	21.04	16.01	15.61

FELDSPAR

	Transitional basalt D7-3		D7-6		Trachyte CAM 1/4			
	grm	mph	ph(c)	grm	grm	grm	grm	grm
SiO_2	51.91	54.37	61.07	64.52	64.52	65.90	66.18	63.52
Al_2O_3	29.00	29.45	26.00	23.62	23.62	21.38	19.66	17.41
CaO	12.26	11.94	6.96	4.41	4.41	2.62	0.77	0.22
Na_2O	3.77	4.16	6.18	7.00	7.00	7.72	6.73	6.31
K_2O	0.33	0.31	0.89	1.75	1.75	3.14	5.61	6.98
Total	98.17	101.50	101.48	101.98	101.98	101.44	99.77	101.25
An(%)	62.92	60.17	36.91	12.20	12.20	12.36	1.08	23.03
Ab(%)	35.05	37.98	58.26	68.69	68.69	60.35	57.27	66.07
Or(%)	2.02	1.84	5.53	18.41	18.41	27.29	41.65	10.90

CLINOPYROXENE

	Transitional basalt D7-6	
	mph	mph
SiO_2	46.06	50.76
TiO_2	3.06	1.52
Al_2O_3	6.04	2.84
Cr_2O_3	0.01	0.01
FeO	11.10	11.05
MnO	0.21	0.28
MgO	11.72	14.11
CaO	20.49	19.21
Na_2O	0.75	0.06
Total	99.48	99.85
Woll	45.07	40.47
En	35.87	41.35
Fs	19.06	18.17

Ph(c), Ph(r) = core and rim of phenocryst respectivley; mph = microphynocryst, grm = groundmass phase.

Table 3. Major oxide (wt%) and trace element (ppm) contents of pillow-fragments

Samples	D4-13A/1			D4-13/B2	
Zones	M	T	C	M+T	C
SiO_2	42.00	41.51	42.60	47.63	44.24
TiO_2	3.29	2.98	2.81	3.18	3.35
Al_2O_3	16.00	16.20	16.60	16.73	15.68
Fe_2O_3	14.10	12.20	10.70	11.57	11.20
FeO	0.40	1.16	1.28	1.40	1.05
MnO	0.17	0.23	0.12	0.14	0.12
MgO	2.30	4.50	3.00	2.09	3.39
CaO	3.80	9.80	7.60	6.35	8.56
Na_2O	2.85	2.85	2.80	3.09	2.99
K_2O	2.50	1.75	2.00	2.56	1.99
P_2O_5	0.69	2.75	2.11	1.03	2.64
H_2O-	5.02	2.15	3.61	2.58	2.72
LOI	11.50	3.70	8.00	4.17	4.78
Total	99.60	99.63	99.62	99.94	99.99
Sr	361	585	307	572	461
Nb	39	40	33	52	36
Y	72	87	33	235	42
Zr	444	368	338	435	379
Ni	56	55	50	63	83
Co	32	47	41	45	43
Cr	88	96	94	91	103
V	200	241	210	248	254

Samples	D4-13B/1		D4-4			D7-5	
Zones	M+T	C	M	T	C	M+T	C
SiO_2	40.00	43.92	40.90	42.70	41.47	46.00	47.38
TiO_2	3.32	3.59	3.14	2.83	3.19	1.97	2.23
Al_2O_3	18.00	16.19	16.30	17.60	13.44	20.70	20.14
Fe_2O_3	13.20	12.23	13.00	11.80	11.60	9.10	8.27
FeO	0.50	0.99	0.50	1.28	1.05	0.75	1.65
MnO	0.10	0.16	0.56	0.06	0.10	0.37	0.10
MgO	5.70	2.66	2.50	3.00	3.31	2.30	3.23
CaO	4.40	7.25	4.80	7.40	10.92	7.20	9.93
Na_2O	2.60	2.76	2.70	2.90	2.47	2.72	2.80
K_2O	1.75	2.18	2.60	2.00	2.00	1.95	1.41
P_2O_5	0.55	2.19	1.11	0.38	1.01	0.34	0.51
H_2O-	3.65	1.70	3.28	2.85	1.96	3.09	2.55
LOI	10.00	5.99	11.46	7.80	9.39	6.80	2.84
Total	100.13	100.11	99.57	99.75	99.94	100.20	100.50
Sr	455	307	449	514	277	517	883
Nb	39	33	42	35	32	26	24
Y	37	47	79	42	42	32	27
Zr	448	338	426	370	308	268	421
Ni	61	74	137	17	47	44	30
Co	28	52	100	20	36	48	32
Cr	97	87	82	82	74	52	46
V	259	255	253	188	180	200	157

M, T, C = zones of pillow: M (marginal); T (transitional); C (central); M+T (marginal and transitional)

Table 4. Major oxide (wt%) and trace element (ppm) contents of volcanic rocks from Karin Ridge, Kilauea Volcano, and Mauna Kea Volcano.

	Karin Ridge (southern area)										Karin Ridge (northern area)					
	D4-4	D4-13G/1	D4-13G/1A	D4-13B/2	D4-13T/1	D3-1	D3-2A	CAM-1/3	D5-2	CAM-1/4	D7-3	D7-5U	D7-5N	D11-3/1	D11-3/2	D11-3A
SiO_2	41.47	44.19	43.60	44.24	47.19	48.81	44.58	47.62	48.71	61.24	47.04	47.38	46.00	47.11	47.23	45.34
TiO_2	3.19	3.26	2.85	3.35	3.27	2.79	2.42	3.82	3.06	1.03	2.95	2.23	1.97	3.64	3.60	3.77
Al_2O_3	13.44	15.95	15.70	15.68	16.92	18.72	17.70	16.29	17.02	16.55	17.28	20.14	20.70	18.25	17.87	17.80
Fe_2O_3	11.60	12.35	10.40	11.20	10.33	5.35	8.70	9.43	6.71	3.75	9.59	8.27	9.10	10.67	9.96	12.78
FeO	1.05	1.06	0.95	1.05	1.84	2.99	1.44	1.70	3.49	0.40	2.27	1.65	0.75	1.30	1.81	1.00
MnO	0.10	0.24	0.29	0.12	0.16	0.09	0.57	0.09	0.13	0.02	0.10	0.10	0.37	0.07	0.11	0.15
MgO	3.31	3.52	3.90	3.39	2.04	2.97	2.60	2.81	2.03	1.43	3.43	3.23	2.30	1.97	2.30	2.03
CaO	10.92	7.74	7.80	8.56	5.99	9.00	8.36	7.97	6.38	1.89	9.30	9.43	7.20	7.59	8.67	7.28
Na_2O	2.47	2.91	2.90	2.99	3.25	3.69	3.52	4.00	3.96	5.73	2.77	2.80	2.72	2.91	3.05	2.91
K_2O	2.00	1.76	1.75	1.99	2.46	2.44	2.53	2.35	3.18	5.04	1.30	1.41	1.95	2.24	1.71	2.14
P_2O_5	1.01	1.33	1.17	2.64	1.39	1.10	2.50	1.05	1.50	0.35	0.52	0.50	0.34	1.11	0.76	1.05
H_2O-	1.96	2.17	3.06	2.72	2.47	1.02	1.40	0.95	1.12	1.09	2.64	2.55	3.09	5.97	4.17	4.09
LOI	9.39	5.71	8.18	4.78	5.11	2.06	4.70	2.66	2.68	2.53	3.45	2.84	6.80	3.14	2.93	2.70
Total	99.94	99.98	99.79	99.99	99.94	100.01	99.62	100.02	99.99	99.99	100.01	100.00	100.20	99.99	99.96	100.01
Rb	38	45	50	46	36	100	73	42	65	102	22	29	35	31	35	42
Sr	277	468	454	461	514	1036	844	691	894	173	326	416	517	325	531	652
Nb	32	39	31	36	36	62	74	58	71	89	23	24	26	33	32	42
Y	42	59	49	42	47	40	50	35	69	43	25	27	32	58	37	41
Zr	308	263	356	379	369	590	614	494	679	763	238	246	268	282	296	354
Ni	47	82	82	83	34	56	65	15	15	38	28	30	44	57	48	30
Co	36	74	74	43	39	23	32	41	31	<10	35	32	48	30	37	39
Cr	74	81	81	103	49	29	57	26	37	32	55	46	52	60	73	66
V	180	149	149	254	277	149	124	255	159	45	231	157	200	250	243	328
Rock Type	AB	AB	AB	AB	AB	HW	HW	HW	HW	TrB	TrB	TrB	TrB	TrB	TrB	TrB

AB = Alkalic basalt; HW = Hawaiite; TR = Trachyte; ThB = Tholeiitic basalt; TrB = Transitional basalt

Table 4. continued

	Karin Ridge (northern area)		Hawaii									
	D8-1	D82	HA-2	HA-3	HA-4	HA-5	HA-8	HA-9	HA-10	HA-11	HA-12	HA-13
SiO_2	45.86	47.62	49.25	49.00	49.24	50.06	45.33	47.00	46.88	51.16	50.00	60.74
TiO_2	3.36	3.21	1.98	1.69	2.15	1.80	1.35	1.67	3.30	2.27	2.49	1.79
Al_2O_3	18.45	17.53	15.30	14.62	14.50	14.05	9.60	9.00	15.90	16.70	18.00	10.50
Fe_2O_3	10.61	9.02	9.22	6.16	3.00	1.80	3.80	2.30	5.00	5.20	3.05	7.20
FeO	2.03	2.42	2.45	5.90	8.40	8.70	7.40	8.43	9.20	6.10	7.61	1.46
MnO	0.10	0.13	0.20	0.19	0.20	0.18	0.19	0.20	0.20	0.29	0.26	0.18
MgO	2.28	1.78	7.30	7.50	8.30	8.70	22.40	22.20	4.80	3.80	4.20	7.40
CaO	6.60	6.85	10.40	10.95	10.24	10.66	6.20	6.20	7.27	6.85	6.00	6.00
Na_2O	2.89	3.10	2.36	2.23	2.17	2.16	1.60	1.60	3.45	3.80	4.50	1.35
K_2O	3.13	3.78	0.43	0.43	0.42	0.41	0.21	0.23	1.82	1.82	1.95	2.35
P_2O_5	1.38	1.84	0.38	0.31	0.27	0.27	0.16	0.20	0.90	0.88	0.82	1.01
H_2O-	3.36	4.24	0.14	0.09	0.17	0.07	0.38	0.20	0.36	0.07	0.10	0.09
LOI	2.31	2.60	0.40	0.65	0.92	0.95	1.40	0.98	0.96	0.70	0.84	0.20
Total	100.00	99.98	99.81	99.72	99.98	99.81	100.02	100.21	100.04	99.64	99.82	100.27
Rb	69	71	11	26	11	12	4	3	51	50	49	31
Sr	1140	883	382	739	415	404	207	213	609	1310	1311	251
Nb	76	71	15	24	17	17	8	8	75	49	50	12
Y	68	69	23	46	24	25	13	12	75	48	47	18
Zr	443	421	193	180	201	205	114	114	400	511	528	147
W	–	–	7	43	13	17	11	14	115	16	20	12
Ni	42	37	48	43	77	95	971	995	6	<10	<10	164
Co	28	22	42	250	45	58	83	81	31	27	15	47
Cr	47	49	147	104	180	226	422	4000	37	31	33	160
V	184	237	228	223	297	282	159	126	195	68	66	235
Rock Type	HW	HW	ThB	ThB	ThB	ThB	ThB	ThB	HW	HW	HW	HW

AB = Alkalic basalt; HW = Hawaiite; TR = Trachyte; ThB = Tholeiitic basalt; TrB = Transitional basalt

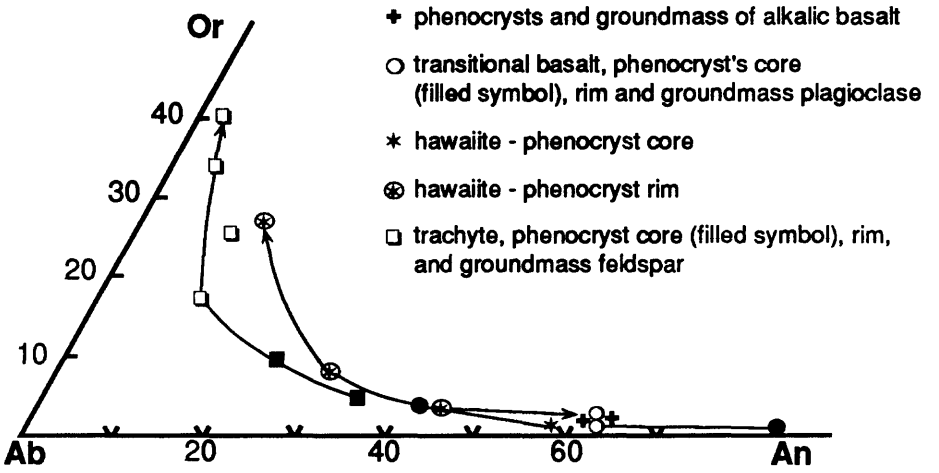

Figure 1. Compositions of feldspars from Karin Ridge lavas. Solid lines show trends of feldspar composition during volcanic rock crystallization.

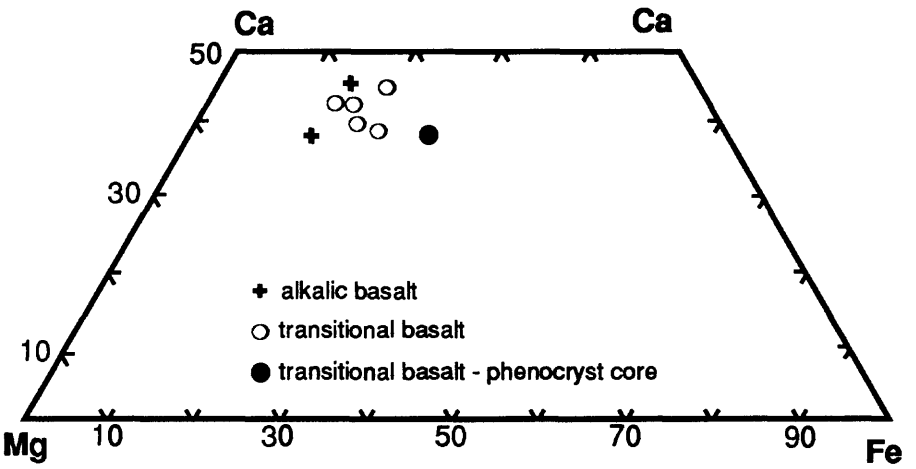

Figure 2. Compositions of clinopyroxene from Karin Ridge lavas.

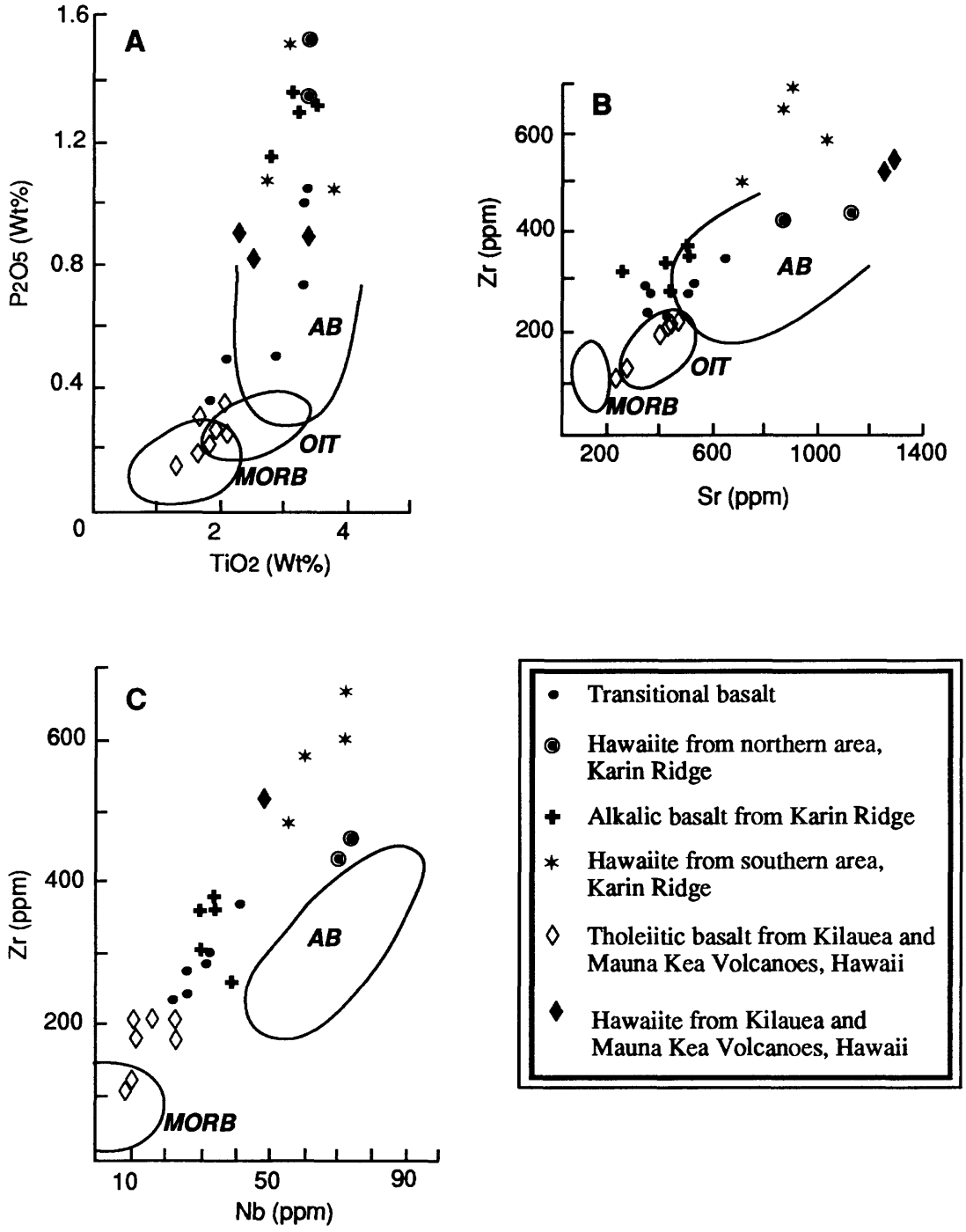

Figure 3A-C. P_2O_5-TiO_2, Zr-Sr, and Zr-Nb plots for magmatic rocks from Karin Ridge. Symbols are the same for figures 3-6. Fields are for alkalic basalt (AB), ocean ridge tholeiite (OIT), and MORB (Bass *et al.*, 1973).

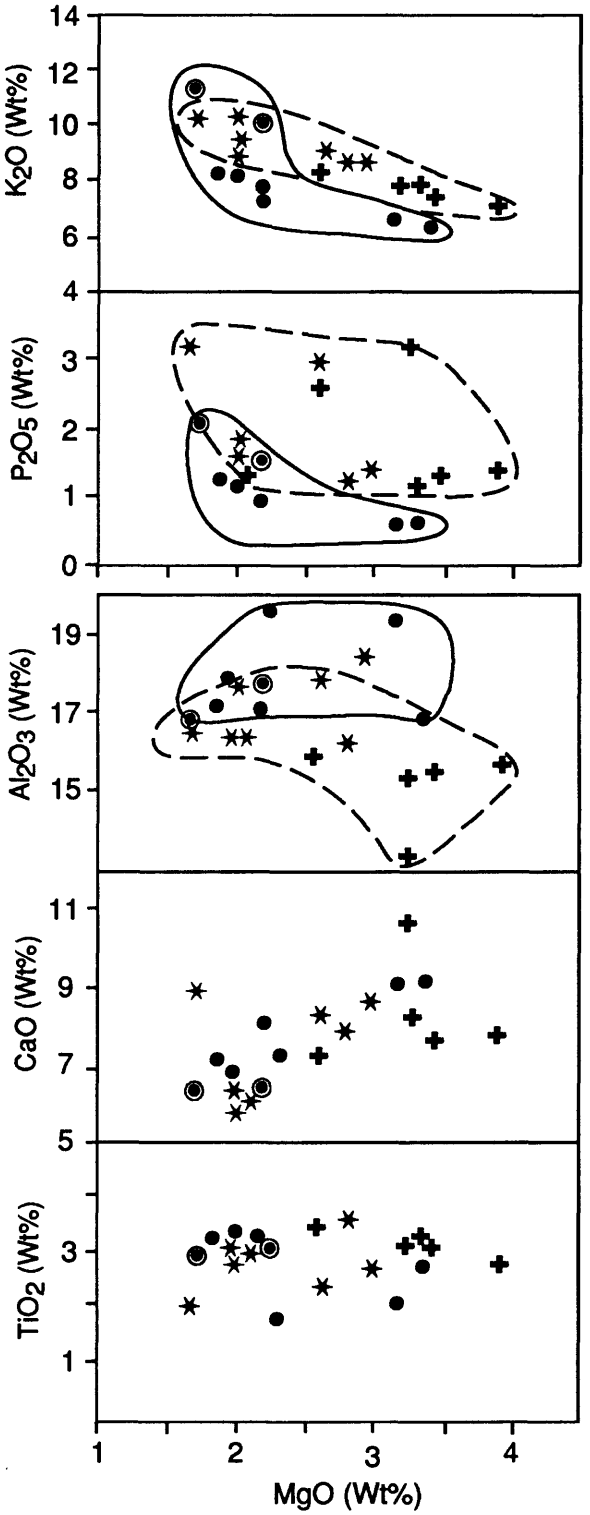

Figure 4. MgO variation diagrams for major oxides. Fields represent volcanic rocks from the northern (solid) and southern (dashed) study areas. Symbols as in Fig. 3.

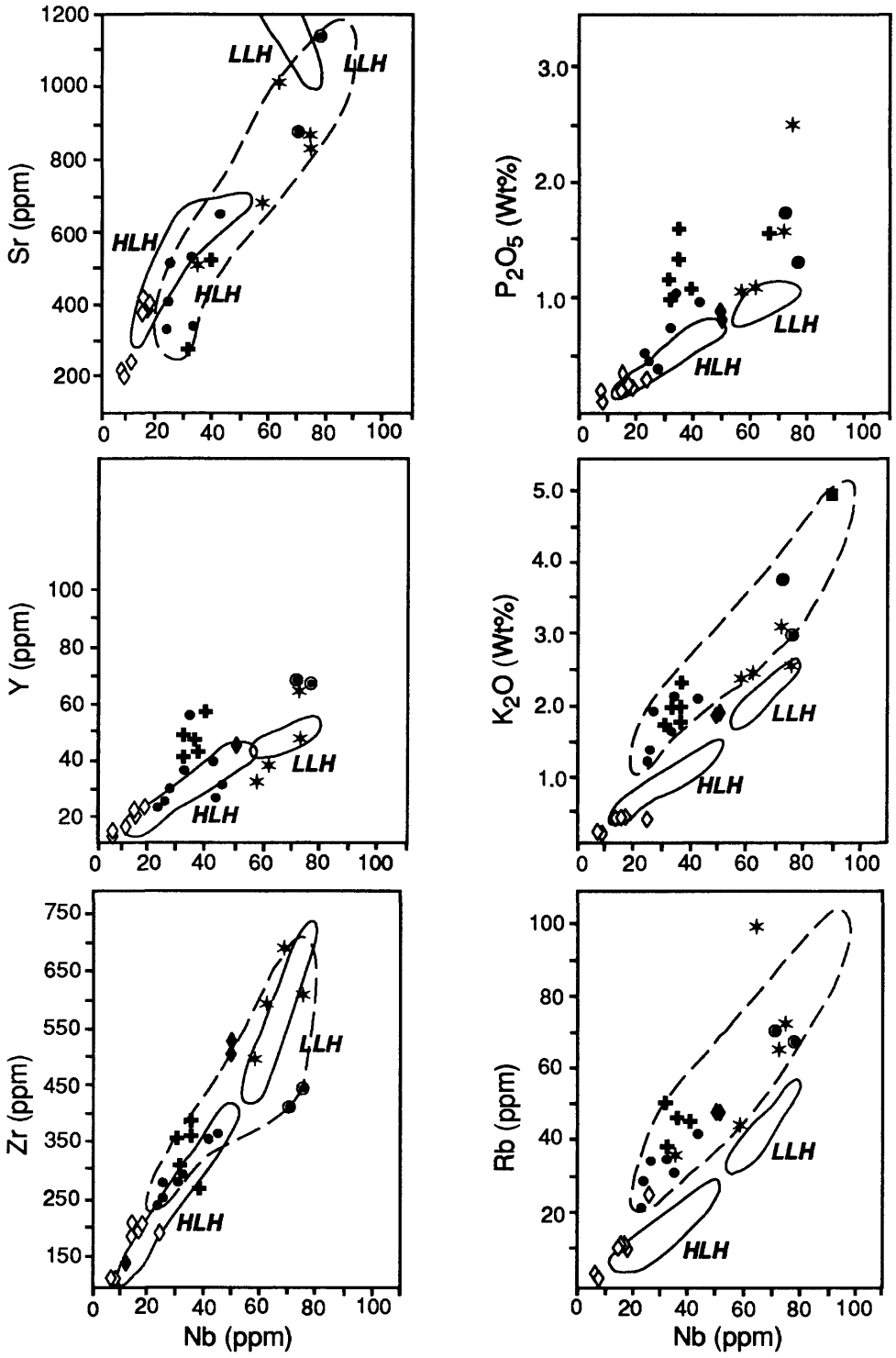

Figure 5 a-f. Abundances of the incompatible elements Rb, Y, Zr, P_2O_5, and Sr versus Nb for Karin Ridge lavas. HLH and LLH are Hamakua and Laupahoehoe lavas from Mauna Kea Volcano, Hawaii (Frey *et al.*, 1990). Symbols as in Fig. 3.

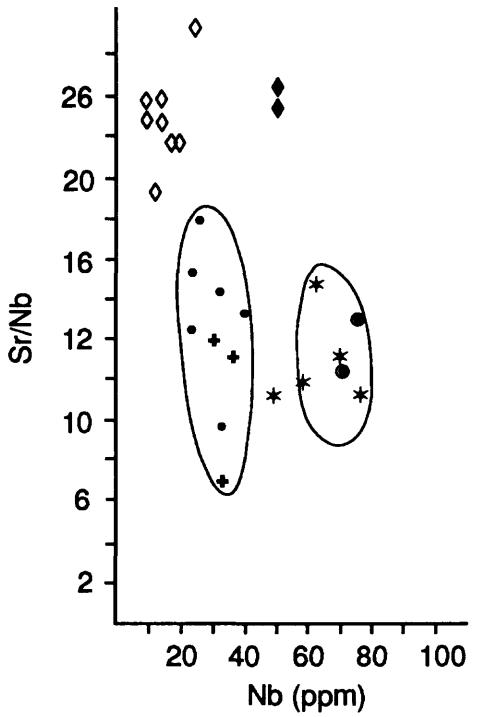

Figure 6. Sr/Nb versus Nb diagram for Karin Ridge lavas. Symbols as in Fig. 3.

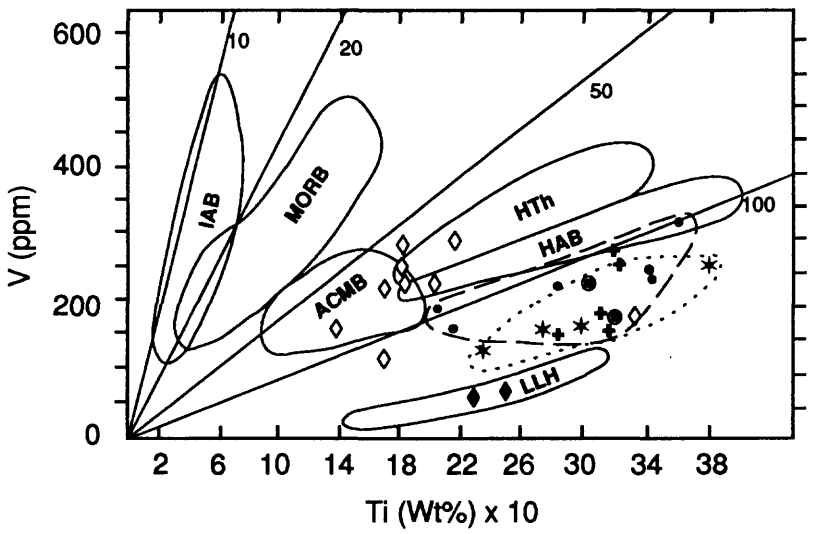

Figure 7. Ti versus V diagram for magmatic rocks from Karin Ridge (modified from Shervais, 1982). Fields of island arc basalts (IAB) and MORB (Shervais, 1982), tholeiites (HTH), alkalic basalts (HAB), and Laupahoehoe Hawaiites (LLH), from Kilauea and Manua Kea volcanoes, Hawaii (Frey *et al.*, 1990, Tilling *et al.*, 1987); and active continetal margin basalts (ACMB) (Martynov, 1990) are shown. Broken line shows the field of plagioclase-phyric basalts and hawaiites from northern area of Karin Ridge; dotted line shows the field for alkalic basalts and hawaiites from southern area of Karin Ridge. Symbols as in Fig. 3.

ACKNOWLEDGEMENTS

Ann Gibbs improved the English and redrafted figures. Alicé Davis reviewed the manuscript.

REFERENCES

Bass, M.N., Moberly, R.M., Rhodes, J.M., Shin, C., and Church, S.E., 1973, Volcanic rocks cored in the central Pacific, Leg 17, Deep-Sea Drilling Project: *in* Winterer, E.L., Ewing, J.I., *et al.* Initial Reports of the Deep-Sea Drill. Project Vol. 17, Washington, (U.S. Government Printing Office), p. 429-503..

Duncan, R.A. and Clague, D.A., 1985, Pacific plate motions recorded by linear volcanic chains: *in* Naim, A.E.M., *et al.*, (eds.) Ocean Basins and Margins. v. 7A, Plenum Press, N.Y., p. 89-121.

Epp, D., 1984, Possible perturbations to hotspot traces and implications for the origin and structure of the Line Islands: Journal of Geophysical Research, v. 89, p. 11,273-11,286.

Frey, F.A., Wise, W.S., Garcia, M.O., West, M.H, Kwon, S.T., and Kennedy, A., 1990, Evolution of Mauna Kea Volcano, Hawaii: Petrologic and Geochemical constraints and postshield volcanism: Journal of Geophysical Research, v. 95, p. 12711300.

Haggerty, J.A., Schlanger, S.O., and Premoli-Silva, I., 1982, Late Cretaceous and Eocene volcanism in the Southern Line Islands and implications for hot spot theory. Geology, v. 10, p. 427-433.

Hein, J.R., Kirschenbaum, M., Schwab, W.E., *et al.*, 1990, Mineralogy and geochemistry of Co-rich ferromanganese crust and substrate rocks from Karin Ridge and Johnston Island, RV *Farnella* cruise F7-86-HW: U.S. Geological Survey Open File Report 90-298, 80 p.

Martynov, Y.A., 1990, Petrology of calc-alkaline basalts of the East Sikhote Aline (Petrologicheskii osobenosti izvestkovo-shchelochnykh basaltov Vostochnogo Sikhote-Alinya): Pacific Geology, v. 5, p. 88-95 (In Russian).

Pearce, J.A., 1983, Role of sub-continental lithosphere in magma genesis at active continental margins: *in* Hawkesworth, C.J. and Nurry, M.J. (eds.), Continental basalts and Mantle xenoliths. Shiva publishing, Nantwich, p. 230-249.

Rona, P.A., 1988, Hydrothermal mineralization at oceanic ridges: Canadian Mineralogist, v. 26, p. 431-465.

Sager, W.W. and Keating, B.N., 1984, Paleomagnetism of Line Islands seamounts: Evidence for Late Cretaceous and early Tertiary volcanism: Journal of Geophysical Research, v. 89, p. 11,135-11,151.

Seyfried, W.E. and Bischoff, J.L., 1979, Low temperature basalt alteration by seawater: An experemental study at 70°C and 150°C: Geochimica et Cosmochimica Acta, v. 43, p. 1937-1947.

Schlanger, S.O., Garcia, M.O., Keating ,B.H., Nanghton, J.J., Sager, W.W., Haggerty, J.A., Philpotts, J.A., and Duncan R.A., 1984, Geology and geochronology of the Line Islands: Journal of Geophysical Research, v. 89, p. 11,261-11,272.

Schlanger, S.O., Jackson, E.D., Kaneps, A.G., and Serocki, S.T., 1976, Introduction and explanatory notes: *in* Schlanger, S.O., Jackson, E.D., *et al.*, Initial Reports of the Deep-Sea Drilling Project, Vol. 33, Washington (U.S. Government Printing Office), p. 5-24.

Shervais, J.W., 1982, Ti-V plots and the petrogenesis of modern and ophiolitic lavas: Earth and Planetary Science Letters, v. 59, p. 101-118.

Tilling, R.I., Wright, T.H., and Millard, H.T, 1987, Trace-element chemistry of Kilauea and Mauna Loa lava in space and time: A reconnaissnce: *in* Decker, R.W., Wright, T.L. and Stauffer, P.H. (eds.), Volcanism in Hawaii, Vol. 1., U.S. Geological Survey Professional Paper 1350, p. 641-691.

Winterer, E.L., 1973, Regional problems: *in* Winterer, E.L., Ewing, J.I., *et al.* Initial Reports of the Deep-Sea Drill. Project Vol. 17, Washington, (U.S. Government Printing Office), p. 911-923.

CURRENT PATTERNS OVER KARIN RIDGE, A SEAMOUNT IN THE CENTRAL PACIFIC

Marlene Noble and Kaye Kinoshita
U.S. Geological Survey, Menlo Park, California 94025

ABSTRACT

Two current-meter moorings were deployed 70 km apart on the cap of Karin Ridge, a deep, narrow seamount in the central Pacific over a 7 month period. The observations show that strong diurnal and semidiurnal internal tides were found over the cap of Karin Ridge. Semi-major axis current amplitudes ranged from 1 to 7 cm/s for diurnal tides, 1 to 10 cm/s for semidiurnal tides. Isotherm deflection amplitudes were 1 to 20 m. The phase speed was downward, toward the cap of the seamount for both currents and isotherm deflections. The phases and amplitudes of the internal tides were constant over the measurement period.

The internal tides were generated at the seamount cap. But the characteristics of the internal tide were not simply related to a uniform, spatially-invariant barotropic forcing. Even though the moorings were deployed at sites that have similar gross topographic characteristics, the internal tides had different amplitudes and phases at the two sites. The amplitudes ratios for tidal constituent within a tidal species were significantly different from the barotropic ratios. For the semidiurnal band, the amplitude ratios were half the predicted values for the northern site, and twice the value at the southern site.

INTRODUCTION

Previous studies of currents over Horizon Guyot, a long, narrow, deeply-submerged seamount located in the central Pacific, suggest that strong internal tides are present over the guyot (Cacchione et al., 1988; Noble et al., 1988; Genin et al., 1989). It is likely that these tides were generated over the crest of the guyot. However, detailed characteristics of the internal tides, their likely presence over seamounts with similar shapes, and the nature of the generation process could not be determined in these initial studies because current records were either too short or confined to one spatial location. In addition, historical data about how tides are generated over deeply submerged seamounts is relatively non existent. Therefore, a small program to study internal tides over large submerged ridges was undertaken.

In September, 1990, two current meter moorings were deployed on the cap of Karin Ridge, a seamount in the central Pacific Ocean near Horizon Guyot. Karin Ridge is a long, narrow seamount with a shape and height similar to Horizon Guyot (Figure 1). It is oriented approximately perpendicular to Horizon Guyot, so it is possible to determine whether orientation of a topographic feature had any effect on the generation or presence of internal tides.

Current meter moorings were deployed at 2 locations on Karin Ridge in order to examine the spatial structure of the tides over the ridge and determine how that structure changed with time, depth and horizontal location. The array was deployed for 7 months. The top current meter on each mooring was located the same distance above the seafloor as was used on Horizon Guyot to allow comparisons with this previous data set.

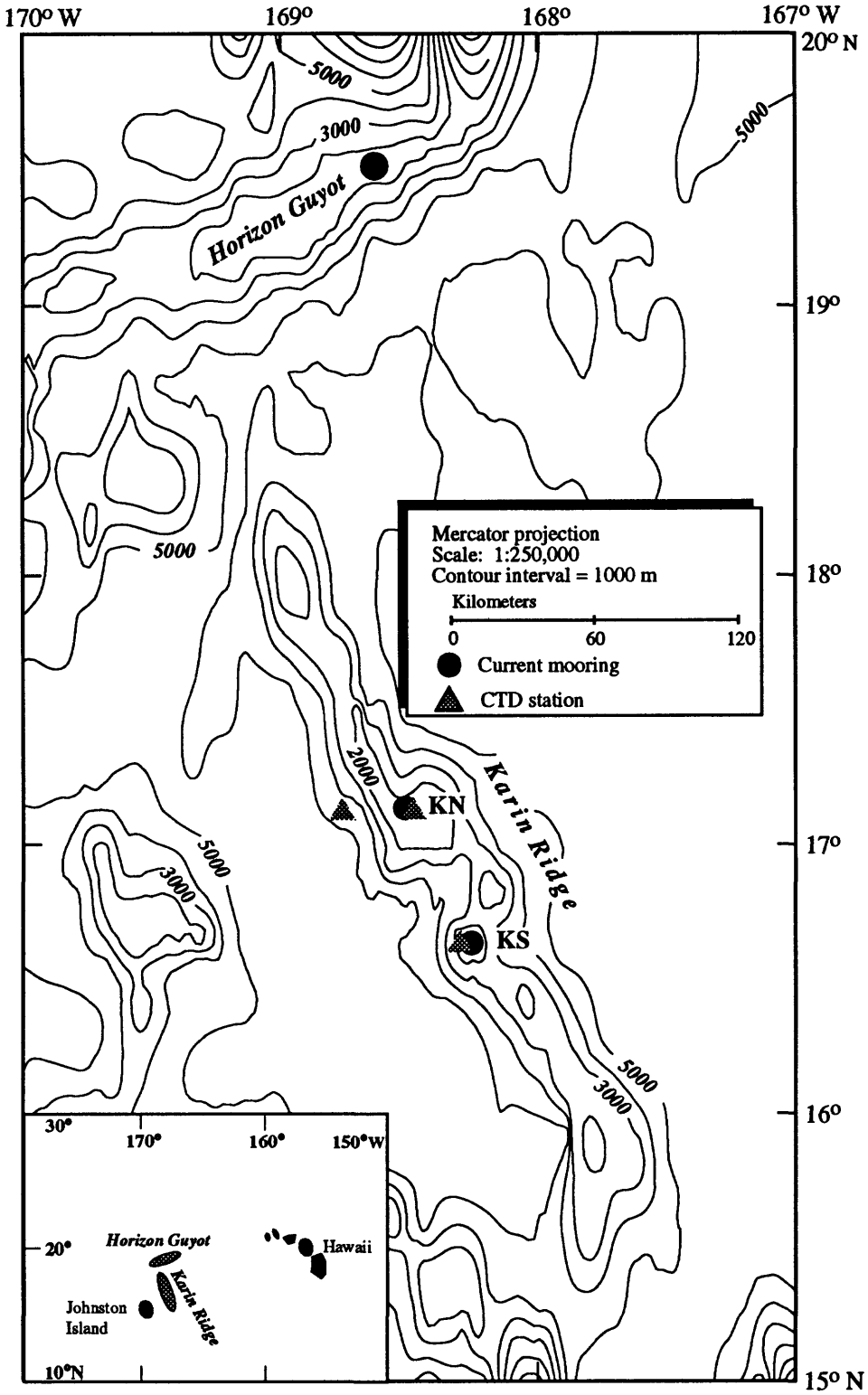

Figure 1. Location map of moorings on Karin Ridge and Horizon Guyot

Data set

Moorings were deployed at 2 sites, designated KN and KS for the northern and southern site, on the top of Karin Ridge (Figure 1). The moorings were placed along the ridge, 70 km apart, at approximately the same depth. Current meters on each mooring were located at 10, 50 and 200 m above the seafloor, in water depths of 1560 and 1615 m for the northern and southern site respectively. Individual records from these instruments are named by the site and water depth. Hence, KN50 is the instrument 50 m above the bed at the northern site. CTD casts were made over and adjacent to the crest of Karin Ridge when the moorings were deployed (Figure 1).

The current records were hour-averaged, then rotated into a coordinate system parallel and perpendicular to the axis of Karin Ridge. The positive along-axis direction is 150°; the positive cross-axis direction is 60°. These records were used to examine the tidal characteristics. The current records were then low-pass filtered to remove oscillations with periods shorter than 66 hours. Hence, tidal currents and inertial oscillations, which have a period of 41 hours, are removed from the filtered records. Since a majority of the variability at shorter periods is in the tidal bands, these lowpass-filtered currents are referred to as subtidal currents.

Temperature records at each site were converted to records of isotherm deflection. The isotherm deflection is defined to be:

$$I = \left(t - \bar{t}\right) \Big/ \frac{\partial t}{\partial z}$$

where I is isotherm deflection, t is temperature, $\bar{t}$ is mean temperature for each record and $\frac{\partial t}{\partial z}$ is temperature gradient.

The temperature gradient was calculated using two different methods. One temperature gradient was determined from the temperature gradient between 1300 and 1700 m measured by a CTD at a site off the seamount at the time the moorings were deployed. A second temperature gradient was calculated from the mean temperature at each instrument site and the instrument depths. Both methods showed that the temperature decreased with depth in a highly linear manner (Figure 2). The correlation coefficients between temperature and depth were greater than 0.996.

The measured gradients had slightly different amplitudes, so the gradient used to convert temperature to isotherm deflection was the average of the two measurements, -0.002372 degrees/meter (dpm). Both temperature profiles fit within a range of 7% around this value. The similarity in slopes between the measured temperature gradient and the mean temperature profile indicated that the temperature gradient was constant over the 9 month record.

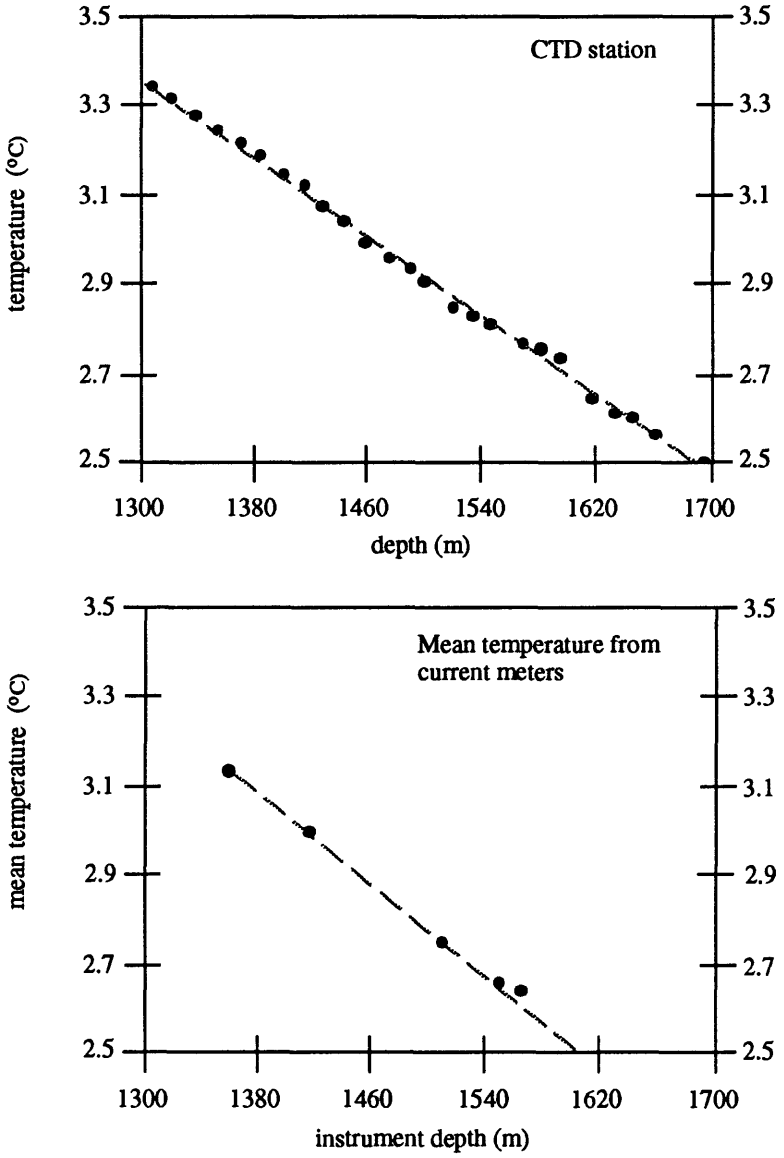

Figure 2. Temperature profiles

Observed characteristics of the data set

The current and isotherm deflection fields over Karin Ridge were dominated by higher-frequency fluctuations due to tidal and inertial processes (Figures 3 and 4). The tidal bands accounted for 35 to 55% of the current variance. Subtidal current fluctuations accounted for less that 10%. The percentage variance due to near-inertial band currents was significant, but generally weaker than tidal currents at the 6 measurement sites. But near-inertial motions were a larger portion of the isotherm deflection field. The dominant isotherm deflection frequency alternated between tidal and near-inertial processes, depending on the mooring site (Kinoshita and Noble, 1993). The inertial-period oscillations were most energetic at KN50 and KN10, weakest at KN200 and KS200.

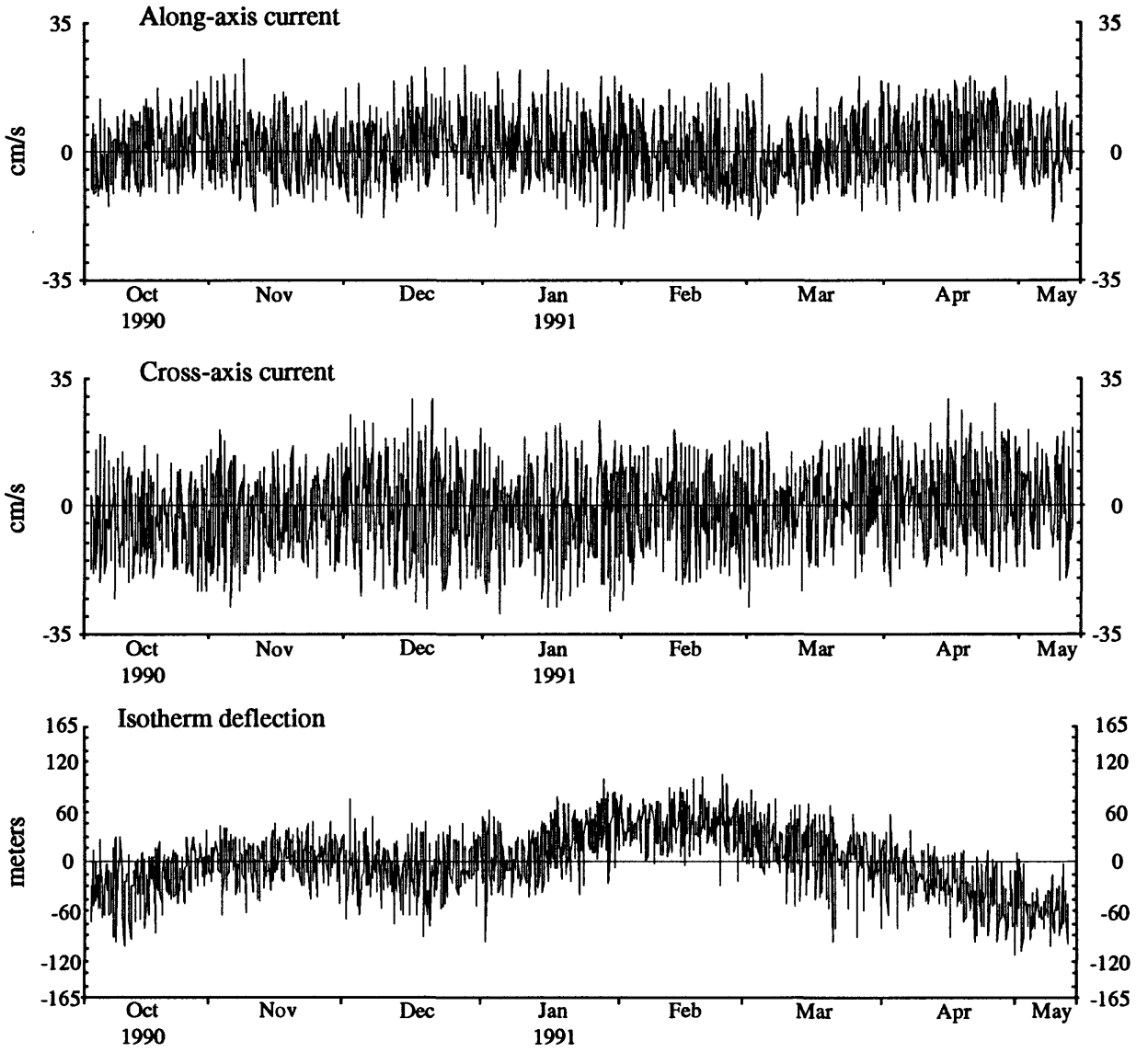

Figure 3. Hour-averaged along-axis and cross-axis current and isotherm deflection at southern mooring, 50 meters above the bottom (KS50).

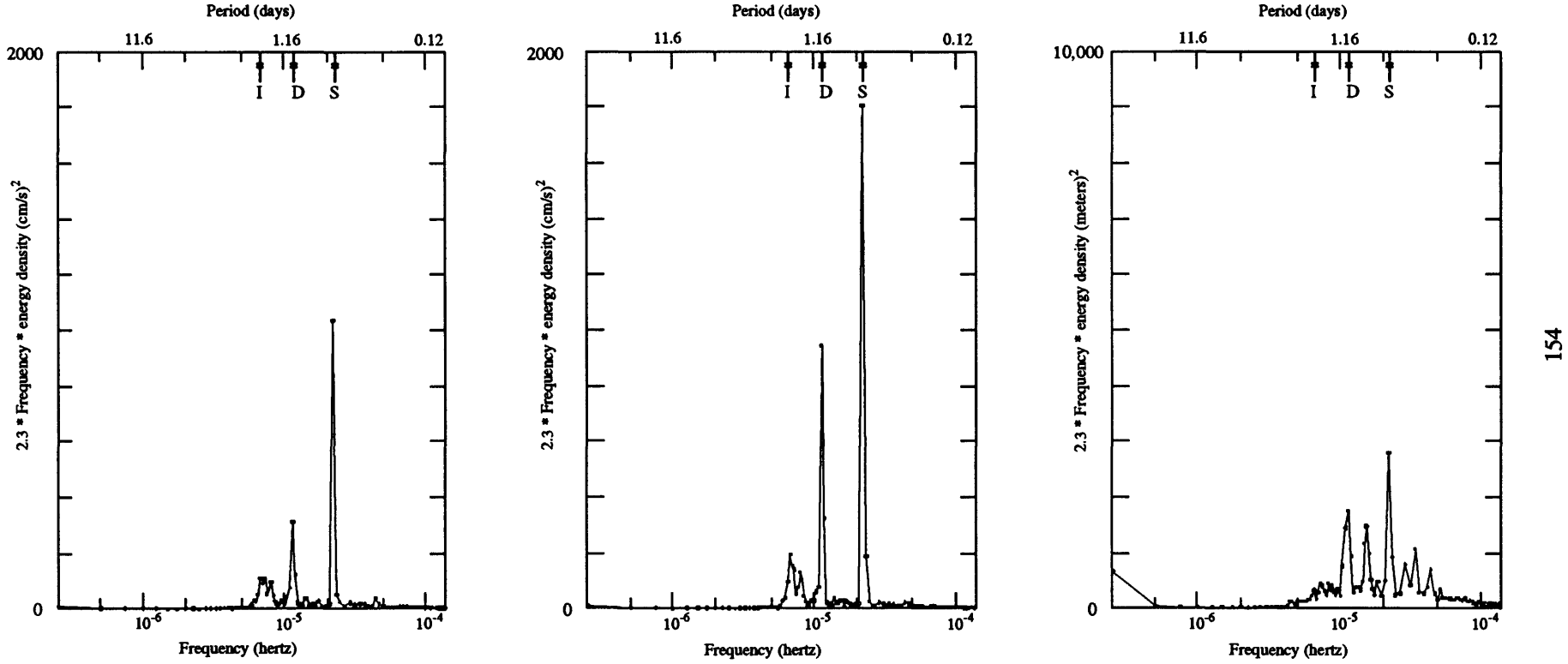

Figure 4. Variance-conserving auto spectra for currents and isotherm deflection at KS50. (I = inertial, D = diurnal, S = semidiurnal).

Subtidal currents

The mean currents over Karin Ridge were similar to each other at each mooring site, but the orientation changed markedly between sites. The mean currents at KN flowed uniformly across the ridge axis toward the east and northeast (Figure 5). The mean currents were weaker and oppositely directed at KS. The strongest mean flows were found near the cap of the seamount. These mean current observations generally represent only the characteristics of the flow for the time period when the moorings were deployed. Statistically, the mean current were not significantly different from zero at the 95% confidence level except at one site, KN10 .

The subtidal currents reflect the mean current pattern. Within 50 m of the cap of the seamount, at KN50 and KN10, the flow was directed across the ridge axis toward the northeast (Figure 6a). The flow was more variable 200 m above the cap, but still shared some similar structure. The largest currents were found during the beginning and end of the measurement period, the weakest in the middle. A correlation analysis suggests that 15-45% of the variability in the cross-axis subtidal currents was coupled over the mooring, with no significant phase lag (Table 1). As expected, the largest percentages of coupled variability were measured between adjacent instrument locations.

A more correlated subtidal flow field was found at KS. Subtidal currents were generally southwestward at all measurement sites in the first two thirds of the measurement period, then changed to an opposite direction at the end of the record (Figure 6b). Between 45 and 60% of the variance in the subtidal KS cross-axis currents were coupled, with no significant lag (Table 1).

The spatial scales for the subtidal currents were smaller than 60 km. The subtidal currents at a particular level above the cap were not correlated between KS and KN.

Station Pairs	Along-axis	Cross-axis
KN200 - KN50	0.54	0.50
KN 50 - KN10	--	--
KN 50 - KN10	--	0.66
KS200 - KS50	0.68	0.74
KS200 - KS10	0.57	0.67
KS 50 - KS10	0.82	0.78

Table 1. Correlations among subtidal currents. Reported correlations are significant at the 90% confidence level. The 95% confidence levelis 0.57.

Diurnal tides

The O_1 tidal currents over Karin Ridge rotated in a clockwise sense (Table 2). The amplitude of the semi-major axis of the current ellipse was about 2 cm/s at most measurement sites. Only the currents at KS200 were significantly smaller, with an amplitude of 1 cm/s. The current ellipse was oriented about 30° counterclockwise of the cross-ridge direction at KN, 30° clockwise of it at KS.

The currents at the top of the mooring led those at the bottom at both seamount sites. The phase propagated toward the top with a uniform speed of 0.27 dpm. However, the phases did not have the same values at the two sites because currents at KS led KN by 75°.

The O_1 isotherm deflection amplitudes were generally between 3 and 7 meters (Table 2). The largest deflections were observed at KS. Isotherm phases propagated downward, but phase speeds were faster than current phase speeds. The isotherm phase speed was 0.7 dpm. The phase offset between sites was 150°; the south led the north. Both the isotherm phase speed and the phase offset between sites were twice the equivalent parameters for currents.

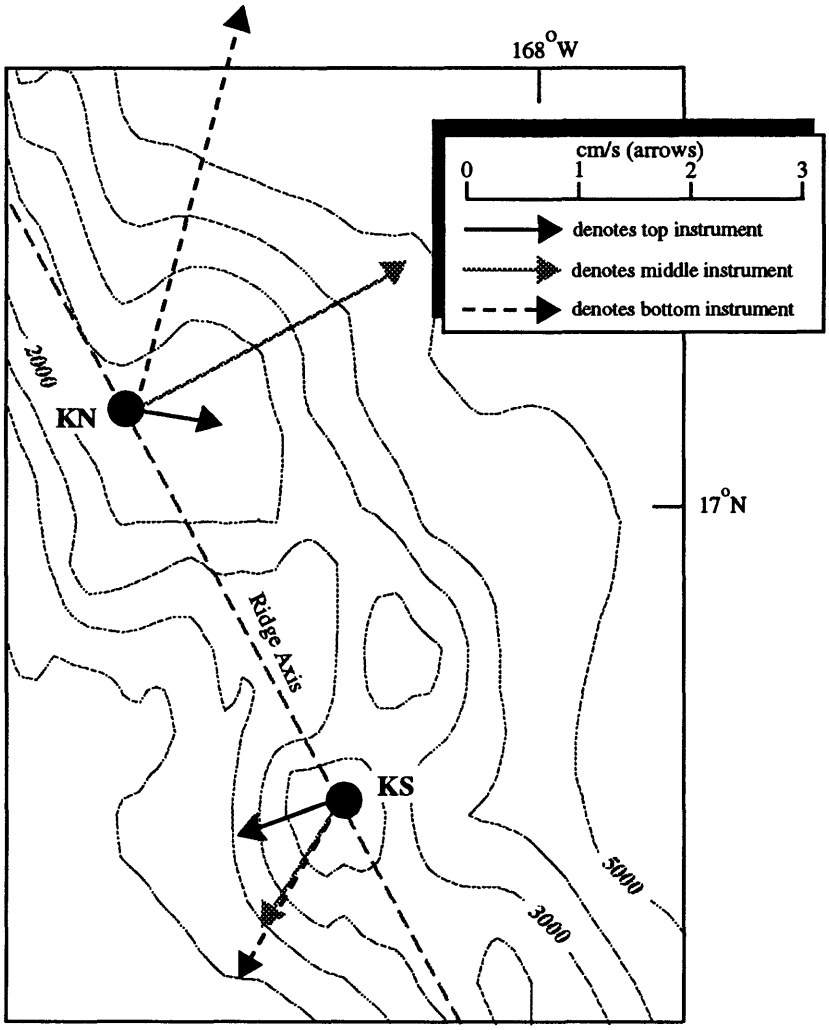

Figure 5. Mean currents on Karin Ridge

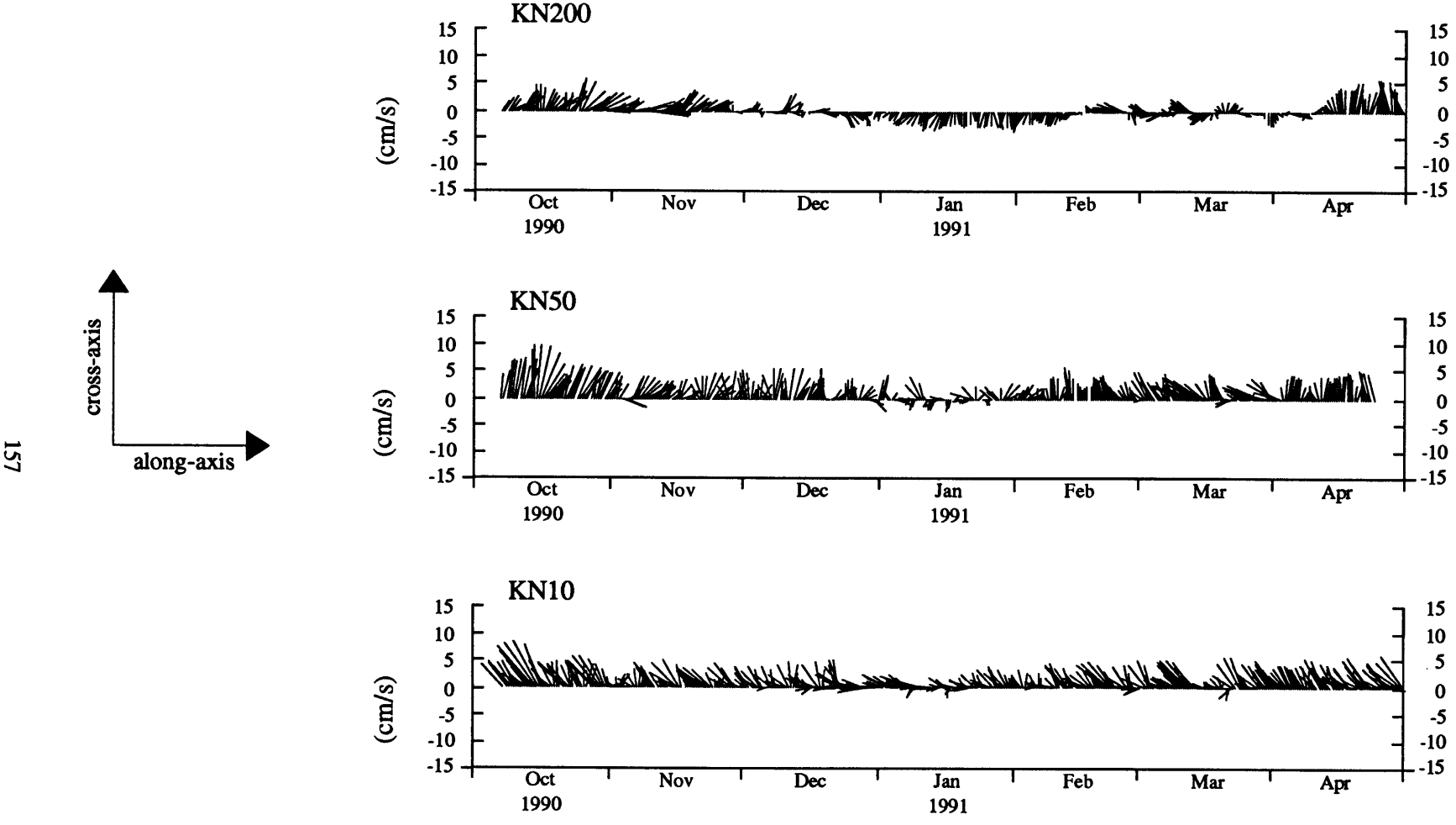

Figure 6a. Subtidal current vectors at the northern mooring (KN).

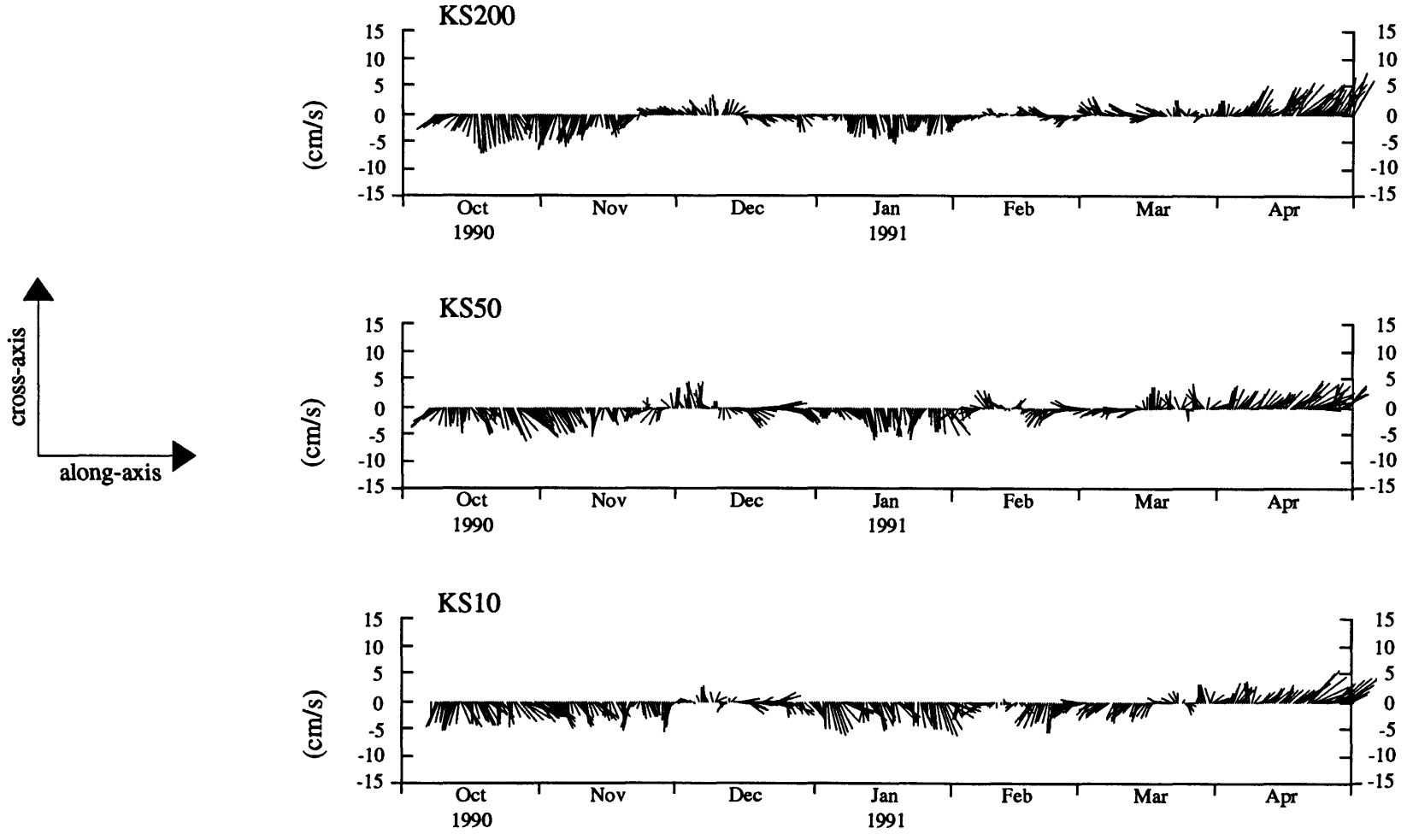

Figure 6b. Subtidal current vectors at the southern mooring (KS).

Station	Semi-major axis current (cm/s)	Semi-minor axis current (cm/s)	Inclination (degrees)	Current phase (degrees)	Isotherm deflection amplitude (meters)	Isotherm deflection phase (degrees)
			O_1			
KN200	2.0	0.5	22	149	3	251
KN 50	2.1	0.8	38	196	2	7
KN 10	1.8	1.0	26	199	3	37
KS 200	1.0	0.6	135	75	4	111
KS 50	2.2	1.0	96	112	7	215
KS 10	1.9	0.4	89	129	7	235
			K_1			
KN200	4.0	2.1	40	148	5	255
KN 50	3.8	1.6	39	182	5	357
KN 10	3.4	1.6	29	186	4	31
KS 200	2.2	0.7	96	109	6	223
KS 50	6.6	2.7	81	146	7	296
KS 10	6.0	2.5	86	169	7	342
			M_2			
KN200	5.4	5.1	152*	174*	20	22
KN 50	4.1	3.1	168	193	7	72
KN 10	4.1	3.2	171	200	3	91
KS 200	9.3	5.2	60	270	17	97
KS 50	9.5	6.7	79	333	5	234
KS 10	5.9	5.1	77	338	4	293
			S_2			
KN200	4.2	2.4	12	254	10	114
KN 50	3.3	1.5	13	267	3	135
KN 10	3.1	1.3	11	263	2	145
KS 200	2.6	0.8	62	282	8	125
KS 50	2.1	0.6	67	328	1	27
KS 10	1.3	0.5	56	323	1	48

Table 2. Tidal parameters. The inclination angle is clockwise from north. The station with the smaller phase leads. All tidal currents rotate in a clockwise direction. (*orientation and phase of the minor axis)

The K_1 tides were larger than, but had characteristics similar to, the O_1 tides. The K_1 tides rotated in a clockwise sense; the semi-major current axis amplitudes ranged between 2 and 7 cm/s (Table 2). The smallest current was measured at KS200. This is the same site with the smallest O_1 tidal current. However, despite the small currents at this one location, the total kinetic energy in the currents at the KS was twice that found at KN. The K_1 and O_1 tides have similar ellipse orientations, roughly 30° counterclockwise of the cross-ridge axis at the KN, 30° clockwise at KS. The ellipse phase speed was downward at 0.25 dpm. The phase offset between sites was 32°. The southern site led the northern.

Isotherm deflections at the K_1 frequency had amplitudes between 4 and 7 m. The largest deflections were at KS. The isotherm phases propagated downward with a phase speed of 0.65 dpm and had a 45° offset between sites.

The phase difference between the major axis of the diurnal current ellipses and the isotherm deflections were highly dependent on measurement location (Table 3). In the K_1 band , the phase difference was near 90° at KN200, near 180° at KN50. The O_1 phase difference was near 180° at KN50 and KN10, near 90° at equivalent locations in the south.

These diverse phase differences are representative of the entire measurement period because the diurnal characteristics did not change markedly over time. Complex demodulation analyses show that amplitudes and phases were constant over the 7 month measurement period (Figure 7a). The phases for the K_1 tidal currents varied less than 90°. There was a bit more temporal variations observed in the isotherm phases, but these variations are not large enough to significantly alter the phase difference calculations given above.

Because the phases of diurnal currents were stable over time, the coherence amplitudes calculated among sites either along a mooring or between sites on different moorings were high. The coherence amplitudes for any current pair at a single site are nearly always above 0.85 and are often larger than 0.90. Between sites, the coherence amplitude for currents measured the same distance off the cap are generally above 0.75 and are above 0.90 for half the station pairs.

Station	Tidal Constituent			
	O_1	K_1	M_2	S_2
KN200	102°	107°	-152°	-141°
KN 50	171°	175°	-121°	-132°
KN 10	-162°	-155°	-109°	-118°
KS200	36°	114°	-173°	-157°
KS 50	103°	150°	-99°	-53°
KS 10	1 06°	173°	-46°	85°

Table 3. Difference between the phase of major-axis currents and isotherm deflections. A positive phase means the current leads.

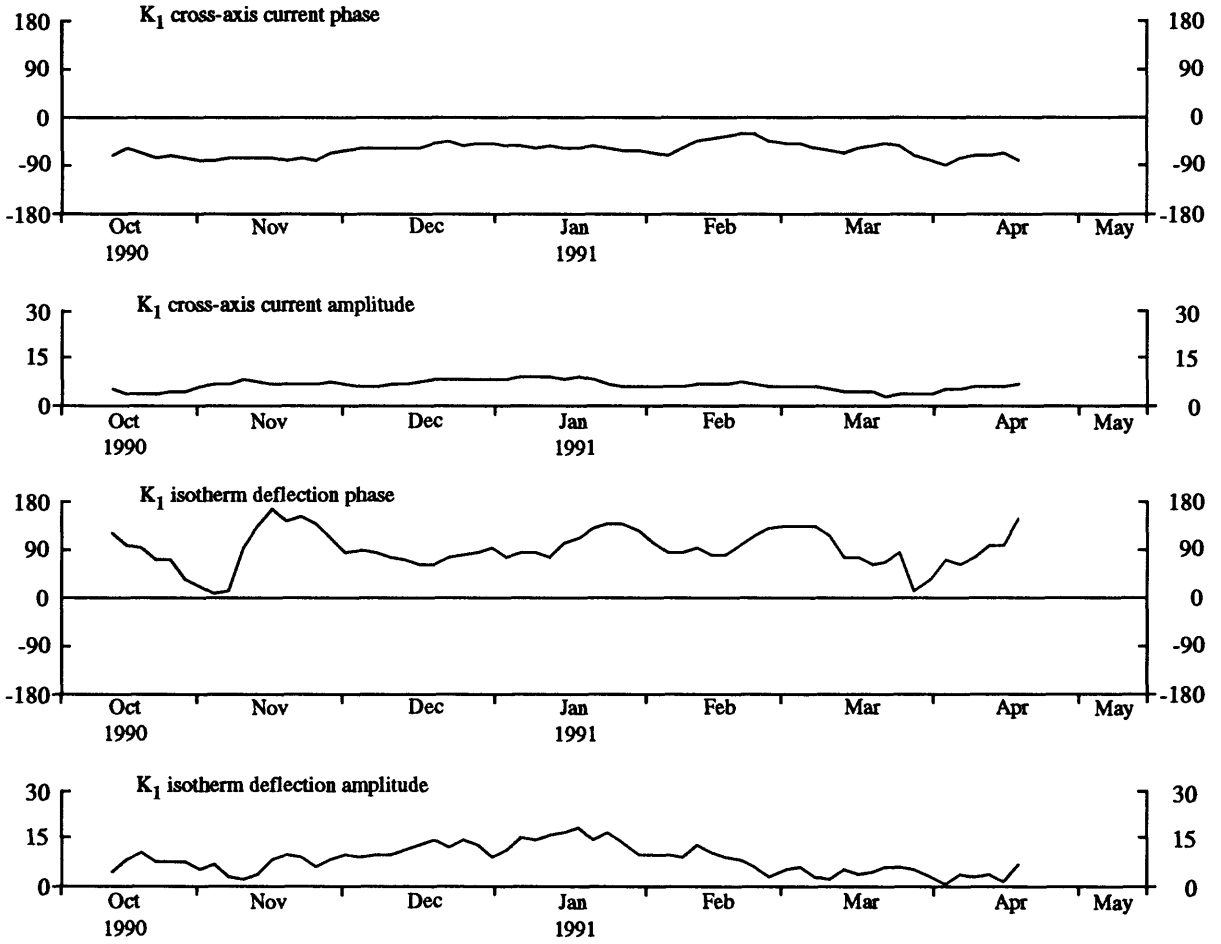

Figure 7a. Phase of the K_1 cross-axis current and isotherm deflection is a function of time at KS50.

Diurnal isotherm phases had more temporal structure than currents. Hence, the coherence amplitude are lower for isotherm pairs than for current pairs. Along a particular mooring, coherence amplitudes range from 0.67 to 0.94. Only one pair, KN200/KN10 at the O_1 frequency was not significant at the 95% confidence level. Between mooring sites, K_1 isotherm deflections were significantly coherent at the 50 and 10 m levels. Diurnal isotherm deflections were not significantly coherent at the 200 m level or at the O_1 frequency

Semidiurnal tides

The M_2 semidiurnal tide was the largest constituent in the tidal bands. The amplitude of currents flowing parallel to the major axis of the current ellipses ranged between 4 and 10 cm/s (Table 2). The strongest currents were found at sites KS200 and KS50. The M_2 current ellipses were fairly round; the ratio of major-axis to minor axis currents was generally less than 1.5. This ratio is significantly smaller than the ratio of 3.4 that is predicted to occur at this

latitude. The phases of the current ellipses did propagate downward, toward the cap of the seamount, with phase speeds between 0.1 and 0.4 dpm. It is not clear whether the two phase speeds are significantly different because moderately round ellipses are subject to larger errors in phase determinations.

The M_2 isotherm deflection amplitudes ranged between 3 and 20 m, with the largest amplitudes observed at the sites furthest from the seamount cap. The isotherm amplitudes scaled linearly with height, with a slope of 0.08. The phase speed of the isotherm deflections was downward.

The M_2 tides at KN and KS were not in phase. There was a 120^o to 140^o phase offset in both currents and isotherm deflections (Table 2). The northern tidal components led the southern.

The measured characteristics of the S_2 semidiurnal tide were similar to M_2. Both components showed downward phase propagation for currents and isotherm deflections. The ellipse orientations at each site were reasonably well aligned with each other. The major difference is that the M_2 tides were stronger at KS, the S_2 tides were larger at KN.

There is no particular pattern in the phase difference between the major axis of the semidiurnal current ellipses and the isotherm deflections (Table 3). One possibility, that the difference phases are scattered because the round M_2 current ellipses introduced noise in the phase of the major-axis current, is not supported by the data set. The S_2 current ellipses are sufficiently narrow and there was still obvious pattern in the difference phases.

The phases of the M_2 currents were constant over the 7 month deployment period at both sites on the seamount (Figure 7b). The S_2 current phase were constant at KS, but were more variable at the energetic KN site. The semidiurnal isotherm deflection phases were stable for periods of several month.

Because the semidiurnal current phases were constant over time, the coherence among M_2 current components at a single mooring site was high, usually larger the 0.96. Coherences amplitudes among S_2 current were also high, above 0.93 for all but KS200/KS50 and KS200/KS10 currents that flow along the ridge axis. The more energetic S_2 cross-axis currents at these stations had correlation amplitude above 0.90.

At KN, the semidiurnal isotherm deflections were highly correlated. Coherence amplitude were larger than 0.85. Semidiurnal isotherm deflections were not coherent at KS, except for the adjacent KS50/KS10 records. Semidiurnal isotherm deflections were not coherent between sites KS and KN except at the 200 m level. At the 200 m level the M_2 coherence amplitude was 0.73, significant at the 95% confidence level.

DISCUSSION

Internal tides over Karin Ridge

Previous observations, summarized in Noble, et. al, 1988, show that the semidiurnal tidal currents in the central Pacific, away from large topographic features, have amplitudes of 2-3 cm/s. It is likely that the majority of these tidal currents are driven by the barotropic tide. Isotherm deflections associated with a barotropic current of this magnitude are small, less than

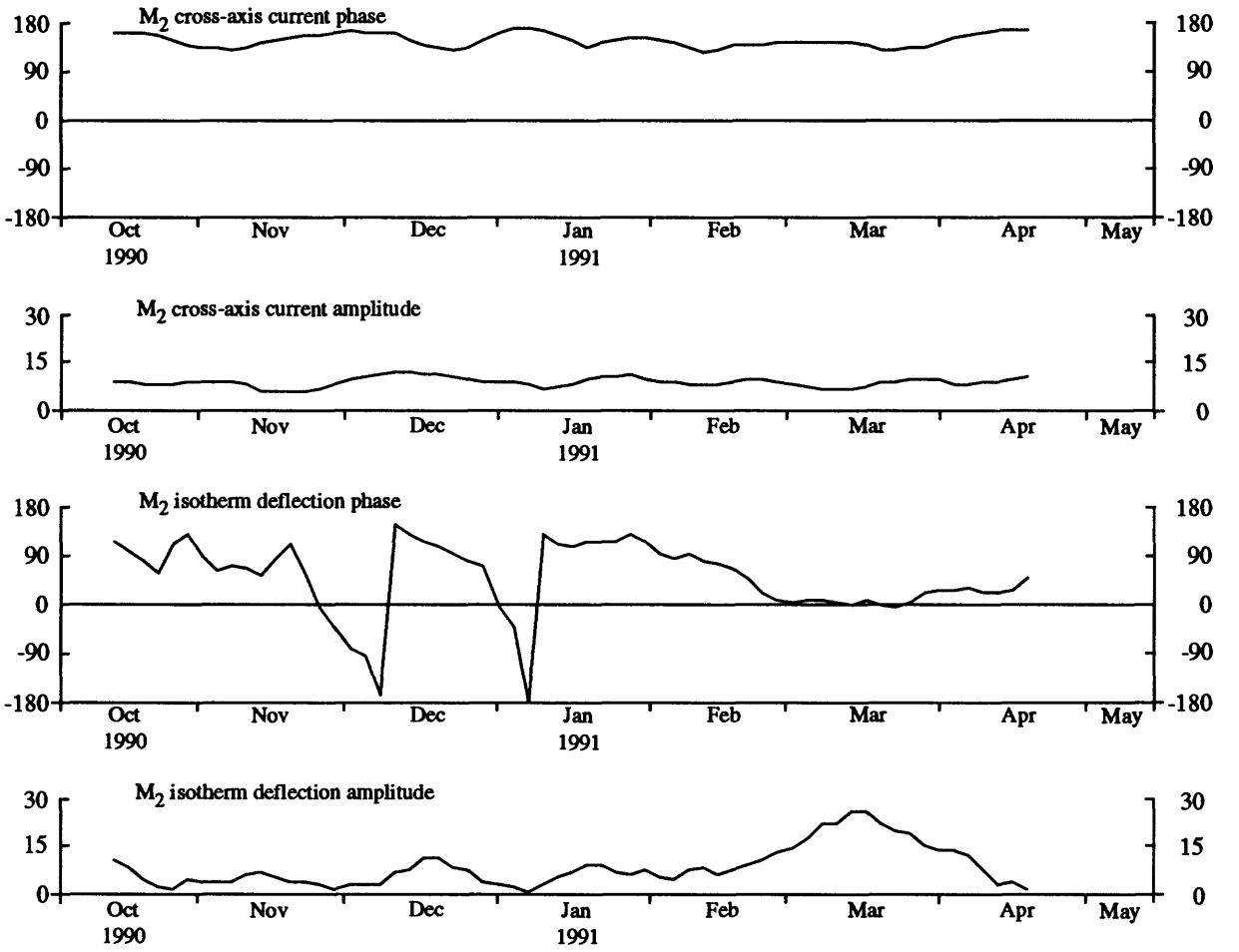

Figure 7b. Phase of the M_2 cross-axis current and isotherm deflection is a function of time at KS50.

1 m. The barotropic diurnal tidal currents are generally smaller than the semidiurnal tides at locations away from large bathymetric features.

The diurnal and semidiurnal tidal currents over Karin Ridge are significantly larger and have amplitudes that change more with location than is typical for tidal currents in the central Pacific. Diurnal current amplitudes range from 1 to 7 cm/s. Semidiurnal currents range between 1 and 10 cm/s. There is no definitive pattern in the amplitude variations. The strongest diurnal currents are found within 50 m of the crest of the seamount at KS. The strongest semidiurnal currents are also found at KS, but between 50 and 200 m above the ridge. The phases of these currents show a uniform downward propagation. Similar characteristics are found for isotherm deflections. Amplitudes are large and variable; phase propagation is uniformly downward. These characteristics indicate that a majority of the variance in the tidal bands is associated with an internal tide.

The constant phases of the diurnal and semidiurnal tidal parameters suggest that the internal tides are not propagating past the seamount from a remote generation site, but are

generated at Karin Ridge. The generation process is continuous throughout the year as indicated by the presence of internal tides during the entire 7 months of record. The observed downward phase propagation shows that the internal tidal energy is traveling up, away from the crest of the seamount. But the internal tidal energy probably not traveling upward along a single ray path. A single, vertically-propagating wave has a phase difference of 90° between the major-axis current and isotherm deflection. This phase difference was found at only 1/4 of our measurement sites.

One might expect the characteristics of the internal tide to be similar at KS and KN because each constituent is generated from a similar constituent in the surface tide. The length scales for the surface tide are large enough that the forcing at both sites will have the same amplitude and phase. However, the tides are definitely not the same at the 2 sites. The M_2 tidal currents at KS are twice the size of those at KN. The S_2 tides are stronger at KN. Therefore, the ratios between the amplitudes of the 2 semidiurnal constituents change markedly with location. They are 1.3 at KN and 4 at KS, about half and 1.5 times the predicted ratios, respectively (Table 4). The diurnal amplitude ratios are equal to the predicted ratio at KN, but are 1.5 times larger at KS. The observed amplitude ratios are specific to a site; the ratio does not change with distance above the seamount cap.

The phases for the internal tides show a significant offset between KS and KN. The phase offset in the diurnal band is 30° to 80° for currents, 50° to 150° for isotherm deflections with KN leading KS (Table 2). The phase offset for semidiurnal tides is 50° to 100° for the currents, 140° to 150° for isotherm deflection, but in this tidal band, KS leads KN. These phase differences cannot be accounted for by the 55 m difference in water depth between KN and KS because the current and isotherm phases change linearly with distance from the cap, not with absolute water depth. The squared correlation amplitudes for a regression of current or isotherm phase with depth above the cap were above 0.96 for all but the S_2 constituent. Equivalent

	Diurnal band		Semidiurnal band	
Station	K_1/O_1	Δ Phase degrees	M_2/S_2	Δ Phase degrees
KN200	2	1	1.3	10
KN 50	1.8	-14	1.2	-74
KN 10	1.9	-13	1.3	-63
KS 200	2.2	34	3.6	-12
KS 50	3.0	34	4.5	5
KS 10	3.2	40	4.5	15
Horizon Guyot	0.7	--	3.3	--
Predicted	2	0	2.9	-22

Table 4. Amplitude ratios and phase differences for tidal currents within a tidal species. The predicted tides are from Schwiderski (1979, 1981a, a981b, 1981c).

squared correlations for a regression against absolute water depth were never higher than 0.36 for currents, 0.63 for isotherm deflections. Squared correlations for the S_2 constituent had the same pattern, but lower values.

The significant changes in the characteristics of the internal tides between the two sites, given a constant, spatially-invariant forcing, suggests that the generation of internal tides is subject to significant local topographic control. With this data set, it is difficult to determine the exact nature of the local control because sites KS and KN share gross topographic characteristics. They are adjacent sites on the crest of a long, narrow, deep seamount. Both sites are located on shallow, roughly circular, smooth, local topographic highs. The radius of the topographic high at KN and KS is 14 and 8 km, respectively. The slopes of the topographic highs are 2^o to 4^o, similar to the slopes of propagating internal diurnal and semidiurnal tides. Hence internal tides could be generated either over the cap itself, where the topographic slopes match the slope of the ray paths, or at the edge of the ridge crest, where the topographic slope suddenly steepens. Given that internal tides usually have wavelengths longer than 35 km (Simpson and Pauling, 1979), it is more likely that the internal tides were generated along the edge of the crest of Karin Ridge. The diameter of the local topographic high, KS, is much smaller than the normal wavelength for internal tides.

A partial explanation for the different tidal characteristics at the two sites is that the moorings may be at different distances from the generation region. KN is nearer the edge of the ridge crest, KS in the middle of the local topographic high. A semidiurnal internal wave, traveling along a ray path, would move up a distance of 200 m, the length of the moorings, in a horizontal distance of 4 km. This distance is half the radius of the smallest local topographic high. Hence, neither the amplitude or the phases of the internal tides would necessarily be the same between KN and KS.

However, this explanation does not account for all the variations observed in the internal tide. In particular, it does not explain why tidal constituents within a tidal species have amplitude ratios that are different from the barotropic forcing ratios or why these ratios change between sites. Models predict that the internal tides within a tidal species will be generated with amplitude ratios similar to the forcing ratio; the generation of an internal tides is not sensitive to slight frequency shifts. The frequency difference between M_2 and S_2 is 3%, O_1 and K_1 is 8%. Yet, the data show that the semidiurnal ratio is much lower than predicted at KN and higher than predicted at KS. The diurnal ratios are closer to the predicted, even thought they have frequencies that are further apart.

Even though it is unclear what processes are responsible for the unusual amplitude ratios in the internal tide, this phenomena is not unique to Karin Ridge. A strongly amplified S_2 internal tide, relative to M_2, was observed propagating past Cross Seamount, located near the Hawaiian Islands (Noble and Mullineaux, 1989). The vertical displacement of isotherms at Ocean Weather Station P, in the north Pacific, was also observed to be dominated by the S_2 tides (Thompson and Tabata, 1982).

Comparison of internal tides over Karin Ridge and Horizon Guyot

Karin Ridge and Horizon Guyot are similar seamounts located in the same region of the central Pacific (Figure 1). They are both long and narrow, with caps near 1600 m. The major difference is that the axis of Karin ridge is oriented approximately perpendicular to the axis of Horizon Guyot. Because of their close proximity, the characteristics of the surface tide, as deduced from Schwiderski's ocean tidal models, are the same at each seamount (Schwiderski, 1979, 1981a, 1981b, 1981c)

A single current-meter was deployed on Horizon Guyot, 200 m above the cap, for 9 months in 1984 (Noble, et. al, 1988). Seven years later, two moorings with current meters 200 m above the cap were deployed for a similar length of time on Karin Ridge. Large semidiurnal internal tides were observed above both seamounts. The internal tides shared many characteristics. Both had stable phases for the observation period. The amplitudes of the currents and isotherm oscillations at Horizon Guyot were within the range seen at Karin Ridge (Table 5). This suggests that the orientation of a submarine ridge with respect to the barotropic tidal currents does not strongly affect whether internal tides will be generated, but the ridge orientation could affect the direction of the internal tidal ray path. .A comparison of ellipse orientations suggests that internal tides are preferentially generated with the major axis of the current ellipse oriented perpendicular, rather than parallel, to the ridge axis. Both semidiurnal current ellipses were aligned across the axis of Horizon Guyot (Table 5). The ellipse axes were aligned within 30^{o} of the cross-axis direction at Karin Ridge for all but the M_2 constituent at KN. However, the M_2 ellipse direction was not well defined at KN because the shape of the ellipse was nearly round.

Station	Semi-major axis current (cm/s)	Semi-minor axis current (cm/s)	Inclination (degrees)	Isotherm deflection amplitude (meters)
		M_2		
KN200	5.4	5.1	152	20
KS 200	9.3	5.2	60	17
Horizon Guyot	7.6	3.1	128	20
		S_2		
KN200	4.2	2.4	78	10
KS 200	2.6	0.8	28	8
Horizon Guyot	2.3	1.0	122	8

Table 5. Semidiurnal tides at Karin Ridge and Horizon Guyot. All current meters were deployed 200 m above the cap of the seamount. All tidal currents rotate in a clockwise direction.

CONCLUSIONS

It is clear that internal tides are commonly generated over large deeply-submerged submarine ridges. The characteristics of the internal tides are more stable over time than is found at other sites where internal tides are generated, such as the shelf break. This is probably because the water in the deep ocean is not subject to seasonal cycles. Also, there are no rapid changes in the density field of the water column in the deep ocean that would either alter the internal wave ray paths or affect parameters in the generation process.

However, it is clear that the generation of internal tides is not a simple process. Even though the characteristics of a particular tidal species were uniform over the water depth at each measurement site, they changed dramatically between sites. The ratios of the tidal amplitudes within a tidal band were significantly different than predicted for the seamount and changed with location along the seamount. The uniform downward phase propagation indicated that the internal tidal energy was moving upward, away from the seamount, along ray paths. But the phase relations between the major axis currents and isotherm deflection were not generally consistent with a sample ray path model.

Clearly, more information is needed before one can understand the complexities in the generation of internal tides. Deep seamounts are an ideal platform to study this process because the signal is continuous and relatively stable over time. Our array on Karin Ridge does provide limited, but critical information on the generation of internal tides. But a greatly expanded array, with instruments both on a seamount and in the far field, are needed before some of the above observations can be adequately understood.

ACKNOWLEDGMENTS

We would like to thank William Strahle, Kevin O'Toole, Walter Olson and Jim Vaughan for preparing, deploying and recovering the many types of instruments used in this project. Francis Hotchkiss decoded and cleaned up the raw data sets. The crews of the research vessels "Farnella" and "Akademik Aleksandr Vinagradov" ably assisted in the deployment and recovery of instruments during the program. This research was sponsored by the Pacific Marine Geology Branch of the U.S. Geological Survey.

REFERENCES

Cacchione, D. A., W. C. Schwab, M. Noble, G. Tate, 1988, Currents, temperature, and sediment movement on Horizon Guyot: Geo-Marine Letters, 8, p 11-17.

Genin, A., M. A. Noble and P. F. Lonsdale, 1989, Tidal currents and anticyclonic motions on two North Pacific seamounts: Deep Sea Research, v. 36, 12A, p. 1803-1816.

Kinoshita, K. and M. Noble, 1994, Current data from Karin Ridge in the Central Pacific, U.S. Geological Survey Open File Report 94-20.

Noble, M., D. A. Cacchione, and W. C. Schwab, 1988, Observations of Strong Mid-Pacific Internal Tides above Horizon Guyot: Journal of Geophysical Research, v. 18, no. 9, p. 1300-1306.

Noble, M. and L. S. Mullineaux, 1989, Internal tidal currents over the summit of Cross Seamount: Deep Sea Research, v. 36, no. 12, p. 1791-1802.

Schwiderski, E. W., 1979, Global Ocean Tides, Part II: The semidiurnal principal lunar tide (M_2): Atlas of tidal charts and maps. Naval Surface Weapons Center, Dahlgren, Virginia, TR 79-414.

Schwiderski, E. W.; 1981a, Global Ocean Tides, Part III: The semidiurnal principal solar tide (S_2): Atlas of tidal charts and maps. Naval Surface Weapons Center, Dahlgren, Virginia, TR 81-122.

Schwiderski, E. W.; 1981b, Global Ocean Tides, Part IV: The diurnal lunar-solar declination tide (K_1): Atlas of tidal charts and maps. Naval Surface Weapons Center, Dahlgren, Virginia, TR 81-142.

Schwiderski, E. W.; 1981c, Global Ocean Tides, Part V: The diurnal principal lunar tide (O_1): Atlas of tidal charts and maps. Naval Surface Weapons Center, Dahlgren, Virginia, TR 81-144.

Simpson, J. J. and C. A.. Paulson, 1979, Observations of upper ocean temperature and salinity structure during the POLE experiment: Journal of Physical Oceanography, 9, p. 869-884

Thompson R. and S. Tabata, 1982, Baroclinic oscillations of tidal frequency at Ocean Weather Station P: Atmosphere-Ocean, 20, p. 242-257.

HYDROLOGICAL PARAMETERS AND WATER STRUCTURE OVER KARIN RIDGE, CENTRAL PACIFIC OCEAN

Ann E. Gibbs[1], Alexander F. Sergeev[2], Anatoly N. Salyuk[2], James R. Hein[1], Valery P. Tapinov[2], and Alexander S. Bychkov[2]

[1]U.S. Geological Survey, 345 Middlefield Road MS 999, Menlo Park, CA 94025, USA; [2]Pacific Oceanological Institute, Far Eastern Branch, Russian Academy of Sciences, 43 Baltiyskaja, Vladivostok 690041, Russia

INTRODUCTION

In this chapter we present hydrological data obtained from continuous CTD measurements and analyses of water bottle samples obtained from deep hydrocasts on and around Karin Ridge. Data were obtained at four locations, two directly over the ridge and two on either side of Karin Ridge, in order to identify and quantify the potential effects of the Ridge on the measured parameters and general water structure of the region. Temperature, pressure, salinity, density, and oxygen information was recovered using CTD and CTD-oxygen instruments. Hydrostation casts recovered similar data as well as water chemistry and alkalinity information.

CTD-oxygen casts (CTDR) were undertaken by the USGS primarily to obtain oxygen data. Total oxygen values and the depth of the oxygen minimum zone (OMZ) have been shown to influence the occurrence, thickness, and metal concentrations of ferromanganese crusts (Hein, Kang, *et al.*, 1990; Hein, Ahn, *et al.*, 1992). CTDR data is compared with results obtained in the Federated States of Micronesia (FSM) and the Marshall Islands (MI), two areas of known Fe-Mn crust occurrence, in order to identify regional trends and support the correlation between oxygen and Fe-Mn crust characteristics. Water temperature, salinity, and density data collected in the same casts are used by Noble and Kinoshita (this volume), in conjunction with current meter data, in order to characterize the current and tidal regimes associated with the ridge.

CTD and hydrocast data obtained under the direction of the POI are used to define water chemistry and water mass characterization and identification. The effect of various parameters on the carbonate system are described in detail by Bychkov *et al.* (this volume) and trace metal concentrations are presented by Orians (this volume).

METHODS

Ten CTD profiles, four CTD-oxygen profiles (CTDR), and three hydrostation profiles (HS) were collected between April 11 and April 23, 1993 (Fig. 1). One hydrostation (HS 15) and five CTD casts were taken over the central summit region of Karin Ridge: four (CTDR 1 and CTD-23, 31, 33) in the northern study area and one (CTDR 2) in the southern study area (Fig. 1). These two areas correspond to current meter sites 356 and 357 described by Noble and Kinoshita (this volume). Four casts (CTDR 3 and CTD 24, 26, 29) were deployed along the southwestern flank and five (CTDR 4 and CTD 35, 37, 39, 40) along the northeastern flank of the study area near stations HS-14 and HS-16, respectively. It should be noted that ship drift and infrequent satellite navigation fixes limit the accuracy of absolute site locations, although the water depths of deployments are well known.

Hydrostation (HS-) samples were collected using 10-liter PVC Niskin-type bottles. Temperature and depth (pressure) were determined by reversing thermometers with a 0.02°C point scale. Salinity measurements were performed on the Guildline Autosal (model 8400) using the analytical technique described in the Autosal Operating Manual. Each sample was run three times. The salinometer was standardized daily with IAPSO Standard Seawater (batch P79). Potential temperature was calculated according to the polynomial of Bryden (1973).

Two instruments were used to make the CTD casts; a portable Guildline system (model 8770) collected ten CTD profiles (CTD) to a depth of 1000 m and a Neil Brown Mark III CTD Instrument collected four CTD-oxygen profiles (CTDR) to depths between 1600 and 3600 m (Table 1).

As a result of difficulties with a new computer system and data processing software, IMS CTD Deck system Software (Saklad, 1990) was used for the CTDR oxygen calculations instead of the commonly used USGS program. We question the accuracy of the absolute oxygen contents calculated from this program because the algorithm used could not incorporate the oxygen contents determined by Winkler titration on water bottle samples. The data generated, however, are mostly consistent with the measured values of oxygen, as well as with regional oxygen values for the Marshall Islands (MI) and Federated States of Micronesia (FSM) (Hein, Kang *et al.*, 1990; Hein, Ahn *et al.*, 1992). We recommend, however, using oxygen contents obtained at the hydrostations determined by Winkler titration (Bychkov *et al.*, this volume).

RESULTS

Water Properties

Vertical profiles of hydrological parameters (potential temperature, salinity, oxygen, and density) for selected CTD and all CTDR casts are given in Figures 2-8. Due to problems with the data acquisition system, data was not recovered for the upper 150 m of the CTDR profiles.

Salinity

Salinity profiles were similar throughout the region. Maximum (34.93-35.14 psu) and minimum (34.21 psu) salinity occurred at mean water depths of 139 m (116-162 m) and 318 m (291-348 m), respectively (Table 1). The minimum salinity layer was slightly deeper along the flanks of the ridge, although for both layers temporal variations of about 40 m were found (Table 1). In all profiles, salinity rapidly increased between the salinity minimum and about 550 m, then increased uniformly at a much slower rate to the bottom of the profiles. An abrupt decrease, or peak, in salinity marked this transition at stations CTDR 1 and 4, both from the northern study area (Figs. 5 and 8).

Temperature

In order to compare temperature distribution for different stations, water depths corresponding to 10 °C were recorded (Table 1). The 10°C isotherm roughly corresponds to the boundary between the seasonal and permanent thermocline in the region and occurs at water depths slightly above the top of oxygen minimum zone (OMZ). The deepest level of the 10°C isotherm was found over the northeastern flank of Karin Ridge (326 m; CTDR 4) and the shallowest level over the northern ridge summit (285 m; CTDR 1). The mean water depth of the 10°C isotherm in the Karin Ridge area during the study period (May 11-18, 1991) was 309 m (Table 1); somewhat deeper than in the FSM (288 m; Oct. 16 - Nov. 8, 1990) and in MI (247 m; Sept. 14 - Oct. 1, 1989) where Fe-Mn crusts occur (Hein, Kang *et al.*, 1990; Hein, Ahn *et al.*, 1992). The 10°C isotherm horizon also showed temporal variations. At station HS-15, fluctuations of up to 29 m were noted over a six day period; at station HS-14, a 22 m variation over a three day period was noted. Spatial variations should be viewed in light of the vertical migration of the isotherm. Overall variation in the depth of the 10°C isotherm in the Karin Ridge area (46 m), however, was less than for the FSM (61 m) and MI (110 m) regions.

Oxygen

Four CTD-oxygen profiles (CTDR) indicate that the water depth to the top of the OMZ was relatively constant throughout the study area and ranged from 450 m at station CTDR 1 to 475 m at stations CTDR 2-4 ; with a mean value of 469 m (Figs. 5-8). This mean depth is nearly one and a half times deeper than in the MI (305m) and the FSM (289 m). Depth of the minimum oxygen value in each profile varied from 492 m (CTDR 4) to 578 m (CTDR 1), with a mean of 548 m (Table 1). These data show good agreement with analysis of water bottle samples by Bychkov *et al.* (this volume).

Differences between the depth of the OMZ in the Karin Ridge region, compared to FSM and MI, can be explained by the proximity to and intensity of equatorial biological productivity zones (Hein, Ahn *et al.*, 1992). Greater quantities of organic matter are produced toward the equator and toward the east (FSM and MI). These materials are oxidized in the water column and, combined with zooplankton respiration, deplete the oxygen in seawater, thereby raising the top boundary of the OMZ.

Water Structure

Water mass types were analyzed using potential temperature versus salinity diagrams (θ-S), and potential temperature versus normalized total alkalinity (θ-NTA). Data was generated from both CTD and hydrocast data. Between 0 and 1000 m, primary emphasis was put on CTD data; below 1000 m data obtained from water bottle samples was used. Results of the θ-S analyses are listed in Table 2 and depicted in Figures 9-11.

Central Karin Ridge and adjacent areas are located in the tropical water mass typically found between 25° N and 15° N, and associated largely with the Northern Passat Current (Radzikhovskaya and Leont'eva, 1986). The upper layer of the water column down to 70 m comprises the North Pacific Tropical Surface water (NPSW), which is uniform in salinity (34.38-34.46 psu) and temperature (26.3-26.5°C). Underlying this surface layer, to a depth of about 200 m, is North Pacific Subsurface (Central) Water (NPCW); NPCW has increased salinity relative to NPSW and formed from surface water in the central part of subtropical anticyclonic gyre (Mamaev, 1987). The NPCW core lies at a depth of about 140 m, with a salinity range of 35.02-35.12 psu, and temperature of approximately 23°C.

Underlying the surface circulation system (NPSW + NPCW) is the North Pacific Intermediate Water (NPIW). It is characterized by a salinity minimum (34.21-34.25 psu) at depths ranging between 300 and 340 m and associated temperatures range from about 9.5 to 10.1°C. The origin and distribution of the NPIW has been extensively discussed (Reid, 1965; Kuksa, 1983; Mamaev, 1987) and different layers can be distinguished within this water mass:

(a) Values of thermohaline characteristics for depths between 200 m and 440-480 m are typical for intermediate water of reduced salinity, formed at the northern polar front (Kuksa, 1983);

(b) Sections of maximum curvature on the θ-S plots occur at a water depth interval of 1200-1280 m and can be interpreted as a transformed core of Antarctic intermediate water of reduced salinity with temperatures of 3.4-3.5°C and salinities of 34.55-34.58 psu (Kuksa, 1983; Mamaev, 1987);

(c) Between North Pacific and Antarctic intermediate water masses, at water depths of 440-480 m and 750-900 m, where the θ-S plot has maximum curvature, a lower intermediate water mass of elevated salinity can be distinguished (Radzikhovskaya and Leont'eva, 1986). Although this water mass is common in the equatorial water mass structure, only traces of it are observed in the Karin Ridge area.

Water below the NPIW displays uniform characteristics. The source, path, and modification of the deep (NPDW) and bottom (NPBW) waters of the North Pacific are described by Reid and Lynn (1971), Mantyla (1975), Mantyla and Reid (1983), and Mamaev (1987). In the Karin Ridge area, the boundary between NPDW and NPBW occurs between 3260 and 3380 m. The position of the upper boundary of the NPDW and its core could not be determined. As a result of the spatial and temporal variability of temperature and salinity above 500 m, and too few measurements of hydrological properties below 1000 m, an accurate description of the core and boundaries of the water masses in this area could not be determined from our CTD data .

Hydrochemical parameters, particularly total alkalinity, however, have been shown to be useful in water mass characterization (Koczy, 1956; Chen *et al.*, 1986; Pavlova *et al.*, 1989). When potential temperature is plotted against normalized total alkalinity (NTA = alkalinity * 35 / S) (semilogarithmic scale), five different trends representing the water masses discussed above can be identified (Fig. 12). In the surficial layer (NPSW 0-70 m), where temperature and salinity are uniform, NTA varies from 2294 to 2307 μeq/kg and has a slope roughly parallel to the x-axis on the θ-NTA diagram. With the transition of NPSW to NPCW (70-200 m depth), the trend changes: a decrease in temperature corresponds to a slight rise in NTA at a rate of about 1 μeq/kg/°C. For the NPIW (200-1500 m depths) this trend has a steeper slope (13 μeq/kg/°C) indicating a higher rate of alkalinity input. The NPDW is characterized by an additional increase of NTA (17 μeq/kg/°C) as a result of calcium carbonate dissolution in the undersaturated deep water. Most carbonates dissolve by the time they reach the NPBW. Therefore this layer does not have a large flux of calcareous material and below about 3300 m NTA decreases to the sea floor (Chen *et al.*, 1986).

The water mass boundaries obtained from the intersection of the θ-NTA trends compare well to the results determined on the basis of θ-S diagrams (Table 2). This method of analysis allows us to identify the boundary between NPIW and NPDW at a depth of about 1500 m; a task that was not possible using only temperature and salinity data. The subdivision of NPIW into the three layers previously discussed is not as straightforward. Through the analysis of all the data sets, however, three water types can tentatively be defined: the lower boundaries of the three layers that compose the NPIW correspond to potential temperatures of about 8.4°C, 5.1°C, and 2.8°C, and depths of 410 m, 800 m, and 1500 m, respectively.

REFERENCES

Bryden, H.L., 1973. New polynomials for thermal expansion, adiabatic temperature gradient and potential temperature of sea water: Deep-Sea Research, v. 20, p. 401-408.

Bychkov, A.S., Pavlova, G.Y., Tishchenko, P.Y., and Salyuk, A.N., 1994. Hydrochemical parameters and carbonate system, Karin Ridge area, this volume, p. 187-218.

Chen, C.T., Rodman, M.R., Wei, C.L., and Olson, E.J., 1986. Carbonate Chemistry of the North Pacific Ocean: U.S. Dept. of Energy Technical Report DOE/NBB-0079, 176 p.

Hein, J.R., Ahn, J.-H., *et al.*, 1992. Geology, geophysics, geochemistry, and deep-sea mineral deposits, Federal State of Micronesia, KORDI-USGS *R.V. Farnella* cruise F11-90-CP: U.S. Geological Survey Open File Report 92-218, 191 p.

Hein, J.R., Kang, J.-K., *et al.*, 1990. Geological, geochemical, geophysical, and oceanographic data and interpretations of seamounts and Co-rich ferromanganese crusts from the Marshall Islands, KORDI-USGS *R.V. Farnella* cruise F10-89-CP: U.S. Geological Survey Open File Report 90-0407, 246 p.

Koczy, F.F., 1956. The specific alkalinity: Deep-Sea Research, v. 3, p. 279-288.

Kuksa, V.I., 1983. Promezhutochnye vody Mirovogo okeana. Gidrometizdat, Moskva, 272 p. (In Russian. Intermediate water masses of the World Ocean. Hydrometeo-Press House, Moscow).

Mamaev, O.I., 1987. Termochalinnyi analiz vod Mirovogo okeana. Gidrometizdat, Moskva, 296 p. (In Russian. Thermohaline analysis of the World Ocean waters. Hydrometeo-Press House, Moscow).

Mantyla, A.W., 1975. On the potential temperature in the abyssal Pacific Ocean: Journal of Marine Research, v. 33, p. 341-354.

Mantyla, A.W. and Reid, J.L., 1983. Abyssal characteristics of the world ocean waters. Deep-Sea Research, v. 30, p. 805-833.

Noble, M. and Kinoshita, K., 1994. Current patterns over Karin Ridge, a seamount in the Central Pacific: this volume p. 149-168

Orians, K.J. and Yang, L., 1994. Cadmium, zinc, nickel, copper, lead, manganese, and cobalt in the western North Pacific: this volume, p. 19-36.

Pavlova, G.Yu., Stashchuk, M.F., and Bychkov, A.S., 1989. Karbonatnaya sistema kak harakteristika vodnykh mass v severo-zapadnoi chasti Tikhogo okeana: Doklady AN SSSR, v. 305/4, p. 973-976. (In Russian. Carbonate system as a characteristics for water masses of the North-West Pacific.)

Radzikhovskaya, M.A., and Leont'eva, V.V., 1986. Struktura vod i vodnye massy: Tikhiy okean. Gidrologiya Tikhogo okeana. Nauka, Moskva, p. 20-68. (In Russian. Water structure and water masses: In: Pacific Ocean. Hydrology of the Pacific Ocean, Nauka, Moscow.)

Reid, J.L., 1965. Intermediate waters of the Pacific Ocean: The Johns Hopkins Oceanographic Studies, No. 2, 85 p.

Reid, J.L., and Lynn, R.Y., 1971. On the influence of the Norwegian-Greenland and Weddell Seas upon the bottom waters of the Indian and Pacific Oceans: Deep-Sea Research, v. 18, p. 1063-1088.

Saklad, H.M., 1990. IMSCTD Deck System Software, v. 3.6. Institute of Marine Science, Univ. of Alaska, Fairbanks.

Table 1. Summary of the selected CTD and CTD-oxygen profiles (CTDR) from the Karin Ridge area

Stations	UTC		Location		10 °C isotherm depth, m	Minimum salinity depth, m	Maximum salinity depth, m	Minimum oxygen depth, m
	date	time	Lat., N	Long., W				
Northern ridge top								
CTDR 1	11/5/91	18:40	17° 7.0'	168° 34.5'	285	305	-	578
CTD-023	12/5/91	04:50	17° 7.6'	168° 30.1'	322	329	138	-
CTD-031	18/5/91	07:06	17° 4.9'	168° 28.3'	295	307	151	-
CTD-033	18/5/91	14:26	17° 10.0'	168° 27.8'	293	291	162	-
Southern ridge top								
CTDR 2	12/5/91	07:13	16° 37.1'	168° 18.3'	320	311	-	553
Southwestern flank								
CTDR 3	15/5/91	01:30	16° 29.9'	168° 30.9'	300	302	-	570
CTD-024	13/5/91	15:45	16° 27.3'	168° 30.6'	311	338	116	-
CTD-026	13/5/91	20:48	16° 31.7'	168° 29.8'	289	312	128	-
CTD-029	16/5/91	01:57	16° 31.8'	168° 29.7'	308	302	162	-
Northeastern flank								
CTDR 4	18/5/91	09:13	17° 15.9'	168° 6.5'	331	343	-	492
CTD-035	21/5/91	16:17	17° 14.0'	168° 7.0'	322	335	129	-
CTD-037	21/5/91	22:50	17° 14.9'	168° 10.9'	314	312	133	-
CTD-039	22/5/91	05:13	17° 17.6'	168° 12.1'	315	307	143	-
CTD-040	23/5/91	07:05	17° 13.0'	168° 6.1'	326	348	132	-

Table 2. Water structure in the Karin Ridge area

Type of water	Depth, m (θ-S diagram)	Depth, m (θ-NTA diagram)	Average characteristics of core		
			Depth, m	θ, °C	Salinity, psu
Surface (NPSW)	0 - 70	0 - 70	-	26.4	34.4
Subsurface (NPCW)	70 - 200	70 - 200	140	23.0	35.1
Intermediate (NPIW)	-	200 - 1500	-	-	-
layer 1	200 - 440/480	200 - 410	340	9.6	34.2
layer 2	440/480 - 750/900	410 - 800	580	6.4	34.5
layer 3	>750/900	800 - 1500	1240	3.5	34.55
Deep (NPDW)	<3260/3380	1500 - 3300	-	<2.8	>34.6
Bottom (NPBW)	>3260/3380	>3300	-	<1.4	34.7

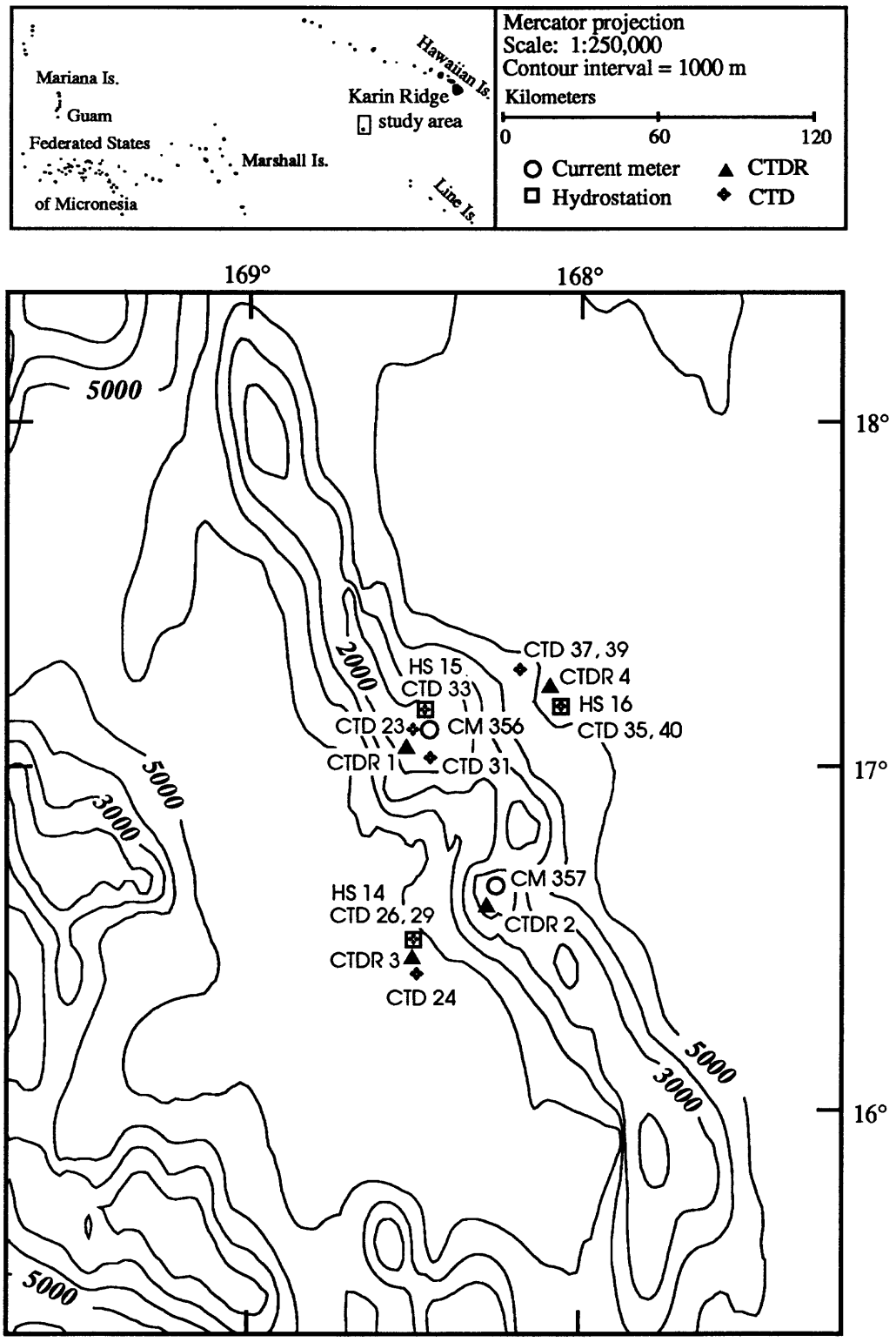

Figure 1. Locations of CTD stations, hydrostations (HS-), and current meter stations (CM-). Station locations are approximate.

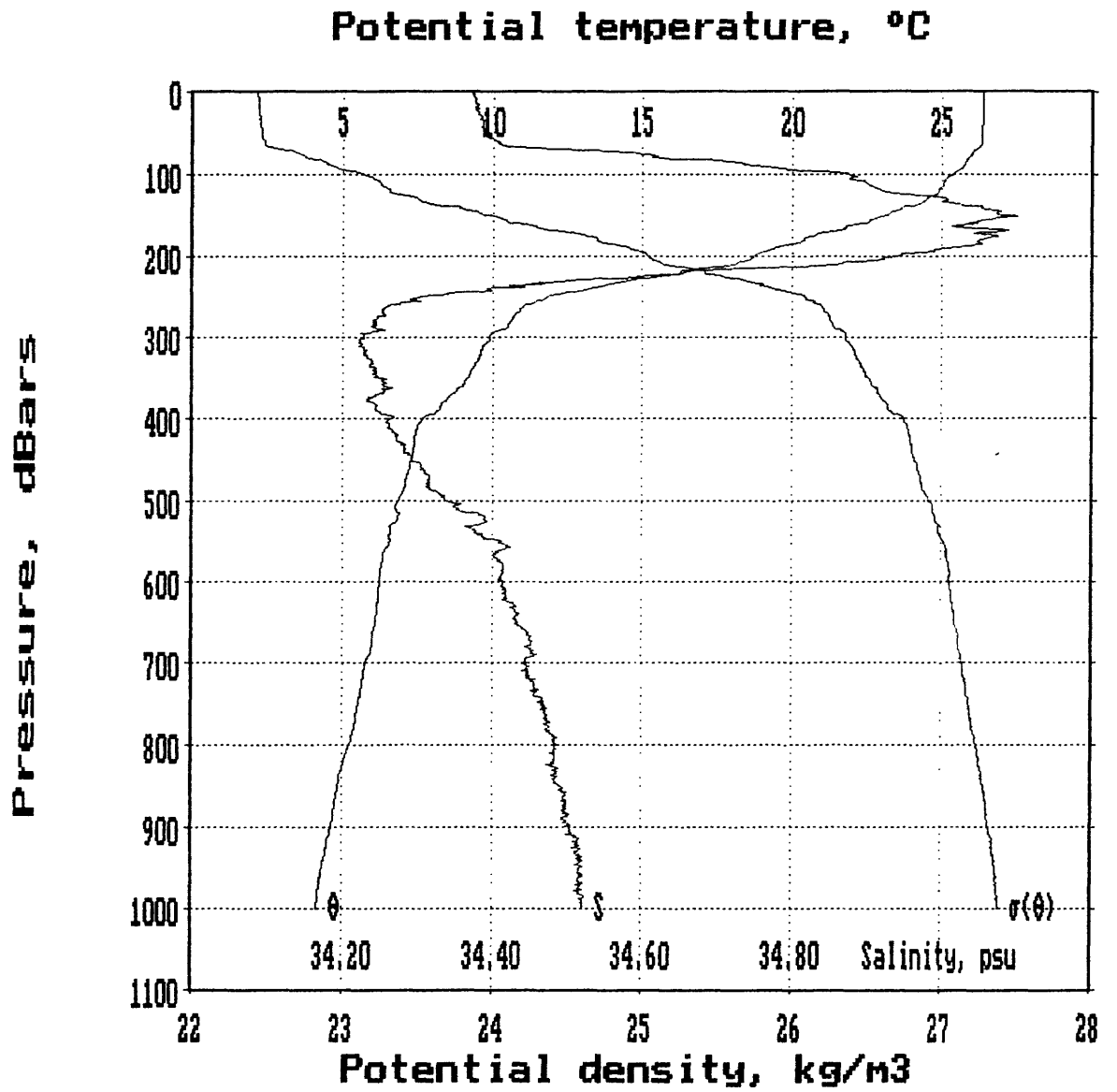

Figure 2. Salinity (S), potential temperature (θ), and density (σ) profiles over the northern top of Karin Ridge (CTD-031).

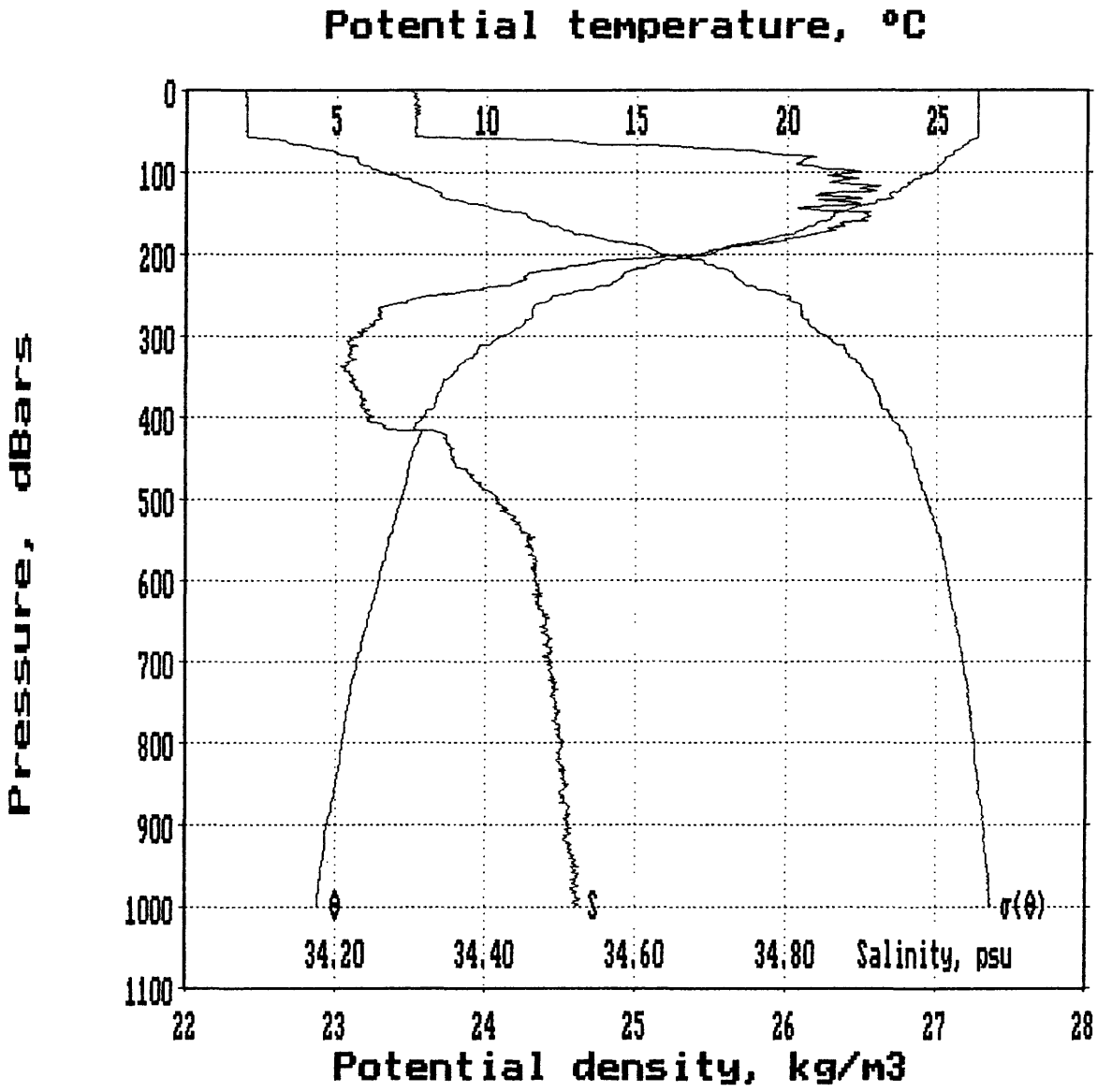

Figure 3. Salinity (S), potential temperature (θ), and density (σ) profiles over the southwestern flank of Karin Ridge (CTD-024).

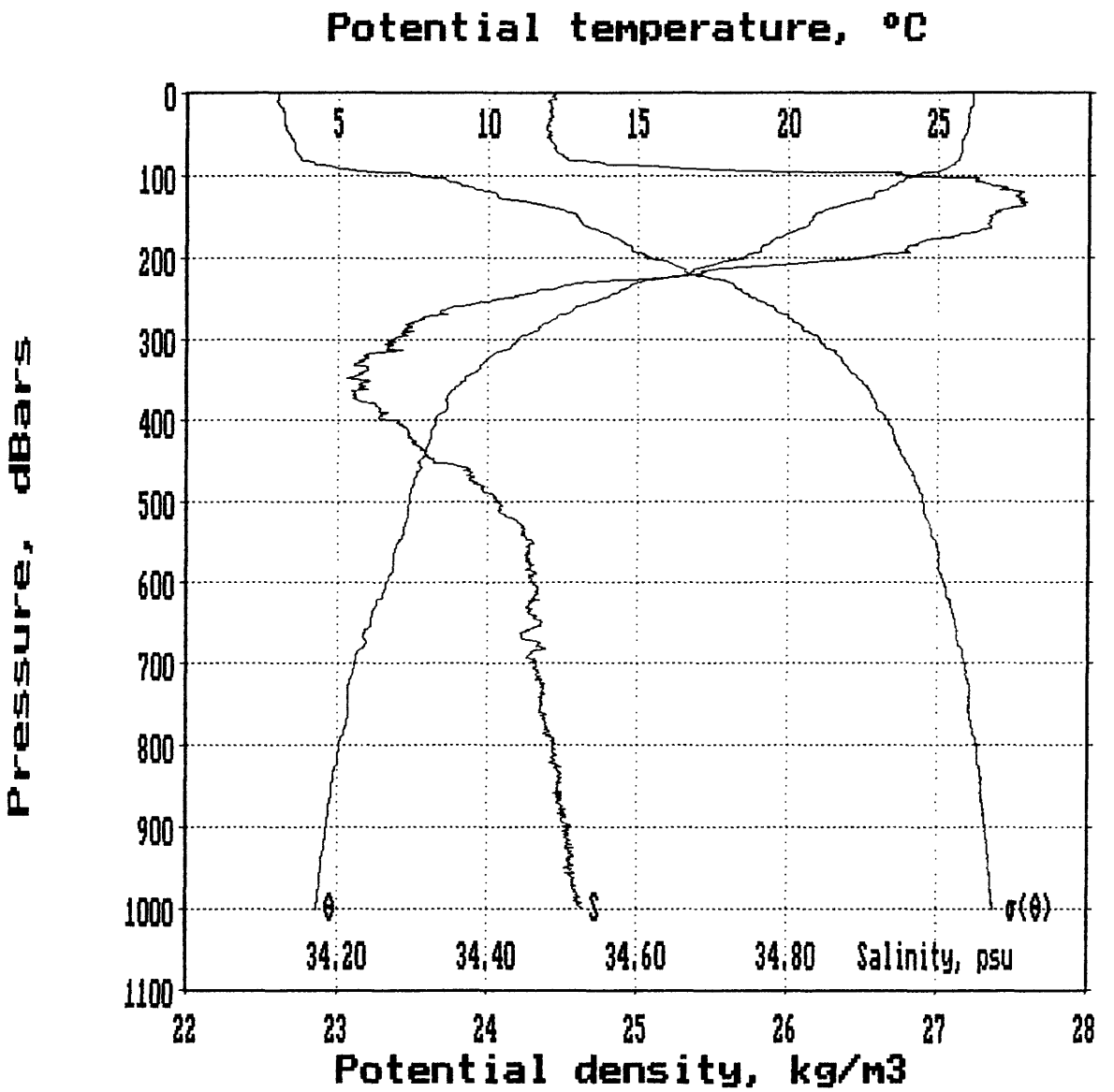

Figure 4. Salinity (S), potential temperature (θ), and density (σ) profiles over the northeastern flank of Karin Ridge (CTD-040).

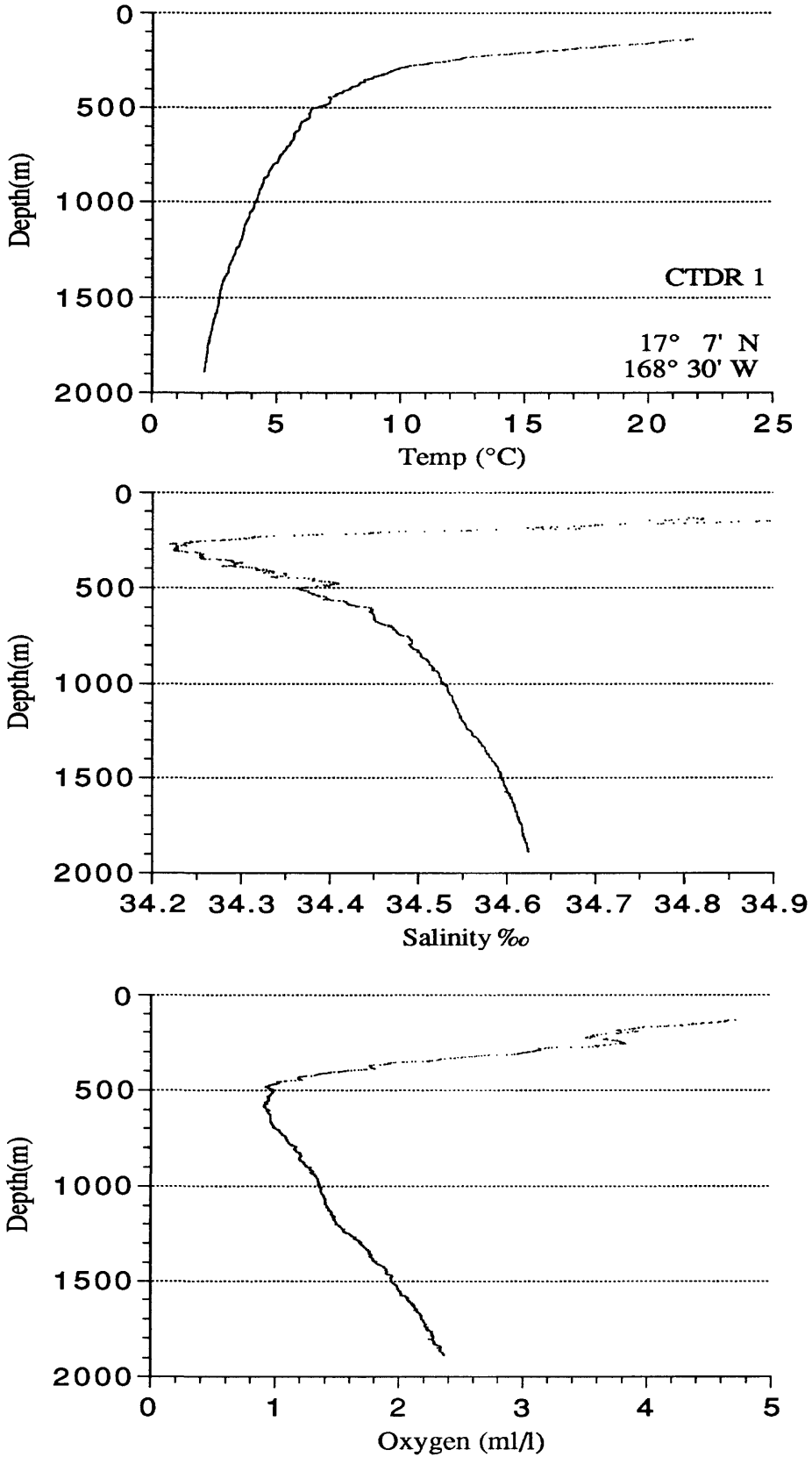

Figure 5. Temperature, salinity, and oxygen content versus water depth for CTDR 1, northern ridge top, Karin Ridge. Water depth at station is 1888 meters.

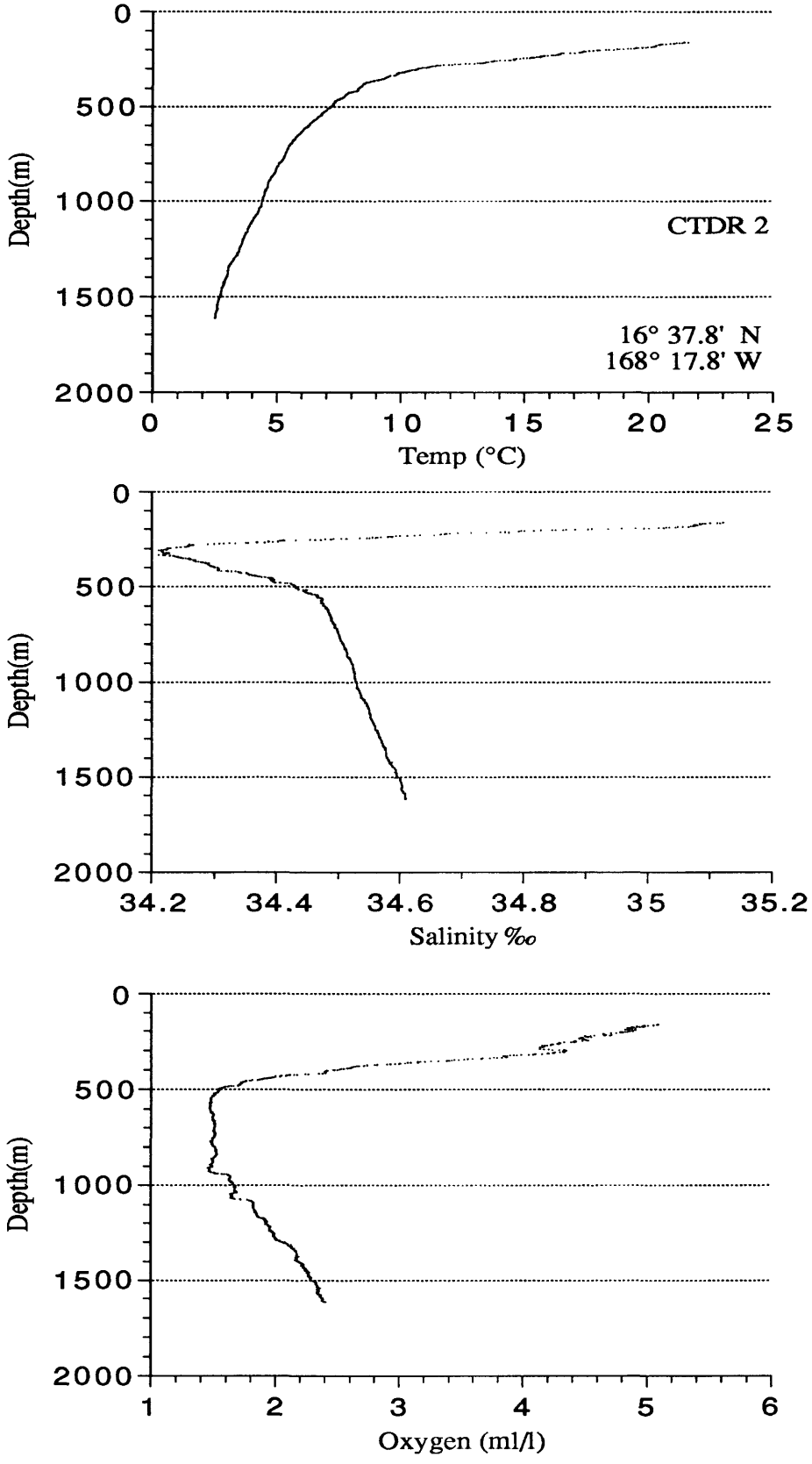

Figure 6. Temperature, salinity, and oxygen content versus water depth for CTDR 2, southern ridge top, Karin Ridge. Water depth at station is 1750 meters.

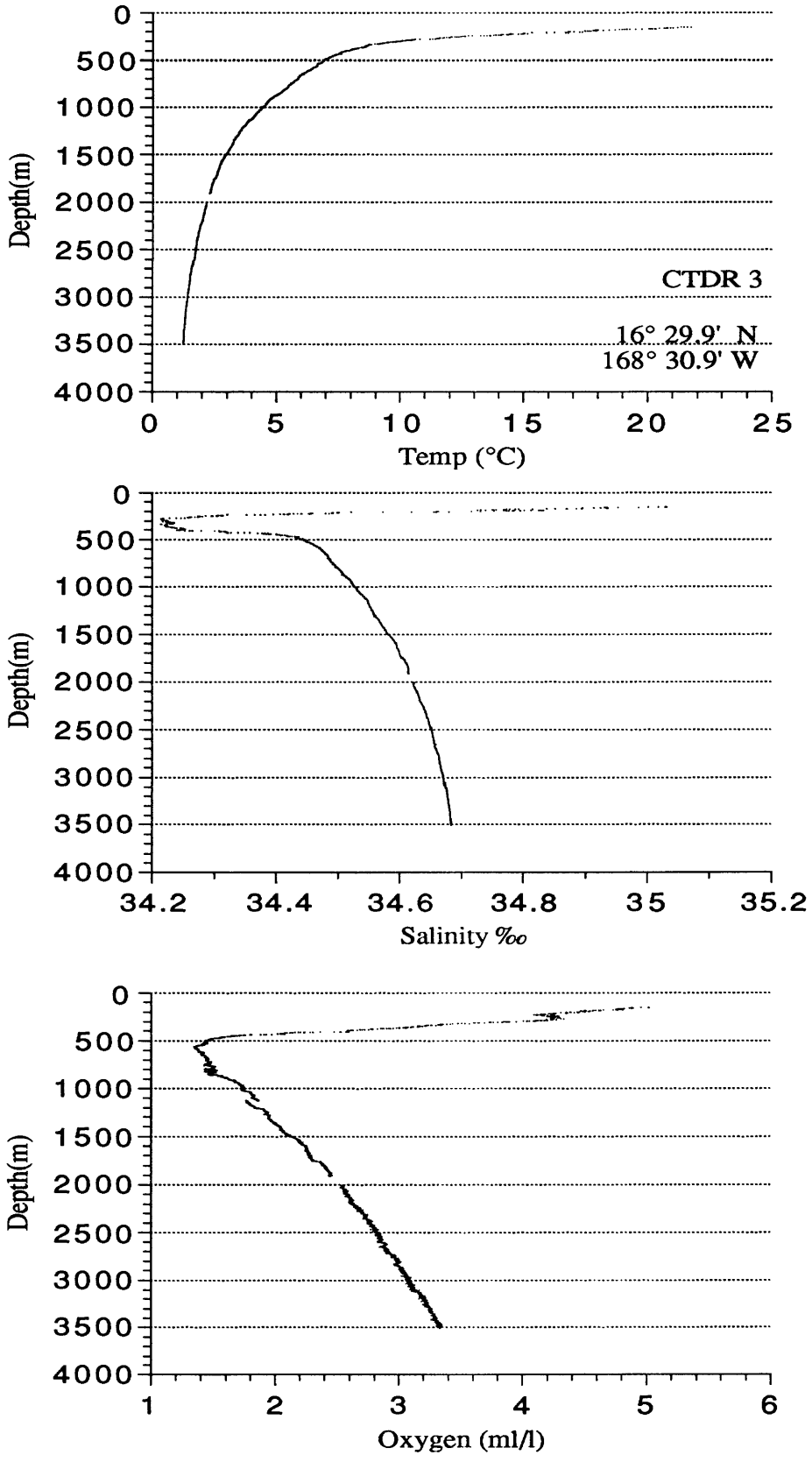

Figure 7. Temperature, salinity, and oxygen content versus water depth for CTDR 3, southern flank, Karin Ridge. Water depth at station is 5100 meters.

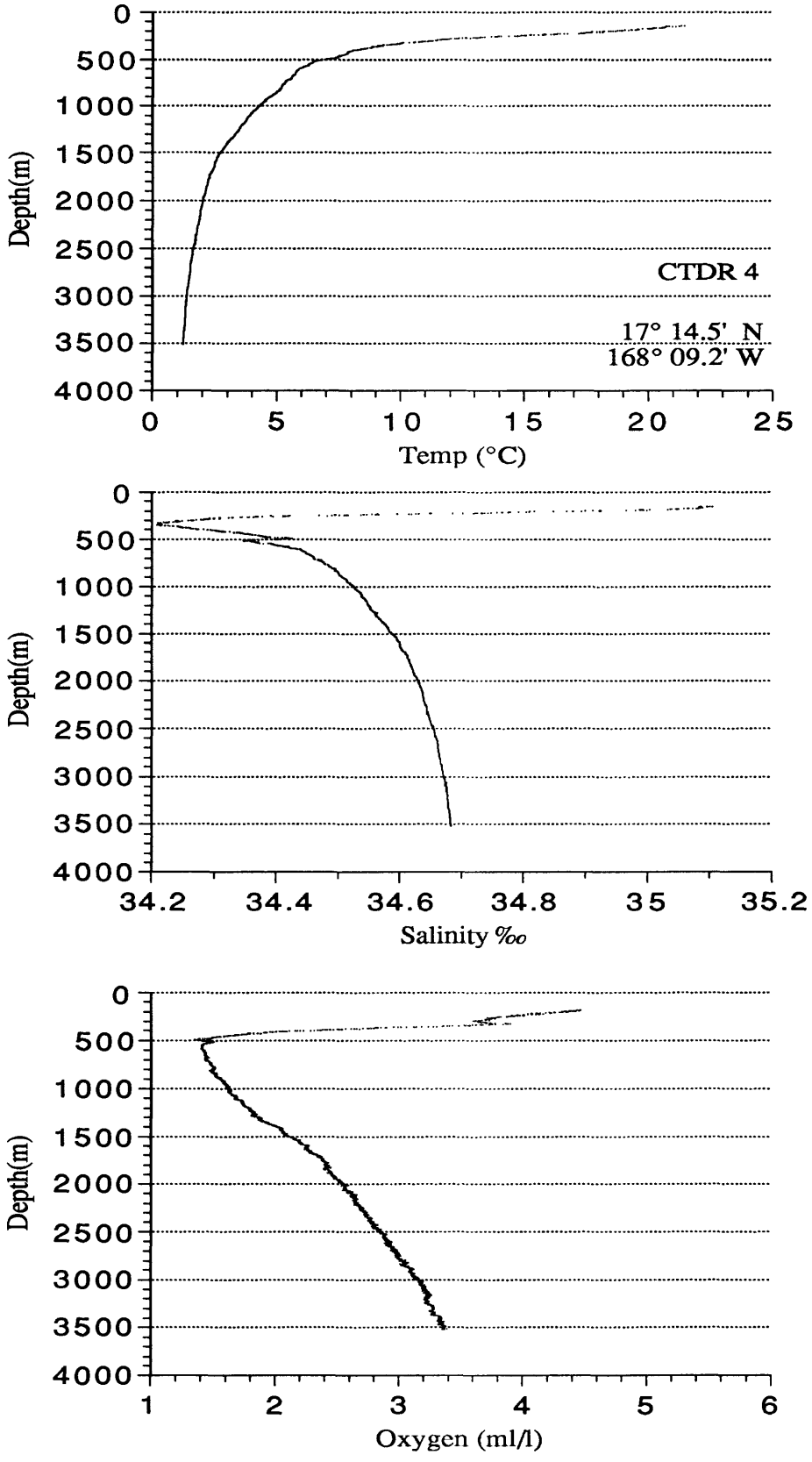

Figure 8. Temperature, salinity, and oxygen content versus water depth for CTDR 4, northern flank, Karin Ridge. Water depth at station is 5100 meters.

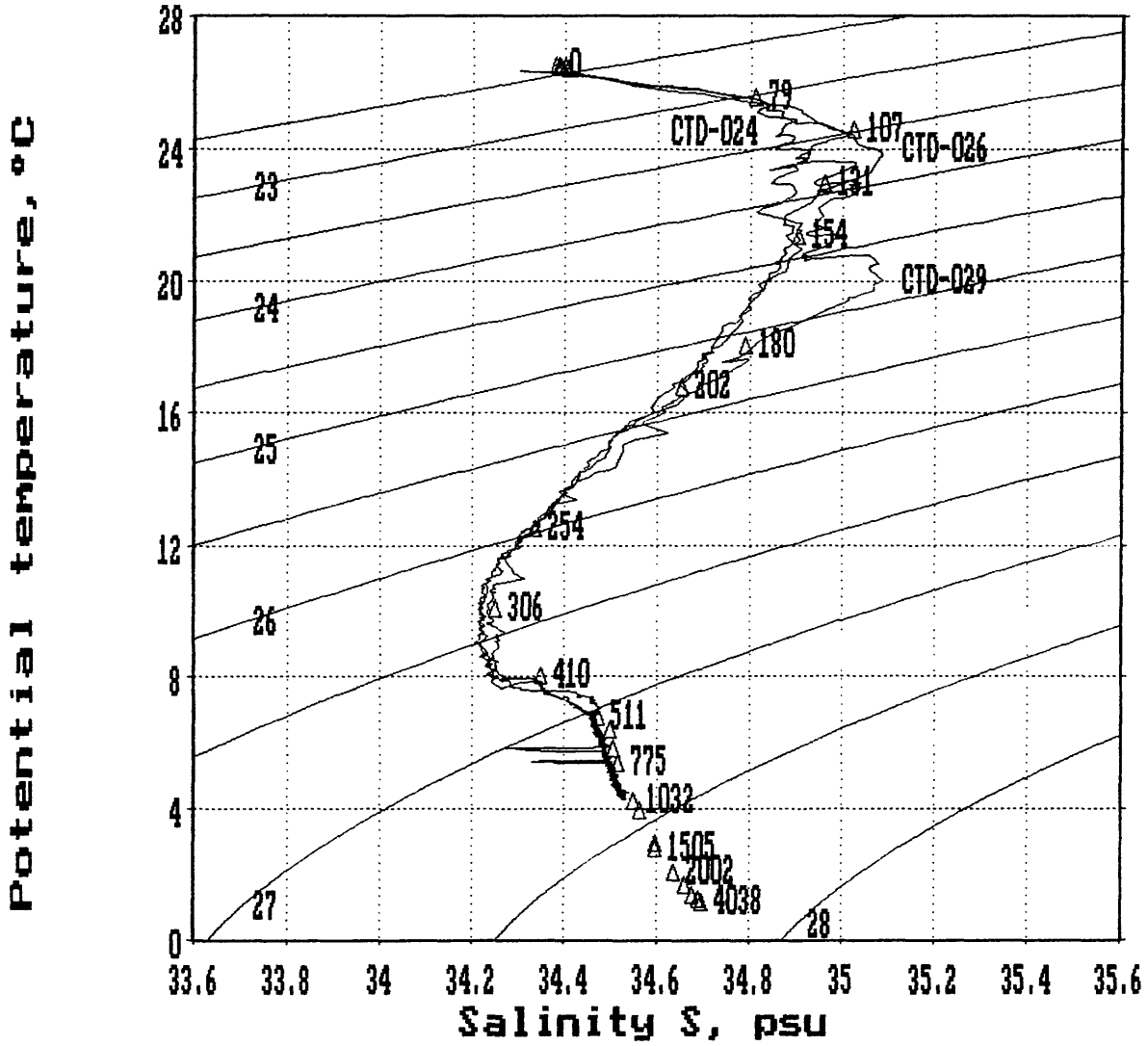

Figure 9. Hydrocast HS-14 and CTD-024, 026, and 029 potential temperature versus salinity diagram over the southwestern flank of Karin Ridge. Numbers beside the plot are depths in meters; subhorizontal lines are isopyknes.

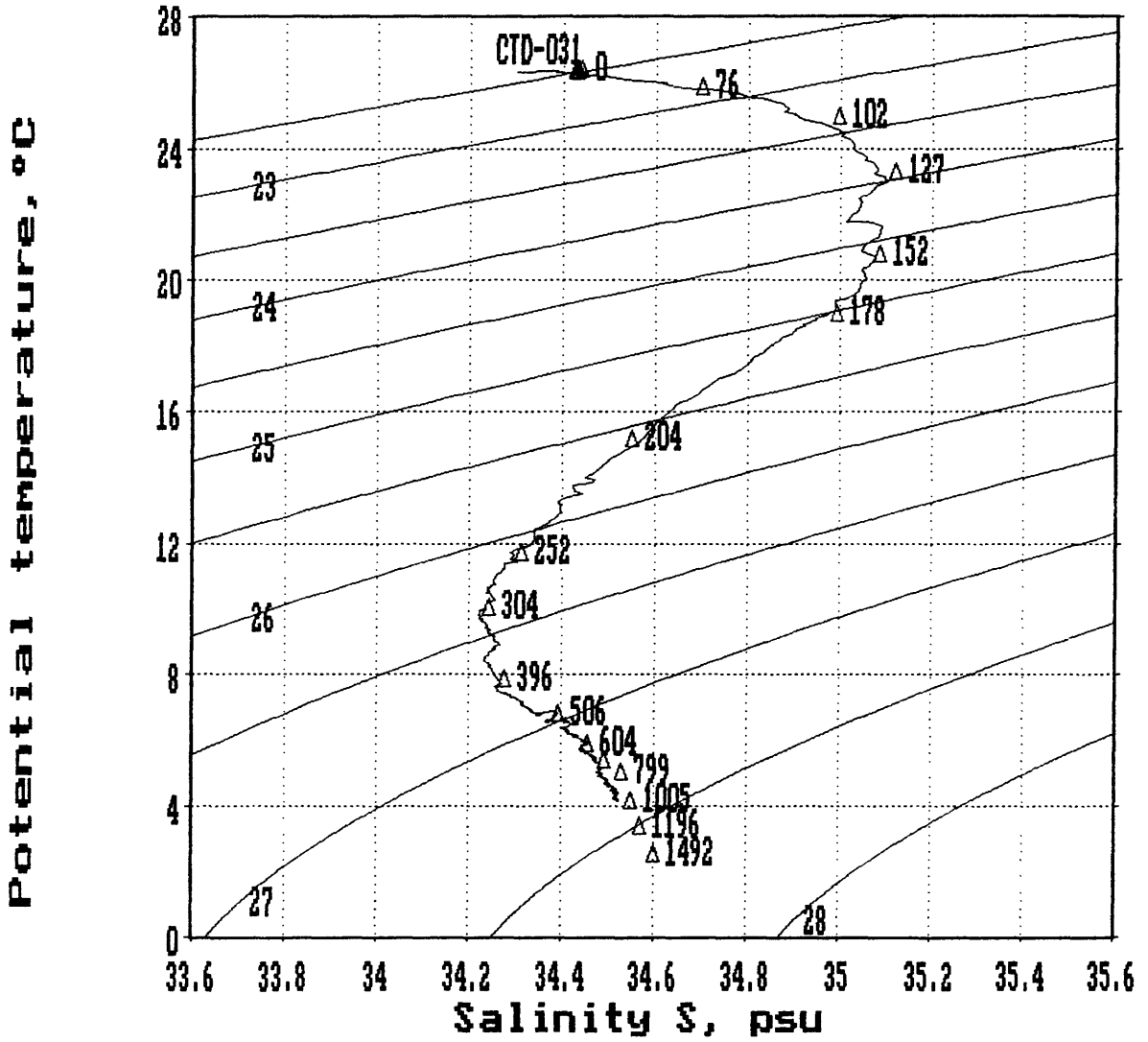

Figure 10. Hydrocast HS-15 and CTD-031 potential temperature versus salinity diagram over the northern top of Karin Ridge. Numbers beside the plot are depths in meters; subhorizontal lines are isopyknes.

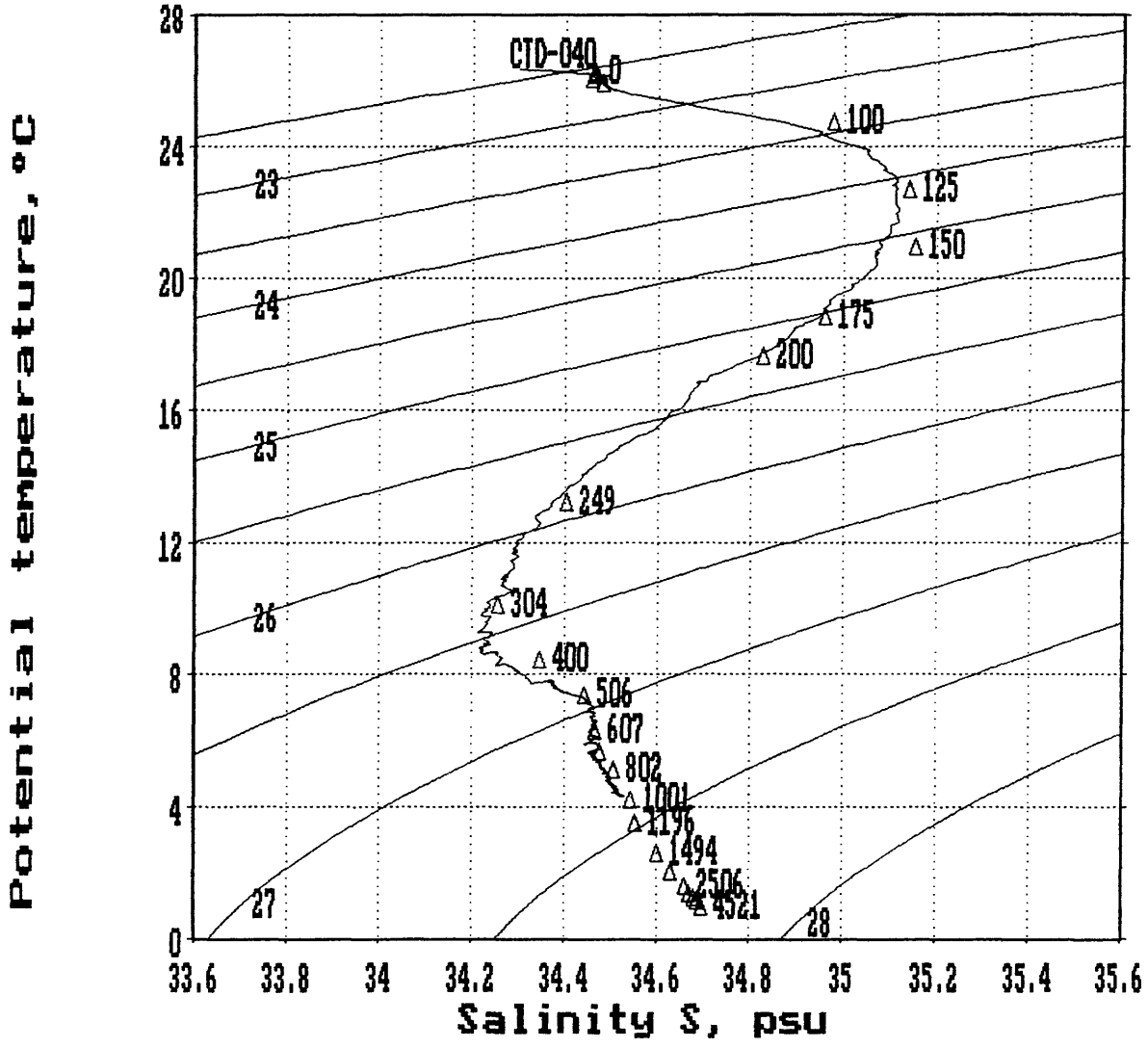

Figure 11. Hydrocast HS-16 and CTD-040 potential temperature versus salinity diagram over the northeastern flank of Karin Ridge. Numbers beside the plot are depths in meters; subhorizontal lines are isopyknes.

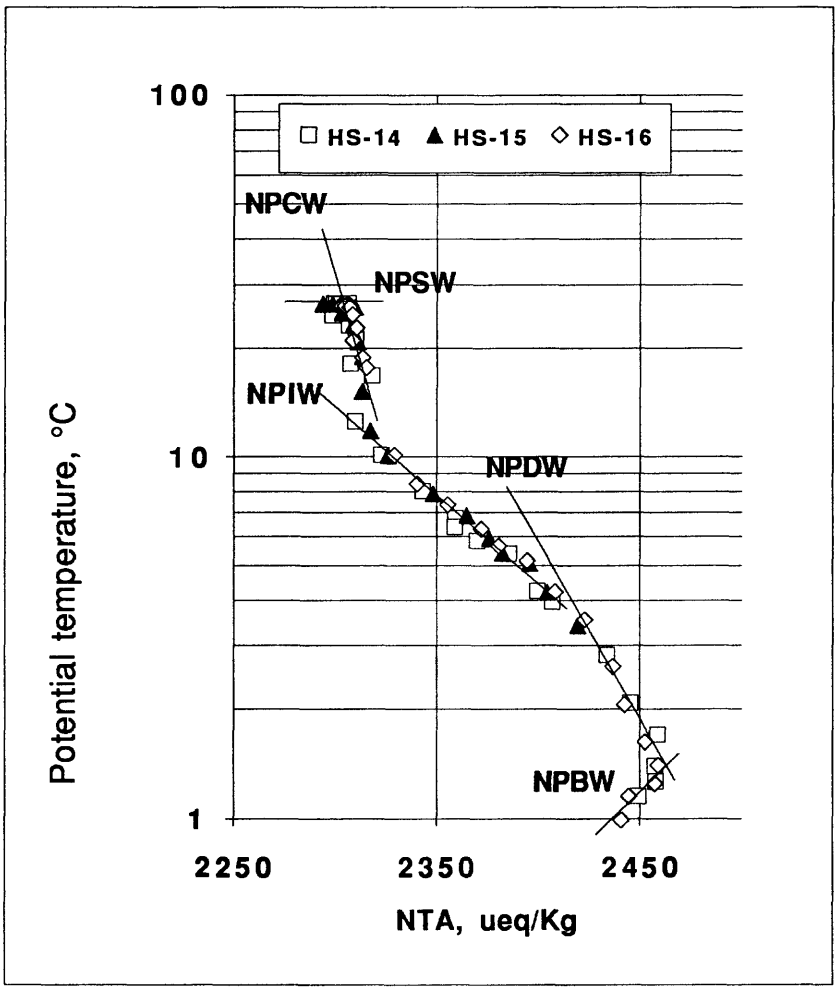

Figure 12. Potential temperature versus normalized total alkalinity diagram over Karin Ridge area. NPSW - North Pacific Surface Water, NPCW - North Pacific Subsurface (Central) Water, NPIW - North Pacific Intermediate Water, NPDW - North Pacific Deep Water, NPBW - North Pacific Bottom Water.

-PAGE 187 FOLLOWS-

HYDROCHEMICAL PARAMETERS AND THE CARBONATE SYSTEM, KARIN RIDGE AREA

Alexander S. Bychkov, Galina Yu. Pavlova, Pavel Ya. Tishchenko, and Anatoly Salyuk

Pacific Oceanological Institute, Far Eastern Branch, Russian Academy of Sciences, 43 Baltiyskaja, Vladivostok 690041, Russia

INTRODUCTION

The carbonate system in seawater is one of the most complex topics in oceanography. This system has long interested oceanographers from various fields because it plays an important role in all the subspheres of our planet: biosphere, lithosphere, and hydrosphere. The carbonate system regulates pH in seawater (Skirrow, 1975) and directly affects the forms and migration of elements, as well as many sedimentological and geochemical processes taking place in the ocean. Accumulation of carbonate sediments is important for mineral formation on seamounts in particular.

Oceanographic investigations in the Karin Ridge area included the following goals: (a) to study the distribution of hydrochemical parameters affected by both shallow decomposition of organic matter and the dissolution of minerals dependent on pressure and temperature; (b) to estimate carbon fluxes generated by organic and inorganic sources; (c) to describe carbonate equilibrium *in situ* including pH, which are essential for manganese system calculations (Gramm-Osipov *et al.*, this volume); and (d) to examine water depths associated with calcium carbonate sedimentation: saturation horizon, lysocline, and compensation depth.

METHODS

Hydrocasts were performed over the northern central summit region (HS-15) and along southwestern (HS-14) and northeastern (HS-16) flanks of Karin Ridge (Table 1).

Seawater was collected using 10-liter PVC Niskin-type bottles. Temperature and pressure (depth) were determined by reversing thermometers with the main scale etched to 0.02°C. Potential temperature and density were calculated according to the polynomials of Bryden (1973) and Millero and Poisson (1981), respectively.

Salinity samples were collected and stored according to WOCE recommendations (Stalcup, 1991) and measurements were carried out on the Guildline Autosal (model 8400). Each sample was run three times. The salinometer was standardized daily with IAPSO standard seawater (batch P79).

Dissolved oxygen samples were taken and analyzed following the micro-Winkler technique (Carpenter, 1965; Culberson, 1991). Standardization and blank determination with potassium iodate prepared from pre-weighed crystals was done daily. A few checks were performed with Sagami potassium iodate standard solution. Both sets agreed well. To estimate apparent oxygen utilization, oxygen solubility was deduced from Weiss' equation (Weiss, 1970).

Nutrients (phosphate, nitrate, and silicate) were measured simultaneously on a Technicon Auto-Analyzer (Hager *et al.*, 1972). Each sample was run twice. Standardization using pre-weighed potassium iodate crystals was used before and after each 22-25 samples to correct instrumental drift during the analyses. Sagami nutrient solutions were applied periodically to control working standards and to establish the shape of the Beer's law curve.

Chlorophyll "a" was analyzed using the well-known fluorescence procedure of Strickland and Parsons (1968). The Turner Designs Fluorometer was calibrated by the spectrophotometric method just before the cruise.

Direct potentiometry was used for pH determination (Bates, 1973). Water was collected according to the recommendations for oxygen (Culberson, 1991) and measurements were conducted immediately after sampling. The analysis was made at 25±0.1° C with glass (OP-0718) and saturated calomel (OP-0830P) electrodes produced by Radelkis Co. (Hungary). Tris-seawater prepared according to Millero (1986) was used as a standard before and after each set. The pH value of this buffer and Nernst slope of the electrode pair were controlled with Russian commercial standards: 6.86 (phosphate buffer) and 4.01 (phtalate buffer). The estimated precision was ±0.006 pH.

The coulometric method (Johnson *et al.*, 1985; 1987) was applied for total inorganic carbon analysis. Samples were taken and stored in a manner described by Dickson and Goyet (1991). To prevent biological activity, the probes were treated with 50 µl of saturated mercuric chloride. For calibration, a stainless steel loop was filled with pure CO_2 (99. 99%) at ambient temperature and pressure. The result of measurement was compared with calculated loop content to ensure that the coulometric system operated adequately. Gas calibration was run at the beginning and end of each set. Every day seawater standards were analyzed to determine the quality of measurements dependent upon the following factors: the complete stripping of CO_2 from the sample, calibration and reproducibility of the automatic pipette delivery, and inaccuracy of current registration. A precision better than ±1 µmol/kg was achieved.

Samples for total alkalinity were obtained in the same manner as described by Dickson and Goyet (1991). They were analyzed during 12 hours by direct titration in an open cell of 25 ml of seawater with 0.02 N HCl (Methods, 1978). The acid was standardized daily with Na_2CO_3 solution prepared from pre-weighted crystals dissolved in deionized water free of CO_2. To remove carbon dioxide during titration the samples and standard were flushed with a continuous stream of air free of CO_2. The mixture of methylene blue and methyl red was used as an indicator. Titration was complete at pH 5.4-5.5 when the green color of the solution turned to pale pink. The precision estimated from analyses of replicates was ±5 µmol/kg.

Total calcium was determined by potentiometric EGTA titration (Kanamori and Ikegami, 1980; Krumgalz and Holzer, 1980). The solution of EGTA (~0.01 N) in 0.36 M NaCl was standardized daily with artificial seawater prepared according to Millero (1986). Calcium-selective electrode (developed at St. Petersburg University on the base of neutral carrier) and saturated KCl silver chloride reference electrode were used for end-point detection. Calcium concentration was calculated by Gran's method. A precision of better than ±10 µmol/kg was achieved.

Concentrations were converted from volumetric to weight units by using density of seawater calculated at the potential temperature for oxygen and temperature of measurements for nutrients, total inorganic carbon, total alkalinity, and total calcium.

The observed results are listed in Tables 3a-5c; abbreviations used are shown in Table 2.

RESULTS

Distribution of Hydrochemical Parameters

The distribution of hydrological parameters and water structure in the Karin Ridge area were described by Gibbs *et al.* (this volume). In Figs. 1-3, the salinity, temperature, and density profiles from water-bottle data are presented to point out some regularities in their behavior. It should be noted that five water masses were found in the study region: surface water (NPSW, above 70 m); subsurface water of elevated salinity (NPCW, 70-200 m); intermediate water characterized by salinity minimum (NPIW, 200-1500 m); deep water (NPDW, 1500-3300 m), and bottom water (NPBW, below 3300 m).

The oxygen distribution (Fig. 4) was similar to that found by others (Smetanin, 1962; Reid, 1965; Duedall and Coote, 1972; Craig *et al.*, 1981). The oxygen minimum zone (with O_2 contents less than 50 µmol/kg) falls in the NPIW between 450 m and 750 m. The minimum oxygen depth was located at about 600 m. The presence of an oxygen minimum is a reflection of the North Pacific circulation system where oxygen decreases downstream from its aeration source, and replenishment is primarily by vertical diffusion (Reid, 1965).

Apparent oxygen utilization (AOU) is a rough measure of the amount of oxygen consumed by oxidation since the waters left their surface source. It is calculated as the difference between the solubility of oxygen (Weiss, 1970) at potential temperature and salinity and the oxygen concentration. If we assume that a parcel of seawater was in equilibrium with the atmosphere before it sank, then a negative AOU means supersaturation with respect to atmospheric oxygen while a positive AOU means undersaturation. In the Karin Ridge area, the surface water above 100 m was supersaturated with oxygen (Table 4a-4c; Fig. 5). Oxidation occurs primarily in the intermediate waters that bring a large organic load from high latitudes (Chen *et al.*, 1986), therefore maximum AOU values (about 260 µmol/kg) are found at depths of approximately 550 m to 1150 m (Fig. 5).

It has long been known that the oxygen minimum water originates in the deep water of the northern North Pacific and is associated with nutrients maxima (Bogojavlensky, 1955; Chen *et al.*, 1986). The vertical distributions of both phosphate (Fig. 6) and nitrate (Fig. 7) show the maxima in NPIW near 1000 m, only slightly deeper than the oxygen minimum. However, the silicate maximum is quite broad and is located in the NPDW at about 3000 m (Fig. 8). This situation is to be expected because silicate is not

remineralized along with the organic matter (Edmond, 1974). The nutrient concentrations were very low (for nitrate even zero) in the surface water above 100 m, agreeing with high biological productivity for the study area.

The vertical distribution of pH (25) (pH at 25°C and 1 atm) is shown in Fig. 9. This parameter was practically constant for NPSW, decreased with depth for subsurface and upper layers of intermediate waters, achieved minimum values of about 7.57 in NPIW between 550 m and 1150 m, continuously increased with depth within NPDW, and was uniform, representing the end of pH trend, for NPBW. Park (1968a, b) discussed two pertinent factors that affect the vertical distribution of pH, AOU and $CaCO_3$ dissolution. In the Karin Ridge area, the pH minimum generally coincided with the AOU maximum, but deep and bottom water trends were mainly caused by calcium carbonate dissolution.

Total alkalinity variations (Fig. 10) down to about 400 m mainly followed changes in salinity (Fig. 1), reflecting its extreme values at depths of approximately 150 m and 350 m. Below the minimum, the distributions of TA and NTA showed the same pattern (Figs. 10 and 26). The normalized total alkalinity was uniform for NPSW and increased with depth for NPCW and NPIW, consistent with previous work (Chen *et al.*, 1986). The further alkalinity increase in the NPDW was a result of calcium carbonate dissolution. The highest values (more than 2430 μeq/kg for TA and 2450 μeq/kg for NTA) were found between 2500 m and 3500 m. For the NPBW, total alkalinity decreased toward the bottom.

The existence of the NTA maximum in the deep Pacific was noted previously (Fiadeiro, 1980; Takahashi *et al.*, 1981; Chen *et al.*, 1986). In the Karin Ridge area the lysocline was determined to be at about 3800 m (See following section: *Saturation degree of $CaCO_3$*). Theoretically, the increasing NTA trend should be found below this depth because of acceleration of calcium carbonate dissolution (Berger, 1967, 1968). Nevertheless, the maximum NTA range is shallower than both the lysocline and the carbonate compensation depth (Fig. 26). This situation can be explained (Chen *et al.*, 1986) if the dissolution rate of $CaCO_3$ in the study region is not rapid enough to overcome the flushing of the low alkalinity bottom water originating from the Southern Ocean (Edmond *et al.*, 1971).

Total alkalinity data confirmed that this parameter can be used as a water mass tracer (Koczy, 1956; Fiadeiro, 1980; Chen *et al.*, 1986; Pavlova *et al.*, 1989). Five linear potential temperature-NTA trends representing different water masses were identified (Fig. 13 - Gibbs *et al.*, this volume). In the surficial 70 m layer (NPSW), NTA forms a line roughly parallel to the x-axis on the plot. Between 70 m and 200 m (NPCW), an insignificant rise in NTA at a rate about 1 μeq/kg/°C corresponds to a temperature decrease. For NPIW (200-1500 m) this trend has a steeper slope (13 μeq/kg/°C) indicating a higher rate of alkalinity input. The NPDW is characterized by an additional increase of NTA (17 μeq/kg/°C) as a result of calcium carbonate dissolution in the undersaturated water. Below a water depth of 3300 m (NPBW), NTA falls with decreasing temperature.

The total inorganic carbon distribution (Fig. 11) is similar to that of AOU and pH (Figs. 6 and 9). TCO_2 and pH are strongly related to the production and consumption of organic matter, therefore, the resemblance is not surprising. The surface TCO_2, which is affected by biological activity and temperature (Chen *et al.*, 1986), was nearly constant down to 100 m. For NPCW and NPIW this parameter increased continuously with depth. The highest values (more than 2345 μmol/kg for TCO_2 or 2370 μmol/kg for $NTCO_2$) were found for NPDW between 1500 m and 2500 m. The maximum TCO_2 range was at a depth of several hundred meters deeper than the AOU maximum and pH minimum core, because calcium carbonate dissolution contributes to the increase of the total inorganic carbon. Below 3000 m the TCO_2 decreased towards the bottom. The explanation for this fact is that the delivery rate of low alkalinity and TCO_2 bottom water in that region is higher than the rate of $CaCO_3$ dissolution (Edmond *et al.*, 1971).

The total calcium concentration (TCa) is plotted in Fig. 12. This distribution seems to follow that of salinity (Fig. 1). Maximum (10247 μmol/kg) and minimum (~10000 μmol/kg) TCa coincided with the salinity extreme values and occurred at the depths of 150 m and about 350 m respectively. TCa rapidly increased between the depth of the calcium minimum and approximately 1500 m, while below it TCa rose uniformly. Normalized calcium is known to be useful for studying water mass circulation mixing and diffusion in the Pacific Ocean (Tsunogai *et al.*, 1973; Horibe *et al.*, 1974; Shiller and Gieskes, 1980; Chen *et al.*, 1982, 1986; Olson, 1982). The too few samples available gave no possibility to consider NTCa-salinity and NTCa-potential temperature correlations for the Karin Ridge area. It should be only noted that generally the NTCa values increased monotonically with depth (Tables 4a-4c) mainly as a result of calcium carbonate dissolution (Tsunogai *et al.*, 1973; Horibe *et al.*, 1974; Brewer *et al.*, 1975; Shiller and Gieskes, 1980; Tsunogai and Watanabe, 1981; Chen *et al.*, 1986).

Carbon Fluxes

General remarks

To estimate the carbon fluxes from different sources, the approach proposed by Chen (Chen, 1978; 1990; Chen *et al.*, 1982; 1986) has been used. Following are the main features:

(a) The combined effect of the dissolution of x moles of $CaCO_3$ and decomposition of y moles of organic matter in 1 kg seawater on the changes of carbonate parameters, nitrate, and oxygen concentrations can be represented as:

$$\Delta NTA = NTA - NTA^\circ = 2x - 17y \quad (1)$$

$$\Delta NTCO_2 = NTCO_2 - NTCO_2^\circ = x + 106y \quad (2)$$

$$\Delta NNO_3 = NNO_3 - NNO_3^\circ = 16y \quad (3)$$

$$\Delta NCa = NCa - NCa^\circ = 0.46288\Delta NTA + 0.074236\Delta NTCO_2 = 0.5\Delta NTA - 0.63\Delta NNO_3 \quad (4)$$

$$\Delta AOU = AOU - AOU^\circ = 138y \quad (5)$$

The above scheme is based on stoichiometry $C:N:P:O_2=106:16:1:(-138)$ for organic matter suggested by Redfield *et al.* (1963). In equation (4), the coefficient 0.63 for nitrate, rather than 0.53, is used to take into consideration the effect of sulfur on TA (Brewer *et al.*, 1975; Chen, 1978).

(b) The ratio of the *in situ* inorganic carbon flux to organic carbon flux can be calculated from equation:

$$IC/OC = x/106y = [0.16038(\Delta TCO_2 + 40) + \Delta TA]/[2(\Delta TCO_2 + 40) - \Delta TA] \quad (6)$$

where $\Delta TCO_2 = TCO_2 - NTCO_2^\circ * S/35$ and $\Delta TA = TA - NTA^\circ * S/35$ (7)

Chen *et al.* (1982) pointed out the importance of the contribution of the fossil fuel CO_2 to the IC/OC ratio and recommended subtractacting an anthropogenic CO_2 signal equal to 40 μmol/kg (Chen and Millero, 1979) from the TCO_2° values.

(c) Previous attempts to evaluate the *in situ* $CaCO_3$ dissolution or organic carbon decomposition (Brewer *et al.*, 1975; Chen, 1978; Tsunogai and Watanabe, 1981) were based on local surface hydrochemical data as references. This method leaves the erroneous impression that differences in concentrations between deep and surface waters should represent the vertical inorganic or organic carbon flux. However, deep water may simply have different initial (pre-formed) chemical properties than surface waters (Edmond *et al.*, 1979; Shiller and Gieskes, 1980). In this case a large portion of the apparent carbonate parameter concentration increase is probably not due to *in situ* chemical processes, but rather due to transport by the water itself (Chen *et al.*, 1982, 1986).

It has long been accepted that the Southern Ocean is the main source of deep waters in the Pacific (Knauss, 1962). Therefore the hydrochemical winter data for the Weddell Sea were recommended as references (Chen, 1990): NCa°=10240 μmol/kg; NTA°=2386 μeq/kg; $NTCO_2^\circ$=2280 μmol/kg; NNO_3°=32.3 μmol/kg; AOU°=130 μmol/kg. The revised GEOSECS data south of 50° N were used to derive equations (Chen, 1990; Chen *et al.*, 1986):

$$NTA^\circ(\mu eq/kg) = 2384 - 4.2*\theta \quad \text{and} \quad NTCO_2^\circ(\mu mol/kg) = 2219 - 11*\theta \quad (8)$$

where θ is the potential temperature.

(d) The average replacement time for the deep North Pacific waters is approximately 600 years (Chen, 1990; Chen *et al.*, 1986).

Calcium carbonate dissolution rate

For deep and bottom waters (below 1500 m) in the Karin Ridge area, average normalized calcium was 10,279 μmol/kg (Tables 4a-4c), being only 39 μmol/kg higher than the Weddell sea value. The difference reflects the $CaCO_3$ flux relative to the water source. Dividing NCa by the average replacement time of the deep North Pacific water, also referenced to the Southern Ocean, we obtained the calcium carbonate dissolution rate of 0.065±0.012 μmol/kg/y (CDR3 in Tables 4a-4c; Fig. 13). Using equations (1)-(4) we obtain a calcium enrichment of 36.5 μmol/kg from NTA and NNO_3 data and 36 μmol/kg from NTA and $NTCO_2$ data (Tables 4a-4c), and, respectively, the calcium carbonate dissolution rate of 0.061±0.007 μmol/kg/y (CDR2 in Tables 4a-4c; Fig. 14) and 0.060±0.007 μmol/kg/y (CDR1 in Tables 4a-4c; Fig. 15). These values are in good agreement with our direct calcium results and the literature data summarized by Chen (1990). In this work, $CaCO_3$ fluxes equal 0.060±0.010 μmol/kg/y and 0.053±0.005 μmol/kg/y as determined from TCa and TA-NO_3 measurements. It should be noted that CDR1 and CDR2 show a tendency to increase with depth for deep water (1500-3000 m) and to decrease with depth for bottom water (below 3000 m).

Organic carbon decomposition rate

A similar method has been used to estimate the organic carbon decomposition rates in reference to the Weddell sea (Tables 4a-4c; Figs. 16-19). Preliminarily, the amount of carbon from organic sources was calculated in two principal ways: from AOU data (OCDR1 and OCDR11) and from equations (2) and (4) as the difference between ΔTCO_2 and ΔNCa (OCDR2 and OCDR3). The OCDR1 values were based on Redfield stoichiometry for organic matter (Eq. 5). The revised ratio for C:N:P:O = 103:16:1:(-172), as proposed by Takahashi *et al.* (1985), was used for the OCDR11 evaluation. The ΔNCa values were calculated from TA and TCO_2 measurements (OCDR2) or TA, TCO_2, and nitrate data (OCDR3). For the deep and bottom waters in the Karin Ridge area, the organic carbon decomposition rate continuously decreased with depth (Figs. 16-19). Below 2000 m the last three data sets were in good agreement with the average OCDR value of 0.071 μmol/kg/y. For these depths the average OCDR1 value was 0.092 μmol/kg/y. The most realistic organic carbon decomposition rates published in the literature for the North Pacific vary within a wide range, from 0.03 to 0.18 μmol/kg/y (Chen, 1990; Chen *et al.*, 1986).

Oxygen consumption rate

Oxygen consumption rates (OCR) reported elsewhere are 0.03-0.19 μmol/kg/y between 1 and 4 km water depths in the North Pacific (Craig, 1969; Chen, 1990). The latest estimate is 0.13±0.002 μmol/kg/y for the North Pacific waters deeper than 2000 m (Chen, 1990). In the Karin Ridge area, OCR values, calculated (Eq. 5) from the deep Weddell sea and our AOU data (Tables 4a-4c) and the replacement time mentioned above, were practically constant for intermediate water and then continuously decreased from 0.15 to 0.07 μmol/kg/y (Tables 4a-4c; Fig. 20). However, the average value for the water depths below 1500 m was 0.12 μmol/kg/y.

Ratio of inorganic to organic carbon flux

IC/OC ratios, calculated from equations (6)-(8), are listed in Tables 4a-4c and are shown in Fig. 21. This parameter increased markedly from 0.1 to 0.35 between 500 m and 2500 m, then was essentially constant with increasing water depths, reflecting the high degradation rates of organic tissue in the upper water column. Thus, our analyses indicate that inorganic $CaCO_3$ dissolution contributes about 26% of the total CO_2 increase in the deep water during its journey from the Southern Ocean to the Karin Ridge area. The oxidation of organic matter generates the larger part of the TCO_2 increase, about 75% for waters deeper than 2500 m.

These results agree well with the few other estimates for the North Pacific: 29% (IC/OC=0. 40) between 1 and 4.5 km (Tsunogai, 1972) and 26% (IC/OC=0. 35) below 2.5 km (Chen, 1990). Lower values in the deep Pacific were reported based on the box model, 20% (Li *et al.*, 1969) and on carbon-13 data, 17% (Kroopnick, 1974). Edmond (1974) found the IC/OC ratio equal to 0.26 at a water depth of 3000 m in the Northeast Pacific, which is probably an underestimate as a result of ignoring the correction for excess CO_2 (Chen *et al.*, 1986; Chen, 1990).

In situ Carbonate Equilibrium

Among the primary objectives for the detailed investigation of the carbonate system in seawater are the *in situ* determination of the partial pressure of carbon dioxide, the carbonate ion concentration, and the pH. The former is important in studies of CO_2 exchange between the atmosphere and the ocean and the second in studies of seawater saturation with respect to calcium carbonate. The pH is essential to determine the forms and migration of elements.

Detailed description of the thermodynamics of the CO_2 system and relations between carbonate parameters (pH, TA, TCO_2, and pCO_2) and species (CO_2, HCO_3^-, CO_3^{2-}, and $B(OH)_4^-$) in seawater is given in the literature (Park, 1969; Skirrow, 1975; Millero, 1979; UNESCO, 1987). The scheme recommended to determine *in situ* carbonate equilibrium is based on the assumption that total alkalinity is the sum of three ionic species: HCO_3^-, CO_3^{2-} and $B(OH)_4^-$ (Edmond and Gieskes, 1970; Skirrow, 1975). To realize this approach the combination of at least two carbonate parameters together with appropriate constants at *in situ* temperature, salinity, and pressure are necessary.

For this investigation the following equations and constants were applied:

- Equation proposed by Weiss (1974) to represent the CO_2 gas solubility as a function of temperature and salinity in accordance with Murray and Riley's (1971) and Weiss' (1974) measurements;

- Equations recommended by Millero (1979) for the temperature and salinity dependence of the apparent dissociation constants for carbonic and boric acids in seawater determined by Mehrbach *et al.* (1973) and Lyman (1956), respectively;
- The partial molal volumes and compressibilities presented by Millero (1979, 1982, 1983) to estimate the pressure effect on the dissociation of carbonic and boric acids in seawater;
- The total borate concentration in seawater assumed to be proportional to salinity based on the summary of Culkin (1965).

The various combinations of measuring the parameters and their subsequent use in the carbon dioxide system calculation have been discussed by Park (1969). UNESCO (1987) Expert Group advocated the determination of TA and TCO_2 as they are independent of temperature and pressure and, especially because each quantity is of intrinsic interest in chemical oceanography. But recently, it was shown that the best pairs to characterize the CO_2 system in the ocean are pH-TCO_2 or pCO_2-TCO_2 (Millero, 1993). In this work the carbonate equilibrium was computed from all available sets: pH-TA, TA-TCO_2, and pH-TCO_2. The results were in satisfactory agreement and only data obtained from the last pair are listed in Tables 5a-5c.

The main features of the pH (p,t) vertical distribution (Fig. 22) practically repeated those of pH (25) (Fig. 9). The lowest pH (p,t) values were found for the oxygen minimum range in the NPIW.

The pCO_2 vertical distribution is shown in Fig. 23. The pCO_2 was essentially constant through the surface water. Different processes regulate the pCO_2 in this layer including photosynthesis, exchange with the atmosphere, and removal of $CaCO_3$ from seawater by shell-building biota (Skirrow, 1975). Below the photic zone and particularly in the NPIW, organic debris is oxidized to CO_2. Therefore, the pCO_2 maximum core located between 450 m and 800 m and coincides with the oxygen and pH minimum range. The behavior of pCO_2 in NPDW was determined by its expenditure on the $CaCO_3$ dissolution (Broecker and Takahashi, 1977). The same process and also the input of low TCO_2 bottom water (Edmond *et al.*, 1971) were responsible for further decreases of pCO_2 below 3500 m.

The carbonate ion distribution for the surface, subsurface, and intermediate waters (Fig. 24) is similar to those of oxygen (Fig. 4) and pH (Fig. 22). This situation is to be expected as the oxidation of organic matter leads to a fall of pH and, accordingly, to the decrease of the CO_3^{2-} concentration in spite of the total inorganic carbon increase. For the NPDW, the concentration of CO_3^{2-} ion continuously increased because the calcium carbonate dissolution contributes to the rise of TCO_2. The increasing CO_3^{2-} trend was obtained also for the NPBW under the TCO_2 maximum. For this water, the pH change probably overcomes the TCO_2 fall.

Water Depths of Calcium Carbonate Sedimentation

Background

Three water depths characterize the calcium carbonate sedimentation in the ocean. The saturation horizon is the depth at which seawater is just saturated with respect to $CaCO_3$ (Skirrow, 1975). The lysocline marks a depth of a sharp increase in the rate of $CaCO_3$ dissolution (Berger, 1967, 1968, 1970). The carbonate compensation depth corresponds to the horizon where an abrupt decrease in abundance of $CaCO_3$ in the sediments occurs (Berger *et al.*, 1976; Biscaye *et al.*, 1976; Kolla *et al.*, 1976). In kinetic terms, the position of the CCD coincides with a depth at which the rate of sedimentation equals that of dissolution (Skirrow, 1975).

A convenient measure of seawater saturation with respect to $CaCO_3$ is the degree of saturation defined as the ion product of the calcium and carbonate concentrations at *in situ* temperature, salinity, and pressure, divided by the apparent solubility products of calcite and aragonite under the same conditions:

$$L_c = (Ca^{2+}) \times (CO_3^{2-}) / K'_c \quad (9)$$

$$L_a = (Ca^{2+}) \times (CO_3^{2-}) / K'_a \quad (10)$$

When L_c or $L_a > 1$, seawater is supersaturated with respect to calcite or aragonite, and conversely, when L_c or $L_a < 1$, seawater is undersaturated with respect to these minerals. The value L_c or $L_a = 1$ corresponds to the saturation horizon. It should be mentioned that the rate of $CaCO_3$ dissolution, and therefore the position of the lysocline and CCD depth, depends on the degree of saturation (Morse and Berner 1972; Morse, 1978; Keir, 1980).

Since the concentrations of the carbonate ions in seawater cannot be directly determined, they were calculated from measured variables such as pH, total inorganic carbon, and total alkalinity, using the

equations of Millero (1979, 1982, 1983) wherein the effect of temperature, salinity, and pressure on the dissociation constants for the carbonate system are described. Calcium data exist only for stations HS-14 and HS-16, therefore calcium concentration was estimated from the salinity and the calcium to salinity ratio (Millero, 1979; Takahashi *et al.*, 1980).

The apparent solubility product of calcite and aragonite in seawater at 1 atm total pressure were taken from works of Ingle (Ingle *et al.*, 1973; Ingle, 1975) and Mucci (1983), respectively. These measurements were verified by a number of studies and were recommended by UNESCO (1987) Expert Group, which selected the equations to represent the temperature and salinity dependence for K'_c and K'_a. The pressure effect on the solubility was estimated from partial molal volume and compressibility data for both minerals and calcium and carbonate ions presented by Millero (1979, 1982, 1983).

Saturation degree of $CaCO_3$

The results obtained from the best pair pH-TCO_2 (Millero, 1993) are listed in Tables 5a-5c and in Figs. 24-26.

Surface water in the Karin Ridge area was highly oversaturated with respect to calcite and aragonite. This fact is in a good agreement with the high temperature (Lyakhin, 1968) and low TCO_2 to TA ratio (Feely *et al.*, 1984) for the surface water in the study region. For the subsurface and intermediate waters, the L_c and L_a were primarily governed by the carbonate ion concentration. Therefore, the fall of pH and consequently CO_3^{2-} (Figs. 22 and 24) caused by the oxidation of organic matter, coincided with a sharp decrease in the saturation degree of $CaCO_3$ between 75 m and 500 m (Figs. 25 and 26). Only small variations of this value were found for the AOU maximum and pH minimum area. The general increasing trend of CO_3^{2-} concentration (Fig. 24) and the continuous decrease in the degree of saturation (Figs. 25 and 26) below the depth at about 1500 m indicate the main role of the apparent solubility product for the deep waters. The L_i distribution in NPDW and NPBW was a consequence of the pressure and temperature effect on the K_i value.

The saturation horizon occurs at the depth 380-390 m for aragonite (Table 5a-5c; Fig. 25) and between 1500 m and 2000 m for calcite (Table 5a-5c; Fig. 26). According to Feely *et al.* (1988), the deepening of the calcite saturation horizon in this region is explained by intensified vertical mixing south of the Subtropical Front. So, practically all of Karin Ridge is located in water undersaturated with respect to both aragonite and calcite. Possibly, only around the top of the ridge is the seawater close to saturation. The scatter of data contributes too much noise for the calcite saturation horizon to be more precisely defined.

Relationship between saturation horizon, lysocline, and CCD

The relationship among the saturation horizon, lysocline, and carbonate compensation depth was investigated intensively to understand the mechanisms that control the distribution of the calcium carbonate sediments (Li *et al.*, 1969; Edmond and Gieskes, 1970; Heath and Culberson, 1970; Lisitzin, 1972; Takahashi, 1975; Broecker and Takahashi, 1978; Chen *et al.*, 1986, 1988).

To determined the position of the lysocline, Peterson (1966) and Berger (1967) performed the well known *in situ* experiment for calcite dissolution in the Central North Pacific (18°49'N, 168°31'W), not far from Karin Ridge, and found that the rate of $CaCO_3$ dissolution increases sharply at the depth of about 3700 m (Fig. 26).

An indirect approach to studying the lysocline was worked out by examining the difference between the pH for calcite-seawater equilibrium and the *in situ* pH (Morse and Berner, 1972; Berner and Morse, 1974). A ΔpH of 0.15 was proposed as an indicator of an abrupt increase in the calcite dissolution rate. For the Karin Ridge area this value gave a lysocline depth of 3200 m (Fig. 26). Later, a ΔpH of 0.08, rather than 0.15, was suggested to be correct (Takahashi, 1975). This later value coincides with the calcite saturation degree of 0.9 (Berner and Wilde, 1972). We adopted this last value as a qualitative reference for the lysocline (Chen *et al.*, 1986) and the depth of about 3400 m was determined for the study region (Fig. 26). In the experiment mentioned above (Morse and Berner, 1972), it was shown that the increase in the calcite dissolution rate took place when ΔCO_3^{2-} exceeded 10 μmol/kg. The ΔCO_3^{2-} is the difference between the carbonate ion concentration for calcite-seawater equilibrium and *in situ*. The depth of the lysocline estimated from ΔCO_3^{2-} (~ 3800 m) is consistent with that determined by Peterson (Fig. 26).

Berger *et al.* (1976) summarized the data on the distribution of $CaCO_3$ in the surface sediments of the Pacific Ocean. Between 15°N and 20°N the carbonate compensation depth was placed at 4200-4400 m, close to the 0.83 L_c contour (Fig. 26).

According to our estimates and also Broecker and Takahashi (1978), Plath *et al.* (1980), and Pytkowicz (1983), the uncertainty in the determination of the saturation horizon ranges from 16 to 35%. Even taking into consideration the maximum value, the saturation horizon in the Karin Ridge area is much shallower than the lysocline and CCD depths. The difference in the water depths of $CaCO_3$ sedimentation can be explained only by kinetics.

CONCLUSIONS

As a result of the oceanographic work performed in the Karin Ridge area, the following conclusions are made:

- All hydrochemical parameters studied show a core structure underlying the salinity minimum layer, nevertheless they can be divided into two groups. The vertical distributions of oxygen, phosphate, nitrate, and pH are affected mainly by the shallow decomposition of organic matter. The oxidation occurs primarily in intermediate waters, which bring a large organic load from high latitudes and therefore, the extreme values of this parameters are located in NPIW at a water depth of about 1000 m. Silicate, total alkalinity, total inorganic carbon, and calcium are also (or mostly) released by minerals dissolution, which is enhanced by pressure increase and temperature decrease. Hence, for these substances the maximum core occurs in NPDW.

- Total alkalinity can be used as a water mass tracer. Different water masses have different trends, which can be identified by the correlation of normalized total alkalinity with potential temperature;

- The calcium data give a $CaCO_3$ flux of 0.065±0.012 µmol/kg/y for waters deeper than 1500 m, referenced to the Weddell sea deep water. The total alkalinity data combined with nitrate or total inorganic carbon results indicate a $CaCO_3$ dissolution rate of 0.061±0.007 µmol/kg/y and 0.060±0.007 µmol/kg/y, respectively. For the same conditions the average organic carbon decomposition rate ranges between 0.071 and 0.092 µmol/kg/y and the corresponding average oxygen consumption rate is 0.12 µmol/kg/y.

- About 26% of the total CO_2 increase in the deep water during its journey from the Southern Ocean to the Karin Ridge area is contributed by inorganic $CaCO_3$ dissolution.

- The carbonate equilibrium *in situ* including pH and the degree of saturation with respect to calcite and aragonite was calculated from all available data sets: pH-TCO_2, pH-TA, and TCO_2-TA. The calcite saturation horizon was found at a depth of approximately 2000 m, much shallower than that of both the lysocline (about 3800 m) and carbonate compensation depth (4200-4400 m).

REFERENCES

Bates, R.G., 1973, Determination of pH theory and practice: Wiley, N.Y., 386 p.

Berger, W.H., 1967, Foraminiferal ooze: Solutions of depths: Science, v. 156, p. 383-385.

Berger, W.H., 1968, Planktonic foraminifera: Selective solution and paleoclimatic interpretation: Deep-Sea Research, v.15, p. 31-43.

Berger, W.H. 1970, Planktonic foraminifera: Selective solution and lysocline: Marine Geology, v. 8, p. 111-138.

Berger, W.H., Adelesk, C.G., and Mayer, L.A., 1976, Distribution of carbonate in surface sediments of the Pacific Ocean: Journal of Geophysical Research, v. 81, p. 2617-2627.

Berner, R.A. and Morse, J.W., 1974, Dissolution kinetics of $CaCO_3$ in seawater. IV. Theory of calcite dissolution: American Journal of Science, v. 274, p. 108-134.

Berner, R.A. and Wilde, P., 1972, Dissolution kinetics of $CaCO_3$ in seawater. I. Saturation state parameters for kinetics calculations: American Journal of Science, v. 272, p. 826-839.

Biscaye, P.E., Kolla, V., and Turekian, K.K., 1976, Distribution of calcium carbonate in surface sediments of the Atlantic Ocean: Journal of Geophysical Research, v. 81, p. 2595-2603.

Bogojavlensky, A.N., 1955, Chemistry of the Kuril-Kamchatka Trench waters: Trudy Instituta Okeanologii Akademiya Nauk SSSR, v. 12, p. 161-176 (In Russian).

Brewer, P.G., Wong, G.T.F., Bacon, M.P., and Spencer, D.W., 1975, An oceanic calcium problem: Earth and Planetary Science Letters, v. 26, p. 81-87.

Broecker, W.S. and Takahashi, T., 1977, Neutralization of fossil fuel CO_2 by marine calcium carbonate: *in* Andersen, N.R. and Malahoff, A. (eds.), The Fate of Fossil Fuel CO_2 in the Oceans. Plenum Press, N.Y., p. 213-241.

Broecker, W.S. and T. Takahashi, 1978, The relationship between lysocline depth and *in situ* carbonate ion concentration: Deep-Sea Research, v. 35, p. 65-95.
Bryden, H.L., 1973, New polynomials for thermal expansion, adiabatic temperatures gradient and potential temperature of sea water: Deep-Sea Research, v. 20, p. 401-408.
Carpenter, J.H., 1965, The Chesapeake Bay Institute technique for the Winkler dissolved oxygen method: Limnology and Oceanography, v. 10, p. 141-143.
Chen, C.T., 1978, Decomposition of calcium carbonate and organic carbon in the deep oceans: Science, v. 201, p. 735-736.
Chen, C.T., 1990, Rates of calcium carbonate dissolution and organic carbon decomposition in the North Pacific Ocean: Journal of the Oceanographic Society of Japan, v. 46, p. 201-210.
Chen, C.T. and Millero, F.J., 1978, Gradual increase of oceanic carbon dioxide: Nature, v. 277, p. 205-206.
Chen, C.T., Feely, R.A., and Gendron, J.F., 1988, Lysocline, calcium carbonate compensation depth, and calcareous sediments in the North Pacific Ocean: Pacific Science, v. 42, p. 237-252.
Chen, C.T., Pytkowicz, R.M., and Olson, E.J., 1982, Evaluation of the calcium problem in the South Pacific: Geochemical Journal, v. 16, p. 1-10.
Chen, C.T., Rodman, M.R., Wei, C.L., and Olson, E.J., 1986, Carbonate chemistry of the North Pacific Ocean: U.S. Dept. of Energy Technical Report DOE/NBB-0079, 176 p.
Craig, H., 1969, Abyssal carbon and radiocarbon in the Pacific: Journal of Geophysical Research, v. 74, p. 5491-5506.
Craig, H., Broecker, W.S., and Spencer, D., 1981, GEOSECS Pacific Expedition, sections and profiles: National Science Foundation, Washington, D.C., v.4 , 251 p.
Culberson, C.H., 1991, Dissolved oxygen: *in* WOCE Operations Manual, WHP Operations and Methods. WOCE Report No 68/91, p. 1-15.
Culkin, F., 1965, The major ion components of seawater: *in* J.P. Riley and G. Skirrow (eds.) Chemical Oceanography. Academic Press, N.Y., v. 1, p. 121-162.
Dickson, A.G. and Goyet, C., 1991, Handbook of methods for the analysis of the various parameters of the carbon dioxide system in seawater: U.S. Department of Energy publication 89-7A.
Duedall, I.W. and Coote, A.R., 1972, Oxygen distribution in the Pacific Ocean: Journal of Geophysical Research, v. 77, p. 2201-2203.
Edmond, J.M., 1974, On the dissolution of carbonate and silicate in the deep ocean: Deep-Sea Research, v. 21, p. 455-480.
Edmond, J.M. and Gieskes, J.M., 1970, On the calculation of the degree of saturation of seawater with respect to calcium carbonate under *in situ* conditions: Geochimica et Cosmochimica Acta, v. 34, 1261-1291.
Edmond, J.M., Chung, Y., and Sclater, J.G., 1971, Pacific bottom water: Penetration east around Hawaii: Journal of Geophysical Research, v. 76, p. 8089-8097.
Edmond, J.M., Jacobs, S.S., Gordon, A.L., *et al.*, 1979, Water column anomalies in dissolved silica over opaline pelagic sediments and the origin of the deep silica maximum: Journal of Geophysical Research, v. 84, p. 7809-7826.
Feely, R.A., Byrne, R.H., Betzer, P.R., Gendron, J.F., and Acker, J.G., 1984, Factors influencing the degree of saturation of the surface and intermediate waters of the North Pacific Ocean with respect to aragonite: Journal of Geophysical Research, v. 89, p. 10631-10640.
Feely, R.A., Byrne, R.H., Acker, J.G., Betzer, P.R., Chen, C.T., Gendron, J.F., and Lamb, M., 1988, Winter-summer variations of calcite and aragonite saturation in the Northeast Pacific: Marine Chemistry, v. 25, p. 227-241.
Fiadeiro, M., 1980, The alkalinity of the deep Pacific: Earth and Planetary Science Letters, v. 49, p. 499-505.
Gibbs, A.E., Sergeev, A.F., Salyuk, A.N., Hein, J.R., Tapinov, V.P., and Bychkov, A.S., 1994, Hydrological parameters and water structure over Karin Ridge, Central Pacific: this volume, p. 169-186.
Gramm-Osipov, L.M., Hein, J.R., and Chichkin, R.V., 1994, Manganese geochemistry in the Karin Ridge region: Preliminary physiochemical description: this volume, p. 99-102.
Hager, S.W., Atlas, E.L., Gordon, L.I., Mantyla, A.W., and Park, P.K., 1972, A comparison at sea of manual and autoanalyzer analyses of phosphate, nitrate and silicate: Limnology and Oceanography, v. 17, p. 931-937.
Heath, G.R. and C.H. Culberson, 1970, Calcite: Degree of saturation, rate of dissolution and the compensation depth in the deep oceans: Geological Society of America Bulletin, v. 81, p. 3157-3160.
Horibe, Y., Endo, K., and Tsubota, H., 1974, Calcium in the South Pacific and its correlation with carbonate alkalinity: Earth and Planetary Science Letters, v. 23, p. 136-140.

Ingle, S.E., 1975, Solubility of calcite in the ocean: Marine Chemistry, v. 3, p. 301-319.
Ingle, S.E., Culberson, C.H., Hawley, J.E., and Pytkowicz, R.M., 1973, The solubility of calcite in seawater at 1 atm pressure and 35% salinity: Marine Chemistry, v. 1, p. 295-307.
Johnson, K.M., King, A.E., and Sieburth, J.M., 1985, Coulometric TCO_2 analyses for marine study: An introduction: Marine Chemistry, v. 16, p. 61-82.
Johnson, K.M., Williams, P.J., Brandstrom, L., and Sieburth, J.M., 1987, Coulometric TCO_2 analysis for marine studies: Automation and calibration: Marine Chemistry, v. 21, p. 117-133.
Kanamori, S. and Ikegami, H., 1980, Computer-processed potentiometric titration for the determination of calcium and magnesium in seawater: Journal of the Oceanographic Society of Japan, v. 36, p. 177-184.
Keir, R.S., 1980, The dissolution kinetics of biogenic calcium carbonates in seawater: Geochimica et Cosmochimica Acta, v. 44, p. 241-252.
Koczy, F.F., 1956, The specific alkalinity: Deep-Sea Research, v. 3, p. 279-288.
Knauss, J.A., 1962, On some aspects of the deep circulation of the Pacific: Journal of Geophysical Research, v. 67, p. 3943-3954.
Kolla, V., Be, A.W., and Biscaye, P.E., 1976, Calcium carbonate distribution in the surface sediments of the Indian Ocean: Journal of Geophysical Research, v. 81, p. 2605-2616.
Kroopnick, P., 1974, Correlations between C-13 and sigma CO_2 in surface waters and atmospheric CO_2: Earth and Planetary Science Letters, v. 22, p. 497-503.
Krumgalz, B. and Holzer, R., 1980, On the determination of Ca^{2+} concentration in seawater: Limnology and Oceanography, v. 25, p. 367-370.
Li, Y.-H., Takahashi, T., and Broecker, W.S., 1969, Degree of saturation of $CaCO_3$ in the oceans: Journal of Geophysical Research, v. 74, p. 5507-5525.
Lisitzin, A.P., 1972, Sedimentation in the World Ocean with emphasis on the nature, distribution, and behavior of marine suspensions: Society for Sedimentary Geology (SEPM) Special Publication 17, 218p.
Lyakhin, Y.I., 1968, Calcium carbonate saturation of Pacific water: Oceanology, v. 10, p. 789-795.
Lyman, J., 1956, Buffer mechanism of seawater: Unpublished Ph.D. Thesis, Univ. of California, Los Angeles, 196 p.
Mehrbach, C., C.H. Culberson, J.E. Hawley, and R.M. Pytkowicz, 1973, Measurement of the apparent dissociation constants of carbonic acid in seawater at atmospheric pressure: Limnology and Oceanography, v. 18, p. 897-907.
Methods of the hydrochemical investigations in the ocean, 1978. Nauka, Moscow, 271 p. (In Russian).
Millero, F.J., 1979, The thermodynamics of the carbonate system in seawater: Geochimica et Cosmochimica Acta, v. 43, p. 1651-1661.
Millero, F.J., 1982, The effect of pressure on the solubility of minerals in water and seawater: Geochimica et Cosmochimica Acta, v. 46, p.11-22.
Millero, F.J., 1983, Influence of pressure on chemical processes in the sea: *in* J.P. Riley and R. Chester (eds.) Chemical Oceanography. Academic Press, N.Y., v. 8, p. 1-88.
Millero, F.J., 1986, The pH of estuarine waters: Limnology and Oceanography, v. 31, p. 839-847.
Millero, F.J., 1993, Describing the ocean CO_2 system: U.S. JGOFS News, v. 44, p. 7-14.
Millero, F.J. and A. Poisson, 1981, International one-atmosphere equation of state of sea water: Deep-Sea Research, v. 28, p. 625-629.
Morse, J.W., 1978, Dissolution kinetics of calcium carbonate in seawater. VI. The near equilibrium dissolution kinetics of calcium carbonate rich sea sediments: American Journal of Science, v. 278, p. 243-261.
Morse, J.W. and Berner, R.A., 1972, Dissolution kinetics of calcium carbonate in seawater. I. A kinetic origin for lysocline: American Journal of Science, v. 272, p. 840-851.
Mucci, A., 1983, The solubility of calcite and aragonite in seawater at various salinities, temperatures and one atmosphere total pressure: American Journal of Science, v. 283, p. 780-799.
Murray, C.N. and Riley, J.P., 1971, The solubility of gases in distilled water and seawater. IV. Carbon dioxide: Deep-Sea Research, v. 18, p. 533-541.
Olson, E.J., 1982, Calcium in the Equatorial Pacific Ocean: Unpublished M.S. Thesis, Oregon State University, 84 p.
Park, K., 1968a, The processes contributing to the vertical distribution of apparent pH in the Northeastern Pacific Ocean: Journal of the Oceanographic Society of Korea, v. 3, p. 1-7.
Park, K., 1968b, Seawater hydrogen-ion concentration: Vertical distribution: Science, v. 162, p. 357-358.
Park, K., 1969, Oceanic CO_2 system: Evaluation of ten methods of investigation: Limnology and Oceanography, v. 14, p. 179-186.

Pavlova, G.Yu., Stashchuk, M.F., and Bychkov, A.S., 1989, Carbonate system as a water mass characteristic in the Northwestern Pacific: Doklady AN SSSR, v. 305, p. 973-976 (In Russian).
Peterson, M.N.A., 1966, Calcite: Rate of dissolution in a vertical profile in the central Pacific: Science, v. 154, p. 1542-1544.
Plath, D., Johnson, K.S., and Pytkowicz, R.M., 1980, The solubility of calcite probably containing magnesium in seawater: Marine Chemistry, v. 10, p. 9-29.
Pytkowicz, R.M., 1983, Solubility of carbonates and related processes: *in* Equilibrium Nonequilibrium and Natural waters. Wiley, N.Y., Chap. 5.
Redfield, A.C., Ketchum, B.H., and Richards, F. , 1963, The influence of organisms on the composition of seawater: *in* M.N. Hill (ed.) The Sea. Wiley, N.Y., v. 2, p. 26-77.
Reid, J.L., 1965, Intermediate waters of the Pacific Ocean: The Johns Hopkins Oceanographic Studies, No 2, 85 p.
Shiller, A.M. and Gieskes, J.M., 1980, Processes affecting the oceanic distribution of dissolved calcium and alkalinity: Journal of Geophysical Research, v. 85, p. 2719-2727.
Skirrow, G., 1975, The dissolved gases - carbon dioxide: *in* J.P. Riley and G. Skirrow (eds.) Chemical Oceanography. Academic Press, N.Y., v.2, p. 1-192.
Smetanin, D.A., 1962, Features of the chemistry of water in the central Pacific: Trudy Instituta Okeanologii Akademiya Nauk SSSR, v. 40, p. 58-71 (In Russian).
Stalcup, M.C., 1991, Salinity measurement: *in* WOCE Operations Manual, WHP Operations and Methods. WOCE Report No.68/91, p. 1-17.
Strickland, J.D.H. and Parsons, T.R., 1968, A practical handbook of sea water analysis. Fish.Res.Board Can., Ottawa, v. 177, 240 p.
Takahashi, T., 1975, Carbonate chemistry of seawater and the calcite compensation depth in the oceans: *in* W.S. Sliter, A.W.H. Be, and W.H. Berger (eds.) Dissolution of deep-sea carbonates. Cushman Foundation, Special Publication 13, p. 159-178.
Takahashi, T., Broecker, W.S., Bainbridge, A.E., and Weiss, R.F., 1980, Carbonate chemistry of the Atlantic, Pacific and Indian oceans: Results of the GEOSECS expedition 1972-1978: Technical Report ICU 1-8, Lamont-Doherty Geological Observatory, N.Y.
Takahashi, T., Broecker, W.S., and Bainbridge, A.E., 1981, The alkalinity and total carbon dioxide concentration in the world ocean. *in* B. Bolin (ed.) Carbon Cycle Modeling. SCOPE 16, p. 271-286.
Takahashi, T., Broecker, W.S., and Langer, S., 1985, Redfield ratio based on chemical data from isopycnal surfaces: Journal of Geophysical Research, v. 90, p. 6907-6924.
Tsunogai, S., 1972, An estimate of the rate of decomposition of organic matter in the deep water of the Pacific Ocean: *in* Y. Takenouti (ed.) Biological Oceanography of the Northern North Pacific. Idemitsu Shoten, Tokyo, p. 517-533.
Tsunogai, S. and Watanabe, Y., 1981, Calcium in the North Pacific water and the effect of organic matter on the calcium-alkalinity relation: Geochemical Journal, v. 15, p. 95-107.
Tsunogai, S., Yamahata, H., Kudo, S., and Saito, O., 1973, Calcium in the Pacific Ocean: Deep-Sea Research, v. 20, p. 717-726.
UNESCO, 1987, Thermodynamics of the carbon dioxide system in seawater: UNESCO Technical Papers in Marine Science, v. 42, 55 p.
Weiss, R.F., 1970, The solubility of nitrogen, oxygen and argon in water and seawater: Deep-Sea Research, v. 17, p. 721-735.
Weiss, R.F., 1974, Carbon dioxide in water and seawater: The solubility of non-ideal gas: Marine Chemistry, v. 2, p. 203-215.

Table 1. Locations of hydrochemical stations in the Karin Ridge area.

Station	UTC		Location		Bottom	Water
	Date	Time	Lat., N	Long., W	depth, m	depth, m[1]
HS-14	14-May-91	01h05m	16° 33.0'	168° 27.4'	5100	4038
HS-15	18-May-91	13h20m	17° 09.8'	168° 28.7'	1550	1492
HS-16	21-May-91	20h50m	17° 14.9'	168° 11.1'	5210	4521

[1] Maximum water depth of sampling

Table 2. Symbols, units, and abbreviations used in the text and tables.

AOU	apparent oxygen utilization, μmol/kg
CCD	carbonate compensation depth, m
CCDR	calcium carbone dissolution rate, μmol/kg/y
Chl.a	chlorophyll "a" concentration, μg/l
IC/OC	inorganic to organic carbon ratio
K'_a	apparent solubility product of aragonite
K'_c	apparent solubility product of calcite
L_a	aragonite saturation degree
L_c	calcite saturation degree
NO_3	nitrate concentration, μmol/kg
NPBW	North Pacific Bottom Water
NPCW	North Pacific Subsurface Water
NPDW	North Pacific Deep Water
NPIW	North Pacific Intermediate Water
NPSW	North Pacific Surface Water
NTA	normalized total alkalinity, μeqv/kg (=TA×35/S)
NTCa	normalized total calcium concentration, μmol/kg (=TCa×35/S)
$NTCO_2$	normalized total inorganic carbon, μmol/kg (=TCO_2×35/S)
O_2	oxygen concentration, μmol/kg
OCDR	organic carbon decomposition rate, μmol/kg/y
OCR	oxygen consumption rate, μmol/kg/y
pCO_2	partial pressure of carbon dioxide, ppm
pH(25)	pH at 25°C temperature and one atmosphere total pressure
pH(p,t)	pH at *in situ* temperature and pressure
PO_4	phosphate concentration, μmol/kg
S	salinity, psu
SiO_4	silicate concentration, μmol/kg
TA	total alkalinity, μeqvl/kg
TCa	total calcium concentration, μmol/kg
TCO_2	total inorganic carbon, μmol/kg

Table 3. Hydrochemical data from the Karin Ridge area.

Corrected depth m	Temp. °C	Salinity psu	Potential temp. °C	O_2 µmol/kg	PO_4 µmol/kg	NO_3 µmol/kg	SiO_4 µmol/kg	TCO_2 µmol/kg	TA µeql/kg	TCa µmol/kg	pH (25) NBS	Chl.a µg/l
HS-14												
0	26.52	34.380	26.52	203	0.10	0.0	1.6	1914.0	2259	10061	8.24	0.025
11	26.50	34.385	26.498	202	0.10	0.0	1.6	1913.5	2259	10062	8.25	0.056
22	26.46	34.390	26.455	203	0.10	0.0	1.5	1914.8	2261	10047	8.26	0.047
34	26.49	34.401	26.482	202	0.10	0.0	1.3	1915.1	2267	10043	8.26	0.050
53	26.45	34.406	26.438	204	0.10	0.0	1.5	1915.3	2261	10041	8.26	0.050
79	25.61	34.811	25.592	208	0.08	0.0	1.5	1942.7	2291	10158	8.25	0.091
107	24.63	35.022	24.607	210	0.06	0.0	1.7	1957.7	2300	10203	8.24	0.110
131	23.02	34.960	22.993	207	0.15	0.0	1.9	1989.3	2304	10173	8.19	--
154	21.43	34.904	21.400	197	0.24	1.1	2.7	2016.0	2304	10165	8.14	--
180	18.10	34.791	18.069	172	0.54	5.7	4.9	2056.3	2294	10141	8.04	--
202	16.84	34.653	16.807	167	0.69	7.8	6.1	2071.8	2295	10095	7.99	--
254	12.54	34.337	12.506	154	1.22	16.0	14.4	2110.3	2266	10023	7.89	--
306	10.12	34.250	10.084	143	1.58	21.5	23.7	2146.1	2273	9975	7.81	--
374	8.77	34.237	8.730	123	1.81	24.5	29.2	2170.5	--	10015	7.74	--
410	8.06	34.349	8.018	67	2.49	33.2	43.9	2240.8	2300	10025	7.62	--
511	6.80	34.474	6.752	38	2.85	38.5	56.4	2283.2	2324	10085	7.58	--
586	6.44	34.499	6.386	36	2.94	39.7	62.2	2293.0	2325	10087	7.57	--
670	5.89	34.508	5.831	46	3.00	41.0	68.9	2301.3	2337	10109	7.57	--
775	5.44	34.518	5.374	45	3.00	41.8	76.2	2310.0	2353	10116	7.56	--
1032	4.32	34.551	4.238	54	3.04	42.4	94.5	2327.3	2369	10142	7.60	--
1096	4.04	34.563	3.955	58	3.03	42.2	99.1	2330.3	2377	10143	7.58	--
1505	2.92	34.596	2.811	77	2.91	40.8	128.8	2344.4	2406	10156	--	--
2002	2.22	34.636	2.078	113	2.82	39.8	143.7	2349.2	2420	10161	7.64	--
2505	1.88	34.659	1.699	126	2.74	38.8	149.6	2346.0	2435	10176	7.66	--
3002	1.62	34.677	1.397	129	2.65	37.8	152.2	2339.5	2435	10181	7.70	--
3515	1.54	34.690	1.266	132	2.58	37.0	152.1	2331.7	2436	10195	7.71	--
4038	1.48	34.696	1.150	154	2.52	36.1	147.1	2321.3	2428	10181	7.71	--
HS-15												
0	26.43	34.439	26.430	204	0.09	0.0	1.5	1916.1	2257	--	8.22	--
10	26.42	34.426	26.418	201	0.09	0.0	1.5	1916.1	2268	--	8.24	--
20	26.43	34.432	26.425	209	0.10	0.0	1.5	1915.5	2266	--	8.24	--
31	26.41	34.426	26.403	204	0.09	0.0	1.5	1915.5	2269	--	8.24	--
52	26.41	34.430	26.398	206	0.09	0.0	1.5	1916.5	2261	--	8.24	--
76	25.93	34.700	25.913	210	0.07	0.0	1.5	1934.5	2290	--	8.23	--
102	25.02	34.998	24.998	209	0.06	0.0	1.5	1953.7	2303	--	8.23	--
127	23.37	35.119	23.344	208	0.07	0.0	1.5	1982.9	2317	--	8.20	--
152	20.86	35.088	20.831	194	0.23	1.4	2.1	2024.9	2317	--	8.12	--
178	19.02	34.994	18.988	188	0.38	3.3	3.2	2041.9	2313	--	8.08	--
204	15.23	34.551	15.199	155	0.94	11.1	9.2	2090.9	2284	--	7.94	--
252	11.78	34.313	11.747	141	1.43	18.0	17.3	2127.4	2272	--	7.83	--
304	10.07	34.243	10.034	139	1.69	21.5	24.1	2149.3	2276	--	7.79	--

Table 3. continued

Corrected depth m	Temp. °C	Salinity psu	Potential temp. °C	O_2 µmol/kg	PO_4 µmol/kg	NO_3 µmol/kg	SiO_4 µmol/kg	TCO_2 µmol/kg	TA µeql/kg	TCa µmol/kg	pH (25) NBS	Chl.a µg/l
HS-15	**cont.**											
396	7.92	34.277	7.880	81	2.40	30.8	44.3	2225.1	2300	--	7.66	--
506	6.88	34.393	6.832	48	2.80	36.8	58.6	2274.4	2324	--	7.57	--
604	5.98	34.458	5.927	44	2.96	39.2	70.1	2295.0	2339	--	7.56	--
701	5.47	34.493	5.410	51	2.99	40.2	77.2	2302.9	2348	--	7.57	--
799	5.12	34.531	5.053	52	3.02	40.7	84.8	2309.1	2364	--	7.57	--
1005	4.28	34.551	4.201	57	3.07	41.4	100.0	2326.4	2374	--	7.57	--
1196	3.50	34.571	3.411	62	3.07	41.1	114.5	2340.5	2390	--	7.59	--
1492	2.64	34.597	2.536	78	2.97	41.0	131.0	2347.6	--	--	7.61	--
HS-16												
0	26.26	34.463	26.260	204	0.10	0.0	1.5	1921.0	2267	10038	8.23	0.047
10	26.20	34.462	26.198	203	0.12	0.0	1.5	1920.3	2272	10048	8.24	0.052
20	26.17	34.459	26.166	204	0.10	0.0	1.5	1920.9	2269	10044	8.23	0.057
30	26.17	34.463	26.163	204	0.12	0.0	1.5	1920.2	2268	10058	8.24	0.067
50	26.06	34.458	26.049	208	0.00	0.0	1.5	1919.4	2269	10029	8.24	0.082
75	25.93	34.479	25.913	208	0.15	0.0	1.5	1922.7	2273	10043	8.24	0.083
100	24.79	34.975	24.768	216	0.15	0.0	1.5	1957.6	2307	10204	8.23	0.126
125	22.76	35.139	22.734	212	0.14	0.0	1.7	1956.7	2320	10235	8.18	--
150	21.02	35.153	20.991	195	0.23	0.5	2.1	2021.4	2319	10247	8.14	--
175	18.88	34.959	18.849	185	0.41	3.5	3.2	2049.3	2311	10191	8.07	--
200	17.68	34.828	17.646	177	0.53	5.7	4.7	2061.0	2304	10154	8.03	--
249	13.23	34.402	13.195	148	1.18	15.1	13.4	2110.9	--	10041	7.88	--
304	10.13	34.258	10.094	137	1.67	21.8	23.9	2149.7	2280	10014	7.80	--
400	8.46	34.348	8.418	69	2.40	31.6	41.1	2232.2	2297	10041	7.63	--
506	7.41	34.443	7.360	41	2.81	36.6	53.0	2271.3	2318	10091	7.56	--
545	6.61	34.415	6.559	43	2.87	38.3	61.2	2280.6	--	10075	--	--
596	6.70	34.497	6.644	35	2.93	39.3	60.8	2287.9	--	10105	--	--
607	6.35	34.467	6.294	41	2.92	39.0	64.9	2291.7	2336	10089	7.56	--
648	6.13	34.457	6.072	40	2.95	39.6	67.6	2294.1	--	10101	--	--
701	5.73	34.478	5.669	46	2.99	39.9	74.1	2301.3	2345	10116	7.56	--
802	5.20	34.505	5.133	53	3.05	40.9	82.7	2311.7	2361	10122	7.55	--
1001	4.30	34.543	4.221	55	3.08	41.9	99.3	2329.6	2377	10135	7.57	--
1196	3.62	34.553	3.530	67	3.07	41.7	112.8	2339.3	2392	--	7.57	--
1494	2.73	34.599	2.625	83	2.96	41.0	132.1	2348.7	2409	--	7.60	--
2001	2.20	34.630	2.059	114	2.87	38.8	142.5	2346.9	2417	10177	7.63	--
2506	1.80	34.659	1.620	123	2.76	38.0	149.5	2344.5	2429	10182	7.66	--
3018	1.63	34.670	1.405	135	2.69	--	152.7	2341.6	2436	--	7.71	--
3510	1.52	34.680	1.247	133	2.65	36.6	152.1	2333.4	2435	10188	7.68	--
4023	1.48	34.687	1.152	153	2.57	36.0	146.3	2321.3	2423	--	7.71	--
4521	1.37	34.696	0.988	167	2.49	--	138.1	2306.5	2420	10194	7.73	--

-- = no data available. See Table 2 for explanation of units and abbreviations.

Table 4. Summary of estimated oxygen consumption (OCR), organic carbon decomposition (OCDR), carbonate dissolution (CDR) rates, and inorganic/organic carbon ratio (IC/OC) in the Karin Ridge area.

Corrected depth meters	AOU	NNO_3	$NTCO_2$	NTA	NTCa	OCR	OCDR1	OCDR11	OCDR2	OCDR3	CDR1	CDR2	CDR3	IC/OC
	µm/kg	µm/kg	µm/kg	µeq/kg	µm/kg	µm/kg/y	µm/kg/y	µm/kg/y	µm/kg/y	µm/kg/y	µm/kg/y	µm/kg/y	µm/kg/y	
HS-14														
0	-1	0.0	1949	2300	10242	--	--	--	--	--	--	--	--	--
11	0	0.0	1948	2299	10242	--	--	--	--	--	--	--	--	--
22	-1	0.0	1949	2301	10225	--	--	--	--	--	--	--	--	--
34	0	0.0	1948	2306	10218	--	--	--	--	--	--	--	--	--
53	-2	0.0	1948	2300	10214	--	--	--	--	--	--	--	--	--
79	-3	0.0	1953	2303	10213	--	--	--	--	--	--	--	--	--
107	-2	0.0	1956	2299	10197	--	--	--	--	--	--	--	--	--
131	7	0.0	1992	2307	10185	--	--	--	--	--	--	--	--	--
154	23	1.1	2022	2310	10193	--	--	--	--	--	--	--	--	--
180	62	5.7	2069	2308	10202	--	--	--	--	--	--	--	--	--
202	72	7.9	2093	2318	10196	--	--	--	--	--	--	--	--	--
254	108	16.3	2151	2310	10216	--	--	--	--	--	--	--	--	--
306	133	22.0	2193	2323	10194	--	--	--	--	--	--	--	--	--
374	162	25.1	2219	--	10238	--	--	--	--	--	--	--	--	--
410	222	33.8	2283	2344	10215	--	--	--	--	--	--	--	--	--
511	259	39.0	2318	2359	10239	0.21	0.16	0.13	0.08	0.08	--	--	--	0.09
586	263	40.3	2326	2359	10233	0.22	0.17	0.13	0.09	0.09	--	--	--	0.08
670	257	41.6	2334	2370	10253	0.21	0.16	0.13	0.10	0.09	--	--	--	0.11
775	262	42.4	2342	2386	10257	0.22	0.17	0.13	0.10	0.09	--	--	--	0.14
1032	261	42.9	2358	2400	10274	0.22	0.17	0.13	0.11	0.11	0.020	0.023	0.057	0.17
1096	259	42.7	2360	2407	10272	0.22	0.17	0.13	0.11	0.10	0.026	0.028	0.053	0.18
1505	249	41.3	2372	2434	10275	0.20	0.15	0.12	0.10	0.10	0.048	0.050	0.058	0.25
2002	219	40.2	2374	2445	10268	0.15	0.11	0.09	0.10	0.10	0.057	0.058	0.047	0.29
2505	209	39.1	2369	2459	10276	0.13	0.10	0.08	0.08	0.08	0.067	0.068	0.061	0.34
3002	209	38.1	2361	2458	10276	0.13	0.10	0.08	0.07	0.07	0.065	0.066	0.060	0.35
3515	207	37.3	2353	2458	10286	0.13	0.10	0.08	0.06	0.06	0.064	0.065	0.077	0.37
4038	186	36.4	2342	2449	10270	0.09	0.07	0.06	0.05	0.05	0.056	0.057	0.051	0.35
HS-15														
0	-1	0.0	1947	2294	--	--	--	--	--	--	--	--	--	--
10	1	0.0	1948	2306	--	--	--	--	--	--	--	--	--	--
20	-7	0.0	1947	2303	--	--	--	--	--	--	--	--	--	--
31	-2	0.0	1947	2307	--	--	--	--	--	--	--	--	--	--
52	-4	0.0	1948	2298	--	--	--	--	--	--	--	--	--	--
76	-6	0.0	1951	2310	--	--	--	--	--	--	--	--	--	--
102	-3	0.0	1954	2303	--	--	--	--	--	--	--	--	--	--
127	4	0.0	1976	2309	--	--	--	--	--	--	--	--	--	--
152	28	1.4	2020	2311	--	--	--	--	--	--	--	--	--	--
178	42	3.3	2042	2313	--	--	--	--	--	--	--	--	--	--
204	92	11.3	2118	2314	--	--	--	--	--	--	--	--	--	--
252	125	18.3	2170	2317	--	--	--	--	--	--	--	--	--	--
304	137	22.0	2197	2326	--	--	--	--	--	--	--	--	--	--

Table 4. continued

Corrected depth meters	AOU	NNO_3	$NTCO_2$	NTA	NTCa	OCR	OCDR1	OCDR11	OCDR2	OCDR3	CDR1	CDR2	CDR3	IC/OC
	µm/kg	µm/kg	µm/kg	µeq/kg	µm/kg	µm/kg/y	µm/kg/y	µm/kg/y	µm/kg/y	µm/kg/y	µm/kg/y	µm/kg/y	µm/kg/y	
HS-15	**cont.**													
396	208	31.4	2272	2349	--	--	--	--	--	--	--	--	--	--
506	249	37.5	2315	2365	--	0.20	0.15	0.12	0.07	0.07	--	--	--	0.11
604	259	39.9	2331	2376	--	0.21	0.16	0.13	0.09	0.09	--	--	--	0.12
701	255	40.8	2337	2383	--	0.21	0.16	0.13	0.09	0.09	--	--	--	0.14
799	257	41.3	2340	2396	--	0.21	0.16	0.13	0.09	0.08	--	--	--	0.17
1005	259	41.9	2357	2405	--	0.21	0.16	0.13	0.10	0.10	0.024	0.026	--	0.18
1196	259	41.6	2370	2420	--	0.22	0.17	0.13	0.11	0.11	0.037	0.038	--	0.21
1492	250	41.5	2375	--	--	0.20	0.15	0.12	--	--	--	--	--	--
HS-16														
0	-1	0.0	1951	2302	10194	--	--	--	--	--	--	--	--	--
10	0	0.0	1950	2307	10205	--	--	--	--	--	--	--	--	--
20	-1	0.0	1951	2305	10201	--	--	--	--	--	--	--	--	--
30	-1	0.0	1950	2303	10214	--	--	--	--	--	--	--	--	--
50	-5	0.0	1950	2305	10187	--	--	--	--	--	--	--	--	--
75	-4	0.0	1952	2307	10195	--	--	--	--	--	--	--	--	--
100	-8	0.0	1959	2309	10211	--	--	--	--	--	--	--	--	--
125	2	0.0	1949	2311	10195	--	--	--	--	--	--	--	--	--
150	26	0.5	2013	2309	10202	--	--	--	--	--	--	--	--	--
175	45	3.5	2052	2314	10203	--	--	--	--	--	--	--	--	--
200	58	5.7	2071	2315	10204	--	--	--	--	--	--	--	--	--
249	110	15.4	2148	--	10215	--	--	--	--	--	--	--	--	--
304	139	22.2	2196	2329	10231	--	--	--	--	--	--	--	--	--
400	217	32.2	2275	2341	10231	--	--	--	--	--	--	--	--	--
506	251	37.2	2308	2355	10254	0.20	0.16	0.12	0.07	0.07	--	--	--	--
545	255	38.9	2319	--	10246	0.21	0.16	0.12	--	--	--	--	--	--
596	262	39.9	2321	--	10252	0.22	0.17	0.13	--	--	--	--	--	--
607	259	39.7	2327	2372	10245	0.22	0.17	0.13	0.08	0.08	--	--	--	0.12
648	261	40.3	2330	--	10260	0.22	0.17	0.13	--	--	--	--	--	--
701	259	40.5	2336	2381	10269	0.21	0.16	0.13	0.09	0.09	--	--	--	0.13
802	255	41.5	2345	2395	10268	0.21	0.16	0.12	0.09	0.09	--	--	--	0.16
1001	260	42.4	2360	2408	10270	0.22	0.17	0.13	0.11	0.10	0.027	0.029	0.049	0.19
1196	254	42.2	2370	2423	--	0.21	0.16	0.12	0.11	0.11	0.040	0.041	--	0.22
1494	245	41.5	2376	2437	--	0.19	0.15	0.11	0.11	0.11	0.051	0.052	--	0.26
2001	218	39.3	2372	2443	10286	0.15	0.11	0.09	0.10	0.10	0.055	0.055	0.077	0.28
2506	213	38.3	2368	2453	10282	0.14	0.11	0.08	0.08	0.08	0.062	0.062	0.071	0.32
3018	203	--	2364	2459	--	0.12	0.09	0.07	0.07	--	0.067	--	--	0.35
3510	206	36.9	2355	2457	10282	0.13	0.10	0.08	0.06	0.06	0.064	0.064	0.070	0.36
4023	187	36.3	2342	2445	--	0.10	0.07	0.06	0.05	0.05	0.053	0.053	--	0.33
4521	174	--	2327	2441	10283	0.07	0.06	0.04	0.03	--	0.048	--	0.072	0.34

-- = no data available; See Table 2 for explanation of units and abbreviations.

Table 5. Measured and calculated carbonate parameters for the Karin Ridge area.

Corrected depth meters	Temp. °C	Salinity psu	TCO_2 µm/kg	TA µeq/kg	pH(25) NBS	pH(p,t) NBS	CO_3 µm/kg	PCO_2 ppm	L_c	L_a	NTA µeq/kg
HS-14											
0	26.52	34.380	1914.0	2259	8.239	8.224	0.224	364	5.21	3.46	2300
11	26.50	34.385	1913.5	2259	8.250	8.235	0.229	353	5.32	3.53	2299
22	26.46	34.390	1914.8	2261	8.256	8.241	0.232	347	5.36	3.57	2301
34	26.49	34.401	1915.1	2267	8.257	8.242	0.233	347	5.37	3.57	2306
53	26.45	34.406	1915.3	2261	8.264	8.249	0.236	340	5.42	3.61	2300
79	25.61	34.811	1942.7	2291	8.247	8.239	0.233	347	5.29	3.52	2303
107	24.63	35.022	1957.7	2300	8.242	8.244	0.233	341	5.22	3.47	2299
131	23.02	34.960	1989.3	2304	8.193	8.210	0.213	369	4.70	3.13	2307
154	21.43	34.904	2016.0	2304	8.141	8.174	0.192	401	4.21	2.80	2310
180	18.10	34.791	2056.3	2294	8.044	8.112	0.157	458	3.39	2.26	2308
202	16.84	34.653	2071.8	2295	7.992	8.073	0.140	499	3.00	2.00	2318
254	12.54	34.337	2110.3	2266	7.887	8.015	0.109	554	2.34	1.56	2310
306	10.12	34.250	2146.1	2273	7.813	7.966	0.092	612	1.95	1.30	2323
374	8.77	34.237	2170.5	--	7.737	7.900	0.077	706	1.63	1.09	--
410	8.06	34.349	2240.8	2300	7.620	7.781	0.060	950	1.25	0.83	2344
511	6.80	34.474	2283.2	2324	7.579	7.748	0.054	1016	1.12	0.75	2359
586	6.44	34.499	2293.0	2325	7.569	7.739	0.053	1028	1.08	0.72	2359
670	5.89	34.508	2301.3	2337	7.571	7.745	0.053	1000	1.07	0.72	2370
775	5.44	34.518	2310.0	2353	7.561	7.736	0.052	1007	1.03	0.69	2386
1032	4.32	34.551	2327.3	2369	7.596	7.783	0.057	874	1.08	0.73	2400
1096	4.04	34.563	2330.3	2377	7.581	7.767	0.055	897	1.02	0.69	2407
1413	3.06	34.596	2342.4	2398	7.615	7.810	0.060	779	1.06	0.72	2426
2002	2.22	34.636	2349.2	2420	7.642	7.836	0.064	682	1.02	0.69	2445
2505	1.88	34.659	2346.0	2435	7.661	7.848	0.067	622	0.98	0.67	2459
3002	1.62	34.677	2339.5	2435	7.696	7.879	0.074	544	0.98	0.67	2458
3515	1.54	34.690	2331.7	2436	7.708	7.881	0.077	510	0.92	0.64	2458
4038	1.48	34.696	2321.3	2428	7.715	7.876	0.078	485	0.85	0.59	2449
HS-15											
0	26.43	34.439	1916.1	2257	8.221	8.207	0.216	380	5.02	3.33	2294
10	26.42	34.426	1916.1	2268	8.236	8.222	0.223	366	5.16	3.43	2306
20	26.43	34.432	1915.5	2266	8.238	8.224	0.224	363	5.18	3.44	2303
31	26.41	34.426	1915.5	2269	8.236	8.222	0.223	365	5.15	3.42	2307
52	26.41	34.430	1916.5	2261	8.238	8.223	0.224	363	5.15	3.43	2298
76	25.93	34.700	1934.5	2290	8.234	8.223	0.226	362	5.14	3.42	2310
102	25.02	34.998	1953.7	2303	8.229	8.227	0.226	357	5.10	3.39	2303
127	23.37	35.119	1982.9	2317	8.199	8.213	0.216	366	4.79	3.19	2309
152	20.86	35.088	2024.9	2317	8.121	8.160	0.185	414	4.06	2.70	2311
178	19.02	34.994	2041.9	2313	8.079	8.138	0.169	431	3.67	2.45	2313
204	15.23	34.551	2090.9	2284	7.937	8.035	0.124	542	2.66	1.77	2314

Table 5. continued

Corrected depth meters	Temp. ° C	Salinity psu	TCO_2 µm/kg	TA µeq/kg	pH(25) NBS	pH(p,t) NBS	CO_3 µm/kg	PCO_2 ppm	L_c	L_a	NTA µeq/kg
HS-15	**cont.**										
252	11.78	34.313	2127.4	2272	7.832	7.967	0.097	621	2.07	1.38	2317
304	10.07	34.243	2149.3	2276	7.785	7.937	0.086	656	1.84	1.23	2326
396	7.92	34.277	2225.1	2300	7.659	7.819	0.064	863	1.35	0.90	2349
506	6.88	34.393	2274.4	2324	7.573	7.740	0.053	1032	1.10	0.73	2365
604	5.98	34.458	2295.0	2339	7.560	7.734	0.051	1033	1.05	0.70	2376
701	5.47	34.493	2302.9	2348	7.567	7.745	0.053	993	1.05	0.70	2383
799	5.12	34.531	2309.1	2364	7.569	7.740	0.052	992	1.02	0.68	2396
1005	4.28	34.551	2326.4	2374	7.572	7.757	0.053	930	1.01	0.68	2405
1196	3.50	34.571	2340.5	2390	7.589	7.781	0.056	858	1.02	0.69	2420
HS-16											
0	26.26	34.463	1921.0	2267	8.230	8.218	0.221	370	5.10	3.39	2302
10	26.20	34.462	1920.3	2272	8.238	8.226	0.225	361	5.18	3.44	2307
20	26.17	34.459	1920.9	2269	8.233	8.221	0.222	366	5.12	3.40	2305
30	26.17	34.463	1920.2	2268	8.244	8.232	0.227	355	5.23	3.48	2303
50	26.06	34.458	1919.4	2269	8.244	8.233	0.227	353	5.19	3.45	2305
75	25.93	34.479	1922.7	2273	8.240	8.229	0.226	355	5.14	3.42	2307
100	24.79	34.975	1957.6	2307	8.230	8.230	0.227	354	5.10	3.40	2309
125	22.76	35.139	1956.7	2320	8.184	8.204	0.206	367	4.55	3.03	2311
150	21.02	35.153	2021.4	2319	8.137	8.175	0.192	399	4.19	2.79	2309
175	18.88	34.959	2049.3	2311	8.073	8.133	0.168	437	3.63	2.42	2314
200	17.68	34.828	2061.0	2304	8.032	8.104	0.153	464	3.29	2.19	2315
304	10.13	34.258	2149.7	2280	7.796	7.948	0.089	640	1.89	1.26	2329
400	8.46	34.348	2232.2	2297	7.630	7.787	0.061	938	1.28	0.85	2341
506	7.41	34.443	2271.3	2318	7.559	7.718	0.051	1091	1.07	0.71	2355
607	6.35	34.467	2291.7	2336	7.556	7.725	0.051	1058	1.04	0.70	2372
701	5.73	34.478	2301.3	2345	7.557	7.731	0.051	1030	1.03	0.69	2381
802	5.20	34.505	2311.7	2361	7.551	7.727	0.050	1024	1.00	0.67	2395
1001	4.30	34.543	2329.6	2377	7.569	7.753	0.053	940	1.01	0.68	2408
1196	3.62	34.553	2339.3	2392	7.574	7.762	0.053	898	0.99	0.67	2423
1494	2.73	34.599	2348.7	2409	7.600	7.795	0.057	799	1.01	0.68	2437
2001	2.20	34.630	2346.9	2417	7.634	7.826	0.063	696	1.00	0.68	2443
2506	1.80	34.659	2344.5	2429	7.661	7.849	0.067	620	0.98	0.67	2453
3018	1.63	34.670	2341.6	2436	7.705	7.889	0.076	531	1.00	0.69	2459
3510	1.52	34.680	2333.4	2435	7.683	7.851	0.072	547	0.86	0.60	2457
4023	1.48	34.687	2321.3	2423	7.715	7.877	0.078	485	0.85	0.60	2445
4521	1.37	34.696	2306.5	2420	7.734	7.888	0.082	444	0.82	0.57	2441

-- = no data available; See Table 2 for explanation of units and abbreviations.

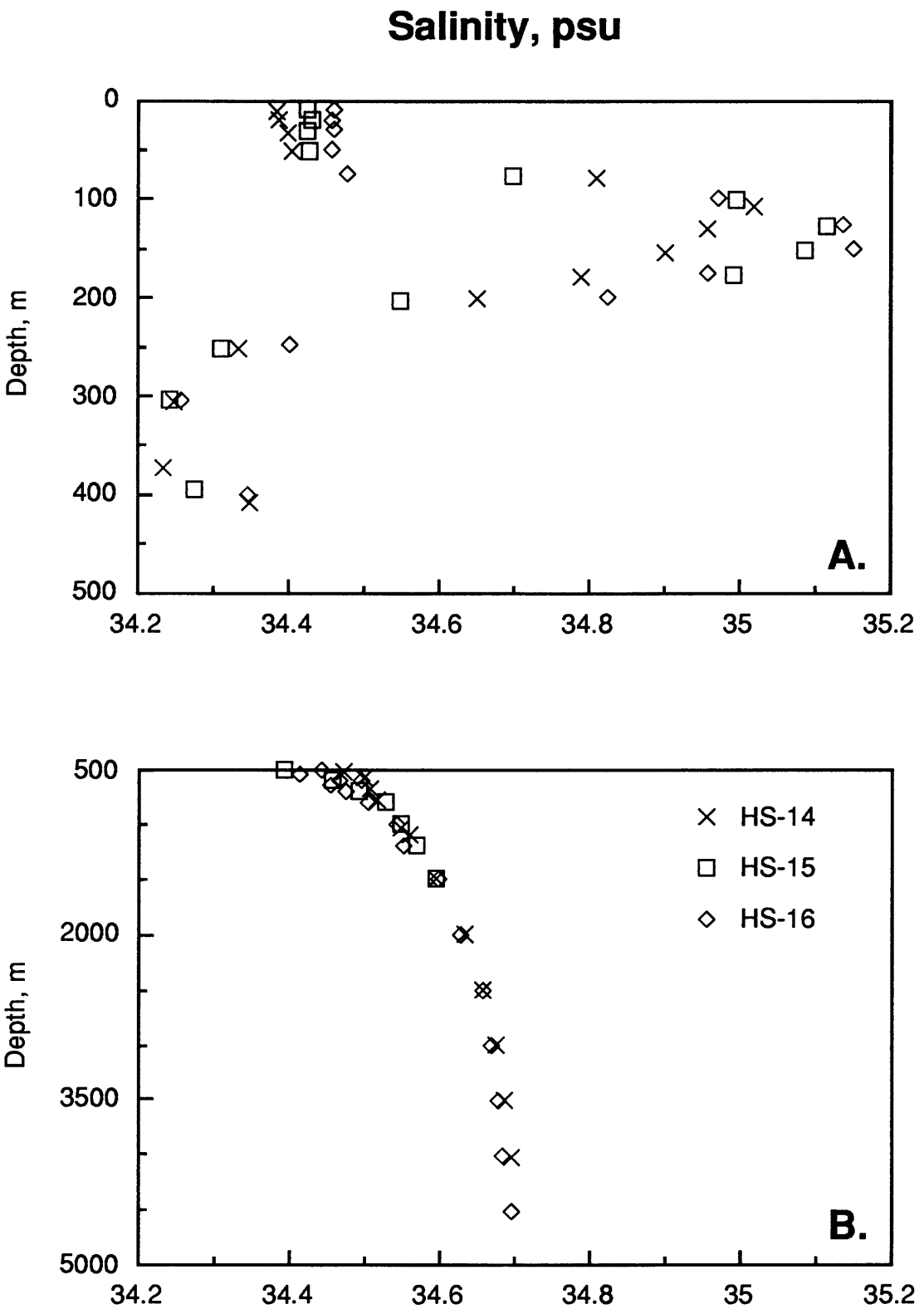

Figure 1. Vertical distribution of salinity in the Karin Ridge area. **A.** 0-500 m; **B.** 500-5000 m.

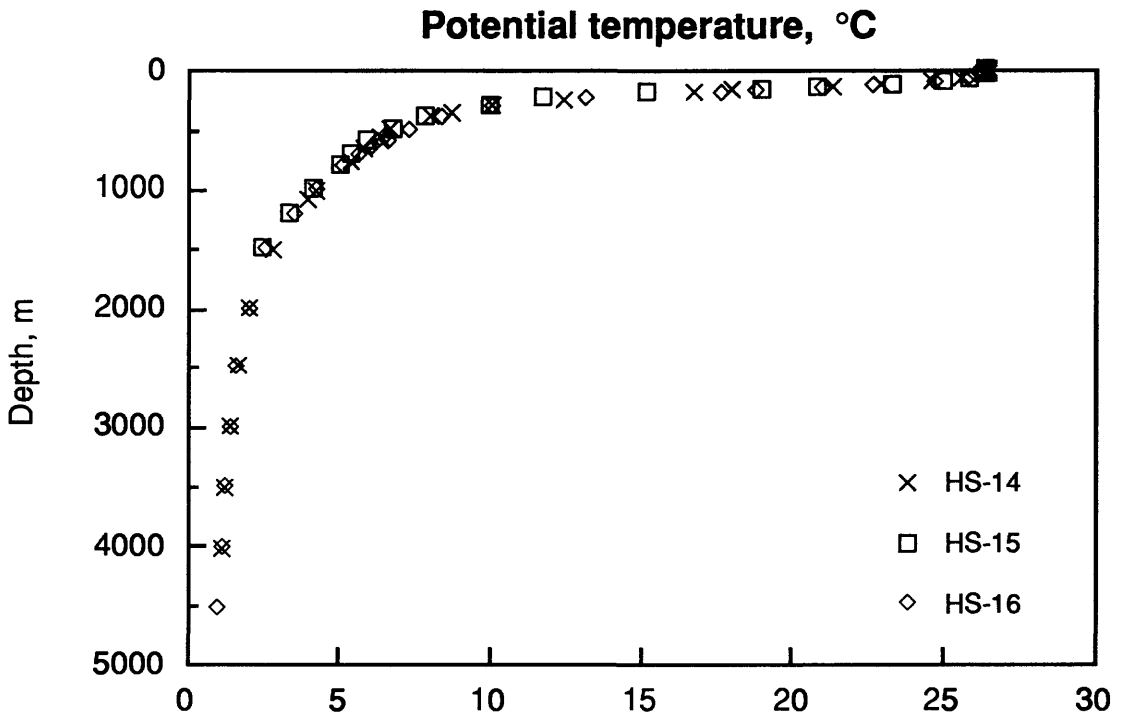

Figure 2. Vertical distribution of potential temperature in the Karin Ridge area.

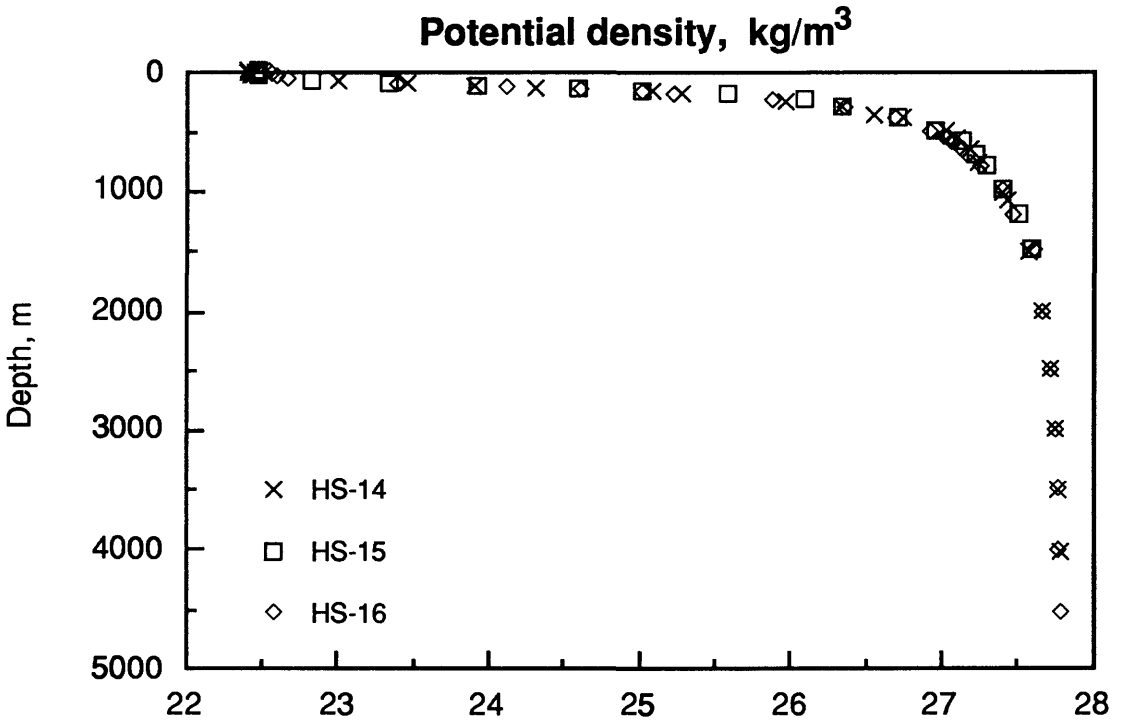

Figure 3. Vertical distribution of potential density in the Karin Ridge area.

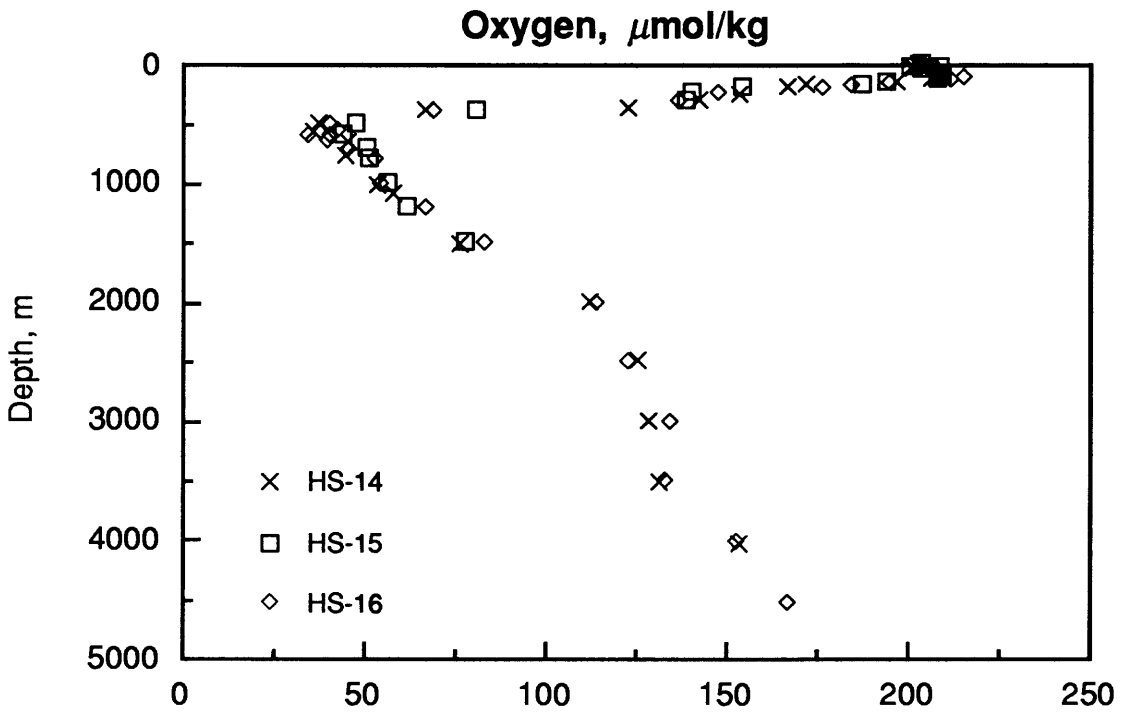

Figure 4. Vertical distribution of dissolved oxygen in the Karin Ridge area.

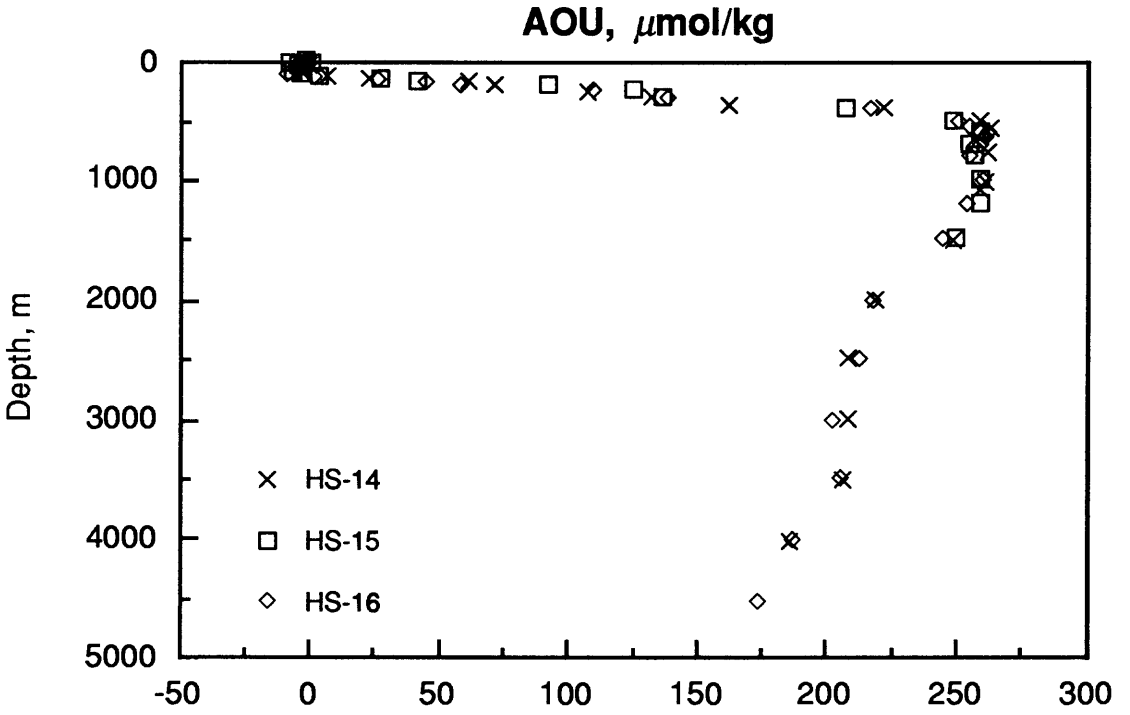

Figure 5. Vertical distribution of AOU in the Karin Ridge area.

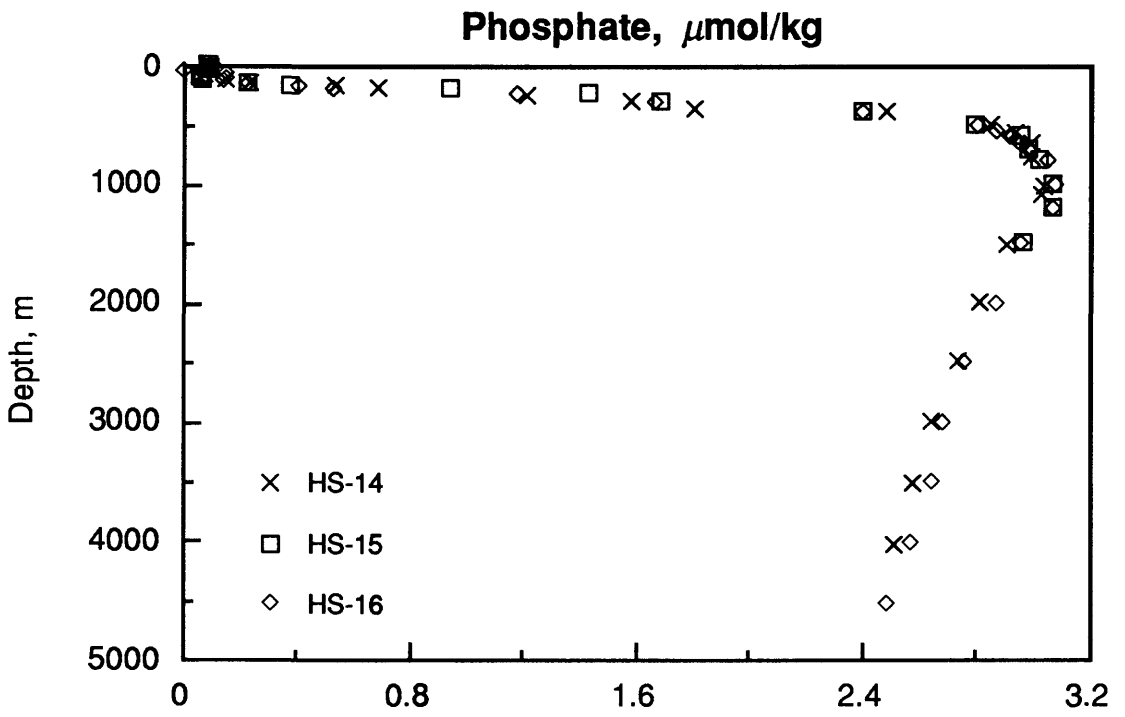

Figure 6. Vertical distribution of phosphate in the Karin Ridge area.

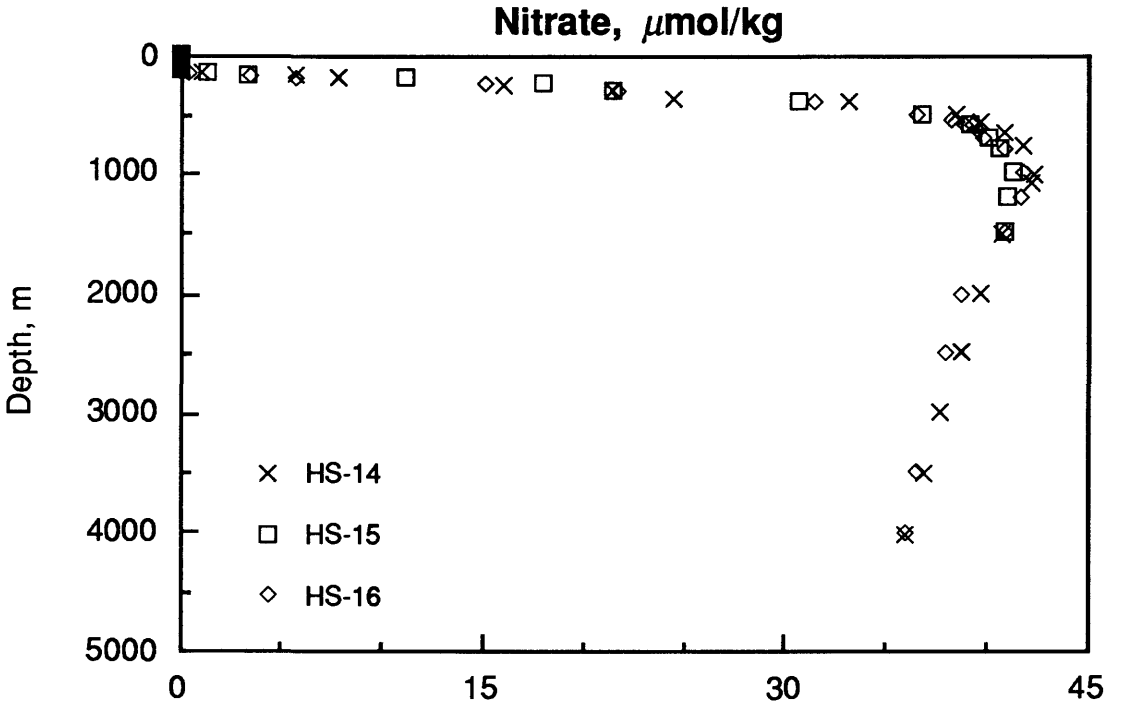

Figure 7. Vertical distribution of nitrate in the Karin Ridge area.

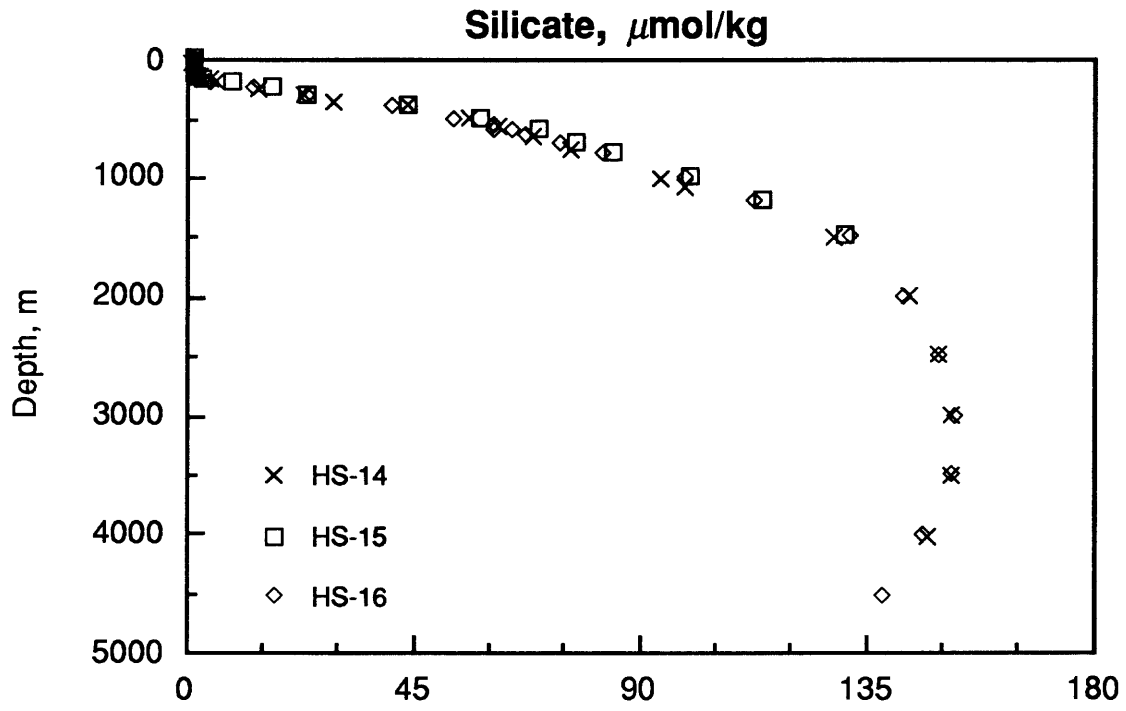

Figure 8. Vertical distribution of silicate in the Karin Ridge area.

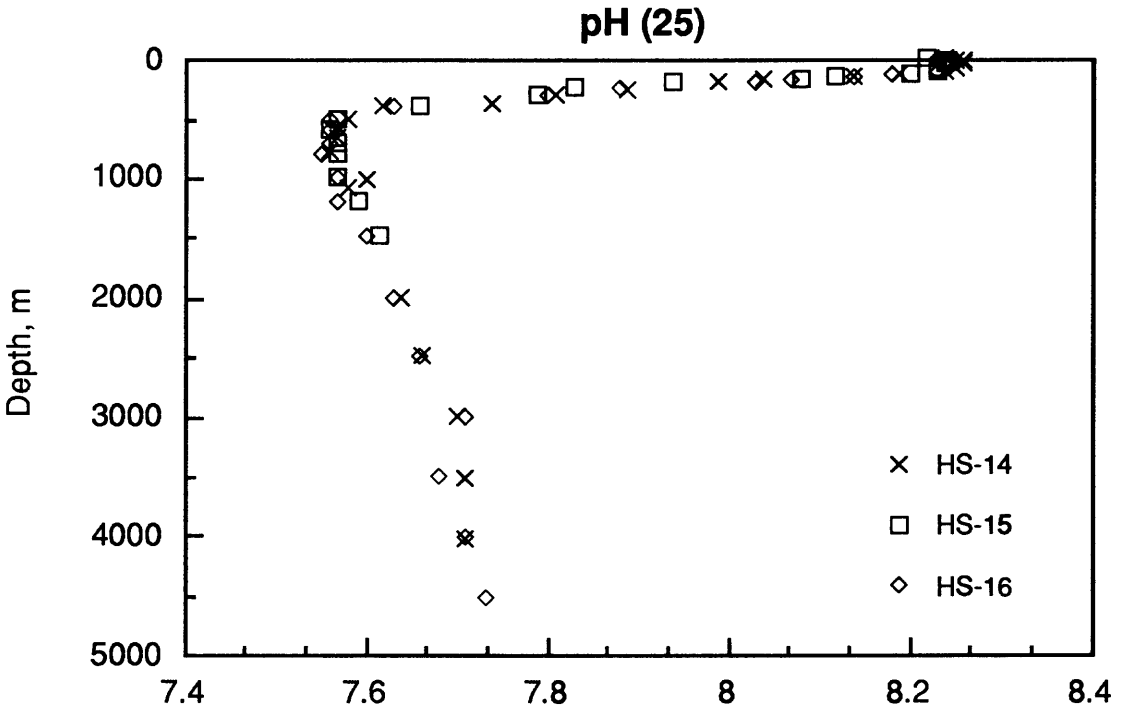

Figure 9. Vertical distribution of pH (25) in the Karin Ridge area.

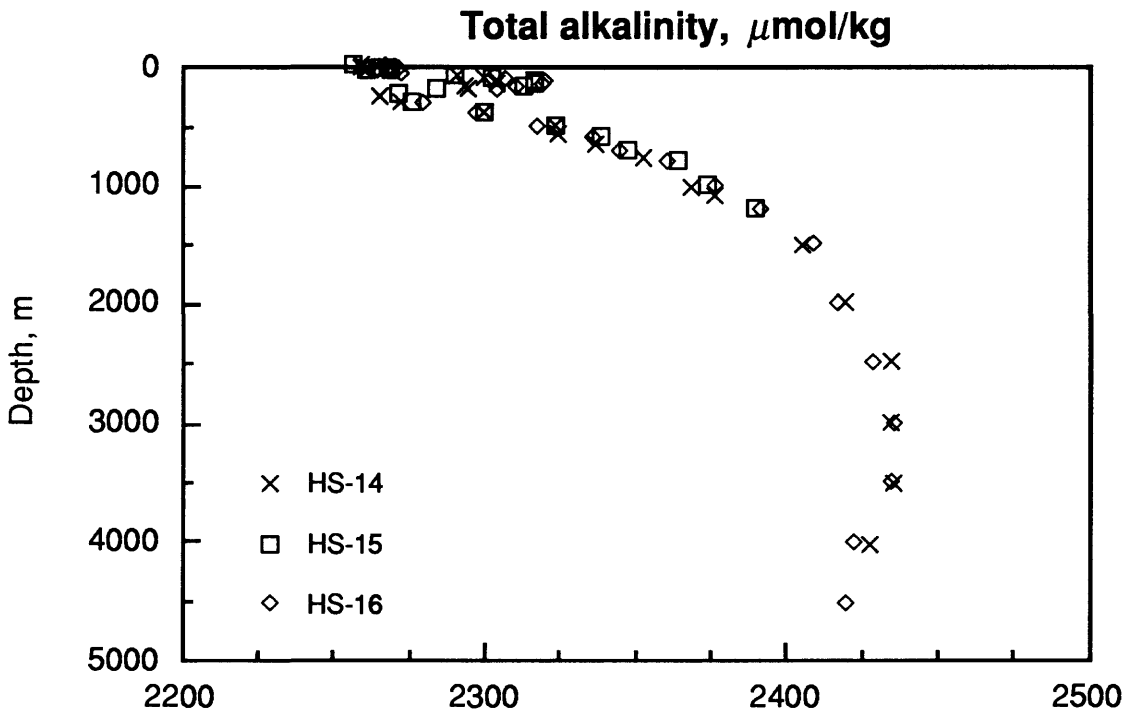

Figure 10. Vertical distribution of total alkalinity in the Karin Ridge area.

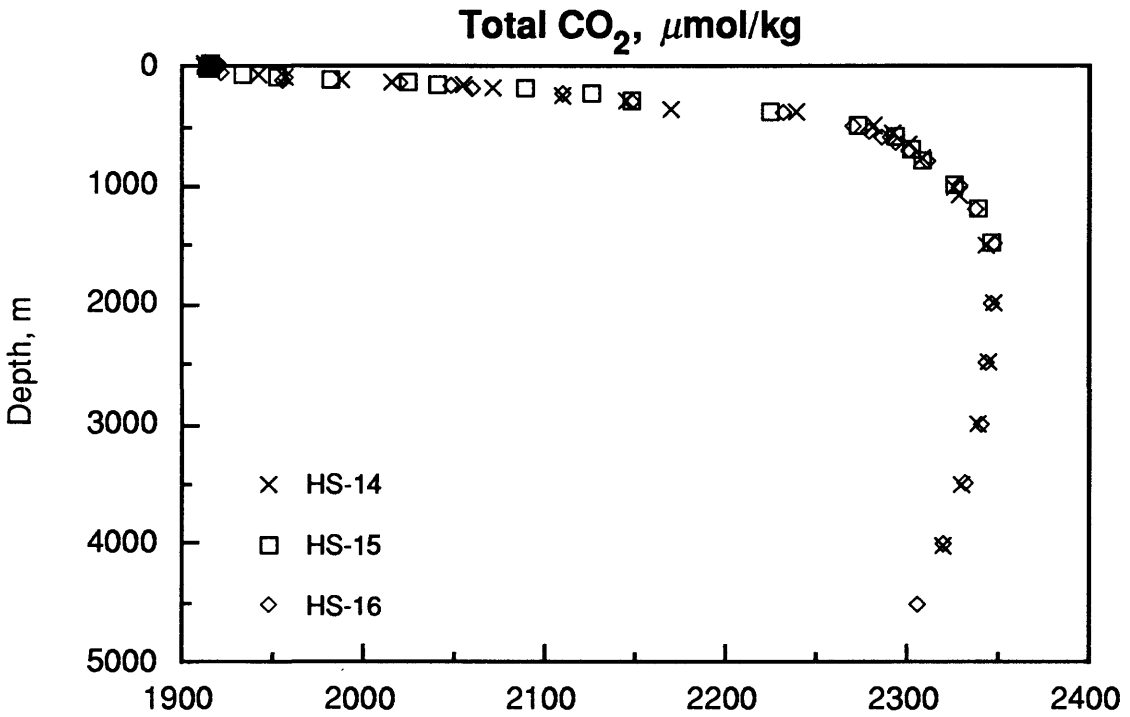

Figure 11. Vertical distribution of total CO_2 in the Karin Ridge area.

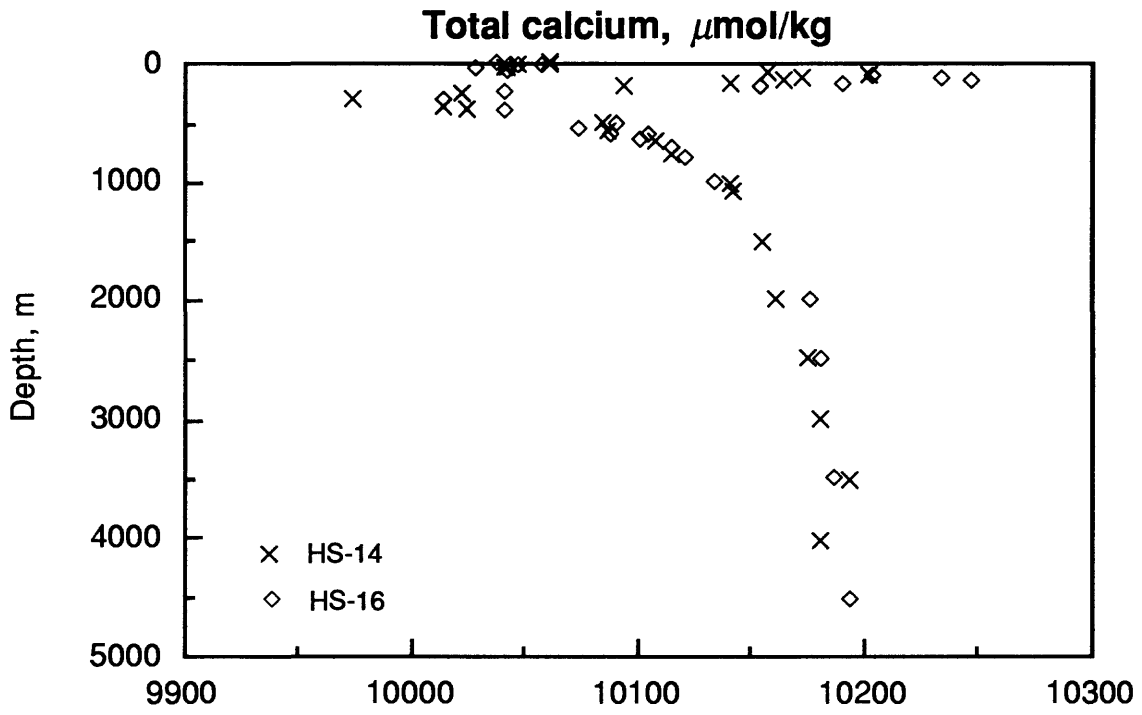

Figure 12. Vertical distribution of calcium in the Karin Ridge area.

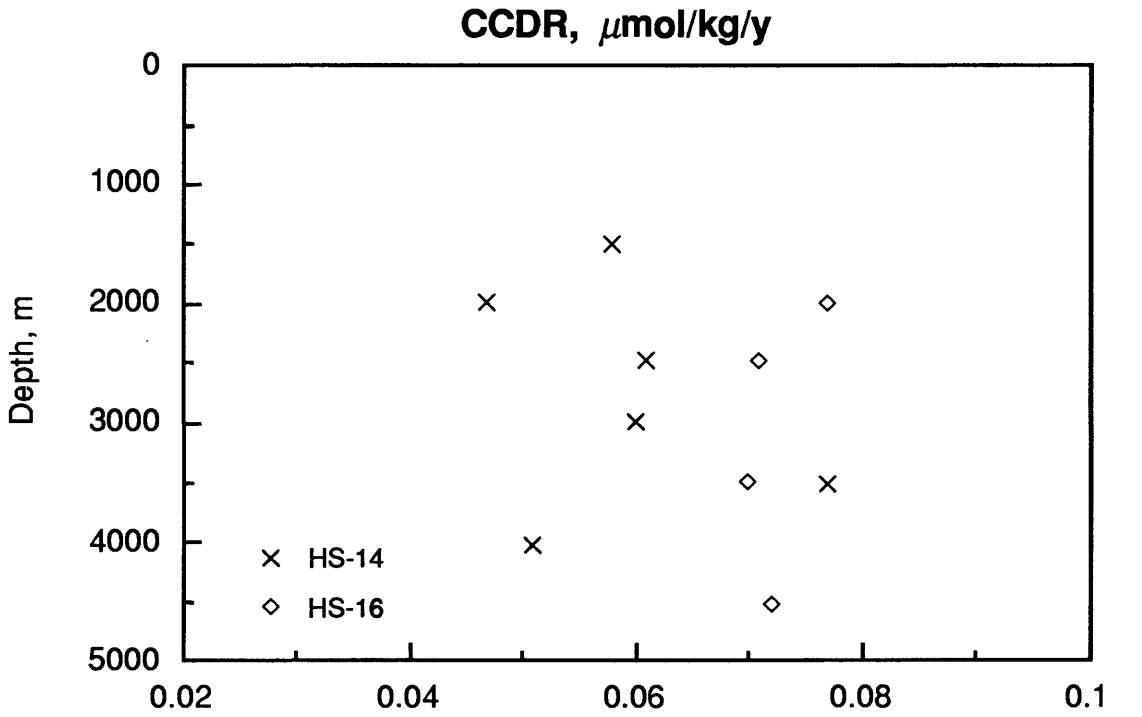

Figure 13. Calcium carbonate dissolution rate (from Ca data; CDR3 in Table 4) in the Karin Ridge area.

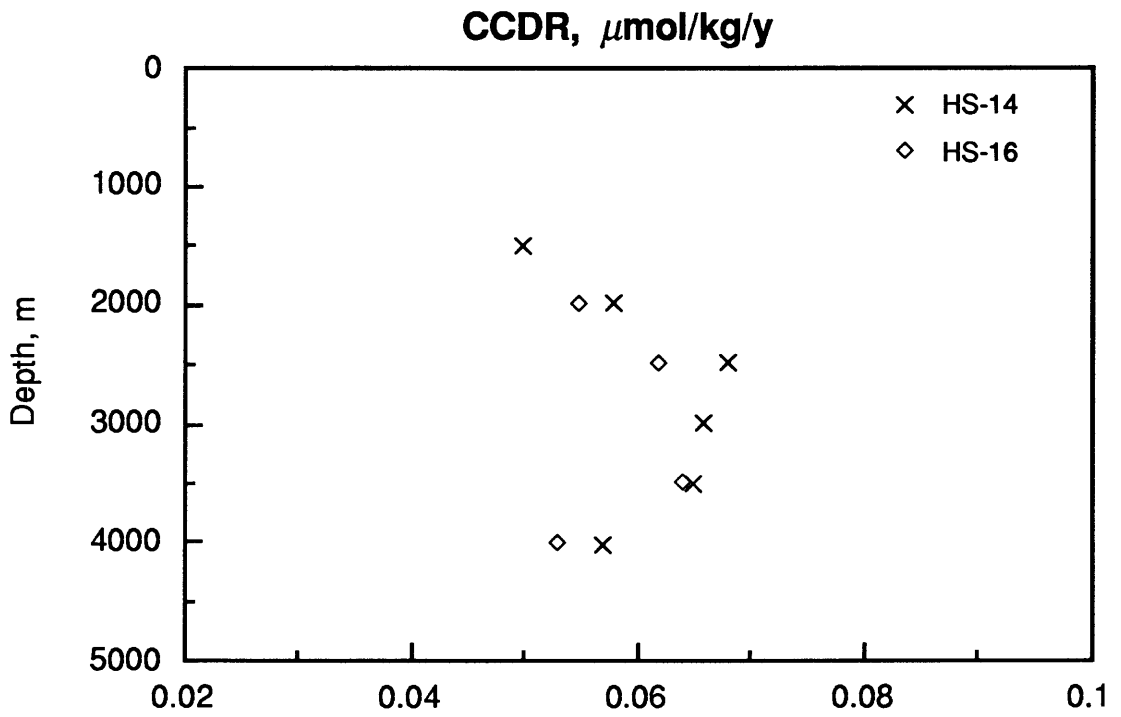

Figure 14. Calcium carbonate dissolution rate (from TA and NO_3 data; CDR2 in Table 4) in the Karin Ridge area.

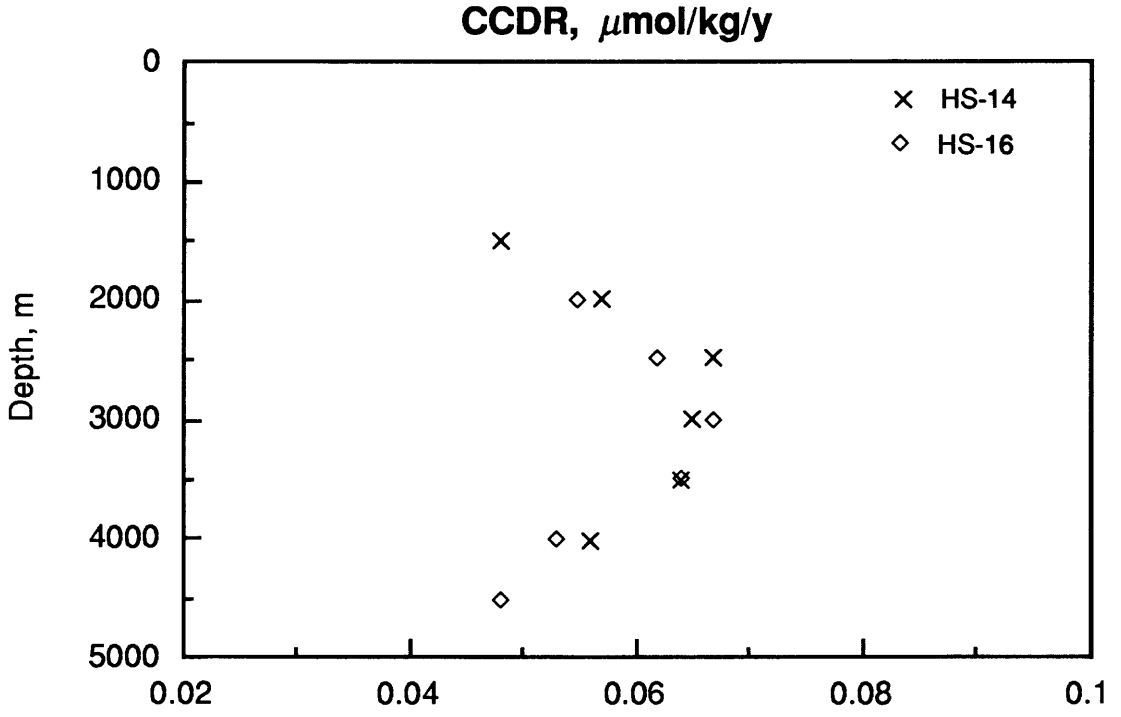

Figure 15. Calcium carbonate dissolution rate (from TA and CO_2 data; CDR1 in Table 4) in the Karin Ridge area.

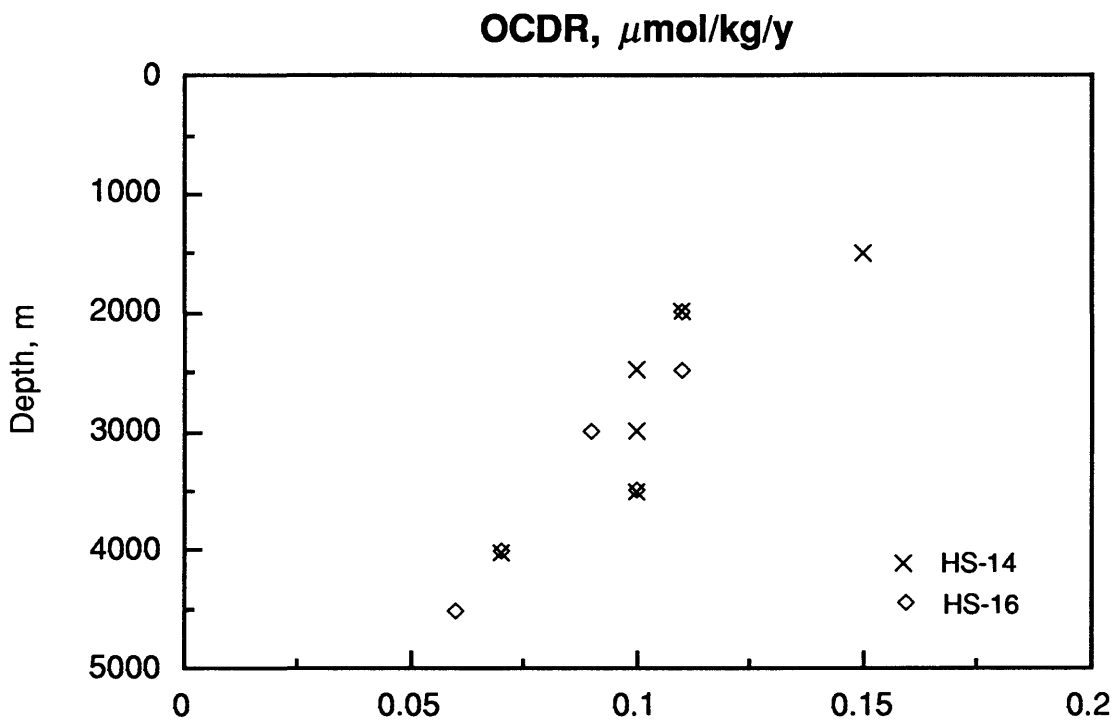

Figure 16. Organic carbon decomposition rate (from AOU data, Redfield model, OCDR1 in Table 4) in the Karin Ridge area.

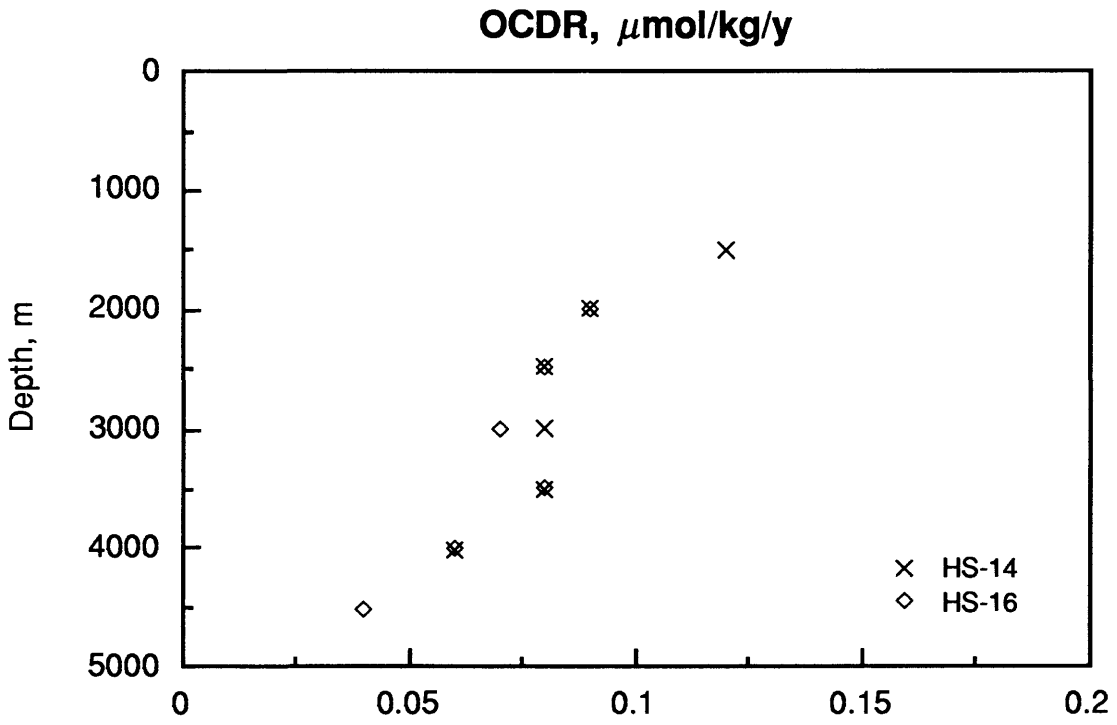

Figure 17. Organic carbon decomposition rate (from AOU data, Takahashi model, OCDR11 in Table 4) in the Karin Ridge area.

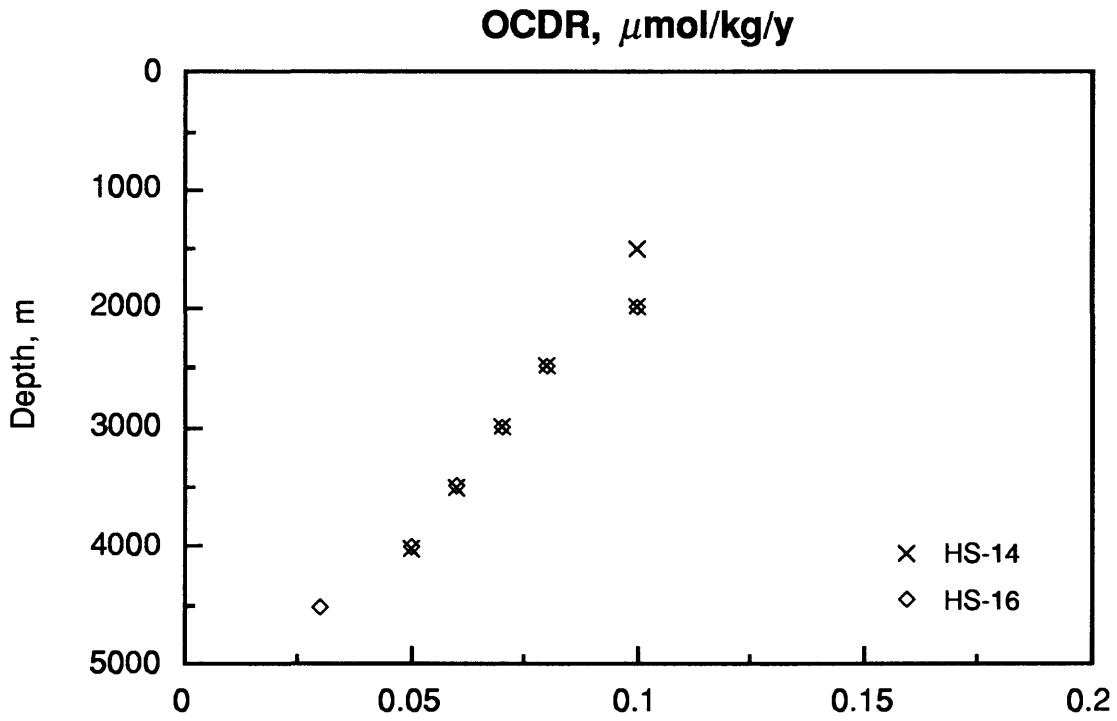

Figure 18. Organic carbon decomposition rate (from TA and TCO_2 data, OCDR2 in Table 4) in the Karin Ridge area.

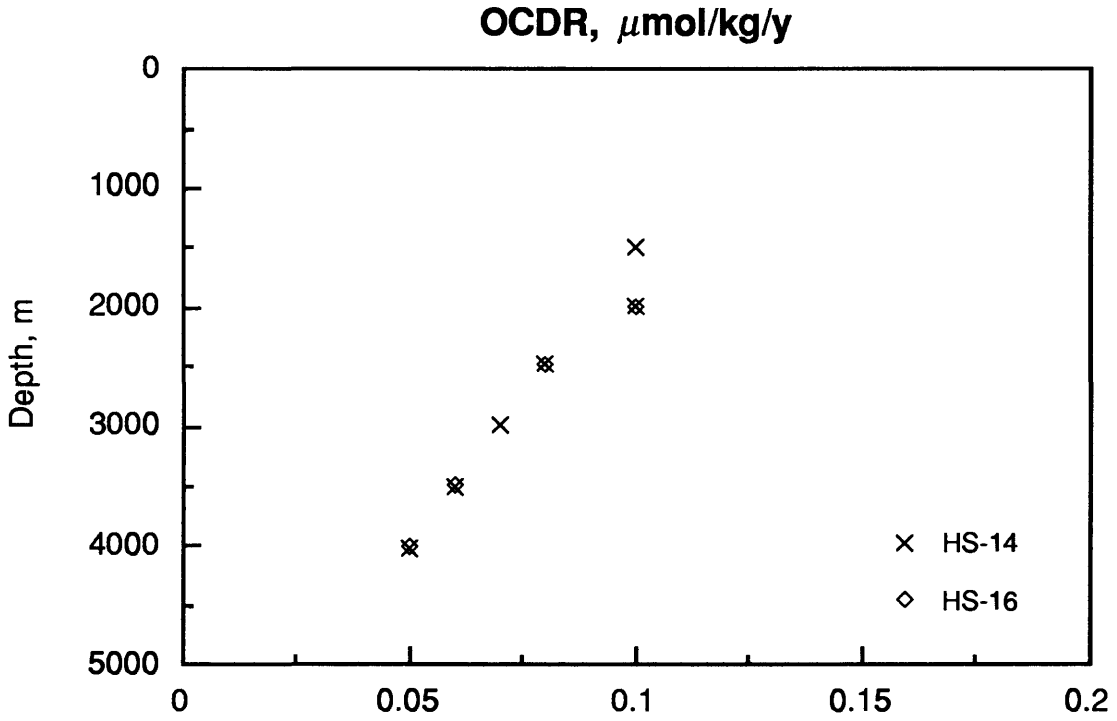

Figure 19. Organic carbon decomposition rate (from TA, TCO_2, and NO_3 data, OCDR3 in Table 4) in the Karin Ridge area.

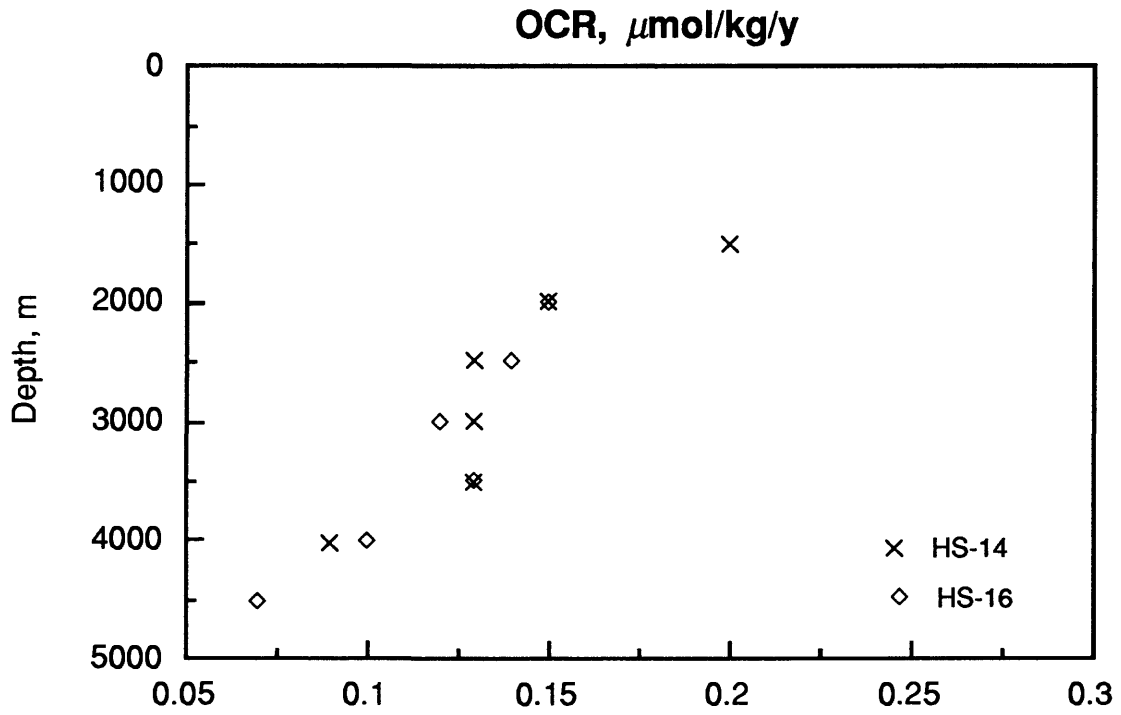

Figure 20. Oxygen consumption rate in the Karin Ridge area.

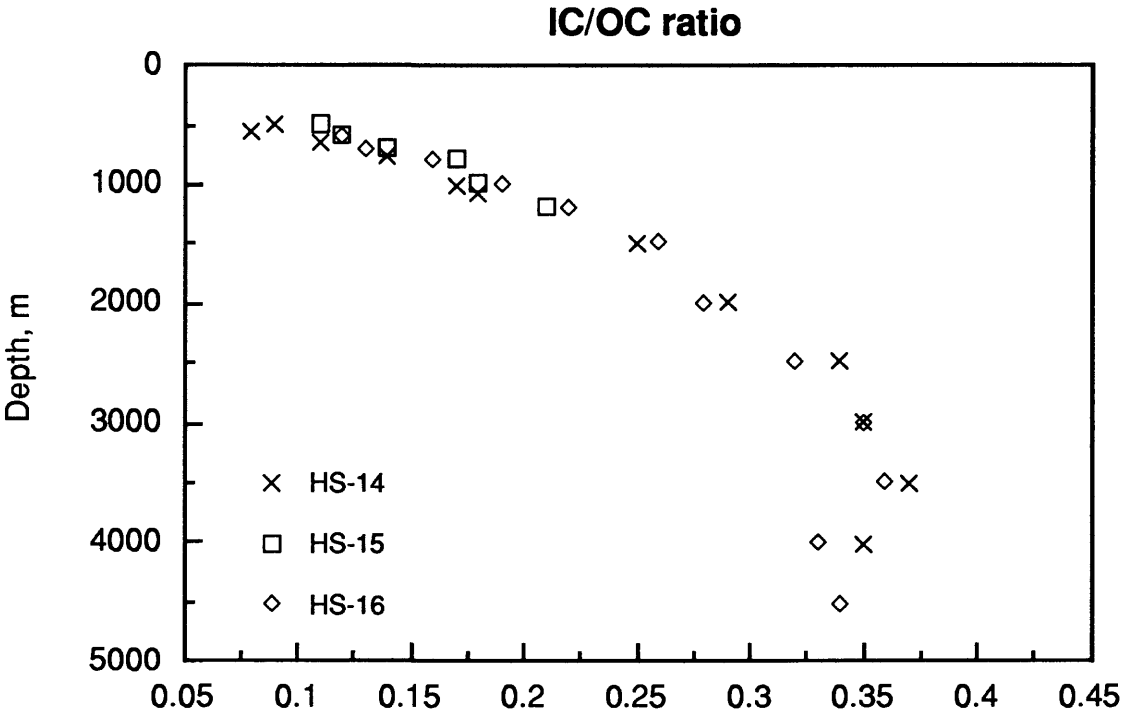

Figure 21. Inorganic/organic carbon ratio in the Karin Ridge area.

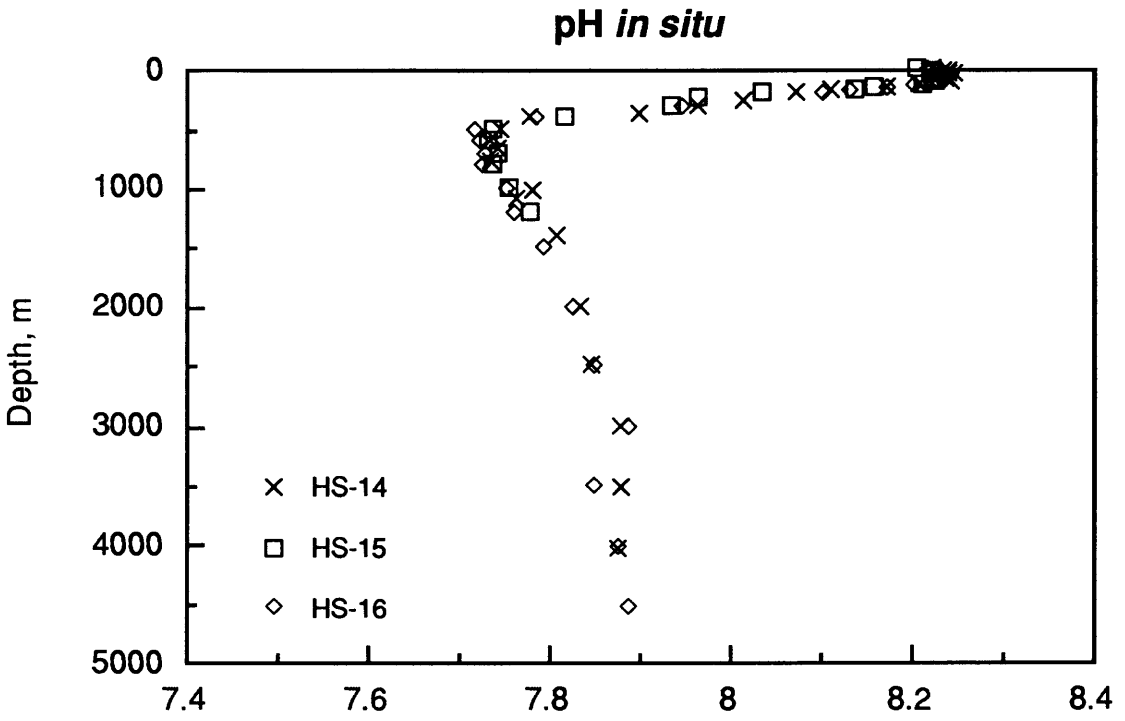

Figure 22. Vertical distribution of pH *in situ* in the Karin Ridge area.

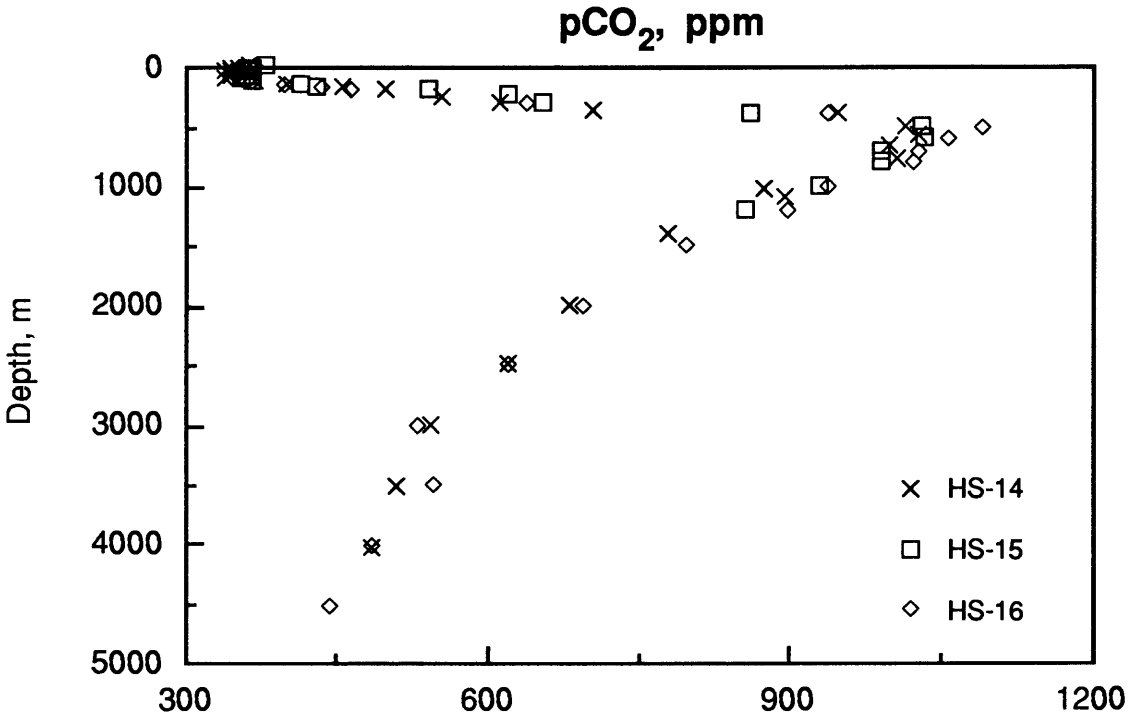

Figure 23. Vertical distribution of partial pressure CO_2 in the Karin Ridge area.

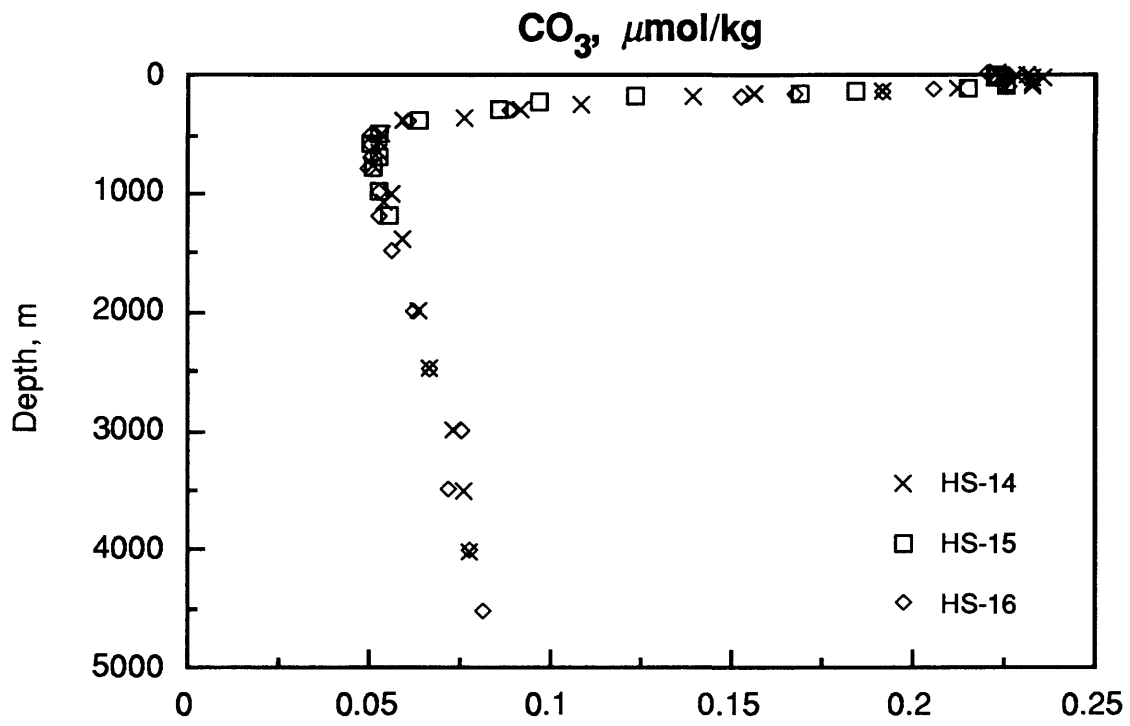

Figure 24. Vertical distribution of carbonate ion in the Karin Ridge area.

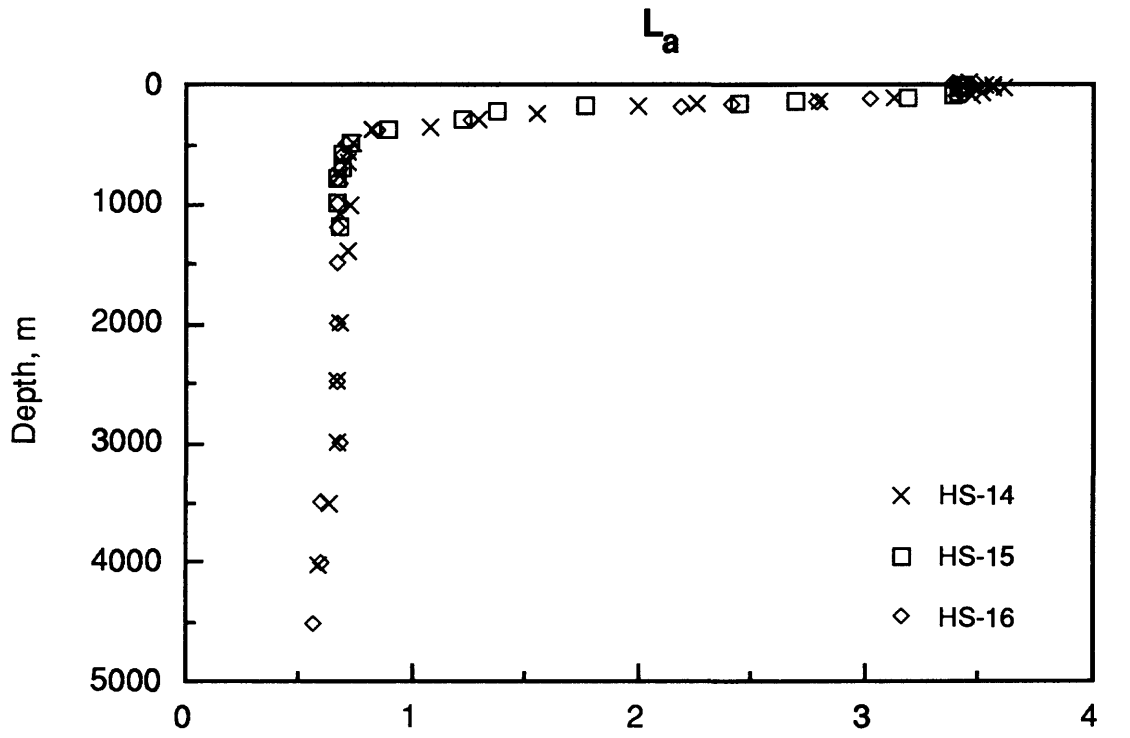

Figure 25. Vertical distribution of degree of aragonite saturation in the Karin Ridge area.

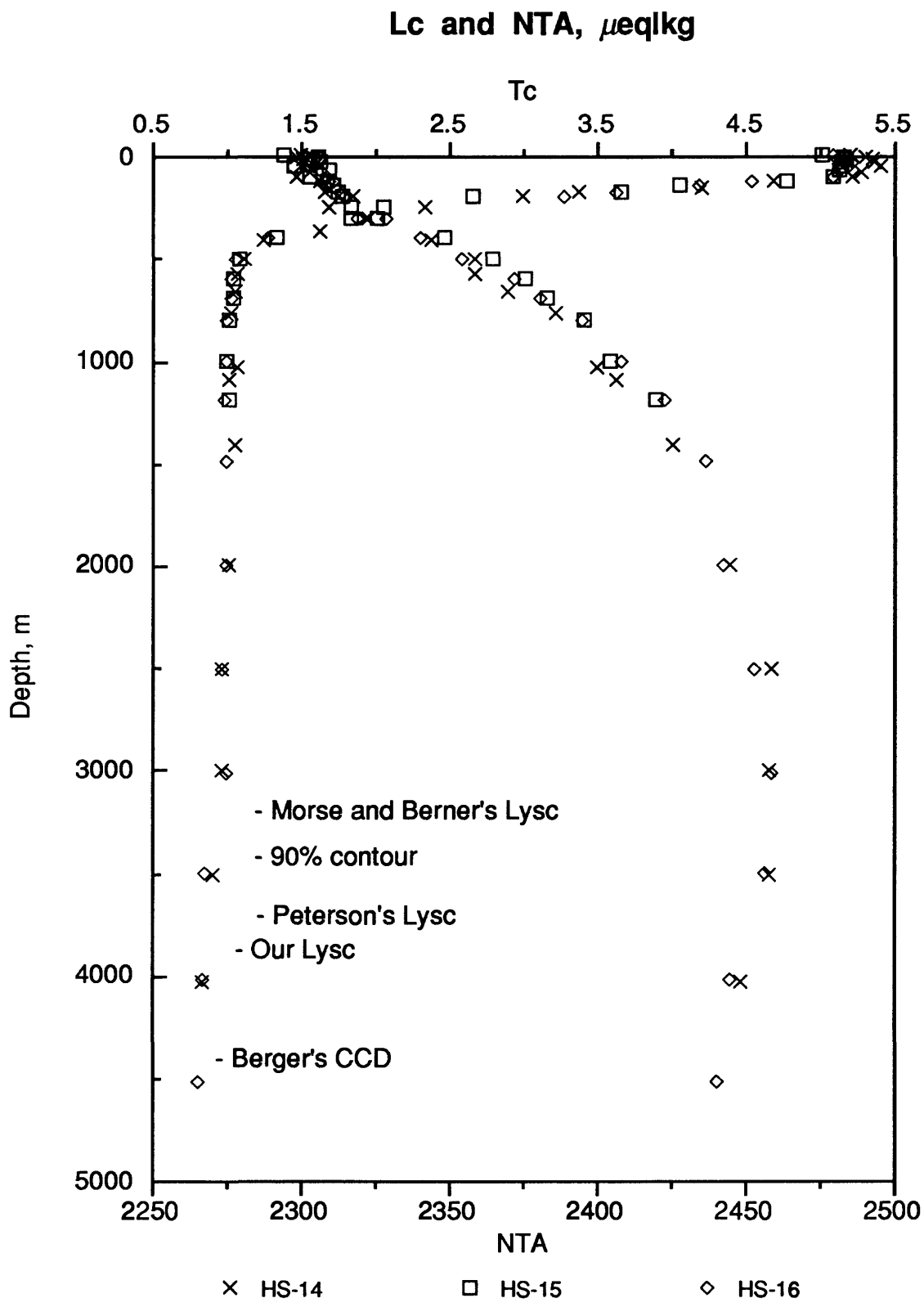

Figure 26. Vertical distribution of degree of calcite saturation and normalized total alkalinity in the Karin Ridge area.

91-AV-19

LEG 4

Northwest Pacific

— PAGE 221 FOLLOWS —

MEASUREMENTS OF OXIDATION-REDUCTION POTENTIAL IN SEDIMENTS FROM THE NORTHWEST PACIFIC

A.M. Pysarevsky[1], L.M. Gramm-Osipov[2], T.D. Shigaeva[1]

[1]St. Petersburg University, Chemical Department, 41 Sredniy Ave., 199004 St. Petersburg, Russia; [2]Pacific Oceanological Institute, Far Eastern Branch, Russian Academy of Sciences, 43 Baltiyskaja, Vladivostok 690041, Russia

INTRODUCTION

Oxidation-reduction potential (Eh) is one of the most important characteristics of the environment where processes of mineralization, migration, and accumulation of chemical elements occur. The environmental characteristics acquire a special importance when attempts are made to describe the processes by means of physical chemistry and thermodynamics. It is then important to determine what can be measured and can those measurements be applied to physiochemical calculations? For example, Eh measurements made in normal-aerated seawater with a Pt electrode were used by a number of geochemists (e.g. Baas-Becking *et al.*, 1960; Crerar and Barnes, 1974) to make geochemical conclusions; however, electrochemists have long known that the redox potential is constant when at non-equilibrium. Contributions of electrochemists (e.g. Gramm-Osipov, 1982; Peshchevitsky *et al.*, 1970) helped clarify these points.

The redox potential of bottom sediments is more complicated. Pysarevsky *et al.* (1989) showed that Eh values obtained by direct measurements for red clays are constant. Only by using a special technique could the equilibrium Eh values be obtained, and they proved to be 80-100 mV higher than expected. No papers exist about Eh values measured in reduced sediments (gray, greenish-gray, steel-gray in color). Some of these points were addressed by the Geochemistry of Marine Sediments Project (GEMS) during the R.V. *Akademik Aleksandr Vinogradov* Cruise 91-AV-19.

Results obtained from previous studies of red clays (e.g. Pysarevsky *et al.*, 1989) emphasize the need for further studies to better understand the natural systems. For example, further work is needed to develop and implement new techniques for reliable measurements of Eh (intensive parameter) with respect to natural systems; estimation of the oxidation (reduction) volume (ß) in sediments (extensive factor); determine what controls oxidation number (n); determine chemical (or physiochemical) effects on other characteristics of the environment, for example, pH, concentrations of Mn^{2+} and S^{2-} in pore water, and so on.

The accomplishment of such an approach will allow for a new, quantitative level of understanding geochemical problems with respect to the nature and the role of redox barriers. Investigations during cruise 91-AV-19 were aimed at working out a concrete version of potentiometric redox measurements in different geochemical (oxidized and reduced) types of bottom sediment.

METHODS

An electrochemical cell was used to obtain direct measurements of Eh, pH, and pNa. Smooth platinum redox-metric electrodes (wire and platinum), and Ti-silicate glass (EO-021) and Fe-silicate glass (EO-035) electrodes developed at the Research Institute of Chemistry of Glass, St. Petersburg University, served as electrode-indicators. Characteristics of redox-electrodes were initially checked against dilute solutions of the system $Fe(CN)_6^{3-,4-}$ (Shulz *et al.*, 1984).

The pH values of marine sediments were determined by means of glass electrode-indicators with liquid (0.1 N HCl) and a special alloy, solid filling developed at St. Petersburg University. Electrodes were calibrated against standard buffer solutions. Electrodes from NAB-161008 glass with solid filling served as Na-selective electrodes. Prior to an experiment, the electrodes were checked using NaCl solutions. In all instances a removable chlorine-silver electrode was used for comparison. EMF (electro-motive force) was measured by pH-150- and pX-150-meters and temperature by mercury thermometers. For better contact, a sediment sample at the electrode-sediment boundary was diluted with seawater (sw) in proportion $V_{sediment}/V_{sw} \approx 10{:}1$.

Solutions of $Fe(CN)_6^{3-,4-}$ ($E° = +360$ mV) were used as mediators for oxidized sediments and complexes of iron with EDTA (ethylendiaminetetraacetic acid, $E°\sim +140$ mV with pH 7) were used for reducing sediments. The mediator interacts with the redox system of the sediments very rapidly and thus the equilibrium potentials are more easily established on electrodes. The amount of the mediator introduced in sediments must not alter the

redox conditions of the environment. It was found that the volume of the mediator must provide a redox-buffer 50-100 times less than the redox-buffer of the environment: $\beta * V_{sed}/C_{med} * V_{med} \geq 50\text{-}100$. The volume of the added mediator is calculated from the above expression. Eh of the mediator solution will optimally be close to the Eh of the sediments.

Oxidation volume (ß) was determined potentiometrically by Pt-electrode. As a redox system, the system $Fe(CN)_6^{3-,4-}$, with ratios of redox components being 1/1, 1/10, and 10/1, was used depending on the Eh of the studied sediments. A redox system added to a sediment either increased (oxidation properties "+") or decreased (reduction properties "-") its redox potential. The values of (ß) were calculated by the formula deduced from Nernst's equilibrium ratios (Shulz *et al.*, 1984):

$$\beta = l_{ox} * l_{red}{}^{(1-A)}/(l_{ox} - l_{red} * A)\, V_{sed}$$

where l_{ox} and l_{red} are equivalents of oxidant (reducer), that is, C_{ox} (or C_{red}) V_o; V_o = the volume of a solution in a redox system, V_{sed} = volume of sediment added; A = inverse log $(E_1 - E_2)/\theta$, θ=59.2 mV at 25°C; for negative values inverse log is deduced from the values $(E_2 - E_1)$. For example:

2 ml of sediment is added to the initial solution (15 ml) $10^{-4}/10^{-3}$ N prepared from seawater of the $Fe(CN)_6^{3-,4-}$ system. In ten minutes the E_2 value becomes 250 mV and remains constant for 30 minutes. If during the test-time the temperature rises more than 0.5°C, a correction is made; the temperature coefficient in solutions of the system $Fe(CN)_6^{3-,4-}$ is about +1 mV/°C

$$\beta = (10^{-7} * 15\text{ ml})\,(10^{-6} * 15\text{ ml})\,(1 - A)\,/\,2\,[(15\text{ ml} * 10^{-7}) + (15\text{ ml} * 10^{-6})\,A]$$

where A = inverse log [(211-250)/59.2] = 0.218

ß = $1.85 * 10^{-6}$ oxidation equivalents/ml or

ß = $1.85 * 10^{-3}$ eqv/l

Thirty minutes is an optimum amount of time to obtain stable E_2 values.

Volumes for both oxidized (red and brown) and gray sediments are determined by using solutions of $Fe(CN)_6^{3-,4-}$ and I_2/I^-.

Measurements of Eh with Redox Mediators

After (ß) was determined, 5-10 ml of sediment was taken into another cell and diluted with seawater (in proportion 5 to 1 volume) and then stirred. Then, 0.5 to 2 ml mediator as needed was added to the cell. The mediator concentration is calculated in order to make the oxidizing (reducing) capacity 50-100 times higher than the amount of equivalent reducer (oxidizer) introduced with the mediator solution. It should be kept in mind that the smaller the amount of mediator the less possibility of error in Eh measurements. On the other hand, the less mediator, the lower the efficiency.

An additional example of Eh determination can be mentioned. Given 10 ml of sediment for Eh determination, the number of oxidizing equivalents is about $1.85 * 10^{-5}$, and as a mediator the $Fe(CN)_6^{3-,4-}$ solution is used with the ratio of concentration $5 * 10^{-5} / 5 * 10^{-4}$ N, then it is possible to add no more than $V < 1.85 * 10^{-5} / 50 * 5 * 10^{-5} < 0.74$ ml of the mediator solution. Experiments show that such amounts of mediator are enough to overcome individual properties of an electrode and to have good reproducibility of measurements.

RESULTS AND DISCUSSION

Results (Table 1) show that there are some discrepancies in distinguishing between oxidized and reduced sediments by color and by the sign of the oxidation volume (ß). Even though the contact observed in stratigraphic profile between these geochemical sediment types is rather distinct, commonly there are parts of the gray sediments that possess properties of oxidized sediment (oxidation "+") (GC-7, GC-27, BC-8, BC-38, GC-39).

We give below a brief description of various types of sediments, as determined by properties other than their sign (ß) ("+"= oxidized, "-" = reduced).

Oxidized Sediments

The interval of Eh^{med} ranges over 270 mV: from 470 (BC-38) to 740 mV (BC-8), while (ß) ranges from $4 * 10^{-8}$ eqv/ml (BC-38) to $3.8 * 10^{-5}$ eqv/ml (BC-27). Conventionally, three groups can be distinguished among the oxidized sediments (by Eh values determined with the help of mediators): 1) 470 - 560 mV; 2) 580 - 620 mV; and 3) 650 - 740 mV.

Measurements without mediators in the Group 1-type sediments are most consistent; that is, measurements with mediators and without them show the least differences. The larger differences are observed for sediments of the second and third groups, where (Eh^{med} - Eh) can exceed 200 mV (GC-13, BC-16, BC-27). The highest values of Eh^{med} are common to sediments of the third group. Samples of oxidized sediment are rather stable over time, and values of Eh^{med} and Eh are reproducible.

For refrigerated samples, results consistent with the initial values of ß were obtained after 15-16 days for sediments in BC-8.

Reduced Sediments

For reduced sediments Eh^{med} ranges from 100 mV (GC-7) to -90 mV (GC-10, GC-32, GC-39); $ß_{red}$ ranges from $-5.81 * 10^{-6}$ to $-4.61 * 10^{-5}$ eqv/ml.

Significant technical problems were encountered in response to the instability of sediment samples with time, even when kept refrigerated. As Eh decreases rapidly, $ß_{red}$ also decreases. It is better to use cells with a noble gas to preserve the original sediment characteristics. "Poisoning" of Pt electrodes (GC-10, BC-14) followed by a drastic drop in potential is common. The use of mediators significantly reduces the chance of "poisoning". Most likely, the preference should be given to glass redox-metric electrodes EO-021.

CONCLUSIONS

This study presents for the first time a technique where mediators were used for studying equilibrium values of Eh in various geochemically distinct types of oceanic bottom sediments. Although this study is preliminary, new results were obtained. Further investigations in this direction will greatly contribute to a better understanding of the geochemistry of oxidation-reduction processes in sedimentary rock formation and may revise concepts of physiochemical behavior for a number of chemical elements during early diagenesis.

ACKNOWLEDGMENTS

Thanks go to Larisa V. Kulchitskaya for her translation work and to Ann E. Gibbs and James R. Hein for improving the English.

REFERENCES

Baas-Becking, L.G.M., Kaplan, I.R., and Moore, D., 1960. Limits of the natural environment in terms of pH and oxidation-reduction potentials. Journal of Geology, v. 8, p. 243-284.

Crerar, D.A. and Barnes, H.L., 1974. Deposition of deep-sea manganese nodules. Geochimica et Cosmochimica Acta, v. 38, p. 279-300.

Gramm-Osipov, V.N.,1982. On redox potential of oceanic waters. Doklady Akademii Nauk SSSR, v. 267, no 2, p. 457-459 (In Russian).

Peshchevitsky, V.I., Anoshchin, G.N., and Erenburg, A.M., 1970. Chemical forms on gold and questions of oxidation-reduction potential of seawater. *in* Chemical Resources in Seas and Oceans. Moscow. Science. p. 141-144 (In Russian).

Pysarevsky, A.M., Tishchenko, P.Ya., Gramm-Osipov, L.M., Nikolayev, Yu.I., 1989. MnO_2 /Mn^2 system as a potential defining factor with Eh control over pelagic strongly oxidized bottom sediments. Doklady Akademii Nauk USSR, v. 306, N1, p. 195-198 (In Russian).

Shulz, M.M., Pysarevsky, A.M, Polozova, B.P.,1984. Oxidation Potential. Leningrad, Chimia, 160 p. (In Russian).

Table 1. Results of potentiometric measurements

Sample interval (cm)	Water depth (m)	Sediment description	pNa	$\beta^{*}10^{2}$ eqv/l	pH	Eh, mV direct. potent.	Eh, mV potent. with mediator
GC-6							
0- 1	5500	Silty clay dusky	0.46	0.001	7.35	+300/+410	+496
2- 5		yellowish-brown	0.43	-2.31	7.40	+20/+40	+ 50
17-19		Silty clay grayish	0.46	-2.71	7.80	+40/-40	- 20
43-45		olive green	0.45	-2.71	7.80	+200/-201	- 5
GC-7							
2- 5	4990	Silty clay dark-	0.45	0.30	6.80	+411/+536	+630
23-25		brown	0.45	0.041	-	+340/+440	+501
40-42		Silty clay light	0.45	0.36	7.30	+470/+490	+505
50-53		olive	0.48	0.07	7.35	+440/+470	+506
73		" - "	0.51	-3.41	7.80	+160/ -20	+ 85
BC-8							
2- 5	5860	Silty clay brown	0.45	0.61	6.90	+520/+580	+645
17-19		" - "	0.46	1.21	6.95	+605/+620	+680
30-32		" - "	-	0.42	-	-	-
36-39		" - "	0.46	1.51	6.85	+620/+640	+706
45-47		" - "	0.46	0.26	6.85	+510/+570	+618
54-57		" - "	0.46	0.03	7.00	+390/+500	+526
GC-9							
0- 1	6100	Silty clay brown	0.46	0.28	7.15	+500/+580	+653
3- 5		" - "	0.46	0.19	7.05	+490/+560	+639
19-21		" - "	0.46	0.29	7.05	+480/+505	+635
73-75		" - "	0.44	0.34	7.20	+520/+540	+640
169-171		" - "	0.46	0.37	7.05	+520/+570	+662
248-250		" - "	0.35	0.40	7.40	+490/+570	+633
GC-10							
0-1	4000	Clayey silt brown	0.48	0.15	7.30	+460/+500	+565
10-12		Clayey silt olive	0.46	-2.81	7.60	+135/-144	- 55
58-60		gray	0.48	-3.41	7.70	- 7/-300	- 30
118-120		" - "	-	-4.41	-	-	-
160		" - "	0.57	-4.51	7.90	+ 35/- 7	- 82
GC-13							
0- 1	2630	Silty clay brown	0.50	0.84	7.40	+250/+430	+610
10-12		Silty clay dusky	0.50	-0.58	7.70	+ 84/+103	+ 35
610-612		yellow green	-	-1.71	7.50	+ 12/+104	- 63
BC-14							
0- 1	2290	Silty clay brown	-	0.44	-	-	+612
38-41		Silty clay olive gray	0.46	-1.21	7.60	+ 19/-285	- 50
BC-16							
0- 3	3815	Silty clay moderate	0.46	0.88	7.20	+360/+450	+607
13-15		brown	0.51	0.71	7.30	-	+607
30-32		Silty clay grayish olive	0.48	-3.71	7.50	+ 4/- 27	- 43
BC-27							
Top	5120	Silty clay brown	0.50	3.71	6.90	+600/+630	+699
Bottom		silty clay olive gray	0.50	0.07	7.15	+500/+530	+540
GC-32							
0- 1	2860	Sand clayey brown	-	0.03	7.40	+530/+560	+599
165-185		Silty clay olive gray	-	-4.61	-	- 20/- 25	- 27
BC-38							
0- 1	5370	Clay moderate brown	0.43	0.43	7.25	+330/+430	+638
2- 4		" - "	0.43	0.43	7.10	-	+667
8-10		" - "	0.43	0.88	7.00	-	+683
14-16		" - "	0.50	0.87	7.00	+370/+520	+660
22-24		Clay pale olive	-	0.08	7.15	+460/+500	+528
48-50		" - "	0.48	0.005	7.15	+440/+480	+468
GC-39							
1- 5	5620	Silty clay moderate	0.46	0.28	7.00	+490/+540	+660
15-22		brown	0.46	0.27	7.00	+400/+540	+565
44-50		Silty clay lt olive	0.46	0.07	7.15	+330/+530	-
63-70		Silty clay grayish	0.46	-2.01	7.35	-	-
110-120		olive green	-	-3.10	-	-1/- 21	- 65
168-175		" - "	0.50	-1.91	7.65	-1/-32	- 59

HYDROCARBONS IN SEDIMENTS OF THE NORTH PACIFIC OCEAN

John B. Rapp and Frances D. Hostettler
U.S. Geological Survey, 345 Middlefield Road MS 999, Menlo Park, CA 94025, USA

INTRODUCTION

In 1991, a co-operative scientific program was undertaken by scientists from Russia, Canada and the United States of America. The GEMS program (GEochemistry of Marine Sediments) consisted of geochemical and geological work in the North Pacific Ocean. This paper reports on hydrocarbons found in sediments taken from Leg 4 of the cruise aboard the Russian Research Vessel *Akademik Alexander Vinogradov*. Objectives were to measure hydrocarbons in the sediment, to determine their possible sources, to measure the gases in the sediment, and to retrieve gas hydrates, if present.

METHODS

Heavy Hydrocarbons

Sampling: Samples were obtained from box cores or gravity cores between July 7 and July 27, 1991 at sites in the North Pacific (Figure 1). The top 8 cm of sediment were subsampled from box cores. The sampling sites varied in water depths from 2340 to 6100 meters. Table 1 contains the field number, water depth, sampling interval below the sediment/water interface and the laboratory number for samples taken for heavy hydrocarbon analysis. The prefix of the field number is either BC for box core or GC for gravity core. Sediments were sampled with an acetone-rinsed, stainless steel cylinder (for box cores) or an acetone-rinsed stainless steel spatula (for gravity cores), placed into glass jars (previously heated to 450° C.) with solvent-rinsed aluminum foil lined lids, and immediately frozen.

Laboratory Preparation: Samples were kept frozen from the time of sampling until they were air dried in the laboratory. The dried sediments were ground until they passed through a 32 mesh screen. A portion was used to determine the organic carbon content by wet combustion, following the procedure of Bush (1970). One hundred gram samples (50 grams for samples 1 and 2) were extracted three times with dichloromethane on a wrist action shaker (200 ml for 2 hr., 100 ml for 2 hr. and 100 ml for 15 min.). The extracts were concentrated to <5 ml on a rotary evaporator and passed through activated copper dust to remove any elemental sulfur. The resultant sulfur-free extract (SFE) was analyzed by gas chromatography and an aliquot was weighed.

The samples were then fractionated by liquid-solid chromatography. The solvent of the SFE was exchanged with hexane on a rotary evaporator, and the extract was applied to a column of 5 g and 2.5 g activated silica gel (Davidson Nos. 923 and 62 respectively) and 2.5 g deactivated (5% water) alumina. The column was eluted with hexane; 20, 40, 60% benzene in hexane; benzene; and methanol to produce 6 fractions. The hexane fraction contained normal alkanes, isoprenoids, and polycyclic biomarkers. The 20% benzene in hexane fraction contained polycyclic aromatic hydrocarbons (PAHs) and many unknown compounds. The fractions were analyzed by gas chromatography (GC). The hexane and 20% benzene in hexane fractions were also analyzed by gas chromatography/mass spectrometry (GC/MS).

Analysis: Gas chromatography of the fractions was performed on a gas chromatograph with a flame ionization detector and a 30 m x 0.3 mm bonded-phase fused-silica capillary column. The temperature program used was: initial temperature = 90° C for 3 minutes followed by a ramp of 4° C/min to 310° C and a final hold for 20 min. Other conditions were: injection port and detector temperature at 300° C, and column inlet pressure at 10 psi helium, splitless injection. GC/MS was performed on a GC/MS system with a 30 m x 0.3 mm bonded phase fused silica capillary column with splitless injection. Two temperature programs were used: 1) initial temperature 60° C, fast ramp to 90° C, 6° C/min to 300° C then hold for 10 min; and 2) initial temperature 150° C, fast ramp to 200° C, 1° C/min to 300° C. Hydrocarbon biomarkers in the hexane fraction were analyzed using selected-ion-monitoring (SIM): monitoring mass to charge (m/z) 191 for terpanes and triterpanes and monitoring m/z 217 for steranes and diasteranes. Biomarker identifications were made as in previous studies (Kvenvolden and others, 1985). Biomarker ratios were calculated using peak heights.

Multivariate Analysis: The multivariate analysis computer program package *Pirouette* (Infometrix Incorporated, Seattle, Washington) was used to study the distribution of aliphatic hydrocarbons in the sediment samples. These compounds were selected for study because they are more stable in the sediment and thus remain unchanged, for a longer period of time than organic compounds containing functional groups. The data matrix contained the normalized values of 18 normal alkanes (n-C_{14} to n-C_{31}), pristane, and phytane in 13 samples. The normalization was done with respect to the sum of all 20 compounds in each sample. The sum of the 20 normalized values for each sample equals 1.00, and thus each sample has the same statistical weighting as any of the other samples. I am studying hydrocarbon systems: if two samples were dominated by one system, the normalized values for the hydrocarbons in the samples would be the same whether the hydrocarbon concentrations were high or low. When concentrations are used in the data matrix, samples with high concentrations dominate the results compared to samples with low concentrations (Two samples dominated by the same system would produce different results: the sample with the high concentration would have larger results than the sample with the low concentration even though they are the same system). This problem is avoided when the normalization procedure is used. A second data matrix contained 6 autoscaled ratios of terpane and sterane biomarkers in 13 samples.

Multivariate analysis consisted of Hierarchical Cluster Analysis (HCA), and Principal Component Analysis (PCA) (Green, 1978). The metric used for HCA was Euclidian distance in n dimensional space (n = total number of variables = 20 for the aliphatic hydrocarbons and = 6 for the terpane and sterane biomarker ratios). The clustering technique used was single linkage because it is generally more robust than the other linkages (Jardine and Sibson, 1971). Varimax rotation was used for PCA to maximize the variance of the loadings.

Gaseous Hydrocarbons

Sampling: Sediment samples for gas analysis were placed in gas tight metal cans prepared with septa-covered ports. To each can was added sufficient sea water to establish a 100 cc headspace when the can was sealed. Sodium azide was added to inhibit bacterial growth and the can was sealed. The can was shaken to dissolve the azide and to suspend the sediment. The can was then stored frozen until analyzed in the laboratory. Evacuated test tubes (vacutainers) were used to sample gas bubbles when they occurred in the cores.

Laboratory Preparation: The samples were thawed and the cans were shaken vigorously (paint can shaker) for ten minutes. Gases partitioned into the headspace, a portion of which was analyzed by gas chromatography.

Analysis: Gases were analyzed on a gas chromatograph equipped with both flame ionization and thermal conductivity detectors. The chromatograph was calibrated with standard mixtures of gases. Concentrations of gases were calculated from integrated peak areas after background blanks were subtracted. Concentrations are referenced to the weight of wet sediment used.

RESULTS AND DISCUSSION

Sulfur Free Extract (SFE)

Table 1 contains the concentrations of the sulfur free extracts (ppm = micrograms of extract per gram of dry sediment), moisture (% H_2O), and organic carbon (% of dry sediment). There is a strong positive correlation (+0.80) between SFE and organic carbon but a strong negative correlation between SFE and %H_2O. The correlation between SFE and %H_2O is -0.62, which is statistically significant at the 95% confidence level. Figure 2 is a plot of the SFE concentration versus %H_2O and illustrates the negative correlation, most of which is due to the GC-10 samples (lab numbers 5,13,14,15) taken near the Aleutian Trench.

When only the GC-10 samples are used, the correlation coefficient becomes -0.94. As the samples increase in depth of burial (5,13,14,15), the water content decreases as would be expected (sediments would be squeezed by increasing amounts of pressure and for longer amounts of time) but this water loss would not explain the increase in SFE concentration because it is reported on a dry weight basis (per gram of dry sediment). One plausible explanation is that the source of extractable organic material has changed from a richer source near the bottom of the core to a poorer source at the top of the core. Thus, the

negative correlation between SFE and $\%H_2O$ might be explained because two variables (SFE and $\%H_2O$), which are correlated to a third variable (depth), would be indirectly correlated to each other. Since GC-10 is the only site with multiple depth samples, this explanation is specific to this site.

Normal Alkanes and Isoprenoids

Figure 3 contains the gas chromatograms of the aliphatic hydrocarbon fraction of all the 13 samples. The major peaks are the normal, straight-chain alkanes and the isoprenoids pristane and phytane. From visual inspection, one can discriminate two major groups of compounds. One group consists of low molecular weight hydrocarbons from n-C_{14} to n-C_{20} with concentrations of adjacent alkanes being similar (no odd or even carbon-number predominance) and the compound of highest concentration being n-C_{16} or n-C_{17}. The second group consists of high molecular weight hydrocarbons from n-C_{23} to n-C_{31} with concentrations of odd carbon-numbered alkanes much higher than concentrations of adjacent even carbon-numbered alkanes (odd predominance) and the compound of highest concentration being n-C_{27}, n-C_{29} or n-C_{31}.

Principal Components Analysis: Multivariate analysis has been used in several organic geochemical studies (Oygard et al., 1984; Shaw and Johns, 1986; Zumberge, 1987; Engel et al., 1988; Rapp, 1991). It is used in this study to determine the systems, when mixed in various proportions, that produce the observed compositions of the samples. One objective is to determine the composition of each "pure" system. This is achieved by observing the principal component loadings. Four rotated principal components account for 99.8% of the variance in the data set. Figure 4 contains plots of the loadings of four principal components. Another objective is to determine which samples are richest in each system in order to form groups of samples for easier interpretation. This is achieved by observing the principal component scores. Figure 5 contains the plots of the scores of the four principal components (PC 1 vs PC 2 and PC 3 vs PC 4). None of the samples have scores near zero in any of the principal components, which indicates that all the samples are mixtures; that is, none are pure end members. If a sample was almost a pure end member, it would have a high score in one of the principal components but would have near zero scores for the other principal components.

Principal Component 1 : This principal component accounts for 33.4% of the variance in the data set. It consists of the low molecular weight normal alkanes n-C_{16} to n-C_{22} and the isoprenoids pristane and phytane. Adjacent alkanes have similar concentrations: there is no preference of odd or even numbered n-alkanes. This pattern of compounds appears to be more mature material. The samples richest in this component are 5,13,9, and 14. The samples from the core GC-10 have decreasing scores with increasing depth (5-13-14-15), indicating that, with time, an increasing proportion of the alkanes being deposited is from more mature material. A possible explanation might be that erosion may have cut into the walls of the Aleutian Trench, exposed and mobilized older material which was then deposited where the core was taken. This might also indicate that the erosion rate in these adjacent areas is increasing with time and thus depositing (at the core site) more mature hydrocarbons at a higher rate compared to the rate of deposition from other sources.

Principal Component 2 : This component accounts for 26.4% of the variance in the data. It consists of mostly n-C_{27}, n-C_{29} and n-C_{31}, increasing in concentration in that order. The adjacent even numbered n-alkanes are very low in abundance and thus there is a very large odd carbon-number predominance. This high molecular weight odd carbon-number predominance is characteristic of a terrestrial source (Cranwell, 1973; Giger, et al., 1974). The samples richest in this component (compared to other sources) are 12, 3, and 4, the mid-ocean sites. The samples with the highest proportion of this terrestrial material are farthest from land. This component may represent terrestrial material that has been transported by air (eolian). Dusts collected over the Atlantic Ocean contain n-alkanes with very large odd carbon-number predominance and concentration maxima in the C_{27} to C_{31} range (Simoneit, 1977).

Principal Component 3 : This component accounts for 12.4% of the variance in the data. It consists of mostly high molecular weight odd carbon-number n-alkanes ranging from n-C_{19} to n-C_{29}. The compound with the maximum concentration is n-C_{27}. The adjacent even number alkanes are in greater abundance then those in PC 2. There is a definite odd carbon-number predominance and is thus terrestrial but the predominance is much less than that in PC 2. The shift in the compound with the maximum concentration from n-C_{31} in PC 2 to n-C_{27} and the decrease in odd carbon-number predominance may indicate that this component is more degraded than PC 2 and/or is from a different source. This component may be water-transported terrestrial material. During the period between leaving the land and being deposited in the marine sediment column, water-transported terrestrial material has had more time (and biological activity)

to be degraded than air-transported terrestrial material. The samples with the highest scores are 1 and 15, both of which illustrate interesting trends. The scores of samples 1, 2 and 3 decrease as the sample sites go from nearer land (1) to open ocean far from land (3), as would be expected if the source was terrestrial. The scores of the core GC-10 samples increase with increasing depth: low score for 5 (top), intermediate scores for 13 and 14 and high score for 15 (bottom), indicating that water-transported terrestrial material was a much higher proportion of the total load of hydrocarbon deposition in the past (sample 15) and has decreased over time to the present (sample 5) minimum.

Principal Component 4 : This component accounts for 27.5% of the variance in the data. It consists of n-C_{14}, n-C_{15}, and n-C_{16}. This component may be an artifact of the laboratory preparation and is due to evaporation. During the solvent exchange from the extracting solvent (dichloromethane) to hexane, the sample is evaporated to near dryness three times to assure that none of the extracting solvent is present in the sample when it goes onto the silica/alumina chromatography column. The very volatile compounds (e.g. low molecular weight alkanes) are lost to varying degrees depending upon their volatility, the temperature and length of time of the evaporation, and the nature of the organic matrix of the sample. This is why many hydrocarbon laboratories report on the C_{15+} fraction. The samples with the highest scores for this component are 14, 9, 13, and 5 (Fig. 5), which are also the samples highest in principal component 1, which has high loadings in the adjacent low molecular weight alkanes (n-C_{17-22})(Fig. 4).

Hierarchical Cluster Analysis : This type of analysis groups samples according to the similarity between samples and/or groups (clusters) of samples. The similarity is measured by the distance (in n-dimensional space, in this case 20 dimensions) between a sample or cluster and another sample or cluster. The results of this analysis (dendogram) are presented in Fig. 6. One cluster, at the top, consists of samples 3, 4, and 12. This cluster corresponds to samples high in principal component 2. These mid-ocean samples are dominated by an eolian hydrocarbon source. The cluster at the bottom consists of samples 9, 14, 5, and 13 and corresponds to samples high in principal components 1 and 4. These samples are dominated by a reworked hydrocarbon source. The rest of the samples form the third cluster, which contains samples high in principal component 3 (samples 15 and 1) and samples which were intermediate in their scores in all 4 principal components (samples 10, 8, 2, and 6).

Biomarkers (Terpanes and Steranes)

Compounds observed in the m/z 191 trace include tricyclic terpanes, especially C_{23} through C_{28} with C_{23} the dominant member, pentacyclic triterpanes from C_{27} through C_{34}, including the hopane series ($\alpha\beta$, the mature geologic configuration, $\beta\beta$, the immature biogenic configuration, and $\beta\alpha$ or moretane, a somewhat intermediate series), and hopenes, with diploptene (C_{30}) and trisnorhopene (C_{27}) as the dominant members. The hopenes are indicative of very recent biogenic (microbial) contribution to the sediments (Philp, 1985).

Ratios which are indicative of the sources and maturity of the samples are presented in Table 2. The two maturity parameters are noted: $\alpha\beta C_{31}$ (S/(S+R)) from the 191 trace and $\alpha\alpha\alpha C_{29}$ (S/(S+R)) from the 217 trace. The hopane parameter reaches equilibrium or full maturity at a value of 0.6 (Ensminger, et al., 1974) and the sterane parameter at about 0.5 (Mackenzie, et al., 1980). The remaining parameters are more descriptive of source. The diploptene and $\beta\beta C_{31}$ ratios compare these two compounds to the major hopane, $\alpha\beta C_{30}$, to give an assessment of the relative amounts of each indicator of immature biogenic input. Although they both indicate immaturity, they seem to vary independently and so reflect different sources. Trisnorhopene seems to vary with the diploptene. Variations in Tm/Ts can indicate variations in facies as well as maturity. High diasterane ratios can indicate high clay sources or overmaturity (Waples and Machihara, 1991). The biomarkers may reflect input from several sources. Highly mature hopanes and steranes may come from petrogenic sources or be reworked sediments. The hopenes come from various immature biogenic sources.

Hierarchical Cluster Analysis : Six ratios of biomarkers in all 13 samples were autoscaled and subjected to cluster analysis. Figure 7 contains the dendograms of the ratios and the samples from the cluster analysis. The $\beta\beta C_{31}/\alpha\beta C_{30}$ ratio is independent of the other ratios and represents biogenic input. The $\alpha\beta C_{31}$ S/(S+R) ratio and the $\alpha\alpha\alpha C_{29}$ S/(S+R) ratio form a single cluster and represent a maturity parameter. The other 3 ratios, $\beta\alpha D_{27}$(S+R)/$\alpha\alpha\alpha C_{29}$(S+R) , C_{23}/C_{30}, and $\alpha\beta C_{29}/\alpha\beta C_{30}$ form a cluster that might represent a source parameter.

The dendogram of the samples has two clusters and several independent samples. The cluster at the top, containing samples 10, 6, 3, and 12, is a mature group with high maturity (S/(S+R)) ratios, high

diasterane ratios, and medium $\beta\beta C_{31}/\alpha\beta C_{30}$ ratios. The next cluster, containing samples 2, 13, 14, 5, and 1, is an immature group with low maturity (S/(S+R)) ratios, low diasterane ratios, and high $\beta\beta C_{31}/\alpha\beta C_{30}$ ratios. Sample 4 is an outlier because it is highest in all three "source" ratios: the ratios are extremely high for C_{23}/C_{30} and for the diasterane ratio. Samples 8 and 9 are both almost completely mature according to the $\alpha\beta C_{31}$ S/(S+R) ratio but the $\alpha\alpha\alpha C_{29}$ S/(S+R) ratio indicates sample 9 has high maturity whereas sample 8 has low to moderate maturity. Samples 8 and 9 have $\beta\beta C_{31}/\alpha\beta C_{30}$ ratios that are much lower than the values of the samples in the mature cluster. Sample 15 is an outlier because it appears to be even less mature than any of the samples in the immature group: the $\alpha\beta C_{31}$ S/(S+R) ratio is much lower than that of the immature group and it has the highest $\beta\beta C_{31}/\alpha\beta C_{30}$ ratio in the whole data set. In summary, the samples that show the highest maturity and corresponding low levels of immature input are samples 3, 4, 6, 8, 9, 10, and 12. The samples that are dominated by immature biogenic input are 1, 2, and the GC-10 core (samples 5, 13, 14, and 15). Biomarker chromatograms are shown (Figure 8 = m/z 191 and Figure 9 = m/z 217) which are typical of samples dominated by immature biogenic constituents (sample 1) and sites dominated by mature constituents (sample 9).

Aromatics

Three samples were examined in detail for aromatic consistuents. Sample 14 contained the largest amounts of polycyclic aromatic hydrocarbons (PAHs). Phenanthrene and alkyl phenanthrene homologs were the most prominent. Naphthalene and its alkylated homologs were also present. In general, the alkylated PAHs are in high enough concentrations relative to their parent PAH that the ratio of alkylated PAH to parent PAH does not appear to be attributable to pyrogenic or combustion-sourced input (Prahl and Carpenter, 1983); a petrogenic source is a possibility. In the PAH group of molecular weight 252, perylene is present in the highest concentration. Perylene has been reported in several deep-water sediments in anomalously high concentrations, and considered to come from unknown biogenic sources (Wakeham and Farrington, 1980). Also in this sample, benz(e)pyrene is present, and its isomer benz(a)pyrene, reported to indicate anthropogenic combustion or pollution sources, is absent. The most prominent peaks in the aromatic fraction are unknown compounds.

The two other samples, 6 and 10, show very, very low amounts of aromatic constituents. The major peaks are again unknown compounds. The PAHs that are present are in only trace amounts; they also have alkylated homologs in high enough relative concentrations that they cannot be attributed to a pyrogenic source.

Gases

The data for samples taken for gas analysis are shown in Table 4. Samples 13 and 15 were taken near the Aleutian Trench and sample 1 was taken near the Japan Trench (and Kuril Islands) . The highest methane levels are in sample 1 (2.5 nl/g wet sediment) and sample 15 (2.3 nl/g). Sample 13, which was stratigraphically higher in the core than sample 15, also showed an elevated level (1.3 nl/g). Sample 11, the deepest core (>6 meters), had only 0.7 nl/g. All the samples had methane levels which were in the range observed by Kvenvolden and Redden (1980) for Bering Sea sediments (after conversion from nl/g to nl/l). Ethane, ethylene, propane, propylene, n-butane and isobutane were sought but not found. Their detection limit was 0.1 nl/g. The carbon dioxide concentrations were low in all samples except sample 2 (0.8 µl/g) and sample 1 (0.3 µl/g). Evacuated test tube samples were taken from bubbles or spaces between the core and liner from cores GC7, GC9 and GC10. All these samples showed methane and carbon dioxide concentrations near the blanks. No gas hydrates were observed in any of the cores taken.

CONCLUSIONS

Statistical analysis of the hydrocarbons indicates that all the samples were very heterogeneous. None were extremely rich in any one source of hydrocarbons. Analysis of the aliphatic hydrocarbon data indicates that there are 3 major sources of alkanes in these sediments. The most significant source is reworked material characterized by low molecular weight hydrocarbons with little or no odd carbon-number predominance. Samples richer in this source are samples from core GC-10 (5, 13, 14) and sample 9. The next most significant source is air-transported, terrestrial material characterized by high levels of n-C_{27}, n-C_{29} and n-C_{31} (maximum at n-C_{31}) with large odd carbon-number predominance. Samples richer in this source are the mid-ocean samples 12, 3, and 4. The third source is water-transported terrestrial material

characterized by high levels of the odd carbon-numbered alkanes n-C_{19} to n-C_{27} (maximum at n-C_{27}) with large odd carbon-number predominance. Samples richer in this source are samples 15, 1, and 2. Samples 1, 2, and 3 are located in a straight line going from nearer land (1) to mid-ocean (3). As would be expected of a terrestrial source, this component increases from mid-ocean to nearer to land. The hierarchical cluster analysis of the biomarker data produced three groups of ratios. The $\alpha\beta C_{31}$ S/(S+R) and the $\alpha\alpha\alpha C_{29}$ S/(S+R) ratios cluster together to form a maturity group. The $\beta\beta C_{31}/\alpha\beta C_{30}$ is an independent ratio. The third group consists of C_{23}/C_{30}, $\alpha\beta C_{29}/\alpha\beta C_{30}$ and $\beta\alpha D_{27}$(S+R)/$\alpha\alpha\alpha C_{29}$(S+R) and may be a source related group. The cluster analysis also produces three groups of samples. A mature group consists of samples 6, 10, 3, and 12 and is characterized by high S/(S+R) ratios, high diasterane ratios, and moderate $\beta\beta C_{31}/\alpha\beta C_{30}$ ratios. An immature group consists of samples 13, 14, 2, 5, and 1 and is characterized by low S/(S+R) ratios, low diasterane ratios, and high $\beta\beta C_{31}/\alpha\beta C_{30}$ ratios. The rest of the samples are outliers (independents) and were detailed in the main text. Samples 4, 9, and 8 are mature, whereas sample 15 is very immature.

The mathematical analysis of the samples from core GC-10 reveals several interesting conclusions. The bottom of the core (sample 15) is the most immature sample in the data set according to the $\alpha\beta C_{31}$S/(S+R) ratio. It also has the highest $\beta\beta C_{31}/\alpha\beta C_{30}$ ratio of the data set indicating highest biological activity. It has the highest water-transported terrestrial and air-transported terrestrial scores of the core samples. The top of the core (sample 5) is the most mature of the core samples according to the $\alpha\beta C_{31}$S/(S+R) ratio. It has the lowest $\beta\beta C_{31}/\alpha\beta C_{30}$ ratio of the core samples indicating the least biological activity in the core. It has the highest reworked material score in the whole data set and the lowest water-transported terrestrial score in the whole data set. The usual trend in a core is that the most immature sample is on the top and the most mature sample is on the bottom. The opposite is true in this particular core because of the steadily increasing proportion of reworked material being deposited with time compared to the other sources of material.

Low concentrations of methane were observed in samples taken near the Aleutian and Japan Trenches where high organic carbon and SFE would be good sources for methane production, but the levels of methane were very much lower than the concentrations associated with gas hydrates. No gas hydrates were observed in any of the cores taken.

REFERENCES

Bush, P.R., 1970, A rapid method for the determination of carbonate carbon and organic carbon: Chemical Geology, v. 6, p. 59-62.

Cranwell, P.A.,1973, Chain-length distribution of n-alkanes from lake sediments in relation to post-glacial environmental change: Freshwater Biology, v. 3, p. 259-265.

Engel, M.H., Imbus, S.W., and Zumberge, J.E., 1988, Organic geochemical correlation of Oklahoma crude oils using R- and Q-mode factor analysis: Organic Geochemstry, v. 12, p. 157-170.

Ensminger, A., van Dorsselaer, A, Spykerelle, C., Albrecht, P., and Ourisson, G., 1974, Pentacyclic triterpanes of the hopane type as ubiquitous geochemical markers- origin and significance: in Tissot, B. and Bienner, G., (eds.), Advances in Organic Geochemistry 1973. Paris, Editions Technip, p. 245-260.

Giger, W., Reinhardt, M., Schatffner, C., and Stumm, W., 1974, Petroleum derived and indigenous hydrocarbons in recent sediments of Lake Zug, Switzerland: Environ. Sci. Technol., v. 8, p. 454-455.

Green, P.E., 1978, Analyzing multivariate data: Hinsdale, Ill., The Dryden Press.

Jardine, N., and Sibson, R., 1971, Mathematical Taxonomy: London, Wiley.

Kvenvolden, K.A., Rapp, J.B., and Bourell, J.H., 1985, Comparison of molecular markers in crude oils and rocks from the North Slope of Alaska: in Magoon, L.B. and Claypool, G.E. (eds.), Alaska North Slope Oil/Rock Correlation Study. American Association of Petroleum Geologists Studies in Geology, v. 20, p. 593-617.

Kvenvolden, K.A., and Redden, G.D., 1980, Hydrocarbon gases in sediment of the shelf, slope and basin of the Bering Sea.: Geochimica et Cosmochimica Acta, v. 44, p. 1145-1150.

Oygard, K., Grahl-Nielsen, O., and Ulvoen, S., 1984, Oil/oil correlation by aid of chemometrics: Organic Geochemistry, v. 6, p. 561-567.

Mackenzie, A.S., Patience, R.L., Maxwell, J.R., Vandenbroucke, M., and Durand, B., 1980, Molecular parameters of maturation in the Toarcian shales, Paris basin, France- I. Changes in configuration of acyclic isoprenoid alkanes, steranes, and triterpanes: Geochimica et Cosmochimica Acta, v. 44, p. 1709-1721.

Philp, R.P., 1985, Fossil Fuel Biomarkers: Amsterdam, Elsevier, 294p.

Prahl, F.G. and Carpenter, R., 1983, Polycyclic aromatic hydrocarbons (PAH)- phase associations in Washington coastal sediments: Geochimica et Cosmochimica Acta, v. 47, p. 1013-1023.

Rapp, J.B., 1991, A statistical approach to the interpretation of aliphatic hydrocarbon distributions in marine sediments: Chemical Geology, v.93, p. 163-177.

Shaw, P.M., and Johns, R. B., 1986, Organic geochemical studies of a recent Inner Great Barrier Reef sediment, II. Factor analysis of sedimentary organic materials in input source determinations: Organic Geochemistry, v. 9, p. 237-244.

Simoneit, B.R.T., 1977, Organic matter in eolian dusts over the Atlantic Ocean: Mar. Chem., v. 5, p. 443-464.

Wakeham, S.G. and Farrington, J.W., 1980, Hydrocarbons in contemporary aquatic sediments, Chapter 1, *in* Contaminants and Sediments, Volume 1, R.A. Baker, ed., Ann Arbor, MI, Ann Arbor Science Publishers, Inc., p. 3-32.

Waples, D.W., and Machihara, T., 1991, Biomarkers for geologists-- a practical guide to the application of steranes and triterpanes in petroleum geology: American Association of Petroleum Geologists, Methods in Exploration, No. 9, 91 pp.

Zumberge, J.E., 1987, Prediction of source rock characteristics based on terpane biomarkers in crude oils: a multivariate statistical approach: Geochimica et Cosmochimica Acta, v. 51, p. 1625-1637.

Table 1. Data for samples taken for heavy hydrocarbons

Field Number	Water Depth (m)	Sediment Interval (cm)	Lab Number	Organic Carbon (%)	SFE (ppm)	H_2O (%)
GC-6	5500	25-31	1	0.8	24.0	68
GC-7	4990	50-57	2	<0.1	8.4	60
BC-8	5860	0-8	3	0.6	3.8	65
GC-9	6100	8-13	4	<0.1	3.6	60
GC-10	4000	0-5	5	0.3	15.7	53
GC-10	4000	65-70	13	0.1	20.6	45
GC-10	4000	100-105	14	0.4	23.5	41
GC-10	4000	147-151	15	0.3	33.9	36
BC-14	2920	0-8	6	0.1	6.8	63
BC-26	2970	0-8	8	<0.1	3.3	54
BC-27	5120	0-8	9	0.3	4.3	53
BC-30	2340	0-8	10	<0.1	4.7	55
BC-38	5370	0-8	12	0.5	4.5	69

Table 2. Biomarker ratios

Lab Number	Tm/ Ts	C_{23}/ C_{30}	$\alpha\beta C_{29}$/ $\alpha\beta C_{30}$	$\alpha\beta C_{31}$ S/(S+R)	Diplop./ $\alpha\beta C_{30}$	$\beta\beta C_{31}$/ $\alpha\beta C_{30}$	$\alpha\alpha\alpha C_{29}$ S/(S+R)	$\beta\alpha D_{27}$(S+R)/ $\alpha\alpha\alpha C_{29}$(S+R)
1	*	0.23	0.33	0.43	0.9	0.95	0.23	0.34
2	2.1	0.51	0.48	0.41	0.0	0.91	0.23	0.38
3	1.3	0.87	0.57	0.54	0.0	0.28	0.31	0.82
4	1.2	3.90	0.75	0.48	0.0	0.52	0.27	1.60
5	*	0.50	0.47	0.47	1.0	0.66	0.24	0.62
13	*	0.35	0.48	0.42	1.2	0.76	0.23	0.42
14	*	0.37	0.43	0.40	1.3	0.74	0.24	0.45
15	*	0.20	0.44	0.32	2.2	1.20	0.26	0.37
6	1.2	0.17	0.46	0.53	0.3	0.37	0.35	0.88
8	1.8	0.33	0.51	0.57	0.0	0.17	0.25	0.47
9	1.9	0.23	0.71	0.58	0.0	0.12	0.40	0.25
10	1.8	0.34	0.50	0.50	0.2	0.41	0.31	0.78
12	1.1	0.75	0.56	0.48	0.0	0.54	0.37	0.85

Identities of the peaks used in these ratios are as follows: (reference Table 3)

Tm/Ts = peak 9 / peak 7
C_{23}/C_{30} = peak 1 / peak 13
$\alpha\beta C_{29}/\alpha\beta C_{30}$ = peak 11 / peak 13
$\alpha\beta C_{31}$ S/(S+R) = peaks 16
Diplop./$\alpha\beta C_{30}$ = peak 18 / peak 13
$\beta\beta C_{31}/\alpha\beta C_{30}$ = peak 20 / peak 13
$\alpha\alpha\alpha C_{29}$ S/(S+R) = peak C(S)/(C(S)+C(R))
$\beta\alpha D_{27}$(S+R)/$\alpha\alpha\alpha C_{29}$(S+R) = (peak A(S) + peak A(R)) / (peak E(S) + peak E(R))

* Tm/Ts can not be accurately measured because of trisnorhopene overlap of Tm

Table 3. Identification of terpanes and steranes.

Peak	Compound	
TERPANES and TRITERPANES (m/z 191)		
1	C_{23} tricyclic terpane	C_{23}
2	C_{24} tricyclic terpane	C_{24}
3	C_{25} tricyclic terpane	C_{25}
4	Triplet: C_{24} tetracyclic terpane	C_{24}
	C_{26} tricyclic terpane (?S)	C_{26}
	C_{26} tricyclic terpane (?R)	C_{26}
5	C_{28} tricyclic terpanes (?S and R)	C_{28}
6	C_{29} tricyclic terpanes (?S and R)	C_{29}
7	18α(H)-22,29,30-trisnorneohopane (Ts)	C_{27}
8	22,29,30-trisnorhop-17(21)-ene	C_{27}
9	17α(H)-22,29,30-trisnorhopane (Tm)	C_{27}
10	17β(H)-22,29,30-trisnorhopane	C_{27}
11	17α(H),21β(H)-30-norhopane	C_{29}
12	17β(H),21α(H)-30-normoretane	C_{29}
13	17α(H),21β(H)-hopane	C_{30}
14	17β(H),21β(H)-norhopane	C_{29}
15	17β(H),21α(H)-moretane	C_{30}
16	17α(H),21β(H)-homohopane(22 S and R)	C_{31}
17	17β(H),21β(H)-hopane	C_{30}
18	17β(H),21β(H)-hop-22(29)-ene (diploptene)	C_{30}
19	17α(H),21β(H)-bishomohopane(22 S and R)	C_{32}
20	17β(H),21β(H)-homohopane	C_{31}
21	17α(H),21β(H)-trishomohopane(22 S and R)	C_{33}
22	17α(H),21β(H)-tetrakishomohopane(22 S and R)	C_{34}
STERANES and DIASTERANES (m/z 217)		
A(S)	13β(H),17α(H)-diacholestane(20S)	C_{27}
A(R)	13β(H),17α(H)-diacholestane(20R)	C_{27}
B(S)	5α(H),14α(H),17α(H)-cholestane(20S)	C_{27}
C(S)	24-ethyl-13β(H),17α(H)-diacholestane(20S)	C_{29}
B(R)	5α(H),14α(H),17α(H)-cholestane(20R)	C_{27}
C(R)	24-ethyl-13β(H).14α(H)-diacholestane(20R)	C_{29}
D(S)	24-methyl-5α(H),14α(H),17α(H)-cholestane(20S)	C_{28}
D(R)	24-methyl-5α(H),14α(H),17α(H)-cholestane(20R)	C_{28}
E(S)	24-ethyl-5α(H),14α(H),17α(H)-cholestane(20S)	C_{29}
E(R)	24-ethyl-5α(H),14α(H),17α(H)-cholestane(20R)	C_{29}

Table 4. Data for samples taken for gas analysis.

Field Number	Water Depth (m)	Sediment Interval (cm)	Lab Number	CH_4 (nL/g)*	CO_2 (μL/g)*
GC-6	5500	34-41	1	2.5	0.3
GC-7	4990	50-57	2	0.2	0.8
GC-9	6100	245-249	4	<0.1	<0.1
GC-10	4000	70-72	13	1.3	0.1
GC-10	4000	156-160	15	2.3	<0.1
GC-20	3430	46-49	7	0.3	<0.1
GC-34	3750	621-625	11	0.7	0.1

* per gram of wet sediment

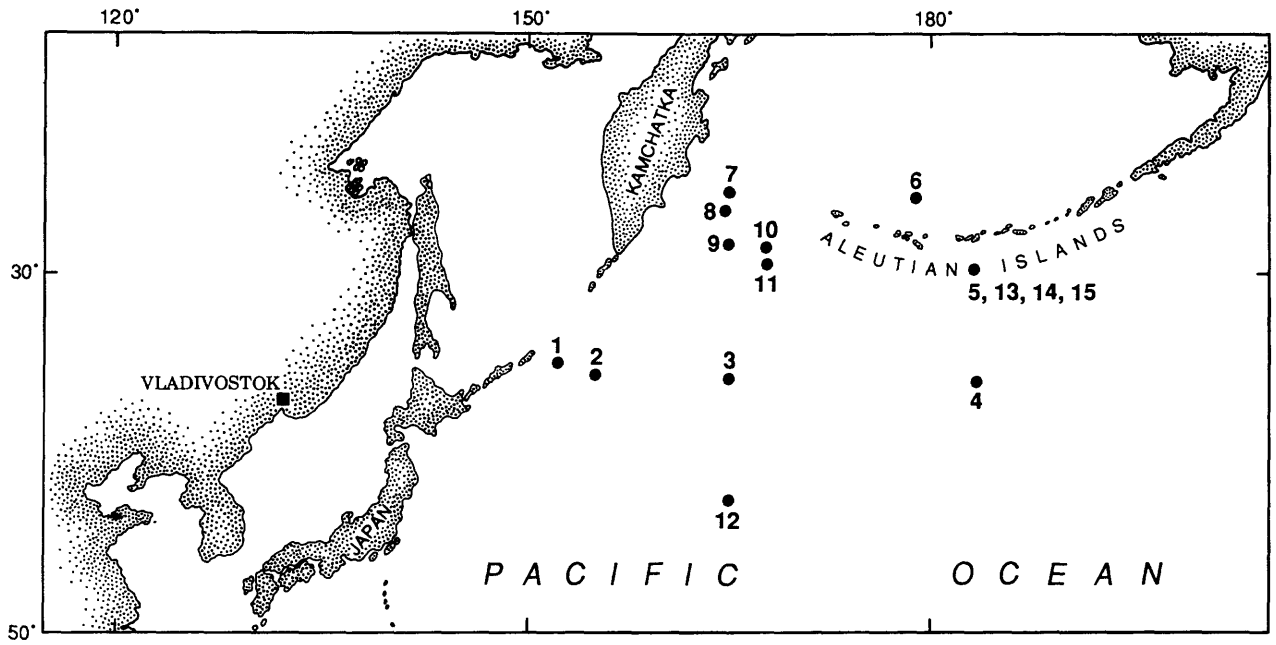

Figure 1. Map of the North Pacific Ocean showing sampling locations (laboratory numbers).

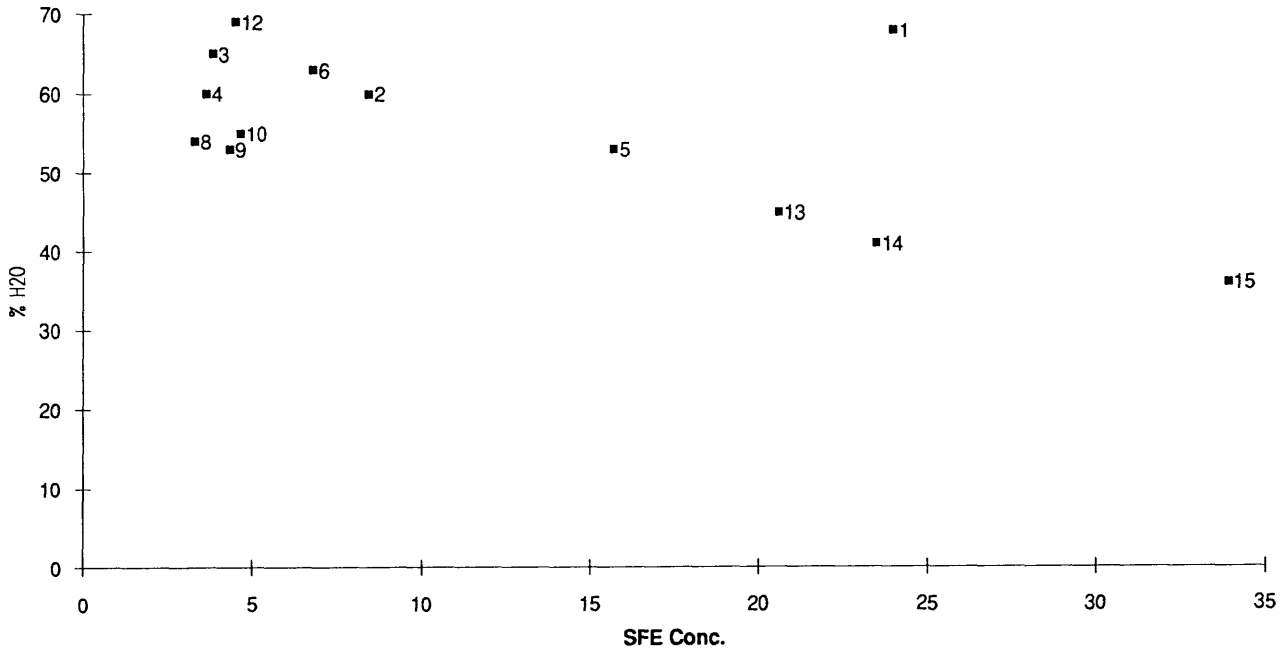

Figure 2. Plot of SFE concentration versus $\%H_2O$ in sediment samples.

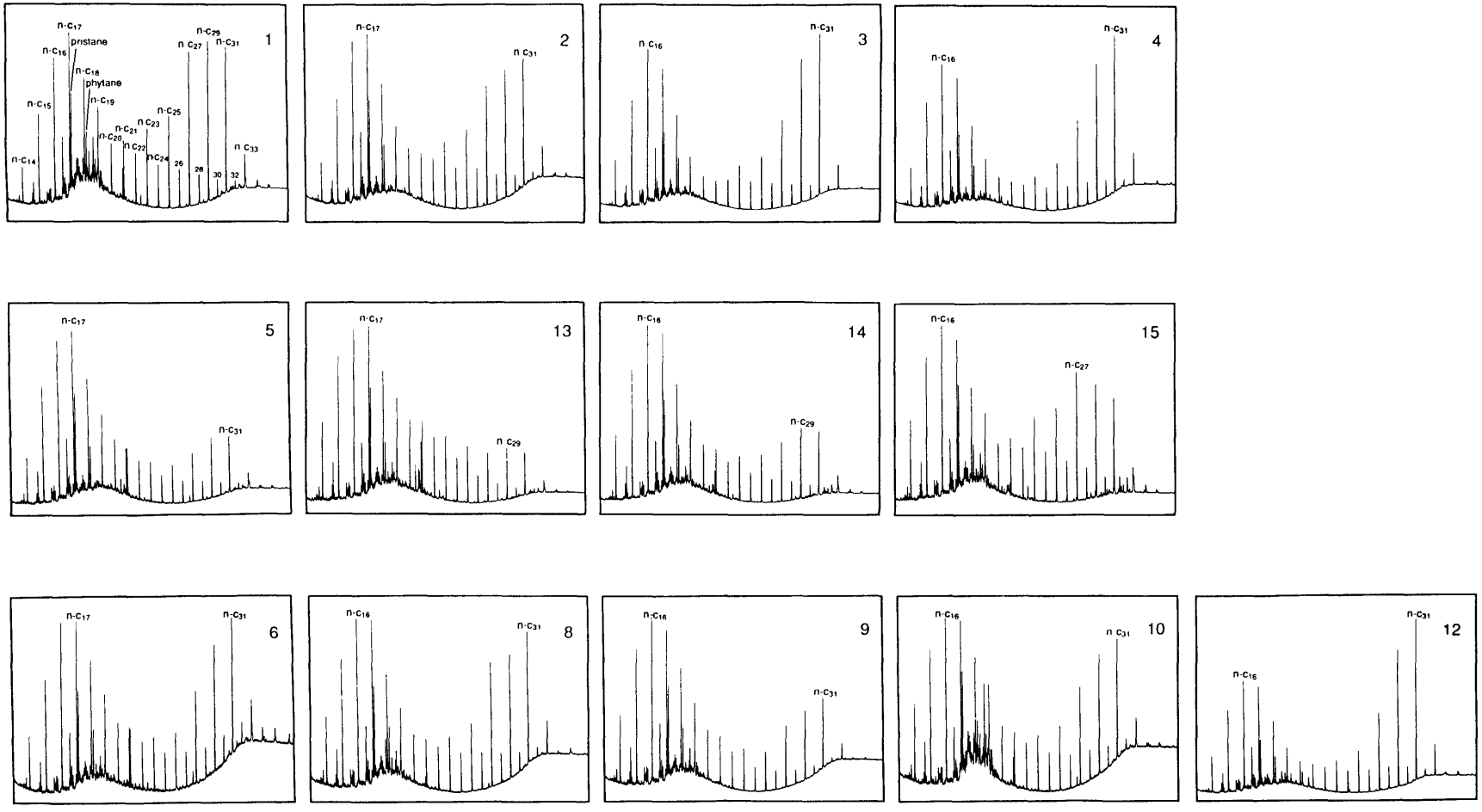

Figure 3. Gas Chromatograms of the aliphatic hydrocarbon fraction of the 13 samples.

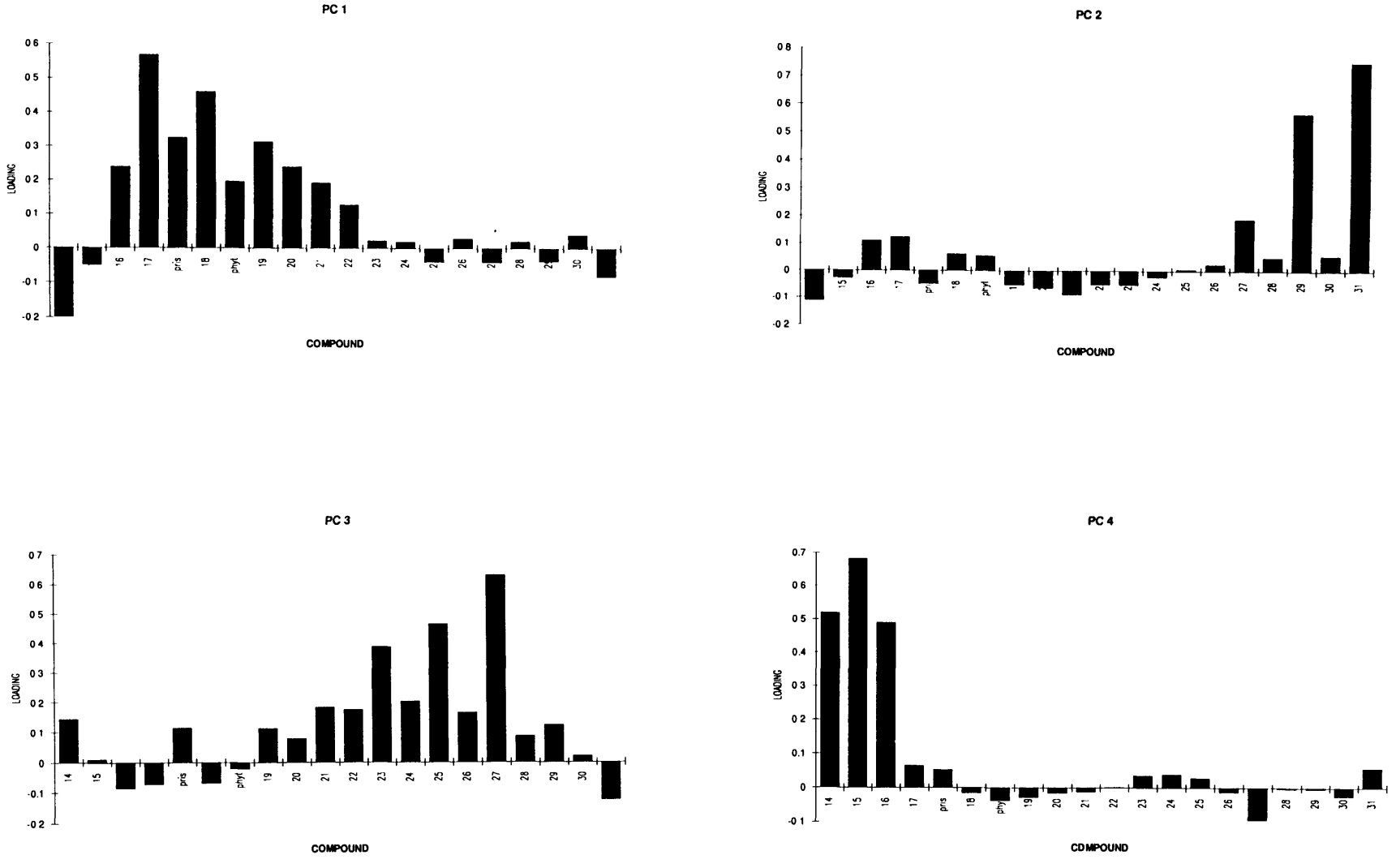

Figure 4. Plots of the loadings of the four principal components of the aliphatic hydrocarbons.

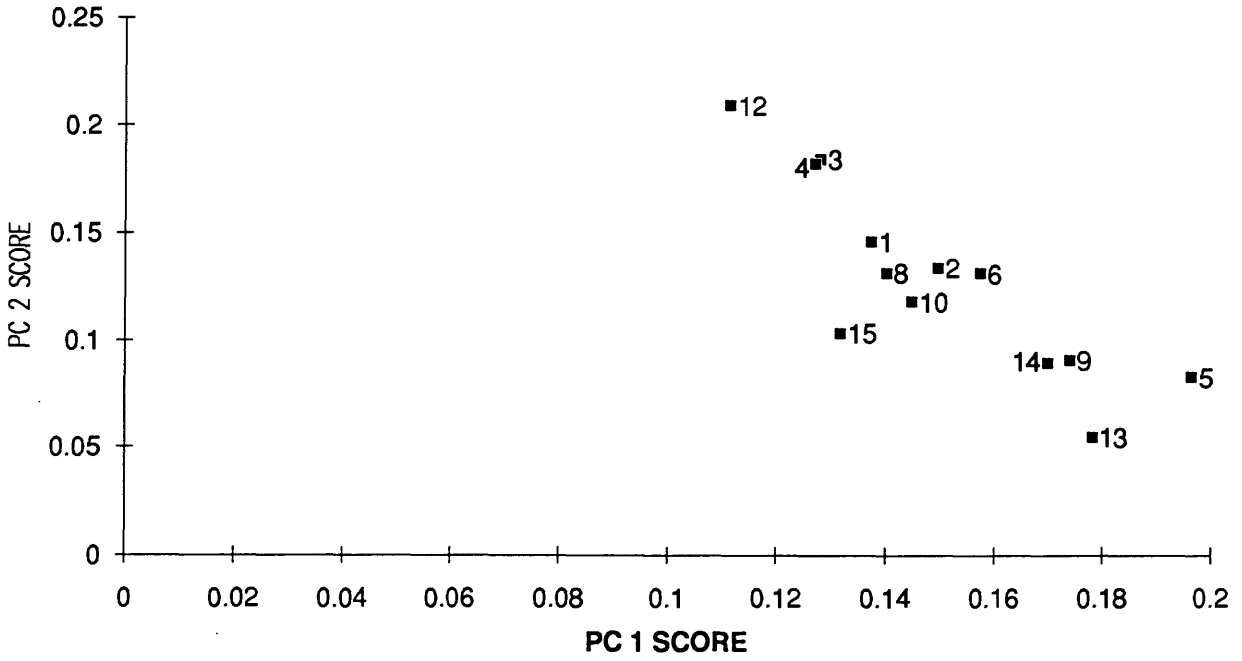

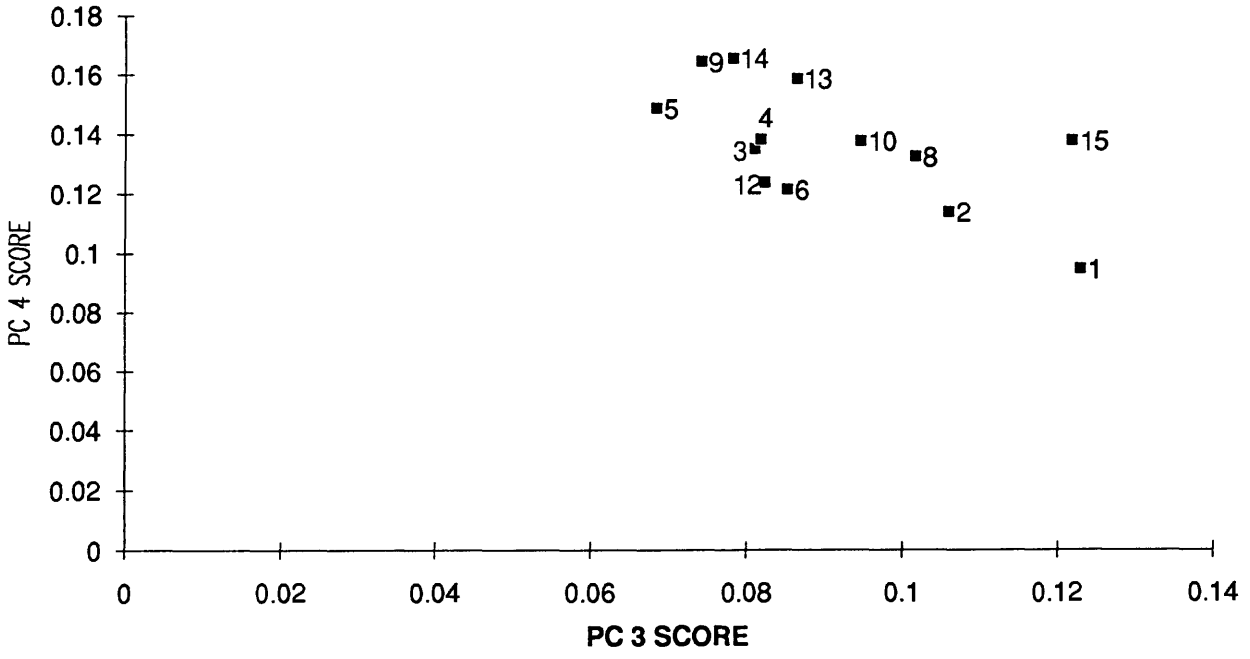

Figure 5. Plots of the scores (1 vs 2 and 3 vs 4) of the four principal components of the aliphatic hydrocarbons.

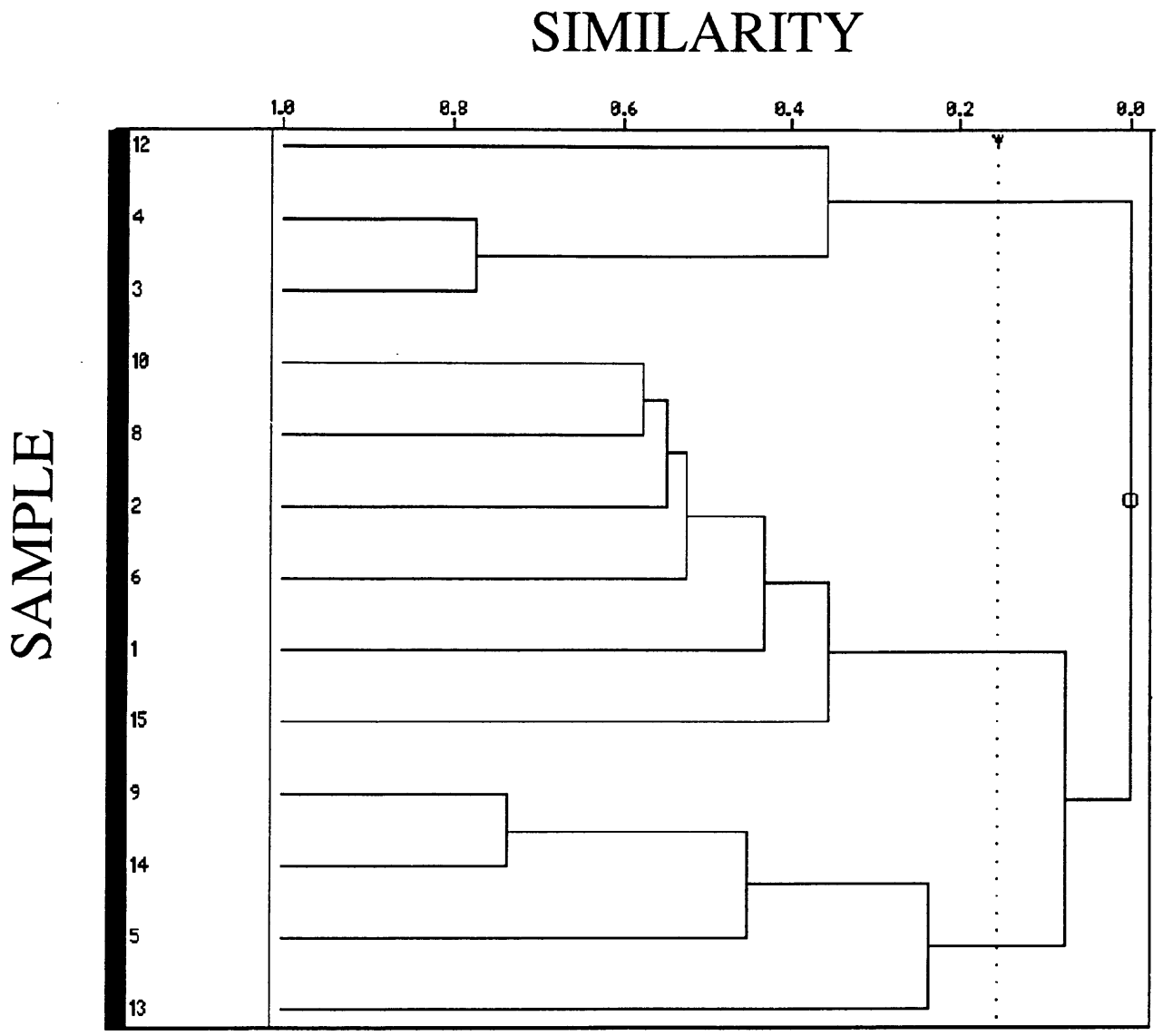

Figure 6. Dendogram of the samples from the alkane cluster analysis

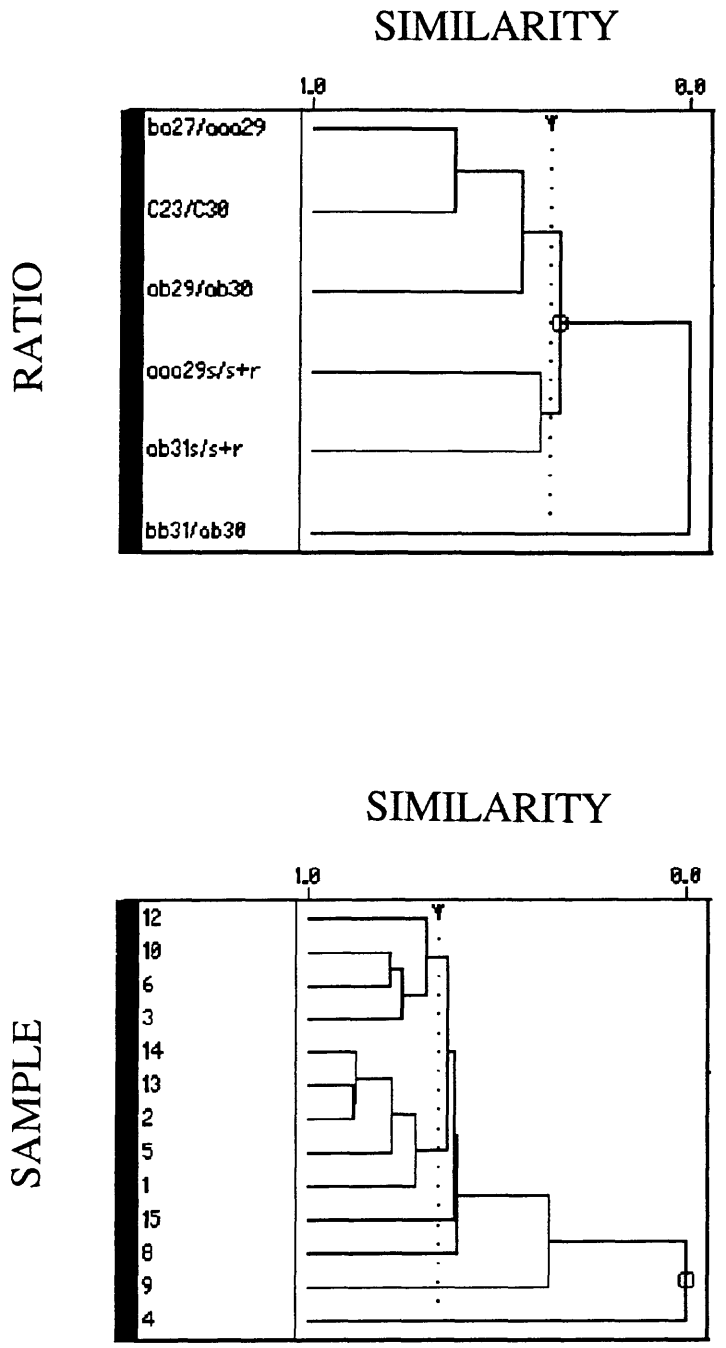

Figure 7. Dendograms of ratios and samples from the biomarker cluster analysis.

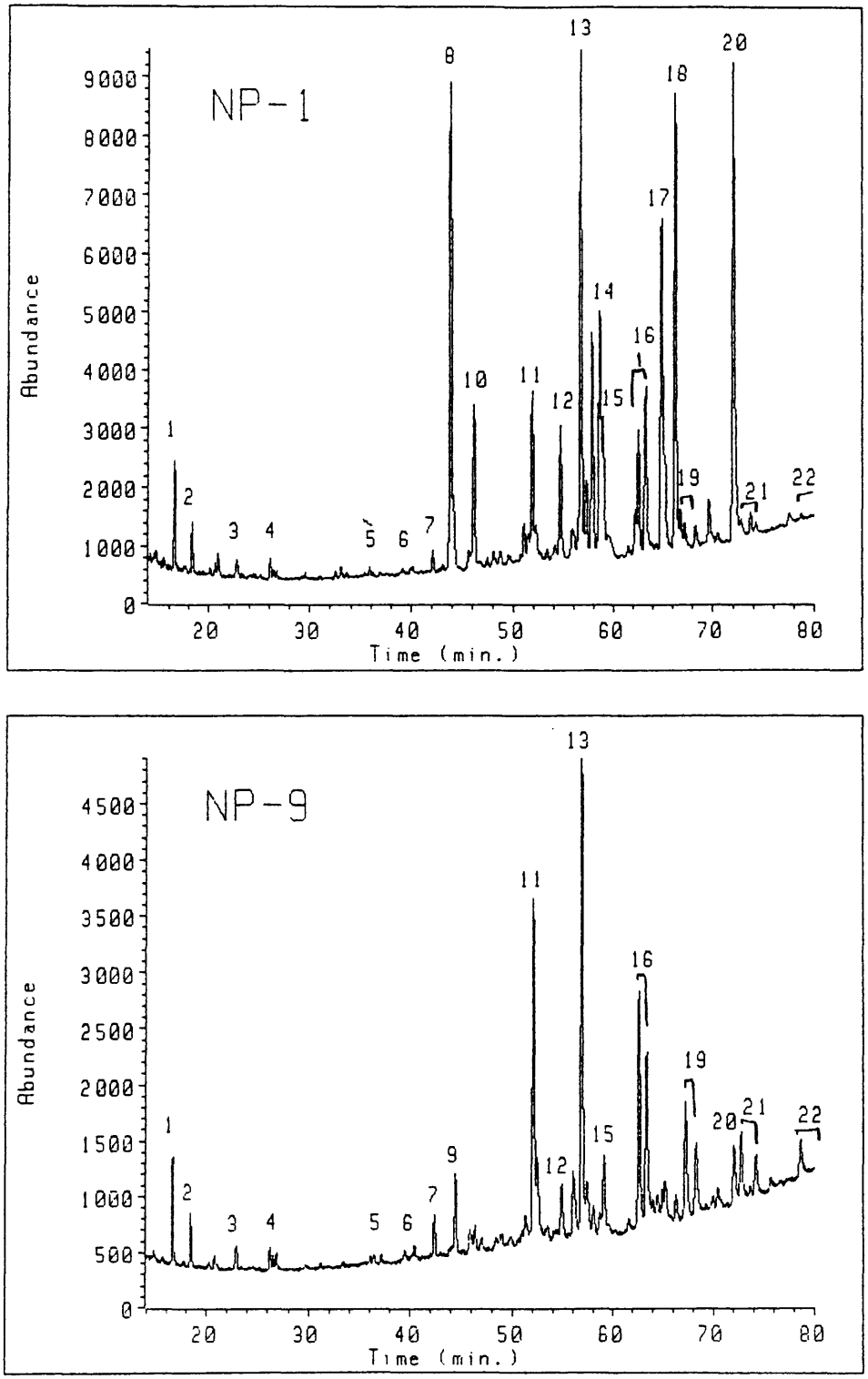

Figure 8. Chromatograms (m/z 191) of samples 1 and 9.

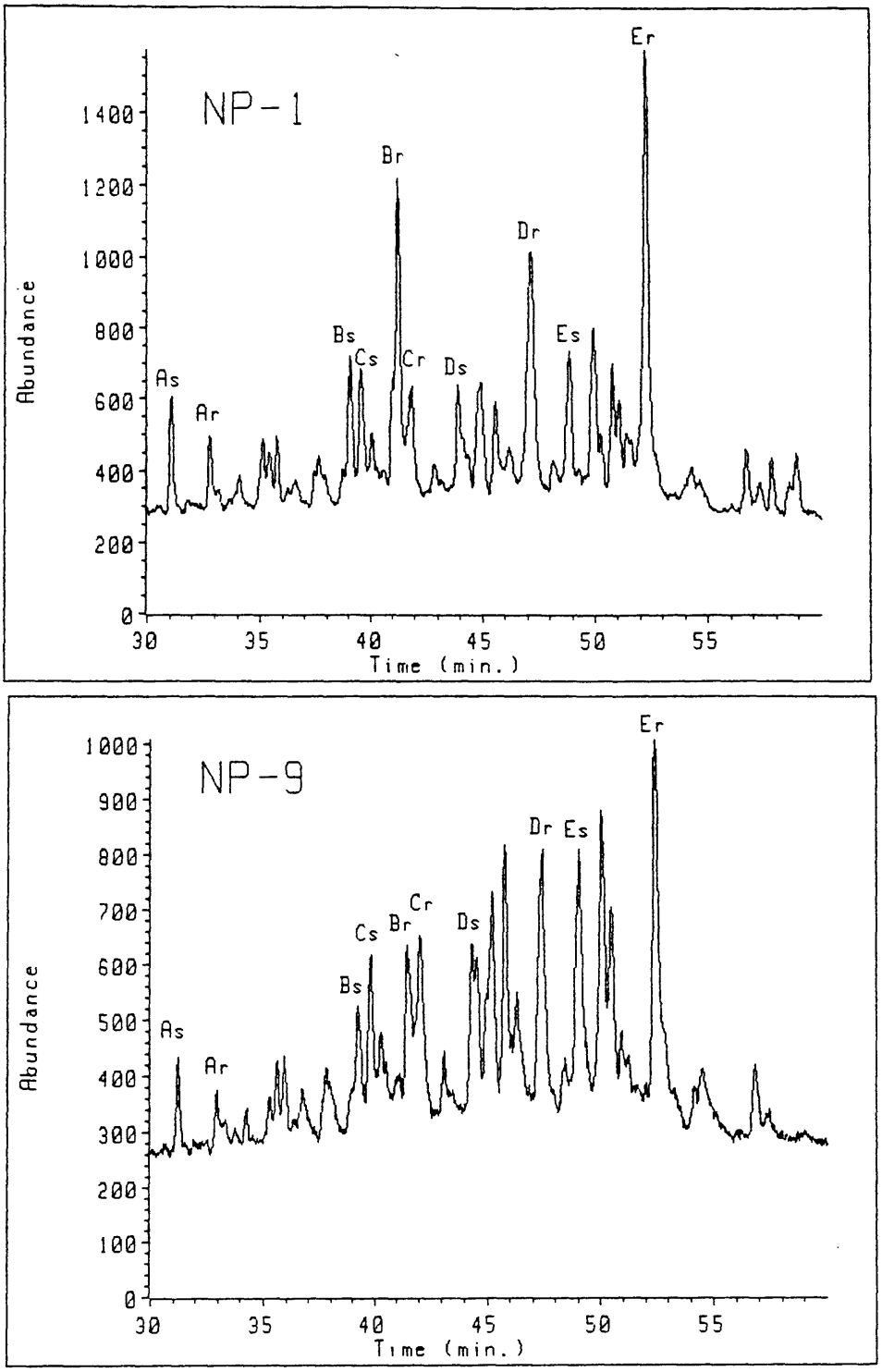

Figure 9. Chromatograms (m/z 217) of samples 1 and 9.

ROCK TYPES AND THEIR DISTRIBUTION FROM DETROIT SEAMOUNT (OBRUCHEV RISE)

Yuri A. Martynov[1], Anatoly N. Kalyagin[2], Rostislav A. Oktyabr'sky[1], and Ziniat Badredtinov[1]

[1]Far East Geological Institute, Far Eastern Branch, Russian Academy of Sciences, Vladivostok 690022, Russia; [2]Pacific Oceanological Institute, Far Eastern Branch, Russian Academy of Sciences, 43 Baltiyskaja, Vladivostok 690041, Russia

INTRODUCTION

According to many investigators, Obruchev Rise represents the northern end of the Emperor Ridge, however other interpretations have been presented (Vasilyev and Udintsev, 1982). Two morphologically distinct seamounts are present on Obruchev Rise: Meiji Seamount to the northwest and Detroit Seamount to the southeast. Up to 1500 m of sediments overlie acoustic basement on Detroit Seamount (Vasilyev and Udintsev, 1982). A DSDP core taken northwest of Detroit Seamount revealed that the acoustic basement consists of pillow lavas of alkalic basalts and trachybasalts (Creager and Scholl, 1973).

Previous dredges taken along the slopes of Detroit Seamount (Vasilyev and Udintsev, 1982; Vasilyev, 1988) recovered a wide variety of rock types; the origin, spatial distribution, and conditions of formation of these rocks continues to be a matter of debate (Vasilyev and Udintsev, 1982; Vasilyev, 1988). As part of this study, Detroit Seamount was dredged, during Leg 4 of the R.V. *Akademik Aleksandr Vinogradov* cruise 91-AV-19, in order to more accurately define the composition of the acoustic basement and the distribution of glacial erratics. According to data presented by B. Ya. Karp (Vasilyev and Udintsev, 1982) and the results of a bathymetric survey, the intended dredging location (D13) was an erosional(?) scarp on the northern upper flank of a single edifice rising more than 1000 m above the plateau surface (Fig. 1).

RESULTS

About 100 kg of rocks were recovered from dredge D13. Material ranged in size from 1 cm to 35 cm (Fig. 2). The composition of the rocks is as follows: 10% - large, equidimensional iron-manganese crusts (1-tabular) with sizes ranging from 5 cm on a side to 15x22x35 cm, with uneven surfaces; 10% cobbles and 20% pebbles of dense, dark-gray, almost black, gabbro, diabase, basalt, andesite, granite, silicic volcanic rocks, crystalline schist, and rarely sedimentary rocks (sandstone, chert); 60% - fine (10% 3-6 cm, 50% 3 cm) pebbles and fragments of the above listed rocks. The entire content of the dredge was divided by composition into groups (intrusive, basic extrusive, volcaniclastic, metamorphic, and sedimentary), and the basic and intermediate igneous rocks and their tuffs were the predominant types by volume (70-80%).

Intrusive Rocks

Silicic intrusive rocks are represented by granites (D-13-2,3; D-13-14-30) and granophyres (D-13-2-1), as well as associated felsic-porphyry dike rocks (D-13-2-2), and andesite-dacite porphyries (D-13-9-1).

Granite and granodiorite are pink to cream colored, medium-grained, altered, and mylonitized rocks, where cracks are healed with quartz, muscovite, and chlorite aggregates. Medium-grained biotite granite has the same amount of plagioclase and orthoclase. Plagioclase forms twinned, zoned crystals (0.8 - 3.0 mm), and biotite (4%), ranging up to 0.5 x 1.7 mm, are often completely replaced by chlorite. Also present are magnetite grains (to 1%) and apatite needles.

In medium-grained sub-alkaline porphyritic granite, phenocrysts (80%) are prevalent over groundmass. The most abundant phenocrysts (50%) are equant, less often tabular plates of orthoclase (from 1 to 5 mm) almost completely altered to clay minerals. Tabular plates of plagioclase (0.7 - 2.5 mm) are half as abundant and also replaced by clay minerals. Tabular crystals (0.4-1.7 mm) of green hastingsite (up to 3%), single grains of quartz (0.7 - 2.0 mm) and pyroxene (up to 0.5 mm) are also present. Pyroxene is typically pseudomorphed by epidote-amphibole-stilpnomelane aggregates. The groundmass is micropegmatitic and consists of micrographic intergrowths of altered orthoclase with quartz, rare amphibole flakes, and magnetite crystals (0.002-0.002 mm).

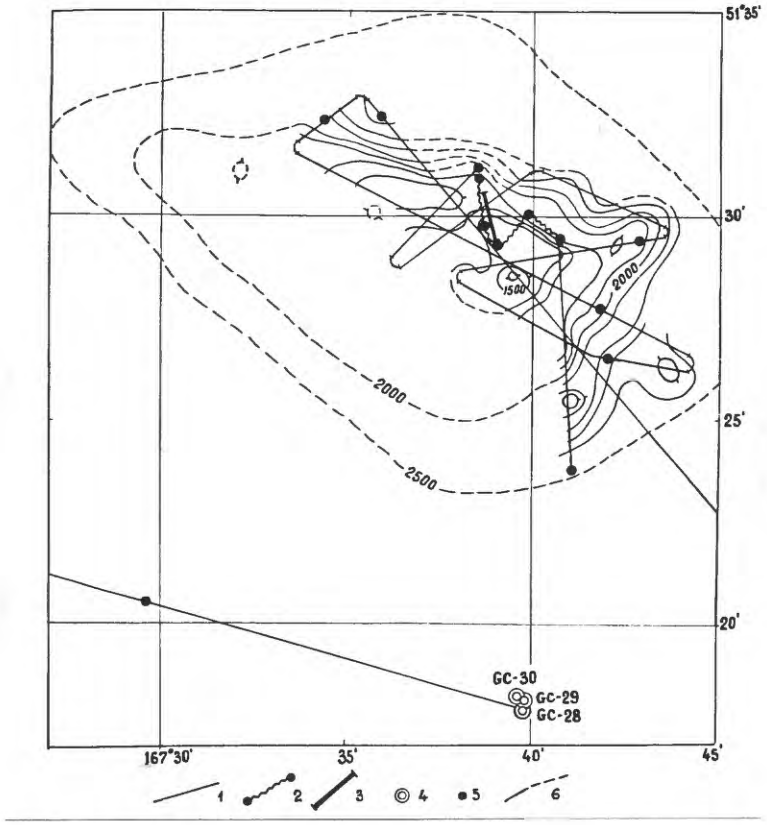

Figure 1. Bathymetric map of the study area, including Detroit Seamount and station locations. 1- tracklines; 2- drift tracks, 3 - dredge site D13; 4 - bottom sediment sampling sites; 5 - sites of observations of ship locations; 6 - isobaths

Figure 2. Rocks recovered at Station D-13.

Porphyritic granophyre is pale gray, tabular (3x4x5 cm), with sharp edges. Rare large phenocrysts (up to 3.0 mm) are represented by microcline altered to clay minerals, muscovite, and less often plagioclase. The groundmass has a micrographic texture consisting of polycrystalline (0.2-1.5 mm) quartz (20%), tabular orthoclase (0.2-1.0 mm), and less often plagioclase (5-10%), rare magnetite crystals (0.02-0.2 mm), sphene, and apatite. Mafic minerals (0.1-0.7 mm) are completely replaced by bluish-green hydrobiotite and magnetite.

Metamorphosed medium-grained granodiorite has hypidiomorphic granular texture and 50% of it consists of tabular (0.2-3.2 mm) twinned, zoned plagioclase (40-25% An) moderately (in places completely) altered to saussurite. Microcline (20%) is formed mainly by poikiloblasts up to 5.0 mm, and it is also noticeably replaced by clay minerals. Interstices are filled by aggregates of xenomorphic quartz (0.2-1.5 mm). Mafic minerals (10%) include clinopyroxene, hornblende, and biotite. Clinopyroxene (1.5-3.0 mm) is pseudomorphed by colorless actinolite and secondary magnetite; green hornblende by pale-green amphibole and epidote; biotite plates (0.2-1.5 mm) by chlorite and sphene. Some single apatite grains are present.

The granites are probably associated with dikes of pinkish and brownish felsite-porphyries, whereas granodiorite supposedly corresponds compositionally with pale-gray quartz andesite-dacite porphyry. Phenocrysts (10-20%) of felsite-porphyrys are mainly plagioclase (albite), less often microcline (0.22 mm up to 2 mm), and rare hornblende (0.2-1.0 mm). Hornblende is completely pseudomorphed by epidote, hydroxides, or magnetite-carbonate-sericite aggregates. Biotite (up to 1.2 mm) is replaced by green chlorite and leucoxene. Plagioclase may have minute inclusions of ilmenite (0.1-0.15 mm) that are replaced by anatase and hematite.

Textures are generally micropoikilitic or felsite-spherulitic. In micropoikilitic matrix, irregular grains of quartz contain needle-shaped microlites of albite, less often apatite (0.5%), and fine crystals (up to 0.01 mm) of magnetite. Spherulite texture is formed by equal amounts of quartz-orthoclase aggregates and yellow-brown spherulites (0.05- 0.1 mm) of devitrified glass, which produces the overall brownish color.

Phenocrysts in andesite-dacite porphyrys are tabular prisms of fallow-green grading to deep-green hornblende and the opaque phase is pseudomorphed by chlorite, epidote, and sphene, as well as plates (0.2-2.0 mm) of zoned plagioclase (30-20% An). The latter typically has inclusions of hornblende and quartz (0.3-1.7 mm). The groundmass contains up to 10% orthoclase laths (0.01-0.05 mm), rare xenomorphic grains of quartz, spicules of apatite and green hornblende, floating in spherulitic plagioclase aggregates.

Basic intrusive rocks consist of rounded debris of leucocratic medium-grained troctolite and pebbles of medium-grained melanocratic gabbro-diorite.

Troctolite with tabular grains is composed of 20% olivine (up to 1.5x2.5 mm) completely replaced by serpentine and single-faceted and deformed crystals of magnetite (0.01-0.12 mm). Other grains include multigrained (0.3-6.0 mm) aggregates of fractured plates and equant plagioclase (58% An), pseudomorphed by prehnite, chlorite, and zeolite. Colorless amphibole rims are formed along the margin between olivine and plagioclase. Gabbro-diorite with tabular grains has the following composition: 2% - small crystals (0.005-0.03 mm), and acicular apatite; 3% - brown biotite and less often, brown and green hornblende, forming around magnetite (0.1-0.3 mm); 10% magnetite in the form of equant rounded grains (0.005-0.1 mm) in clinopyroxene or together with apatite in the interstices; 50% greenish clinopyroxene, formed of well-developed, equant, often tabular crystals (0.3-1.5x3.0 mm) and typically rimmed by deep-green ferroactinolite, occasionally with inclusions of magnetite and apatite; 35% (0.1-1.5 mm) xenomorphic grains of mottled plagioclase (48% An), commonly replaced by scapolite.

Extrusive Rocks

Dolerites are dark gray fine-grained massive rocks with porphyritic and subophitic textures. Fresh two-pyroxene dolerite (the largest part of pillows) contains 70-80% minerals, among which, plagioclase (0.15-1.5 mm) is prevalent (65%) (60% An in core, 40% An at margin). Less abundant (20%) equant tablets of clinopyroxene, plates of orthopyroxene (0.5-1 mm) with pink pleochroism, and 5% magnetite occur. Tholeiitic groundmass is mineralogically similar to phenocrysts, except that orthopyroxene is partly replaced with bastite. Altered subophite dolerite (diabase) occurs as pebbles of fine-grained trachydolerites and quartz-bearing (5%) fine-grained dolerite. Trachydolerite contains about 10% pinkish-fallow titanaugite in the form of equant to tabular (0.3-2.8 mm) grains between lath-shaped zoned plagioclase (55% An in core; 35% An in margin). Plagioclase is extensively replaced by (5-40%) saussurite and hydromica; clinopyroxene by bluish-green fibrous hornblende, hydrobiotite, and chlorite. A characteristic trachydolerite feature is the presence of up to 2% biotite flakes (0.1-1.0 mm), which occurs

in the angular interstices, and is replaced with chlorite and hydrobiotite. Spicules and grains of zircon (0.05-0.1 mm) with pleochroic halos also occur.

Quartz-bearing dolerite, like trachydolerite, contains 5% titanmagnetite (0.05-0.2 mm), replaced by sphene. Plagioclase is more sodic (25-10% An) and moderately replaced by epidote and chlorite. Clinopyroxene converted to bluish-green amphibole is also present.

Basalts are both massive and amygdaloidal. Amygdules (1-20%) are round and oval and range from 0.05 to 4.5 mm in size. They are filled by chlorite, epidote, zeolite, chalcedony, carbonate, and sericite.

The freshest samples are one of basalt and one of basaltic lava breccia. Basalt has microporphyritic and porphyritic texture. Phenocrysts compose from 7 to 20% of the rock and include skeletal olivine (0.1-0.2) with inclusions of magnetite (0.01 mm), single crystals of magnetite (0.2-0.3 mm), small amounts of equant grains or glomerocrysts of clinopyroxene (2-3%, 0.1-0.7 mm), and plagioclase (from 0.2 to 1x2.0 mm) (65-50% An) with inclusions of glass. Itersertal minerals consist of small magnetite grains (0.001-0.07 mm; up to 7-10%), 30% spicules, grains of fresh clinopyroxene, and 30-60% plagioclase laths (0.02-0.25 mm) (50% An). The remaining angular interstices are filled with yellow-brown glass and iddingsite.

Volcanic lava breccia is composed of clasts (0.3-3.0 mm) of plagioclase-phyric basalt (70% An), clinopyroxene-plagioclase basalt, and dolerite-basalt.

Metabasalts are more abundant than fresh ones, and contain more (20-50%) phenocrysts. They have porphyritic and seriate-porphyritic textures. One sample is a fragment of pillow lava.

Phenocrysts are equant, rhomb-shaped olivine (0.1-0.4 mm; 3-10%) that may be completely replaced by serpentine, chlorite, hydroxides, smectite, carbonate, or a yellow-brown mica, varying amounts of pyroxene (0-20%), plagioclase (10-30%), and less often fine (0.12-0.3 mm) crystals of magnetite, that in places occur as inclusions in clinopyroxene. Equant clinopyroxene grains (from 0.2-2x6 mm) are rarely replaced by chlorite and contain inclusions of magnetite. Zoned crystals may have a colorless or pink (titanaugite) core. Orthopyroxene occurs in clinopyroxene cores, but in sample D13-6-1 it is present in amounts greater than clinopyroxene, where the latter forms rims around orthopyroxene.

Plagioclase laths (70-50% An) are moderately or completely replaced by carbonate, chlorite, saussurite, albite, and epidote.

Groundmass textures of metamorphosed basalts vary from a prevalence of microlitic to hyalopilitic textures composed of approximately equal proportions of plagioclase laths (50% An), clinopyroxene grains, dust-like magnetite, and yellow-brown glass, often replaced by chlorite.

Extrusive rocks of intermediate composition occur as sharp-angular debris, predominantly of volcaniclastic breccia, with andesite (D13-7-6) and altered diorite (D13-12-1) clasts. Andesites are serial-porphyritic rocks, containing 3-20% phenocrysts, among which crystals of weakly-zoned (0.1-2.5 mm) plagioclase are notably most abundant. Some plagioclase phenocrysts are replaced by colorless zeolite. Phenocrysts of magnetite are rarely found.

Clinopyroxene (0.5-3%) forms equant to tabular yellow-brown grains (0.2-1.5 mm) with inclusions of plagioclase, magnetite, and apatite. Magnetite, although abundant in the groundmass, is seldom important as phenocrysts (up to 0.5-2.0%). Microlite groundmass is mainly composed (50-60%) of plagioclase laths (0.1-0.2 mm) (45-30% An) and pale, slightly devitrified glass. Tabular crystals of clinopyroxene and magnetite, and less often apatite, are present.

Volcaniclastic Rocks

Volcaniclastic breccia is a dense, greenish, almond-shaped, amygdaloidal rock. Amygdules (7%) are filled by colorless chlorite, in places yellowish-brown in the center. The rock is altered with veinlets of zeolite, albite, and quartz. Andesite clasts have 30% pyroxene and plagioclase phenocrysts. Plagioclase (20% An) is predominant, and in places forms glomerocrysts of 1.5x2.0 mm. Rare crystals of clinopyroxene occur in clusters with magnetite. Hyalopilitic groundmass consists of rare plagioclase laths and clinopyroxene crystals (2-5% each; 0.01-0.05 mm) floating in brown devitrified glass that is filled with dust-like grains of an opaque mineral, replaced by hydroxides.

In fragmental diorite, fractures are filled with quartz, epidote, and chlorite. The texture is glomeroporphyritic (15% of phenocrysts). The predominant plagioclase phenocrysts (40-10% An) are moderately or completely replaced by chlorite-epidote aggregates. Clinopyroxene (0.2 - 1.5 mm) replaced by epidote occurs in clusters with plagioclase. Magnetite and biotite are altered to leucoxene and chlorite, respectively. Groundmass textures vary from micro-dolerite to tholeiitic and are composed of plagioclase (40-10% An) severely altered to clay minerals, xenomorphic grains of quartz (3-5%), and clinopyroxene replaced by leucoxene epidote.

Tuffs of intermediate and silicic composition occur as rock fragments and pebbles of gray, greenish, and brown color, mainly greenstone, banded, and shaly. The amount of grains varies from 15 to 80% and include plagioclase (prevails), clinopyroxene (0.1-1.5 mm), quartz, magnetite, and orthoclase, and less commonly brown hornblende (0.1-0.4 mm), flakes of biotite, and apatite. Rock fragments include yellow-brown porphyrites, andesite, dacite, devitrified silicic glass, tuff, and rarely micropegmatite. Cement is gray, vitreous, decomposed grains, with zeolite, carbonate, epidote, and quartz as secondary mineral phases.

Metamorphic Rocks

Metamorphic rocks are represented by schists: epidote-amphibole-plagioclase, biotite-quartzose, and sericite-siliceous-argillaceous. Epidote-amphibole-plagioclase crystalline schists with poikiloblastic textures is composed by rare crystals of magnetite (1-2%), single prisms (0.08x0.3 mm) of zircon, sphene, more abundant apatite (up to 0.01 mm), epidote (0.1-0.3 mm), xenomorphic quartz (0.05-0.8; 3-5%), noticeable amounts (15%) of large (up to 1.5 mm) crystals of greenish-blue hornblende all in fine-grained (0.1-1.0 mm) plagioclase aggregate. Rare flakes of biotite replaced with chlorite are also present.

Biotite-quartzose schists are fine-grained with augen or lepidoblastic textures. Augen are composed by lens-like grains (0.2-0.5 mm) of quartz and plagioclase, or larger lenses (2x6 mm) of carbonaceous quartzite. The rock is primarily composed of subequal proportions of biotite flakes and grains of quartz, as well as single crystals of epidote, zircon, and apatite (0.01-0.02 mm).

Sericite-siliceous-argillaceous schists are fine-grained, massive, with pelitic textures. They have 3-5% crystals and 5% sericite. The rest is yellow-brown argillaceous material.

Sedimentary Rocks

Sedimentary rocks are composed of greenschist facies, fine-grained polymictic sandstones, altered silty-sandstones, and siltstones.

Metamorphosed polymictic sandstones of blastopsammitic texture contain 50-70% angular grains (0.05-0.7 mm) of plagioclase (30% An), rare grains of magnetite, orthite, green-yellow-brown hornblende (up to 0.5 mm), apatite (0.03 mm), and biotite, in a carbonaceous-sericite-siliceous-argillaceous matrix. The rock is cut by veins of quartz and carbonate and contains secondary epidote, chlorite, and sericite.

Some silty-sandstone fragments are gray, massive, and contain 75% grains of mainly quartz and plagioclase, rarely sphene (0.05-0.1 mm), epidote, orthite, up to 5% crystals of magnetite (0.02-0.08). Cement is tuffaceous, siliceous-argillaceous with admixtures of biotite flakes (up to 0.2 mm), and less commonly muscovite, chlorite, and smectite.

Siltstone has a poorly developed shaly texture with lens-like pelitic structures in a silty groundmass. Grains comprise 50% and include magnetite, 3-5% feldspar, and predominantly quartz. The matrix is pelitic with admixtures of muscovite flakes (up to 0.2 mm), in places replaced by chlorite.

DISCUSSION AND CONCLUSIONS

The described rocks show a heterogeneous metamorphic character, the grade of which varies from lower greenschist facies to amphibolite facies. At the same time in some samples, dislocational metamorphism is noted, while in other samples, changes that characterize a proto-pneumatolytic stage in the establishment of plutons is noted. The majority of rocks underwent regional metamorphism of various temperature facies; some samples show subsequent input of sodium that led to the intensive albitization of plagioclase. The highest level of metamorphism is seen in crystalline schists, and their protolith remains unknown. The recovered rocks allow us to conclude that there is a lack of general uniformity in the character of metamorphism represented in the rocks.

Petrographic study of the rocks allows us to make the following assumptions. Silicic intrusive rocks include medium-grained subalkaline pyroxene (?)-hastingsite granites (D13-5-2), and analogous rocks are exposed in the area of Provideniye Bay on Chukotka (Geology of the USSR, 1970). Basic intrusive rocks are derived from the upper part of the third layer of oceanic crust, that is exposed by faulting, for example, troctolites similar to those in the Parese Vella basin in the Philippine Sea (Scheka *et al.*, 1986) or gabbro-diorites (D13-4-2) similar to those on the seamounts in the South Pacific northeast of New Zealand (Puschin *et al.*, 1990).

Dolerites, basalts, andesites, and various tuffs are generally comparable to rocks of the Aleutian Arc (Magmatic rocks. Basic rocks, 1985), which is supported by the greenschist grade of their metamorphism,

wide development of orthopyroxene, titanaugite, zoned clinopyroxene with colorless core, presence of biotite, and zircon in trachydolerite (D13-5-1). The formation of some basalts under subaerial conditions is supported by secondary magnetite rims around clinopyroxene (D13-10). Earlier, Vasilyev (1988) correlated similar extrusive rocks dredged from Detroit Seamount with rocks of the Iruneisk suite found on Kamchatka, and he also pointed out that formation of part of the effusive rocks occurred under subaerial conditions. Relatively fresh basalt (D13-6-2, D6-5) and volcaniclastic breccia composed of plagioclase-phyric basalt clasts (D13-6-6A) can be identified as oceanic basalts, for example with sub-alkaline basalts of oceanic basement, seamounts, ridges, or islands of the Hawaiian type (Magmatic rocks. Subsilicic rocks, 1985).

The character and composition of grains (hornblende, biotite, orthite) of sedimentary rocks and the poor roundness of grains (D13-5-3) suggest that they formed on the shelf of an island arc. Vasilyev and Udintsev (1982) suggested that similar volcaniclastic rocks of basic and intermediate composition, composing the top of the Detroit Seamount, can be considered young superficial deposits on the volcano that subsided not long ago. This conclusion, however, is not supported by the data from deep sea drilling and the discovery of oceanic subsilicic rocks in samples studied here.

ACKNOWLEDGEMENTS

Ann Gibbs and James Hein improved the English. Alicé Davis reviewed the paper.

REFERENCES

Creager, J.S., Scholl, D.W., *et al.*, 1973, Initial Reports of the Deep Sea Drilling Project, Vol.19., Washington (US Government Printing Office), 913 p.

Geology of USSR, 1970, Northwestern USSR, Geological Description, Book 2, Moscow, Nedra, v.30, 536p.

Magmatic Rocks. Basic Rocks, 1985, Moscow, Nauka, v. 3, 486 p.

Magmatic rocks. Subsilicic rocks,1985, Moscow, Nauka, 475 p.

Puschin, I.A., 1985, Magmatic Rocks. Basic Rocks: Vol.3, Moscow, Nauka, 486 p.

Puschin, I.A., Tararin, I.A., Sakhno, V.G., Oktyabr'sky, R.A, and Chudayev, O.V., 1990, The upper layer of ophiolitic association in the southwestern Pacific northeast of New Zealand: Doklady Akademii Nauk, USSR, v. 315, p. 945-949.

Scheka, S.A., Kulinich, R.G., Vysotsky, S.V., *et al.*, 1986, New data on geology of Japanese faults and the central part of the Philippine Sea: Doklady Akademii Nauk USSR, v. 286, p. 417-421 (In Russian).

Vasilyev, B.I., 1988, Major geological characteristics of the northwestern Pacific, Vladivostok, DVO AN USSR, 191 p.

Vasilyev, B.I. and Udintsev, G.B., 1982, New data on continental composition of the Obruchev Rise: Doklady Akademii Nauk USSR, v. 267, p. 694-698.

QUATERNARY BIOSTRATIGRAPHY OF THE NORTHWEST PACIFIC: R/V VINOGRADOV CRUISE 91-AV-19 LEG 4

Irina B. Tsoy, Irina O. Ryaben'kaya, and Sergey P. Pletnev

Pacific Oceanological Institute, Far Eastern Branch, Russian Academy of Sciences, 43 Baltiyskaja, Vladivostok 690041, Russia

Results of microfossil analyses from gravity cores collected on Bowers Rise (GC-11) in the Bering Sea, and Meiji Guyot (GC-24) and Detroit Seamount (GC-32, GC-36) in the northwest Pacific (Table 1) agree well with results of previous biostratigraphic studies in these regions (Zhuze, 1962; Sancetta, 1979, 1983; Sancetta and Robinson 1983; Sancetta and Sylvestri, 1984; and others). The Pleistocene-Holocene boundary was recognized in all four cores, and the middle Wisconsin glaciation was recognized in two cores.

Table 1. Locations of gravity cores

Core	Latitude - N	Longitude - E	Water depth (m)
GC-11	53° 31.1	178° 51.1	3060
GC-24	52° 58.2	164° 43.1	2970
GC-32	51° 03.4	167° 52.6	2860
GC-36	50° 24.7	167° 43.9	3300

DIATOMS

Diatom samples were processed by boiling in distilled water with sodium pyrophosphate and subsequent settling to remove clay-sized material. A 22 x 22 mm cover slip and NAPHRAX mounting medium were used to prepare slides from the remaining sample. Diatom number was determined for each sample by counting 200 or 300 specimens encountered in random traverses at 900x magnification.

Gravity Core 11

GC-11 was taken on the western slope of Bowers Rise at a water depth of 3060 m. The core is 660 cm long and composed primarily of silty clays. Diatoms are abundant and well-preserved throughout the core (Table 2) except for the interval between 170-139 cm where they are somewhat less abundant. Three units were distinguished based on floral and lithologic characteristics.

Unit 1 (0-161 cm) consists of muds and diatomaceous clays characterized by abundant *Neodenticula seminae*, a species that is presently common in moderately warm waters (10°C) with moderate salinities (32.5 %) (Sancetta *et al.*, 1985). *Rhizosolenia hebetata f. hiemalis, Thalassiosira latimarginata, Actinocyclus curvatulus,* and *Coscinodiscus-oculus iridis* are relatively abundant throughout this unit while *Stellarima microtrias, Asteromphalus robustus, and Thalassiosira oestrupii* occur consistantly. Low concentrations of species common in shelf and icy waters with low salinities, including *Thalassiosira gravida* and other species of this genus, are also present in Unit 1. The occurrence of benthic forms is sporadic. Unit 1 likely represents the Holocene post glacial, approximately the past 10,000 years.

Unit 2 (161-510 cm) consists of clays interbedded with pebbles and sand. This interval is characterized by a sharp decline in the abundance of *Neodenticula seminae* and a considerable increase in the abundance of the *Antinocyclus curvatulus/Thalassiosira latimarginata* group; these species are characteristic of basins subject to prolonged ice cover and weak summer mixing (Sancetta and Robinson, 1983; Sancetta *et al.*, 1985). The genus *Thalassiosira* is well represented and some species, such as *T. gravida*, are abundant. A relative increase in displaced benthic species was observed in this unit. Unit 2 likely represents the late Wisconsin glaciation and onset of de-glaciation which occurred between about 25,000 and 10,000 y.b.p. (years before present).

Unit 3 (510-660 cm), consisting of muds and diatomaceous clays, is characterized by diatom floras similar to those in Unit 2, although *Neodenticula seminae* is the dominant species. This diatom assemblage is characteristic of the middle Wisconsin (approximately 65,000-25,000 y.b.p).

Gravity Core 24

GC-24 was taken on the top of Meiji Guyot at a water depth of 2970 m. The core recovered 94 cm of sandy clay interbedded with volcanic ash and pebbles. Diatoms are abundant and well-preserved throughout most of the core (Table 3). Unit 1 (Holocene) and Unit 2 (Late Wisconsin), described above for the Bowers Rise core also apply to this core.

Unit 1 (0-33 cm) consists of calcareous, sandy clays characterized by the dominance of *Neodenticula seminae* and abundant *Thalassiosira gravida, T. latimarginata, Coscinodiscus marginatus, Actinocyclus curvatulus, Rhizosolenia hebetata f. hiemalis,* and *Thalassiosira oestrupii. Asteromphalus robustus* is pervasive throughout this unit.

Unit 2 (33-94 cm) consists of homogenous sandy clays characterized by a relative decrease in the overall abundance of diatoms. Dominant species include *Actinocyclus curvatulus* and *Thalassiosira latimarginata.* Diatom floras show a sharp decrease in number of *Neodenticula seminae, Coscinodiscus marginatus,* and *Rhizosolenia hebetata f. hiemalis.* The number of benthic species belonging to *Cocconeis, Delphineis, Navicula, Diploneis,* and other genera increase along with re-deposited Neogene species, such as *Thalassiosira zabelinae, Neodenticula kamtschatica, Nitzschia extincta,* and *Hyalodiscus obsoletus.*

Gravity Core 36

GC-36 was taken at a water depth of 3300 m at the base of Detroit Seamount. The core recovered 336 cm of silty clays with admixed sand in the interval 0-89 cm, and multiple interbeds of different colors and densities in the interval 90-336 cm. Sediment in the lower interval is bioturbated and contains abundant fecal pellets. Diatoms are numerous throughout the core except from 90-281 cm where a relative drop in abundance is observed. Floral characteristics allowed us to distinguish three units corresponding to the Holocene, late Wisconsin, and middle Wisconsin (Table 3). Diatom floras are similar to the floras of corresponding units distinguished in Bowers Rise and Meiji Guyot cores.

Unit 1 (0-89 cm) consists of silty clays with fine sand and is characterized by a dominance of *Neodenticula seminae* as well as *Actinocyclus curvatulus, Thalassiosira latimarginata, T. oestrupii, and Stellarima microtrias.*

Unit 2 (90-334 cm) consists of terrigenous silty clays characterized by the dominance of *Actinocyclus curvatulus/Thalassiosira latimarginata* group diatoms and an associated decrease in the abundance of *Neodenticula seminae,* as well as other oceanic species. Neritic species *Odontella aurita, Pyxidicula turris, Actinoptychus senarius, and Paralia sulcata* and a wide variety of benthic and Neogene species (*Hyalodiscus dentatus, Neodenticula kamtschatica*) are present.

Unit 3 (335-336 cm) consists of silty clays similar to those of Unit 2. The diatom flora is similar to Unit 2, but as at Bowers Rise, *Neodenticula seminae* is the dominant species.

PLANKTONIC FORMAMINIFERS

The number of planktonic foraminiferal tests within cores GC-32 and GC-36 varies from zero to several hundreds of individuals per gram of dry sediment. Intervals with low total abundances are due to dissolution of foraminiferal tests deposited close to the carbonate compensation depth (CCD).

Neogloboquadrina pachyderma (sinistral) and *Globigerina bulloides* are common in the foraminiferal assemblage, and *Globigerina quinqueloba, Globigerinita uvula, Globorotalia scitula,* and *Neogloboquadrina pachyderma* (dextral) are less abundant.

Paleotemperature analysis was conducted using the proportion of sinistral *Globigerina bulloides* to the total number of individuals of this species. This method was suggested by Boltovskoy (1973) based on plankton data collected in the northwest Atlantic. Boltovskoy noted a nearly linear relationship between the two variables, such that when the temperature increased from 3-4°C to 15°C, the proportion of sinistral *G. bulloides* to the total number of this species decreased from 80% to 60%. Boltovskoy further noted that this relationship is most accurate for his area of study, although the method can be used for other areas, with a slight loss in precision. We chose this method over the more reliable method of paleotemperature reconstruction using the sinistral and dextral forms of *Neogloboquadrina pachyderma* because of the abundance of *G. bulloides* in our samples.

Interpretation of paleotemperature curves (Fig. 1) allows us to distinguish the Holocene from the Wisconsinan glacial stage. Gravel in the core suggests increased ice rafting and supports the idea of the glacial stage.

RADIOLARIANS

Radiolarians were studied only in GC-36 from Detroit Seamount. The core was sampled mainly at 5 or 10 cm intervals. Sample preparation followed procedures described by Tochilina (1985). Radiolarian abundance was determined by counting the number of specimens of each taxon in 4-5 mg samples and subsequently recalculated as per gram of air dried sample (Tochilina and Ryaben'kaya, 1991). Six radiolarian assemblages were distinguished based on taxonomic diversity and species dominance (Table 5; Fig. 2).

The total number of radiolarians in the lowest interval (335-300 cm) varies from 91,250 to 22,826 per gram of air-dried sediment. Radiolarians are well preserved, and 44 taxa were identified. The *Cycladophora davisiana* Ehr.-*Cycl.* sp. group is dominant (335 cm-32.5%, 330 cm-30.1%, 320 cm-12.5%, 310 cm-32.6%, 300 cm-26.6%), and *Cycladophora davisiana* reaches its maxima for the entire core in this interval from 300-335 cm. Sub-dominant species include *Tholospiris borealis* (Bailey) (335 cm-16.7%, 330 cm-9.5%, 320 cm-6.8%, 310 cm-5.8%, 330 cm-6.6%), *Stylatractus pyriformis* (Bailey) (335 cm-3.5%, 320 cm-4.54%), *Diplocyclas cornuta* (Bailey) (335 cm-3.1%, 320 cm - 8.0%, 310 cm - 4.9%), and *Lithomitra lineata* (Ehr) (320 cm - 5.1%, 300 cm - 6.6%). Radiolarians of the *Spumellaria* group, such as *Haliomma circumtextum* Hck. (330 cm - 5.4%, 320 cm - 4.5%, 310 cm - 4.2.%. 300 cm - 5.7%), are somewhat abundant. Additional species, including *Stylochlamydium venustum* (Bailey), *Lithelius nautiloides* (Popofsky), *Tholospira* sp. aff *dendrophora* Hck., *Lithatractus jugatus* Hck., *Amphisphaera cronos* Hck., *Hexacromyum sexaculatum* (Stohr), *Carposphaera nodosa* Hck., *Stylodictya stellata* (Bailey), *Cromyechinus dodecanthus* Hck., and *Stylosphaera lithatractus* Hck. were encounted only as single specimens. Radiolarians from the *Nassellaria* group, including *Prunopyle antarctica* (Dreyer) (335 cm - 3.6%, 330 cm- 1.4% , 320 - 2.27%, 310cm - 1.0%, 300 cm - 3.8%), *Bathropyramis* sp. (330 cm - 1.4%, 320 cm 4.5%, 310 cm - 2.1%, 300 cm - 3.8%), *Cyrtolagena laguncula* (Hck.), *Cornutella profunda* (Ehr.), *Pseudodictyophimus gracilipes* (Bailey), *Ceratospyris* sp., *Plectopyramis* sp., *Pteroscenium pinatum* (Hck.), and *Tricolocapsa papiosa* (Ehr.), are sparse. One subspecies of *Lychnocanium grande* (Campbell and Clark) present in the assemblage was widespread in the Bering Sea region during the Pleistocene and became extinct about 50,000 y.b.p. (Morley et al., 1982; Tochilina, 1985). Absence of *L. grande* in the upper part of the core suggests an age of approximately 50,000 years for the 335-300 cm interval.

The interval from 290-250 cm is also dominated by *Cycladophora davisiana,* although in lower concentrations. The total number of radiolarians is lower (1,910 to 30,000 per gram of dry sediment) and the assemblage is represented by an average of 40 taxa. GC-36 contains an ashy layer (291-290 cm) with very low radiolarian content (25 taxa). Similar taxonomic associations were observed in other cores with ash layers taken nearby. A somewhat higher content of *Cycl. davisiana*--7 specimens, *Styl. venustum* (Bailey)--5 specimens, *Tholospyris borealis*--5 specimens, were observed in the interval 290-250 cm. Although *Cycladophora davisiana* (Ehr) is still dominant in this interval (280 cm- 16.4%, 270 cm -18.9%, 260 cm-21%, 250 cm - 12.8%), the composition of the sub-dominant group has changed to an increase in the abundance of *Cromyechinus dodecanthus* (Hck.) (280 cm-5.7%, 270cm-6.1%, 260 cm-3.9%, 250 cm-14.5%), *Dictyophimus crisiae* (Ehr) (280 cm-5.7%, 270 cm-5.3%, 260cm-2.2%, 250cm-10.6%), and *Prunopyle antarctica* (Dreyer) (280 cm-4.1%, 270 cm-1.1%, 260 cm-4.5%, 250 cm-2.3%). Less abundant in the association are *Acrosphaera spinosa* Hck., *Lithatractus jugatis* (Hck.), *Styl. pyrifomis, Spongodiscus, Lith. nautiloides* (Popofsky), *Stylosphaera lithatractus* (Hck.), *Pylospira octopyle* (Hck.), *Carp. nodosa* (Hck.), *Thol. borealis* (Bailey), *Thol. tripodiscus* (Hck.), *Pseudodictyophimus gracilipes* (Bailey), *Androcyclas gamphonycha* (Jorgensen), *Cyrtolagena laguncula* (Hck.), *Artostrobus* sp., and *Bathropyramis* sp.

Within the interval from 241-180 cm, the maximum number of radiolarians (202,000-222,000 specimens per gram) was observed at 240 cm. Throughout the rest of the interval (241-180 cm), the total number of radiolarians are 24,000-45,000 per gram. The dominant species in this interval is *Cromyechinus dodecanthus* (Hck.) (240 cm-9.9%, 230 cm-8.1%, 220 cm-8.2%, 210 cm-14.4%, 200 cm-26% (max.), 190 cm -11.5%, 180 cm-8.1%). The sub-dominant group also differs from those described above; *Dictyophimus crisiae* (240 cm-8.8%, 230 cm- 12.3%, 220 cm-7.1%, 210 cm- 9.4%, 200 cm-9.2%, 190 cm-4.4%, 180 cm-6.3%), *Th. borealis:* 240 cm-7.7%, 230 cm-4.1%, 220 cm-3.6%, 210 cm-8.5%, 200 cm-6.2%, 190 cm - 5.6%, 180 cm-9.4%). The total number of *Cycladophora davisiana* (Ehr) decreases, and is the dominant species only at 240 and 220 cm, (about 15.3%). The abundance of the *Spongodiscus-Spongotrochus* group increases (240 cm-8.8%, 230 cm-13.9%, 220 cm-14.2%, 210 cm-6.8%, 200 cm-4.6%, 190 cm-5.3%, 180 cm-3.1%) and there are fewer occurrences of *Euscenium cucoplium* Hck., *Lith nautiloides* (Popfsky), *Carposphaera nodosa* Hck., *Prunopyle antarctica* (Dreyer), *Pseudodictyophimus gracilipes* (Bailey), *Lithatractus fragilis* (Hck.), *L. jugatus* (Hck.), *Haliomma circumtextum* (Hck.), *Stylatractus pyrifomis* (Bailey), and *Dictyophimus mawsoni* (Riedel).

Cycladophora davisiana and the group *Stylodictya-Porodiscus* dominate the interval from 171 to 105 cm. The total number of radiolarians varies from 195,000 to 27,000 per gram of dry sediment. The abundance of *Cycladophora davisiana* is doubled (170 cm-8%, 160 cm-17.8%, 150 cm-24.6%, 140 cm-22.1%, 130 cm-29.3%, 120 cm-17.5%, 110 cm-17.8%, 105 cm-6.4%), but except for the interval between 120 and 130 cm, it is sub-dominant to the *Stylodictya-Porodiscus* group (160 cm-9.9%, 150 cm-15.4%, 140 cm-17.5%, 110 cm-12.5%, 105 cm-13.3%). The distribution of the major groups composing the radiolarian assemblages is graphically presented in Fig. 3. *Spumallaria* present include *Carposphaera nodosa* (Hck.), *Cenosphaera compacta* (Hck.), *Haliomma lirianthus* (Hck.), *Acrosphaera spinosa* (Hck.), *Haliomma compactum* (Hck.), *H. circumtextum* (Hck.), *Actinomma* sp., *Collosphaera* sp., *Styl. lithatractus* (Hck.), *Lith. jugatus* (Hck.), *Styl. pyrifomis* (Bailey), *Lithelius nautiloides* (Popofsky), and *Druppatractus ostracion* (Hck.). *Nassellaria* represented by single specimens are *Cornutella profunda* (Ehr.), *Lithomitra lineata* (Ehr.), *Bathropyramis* sp., *Diplocyclas cornuta* (Bailey), *Tricolocapsa papilosa* (Ehr.), *Cyrtolagena laguncula* (Hck.), *Clathrocyclas bicornis* Popofsky, *Dictyophimus mawsoni* (Riedel), *Ceratocyrtis* sp., and *Pseudodictyophimus gracilipes* (Bailey).

Lithatractus jugatus and *Crom. dodecanthus* dominate the interval between 99 and 87 cm. The total number of radiolarians noticeably decreased to about 24,000-30,000 per gram of dry sediment, and the abundance of *Cycladophora davisiana* (Ehr.) decreased as well (99 cm-1.7%, 96 cm-0.8%, 87 cm-8.9%). The dominant species in the assemblage are *Lith. jugatus* (99 cm-8.9%, 96 cm-12.8%, 87 cm-4.1%) and *Crom. dodecanthus* (99 cm-8.1%,96 cm-9.6%, 87 cm-8.9%). The co-dominant group includes *Haliomma circumtextum* Hck. (99 cm-8.1%, 96 cm-7.2%, 87 cm-1.6%), *Carposphaera nodosa* Hck., and *Dictyophimus crisiae* (99 cm-2.7%, 96 cm-4%, 87 cm-2.4%). According to Morley *et al.*, (1982), a sharp decrease in the abundance of *Cycl. davisiana* occurs at the Pleistocene-Holocene boundary. Based on the observation that in the upper part of the core *Cycladophora davisiana* occurs in low percentages, the interval with *Lith. jugatus* and *Crom. dodecanthus* can be considered as transitional to the Holocene.

The *Tholospyris borealis* and *Thol. tripodiscus* assemblage present from 75-0 cm is assigned to the Holocene. Radiolarian abundance in this interval is the lowest for the core, and the total number of taxa is also reduced. The dominant species, *Thol. borealis* (Bailey) and *Thol. tripodiscus* Hck., constitute from 50% (at 75 cm and 66 cm) to 17.7% (at 54 cm), and from 7% (at 42 cm) to 15% (at 75 cm), respectively of the assemblage. *Cycl. davisiana* Ehr. does not exceed 7% (66 cm). Other members of the radiolarian assemblage are represented by single specimens.

ACKNOWLEDGMENTS

Ann Gibbs redrafted figures and tables. Paula Quinterno reviewed the paper and improved the English.

REFERENCES

Boltovskoy, E., 1973, Note on the determination of absolute surface water paleotemperature by means of the foraminifer *Globigerina bulloides*, d'Orbigny: Palaontol. Ztscchr., v. 47, p. 152-155.

Morley, J.J., Hays, J.D., and Robertson, J.H., 1982, Stratigraphic framework for the late Pleistocene in the Northwest Pacific Ocean: Deep-Sea Research, v. 29, p. 1485-1499.

Sancetta, C., 1979, Oceanography of the North Pacific during the last 18,000 years: Evidence from fossil diatoms: Marine Micropaleontology, v. 4, p. 103-123.

Sancetta, C., 1983, Effect of Pleistocene glaciation upon oceanographic characteristic of the North Pacific Ocean and Bering Sea: Deep-Sea Research, v. 30, p. 851-869.

Sancetta, C. and Robinson, S.W., 1983, Diatom evidence on Wisconsin and Holocene events in the Bering Sea: Quaternary Research, v. 20, p. 232-245.

Sancetta, C. and Silvestri, S., 1984. Diatom stratigraphy of the Late Pleistocene (Brunhes) Subarctic Pacific: Marine Micropaleontology, v. 9, p. 263-274.

Sancetta, C., Heusser, L., Labeyrie, L., Naidu, A.S., and Robinson, S.W., 1984, Wisconsin-Holocene paleoenvironment of the Bering Sea: Evidence from diatoms, pollen, oxygen isotopes, and clay minerals: Marine Geology, v. 62, p. 55-68.

Tochilina, S.V., 1985, Biostratigraphy of the Cenozoic of the northwest Pacific: M. Nauka, 133 p.

Tochilina, S.V. and Ryaben'kaya, I.O., 1991. Ecozonal stratigraphic Pleistocene scale according to results of quantitative radiolarian analysis: *in* Paleontological and stratigrahphic investigation of Phanerozoic in the Far-Eastern region. Vladivostok, p. 111-127 (In Russian).

Zhuze, A.P., 1962, Stratigraphic and paleogeographic investigations in the northwest Pacific: Akademii Nauk USSR, 259 p. (In Russian).

Table 2. Diatom distribution in core GC-11.

Diatoms	Interval (cm)												
	Unit 1					Unit 2					Unit 3		
	0-1	30-31	60-61	90-91	120-121	170-171	240-241	310-311	390-391	470-471	560-561	620-621	659-660
Achnanthes brevipes Ag.												1	
Actinocyclus curvatulus Janisch	12	16	24	20	10	38	50	82	32	87	50	34	43
A. ochotensis Jousé	1	2			1	4	2	1	4	6	8	4	2
A. oculatus Jousé		1		1		6	4	2		4	1		2
Actinoptychus bipunctatus Lohman		1	1										
A. senarius (Ehr.)Ehr.						2					1		
Amphora sp.					*								
Arachnoidiscus ehrenbergii Bailey	1				1								
Asteromphalus robustus Castr.	2	2	2	1								2	
Aulacoseira italica (Ehr.) Ktz.					*								
Bacterosira fragilis Gran	1						2	2	1			1	
Chaetoceros affinis Lauder	1	1											
C. furcellatus Bailey			1				2	2	1		1	1	
C. subsecundus (Grev.) Hust.	1			2	1								
Chaetoceros spp.	11	2	5			10	4	4	6				
Clavicula polymorpha Grun. et Pant.	1												
Cocconeis costata Greg.	2	2		1	1	2	2			1	1		
C. dirupta Greg.								1					1
C. marginata Ktz.										1			
C. scutellum Ehr.						2	2	1	1		2		3
C. vitrea Brun									1				3
Cocconeis spp.						1				1			
Cocconeis sp. (*sensu* Sancetta, 1982)		1											
Coscinodiscus marginatus Ehr.	10	4	8	10	2	6	4	10	2	6	6	1	10
C. nitidus Greg.										1			
C. oculus iridis Ehr.	18	24	18	8	2	8	6	16	5	8	4	1	14
C. tabularis v. *egregius* (Rattr.) Hust.	1	2	2										
Cyclotella sp.	1												
Delphineis surirella (Ehr.) Andrews	1				1	2	1	1					
Denticulopsis hyalina (Schrader) Sim.								*					
Denticulopsis sp.			1										
Detonula confervaceae(Cl.) Gran									4				2
Diploneis smithii (Breb.) Cl		3				1	2						
Diploneis subcincta (A.S.) Cl.										1			
Diploneis sp.				1									
Grammatophora sp.			*		1								
Hyalodiscus obsoletus Sheshuk.				1									
Kisseleviella carina Sheshuk.			*										

Table 2. GC-11 continued

	Interval (cm)												
	Unit 1					Unit 2					Unit 3		
Diatoms	0-1	30-31	60-61	90-91	120-121	170-171	240-241	310-311	390-391	470-471	560-561	620-621	659-660
Navicula spp.						1		1					
Neodenticula kamtschatica (Zabelinae) Akiba et Yanagisawa	1		1						1				
N.seminae (Sim.et Kan.) Akiba et Yanag.	108	146	138	140	160	12	60	30	86	16	30	84	75
Odontella aurita (Lyngb.) Breb.et Godey	1	4	4	4	1	2		1	2	6	16	18	14
Paralia sulcata (Ehr.) Cl.					4	2	2	2	1	8	6	1	2
P. sol (Ehr.) Ktz.		1	1		1		2						*
Plagiogramma staurophorum (Greg.)Heib.											1		
Porosira glacialis (Grun.)Jorg.					1						2		
Pyxidicula turris (Grev. et Ar.) Str. et Nik.	2			2	10	1		2	4		4	2	2
Rhabdonema sp.			*										
Rhizosolenia curvirostris Jousé					2								1
R.hebetata f.hiemalis Gran	54	40	14	18	10	10	6	16	25	40	16	10	12
R.styliformis Bright												2	
Stellarima microtrias (Ehr.) Hasle et Sims	6	6	4	2	2	2							
Thalassionema nitzschioides Grun		4	6	2	2			4				1	
Thalassiosira antiqua A. Cl.	2												
T. bramaputrae v. *septentrionalis* (Grun.) Makar.						1				1			
T. decipiens (Grun.) Jorg.				2		2							
T.eccentrica (Ehr.) Cl.			2		10			8			4		
T. gravida Cl.		4	6	14	20	24	60	12	14	12	30	36	25
T.hyalina (Grun.) Gran		1	1	2							4	4	
T.latimarginata Makar.	24	6	39	50	40	42	76	80	86	78	93	90	60
T. nordenskioldii Cl.				2								1	
T. oestrupii Ostf.	7	8	4	10	4				2	6	2	2	
T. pacifica Gran et Angst.					4	2					10		
Thalassiosira spp.	10	6	8	2	2		4	4					8
Thalassiothrix longissima Cl. et Gr.	20	10	10	6	8	8	6	28	20	18	8	4	20
Specimens counted	300	300	300	300	200	300	300	300	300	300	300	300	300

* = presence of taxa fragments

Table 3. Diatom distribution in core GC-24

Diatoms	Interval (cm) Unit 1 0-1	6-7	9-10	15-16	26-26	Unit 2 45-46	65-66	85-86	93-94
Actinocyclus curvatulus Janisch	20	14	16	12	14	24	46	62	76
A. ochotensis Jousé	2	1	1	2				1	
A. oculatus Jousé							4	4	
Actinoptychus senarius (Ehr.) Ehr.			1						
Asteromphalus robustus Castr.	2	1	6						
Bacterosira fragilis Gran				3					1
Chaetoceros furcellatus Bail.	1								
Chaetoceros spp.	4	1	2	6				1	1
Cocconeis scutellum Ehr.								1	
Coscinodiscus marginatus Ehr.	10	14	12	8	18	6	1	2	6
C. obscurus A.S.				1					
C. oculus iridis Ehr.	4	4	8	4	6	1	1	2	2
C. tabularis v.egregius (Rattray) Hust.				1		1			
Delphineis surirella (Ehr.) Andrews						1	3		
Delphineis sp.								*	
Eunotia sp.						*			
Grammatophora sp.				1					
Hyalodiscus obsoletus Sheshuk.									1
Navicula spp.					1			1	1
Neodenticula kamtschatica (Zab.) Ak. et Yanag.						1	2		1
N.seminae (Sim.et Kan.) Akiba et Yanagisawa	82	66	76	88	70	14	4	10	2
Nitzschia excincta Koz. et Sheshuk.							1		
N. Grunowii Hasle								1	
Nitzschia sp.								*	
Odontella aurita (Lyngb.) Breb. et Godey		2		3		1			
Paralia sulcata (Ehr.)Cl..					2	2			
Pyxidicula turris (Grev. et Arn.) Streln. et Nikol.						1			
P. zabelinae (Jousé) Makar.et Moiss.								1	
Rhizosolenia hebetata f. hiemalis Gran	10	16	24	5	8	12	7	4	
Stellarima microtrias (Ehr.) Hasle et Sims					4				
Thalassiosira gravida Cl.	36	64	40	42	51	27	5	10	10
T.nordenskioldii Cl.				6					
T. oestrupii (Ost.) Hasle	6	2	2	2					
T. pacifica Gran et Angst.					4			4	4
T. latimarginata Makar.	20	16	16	12	18	108	124	95	92
Thalassiothrix longissima Cleve et Grun.	3	4	2	4	4	2	2	1	2
Specimens counted	200	200	200	200	200	200	200	200	200

* = presence of taxa fragments

Table 4. Diatom distribution in core GC-36

	Interval (cm)											
	Unit 1			Unit 2								Unit 3
Diatoms	0-1	30-31	60-61	90-91	120-121	150-151	180-181	210-211	250-251	280-281	310-311	335-336
Actinocyclus curvatulus Janisch	18	10	20	25	58	30	50	38	50	46	48	30
A. ochotensis Jousé	2				2	1	4	6	4	6	1	1
A. oculatus Jousé	2			2		2			4	2	1	
Actinoptychus senarius (Ehr.) Ehr.										1	1	1
Amphora terroris Ehr.				1								
Amphora sp. Castr.							*				1	
Asteromphalus robustus	2		1									1
Aulacoseira islandica (O.Müll.) Sim.							1					
Chaetoceros furcellatus Bail.		1								1	1	
C. ingolphianus Ostf.					1							
C. subsecundus (Grev.) Hust.			1									
Chaetoceros spp.	4	10	3							2	4	
Cocconeis costata Greg.		1		1	1					1		
C. scutellum Ehr.							*	1				
C. vitrea Brun Ehr.												1
Coscinodiscus marginatus	12	10	2	2	2	2	4	4	6	1	2	4
C. nitidus Greg.						*						
C. oculus iridis Ehr.	6	4	8		2	1	2	2	6	2	2	4
C. tabularis v.egregius (Rattray) Hust.	2	1										
Delphineis surirell (Ehr.) Andrews					1					1		
Diploneis smithii (Breg.) Cl.								1				
Diploneis sp.							*					
Hyalodiscus dentatus Korotk.							1					
Navicula spp.								1	1			
Neodenticula kamtschatica (Zabel.) Akiba et Yanag.								2				1
N.seminae (Sim.et Kan.) Akiba et Yanag.	100	134	100	20	40	14	14	26	16	26	48	100
Nitzschia excincta Koz.et Sheshuk.											1	
N. Grunowii Hasle			1	1								
N. punctata (W.Sm.) Gran et Godey					1							
Odontella aurita (Lyngb.)	2			37	2		4	4	2	2	10	
Paralia sulcata (Ehr.) Cl.	2				2			4		2		
P. sol (Ehr.) Ktz.					1							
Pyxidicula turris (Grev.et Arn.)			1	2	3	1		2	1	1	2	4
Rhaphoneis margarita-limbata Mertz	*											
Rhizosolenia curvirostris Jousé				2		1						

Table 4. GC-36 continued

	Interval (cm)											
	Unit 1			Unit 2								Unit 3
Diatoms	0-1	30-31	60-61	90-91	120-121	150-151	180-181	210-211	250-251	280-281	310-311	335-336
R.hebetata f.hiemalis Gr.	14	6	6	13	6	6	6	16	6	10	8	8
R.styliformis Bright								1		1	1	
Stellarima microtrias (Ehr.)	4	2	20	2				1		2	2	4
Thalassionema nitzschioides	2			4		4		2				
Thalassiosira bramaputrae Ehr.									1			
v.*septentrionalis* (Grun.) Makar												
T.decipiens (Grun.) Jorg.		2										
T.eccentrica (Ehr.) Cl.								16	6	18	4	6
T.gravida Cl.	2	12	6	32	18	56	46	28	4	14	10	6
T.latimarginata Makar.	14	12	20	60	60	80	70	28	78	60	40	25
T.oestrupii (Ost.) Hasle	8	2	2		2			2		1		10
T.pacifica Gran et Ang.		1	4	2				4				
T.nordenskioldii Cl. Cl.et Grun.											2	
Thalassiothrix longissima Cl.et Grun.	8	2	6	4	1	3	1	12	6	2	10	4
Specimens counted	200	200	200	200	200	200	200	200	200	200	200	200

* = presence of taxa fragments

Table 5. Counts of radiolarian taxa in 4-5 mg samples, GC-36.

Radiolarian	Interval (cm)					
	46-46	96-97	110-111	210-211	260-261	334-335
Acrospheara spinosa (Hck.)	3	1	1	3	4	2
Collosphaera sp.			2	2	1	6
Stylatractus pyriformis (Bailey)		5		4	11	8
Lithatractus jugatus Hck.	5	16	6	6	3	3
Stylosphaera lithotractus Hck.		4	5	1		
Stylosphaera sp.		1	1		1	
Stylocontaryum sp.		1				
Stylochlamidyum venustum (Bail.)	1		1	4	9	3
Stylochlamidyum sp.				1	1	1
Perychlamidyum sp.	1	1				
Spongodiscus osculosus (Dreyer)	3	8	2	1		1
Spongodiscus sp.			12	12	6	6
Spongotrochus glacialis Popofs.	1	1	2	13		2
Stylodictya stellata st. Bailey	1	12	13	2	3	6
St. heliospira Hck.			1	1		
Stylodictya sp.			10			
Porodiscus microporos (Stöhr)			6			
Porodiscus sp.		7		2		
Lithelius nautiloides Popofsky				3	1	1
Lithelius sp.		2	2			
Hexacromyum sexaculatum (Stöhr)		2	7	11	4	6
H. octahedrum Hck.					1	1
Hexacromyum sp.			1	2		
Acanthasphaera reticulata Hck.					4	
Actinomma sp.	1	6	4		2	3
Cenosphaera compacta Hck.	2	3	6	2		
C. cristata Hck.	1			2		1
Cenosphaera sp.			4			
Carposphaera nodosa Hck.	1	1	2	2		
Carposphaera sp.			2			
Heliosphaera pectinata Hck.			1			
Echinomma quadrisphaera	1				2	1
Ech. delicatulum (Dogiel)					1	1
Echimomma sp.			3			
Haliomma cyrcumtextum Hck.	1	9	3	1		7
Haliomma sp.					2	
Hexalonche aristarchi Hck.						1
Heliosoma (?) radians Hck.	1					
Cromyechinus dodecanthus Hck.	6	12	21	31	7	5
C. isocantus Hck.				4		

Table 5. GC-36 continued

Radiolarian	Interval (cm) 46-46	96-97	110-111	210-211	260-261	334-335
Prunopyle antarctica Dreyer	2	6	9	7	8	8
Prunopyle sp.					1	
Sphaeropyle robusta Kling		1	1		4	
Tholospira sp.aff *cervicornis*	2					1
Tholospira sp.		2	4		1	3
Pylospira octopyle Hck.				1	2	2
larcoidea			4			
Amphitolus ariscus Hck.			1			
Spongurus pilomaticus Riedel		4	2	2		
Cromyodruppa sp.		1				
Sphaeridae		5		2	2	3
Androcyclas gamphonicha Jorg.					1	1
Bathropyramis sp.	1	2		6	2	2
Sethopyramis sp.	1					
Plectopyramis polypleura Hck.	2			1		
Cyrtolagena languncula (Hck.)			3	1	1	2
Clathrospyris sp.	1		1		1	
Ceratospyris sp.		1	2	2	3	1
Cycladophora davisiana Ehr.	2	1	23	16	29	55
Cycladophora sp.	3		11	7	9	18
*Dyplocyclas cornuta (*Bailey)	4		9	3	7	7
Dictyophimus crisae (Ehr.)	2	5	9	21	4	4
D. mawsoni Riedel				2		
Pseudodictyophimus gracilipes		1	4	2	2	6
Eucyrtidium sp.	1		1			
Artostrobus annulatus			1			2
Tricolocampe sp.			1			
Pterocanium pinnatum Hck.	1	1	2	3		5
Pteroscenium (?) sp.					3	
Lithomitra lineata (Ehr) gr.			5	4	7	4
Lithomitra arachnea	5					
Tricolocapsa papilosa (Ehr)						1
Eucyrphalus sp.						1
Lychnocanium grande Clark &Campbell						2
Botriopera boreale (Ehr) gr.	1					
Calimitra sp.aff *carolota* Hck.	1					
*Tholospiris borealis (*Bailey)	36	1	16	19	22	26
Tholospiris tripodiscus Hck.	11				2	
Cornutella profunda Ehr.	1		1			
Unknown radiolaria	4		16	5		5

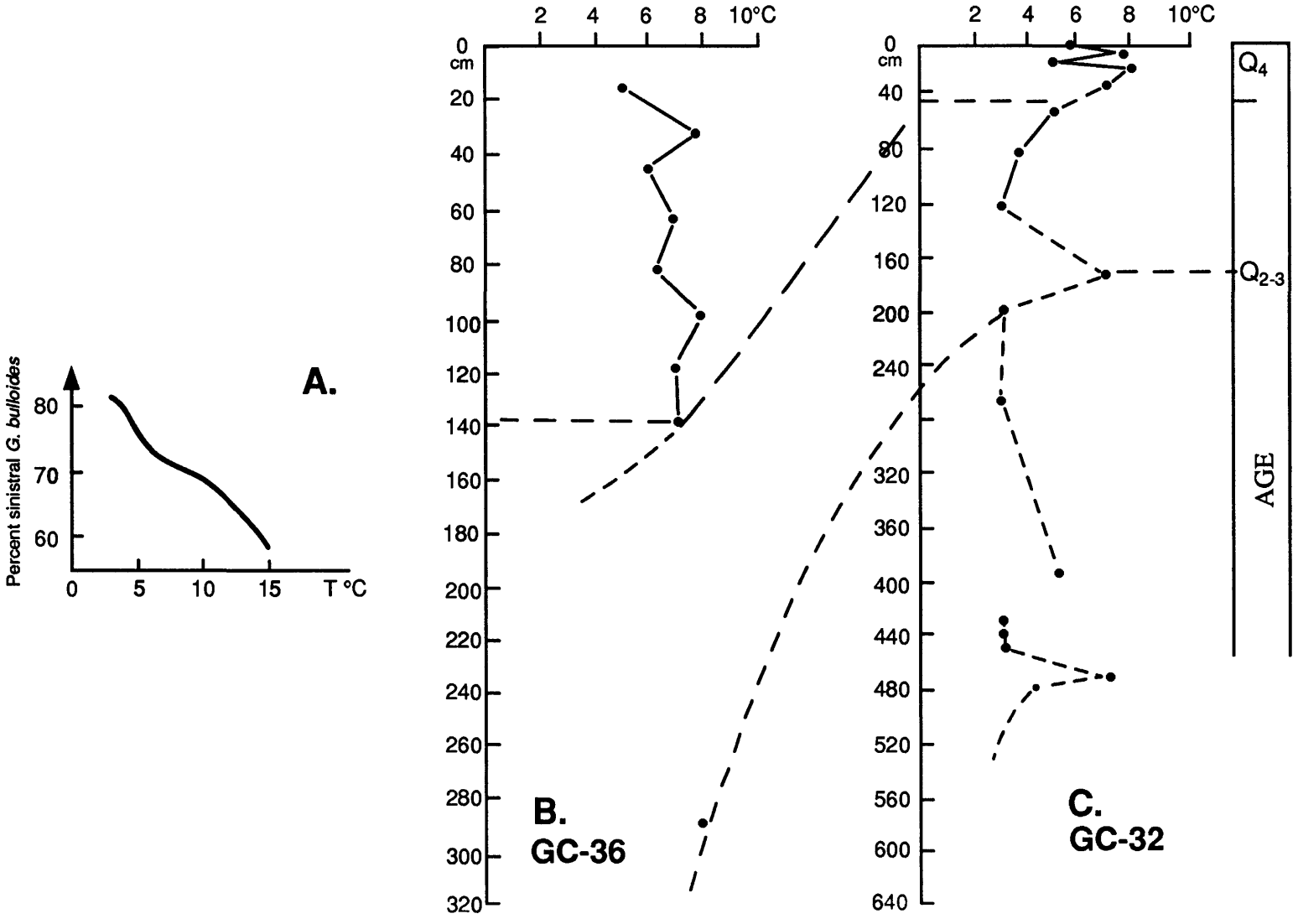

Figure 1. A. Ratio of sinistral/total *G. bulloides* plotted against temperature (Boltovskoy, 1973). B-C. Paleotemperature curves based on the ratio of sinistral/dextral forms of *N. pachyderma* in GC-36 and GC-32, Detroit Seamount. Q_{2-3} = Late Pleistocen (undefined); Q_4 = Holocene.

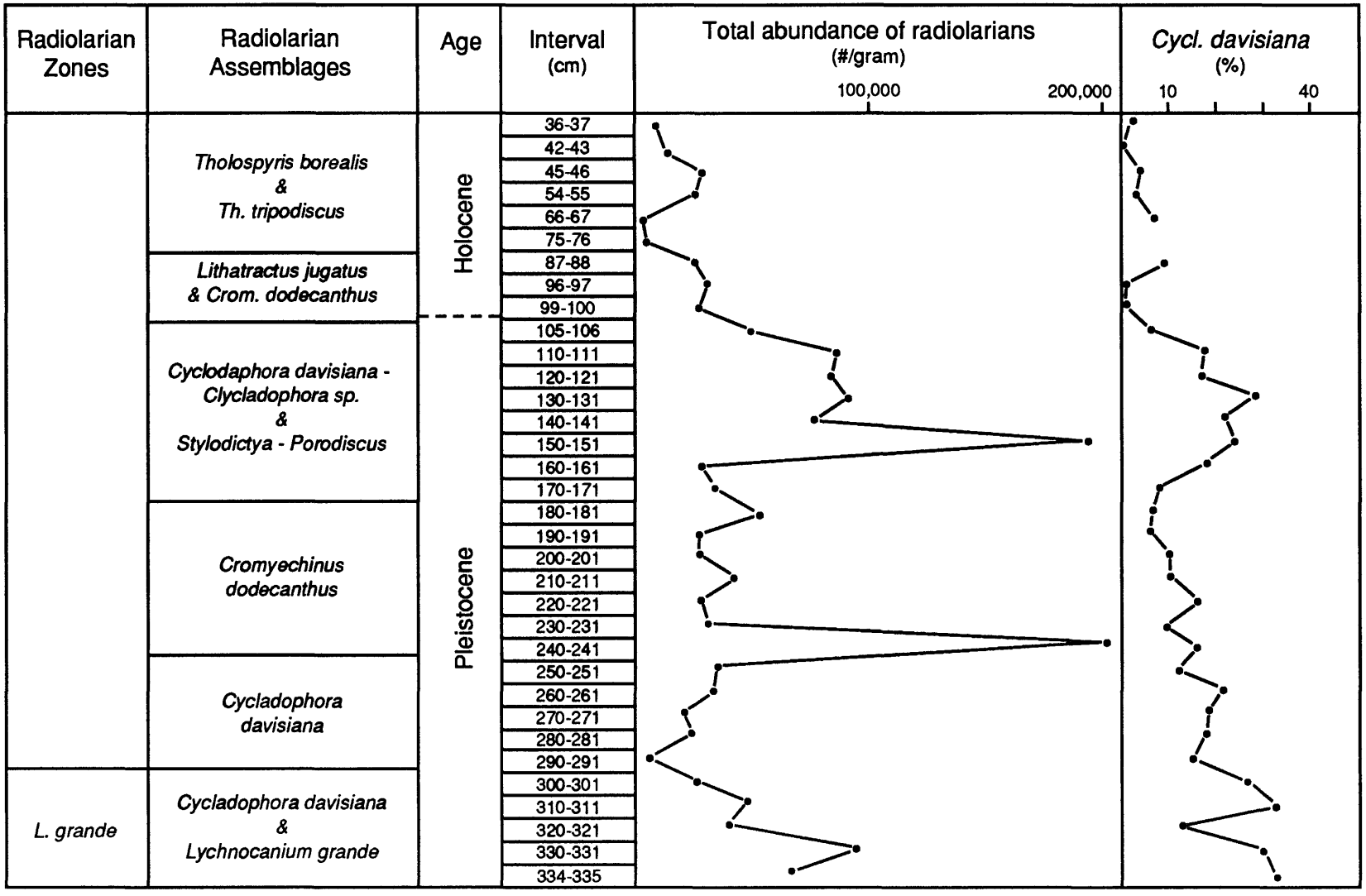

Figure 2. Stratigraphic and quantitative distribution of radiolarians below 87 cm, GC-36.

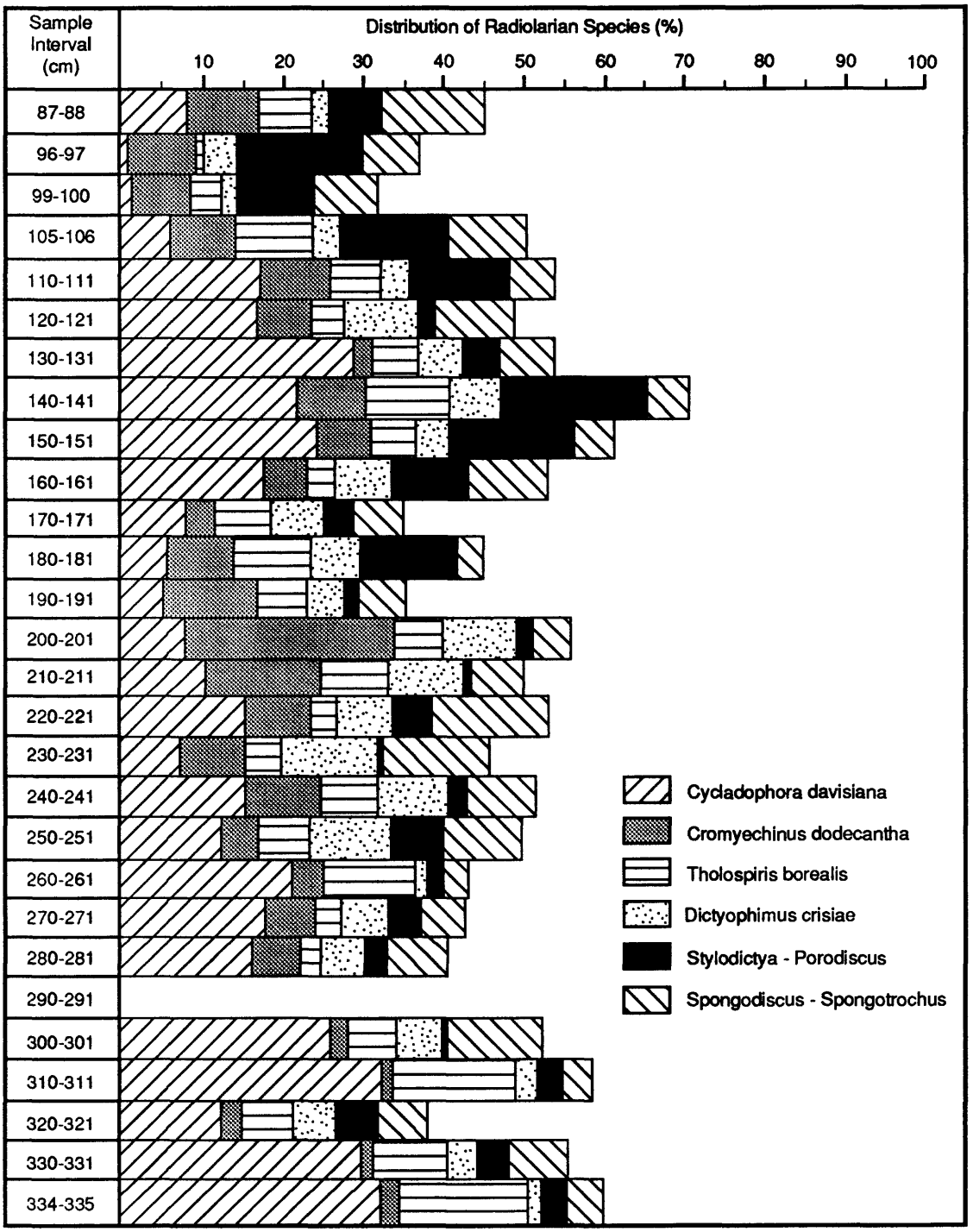

Figure 3. Distribution of dominant radiolarian assemblages and number of radiolarians per gram of sediment in core GC-36.

LATE PLEISTOCENE AND HOLOCENE ACCUMULATION OF CALCIUM CARBONATE, OPAL, AND TERRIGENOUS DETRITUS: DETROIT SEAMOUNT (NORTHWESTERN PACIFIC) AND BOWERS RIDGE (SOUTHERN BERING SEA)

Sergei A. Gorbarenko and Svetlana G. Pliss

Pacific Oceanological Institute, Far Eastern Branch, Russian Academy of Sciences, 43 Baltiyskaja, Vladivostok 690041, Russia

INTRODUCTION

Calcium carbonate content of sediments is often used for stratigraphic divisions of Quaternary deposits and investigations of seawater paleochemistry (Zahn *et al.*, 1991). Bottom accumulation of carbonate carbon, however, depends on the depositional region. For example, the calcium carbonate content in Atlantic Ocean sediments decreased during periods of glaciation and increased during warm interglacial periods (Crowley, 1985). In contrast, calcium carbonate content in equatorial Pacific sediments increased during cold periods and decreased during warm ones (Volat *et al.*, 1980).

Calcium carbonate content in sediments is determined by three factors: 1) photic zone productivity and carbonate shell supply to the bottom; 2) dissolution of shells in the water column and surface sediments; and 3) dilution by terrigenous and other materials. Most investigators agree that carbonate dissolution is the most important factor. Dissolution, which is determined by the degree of seawater undersaturation relative to the carbonate ion, varies considerably in the World Ocean, depending on water depth, oxygen ventilation, and bottom water chemistry. Thus, the identification of regional trends in calcium carbonate content is important toward understanding of regional stratigraphy and variations of bottom-water composition in the past.

The calcium carbonate content trend in sediments from the northwest Pacific differs from that in the Atlantic Ocean and the equatorial Pacific. Only limited investigations of the northwest Pacific using modern methods of dating and stratigraphy have been undertaken. Therefore, data presented here for three cores from the northwest Pacific, and one core from the southern part of the Bering Sea, will help establish primary trends in the variations of biogenic (mainly calcium carbonate) and terrigenous material, and also help in formulating hypotheses regarding the paleoceanographic conditions responsible for these variations.

METHODS AND MATERIALS

Four gravity cores (GC-11, GC-28, GC-32, and GC-36) were obtained during Leg 4 of the R.V. *Akademik Aleksandr Vinogradov* cruise 91-AV-19. One core was obtained on the western slope of Bowers Ridge (GC-11), the other three on the upper part (GC-28), eastern slope (GC-32), and foot of the southern slope (GC-36) of Detroit Seamount (Fig. 1; Table 1). Visual lithologic description of the cores was carried out aboard the research vessel (Table 1). Carbonate and organic carbon contents were determined by the coulometric method and carbon analyzer AH-7529. Total carbon was extracted from sediment by heating samples to 1050 °C and decomposition in dilute HCl, with standard removal of water vapor and sulfur compounds from the evolved gas. Organic carbon content was calculated as the difference between total and carbonate carbon.

Magnetic susceptibility of sediments was determined on board the vessel immediately after sampling along an undisturbed core, using a magnetic susceptibility registrar.

RESULTS AND DISCUSSION

Lithologic data, calcium carbonate and organic carbon contents, and magnetic susceptibility of sediments from cores GC-11, GC-28, GC-32, and GC-36 are shown in Figs. 3 - 6 and Table 2.

Time Control

Oxygen isotope stratigraphy data and AMS radiocarbon dating for cores RAMA 44PC, collected on Meiji Seamount (53° 00' N, 164°39' E) (Keigwin *et al.*, 1992) and CH84-14, collected close to the Tsugaru Strait (41° 44' N, 142° 33' E) (Kallel *et al.*, 1988), and the oxygen isotope record for core K-119, collected on Detroit Seamount (Gorbarenko, 1991b) (Fig. 2) can be used to produce a time scale for regional variations in calcium carbonate content in sediments.

The calcium carbonate content of core CH84-14 has not been determined, however, the number of planktonic foraminifera *N. pachiderma sin.* and *G. bulloides* in 1 g of sediment was calculated. Theses two species are coeval and represent the bulk of the carbonate component in sediments of the region under discussion.

Oxygen isotope records obtained in the region and other parts of the World Ocean reflect a two-stage transition from conditions of the last glaciation (isotope stage 2) to post-glaciation conditions (stage 1). The reason for this transition is that glacial melting occurred non-uniformly. In the Atlantic Ocean, initial acceleration in the glacial melting rate occurred from 14.5 to 11.5 ka (Termination 1a); the second occurred from 10.4 to 8.5 ka (Termination 1b) (Fairbanks, 1989). Distinguished in each termination are maximum melting rates and corresponding melt water pulses (MWP) 1A and 1B that occurred at about 12 and 9.5 ka, respectively (Fairbanks, 1989) In oxygen isotope records, the MWP are reflected by abrupt shifts in planktonic foraminifera $\delta^{18}O$ toward negative values (Fairbanks, 1989). Analysis of sediments in the northern part of the Atlantic Ocean revealed a relatively pervasive "Heinrich layer 1" (HL1) containing the highest abundance of ice-rafted debris and maximum sediment magnetic susceptibility. This layer corresponds to the maximum melting rate for continental glaciers that occurred at 13.6-13.5 ka ago (Laberie *et al.*, 1992). In planktonic foraminifera $\delta^{18}O$ records for RAMA 44PC (Keigwin *et al.*, 1992) and CH 84-14 (Kallel *et al.*, 1988), the isotope shifts corresponding to MWP 1A are dated as 12.9 and 12.5 ka, and the shifts caused by MWP 1B (less well developed) correspond to ages of 10.5 and 9.5 ka. Thus, the negative $\delta^{18}O$ curve shifts reflecting 1A and 1B events occurred in the northwestern Pacific during the period of transition from the last glaciation to the Holocene, were coincident with desalination of surface water, and took place almost simultaneously with similar events in the north Atlantic, which was being supplied with fresh water at an earlier date.

Carbonate Content in Sediments

Calcium carbonate content records for cores RAMA 44PC, CH 84-14 (Fig. 2), and GC-36 (Fig. 5), that were recovered from areas of relatively high sedimentation rates (less elevated areas, less steep slopes), show in their upper parts, two large peaks in carbonate content directly following the "negative" oxygen isotope shifts corresponding to MWP 1A and MWP 1B dated by Keigwin *et al.* (1992) and Kallel *et al.* (1988). According to radiocarbon ages available for the RAMA 44PC and CH 84-14 cores, the carbonate peaks correspond to ages of 12.8 - 11.0 ka and 10 - 9 ka, respectively. It is likely that these carbonate peaks reflect intensification of surface water stratification, surface water desalination, and moderation of bottom-water aeration. Low oxygen contents in bottom waters lead to organic carbon destruction in surface sediments by means of sulphur reduction preferentially, and to changes of CO_3^{2-} ion concentration in pore water and $CaCO_3$ preservation in sediments. Arguments in favor of a cause and effect relationship between processes that produce the carbonate peaks and conditions that produced the oxygen isotope MWP 1A and 1B shifts make it possible to designate the carbonate peaks as 1A and 1B respectively. In core GC-36 a distinct separate peak occurs at the base of the first carbonate peak 1A. Whether this short-lived, abrupt change in calcium carbonate content is an artifact or reflects true calcium carbonate accumulation in the region, is yet to be established. Calcium carbonate content in sediments remained high into the Holocene, especially in its earlier part.

In cores with a lower sedimentation rate (GC-32, GC-38, K-119; Gorbarenko, 1991b) carbonate peaks of the last 13 ka have not been preserved due to extensive bioturbation. In the upper part of the cores, only one peak is apparent.

Organic Carbon and Opal Content

In addition to the regular variations of calcium carbonate content, trends in organic carbon and opal contents are also observed in the upper parts of the cores. Opal occurs mostly as diatom remains. In all cores, sediments that formed during the transition from glacial to postglacial conditions are marked with organic carbon contents that increase uniformly before the 1A carbonate peak and decrease simultaneously with the fall of the 1B carbonate peak. Similar variations in organic carbon contents were observed in core RAMA 44PC recovered from Meiji Seamount (Keigwin *et al.*, 1992) suggesting that this trend is common for sediments investigated in this study from the Pacific and the southern part of the Bering Sea.

In the transition from glacial to postglacial sediments, opal contents change in unison with the 1A carbonate peak (Figs. 2-6). A marked increase in the concentration of opal in these sediments causes considerable changes in the physical properties of the sediments, e.g. magnetic susceptibility and dry bulk density decrease (Keigwin *et al.*, 1992) and sediment color changes from gray to light olive-gray (5Y5/2) and olive-gray (5Y3/2). These changes are most pronounced in cores with higher sedimentation rates (i.e. GC-36

and RAMA 44PC). Thus, opal content in sediments of the region, along with other biogenic components, were subject to systematic changes in the past. Bering Sea opal content variations, however, unlike carbonate and organic carbon changes, differ from trends occurring in the far northwest Pacific. In core GC-11, the increase in opal content and accompanying change of physical properties was considerably less than in cores from the northwest Pacific and silica content significantly increases in Holocene deposits.

Terrigenous Component Variations

Variations in biogenic component contents discussed previously are distinguishable above background variations in coarse-grained terrigenous components that are common to the entire region. As evident from RAMA 44PC (Keigwin *et al.*, 1992), and GC-11 and GC-36 core data (Fig. 2), the coarse-grained terrigenous component predominates in glacial deposits, but becomes several times less abundant before the start of carbonate peak 1A. The sediment size fraction in which the quantity of coarse-grained terrigenous component was determined, differed in cores 44PC, GC-11, and GC-36, and was 150, 65, and 100 μm, respectively. However, these different sizes did not significantly influence the general trend in changes of the coarse component, which is mostly represented by ice-rafted debris, because in the 65 and 100 μm fractions more diatom and small foraminifera contributions were taken into account. Although there was no analysis of the changes in the coarse-grained terrigenous component in cores GC-28 and GC-32, according to their lithological description it is possible to infer that the coarse-grained terrigenous component is greatest in glacial deposits. We believe that changes in the rate of accumulation of the terrigenous component was caused by a change in sediment transport direction resulting from sea level variations and opening of the Bering Strait. During the last glaciation and sea level regression, the Bering Strait closed and most of the northeastern Bering shelf was above sea level. The remaining Bering Sea served as a reservoir for the collection of terrigenous material from the shelf, Chukotka, the Bering Bridge, and Alaska. Cyclonic surface water circulation typical of the Bering Sea carried fine terrigenous material, sea ice, and icebergs containing coarse-grained sediment through the western straits of the Aleutian islands arc (mostly through the Kamchatka Strait) to the western part of the Pacific. The abrupt decrease in accumulation of ice-rafted material in sediments of the Bering Sea and adjacent area of the Pacific is probably related to the Bering Strait opening and subsequent transport of most of the terrigenous material to the Chukchi Sea and the northern part of the Bering Sea. On the basis of radiocarbon dating results for the Bering-Chukchi shelf, McManus and Creager (1984) concluded that the Bering Sea opening occurred 14.6 to 14.4 ka, and the present surface water circulation system developed by 12 ka. The beginning of the decrease in the amount of ice-rafted material noted in sediments from the region (cores GC-11; GC-36) is consistent with the opening of the Bering Strait, as determined by McManus and Creager (1984), however, according to data of MWP 1A in the NW Pacific, the present type of surface currents had set in earlier - about 13.5 ka (prior to carbonate peak 1A). A short-lived increase in the terrigenous component accumulation in sediments from the region during the period between the accumulation of carbonate peak 1A and accumulation of carbonate peak 1B was probably caused by the event when the climate became relatively cold (the Younger Dryas event) and Alaska glaciers expanded prior to the Holocene (Porter *et al.*, 1986).

The cores covering relatively long records of climatic events (GC-11, GC-28, GC-32) show in older deposits the presence of two horizons (III and V, Fig. 3) enriched in calcium carbonate, although less enriched than in the upper horizon I. Similar findings on calcium carbonate and opal accumulation in upper Quaternary sediments of the Okhotsk and Bering Seas and the northwestern Pacific was presented earlier (Bezrukov *et al.*, 1960; Romankevich, 1963; Juise, 1962). Horizons I, III, and V, as distinguished by the just listed and other scientists, contain sediments of relatively higher calcium carbonate and opal contents, and, according to diatom results (Juise, 1962), indicate relatively warm conditions in the region. Horizons II and IV, primarily composed of terrigenous sediments, have a very low content of siliceous and carbonate skeletons, and correspond to glaciation periods. On the basis of oxygen isotope records, an analogous trend in the change of biogenic component content was identified to occur in Okhotsk Sea sediments (Gorbarenko, 1988). Stratigraphic position of horizons I-V was clarified as well (Gorbarenko *et al.*, 1988; Gorbarenko, 1991a). Horizon III, with a high calcium carbonate content, corresponds to the warm isotopic event 3.3., and horizon V, to the isotopic event 5.5. Taking into consideration the stratigraphic location pattern of the carbonate-rich and carbonate-poor horizons in the region under study (including the marginal seas) and synchroneity of horizon I, we suggest that the other horizons are synchronous as well. Thus, stratigraphic location of horizons III and V is most likely similar to that determined for the Okhotsk Sea (Gorbarenko, 1988). A peak in the magnetic susceptibility of sediments, corresponding to the maximum flux of terrigenous ferromagnetic minerals into the region, has been distinguished to occur in the lower part of the "glacial" horizons in cores GC-32 and GC-28.

SUMMARY

Lithology, magnetic susceptibility, carbonate and organic carbon contents, and terrigenous components of sediments were determined from three cores taken on Detroit Seamount and one from Bowers Ridge (southern Bering Sea). All cores studied show abrupt increases in carbonate content directly after the first maximum rate of glacial melting (carbonate peak 1A) and also after the second maximum in rate of melting (peak 1B) during the transition period from the latest glaciation to the Holocene. Also noted was a considerable decrease in the accumulation of terrigenous material, which resulted from the opening of the Bering Strait and transport of material to the north, prior to carbonate peak 1A. A less distinct increase in carbonate content during the Wisconsin glaciation interstadial and the Sangamon interglaciation (isotope stage 5e) has been distinguished in older deposits of the region

Table 1. Locations and descriptions of cores

Station	Location	Latitude-Longitude	Water Depth, m	Lithology
GC11	Western slope of Bowers Ridge	53° 31.0' N 178° 51.0' E	3060	0-230 cm Silty and sandy clay siliceous and calcareous grayish brown (5YR 3/2) 0-13 cm and olive gray (5Y 3/2) 13-230 cm 230-457 cm Silty clay siliceous olive gray (5Y 3/2) with rubble at 263 cm 457-462 cm Silty and sandy clay siliceous and calcareous olive gray (5Y 3/2)
GC28	Flat top of Detroit Seamount	51° 18.0' N 167° 39.9' E	2340	0-22 cm Foram sand clayey: dark yellowish brown (10YR 4/2) in 0-5 cm and light olive gray (5Y 5/2) 5-22 cm. There are ash lenses yellowish gray (5Y 7/2) at 7 cm 22-39 cm Sandy clay calcareous grayish olive (10Y 4/2) with pale olive (10Y 6/2) spots, bioturbated 39-450 cm Silty and sandy clay: olive gray (5Y 3/2) 39-282 cm, grayish olive green (5GY 3/2) 303-317 cm, dusky yellow green (5GY 5/2) 320-335, 350-370, and 378-450 cm, dark greenish gray (5G 4/1) 335-350 and 370-378 cm. There are ash layers: brownish black (5YR 2/1) 170-180 cm (1 cm in thickness, oblique to the core axis) and light olive gray (5Y 6/1) 317-320 cm (3 cm in thickness)
GC32	Eastern slope of Detroit Seamount	51° 03.4' N 167° 52.8' E	2860	0-19 cm Foram sand clayey: dark yellowish brown (10YR 4/2) in 0-12 cm and light olive (10Y 6/2) 12-19 cm 19-35 cm Sandy clay calcareous light olive gray (5Y 5/2) with light olive brown (5Y 5/6) and grayish olive (10Y 4/2) spots, bioturbated 35-575 cm Sandy and silty clay: olive gray (5Y 3/2) 35-320 and 360-380 cm, dusky yellow green (5GY 5/2) 320-345 cm, and grayish olive green (5GY 3/2) 345-360 cm and 380-575 cm. There are ash layers: brownish black (5YR 2/1) at 193 cm (7mm in thickness), moderate brown (5YR 3/4) 517-520 cm (3 cm in thickness) and 545-575 cm (1-3 cm in thickness - core in this interval is disturbed)
GC36	Southern slope of Detroit Seamount	50° 24.7' N 167° 43.9' E	3300	0-56 cm Sandy clay calcareous: dark yellowish brown (10YR 4/2) 0-45 cm and light olive gray (5Y 5/2) 45-56 cm 56-336 cm Silty clay siliceous: graish olive (10Y 4/2) 56-85 cm and moderate gray (N4) 85-336 cm. There is ash layer light olive gray (5Y 5/2) 292-294 cm

Table 2. Calcium carbonate and organic carbon content (% per 1g of dry bulk sediment) and magnetic susceptibility of sediments (10^{-6} unit CGS).

Interval (cm)	$CaCO_3$	C organic	Magnetic suscept.	Interval (cm)	$CaCO_3$	C organic	Magnetic suscept.
Core GC- 11							
2-4	0.75	0.51		97-99	3.92	0.63	
5			64	100			210
7-9	0.92	0.51		102-104	11.25	1.35	
10			45	105			240
12-14	3.67	0.40		107-109	7.50	0.75	
15			52	110			280
17-19	1.67	0.60		112-114	2.92	0.70	
20			48	115			300
22-24	2.92	0.55		117-119	1.75	0.85	
25			56	120			240
27-29	3.17	0.52		122-124	3.33	0.95	
30			68	125			220
32-34	1.67	0.80		127-129	6.66	1.10	
35			75	130			220
37-39	2.50	0.80		132-134	6.25	1.15	
40			60	135			220
42-44	4.33	0.68		137-139	11.66	1.20	
45			88	140			200
47-49	5.25	0.57		142-144	12.99	1.24	
50			80	145			210
52-54	5.41	0.65		147-149	6.66	1.47	
55			80	150			230
57-59	6.25	0.45		152-154	6.25	1.45	
60			87	155			230
62-64	5.00	0.46		157-159	3.00	1.29	
65			82	160			230
67-69	5.00	0.60		162-164	3.33	1.06	
70			58	165			250
72-74	7.16	0.54		167-169	1.67	0.98	
75			40	170			240
77-79	5.16	0.68		172-174	2.08	0.85	
80			95	175			270
82-84	5.00	0.70		177-179	2.08	0.75	
85			210	180			260
87-89	4.17	0.72		182-184	1.42	0.78	
90			240	185			240
92-94	4.17	0.65		187-189	2.00	0.56	
95			250	190			220
192-194	1.67	0.76		372-374	0.75	0.71	
200			240	377	0.83	0.65	
197-199	2.50	0.60		382	0.58	0.71	
205			245	387	0.75	0.63	
202-204	1.50	0.62		392	0.58	0.58	
210			270	397	0.83	0.60	
207-209	1.08	0.72		402	1.50	0.62	
215			260	407	1.83	0.60	
212-214	2.08	0.73		412	0.50	0.56	
220			220	417	0.58	0.55	
217-219	1.67	0.66		422	1.00	0.54	
225			240	427	0.50	0.60	
222-224	1.00	0.62		432	0.92	0.59	
227-229	1.25	0.65		437	0.92	0.62	
232-234	1.17	0.58		442-444	0.92	0.54	
237-239	1.67	0.70		447-449	0.75	0.58	
242	1.33	0.74		452-457	0.83	0.65	

Table 2. continued

Interval (cm)	$CaCO_3$	C organic	Magnetic suscept.	Interval (cm)	$CaCO_3$	C organic	Magnetic suscept.
Core GC-11 continued							
247	1.50	0.64		457-459	1.17	0.60	
252	1.00	0.64		462-464	1.25	0.67	
257	0.83	0.62		467-469	1.08	0.49	
262	1.00	0.68		472-473	0.92	0.51	
267	0.83	0.66		477-479	1.75	0.59	
272	1.00	0.68		482-484	1.17	0.60	
277	1.17	0.70		487-489	2.08	0.65	
282	1.67	0.70		492-494	2.25	0.71	
287	1.42	0.67		497-499	2.17	0.64	
292	1.58	0.74		502-504	2.08	0.71	
297	1.17	0.66		507-509	2.92	0.75	
302	0.75	0.66		512-514	0.75	0.71	
307	0.75	0.61		517	0.75	0.73	
312	0.75	0.61		522	0.75	0.61	
317	0.75	0.66		527	0.75	0.65	
322	0.58	0.73		532	0.67	0.62	
327	0.67	0.62		537	0.75	0.61	
332	0.50	0.64		542	0.67	0.70	
337	0.92	0.59		547	1.25	0.60	
342-344	0.50	0.69		552	0.50	0.71	
347-349	0.75	0.66		557	1.00	0.60	
352-354	0.83	0.85		562	1.17	0.72	
357-359	0.83	1.00		567	1.17	0.59	
362-364	0.83	0.66		572	1.67	0.62	
367-369	0.75	0.69		577	1.83	0.73	
582	2.08	0.65		614	3.83	0.72	
587	3.17	0.78		624	3.67	0.66	
592	2.00	0.68		634	4.66	0.69	
597	2.67	0.71		642	2.75	0.70	
602	3.67	0.50		654	1.00	0.50	
Core GC-28							
1-3	22.49	1.02		75			100
0			96	130-131	1.25	0.45	
5-6	25.82	0.84		80			95
5			100	140-141	1.25	0.62	
10-11	27.66	0.66		85			100
10			100	150-151	1.33	0.54	
15-16	28.32	0.78		90			100
15			90	160-161	3.08	0.53	
21-22	25.82	1.14		95			100
20			90	170-171	5.08	0.69	
25-26	23.82	1.18		100			110
25			84	180-181	2.83	0.44	
35-36	20.41	1.84		105			110
30			61	190-191	5.41	0.67	
40-41	6.00	1.21		110			95
35			88	200-201	8.91	0.55	
50-51	3.25	0.98		115			96
40			95	210-211	2.25	0.53	
60-61	3.83	0.87		120			100
45			100	220-221	1.83	0.58	
70-71	3.42	0.86		125			90
50			90	230-231	1.33	0.74	
80-81	3.17	0.77		130			80
55			110	240-241	1.17	0.76	
90-91	1.75	0.85		135			80
60			160	251-252	0.92	0.69	

Table 2. continued

Interval (cm)	$CaCO_3$	C organic	Magnetic suscept.	Interval (cm)	$CaCO_3$	C organic	Magnetic suscept.
Core GC-28 continued							
100-101	1.08	0.66		140			88
65			100	261-262	0.42	0.57	
110-111	1.25	0.59		145			88
70			100	271-272	0.58	0.59	
120-121	1.08	0.69		150			90
281-282	0.67	0.62		430-431	3.08	0.43	
155			86	255			90
291-292	0.92	0.59		431-432	2.17	0.54	
160			85	260			110
295-296	1.83	0.68		435-436	3.50	0.33	
165			96	265			100
311-312	0.58	0.48		270			120
170			95	275			100
319-320	0.42	0.11		280			100
175			100	285			80
331-332	3.00	0.74		290			68
180			96	295			52
341-342	0.75	0.61		300			58
185			70	305			90
351-352	3.42	0.55		310			80
190			76	315			71
361-362	8.83	0.58		320			63
195			77	325			61
371-372	0.58	0.63		330			55
200			85	335			72
381-382	1.25	0.51		340			74
205			88	345			79
385-386	1.92	0.67		350			84
210			78	355			85
390-391	2.67	0.74		360			72
215			90	365			70
395-396	1.50	0.67		370			72
220			100	375			65
400-401	0.25	0.87		380			52
225			68	385			55
405-406	0.75	0.77		390			64
230			62	395			71
411-412	1.00	0.68		400			80
235			66	405			85
415-416	1.00	0.58		410			86
240			76	415			79
421-422	3.08	0.58		420			60
245			68	425			56
425-426	2.25	0.43		430			53
250			52	435			33
Core GC-32							
1-2	19.58	0.45		141-142	0.50	0.62	
0			96	105			100
4-5	21.66	0.50		151-152	0.58	0.63	
5			100	110			80
7-8	21.82	0.50		161-162	0.67	0.72	
10			80	115			90
10-11	24.16	0.38		171-172	1.00	0.68	
15			58	120			90
13-14	24.57	0.30		181-182	2.08	0.55	
20			31	125			80
16-17	25.57	0.43		191-192	2.00	0.36	

Table 2. continued

Interval (cm)	$CaCO_3$	C organic	Magnetic suscept.	Interval (cm)	$CaCO_3$	C organic	Magnetic suscept.
Core GC-32 continued							
25			33	130			90
19-20	25.99	0.58		196-197	1.42	0.41	
30			52	135			80
22-23	17.66	0.73		201-202	3.33	0.40	
35			62	140			80
25-26	19.16	0.95		211-212	0.80	0.48	
40			91	145			90
27-28	15.66	0.92		221-222	5.00	0.51	
45			58	150			90
31-32	11.25	1.05		231-232	1.67	0.45	
50			105	155			90
41-42	1.58	0.83		241-242	1.00	0.38	1.00
55			110	160	80		80
51-52	2.08	0.65		250-251	0.58	0.63	
60			110	165			100
61-62	2.08	0.71		261-262	0.42	0.77	
65			100	170			100
71-72	1.00	0.83		271-272	0.58	0.58	
70			100	175			90
81-82	2.00	0.61		281-282	0.58	0.68	
75			100	180			80
91-92	1.08	0.67		291-292	0.58	0.58	
80			100	185			90
101-102	0.83	0.61		301-302	0.42	0.60	
85			100	190			90
111-112	0.42	0.57		311-312	0.58	0.48	
90	100		100	195			150
121-122	0.67	0.55		321-322	0.75	0.48	
95	100		100	200			80
131-132	0.83	0.43		326-327	0.83	0.76	
100	100		100	205			76
331-332	0.83	0.75		501-502	0.42	0.65	
210			80	315			105
336-337	0.67	0.67		511-512	0.58	0.58	
215			80	320			100
341-342	0.67	0.95		521-522	0.42	0.47	
220			80	325			80
351-352	1.83	0.34		531-532	0.67	0.45	
225			78	330			75
361-362	0.67	0.52		551-552	0.50	0.54	
230			80	335			70
371-372	0.92	0.72		561-562	0.58	0.58	
235			80	340			80
375-376	2.17	0.47		571-572	0.58	0.43	
240			100	345			50
381-382	1.08	0.65		631-632	0.58	0.71	
245			90	350			70
391-392	0.75	0.61		355			80
250			110	365			70
401-402	1.67	0.50		370			72
255			90	375			75
410-411	5.08	0.49		380			73
260			82	385			86
421-422	4.75	0.45		390			90
265			80	395			82
431-432	12.50	0.40		400			90
270			85	402			100

Table 2. continued

Interval (cm)	$CaCO_3$	C organic	Magnetic suscept.	Interval (cm)	$CaCO_3$	C organic	Magnetic suscept.
Core GC-32 continued							
441-442	1.42	0.48		405			110
275			100	410			100
451-452	0.67	0.60		415			87
280			100	420			82
461-462	1.42	0.42		425			84
285			130	430			58
466-467	0.50	0.44		435			57
290			130	440			190
468-469	1.67	0.42		442			700
295			140	445			72
471-472	0.67	0.42		450			60
300			120	455			42
481-482	2.00	0.51		460			76
305			120	465			120
491-492	0.50	0.59		470			110
310			110	475			100
480			100	515			105
485			100	520			110
490			110	525			160
495			120	530			130
500			110	535			60
505			110	540			90
510			105	545			90
Core GC-36							
2-3	22.49	0.30		85			47
5-6	24.66	0.39		64-65	22.91	0.75	
8-9	21.66	0.50		90			72
11-12	20.41	0.65		66-67	22.07	0.45	
14-15	22.49	0.40		95			78
17-18	21.32	0.44		68-69	18.41	0.89	
20-21	24.16	0.60		100			78
26-27	32.49	0.30		70-71	21.66	0.50	
31-32	30.82	0.30		105			83
34-35	26.74	0.29		72-73	17.49	1.25	
35			66	110			87
36-37	24.16	0.30		74-75	18.33	0.90	
40			67	115	90		90
38-39	26.24	0.45		76-77	14.58	1.15	
45			50	120			90
40-41	25.82	0.50		78-79	17.49	1.00	
50			47	125			105
42-43	25.49	0.44		80-81	11.25	0.90	
55			30	130			110
44-45	21.24	0.65		85-86	13.49	1.02	
60			22	135			97
50-51	17.49	0.60		91-92	2.83	0.76	
65			25	140			100
52-53	12.50	0.75		95-96	2.17	0.84	
70			22	145			100
54-55	15.41	0.65		96-97	2.08	0.75	
75			25	150			100
60-61	18.33	0.45		100-101	2.08	0.95	
80			38	155			100
62-63	19.99	0.70		102-103	2.50	1.10	
160			100	191-192	0.67	0.52	
106-107	1.83	0.93		270			90
165			92	196-197	1.08	0.67	

Table 2. continued

Interval (cm)	$CaCO_3$	C organic	Magnetic suscept.	Interval (cm)	$CaCO_3$	C organic	Magnetic suscept.
Core GC-36 continued							
108-109	1.67	0.75		275			80
170			82	206-207	1.17	0.66	
111-112	1.67	0.78		280			90
175			110	211-212	1.58	0.65	
114-115	1.50	0.82		285			80
180			120	221-222	0.75	0.71	
117-118	1.25	0.75		290			95
190			110	226-227	2.17	0.84	
120-121	1.67	0.90		292			140
195			110	231-232	0.83	0.60	
123-124	1.92	0.97		295			100
200			110	236-237	0.50	0.70	
126-127	2.33	0.82		300			80
205			100	241-242	0.58	0.50	
131-132	1.42	0.83		305			75
210			80	246-247	0.83	0.55	
136-137	2.42	0.71		310			75
215			90	251-252	0.67	0.42	
141-142	1.08	0.87		315			80
220			95	256-257	0.58	0.73	
146-147	1.08	0.69		320			75
225			85	261-262	2.33	0.72	
151-152	1.17	0.74		325			75
230			90	266-267	1.17	0.71	
156-157	1.33	0.54		330			65
235			80	271-272	0.92	0.41	
161-162	0.50	0.69		276-277	0.67	0.47	
240			75	286-287	2.08	0.36	
166-167	0.67	0.70		291-292	1.08	0.62	
245			80	296-297	0.83	0.46	
171-172	1.25	0.65		301-302	2.25	0.48	
250			70	306-307	5.83	0.55	
176-177	0.83	0.70		311-312	7.50	0.60	
255			80	316-317	1.08	0.67	
181-182	0.67	0.67		321-322	1.00	0.38	
260			80	326-327	0.83	0.60	
186-187	0.67	0.54		331-332	1.08	0.77	
265			90				

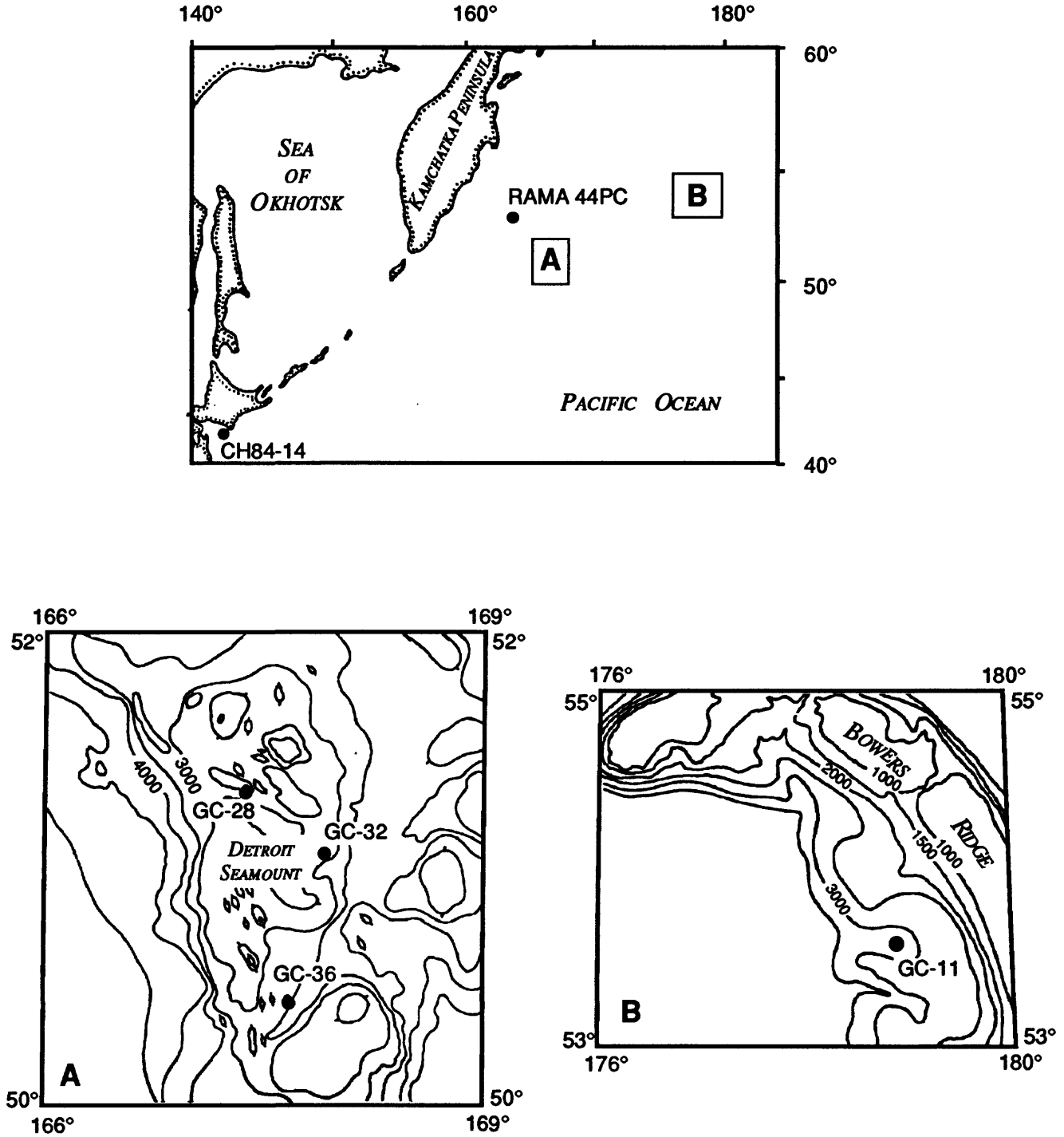

Figure 1. General location map of the northwest Pacific showing location of core sites discussed in text. (RAMA 44PC - Meiji Seamount, Keigwin *et al.*, 1992); CH 84-14 near Tsugaro Strait, Kallel *et al.*, 1988). **A.** Bathymetric map of Detroit Seamount showing locations of gravity cores GC-28, GC-32, and GC-36. **B.** Bathymetric map of Bowers Ridge, in the southern Bering Sea, showing location of gravity core GC-11. Contour interval is 500 m.

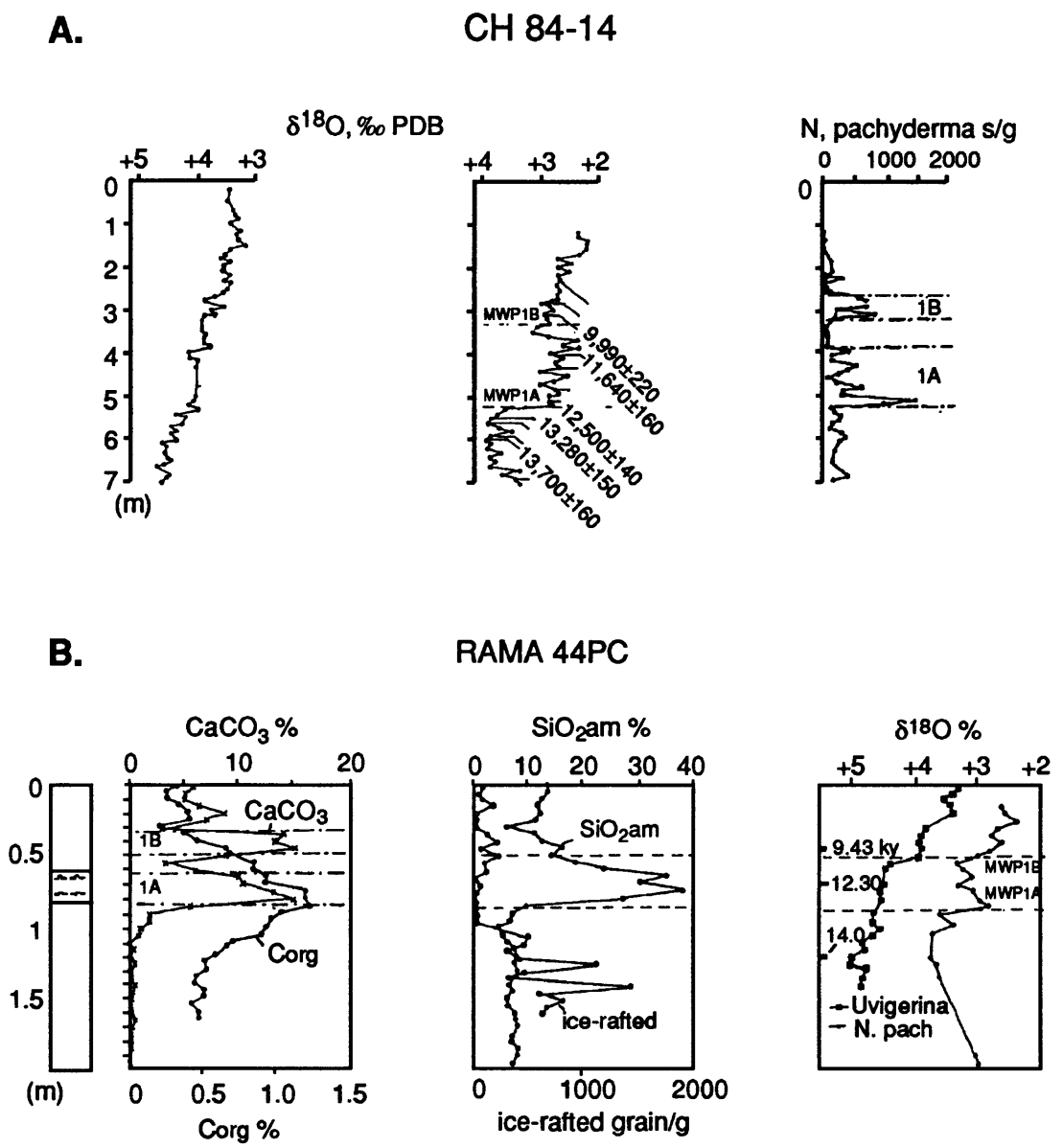

Figure 2. A: $\delta^{18}O$ values of *Uvigerina* and *N. Pachiderma sin.* shells per 1 g of dry bulk sediment for core CH 84-14; AMS ^{14}C dating after Kallel *et al.*,1988. B: Content of calcium carbonate, organic carbon, opal, and ice-rafted debris per 1 g of dry bulk sediment, and $\delta^{18}O$ of *Uvigerina* and *N. Pachiderma sin.* in per mil with respect to PDB for core RAMA 44PC (after Keigwin *et al.*, 1992).

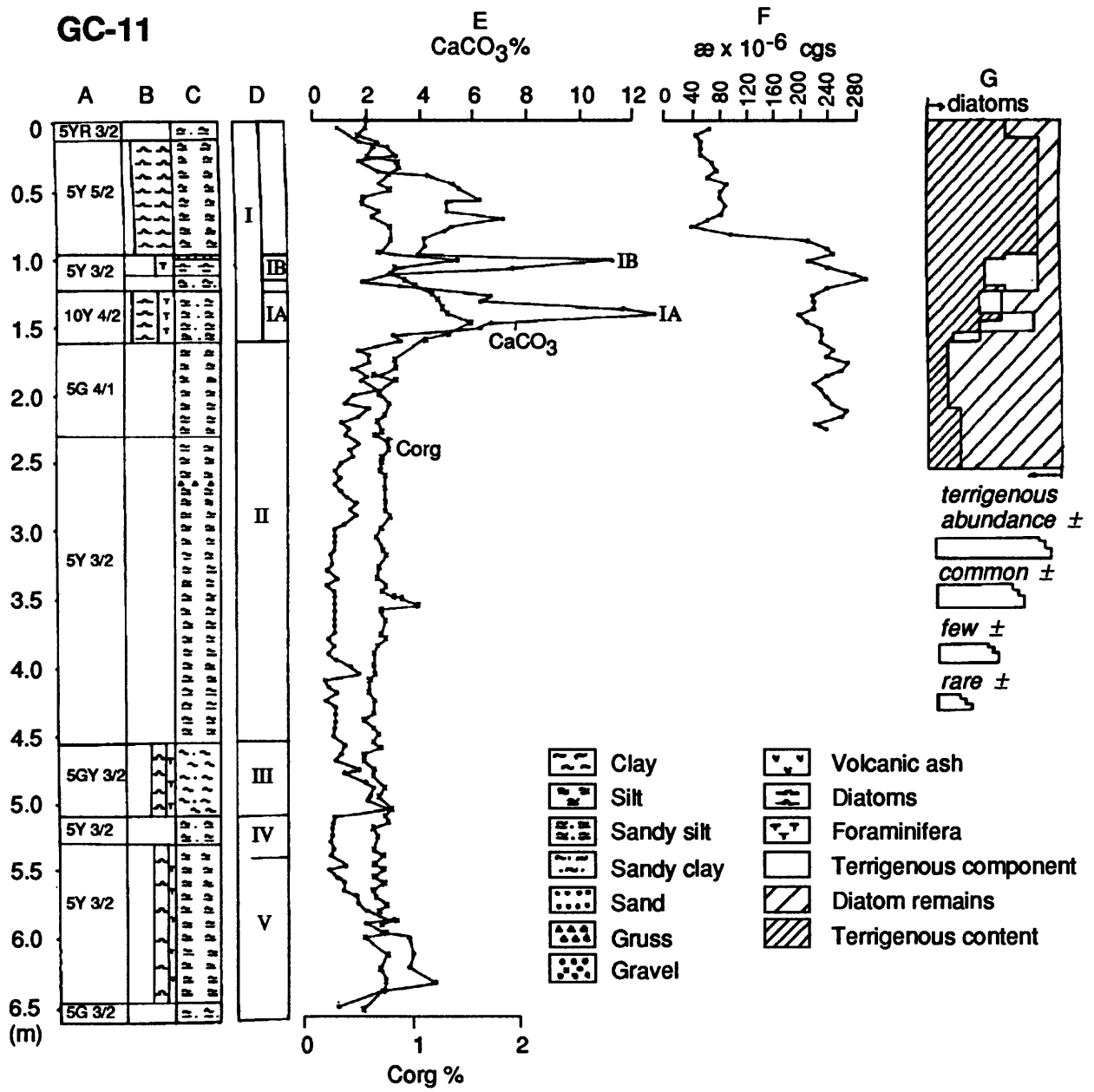

Figure 3. Log for gravity core GC-11. A = sediment color; B = sediment composition; C = sediment structure and admixtures of other origin; D = lithologic horizons; E = calcium carbonate content in % per 1 g of dry bulk sediment; F = mangetic susceptibility of sediments; G = semi-quantitative content of diatom remains and terrigenous content in < 65 micron sediment fraction in GC-11 and < 100 micron fraction in GC-36.

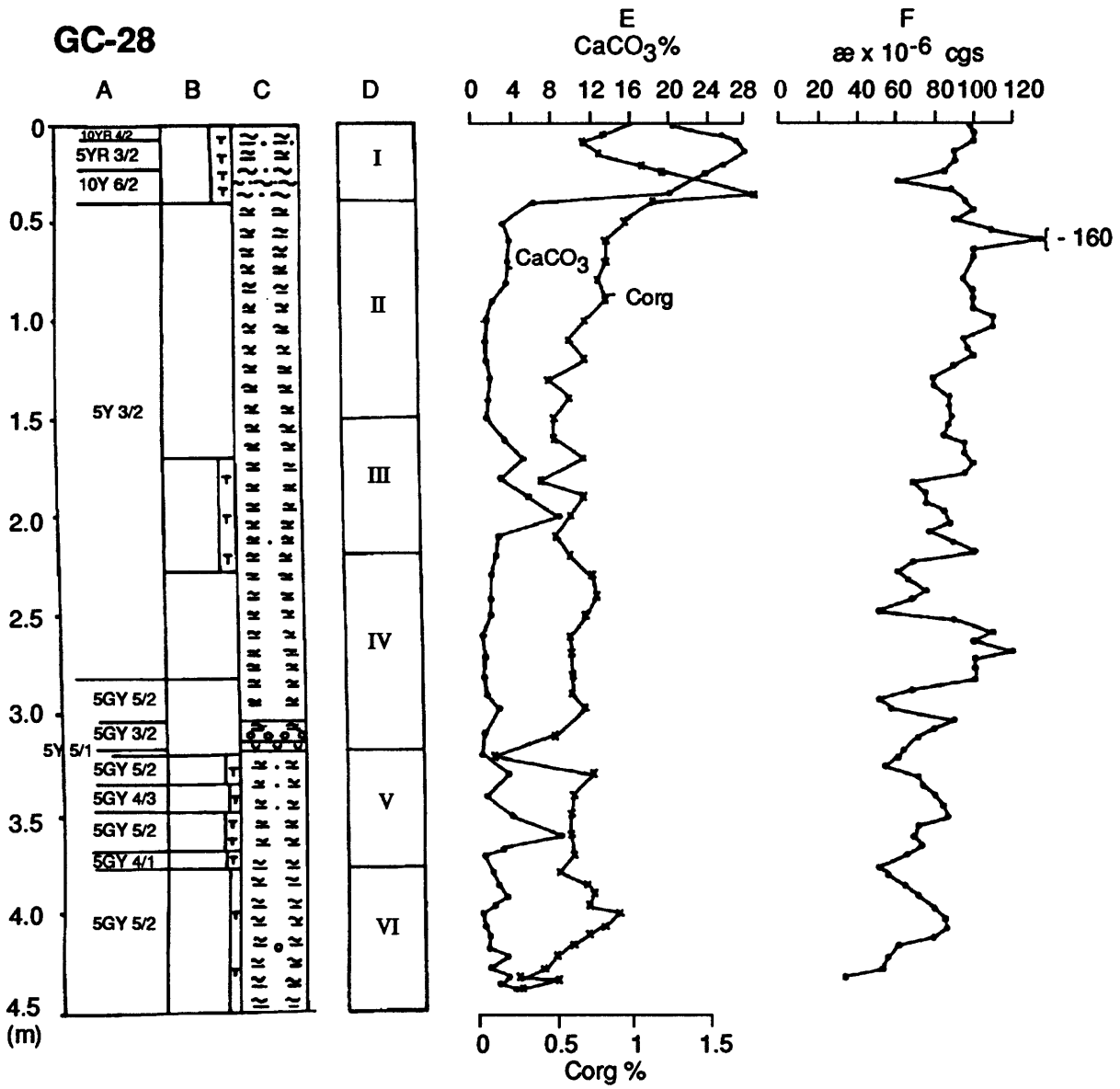

Figure 4. Log of gravity core GC-28; symbols are the same as in Fig. 3.

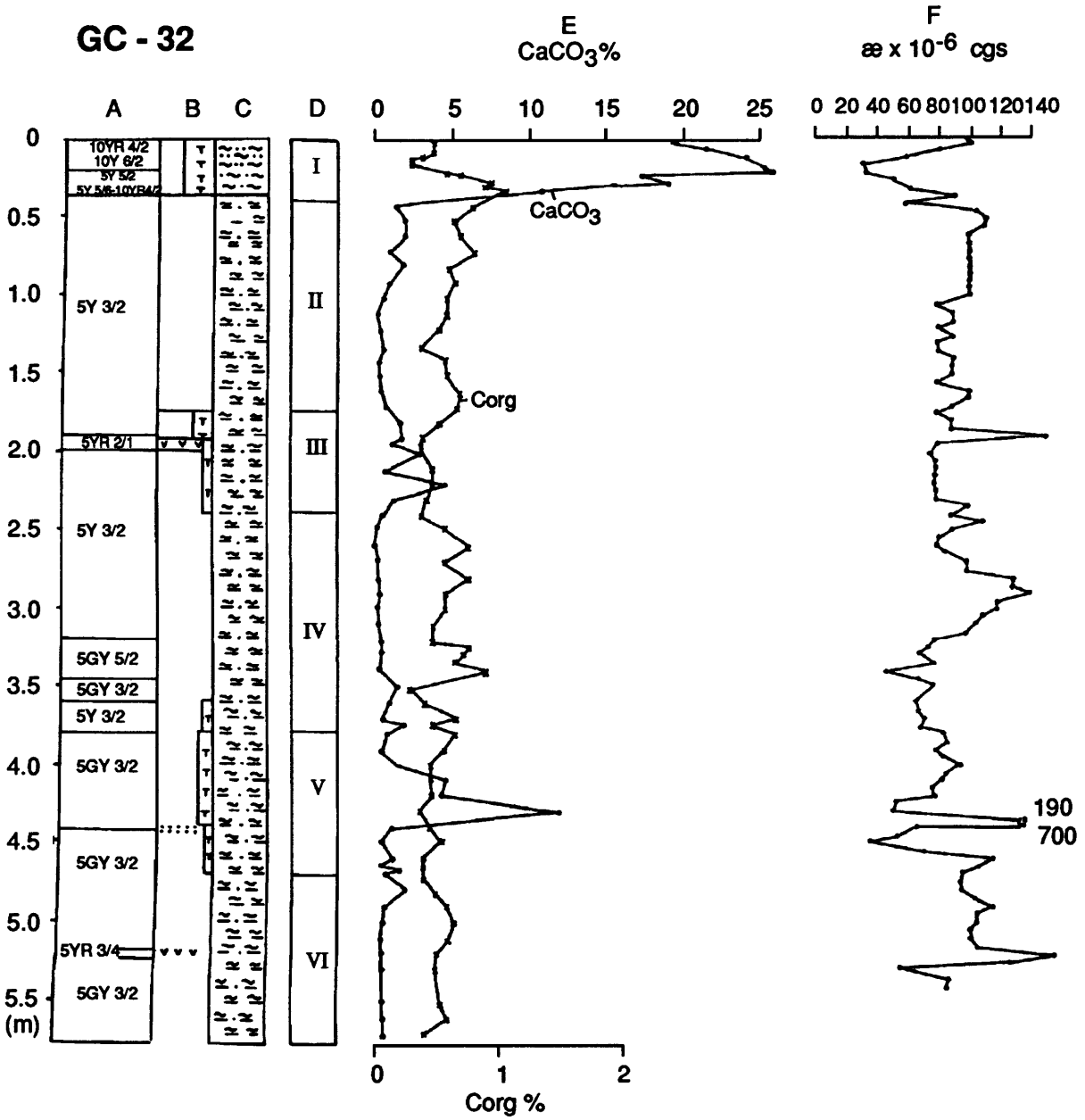

Figure 5. Log of gravity core GC-32; symbols are the same as in Fig. 3.

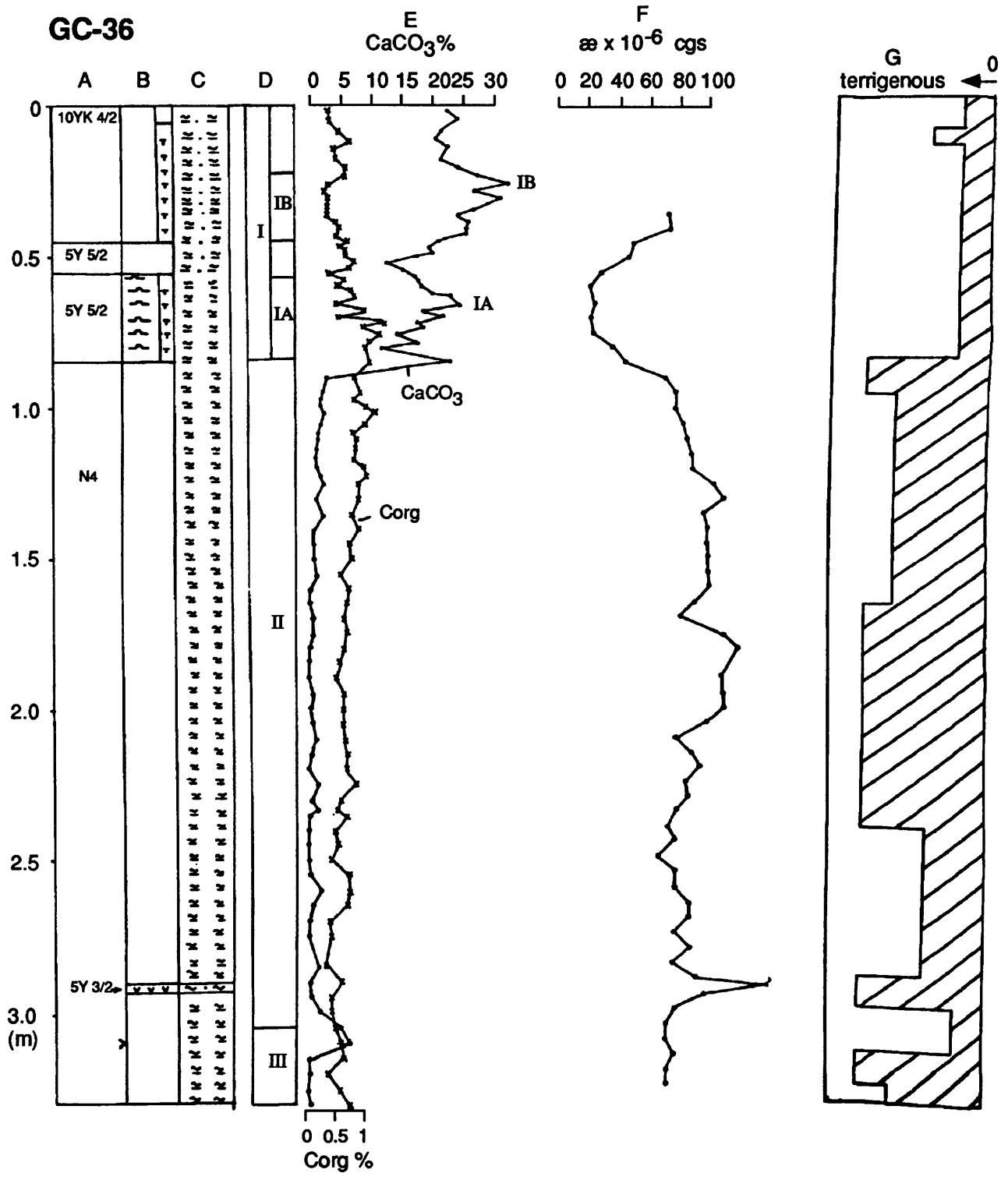

Figure 6. Log of gravity core GC-36; symbols are the same as in Fig. 3.

ACKNOWLEDGMENTS

We thank Lloyd Keigwin for helpful discussions on problems of paleoceanography of the northwestern Pacific, which directly influenced the present paper. We thank James Hein, Lloyd Keigwin, Frank Whitney, and Aleksandr Bychkov for assistance in organizing the expedition and work during the expedition. The authors express their gratitude to all colleagues who participated in the sampling and processing of the sediments: Frank Aben, Gennadiy Krainikov, Victor Nechaev, Yury Martynov, Anna Sorochinskaya, Yevgueniy Mikhalik. Ann E. Gibbs and James R. Hein improved the English and reviewed this paper.

REFERENCES

Bezrukov, P.L. and Romankevich, E.A., 1960, The stratigraphy and lithology of bottom sediment from the northwestern part of the Pacific: Doklady Akad. Nauk SSSR, v. 130, p. 417-420 (In Russian).

Crowley, T.J., 1985, Late Quaternary carbonate changes in the North Atlantic and Atlantic/Pacific comparison: *in* Sundquist, E.T. and Broecker, W.S. (eds.), The carbon cycle and atmospheric carbon dioxide: Natural variations from Archean to present. American Geophysical Union, Geophysical Monograph 32, p. 271-284.

Fairbanks, R.G., 1989, A 17,000-year glacio-eustatic sea level record: Influence of glacial melting rates on the Younger Dryas event and deep-ocean circulation: Nature, v. 342, p. 637-642.

Gorbarenko, S.A., Kovalyukh, N.N., *et al.*, 1988, Okhotsk Sea upper Quaternary sediment and reconstruction of paleoceanographic conditions: Tikhookeanskaya geologiya, v. 2, p. 25-34 (In Russian).

Gorbarenko, S.A., 1991a, Stratigraphy of the Upper-Quaternary sediments from the central part of the Okhotsk Sea and its paleoceanology by the isotopic-oxygen method data and other methods: Okeanologiya, v. 31, p. 1036-1042 (In Russian with English abstract).

Gorbarenko, S.A., 1991b, Deep-sea circulation of the northwestern part of the Pacific during the last glaciation: Doklady Akad. Nauk SSSR, v. 316, p. 979-983 (In Russian).

Juise, A.P., 1962, Stratigraphic and paleogeographic studies in the northwestern part of the Pacific Ocean. Moscow, 258 p (In Russian).

Kallel, N., Labeyrie, L.D., Arnold, M., Okada, H., Dudley, W.C., and Duplessy, J-C., 1988, Evidence of cooling during the Younger Dryas in the Western North Pacific: Oceanologica Acta, v. 11, p. 369-375.

Keigwin, L.D., Janes, G.A., and Froelich, P.N., 1992, A 15,000 year paleoenvironmental record from Meiji Seamount, far northwestern Pacific: Earth and Planetary Science Letters, v. 111, p. 425-440.

Labeyrie, L., Duplessy, J.C., Arnold, M., Duprat, G., Bond, G., and Broecker, W., 1992, North Atlantic surface waters and the conveyor belt: Variability during the past 30 ka: Abstract Fourth International Conferance on Paleoceanography, IGP IV, Short and long term global change: records and modeling. Kiel, Germany, 174 p.

McManus, D.A. and Creager, J.S., 1984, Sea-level data for parts of the Bering-Chukchi shelves of Beringia from 19,000 to 10,000 ^{14}C yr BP: Quaternary Research, v. 21, p. 317-325.

Porter, S.C., Pirs, C.L., and Hamilton, T.D., 1986, Late Wisconsin mountain glaciation in the western part of the U.S.A.: *in* Wright H.E. (ed.), Late Quaternary environments of the United States. Leningrad, p. 58-75 (In Russian).

Romankevich, E.A., 1963, Quaternary deep water beds of the northwestern part of the Pacific Ocean and their paleogeographic importance: Izv. Akad. Nauk SSSR, Ser. Geogr., p. 35-49 (In Russian).

Volat, J.-L., Pastouret, L., and Vergnoud-Grazzini, C., 1980, Dissolution and carbonate fluctuations in Pleistocene deep-sea cores: A review: Marine Geology, v. 34, p. 1-28.

Zahn, R., Rushdi, A., Pisias, N.G., Bornhold, B.D., Blaise, B., and Karlin, R., 1991, Carbonate deposition and benthic $\delta^{13}C$ in the sub-arctic Pacific: Implications for changes of the oceanic carbonate system during the past 750,000 years: Earth and Planetary Science Letters, v. 103, p. 116-132.

91-AV-19

LEGS 1-4

—PAGE 283 FOLLOWS—

GEOMORPHOLOGY OF PARTS OF THE NORTHWEST PACIFIC

Alexander S. Svarichevsky[1] and Galina L. Kirillova[2]

[1]Pacific Oceanological Institute, Far Eastern Branch, Russian Academy of Sciences, 43 Baltiyskaja, Vladivostok 690041, Russia; [2]Institute of Tectonics and Geophysics, Far East Branch Russian Academy of Sciences, Vladivostok, Russia

INTRODUCTION

Geomorphologic investigations were undertaken across the northwest Pacific Ocean during Legs 1, 2, and 4 of the R.V. *Akademik Aleksandr Vinogradov* cruise 91-AV-19. The goals of these investigations were to obtain geomorphologic information along the ship routes, to provide bathymetric data for other studies, and to determine the geomorphology at various stations. Special attention was paid to identification of fault zones delineated by scarps and troughs. Bathymetric surveys were performed over a total distance of 25,443 kilometers, as follows: Vladivostok-Hilo - 5891 km; Hilo-Karin Ridge - 1358 km; Hilo-Gaosun-Vladivostok - 8577 km; Vladivostok-Northwest Pacific-Vladivostok - 9617 km (Fig. 1).

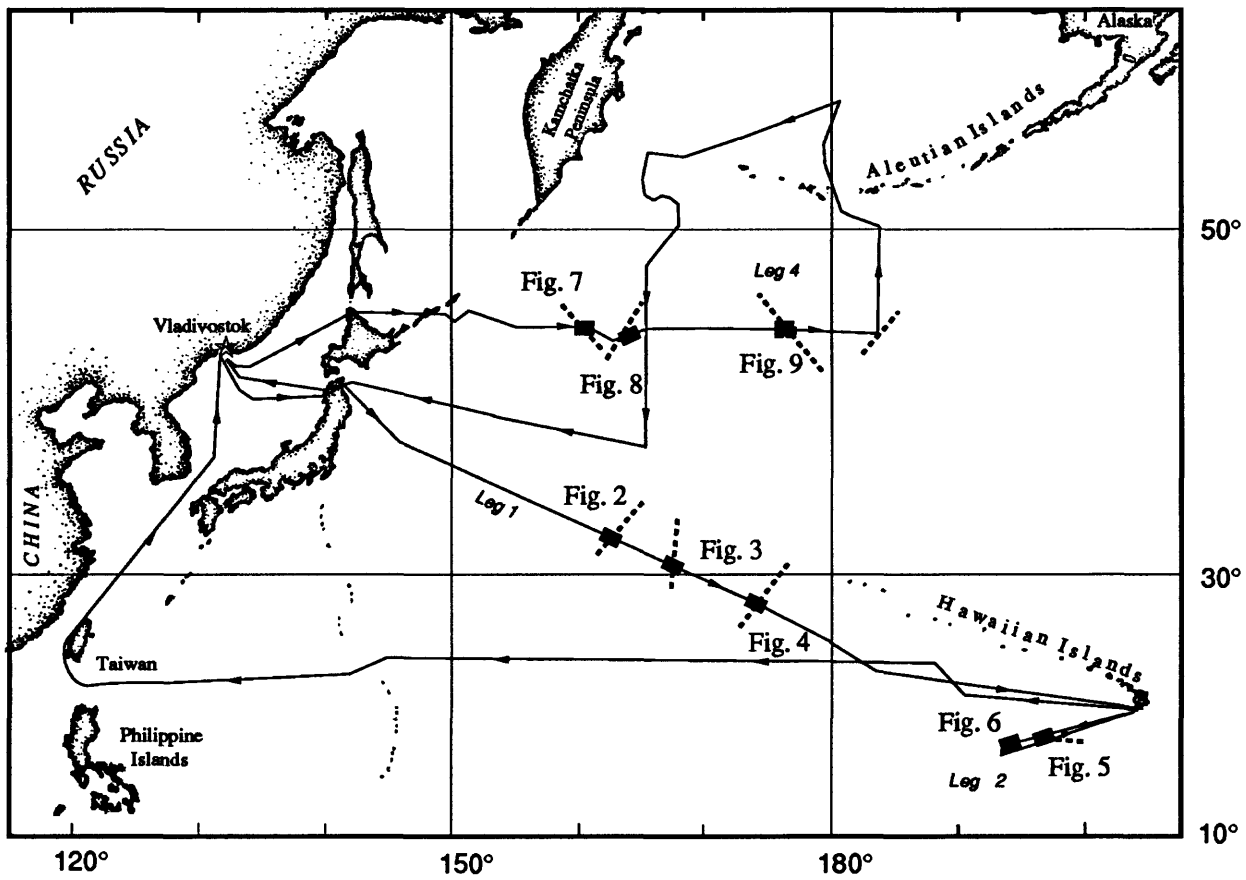

Figure 1. Index map of the North Pacific showing the trackline of R/V *Akademik Aleksandr Vinogradov* cruise 91-AV-19. Black boxes show the location of figures 2-9. Dashed lines indicate locations of fault zones and troughs described in text.

METHODS

Echo sounding was the primary method used to obtain geomorphologic information. Two echo sounding units (GEL-3) were used where appropriate within the optimal recording range of measurement: 0-2500 m, phased for 2500-5000 m and 5000-7500 m. Under favorable weather conditions the echo sounders successfully recorded bathymetry at all encountered depths.

Analog results were recorded on electrothermal paper (ETP-4, 510 mm wide) at a scale of 5 m/mm. Instrumental error was ± 3.25 m for depths less than 2500 m, increasing to ± 15 m for depths between 2500 m and 10,000 m. The velocity of sound in the water column used was 1500 m/s, with no correction for the deviation from the virtual sound velocity in water. The operating frequency of the radiator impulse was 12 kHz and the value of the directivity diagram of the supersonic cone was about 7.

An auxiliary echo sounder (LAZ 72) was used when hydrometeorological and hydroacoustical interference caused excessive loss of data with the GEL units. Because the chart width of the LAZ 72 is only 230 mm, a scale of 10 m/mm was required to obtain the optimum range at all depths (0-2000 m, phased up to 6000 m). Other parameters (frequency, directivity diagram) are similar to those provided by GEL-3 units.

Bathymetric surveys of the Karin Ridge area (Leg 2) were completed along with GLORIA side-scan sonar surveys by the U.S. Geological Survey, so additional surveys were not required on the 91-AV-19/2 cruise.

Geological, geochemical, and hydrochemical stations were located using the navigational satellite system "Transit". The transceiver (JLE-3200) had a capability of receiving six satellites. The discreteness of ship positioning was from 2-3 per hour to 1 within 3 hours. Instrumental error of positioning was 0.2-0.3 cable's length on the drift provided a favorable trajectory of a satellite. An auxiliary satellite navigational system "Tsikada" was used, that has similar accuracy of observations, but working with larger discrete intervals and a different coordinate system. Between satellite fixes, position was calculated using course and speed with a subsequent adjustment of passes.

RESULTS

Leg 1: Sangar Strait to Hilo

During the traverse from Sangar Strait to Hilo, the ship's course crossed several interesting geomorphic features, including Tuscarora fault zone, the east terraced slope of Shatsky Rise, a fault zone east of Shatsky Rise in the Mercator basin, two scarps within the Mendocino fault zone, and several smaller faults to the south of the Hawaiian Ridge.

Tuscarora Fault Zone

The southern part of the Tuscarora fault zone (Gnibidenko *et al.*, 1981) was crossed at Nakwe Channel (Mammerickx, 1980). In this area, the fault zone consists of a western section, along 150° E longitude, and an eastern section, along 150° 30' E, both characterized by a series of troughs and ridges at depths of 5800-5950 m and 5700-6000 m, respectively. The rise separating both segments is poorly defined, reaching water depths of 5700-5800 m. The width of the two sections is about 46 km. The sections possibly have independent tectonic origins, as they have different trends, nearly N-S and NW, compared to neighboring bottom profiles obtained earlier.

Shatsky Rise

Three scarps occur between 3800 and 4500 m water depths on the eastern flank of the Shatsky Rise (Fig. 2). The scarps are 100-300 m high and show an E-W orientation.

East of Shatsky rise, within the Mercator basin (Long. 165° 30' E), we observed an E-W oriented, 200 m high scarp with a base at more than 6000 m (Fig. 3). Together with structures identified earlier, this scarp may be part of a larger fault zone of nearly N-S or N-NE trend; perhaps it is the northern end of the Ortellius fault zone described by Mammerickx (Atwater and Severinhaus, 1988).

Mendocino Fault Zone

The Mendocino fault zone southwest of the Hawaiian ridge (Waghenaer fault zone on the latest tectonic map of Atwater and Severinhaus (1988)), was investigated in detail by earlier studies (Mammerickx, 1983; Svarichevsky and Andreev, 1988). At the site of our crossing, two large scarps were observed (Long 171° E and 172°30' E) with heights of 200 m (eastern scarp) and 400 m (western scarp). The scarps are oriented E-W, with their bases at 5800 m water depth (Fig. 4).

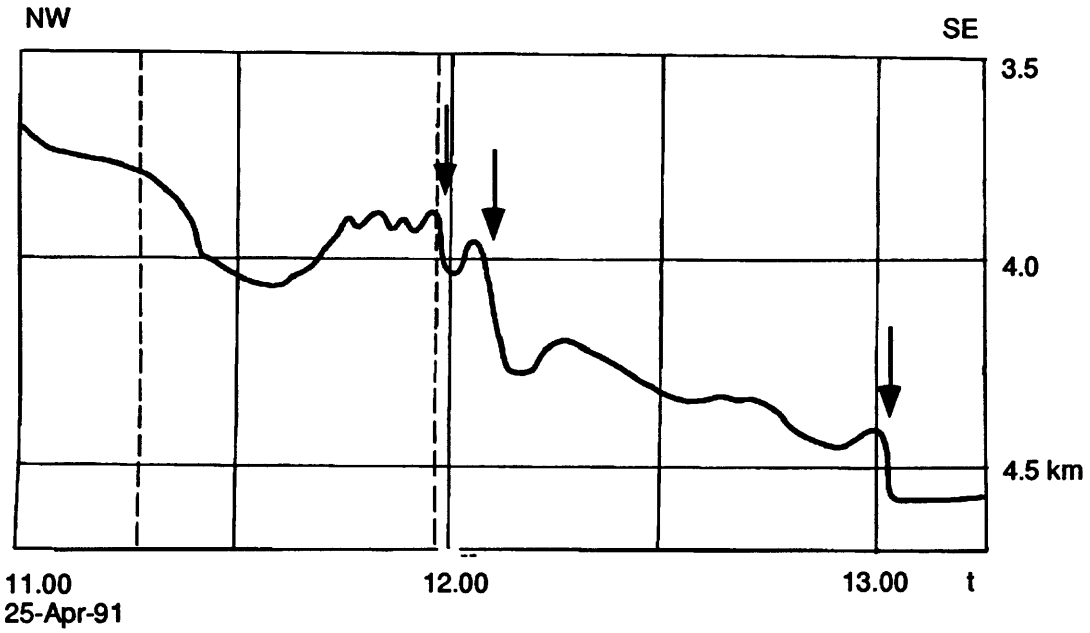

Figure 2. Bathymetric profile of the eastern slope of Shatsky Rise showing three eastward oriented scarps (arrows) between 3800 m and 4500 m. Vertical scale in kilometers; horizontal scale in hours. VE = 1:20

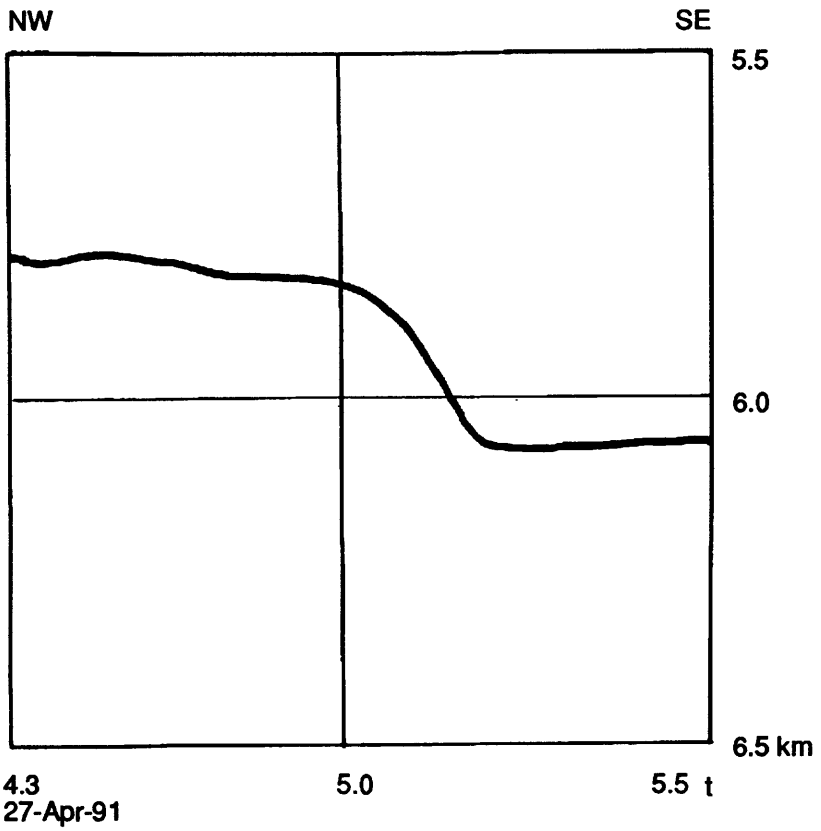

Figure 3. Bathymetric profile of the fault zone east of Shatsky Rise showing an eastward oriented, 200 m high scarp. Vertical scale in kilometers; horizontal scale in hours. VE = 1:20

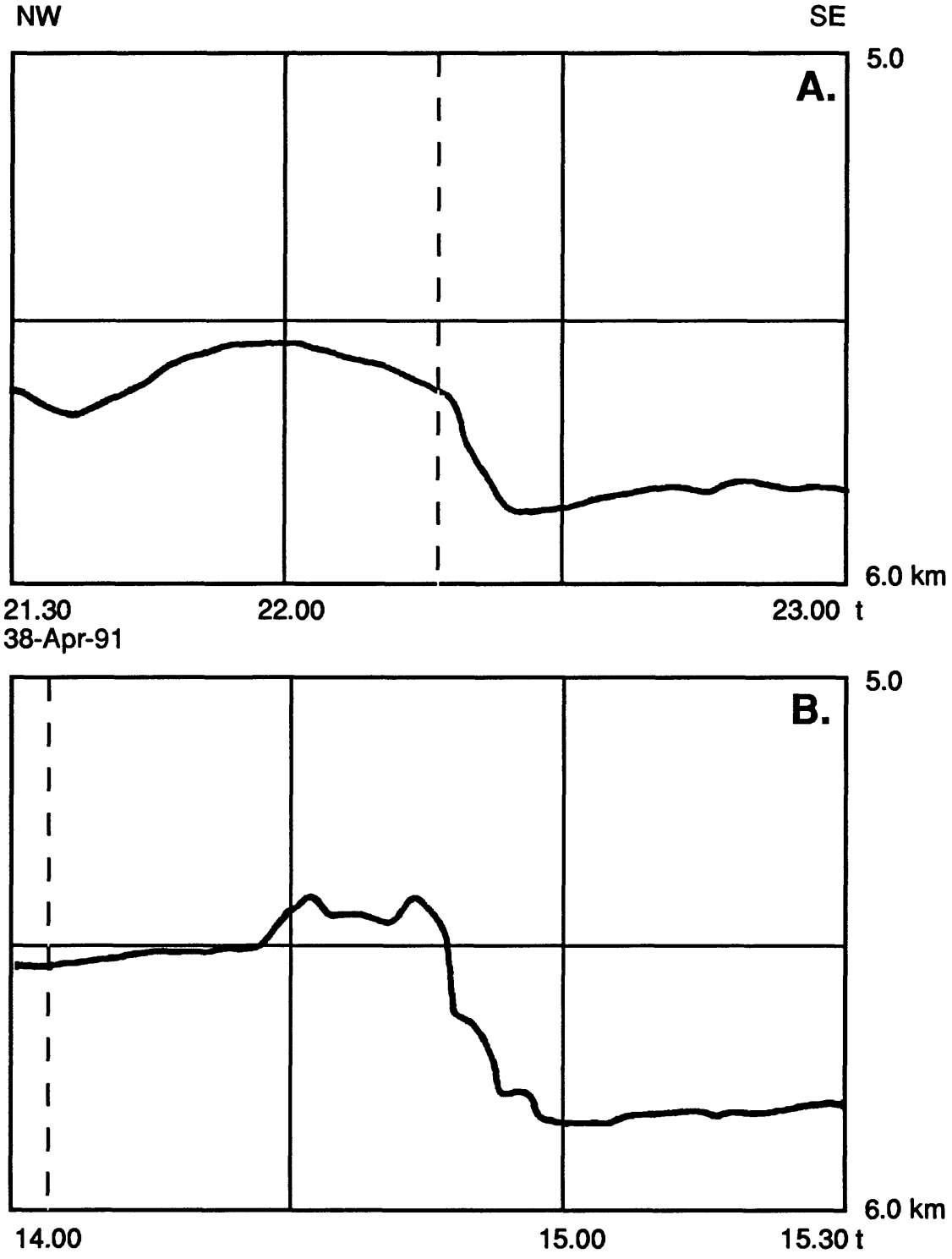

Figure 4. Bathymetric profile of the Mendocino fault zone (Vagenier fault zone of Atwater and Severinhaus, 1988). A. Northeast crossing; B. Southwest crossing. Vertical scale in kilometers; horizontal scale in hours. VE = 1:20

South of the Hawaiian Ridge

Several west and northwest oriented scarps, 100-400 m high, were observed to the south of the Hawaiian Ridge, between longitudes 177° E and 176°30' E. These features correlate with structures identified during previous Far East Branch of the Russian Academy of Sciences cruises (unpublished data from 23 R.V. *Pegas* and 21 R.V. *Morskoy Geofizik*, 1982). These data indicate that the trends of the scarps are most likely northeast, similar to the trend of the Pioneer and Murray fracture zones north of the Hawaiian ridge, which may suggest some structural connection.

Hilo to Karin Ridge

On the traverse from Hilo, Hawaii to Karin Ridge area, an 11 km wide graben-like fault trough was observed (Long. 163°30' E). This feature was first discovered using geophysical techniques during Leg 33 of the "Glomar Challenger" (Schlanger, Jackson, *et al.*, 1976). The graben walls and bounding ridges are roughly 500-900 m high (Fig. 5). Data obtained during this survey indicate the trend of the trough is roughly E-W.

Leg 2: Karin Ridge

Karin Ridge is part of the Line Islands ridge, whose structural type is intermediate between grouped chains and monolithic ranges (Svarichevsky, 1984). Data obtained during this survey indicate that Karin Ridge consists of several volcanic edifices rising from a single foundation. These edifices have slopes of various steepnesses and are intensely dissected by lateral depressions (Fig.6). Scarps on their slopes have a northwest trend, in agreement with the general orientation of the ridge. The summits of the ridges are smoothed in places, giving the appearance of guyots. The margin of these plateau-like summits occurs at 1800-2000 m water depth, which is characteristic of Early Cretaceous guyots in the Northwest Pacific. The planation of the summit was probably due to submarine erosion. Unconsolidated sediments on the ridge are reworked by currents and commonly display ripple marks.

Leg 3: Hilo to Gaosun

The traverse from Hilo to Gaosun (Taiwan), which followed the 24° N meridian for most of the route, crossed the southern flank of the Mendocino fault zone and the northern flank of the Parece-Vela and Okinawa-Luzon fault zones in the Philippine Sea.

Mendocino Fault Zone

Two graben-like troughs at longitudes 166° and 168° E mark the southern flank of the Mendocino fault zone. The grabens floor are at more than 6 km water depth (6350 m - 6100 m) and are 19 and 11 km wide, respectively. We believe a 250 m high, E-W oriented scarp observed at 167° E should also be included in this fault zone. The presence of these grabens indicates that the Mendocino fault zone extends toward the southwest to at least 24° N.

Parece-Vela Fault Zone

In the Philippine Sea, the traverse shifts south to 23°30' N and a graben-like trough is crossed at longitude 139°20' E. The trough is flat-bottomed, about 11 km wide, and occurs at 5300 m water depth. This feature is probably associated with a system of diagonal faults in the middle part of the elevated Parece-Vela basin. The southern part of this basin was studied in greater detail by Svarichevsky (1989a) and Svarichevsky and Khanchuk (1990).

In the West Philippine basin, a deep (6200 m water depth) trough was observed at 129°30' E. This trough is probably part of the nearly N-S oriented fault system that forms the eastern boundary of the Urdanet rise. It is possible that this zone is part of a transform fault identified by magnetic data and associated with the Central-Philippine rift system of the West Philippine basin (Chang, 1980). A near-fault trough with a bottom depth of about 6 km encountered at longitude 127° E is morphologically similar to the fault zone described above.

Okinawa-Luzon Fault Zone

The Okinawa-Luzon fault zone (Svarichevsky, 1989b; Svarichevsky and Wang, 1992) consists of a series of grabens with a northeast trend. The grabens occur at 5800-6000 m water depth and are separated by sharp ridges at water depths of 4900-5150 m. This zone was crossed between longitudes 125° and 125°30' E.

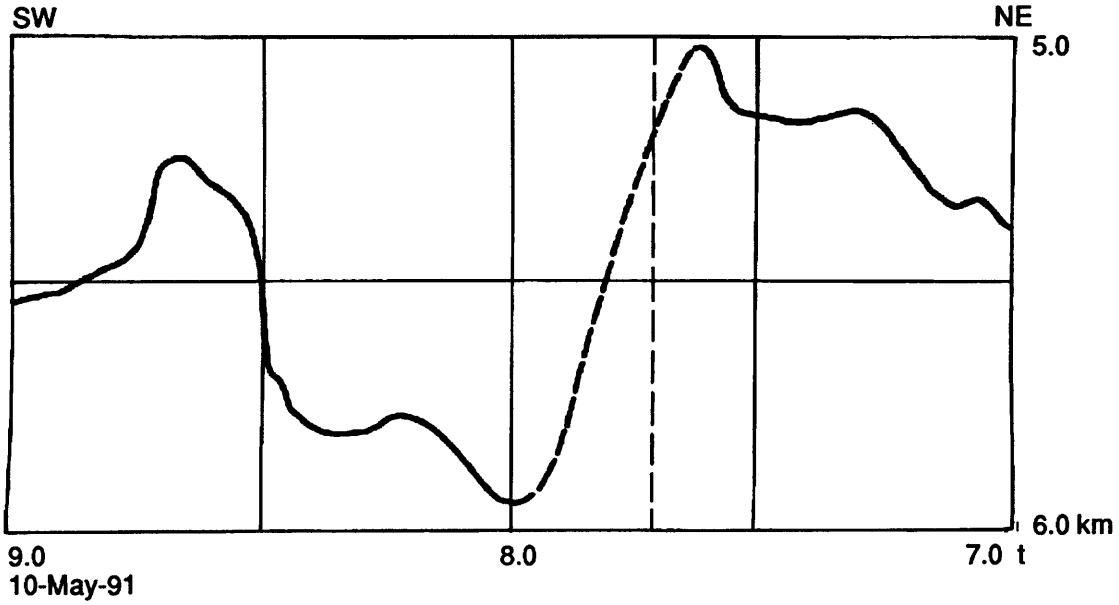

Figure 5. Bathymetric profiles of fault zone south of the Hawaiian Ridge. Vertical scale in km; horizontal scale in hours. VE = 1:20

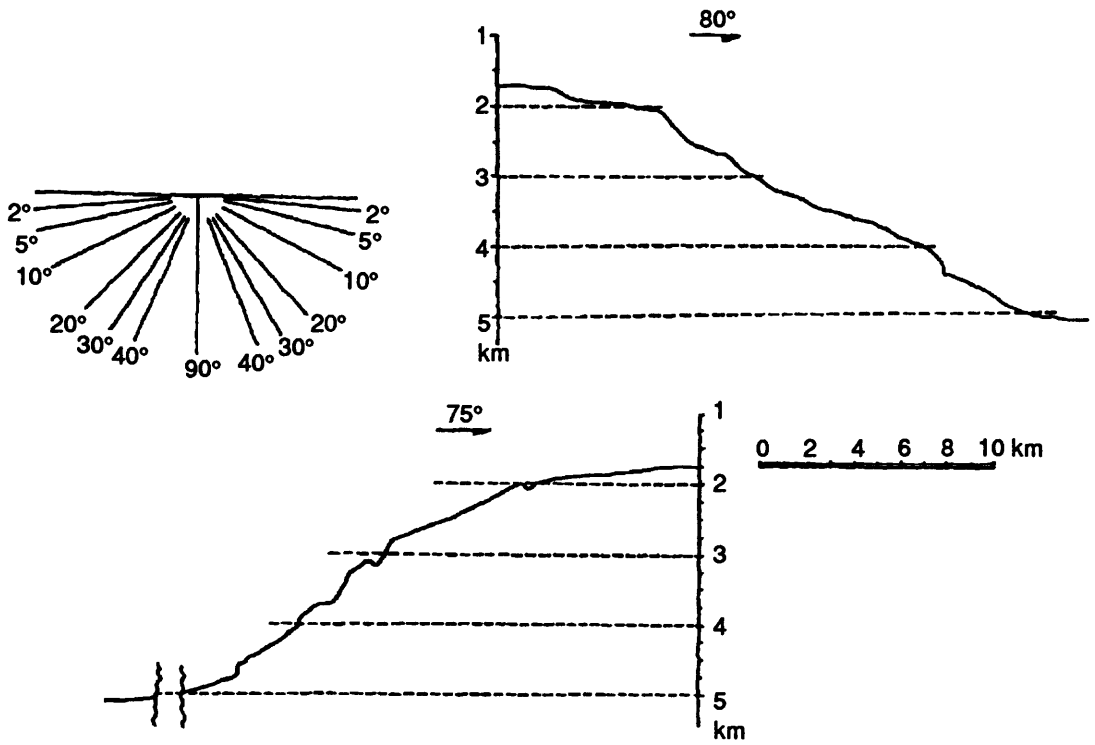

Figure 6. Bathymetric profiles of Karin Ridge slopes within the study area. The pallet is shown to determine the virtual angle; arrows with numbers indicate the vector and azimuth of the profile in degrees. VE = 1:3

Leg 4: Northwest Pacific

The traverse along latitude 45° N, across the northwest Pacific and parts of the northeast Pacific, crossed several large fault zones of the marginal oceanic Zenkevitch swell, as well as the Matua fracture zone, and Hokkaido and Emperor troughs.

Zenkevitch Swell

The fault zone of the Zenkevitch swell (Vasilyev *et al.*, 1979; Svarichevsky, 1987) was crossed at longitude 155°10' E. It is formed by a graben-like trough with a flat bottom 19 km wide at more than 5500 m water depth. The relative depth to the top of the swell is almost 500 m.

Matua Fault

The Matua fault, discussed by Mammerickx and Sharman (1988), but discovered during earlier expeditions of the Institute of Oceanology and the Far East Branch of the Russian Academy of Sciences, is structurally heterogeneous. This fault is represented by graben-like troughs and scarps, or a combination of the two within its different sections. We crossed this fault near mount Morozko, where it is composed of a poorly-defined low scarp (100 m) at the western base of the mount (Fig. 7). In general, the fault zone has a southeastern orientation and is joined with the Hokkaido trough.

Hokkaido Trough

The Hokkaido trough was crossed almost at a right angle in the area where it joins the Matua fault zone. According to available data (POI, unpbl.), the Hokkaido trough has a southwest orientation. At the place of our crossing (Long 161° E), the trough is flat-bottomed and 9 km wide. The floor of the trough is at 6100 m while the associated ridges are at 5000 m water depth, resulting in a relative vertical difference of 1100 m (Fig. 8).

Emperor Trough

The largest morphostructural element encountered during Leg 4 was the Emperor trough (Erickson *et al.*, 1970). We crossed the trough at 174° E (Fig. 9) and observed relatively simple structures of a not very deep trough with even terraced slopes and a flat bottom. At the base, the trough is 9 km wide and occurs at 7200 m water depth. The trough is bounded on the east by a large ridge that rises to 5000 m water depth. To the west are two relatively low and narrow ridges that are separated by a deep (nearly 6500 m water depth) lateral trough. The relative depth of the Emperor trough reaches more than 2000 m within our area of observation.

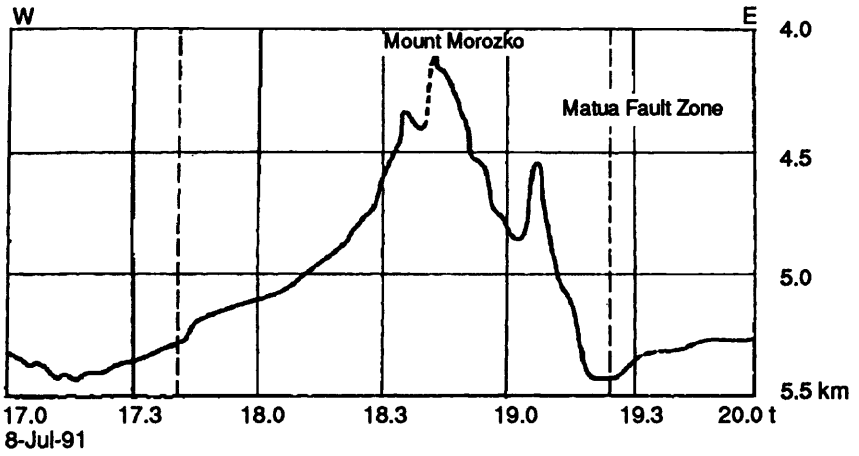

Figure 7. Bathymetric profile of Mount Morozko in the area of the Matua fault zone. Vertical scale in kilometers; horizontal scale in hours. VE = 1:20.

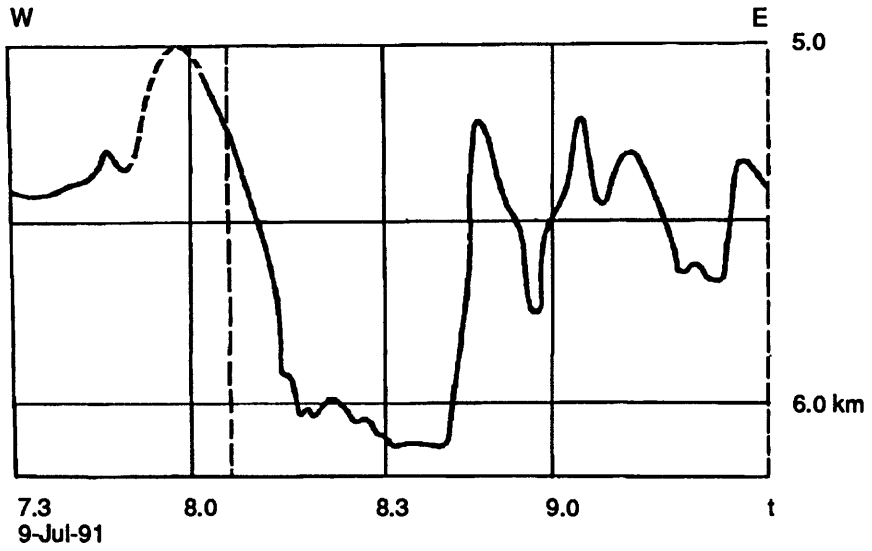

Figure 8. Bathymetric profile of the Hokkaido fault zone. Vertical scale in kilometers; horizontal scale in hours. VE = 1:20.

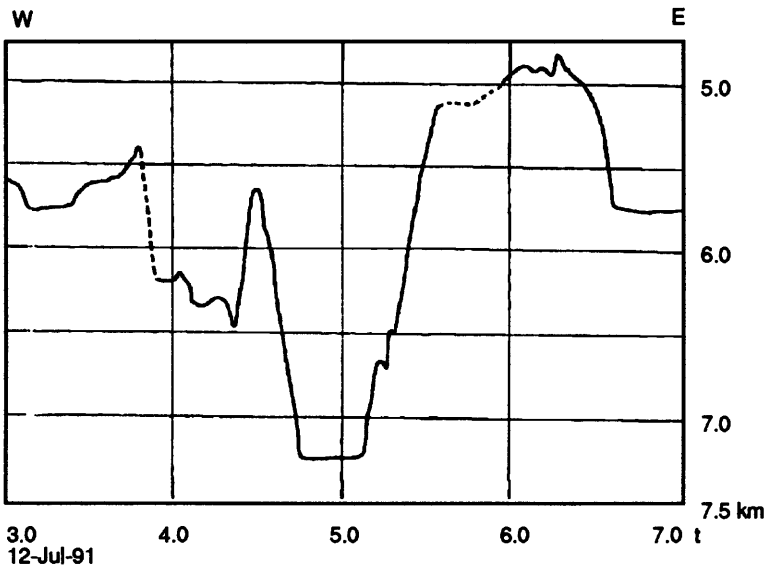

Figure 9. Bathymetric profile of the Emperor fault zone. Vertical scale in kilometers; horizontal scale in hours. VE = 1:20.

Unnamed Fault Zone

Toward the eastern end of the 45°N traverse of Leg 4, at 177°E, another fault zone was crossed at a sharp angle, consequently, the shape of this feature is not well defined, but appears to be a graben-like trough at 6100 m water depth surrounded by lateral ridges with their tops at a depth of 5000 m. This trough has an eastern to northeastern orientation, similar to the orientation of the Chinuk fault zone, located 130 km to the south.

Obruchev Rise

At the nearly N-S traverse along longitude 165° E, we crossed Obruchev Rise, and morphostructural elements of the North-West basin. Obruchev Rise is a swell, elongate in a northwest direction along the Komandor section of the Aleutian trench. The rise consists of two seamounts -- Meiji Seamount to the northwest and Detroit Seamount to the southeast.

Meiji Seamount

Meiji Seamount is elongate in a northwest direction and has an asymmetric cuesta-like longitudinal profile with a smoothed, rolling northeast flank and a steep, terraced southwest flank. A scarp on the terraced flank, between 3900 and 4900 m water depth, has been interpreted as a tectonic scarp (Vasilyev *et al.*, 1984; Svarichevsky, 1987). The summit of the seamount is a plateau between 2900 and 3100 m water depth. The southern part of the plateau is complicated by a wide (up to 19 km), nearly E-W depression, with water depths increasing to about 3000 m. In cross-section, the summit platform measures about 60 km by 170 km.

Detroit Seamount

Detroit Seamount conforms to the structure of a plateau and is elongate nearly N-S. The flat summit of the plateau is found at a water depth of about 3000 m and supports smaller flat-topped elevations with summits at about 2300 m water depth. In addition, a single large edifice rises above the plateau and has three summits that vary in water depth from 1600 - 1400 m. The summits are typically flat. We suggest that the summits were leveled by erosion, at least the elevated parts of Detroit plateau at water depths of 2300-1600 m.

South of Obruchev Rise To 38° N

South of Obruchev Rise, to 38° N, occurs the largest graben-like trough composing the northeast flank of the Hokkaido fault zone near its junction with the Avachinsk fault zone. The bottom depth of this trough exceeds 6000 m water depth.

ACKNOWLEDGMENTS

Ann E. Gibbs and James R. Hein improved the English and reviewed the paper.

REFERENCES

Atwater, T. and Severinhaus, J., 1988. Tectonic map of North Central Pacific Ocean: Geological Society of America, Boulder, Colorado.

Chang, S.T., 1980. Marine magnetic anomalies from the Western Philippine Sea: Implications for the evolution of marginal basins: *in* Hayes, D.E. (ed.) The tectonic and geologic evolution of Southeast Asian seas and islands. American Geophysical Union Monograph 23, p. 49-75.

Erickson, B.H., Naugler, F.P., and Lucas, W.H., 1970. Emperor fracture zone: A newly discovered feature in the Central North Pacific: Nature, v. 225, p. 53-54.

Gnibidenko, H.S., Svarichevsky, A.S., Sedelnikova, S.P., and Zhigulev, V.V., 1981. The structure of Tuscarora fracture zone, Northwestern Pacific: Geo-Marine Letters, v. 1, p. 221-224.

Mammerickx, J., 1980. A deep-sea channel in the North-West Pacific basin: Marine Geology, v. 34, p. 207-218.

Mammerickx, J., 1983. Depth anomalies over Mesozoic crust in the Western Pacific: *in* Hilde, I.W.C, Uyeda, S. (eds.), Geodynamics of the Western Pacific - Indonesian Region. American Geophysical Union, p. 63-73.

Mammerickx, J. and Sharmon, G.F., 1988. Tectonic evolution of the North Pacific during the Cretaceous quiet period: Journal of Geophysical Research, v. 93, p. 3009-3024.

Schlanger, S.O., Jackson, E.D., *et al.*, 1976. Initial Reports of the Deep Sea Drilling Program, Vol. 33: Washington (U.S. Government Printing Office), 973 p.

Svarichevsky, A.S., 1984. Evolutional series of the mountain chains in the Northwest Pacific: *in* Geology of oceans and seas: T. 2, M.: (In Russian: Evolutsionnyi ryad gornyh tsepey v severo-zapadnom sektore Tihogo okeana/Geologiya okeanov i morey. Tezisy dokl. 6 Vsesoyuznoy shkoly morskoy geologii).

Svarichevsky, A.S., 1987. Geomorphologic Map. Scale 1:1,500,000. Geological geophysical atlas of the Kuril-Kamchatka island arc: Leningrad, VSEGEI. (In Russian: Geomorfologicheskaya karta. M-b: 1:1,500,000. Geologo-geofizichesky atlas Kurilo-Kamchatskoy ostrovnoy sistemy).

Svarichevsky, A.S., 1989a. New data on the morphostructure of the Parece-Vela basin (the Sea of Philippine): in Geology of the Pacific bottom and the transitional zone to the Asian continent: Vladivostok, DVO AN SSSR, p. 191-198. (In Russian: Noviye danniye po morfostrukture kotloviny Parese-Vella (Filippinskoye more)/Geologiya dna Tihogo okeana i zony perehoda k Aziatskomu kontinentu:).

Svarichevsky, A.S., 1989b. Morphostructural mapping of the Philippine Sea: *in* Geological-geophysical mapping of the Pacific Region. Abs., International symposium, USSR Academy of Sciences, Far East Branch, Institute of Marine geology and geophysics, Yuzhno-Sakhalinsk, p. 119-121.

Svarichevsky, A.S. and Andreev, A.A., 1988. Characteristics of the Mendocino fault zone west off the Hawaiian islands: Okeanologiya, v. 2, p. 280-285 (In Russian: Harakteristika razlomnoy zony Mendosina k zapadu ot Gavayskih ostrovov).

Svarichevsky A.S. and Khanchuk, A.I., 1990. Morphostructure of Parase-Vela basin: Pacific Geology, p. 31-66, (In Russian).

Svarichevsky, A.S. and Wang, C., 1992. The Luzon-Okinawa fault zone in the West Philippine Basin: *in* Proceedings of the Fourth Symposium on Geophysics, p. 465-475.

Vasileyev, B.I., Putintsev, V.K., and Udintzev, G.B., 1984. Geologic structure of the northwest Pacific Ocean and problems in subduction: *in* Milanovdkiy, Y.Y., Kropotkin, P.N., Pushcarovskiy, Y.M., and Filatora, L.I. (eds.), Problems of expansion and pulsation of the Earth. Nauka, Moscow, p. 141-149. (In Russian: Geologicheskoe stroenie severo-zapadnoy chasti Tihogo okeana i problema subduktsii//Problemy rasshireniya i pulsatsii Zemli).

Vasileyev, B.I., Zhiltsov, E.G., and Suvorov, A.A., 1979. Geological structure of the southwest part of the Kuril system Arch-Trench: Nauka, Moscow, 105 p. (In Russian: Geologicheskoe stroenie yugo-zapadnoy chasti Kurilskoy sistemy duga-zhelob).